NAS1.55:3056

NASA Conference Publication 3056

MAR 0 3 1990

Space Electrochemical Research and Technology (SERT) 1989

Proceedings of a conference held at
NASA Lewis Research Center
Cleveland, Ohio
April 11-13, 1989

Au

NASA

I

NASA Conference Publication 3056

Space Electrochemical Research and Technology (SERT) 1989

Richard S. Baldwin, *Editor*
Lewis Research Center
Cleveland, Ohio

Proceedings of a conference held at
NASA Lewis Research Center
Cleveland, Ohio
April 11-13, 1989

NASA
National Aeronautics and
Space Administration
Office of Management
Scientific and Technical
Information Division

1989

FOREWORD

Electrochemical energy storage devices will continue to play an important role in our nation's space program. Space power technology requirements for future spacecraft and missions are diverse and rapidly expanding; higher power and energy levels will be required, and the challenges to decrease mass and to increase efficiency, life, and reliability will remain as significant goals. The development of advanced electrochemical energy storage technologies and systems must continue in order to meet NASA's mission needs and to enable new space opportunities in the future.

A wide variety of advanced electrochemical system concepts are in various stages of development, new cell electrochemistries are being studied in the laboratory, and programs which are directed towards the optimization of components and the development of new materials are actively being pursued. High energy density secondary batteries and regenerative fuel cell systems currently under development, as well as other advanced energy storage concepts which are being conceived and investigated, may represent the enabling technologies for future space missions and extraterrestrial surface power applications.

The second NASA Space Electrochemical Research and Technology (SERT) Conference was held at the Lewis Research Center on April 11-13, 1989. The objectives of the conference were to examine current technologies, research efforts, and advanced concepts, and to identify technical barriers which affect the advancement of electrochemical energy storage systems for space applications. The conference provided a forum for the exchange and discussion of ideas and opinions of a proper mix of research scientists, mission planners, technology advocates, and power system engineers, representing forty-eight industrial, academic, and governmental organizations.

The conference opened with a series of related overviews in the areas of NASA advanced mission models (Low-Earth-Orbit (LEO) and Geosynchronous-Earth-Orbit (GEO) Missions, Unmanned Planetary Missions, and Human Exploration Mission Studies). The technical sessions that followed consisted of papers grouped into the following theme areas:

(1) Advanced Concepts
(2) Hydrogen-Oxygen Fuel Cells and Electrolyzers
(3) Nickel Electrode
(4) Advanced Rechargeable Batteries

The technical sessions were chaired by highly respected investigators who are extremely knowledgeable in the practical aspects of complete electrochemical system considerations.

Following the technical presentations, concurrent workshop sessions were held to discuss in depth the critical issues that related to the technical theme areas. These workshops, which were led by the technical session chairpersons, provided a forum for general discussions to coalesce views and findings into conclusions on progress in the field, prospects for future advances, areas overlooked, and the directions of future efforts.

This proceedings includes the related overviews, the technical papers, and the viewgraphs of the workshop summary presentations, which were prepared by the session chair- and co-chairpersons.

On behalf of the Power Technology Division and the Lewis Research Center staff, I would like to thank all of the conference attendees for their active participation and contributions. Sincere appreciation is also extended to Dr. Patricia O'Donnell, who chaired the conference, and to the staff of the Electrochemical Technology Branch, Jo Ann Charleston, the Lewis Conference Planning Office, and ERCI/D-K Associates, Inc. for their assistance and guidance.

Richard S. Baldwin
1989 SERT Conference Coordinator

CONTENTS

Page

RELATED OVERVIEWS

OVERVIEW OF BATTERY USAGE IN NASA/GSFC LEO AND GEO SPACECRAFTS
Thomas Y. Yi, NASA Goddard Space Flight Center 1

THE IMPORTANCE OF BATTERIES IN UNMANNED MISSIONS
John W. Klein, Jet Propulsion Laboratory 5

HUMAN EXPLORATION MISSION STUDIES
Robert L. Cataldo, NASA Lewis Research 9

ADVANCED CONCEPTS

A SURVEY OF ADVANCED BATTERY SYSTEMS FOR SPACE APPLICATIONS
Alan I. Attia, Jet Propulsion Laboratory 17

ADVANCED RECHARGEABLE SODIUM BATTERIES WITH NOVEL CATHODES
S. Di Stefano, B.V. Ratnakumar and C.P. Bankston, Jet Propulsion Laboratory 33

MONOLITHIC SOLID OXIDE FUEL CELL DEVELOPMENT
K.M. Myles and C.C. McPheeters, Argonne National Laboratory 41

THE ELECTROCHEMCIAL GENERATION OF USEFUL CHEMICAL SPECIES FROM LUNAR MATERIALS
Kan J. Tsai, Daniel J. Kuchynka and Anthony F. Sammells, Eltron Research, Inc. 51

A NEW CONCEPT FOR HIGH-CYCLE-LIFE LEO: RECHARGEABLE MnO_2-HYDROGEN
A.J. Appleby, H.P. Dhar, Y.J. Kim and O.J. Murphy,
Texas A&M University 61

CHARACTERIZATION TESTING OF A 40 AHR BIPOLAR NICKEL-HYDROGEN BATTERY
Jeffrey C. Brewer, NASA Marshall Space Flight Center, and
Michelle A. Manzo and Russel P. Gemeiner,
NASA Lewis Research Center 69

ADVANCED DOUBLE LAYER CAPACITORS
S. Sarangapani, P. Lessner, J. Forchione, A. Griffith and
A.B. LaConti, Giner, Inc. 83

HYDROGEN-OXYGEN FUEL CELLS AND ELECTROLYZERS

RECENT ADVANCES IN SOLID POLYMER ELECTROLYTE FUEL CELL TECHNOLOGY WITH LOW PLATINUM LOADING ELECTRODES
Supramaniam Srinivasan, David J. Manko, Hermann Koch,
Mohammad A. Enayetullah and A. John Appleby, Texas A&M University . . 95

THE APPLICATION OF DOW CHEMICAL'S PERFLUORINATED MEMBRANES IN PROTON-EXCHANGE MEMBRANE FUEL CELLS
G.A. Eisman, The Dow Chemical Company 115

HYDROGEN-OXYGEN PROTON-EXCHANGE MEMBRANE FUEL CELLS AND ELECTROLYZERS
R. Baldwin, NASA Lewis Research Center, M. Pham, NASA Lyndon B. Johnson Space Center, and A. Leonida, J. McElroy and T. Nalette, Hamilton Standard 127

ELECTROCATALYSIS FOR OXYGEN ELECTRODES IN FUEL CELLS AND WATER ELECTROLYZERS FOR SPACE APPLICATIONS
Jai Prakash, Donald Tryk and Ernest Yeager, Case Western Reserve University 137

OXYGEN ELECTRODES FOR RECHARGEABLE ALKALINE FUEL CELLS-II
L. Swette and N. Kackley, Giner, Inc. 149

NON-NOBLE ELECTROCATALYSTS FOR ALKALINE FUEL CELLS
S. Sarangapani, P. Lessner, M. Manoukian and J. Giner, Giner, Inc. 165

CORROSION TESTING OF CANDIDATES FOR THE ALKALINE FUEL CELL CATHODE
Joseph Singer and William L. Fielder, NASA Lewis Research Center 171

NICKEL ELECTRODE

STRUCTURAL COMPARISON OF NICKEL ELECTRODES AND PRECURSOR PHASES
Bahne C. Cornilsen, Xiaoyin Shan and Patricia Loyselle, Michigan Technological University 181

IMPEDANCE STUDIES OF Ni/Cd AND Ni/H_2 CELLS USING THE CELL CASE AS A REFERENCE ELECTRODE
Margaret A. Reid, NASA Lewis Research Center 197

THE APPLICATION OF ELECTROCHEMICAL IMPEDANCE SPECTROSCOPY FOR CHARACTERIZING THE DEGRADATION OF $Ni(OH)_2$/NiOOH ELECTRODES
D.D. Macdonald and B.G. Pound, SRI International, and S.J. Lenhart, Ford Aerospace 211

KOH CONCENTRATION EFFECT ON THE CYCLE LIFE OF NICKEL-HYDROGEN CELLS. IV. RESULTS OF FAILURE ANALYSES
H.S. Lim and S.A. Verzwyvelt, Hughes Aircraft Company 243

ADVANCES IN LIGHTWEIGHT NICKEL ELECTRODE TECHNOLOGY
Dwaine Coates, Gary Paul and Paul Daugherty, Eagle-Picher Industries, Inc. 259

ADVANCED RECHARGEABLE BATTERIES

MULTI-MISSION Ni-H_2 BATTERY CELLS FOR THE 1990's
Lee Miller, Jack Brill and Gary Dodson, Eagle-Picher Industries, Inc. 269

NICKEL-HYDROGEN CAPACITY LOSS ON STORAGE
Michelle A. Manzo, NASA Lewis Research Center 279

SODIUM SULFUR-BATTERY FLIGHT EXPERIMENT DEFINITION STUDY
Rebecca Chang and Robert Minck, Ford Aerospace Corporation 297

ADVANCED HIGH-TEMPERATURE BATTERIES
P.A. Nelson, Argonne National Laboratory 307

ADVANCES IN AMBIENT TEMPERATURE SECONDARY LITHIUM CELLS
S. Subbarao, D.H. Shen, F. Deligiannis, C-K. Huang and
G. Halpert, Jet Propulsion Laboratory 325

TECHNICAL WORKSHOP SUMMARY PRESENTATIONS

ADVANCED CONCEPTS WORKSHOP
Chairperson: John Appleby, Texas A&M University 339

HYDROGEN-OXYGEN FUEL CELLS AND ELECTROLYZERS WORKSHOP
Chairperson: James Huff, Los Alamos National Laboratory 343

NICKEL ELECTRODE WORKSHOP
Chairperson: Albert Zimmerman, Aerospace Corporation 347

ADVANCED RECHARGEABLE BATTERIES WORKSHOP
Chairperson: Gerald Halpert, Jet Propulsion Laboratory. 351

OVERVIEW OF BATTERY USAGE IN NASA/GSFC LEO AND GEO SPACECRAFTS

Thomas Y. Yi
NASA Goddard Space Flight Center
Greenbelt, Maryland 20771

A survey of the batteries used in the LEO and GEO missions at the Goddard Space Flight Center is described. For each spacecraft, tentative launch date is given, along with relevant battery parameters including battery size and description, depth-of-discharge, predicted mission temperature, and life requirement.

INTRODUCTION

The Goddard Space Flight Center (GSFC) has a role to expand human knowledge of the Earth, its environment, the solar system, and the universe. And as such, the Center has been at the forefront of space research and exploration through a myriad of spacecrafts, both low Earth orbiting (LEO) and geosynchronous Earth orbiting (GEO) vehicles. A number of these satellites are listed in Table 1 which shows the relevant battery paramters associated with each spacecraft. All the spacecrafts listed in the table have baselined the nickel-cadmium batteries. All the cells used in these batteries are manufactured by Gates Aerospace Batteries (GAB) in Gainesville, Florida.

BATTERY USAGE

In July 1989, Cosmic Background Explorer (COBE) will be launched on a Delta rocket from the Western Test Range. COBE is an in-house program to study the big-bang theory. COBE was originally scheduled for a shuttle launch and it was designed with two 50Ah NASA Standard batteries containing 22 cells per battery. However the launch vehicle was changed to a Delta rocket, and the whole spacecraft was redesigned to fit this vehicle. The battery design was changed to a modified 20Ah NASA Standard battery, 18 cells per battery. The battery usage profile is benign. The mission requirement is for 1 year of battery usage with a predicted mission depth-of-discharge (DOD) of 0 to 24% over one 63-day eclipse season. The batteries will be subjected to a temperature range of 16 to 22°C. McDonnel-Douglas Company is the prime for the batteries.

The next GSFC spacecraft to be launched is National Oceanic and Atmospheric Administration satellite (NOAA-D) in December 1989 for weather observation purposes. This spacecraft is among a series of NOAA weather satellites which GSFC is cooperating with the National Oceanic and Atmospheric Administration on. NOAA-D is in a LEO/Polar morning orbit with a predicted mission DOD of 0 to 16%. There are two 26.5Ah batteries in the spacecraft, 17 cells per battery. The mission duration is 2 years with predicted mission temperature of 5°C. The next spacecraft, NOAA-I, is scheduled to be launched in May 1989. NOAA-I will operate in a LEO/Polar afternoon orbit with 18% DOD, 5°C predicted mission temperature, and 2 year mission duration. It will have three 26.5Ah batteries, 17 cells per battery. NOAA-J is planned for July 1992 launch, and NOAA-K, November 1993. The batteries planned for the NOAA-K, L, and M spacecrafts will utilize the GAB lightweight 50Ah NiCd design with salient characteristics of the NASA Standard cell. General Electric-Astro, East Windsor is the prime contractor for NOAA satellites.

After NOAA-D, Gamma Ray Observatory (GRO) will be launched from STS 37 in April 1990. The primary objective of the satellite is to study the gamma ray radiation phenomenon. The spacecraft is in a LEO orbit with predicted mission DOD of 15% at 15°C. The battery requirement is for 2.5 years of operation. There are six NASA Standard 50Ah batteries in GRO, 22 cells per battery. These batteries are part of two modular power systems (MPS) made by McDonnel-Douglas Company, each MPS containing 3 batteries.

In July 1990, the first of the second generation Geostationary Operational Environmental Satellite (GOES) will be launched for weather observation purposes. This satellite, GOES-I, is in a GEO orbit with battery parameters of 60% DOD, 7°C average temperature, and 5 years life requirement. There are two 12Ah batteries in the spacecraft, 28 cells per battery. The remaining GOES have the same battery parameters. GOES-J is scheduled for November 1991 launch, and GOES-K, May 1992 launch. The launch dates for GOES-L and GOES-M have not been finalized. Ford Aerospace and Communications Company is the prime for GOES.

The last GSFC satellite scheduled for launch in 1990 is the Tracking and Data Relay Satellite (TDRS) in December 1990. TDRS-E will be launched to a GEO orbit for communication purposes. The spacecraft will contain three 40Ah batteries, 24 cells per battery. Relevant battery parameters include the predicted mission DOD of 50%, mission temperature of 5°C, and duration of 10 years. The next satellite, TDRS-F is scheduled for December 1992 launch, and TDRS-G, May 1994. The next generation of TDRS will probably utilize other cell designs such as advanced NiCd or NiH_2 instead of the existing NiCd design. TRW is the prime for present generation of TDRS.

In August 1991, the first of the GSFC explorer platform satellites will be launched. Extreme Ultraviolet Explorer (EUVE), which is in a LEO regime, will have one MPS which contains three NASA Standard 50Ah batteries. The batteries will be subjected to a predicted mission DOD of 15%, temperature of 15°C, and life of 3 years.

Upper Atmosphere Research Satellite (UARS) is planned to be launched from STS 50 in December 1991 to study the Earth's ozone layer and other environmental concerns. This spacecraft is in a 56° inclination LEO. Like EUVE, UARS contains one MPS. The predicted mission DOD is 0 to 24%, temperature, 10 to 16°C, and mission duration, 3 years.

In addition to these missions, the GSFC has a number of Small Explorer satellites which will be launched from Scout rockets. Battery requirements for these spacecrafts have not yet been finalized.

TABLE 1. - OUTLINE OF GSFC MISSIONS AND ASSOCIATED BATTERY PARAMETERS

MISSION	LAUNCH	BATTERY	ORBIT
COBE	7/89	2 20 Ah Batteries 18 Cells/Battery	LEO/Polar 0-24% DOD, 63-day Eclipse 1 Year Mission 16-22°C
NOAA-D	12/89	2 26.5 Ah Batteries 17 Cells/Battery	LEO/Polar Morning 0-24% DOD 2 Year Mission 5°C
GRO	4/90	6 50 Ah Batteries 22 Cells/Battery	LEO 15% DOD 2.5 Year Mission 15°C
GOES-I GOES-J GOES-K	5/90 11/91 5/92	2 12 Ah Batteries 28 Cells/Battery	GEO 60% DOD 5 Year Mission 7°C
TDRS-E TDRS-F TDRS-G	12/90 12/92 5/94	3 40 Ah Batteries 24 Cells/Battery	GEO 50% DOD 10 Year Mission 5°C
NOAA-I	5/91	3 26.5 Ah Batteries 17 Cells/Battery	LEO/Polar Afternoon 18% DOD 2 Year Mission 5°C
EUVE	8/91	3 50 Ah Batteries 22 Cells/Battery	LEO 15% DOD 3 Year Mission 15°C
UARS	12/91	3 50 Ah Batteries 22 Cells/Battery	LEO, 56° Inclination 0-24% DOD 3 Year Mission 10-16°C

THE IMPORTANCE OF BATTERIES IN UNMANNED MISSIONS

John W. Klein
Jet Propulsion Laboratory
California Institute of Technology
Pasadena, California 91109

Introduction

The planetary program has historically used batteries to supply peak power needs for mission specific applications. Any time that additional power has been required in order to meet peak power demands or those applications where only limited amounts of power were required, batteries have always been used. Up until the mid to late 70's they have performed their task admirably. Recently, however, we have all become aware of the growing problem of developing reliable NiCd batteries for long mission and high cycle life applications. Today we will talk about the role rechargeable batteries will play for future planetary and earth observing spacecraft.

Historical Uses of Batteries

Planetary

Batteries have always been used whenever there was a need for power in excess of what a standard primary power source could develop, whether it be from solar arrays or radioisotope thermoelectric generators. Primary batteries have been used in probes and other small spacecraft where limited mission life (on the order of hours) is required. Where peak power needs exceed those available from a primary source and are cyclic in nature, then secondary or rechargeable batteries have been used.

Ranger

Ranger was the first spacecraft to use rechargeable batteries. It utilized a AgZn battery to augment the power produced from solar arrays. No battery failures occurred during these set of launches.

Mariner

The Mariner series of spacecraft saw the development of the power system as we know it today. It started with AgZn batteries for Mariners 1 through 7. On Mariner 8, which launched in May 1971, NiCd batteries were used for the first time. Due to the careful development and preflight testing of these batteries, no failures occurred in the Mariner 7 and 8 power system, which were identical. Similarly, Mariner 9 and 10 flew NiCd batteries successfully.

Viking

Following the successes of the Mariner series of spacecraft, it was decided to develop a lander and an orbiter for Mars observation. In both cases, due to the success of the NiCd batteries of the Mariner series, NiCds were used. Even on the lander, which had a much different environment than had been encountered in space, NiCds were the battery of choice. As in the Mariner case the NiCds performed as expected with no failures.

Leo/Geo

Planetary is not the only mission set where batteries have a historical base. As we are all aware, they have been used successfully in Leo and Geo orbits. The list of these missions is long and marked with great successes due to the careful planning, engineering, and test of the spacecraft subsystems. To list just a few of these include Seasat, the TIROS series, and the whole range of our communications capabilities today.

Recent Experiences

I would like to spend just a little bit of time to talk about some of the more recent experiences with NiCds, however, and solicit the support of this group of engineers and scientists to give to the power system designer that critical tool that has eluded him, a reliable secondary battery.

Magellan

Let us start with a rather benign mission and see how the project insured proper battery operation. First of all, the mission profile for Magellan is rather benign for the batteries. The battery life is projected at 2100 cycles at a depth of discharge no greater than 40%. This has kept the Magellan batteries well out of the operational area of concern, high cycle count, coupled with large depths of discharge.

Gro

An Earth Observing spacecraft, however, is the first to stress the batteries directly in the operational area of concern. Its high number of cycles has been a major concern to the industry and has warranted careful monitoring of the Gro project. As all of you are aware, the Gro test cells have degraded prematurely using the standard Crane accelerated test. This implies that the batteries may not perform as expected or required for the Gro mission.

Mars Observer

Noting this failure, the Mars Observer project has similar concerns. The Mars Observer mission profiles calls for almost 9000 cycles, well beyond the area of concern. To insure proper operation of the batteries, early coordinated efforts between JPL and the Mars Observer prime contractor GE ASD have led to a new design that both parties feel will meet the mission requirements. Unfortunately, it is not a design that has either been qualified or flown before. Thus, early in the program, test cells will be procured and cycled to see what operational concerns arise. Unfortunately, the project has decided not to continue into mission profile testing.

TOPEX

TOPEX is an Earth Observing mission with a similar type of battery profile. It has a cycle life requirements of 20,000 cycles with a maximum depth of discharge of 15%. While the DOD is not as severe as the Mars Observer condition, the large number of cycles is a real concern. TOPEX and MO have teamed together to perform cell testing in order to verify the battery design, separator material, and lifetime. Until these test are completed in 1991, no battery decision can be made for either TOPEX or Mars Observer on the final design.

Solution

Thus, what power system engineers around the US and the world need is a rechargeable battery that is reliable, that has been qualified, and that can meet the strenuous requirements as posed by some of the more advanced scientific missions. Thus, I would like to solicit support from this austere body to continue to develop batteries that return to the reliability levels seem in the late 70's. To do this, two steps must be taken.

Rigorous Quality Control

First, a rigorous quality control plan must be developed that oversees the development of new battery designs and insures their reliability. In addition, this plan must take into account the new developments that will occur over the coming years. We must incorporate advances as they become available, but what does not need to occur is the wholesale change of a battery design before it has been proven.

The recent battery workshops held on the NiCd problem have taken the lead in understanding and remedying the problems seen today. These efforts must not stop there but continue to improve the reliability and quality of batteries.

Rigorous Acceptance Testing

In addition to quality control, rigorous acceptance and accelerated life testing must continue on all cells that will fly on strenuous missions. This is a hard pill to swallow in today's world where every dollar has to be justified. However, I hope that the recent GRO experience will convince project managers across the US to take seriously the advantages of rigorous acceptance and life testing.

Mission Profile Testing

A caveat to the acceptance test concept is to also perform mission profile testing so that the true nature of the long term performance is understood. Without performing such long term tests, there is no way to predict the true operating characteristics of the battery that is in flight. In addition, if something occurs within the battery and/or the power system and one battery is lost, having a battery that has gone through some mission profile testing is invaluable to the understanding of future operational issues. Of particular interest is how far can the battery be discharged safely, when does it need to be reconditioned, how can the most energy be extracted from the battery under the new operating condition.

Closing

In conclusion, NiCds have been and will continue to be the mainstay of the power system engineers tools for peak power production. Recent experience has tarnished its once sterling reputation. However, the industry has stood up to this challenge and implemented wide ranging plans to rectify the situation. These efforts should be applauded and supported as new designs and materials become available.

In addition, project managers must become aware of their responsibility to test "their" batteries and insure quality and mission operating characteristics. Without this teamwork, the role of NiCds in the future will diminish, and other batteries, not as optimum for high performance application (low mass and volume) will take their place. Let us not let this happen, but to continue to strive to develop batteries that are reliable, rugged, and qualified.

HUMAN EXPLORATION MISSION STUDIES

Robert L. Cataldo
National Aeronautics and Space Administration
Lewis Research Center
Cleveland, Ohio 44135

The nation's efforts "to expand human presence and activity beyond Earth orbit into the solar system" was given renewed emphasis in January of 1988 when the Presidential Directive on National Space Policy was signed into effect. The expansion of human presence into the solar system has particular significance, in that it defines long-range goals for NASA's future missions. To embark and achieve such ambitious ventures is a significant undertaking, particularly compared to past space activities.

INTRODUCTION

Two major efforts recently released, the National Commission on Space Report, "Pioneering the Space Frontier," 1986, and astronaut Dr. Sally Ride's task force report, "Leadership and America's Future in Space," 1987, have helped set goals and give focus to NASA's future direction. Dr. Ride's task force formulated a plan to achieve the Commission's proposed agenda for the civilian space program. The task force recommended four initiatives: (1) Mission Planet Earth, (2) Exploration of the Solar System, (3) Outpost on the Moon, and (4) Humans to Mars. The first two initiatives, to a great degree, are being pursued by NASA's Office of Space Science and Applications. However, the last two initiatives prompted the task force to recommend that a special NASA office be established to coordinate and lead human exploration studies. Therefore, the Office of Exploration was established to provide a focal point for these activities. These include establishing a mature understanding of mission options and opportunities and defining those near-term activities that can provide the greatest impact on future missions.

The Office of Exploration has established a process whereby all NASA field centers and other NASA Headquarters offices participate in the formulation and analysis of a wide range of mission strategies. These strategies were manifested into specific scenarios or candidate case studies. The case studies provided a systematic approach into analyzing each mission element. First, each case study must address several major themes and rationale including: national pride and international prestige, advancement of scientific knowledge, a catalyst for technology, economic benefits, space enterprise, international cooperation, and education and excellence. Second, the set of candidate case studies are formulated to encompass the technology requirement limits in the life sciences, launch capabilities, space transfer, automation and robotics, in-space operations, power, and propulsion.

The first set of reference case studies identify three major strategies: (1) human expeditions, (2) science outposts, and (3) evolutionary expansion. During the past year, four case studies were examined to explore these strategies. The expeditionary missions include the Human Expedition to Phobos and Human Expedition to Mars case studies. The Lunar Observatory and Lunar

Outpost to Early Mars Evolution case studies examined the later two strategies. This set of case studies established the framework to perform detailed mission analysis and system engineering to define a host of concepts and requirements for various space systems and advanced technologies. This paper describes the details of each mission and, specifically, the results affecting the advanced technologies required to accomplish each mission scenario.

MISSION STUDIES

The Office of Exploration has established a process whereby reference case studies are examined yearly. This allows for a reasonable subset of options to be studied in some detail in order to establish first order effects and trends in various system elements. Once the study has been characterized in sufficient depth, different system elements can be replaced with new options so that the overall system performance sensitivities can be analyzed. The broad scope in case studies is engineered to provide a wide range of mission options and to avoid making priorities between exploring the Moon or Mars.

The following candidate case studies are the first set of options studied in 1988. These options are not the final set, in fact, during the coming years these cases may be refined and new cases added, to form a comprehensive set of options so that qualified engineering decisions can be made in the final selection process for those studies that will be carried forward into a program phase A/B.

HUMAN EXPEDITION TO PHOBOS

A manned expedition to Phobos, the inner Martian moon, would establish an early U.S. exploration leadership. Activities such as exploration, resource survey and science station set up would be conducted. Also, a fleet of small teleoperated "low-tech" rovers could provide enhanced exploration of the Martian surface. The expedition to Phobos satisfies two objectives, that of human exploration and previously studied robotic missions with sample return options.

Past spectral analysis of both Phobos and Deimos suggest that materials are present that could justify leveraging rocket propellants for future return trips from Mars. Propellant production plants could allow vehicles to carry fuel only for the trans Earth-Mars leg, and refuel at Phobos or Deimos for the trans Mars-Earth leg. Earth to orbit (ETO) mass could be significantly reduced, particularly with an evolutionary Mars mission. The Phobos mission also relieves the pressure on the launch transportation systems, because of reduced propellant mass required by not landing on Mars itself.

Mission Scenario

The Phobos expedition employs a "split/sprint" transportation scheme where a cargo vehicle carrying science equipment, crew return propellant and Mars rovers would be launched on a minimum energy trajectory. About 10 months later, the vehicle carrying a crew of four on a high-energy sprint class trajectory is launched. Nine months later the crew vehicle mates with the cargo vehicle in Mars orbit. Two crew members then board an excursion vehicle and conduct the mission objectives on Phobos. The two remaining crew members teleoperate rovers on the Martian surface and transfer propellant from the cargo vehicle. After about 30 days in the Mars system the four crew members return to Earth having been away from Earth a total of 14 months.

HUMAN EXPEDITION TO MARS

Since the invention of the telescope, Mars, with its observed global dust storms and "canali", has been a favorite destination for planetary exploration and colonization. Mars has been called Earth's sister planet because of their similarities, although it is not a very hospitable planet for humans. Scientists have speculated that Mars had more of Earth's characteristics, denser atmosphere water for example, which could have supported lifeforms early in its evolution. Thus, there is a large international segment of the population that suggests we return to explore Mars with manned missions.

Mission Scenario

The Mars Expedition calls for three separate segments launched on successive opportunities. The first segment includes a cargo vehicle preceding the eight member crew on a split/sprint approach as in the Phobos mission. However, the cargo vehicle that transports rovers, surface habitats, and exploration and science equipment is placed in Mars orbit. After spacecraft rendezvous, four crew members descend to the surface in the landing craft for a 20 day stay. The exploration party will perform science experiments and possibly explore the surface for water, minerals, volatiles, and biological traces of present and past lifeforms. The crew will live in the pre-landed habitats and utilize the rover for extended exploration. The remaining crew members in orbit will transfer propellant from the cargo vehicle, perform orbital science and support surface operations. The surface crew will unite with the orbit craft and return to Earth. The total length of the mission would span about 14 months. On ensuing trips exploration of Phobos and Deimos would also be included in the scenario along with different landing sites on Mars.

LUNAR OBSERVATORY

The Lunar Observatory, comprised of optical telescope arrays, stellar monitoring telescopes, and radio telescopes would encompass both the radio and optical spectrum. An observatory, constructed on the far or backside of the moon, could provide scientists with information orders of magnitude greater than could be achieved from one in earth or in low-Earth-orbit. Significant benefits of lunar locations are; circumventing Earth's atmospheric impediments, shielding of electromagnetic waves and providing a stable foundation for large instruments and arrays.

Mission Scenario

An estimated four flights to the Moon's far side would be required to emplace the observatory. Two launches a year, one cargo and one crew, make up the mission set. One combined crew/cargo flight per year would follow. The crew of four would remain on the Moon's surface only during the Lunar day using their lander vehicle as a habitat, similar to the Apollo missions. A permanent base is not required because of the short stay periods for maintaining the observatory about every 3 years and other exploration missions would land at different sites.

Unpressurized rovers would be used as crew transports during the observatory set up and maintenance, as well as automated machinery used for material handling and scientific equipment transport.

LUNAR OUTPOST TO EARLY MARS EVOLUTION

An evolutionary approach to space exploration is by building on the experience of living and working on the Moon. The Moon is very attractive to accomplish this since the transfer time back to Earth is only several days in case an emergency situation would occur. A sustained human pressence on the lunar surface would provide valuable data on working in reduced gravity, human factors considerations with long duration planetary missions and learning how to extract and utilize local resources.

A recommendation of the National Commission on Space (NCOS) was that a "bridge between worlds" be built with the first step to develop the Moon then continue on to Mars. This case study defines the methodology necessary to achieve that goal, by building a space exploration infrastructure that would lead to nearly self-sufficient space habitation. This, the most complex and ambitious scenario, stretches the limits of technological advances in space construction, utilization of indigenous resources, life support, artificial gravity, chemical and electric propulsion, aerocapture, material and propellant production and space power.

Mission Scenario

A series of both piloted and cargo flights would embark for the Moon. Cargo would be sent on longer transfer trajectories using electric propulsion and crews sent on fast chemically propelled transfer vehicles. It could take several years to fully construct a surface facility, possibly with expediated construction by vehicles operated from Earth. The principle goals of the base is to produce materials and liquid oxygen used for Mars flights. The effort to produce these products is leverage against the mass otherwise launched from Earth.

Sometime later, possibly 6 to 10 years, the Mars flights would begin once capabilities are sufficient for the successful Mars trip. First, an electric cargo vehicle would transport surface equipment, communications orbiters, rovers, Mars-Phobos transfer vehicles, scientific experiments and a Phobos propellant plant. As the vehicle approaches Mars, it would deploy: areosynchronous communication orbiters, robotic equipment to Deimos; and a fuel processing plant to Phobos. The plant would produce fuel for future crew return flights.

During the next Earth-Mars launch opportunity, the lunar electric cargo vehicle will be reused to transfer the crew's transport vehicle to lunar orbit for lunar derived oxygen fueling. The cargo/crew vehicle returns to Earth orbit, and separates. The cargo vehicle stays in orbit for use as the next ferry trip to the Moon, and the crew transport is boarded by the Mars crew. After a systems checkout, they begin their 8 month journey. Several options exist as to Mars stay times; 60 days, 1 year, and 2 years. Continued flights to Mars could occur every Earth-Mars opportunity which is about 26 months apart.

MISSION TECHNOLOGY REQUIREMENTS

As the case studies become more mature and focused, better defined requirements will emerge. However, the preliminary analysis of the 1988 case studies have surfaced many technology areas needing further development. These major areas include the following; surface exploration systems, fluid management, propulsion, automation and robotics in-space operations, aerocapture and power. Table I illustates key technologies as evaluated in relation to the four case studies. Programs such as Pathfinder and the Civil Space Technology Initiative are planned to advance certain technologies that will enable these missions. The requirements refined over the next few years will provide these programs with mission technology goals. On the other hand, the technologists must predict the degree to which the objective can be met considering the techological barriers and funding levels so that the proper estimates can be integrated into the case studies. Significant scenario augmentation reflecting the change in technology status may be necessary to accomplish mission objectives.

POWER SYSTEM REQUIREMENTS

By design, the case studies span a range of complexity with the more basic being the Expedition to Phobos and the more complex the Lunar Outpost to Early Mars. The Lewis Research Center has been chartered by OEXP to perform the power system analyses. These tasks include doing broad trades as well as in depth investigations. Major study areas include power systems for exploration elements such as; electric cargo vehicles, planetary orbit transportation/staging nodes, mobile equipment resource processing plants, surface science outposts and habitated bases.

The power levels presented in table II are first cut estimates. As future systems analysis are performed, the values will become more mature. One objective of the power system studies is to discover those technologies that provide the greatest leverage; either by possessing significant mass or reliability advantages, or having a high degree of commonality. Thus, we will be able to focus our resources on those technologies that have the highest pay off.

CRITICAL TECHNOLOGY	HUMAN EXPEDITION TO PHOBOS	HUMAN EXPEDITION TO MARS	LUNAR OBSERV.	LUNAR OUTPOST TO EARLY MARS EVOLUTION
CRYOGENIC FLUID MANAGEMENT	○	●	○	●
AUTOMATED RENDEZVOUS AND DOCKING	●	●	●	●
AUTONOMOUS ROVERS		●		●
MARS AND EARTH AEROCAPTURE	○	○	○	○
ON-ORBIT ASSEMBLY & CONSTRUCTION		○	○	●
SURFACE EXTRA VEHICULAR ACTIVITY SUITS		●	●	●
SURFACE POWER (INCLUDING SP-100)		○	○	○
ADVANCED CHEMICAL PROPULSION	○	○	○	○
NUCLEAR ELECTRIC PROPULSION				○
IN-SITU PROPELLANT PRODUCTION				○
ADVANCED LIFE SUPPORT	●	●		○

LEGEND: ○ INDICATES REQUIRED TECHNOLOGY

● INDICATES CRITICAL PACING ELEMENT

TABLE I - ASSESSMENT OF PREREQUISITE TECHNOLOGY

SYSTEM ELEMENT	POWER	COMMENT
PLANETARY UTILITY VEHICLE	1 - 2 kW	RECHARGEABLE
PLANETARY MINING VEHICLE	5 - 10 kW	RECHARGEABLE/PEAKING
PLANETARY CONSTRUCTION VEHICLE	15 kW	RECHARGEABLE/PEAKING
PLANETARY MANNED EXCURSION	30 kW	CONTINUOUS
LUNAR OBSERVATORY	30 - 50 kW	FULL NIGHT POWER
LUNAR PROCESSING	150 - 300 kW	ELECTRIC/THERMAL
LUNAR BASE	100 kW	CREW OF EIGHT
MARS OUTPOST	20 kW	40 DAYS
MARS BASE	40 - 50 kW	2 YEARS
PHOBOS/DEIMOS PROCESSING	1000 kW	
CARGO VEHICLE	5000 kW	
STAGING NODES	TBD	
FUEL DEPOT	TBD	

TABLE II - ESTIMATED EXTRATERRESTRIAL POWER REQUIREMENTS OF SIGNIFICANT SYSTEM ELEMENTS

A SURVEY OF ADVANCED BATTERY SYSTEMS FOR SPACE APPLICATIONS

Alan I. Attia
Jet Propulsion Laboratory
California Institute of Technology
Pasadena, California 91109

The results of a survey on advanced secondary battery systems for space applications are presented. Fifty-five battery experts from government, industry and universities participated in the survey by providing their opinions on the use of several battery types for six space missions, and their predictions of likely technological advances that would impact the development of these batteries. The results of the survey predict that only four battery types are likely to exceed a specific energy of 150 Wh/kg and meet the safety and reliability requirements for space applications within the next 15 years.

1.0 INTRODUCTION

The Jet Propulsion Laboratory, under the NASA Headquarters sponsorship of the Advanced Battery Concepts Task, recently completed an evaluation of various advanced battery concepts to replace the current Ni-H_2 and Ni-Cd space qualified batteries. The goals were: 1) to identify advanced battery systems capable of outperforming present day batteries by a significant margin; 2) to obtain an accurate estimate of the anticipated improvements afforded by some technologies; and 3) to obtain a consensus as to which of the large number of possible systems are likely to yield the desired improvements with the highest likelihood of success by the year 2005, if properly funded.

2.0 APPROACH

Following an initial analysis by JPL of various electrochemical energy storage devices, the opinion of battery experts was solicited through a 5-part questionnaire. A brief description of each battery system considered by JPL was included with the questionnaire as background information, together with estimates of theoretical and practical energy densities derived from our initial analysis. Participants were asked to submit comments and answer the questions only within their areas of expertise.

3.0 APPLICATIONS REQUIREMENTS

A long shelf life, from 3 to 7 years, is a firm requirement in most space applications; however, capacity, cycle life and rate requirements tend to vary depending on the specific application. The energy storage requirements of six anticipated space missions are shown in Table 1. The requirements vary widely within the following limits: (a) charge time of 2 hours to 22 days; (b) discharge time of 0.6 hour to 17 days; (c) cycle life from 80 to 50,000 cycles; and peak power from 0.5 kW to 100 kW.

3.1 Currently Available and Near-Term Systems

The systems currently in use for space applications include the Ni-Cd, Ni-H_2 and Ag-Zn batteries. Near-term advanced systems include the advanced Ni-Cd battery and the bipolar or common pressure vessel Ni-H_2 batteries. JPL estimates of the characteristics of the space qualified and the near-term advanced systems are summarized in Table 2. As is immediately noticed, substantial reductions in the overall weight of the battery system would result from a battery capable of a specific energy in excess of 200 Wh/kg. However, the importance of long cycle life, safety, and reliability cannot be overemphasized; and high energy density alone cannot be the only factor to be taken into consideration when assessing the potential of a specific technology for space applications.

4.0 RESULTS OF OPINION SURVEY

4.1 Respondents Profile

The questionnaire together with background information was sent to 205 specialists selected from all sectors of industry, government, the universities and research institutes. Fifty-five respondents returned the questionnaire, including a low percentage of responses from universities. Table 3 shows a summary of the make-up of the respondents group.

4.2 Energy Density Critique

As a starting point for the survey, we had identified a total 23 advanced power sources capable of significant improvements over present day technology. Six types of power systems were represented: aqueous, molten salts, solid electrolytes, lithium-halogens, lithium-intercalation systems, and regenerative fuel cells. The participants were asked to evaluate the accuracy of our estimates of achievable specific energies for the proposed systems and to comment in general on the various systems presented to them for consideration.

Their responses are summarized in Table 4. On average, the respondents' estimates were slightly more conservative than JPL's estimates, but the range of estimates is much wider for systems still in their early stage of development. For example, the respondents estimate for the advanced nickel-hydrogen system is 75 ± 6 Wh/kg vs JPL's estimate of 76 Wh/kg. For the solid electrolyte Li/S system the respondent's estimate is 335 ± 179 compared to JPl's value of 500 Wh/kg.

4.3 Risk to Develop Successful Aerospace Batteries

The respondents were asked to give their best estimates of the likelihood of developing the proposed battery systems by the years 1995, 2000 and 2005 and to list the main obstacles to be overcome for each system. The estimates of these probabilities are summarized in Table 5. The systems with an acceptable risk for development are marked with an asterisk. Although the ranges of the estimates are fairly wide, certain trends are clearly evident.

The standard deviations for the estimates are lower for systems under active and well funded development; the likelihood of their development by the year 2005 is also high. Regenerative fuel cells, Advanced Nickel-Hydrogen and Sodium-Sulfur are typical examples and are all rated high.

Solid electrolyte systems based on Beta" Alumina and metal chloride cathodes are rated somewhat lower than Na/S but with acceptable development risks. The same is true for $LiAl/FeS_2$, lithium-intercalation systems (including those with polymer electrolytes,) and solid electrolyte fuel cells. Here again the intermediate rating seems to reflect the lower degree of funding for those systems.

A few systems are consistently rated "high risk", the lithium-halogens, the solid electrolyte Na/Cl_2 and Li/S, and the molten salt Be/NiF_2.

A list of the most frequently mentioned comments and perceived main obstacles on the most promising candidates is presented in Table 6. Li/S and Li/halogens are included in the list although these two systems were judged poor prospects for development.

4.4 Worthwhile Systems Omitted from JPL List

The respondents were also asked to identify other advanced battery candidates omitted or overlooked by JPL, and to give their best estimate of the realizable specific energy for each system.

Within five of the six categories of systems identified as potential candidates in our questionnaire, the following additional systems were suggested as having potential for achieving specific energies approaching 200 Wh/kg:

(a) Molten Salts:

At 240 Wh/kg, the bipolar "Upper Plateau" $LiAl/FeS_2$ battery offers outstanding peak power, in excess of 500 W/kg throughout its discharge period, over a wide range of states of charge.

(b) Solid Electrolytes:

Li/O_2 and Ca/O_2 are being explored in conjunction with a solid oxide ionic conductor operating at high temperatures (>700 C). Practical energy densities in excess of 200 Wh/kg are conceivable.

(c) Lithium-Halogens:

Systems of the type Lithium/SO_2 inorganic electrolyte/Metal Halides are considered by some as safer and more practical alternatives to the lithium-halogens systems. These systems are capable of achieving 200 Wh/kg at high rates of discharge, but safety is a concern.

(d) Li/Intercalation Cathodes:

Several systems with metal oxide cathodes, not mentioned in our original list of potential candidates, were considered capable of achieving high specific energy. Li/CoO_2 (150 Wh/kg) is one such candidate but requires a suitable electrolyte to achieve long cycle life. Li/MnO_2 (currently at 125 Wh/kg) is another and could reach a substantially greater specific energy in bigger cells, due to the improved packaging factor in large cells. The cell voltage of 2.8 V for Li/MnO_2 is inside the electrochemical window of the current most promising organic electrolytes.

As a whole the class of Lithium/Intercalation Cathodes offers specific energies from 100 to 200 Wh/kg, and presents opportunities for both solid polymer electrolytes as well as ambient temperature conventional electrolytes.

(e) Regenerative Fuel Cells:

The solid polymer electrolyte (SPE) H_2/O_2 fuel cell is a major candidate for the space station. A breadboard system successfully operated for more than 1000 cycles at NASA/JSC. NASA is currently funding a study to conduct a flight experiment on a reversible regenerative SPE fuel cell with all passive fluid and thermal controls. For large systems a specific energy in excess of 200 Wh/kg appears quite feasible. In many respects this system is very similar to the alkaline RFC and could be considered as a direct replacement for it.

(f) Supercapacitors:

A most interesting development which may impact energy storage technology in the future is the supercapacitor. To date devices with specific energies approaching 5 Wh/kg have been successfully demonstrated. These devices offer the additional advantages of ruggedness, high power density (up to 200 W/cc) and potentially unlimited cycle life.

4.5 Suitability of Systems for Space Applications

The fourth question set required the survey participants to estimate the degree of suitability of the proposed systems for several space applications. The panelists were requested to rate each battery system as highly suitable (H), moderately suitable (M) or not suitable (L) for each of six types of space missions. The responses are tabulated in Table 7 for each of the most promising systems. Based on those estimates, the development priorities are shown in Table 8.

For the six missions listed, the Beta" solid electrolyte (BASE) systems, Na/BASE/S and Na/BASE/metal chlorides battery are considered best for four missions; the H_2/O_2 alkaline RFC is ranked best for two missions. The U.P. $LiAl/FeS_2$ system was found worthwhile in 3 missions, whereas the Li/TiS_2, as a representative of a lithium/intercalation cathode system, was deemed useful in three applications. The Ni/H_2 was also highly rated for nearly all applications but was not considered an advanced battery candidate because of its lower specific energy and advanced stage of development. Some of the matches are quite evident, as discussed below.

(a) Lithium-Intercalation Batteries for the Planetary Rover:

The planetary rover has requirements that are well suited to ambient temperature lithium-intercalation batteries, both in terms of cycle life and rate. The fact that these batteries have no special temperature control requirements, and can be packaged and temperature controlled like the rest of the vehicle equipment is an important plus. The fact that they do not require a close temperature control is an advantage also. Several chemistries are available, including polymeric electrolytes, giving flexibility in a final choice.

(b) Regenerative Fuel Cell for Lunar Base:

The lunar mission is unique in that it requires very long operating times (days vs hours). In such applications the dominant weight of the energy storage system is in the reactants. The regenerative H_2/O_2 fuel cell has a very high specific energy for this application, approaching 500 Wh/kg, as most of its weight would be in the light weight reactants and their required tankage.

(c) Upper Plateau (U.P.) $LiAl/FeS_2$ for GEO:

The basis for recommending this system for development is its high energy density capability and its very high expectations of success. Recent results obtained at Argonne National Laboratory have shown that the system is capable of a cycle life in excess of 1000 cycles and a specific energy approaching 200 Wh/kg. The only other candidate system for GEO, aside from the Ni/H_2 system, would be the Na/S system. Although significantly more dollars were spent on Na/S, the U.P. $LiAl/FeS_2$ system shows expectations of having a greater energy density, lower risk of catastrophic failure, less risk of premature shorting, better high rate and peak power capability, less temperature variation during cycling, and less safety concerns for manned Shuttle launches. In addition, the U.P. $LiAl/FeS_2$ system can be activated prior to launch.

(d) Na/BASE/S or $FeCl_2$ or $NiCl_2$ for LEO and Planetary Orbiters:

The requirements for LEO are very strenuous with respect to cycle life and can only be met by very few systems (Ni-Cd or $Ni-H_2$). Currently the Na/S system is being developed for LEO but is still considered a high risk due to its high operating temperature. The Na/Metal Chlorides are attractive alternatives for this application because of their lower operating temperature and lower current density, hence lower risk of premature failure.

4.6 Technological Breakthroughs

Finally an estimate of the likelihood of occurrence of several new technological breakthroughs by the years 1995, 2000 and 2005 was requested from the participants. Only those estimates which show a reasonable degree of certainty are included in Table 9.

5.0 CONCLUSIONS AND FUTURE WORK

The results appear to support the following conclusions:

a) Most experts believe that the technical problems of the sodium-solid electrolyte systems, if continued to be funded at their current level, will be resolved by 2005. This type of system will provide an intermediate specific energy storage device (130 Wh/kg).

b) Key requirements for the development of lithium-intercalation systems appear well underway to being resolved by 2005, the main obstacle at this time being the plating efficiency of the lithium electrode.

c) The molten salt U.P. $LiAl/FeS_2$ system will be a serious high specific energy (180 Wh/kg) contender by 2005.

d) The development of a passive regenerative fuel cell is very likely by 2005. However, the parallel development of a bifunctional oxygen electrode is far from being certain.

e) The halogen-based systems, whether with lithium or sodium, are unlikely to be developed by the year 2005.

f) In general, the survey results are conservative. Participants in the survey are pessimistic about the chances of success of high risk developments with high potential payoffs, such as the lithium/solid ion conductor/sulfur or lithium-halogen battery, maybe due to the current low level of funding for their development.

As a follow up to this survey, the participants will be given a chance to comment on the results and conclusions.

TABLE 1

ENERGY STORAGE REQUIREMENTS OF SIX ANTICIPATED SPACE MISSIONS

PRIORITY	CHARGE/ DISCHARGE DURATIONS	TYPICAL OPERATIONAL CYCLES REQUIRED			TYPICAL PEAK POWER AND ENERGY STORAGE REQUIRED
		ACTUAL	QUAL*	DESIRED	
#1 Outer Planetary Orbit	C - 2 hr D - 0.7 hr	500	1,000	2,000	0.5 C (1 KWH)
#2 Inner Planetary Orbit	C - 2 hr D - 0.7 hr	3,000	6,000	10,000	1.5 C (2 KWH)
#3 GEO	C - 22.8 hr D - 1.2 hr	1,000	1,500	4,000	1.5 C (5 KWH)
#4 Planetary Rover	C - 12 hr D - 3 hr	300	600	800	1.3 C (3 KWH)
#5 Lunar Base	C - 11 Days D - 17 Days	80	160	350	0.02 C (5 MWH)
#6 LEO	C - 1 hr D - 0.6 hr	30,000	35,000	50,000	1.1 C (25 KWH)

GEO = Geosynchronous Orbit
LEO = Low Earth Orbit
*QUAL = Minimum number of cycles needed to qualify for application

TABLE 2

SECONDARY BATTERIES FOR SPACE APPLICATIONS

SYSTEM	SPECIFIC ENERGY (Wh/kg)	ENERGY DENSITY (Wh/l)	CYCLE LIFE (40% DOD)	OPERATING TEMPERATURE (°C)
SYSTEMS CURRENTLY IN USE				
Ni-Cd	34*	70	20,000**	10 - 20
$Ni-H_2$ (IPV)$	45	25	25,000	10 - 20
Ag-Zn	90	80	50	10 - 20
ADVANCES IN STATE-OF-THE-ART				
Advanced Ni-Cd	36	110	35,000	10 - 20
$Ni-H_2$ (CPV)#	60	70	15,000	10 - 20

---

* NASA standard, 50 Ah battery
** Standard Cell Qualification Test
$ IPV = Individual Pressure Vessel
# CPV = Common Pressure Vessel

TABLE 3

PROFILE OF CONTRIBUTORS TO SURVEY ON ADVANCED BATTERIES

Occupation	Number of Respondents
Aerospace Industry	6
Battery Manufacturers	15
Other Manufacturers	8
Government	14
Universities	3
Institutes	9
TOTAL	55

TABLE 4

ESTIMATES OF ACHIEVABLE SPECIFIC ENERGY FOR ADVANCED BATTERIES (Wh/kg)

System	JPL Estimate	Panel's Estimate	Range	Number of Responses
AgO/Fe	90	85 +/-13	60-110	18
Advanced Ni/H_2	76	75 +/-6	60-80	25
U.P.LiAl-FeS_2	180	154 +/-33	75-188	31
Be-NiF_2	185	156 +/-43	95-185	9
LiAl-NiS_2	180	155 +/-35	75-184	19
Na/BASE/S	130	132 +/-26	80-220	29
Na/BASE/Cl_2	200	197 +/-70	100-350	9
Na/BASE/TCNE	100	95 +/-12	70-100	10
Na/BASE/$CuCl_2$	160	132 +/-30	80-160	11
Na/BASE/$FeCl_2$	150	130 +/-20	80-150	19
Na/BASE/$NiCl_2$	160	137 +/-24	80-160	17
Li/Solid Ion Conductor/S	500	335 +/-179	100-510	14
Lithium/Polymer electrolyte	250	183 +/-67	50-250	28
Li/Cl_2	500	375 +/-173	80-500	15
Li/Br_2	200	170 +/-56	70-250	14
Li/TiS_2	90	95 +/-13	73-130	28
Li/$NbSe_3$	100	105 +/-15	80-150	25
Li/Mo_6S_8	140	126 +/-28	50-180	22
Li/V_2O_5	150	143 +/-27	75-200	24
Li/a-Cr_3O_8	200	176 +/-37	75-200	22
Zn/O_2	100	99 +/-15	60-140	17
Alkaline RFC	100	152 +/-113	100-500	14
Solid Oxide H_2/O_2	200	252 +/-180	120-750	10

BASE = Beta" alumina solid electrolyte

TABLE 5

LIKELIHOOD OF DEVELOPMENT OF ADVANCED BATTERY SYSTEMS

System	Estimates of Probability of Development by		
	1995	2000	2005
AgO/Fe	37 +/- 32	47 +/- 33	54 +/- 38
Advanced Ni/H_2*	56 +/- 25	71 +/- 19	81 +/- 17
U.P.LiAl-FeS_2*	36 +/- 26	52 +/- 31	60 +/- 30
Be-NiF_2	12 +/- 16	25 +/- 24	35 +/- 35
LiAl-NiS_2	28 +/- 25	41 +/- 28	46 +/- 31
Na/BASE/S*	56 +/- 28	72 +/- 25	80 +/- 22
Na/BASE/Cl_2	17 +/- 18	31 +/- 25	29 +/- 29
Na/BASE/TCNE	23 +/- 20	33 +/- 28	42 +/- 33
Na/BASE/$CuCl_2$*	27 +/- 19	47 +/- 26	60 +/- 29
Na/BASE/$FeCl_2$*	36 +/- 23	53 +/- 28	66 +/- 29
Na/BASE/$NiCl_2$*	35 +/- 21	54 +/- 25	66 +/- 27
Li/Solid Ion Conductor/S	18 +/- 19	29 +/- 25	39 +/- 28
Lithium/Polymer electrolyte*	33 +/- 29	45 +/- 31	55 +/- 30
Li/Cl_2	10 +/- 14	19 +/- 18	32 +/- 25
Li/Br_2	12 +/- 13	21 +/- 18	33 +/- 26
Li/TiS_2*	44 +/- 26	57 +/- 29	66 +/- 31
Li/$NbSe_3$*	42 +/- 27	57 +/- 31	66 +/- 30
Li/Mo_6S_8	34 +/- 28	50 +/- 31	58 +/- 34
Li/V_2O_5*	34 +/- 23	48 +/- 28	58 +/- 32
Li/a-Cr_3O_8*	27 +/- 18	43 +/- 24	55 +/- 28
Zn/O_2	33 +/- 23	44 +/- 25	58 +/- 24
Alkaline RFC*	49 +/- 30	63 +/- 28	77 +/- 26
Solid Oxide H_2/O_2*	30 +/- 24	47 +/- 27	59 +/- 30

---

* These systems present acceptable development risks

TABLE 6

OBSTACLES TOWARD THE DEVELOPMENT OF ADVANCED BATTERIES

System	Obstacle
Advanced Ni/H2:	2-electron nickel electrode is unlikely No obstacle to improved Ni/H2 (CPV and/or Bipolar)
U.P. LiAl FeS2:	Corrosion and materials compatibility
Na/Beta"/S or Metal Chlorides	Reliability of ceramic electrolyte and seals
Lithium-Sulfur:	Development of lithium ion conducting electrolyte
Thin Film lithium/ polymer electrolyte:	Need for higher ionic conductivity in polymer Low cycle life
Lithium-Halogens:	Material compatibility and corrosion
Lithium-Intercalation Cathodes:	Lithium cyclability Poor electrolyte stability
Alkaline RFC:	Development of the oxygen bifunctional electrode
Solid Oxide Fuel Cell:	Materials compatibility

TABLE 7

SUITABILITY OF ADVANCED BATTERY SYSTEMS FOR SPACE APPLICATIONS
(L= Not Suitable; M= Moderately Suitable; H= Highly Suitable)

SYSTEM	PLANETARY INNER ORBIT	OUTER ORBIT	GEO	ROVER	LUNAR BASE	LEO
Advanced Ni/H_2	L=5	L=7	L=2	L=10	L=14	L=3
	M=9	M=5	M=6	M=9	M=8	M=7
	H=13	H=14	H=20	H=9	H=7	H=20
U.P.LiAl-FeS_2	L=7	L=7	L=8	L=8	L=8	L=18
	M=13	M=11	M=7	M=5	M=12	M=7
	H=6	H=8	H=11	H=14	H=6	H=2
Na/BASE/S	L=5	L=3	L=2	L=3	L=5	L=13
	M=15	M=15	M=13	M=16	L=11	L=12
	H=10	H=12	H=15	H=11	H=16	H=6
Na/BASE/$FeCl_2$	L=5	L=3	L=2	L=4	L=6	L=10
	M=11	M=12	M=12	M=13	M=8	M=8
	H=6	H=6	H=6	H=4	H=9	H=4
Na/BASE/$NiCl_2$	L=5	L=3	L=2	L=3	L=6	L=9
	M=10	M=10	M=10	M=11	M=7	M=8
	H=7	H=8	H=8	H=6	H=9	H=5
Lithium/Polymer electrolyte	L=18	L=11	L=10	L=9	L=12	L=23
	M=5	M=9	M=10	M=10	M=6	M=1
	H=4	H=6	H=6	H=8	H=9	H=3
Li/TiS_2	L=21	L=11	L=11	L=10	L=16	L=28
	M=8	M=15	M=13	M=13	M=8	M=5
	H=4	H=7	H=8	H=10	H=6	H=1
Li/V_2O_5	L=24	L=15	L=13	L=12	L=16	L=30
	M=8	M=14	M=12	M=11	M=11	M=5
	H=1	H=3	H=8	H=9	H=6	H=0
Li/a-Cr_3O_8	L=21	L=12	L=11	L=9	L=13	L=26
	M=8	M=14	M=14	M=11	M=11	M=5
	H=1	H=4	H=5	H=9	H=6	H=0
Alkaline RFC	L=9	L=8	L=6	L=6	L=1	L=9
	M=11	M=12	M=13	M=16	M=8	M=9
	H=3	H=3	H=5	H=2	H=16	H=6
Solid Oxide H_2/O_2	L=10	L=9	L=7	L=8	L=1	L=9
	M=7	M=7	M=8	M=9	M=5	M=7
	H=3	H=4	H=6	H=4	H=17	H=6

TABLE 8

RANKING OF ADVANCED BATTERY SYSTEMS

Mission	Recommended Systems (Ranking)
Planetary Inner Orbit	Na/BASE/S or $FeCl_2$ or $NiCl_2$ (1) U.P. $LiAl-FeS_2$ (2) H_2/O_2 Alkaline RFC (3)
Planetary Outer Orbit	Na/BASE/S or $FeCl_2$ or $NiCl_2$ (1) U.P. $LiAl/FeS_2$ (2) Li/TiS_2 (3)
GEO	Na/BASE/S or $FeCl_2$ or $NiCl_2$ (1) H_2/O_2 Alkaline RFC or U. P. $LiAl/FeS_2$ (2) Li/TiS2 (3)
Planetary Rover	Na/BASE/S or $FeCl_2$ or $NiCl_2$ (1) U.P. $LiAl/FeS_2$ (2) Li/TiS_2 or Alkaline RFC (3)
Lunar Base	H_2/O_2 Alkaline RFC or Solid Oxide (1) Na/BASE/S or $FeCl_2$ or $NiCl_2$ (2) U.P.$LiAl/FeS_2$ (3)
LEO	H_2/O_2 Alkaline RFC or Solid Oxide (1) Na/BASE/S or $NiCl_2$ or $FeCl_2$ (2)

The advanced Ni-H_2 system was not included in the rankings as this system is much further ahead in its development stage.

TABLE 9

PROJECTED PROSPECTS FOR TECHNOLOGICAL BREAKTHROUGHS

	% Probability		
Future Event	1995	2000	2005
Improved Beta" alumina suitable for prismatic cells	39+/-26	53+/-27	66+/-27
Improved ceramic seals for Beta" Alumina	57+/-27	71+/-27	82+/-24
Hermetic seals for high temperature molten salt lithium batteries	29+/-32	61+/-31	71+/-28
A metal oxide intercalation electrode for lithium batteries with cycle life of 100	44+/-26	60+/-25	73+/-30
A reversible lithium electrode capable of 1000 cycles in organic electrolyte at 25C (e.g., Li/TiS$_2$ or Li/Metal Oxide)			
a) Medium voltage cells (~2 V.)	42+/-28	57+/-28	66+/-29
b) High voltage cells (~3V.)	33+/-24	47+/-25	59+/-28
Chemical overcharge protection for Li-Al/FeS$_2$ molten salt system	46+/-26	59+/-25	69+/-26
The development of very thin, suitable polymer electrolytes for thin Li cells	41+/-29	52+/-28	66+/-28
Development of hot-launch, ready to use, high temperature rechargeable batteries			
a) Na/Beta" Alumina/S	50+/-29	59+/-29	70+/-29
b) Li-Al/FeS$_2$	44+/-30	54+/-29	69+/-31
Development of practical rechargeable designs for			
a) Li/Cl$_2$	11+/-13	24+/-18	33+/-22
b) Li/Br$_2$	16+/-17	28+/-20	37+/-23
High rate (100mA/cm^2), reversible, long life, oxygen electrode for alkaline fuel cells	36+/-21	48+/-27	61+/-29

ADVANCED RECHARGEABLE SODIUM BATTERIES WITH NOVEL CATHODES

S. Di Stefano, B.V. Ratnakumar and C.P. Bankston
Jet Propulsion Laboratory
California Institute of Technology
Pasadena, California 91109

Abstract

Various high energy density rechargeable batteries are being considered for future space applications. Of these, the sodium sulfur battery is one of the leading candidates. The primary advantage is the high energy density (760 Wh/kg theoretical). Energy densities in excess of 180 Wh/kg have been realized in practical batteries. More recently, cathodes other than sulfur are being evaluated. We at JPL are evaluating various new cathode materials for use in high energy density sodium batteries for advanced space applications. Our approach is to carry out basic electrochemical studies of these materials in a sodium cell configuration in order to understand their fundamental behaviors. Thus far our studies have focused on alternate metal chlorides such as $CuCl_2$ and organic cathode materials such as TCNE.

Introduction

Rechargeable batteries play a significant role in NASA's space programs including planetary missions and satellite applications such as Geosynchronous Earth Orbit (GEO) and Low Earth Orbit (LEO) missions. There is an increasing need for a light weight high energy battery with long active and cycle lives. Typically, the efforts at various organizations are aimed at developing a battery system with an energy density $\geq$ 200 Wh/kg at power densities $\geq$ 100 W/kg, cycle life of 1000 cycles and active life of ten years. The interest for many years has been focussed on sodium-sulfur battery which has a high formula energy density (~750 wh/kg) a good portion of which has been realized in practical cells for several hundreds of charge/discharge cycles (1). The battery typically operates at 300-400°C where the β" alumina solid electrolyte (BASE) is highly conductive to sodium ions allowing high power densities drawn from the battery. Together with these advantages, there are certain deterrent factors associated with the use of the sodium sulfur battery which partly protracted the development. R. M. Dell et al. (2) have given an excellent account of the status of the NaS battery in their recent review. Many of these operational and safety problems stem from sulfur electrode, e.g., the excessively corrosive nature of the discharge product, sodium polysulfide, towards steels, the high vapor pressure of liquid sulfur above 700°C, the possible degradation of BASE in polysulfide melts, (3) the insulating nature of liquid sulfur, in particular the way in which it isolates regions of BASE during recharge, etc. Alternatives to liquid sulfur cathode are therefore being sought and there are some examples in the literature based on fused salt electrolytes (4-6). In this paper, we review our studies on alternate organic and inorganic cathodes in sodium batteries. In both cases, the cell contains sodium tetrachloroaluminate as the secondary molten electrolyte and BASE as primary electrolyte.

Carbonitriles are a class of relatively stable organic compounds that have high reduction potentials and energy densities. Tetracyanoethylene (TCNE) in particular has an energy density of ~620 Wh/kg at a high potential of ~3.0 V vs. Na^+/Na and a low melting point. Therefore, TCNE has been examined as a possible liquid cathode in sodium batteries. Among the inorganic cathode materials, transition metal dichlorides (e.g., $FeCl_2$ and $NiCl_2$) are gaining increasing attention as solid, insoluble rechargeable cathodes in place of liquid sulfur (8-11). These systems can operate at lower temperatures ~170°C, where the corrosion problems are proportionately less severe. The safety problem is considerably reduced due to the inherent sluggish kinetics of the chemical reaction between liquid sodium and $NaAlCl_4$ molten electrolyte in the event of ceramic failure (12). Further, the molten electrolyte remains invariant during charge/ discharge preventing polarization losses and localized high current densities on the BASE surface. High energy densities ~150 Wh/kg and long cycle life have been demonstrated with ferrous chloride and more recently with nickel chlorides. We summarize below our electrochemical studies on the ferrous chloride and nickel chloride cathodes and also on another promising metal chloride, copper chloride.

Experimental

The experimental cell adopted for these studies is described in detail in. (7) The cell essentially has a central-cathode design with a provision to seal the anode half-cell. The cell is heated electrically with a heating tape wound around a stainless steel tube acting as a container for sodium. For the studies involving TCNE, either Pt or C is used as the positive current collector. Metal chloride positive electrodes were initially fabricated by impregnating commercially available sintered nickel grids (used in Ni-Cd batteries) with the depolarizer by immersing the grid into a concentrated chloride solution. Copper electrodes cannot however be made in this manner for long-term studies due to the preferential dissolution of nickel to copper in the impregnating solution. Perforated copper grids were therefore used to make electrodes in the discharged state either by hot pressing with a binder (Teflon) or by sintering the powders in an inert atmosphere at temperatures below the melting point of NaCl. Conventional electrochemical equipment consisting of E G & G 273 potentiostat/Galvanostat and E G & G 5301 lock-in amplifier interfaced with an Apple IIe computer were used. AC and dc measurements were carried out using E G & G ac impedance and Softcorr software. Various techniques such as potentiodynamic polarization, dc linear polarization and ac impedance were employed to obtain information on the kinetic parameters of the cathode reactions. Discharge/charge cycling was also carried out galvanostatically in a controlled fashion using the above electrochemical equipment. All the chemicals TCNE, $NaAlCl_4$, NaCl and metal powder were of analytical grade and were used as received. BASE tubes were cleaned by etching in hot phosphoric acid. All the cell fabrication operations were carried out in an argon-filled glove box.

Results and Discussions

The findings of our studies on TCNE as a cathode material in sodium batteries are described in detail elsewhere. (7) Briefly, TCNE reduces at 3.0 V vs. Na^+/Na reversibly with a coulombic yield of >60% at 1 ma/cm^2 on either the Pt or C current collector. Fig. 1 gives the typical voltage-time curves of TCNE during discharge and charging. The exchange current density on either Pt or C is of the order of 10^{-3} A/cm^2 in a catholyte containing typically 10% of TCNE. The kinetics of TCNE reduction are essentially governed by the rate of mass transfer in the cathode as evidenced from ac impedance and dc potentiodynamic polarization data. In TCNE-rich catholytes there is a kinetic hindrance to the reduction of TCNE reflected in increased polarization (ohmic, concentration as well as charge transfer) losses. As a result, the coulombic yield as well as diffusion coefficient of TCNE decrease with increasing TCNE concentration in the catholyte. The sluggish kinetics at higher TCNE concentrations is related to the degradation processes occurring in TCNE at operating temperatures of ~230°C forming an adduct. FTIR studies point to a possible polymerization of TCNE under the experimental conditions. Due to the sluggish kinetics at higher TCNE concentrations, it may not be possible to achieve high power densities from TCNE. On the other hand, for medium to low power applications, TCNE is a good cathode material, since the electrochemical activity and reversibility of TCNE are retained even after polymerization.

Metal Dichloride Cathodes

Figure 2 shows the typical charge/discharge curves of a ~16 mAh $NiCl_2$ electrode (made by impregnating $NiCl_2$ into sintered Ni plaque) at 200°C and at 2 mA/cm^2 in the first two test cycles. The discharge as well as charging curves are flat at nominal voltages of 2.56 and 2.63 V vs. Na^+/Na respectively. There is not much polarization loss from the open circuit voltage of 2.59 V.

The coulombic yield is nearly 100% and there is no loss in capacity during cycling in the first few test cycles. Figure 3 illustrates the high rate discharge capability of the electrode. The discharge curves at higher current densities, i.e., 4 mA/cm^2 and 8 mA/cm^2 are also flat with mid-point voltages of 2.54 and 2.5 V and coulombic yields of 98% and 90% respectively. Ferrous chloride electrodes (made by sintering dry powders of sodium chloride and iron) exhibit a lower operating potential of ~2.3 V as may be seen from the discharge and charge curves of a ~230 mAh electrode in Figure 4. The discharge curve is flat in this case also, with a coulombic yield in excess of 90%. The copper chloride cathode is expected to give higher voltage than nickel chloride, from the electrode potentials of Cu^{+2}/Cu and Ni^{2+}/Ni couples. Accordingly, higher energy densities may be possible with copper chloride as compared to ferrous chloride or nickel chloride especially at high power densities due to a high electronic conductivity of copper formed in the course of discharge. The essential requirement for a successful operation of metal chloride cathode in the above sodium batteries is total insolubility of the chloride in a $NaAlCl_4$ melt. Analytical studies carried out on the catholyte with $CuCl_2$ and $NiCl_2$ revealed no extra dissolution of copper over nickel. Initial studies with copper chloride (electrode made by impregnation of $CuCl_2$ into sintered Ni plaque) show a higher operating voltage than $NiCl_2$ or $FeCl_2$ (Figure 5). The discharge (as well as charging) curve is, however, not flat in this case as with $FeCl_2$ or $NiCl_2$ which may be due to the mechanism of reduction being different with the possible formation of a monovalent copper.

DC polarization studies were carried out on these cathode materials to obtain information on the kinetics of their reduction. The potentiodynamic polarization curves of $NiCl_2$, $FeCl_2$ and $CuCl_2$ (Figure 6) illustrate the high rate capability of these electrodes. There exist mass transfer effects at high discharge rates interfering with the charge transfer processes due to which limiting currents are observed at high overpotentials $\geq$ 300 mV. The limiting currents may be due to a relatively slow diffusion processes inside the porous cathode. Nevertheless, the limiting current densities are reasonably high and are of the order of 15-25 mA/cm^2. The charge transfer kinetics appear to be rapid as evidenced by high exchange current densities of 2 mA/cm^2, 0.65 mA/cm^2 and 0.4 mA/cm^2 for $NiCl_2$, $FeCl_2$ and $CuCl_2$, respectively, based on the geometric areas of these electrodes. Linear polarization experiments (i.e., at low perturbations) were also carried out to derive similar information on the exchange current densities. The current potential curves at these potentials are linear (e.g., $FeCl_2$ in Figure 7) the slopes of which give the polarization resistances. The exchange current densities thus obtained are 4.6 mA/cm^2, 1.5 mA/cm^2 and 0.39 mA/cm^2 for $NiCl_2$, $FeCl_2$ and $CuCl_2$, respectively.

The complex plane impedance spectrum of $NiCl_2$ (Figure 8) shows a large inductance at high frequencies not shown in the figure attributed to the porous nickel grid and a low frequency semi-circle ascribed to charge transfer kinetics. The exchange current density calculated therefrom is 6.9 mA/cm^2. There is no evidence of diffusional impedance in the frequency range studied (i.e., $\geq$ 0.01 Hz). The complex plane impedance spectrum of $CuCl_2$ (sintered) electrode, on the other hand, contains two relaxation loops. The exchange current density evaluated from the first relaxation loop is 0.9 mA/cm^2. It is however not clear yet as to whether the second relaxation loop is related to the formation, if any, of monovalent copper during the reduction of $CuCl_2$.

Conclusions

Among the cathode materials studied at JPL as alternatives to sulfur cathode in sodium batteries, TCNE is suitable for low to medium power applications. Metal dichloride cathodes, on the other hand can deliver energy densities comparable to sodium-sulfur batteries at high power densities without many of the operational and safety problems associated with the use of sodium-sulfur batteries and are thus suitable for various applications including space, EV load-levelling, etc. The electrochemical studies carried out so far indicate high exchange current densities for the reduction of these cathodes.

Acknowledgement

The work described here was carried out at the Jet Propulsion Laboratory, California Institute of Technology, under contract with the National Aeronautics and Space Administration. One of the authors (B. V. Ratnakumar) acknowledges the National Research Council for providing his Research Associateship during this work.

References

1. J. Sudworth and A. R. Tilley (Eds.), "The Sodium/Sulfur Battery," Chapman and Hall, New York 1985.
2. R. M. Dell and R. J. Bones, B. Electrochem., 4, 319 (1988).
3. M. Liu and L. C. De Jonghe, J. Electrochem. Soc., 135, 741 (1988).
4. J. Werth, U.S. Patent 3,877,984 (1975).
5. G. Mamantov, R. Marassi, M. Matsunaga, Y. Ogata, J. P. Wiaux and E. J. Frazer, J. Electrochem. Soc., 127, 2319 (1980).
6. K. M. Abraham, L. Pitts and R. Schiff, J. Electrochem. Soc., 127, 2595 (1980).
7. B. V. Ratnakumar, S. Di Stefano, G. Nagasubramanian, R. M. Williams and C. P. Bankston, Extd Abstr. #74, ECS Fall Meeting, Chicago, IL, October 9-14, 1988. Manuscript submitted for publication.
8. J. Coetzer and M. Thackeray, U.S. Patent 4,288,506.
9. J. Coetzer, J. Power Sources, 18, 377 (1986).
10. R. C. Galloway, J. Electrochem. Soc., 134, 286 (1987).
11. B. J. Jones, J. Coetzer, R. C. Galloway and D. A. Teagle, J. Electrochem. Soc., 134, 2379 (1987).
12. R. T. Wedlake, A. R. Tilley and D. A. Teagle, B. Electrochem., 4, 41 (1988).

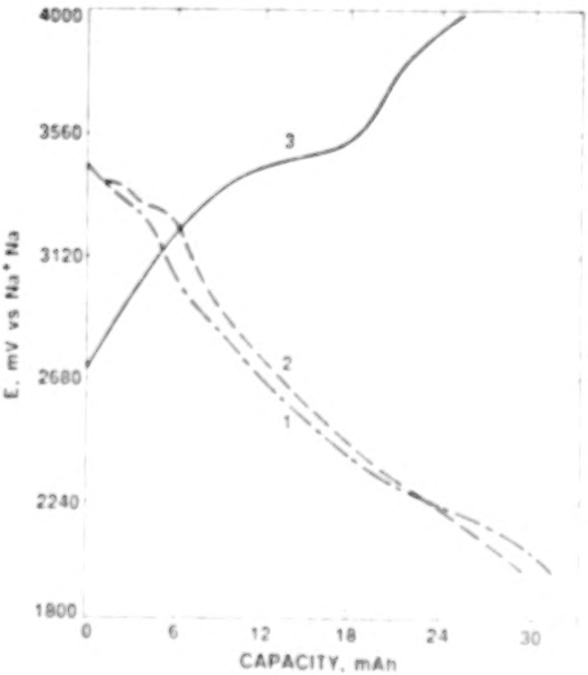

Figure 1. Typical Charge/Discharge Curves of [illegible] ([illegible] mAh) at [illegible] °C: (1) Fourth Discharge, (2) Fifth Discharge, and (3) Charge

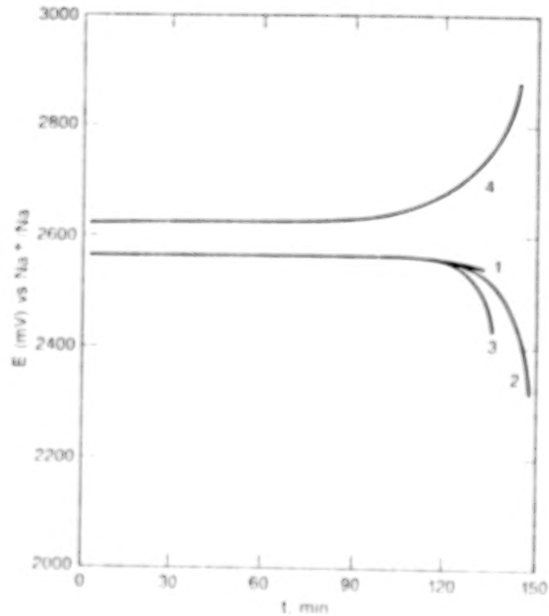

Figure 2. Typical Charge/Discharge Curve 16 mAh Electrode at 200 °C During (1) Second, (2) Third, (3) Fourth Discharge, and (4) Charge at 2 mA/cm^2

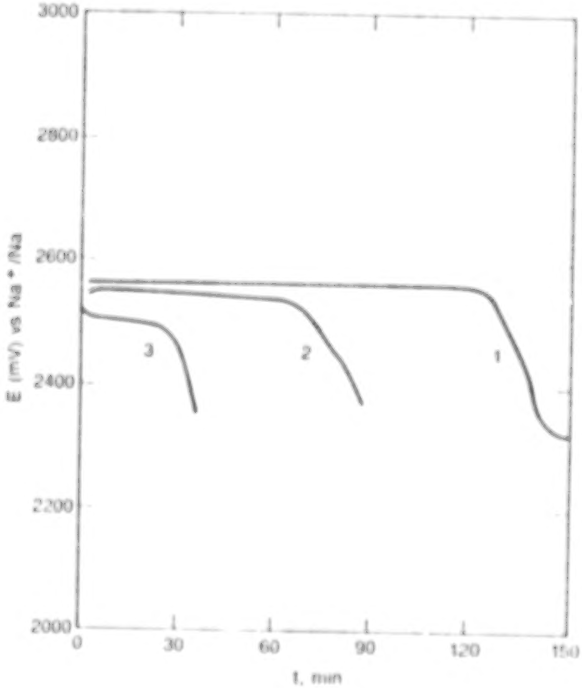

Figure 3. Discharge Curves of 16 mAh NiCl$_2$ Electrode at 200 °C and at Current Density of (1) 2 mA/cm^2, (2) 4 mA/cm^2, and (3) 8 mA/cm^2

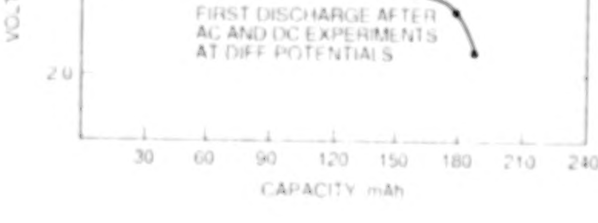

Figure 4. Initial Charge/Discharge Curves of FeCl$_2$ Cathode

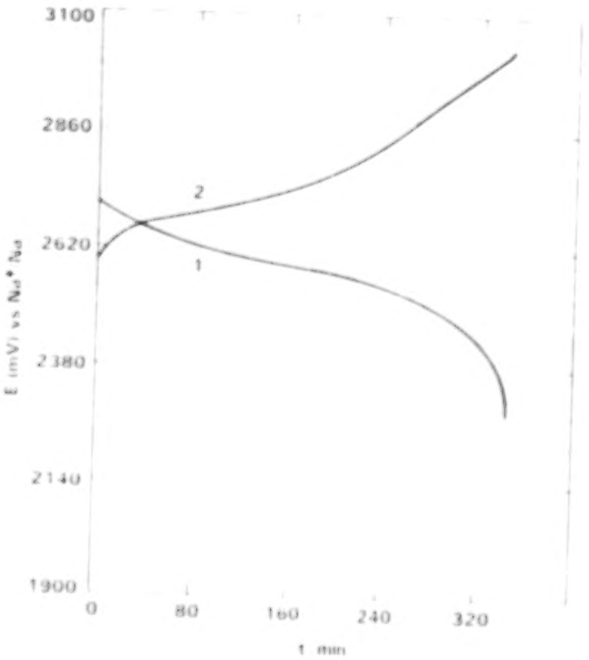

Figure 5. Charge/Discharge Curves of $CuCl_2$ Electrode (Made by Impregnating $CuCl_2$ into a Sintered Nickel Grid) at 200°C

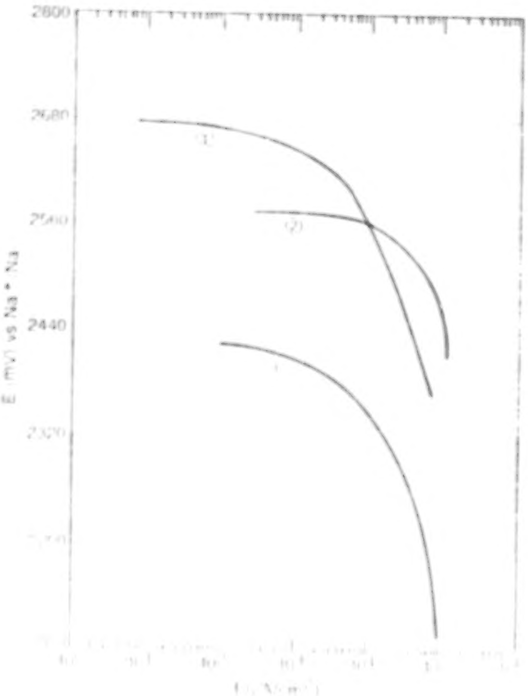

Figure 6. Potentiodynamic Polarization Curves of (1) $CuCl_2$, (2) $NiCl_2$, and (3) $FeCl_2$

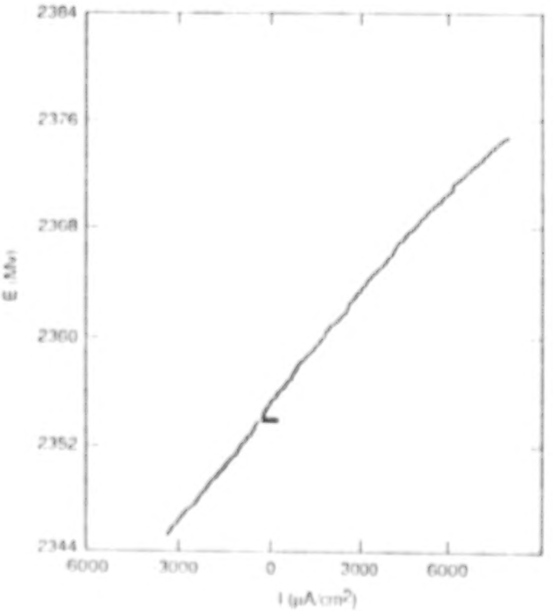

Figure 7. Linear Polarization Curve for $FeCl_2$ from which an Exchange Current Density of 1.5 mA/cm² is Calculated

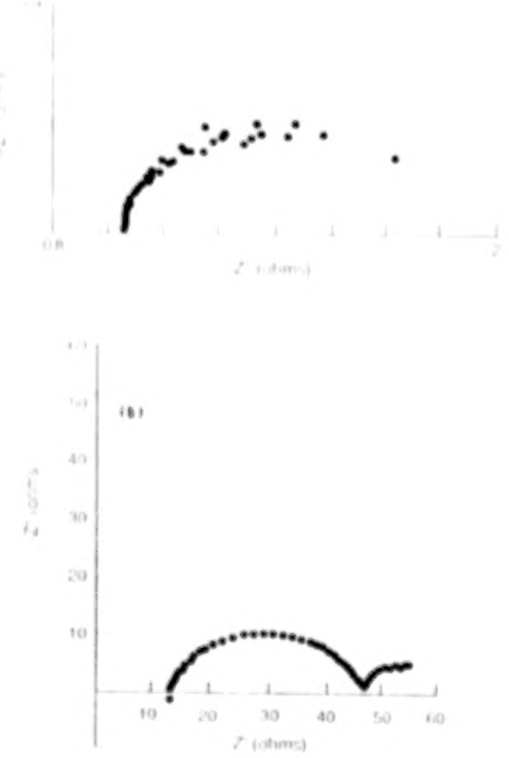

Figure 8. Complex Plane Impedance of (a) $NiCl_2$ and (b) $CuCl_2$

MONOLITHIC SOLID OXIDE FUEL CELL DEVELOPMENT

K.M. Myles and C.C. McPheeters
Argonne National Laboratory
Argonne, Illinois 60439

INTRODUCTION

The Monolithic Solid Oxide Fuel Cell (MSOFC) is being developed by a recently formed team consisting of Argonne National Laboratory, Allied-Signal Aerospace/AiResearch, and Combustion Engineering. The MSOFC (ref. 1) is an oxide-ceramic structure in which appropriate electronic and ionic conductors are fabricated in a "honeycomb" shape similar to a block of corrugated paperboard. The electrolyte that conducts oxygen ions from the air side to the fuel side is yttria-stabilized zirconia (YSZ). All the other materials are electronic conductors, including the nickel-YSZ anode, the strontium-doped lanthanum manganite cathode, and the doped lanthanum chromite interconnect (bipolar plate). These electronic and ionic conductors are arranged to provide short conduction paths to minimize resistive losses. The power density achievable with the MSOFC is expected to be about 8 kW/kg or 4 kW/L (ref. 2) at fuel efficiencies over 50%, because of small cell size and low resistive losses in the materials. The MSOFC operates in the range of 700 to 1000°C, at which temperatures rapid reform of hydrocarbon fuels is expected within the nickel-YSZ fuel channels.

Tape casting (ref. 3) and hot roll calendering (ref. 4) are used to fabricate the MSOFC structure. The tape casting process consists of spreading a ceramic slurry (slip) uniformly on a substrate, such as glass or polymer film, using a doctor blade. After the slip is dry, the ceramic layer is stripped off the substrate in the form of a flexible "tape." The hot roll calendering process consists of mixing ceramic powder with organic binder and plasticizer and rolling the warm mixture into a thin tape. The green tapes are cut to the desired dimensions, and the electrode tapes are corrugated to form the gas flow channels. The corrugations are formed by folding the tape onto a warm mold. After cooling, the tape retains the corrugated shape. Corrugated electrode tapes and flat electrolyte and interconnect composite tapes are stacked up to form the MSOFC structure. The layers are bonded together in the green state by heating the polymer binder slightly above its glass transition temperature under a small weight. The bonded green structure is then heated according to a precise firing schedule to the sintering temperature to form the monolithic ceramic structure.

The performance of the MSOFC has improved significantly during the course of development. The limitation of this system, based on materials resistance alone without interfacial resistances, is 0.05 ohm-cm^2 area-specific resistance (ASR). The current typical performance of MSOFC single cells is characterized by ASRs of about 0.4 to 0.5 ohm-cm^2. With further development, the ASR is expected to be reduced below 0.1 ohm-cm^2, which will result in power levels greater than 2.5 W/cm^2.

SYSTEM PERFORMANCE

Because of the high temperature of operation of the MSOFC and the compact fuel cell design, systems that incorporate the MSOFC for power production are very simple. The high temperature combined with use of nickel in the fuel electrode allows internal reform of hydrocarbon fuels within the fuel channels, obviating the need for a separate fuel reformer. In addition, existing fuel logistics systems can be used with the MSOFC with essentially no modifications. Space-based systems that are required to regenerate the hydrogen fuel from the reaction product water are simplified by the fact that the MSOFC can use the same unit for power production and fuel regeneration. The high operating temperature of the MSOFC allows the waste heat to be rejected at a high temperature, thus minimizing the size of the heat rejection system. The MSOFC systems are flexible in terms of their ability to operate as an open cycle, closed cycle, or a combination of open and closed cycles.

Two types of systems are briefly described in the following paragraphs: (1) a power system for terrestrial vehicle propulsion using hydrocarbon fuel, and (2) an open-cycle, pulse-power system for use in space. Figure 1 is a schematic flow diagram of a 60 kWe vehicle propulsion power system designed to operate on a methanol/water solution. The fuel is evaporated using residual heat from the spent fuel system. The incoming fuel flows through an eductor where a fraction of the spent fuel is caused to recirculate to provide heating and sufficient water for the reform reaction. The remaining spent fuel flows to the spent fuel burner where it is combined with the air exhaust stream, and the heat from burning the spent fuel is used to preheat the incoming air. The preheated air is further heated by recirculating most of the hot air exhausted from the fuel cell. This air recirculation is possible because very little of the oxygen is used in the electrochemical reaction. The primary function of the air flow is to remove waste heat from the fuel cell core. Recirculating about two-thirds of the air minimizes the size of the air preheater heat exchanger. In terms of size and weight of components, the fuel cell and air preheater are approximately equivalent, and the other components are considerably smaller. All the components shown in this flow diagram are enclosed in a high-temperature insulated box, and other components such as the fuel pump, air blower, and control systems are essentially at room temperature.

The volume power density of this system is approximately 1 kW/L, so the 60 kWe system shown in figure 1 occupies about 60 L volume (~2 ft^3). Operation of the MSOFC system for vehicle propulsion will require tolerance to rapid changes in thermal gradients. When a fuel cell operates at full power, the temperature of the downstream region rises due to generation of waste heat. Operation of the fuel cell at low power produces a shallow temperature gradient because the quantity of waste heat is low. Vehicle driving profiles typically require rapid shifting from high power to low power and vice versa. Because the temperature gradients will change as the power level changes, the MSOFC materials must be able to withstand rapid temperature oscillations. The thin sections and honeycomb structure of the MSOFC are particularly adapted to these rapid temperature changes. The coefficients of thermal expansion of the four materials used in the MSOFC are well matched (ref. 5); thus, changes in temperature do not cause significant stresses between the layers.

Coupling a nuclear reactor with a MSOFC appears attractive for space-based pulse power systems. The MSOFC combines hydrogen and oxygen to produce the power pulse, and the product water is stored on board. Following a test power pulse, the fuel cell is run in reverse to regenerate the hydrogen and oxygen. A relatively small nuclear reactor provides the power input for the reverse operation. Reject heat from the reactor may be used to maintain the fuel cell in a "hot standby" mode for rapid response to demands for power.

The hydrogen and oxygen are stored as gases in tanks at elevated temperatures and pressures, as shown in figure 2. Emerging from the storage tank, the oxygen stream passes through a blower and is preheated by mixing with an oxygen recycle stream before entering the fuel cell. Similarly, the hydrogen passes through a blower and preheater before entering the fuel cell. Within the fuel cell, DC power is produced as oxygen is consumed and hydrogen is converted to water vapor. The heat generated in the process is rejected as the oxygen recycle stream passes through the radiator. After a reduction in temperature, the gaseous products are stored. A sliding seal (or rolling diaphragm) is used to separate reactants and products which are stored within the same tank.

The system can be operated in the reverse mode to regenerate the power capability. The same monolithic fuel cell modules can be run backwards for the regeneration: a separate electrolysis unit is not required. The length of time required for regeneration is determined by the size of the external power source. The overall efficiency of the system is attractive. The projected performance of the system is to recover 72% of the heat of reaction in the discharge mode and store 92% of the input electrical energy as chemical energy in the electrolysis mode. The overall round-trip electrical efficiency is projected to be 66%.

The open-cycle concept is much simpler in system design and operation. A simple once-through system that has excess hydrogen available for cooling the fuel cell and for providing the chemical energy for the electrochemical process is shown in figure 3. The waste heat is carried out of the fuel cell core with the hydrogen stream, and the hydrogen and product water are dumped overboard. The oxygen stream is recycled with only a small bleed stream to eliminate any impurities that might accumulate. The system components include heat exchangers to heat the incoming oxygen using waste heat from the fuel cell exhaust streams, an eductor to recycle the hydrogen stream, and the fuel cell. Other components include the insulated box, current collectors, and appropriate control systems.

This very simple system has application only in very special cases where very high power densities are needed and an essentially "unlimited" source of hydrogen is available. Specialized space power systems are the only currently known applications for such a system, and this concept offers an interesting example of a compact, high power density system for space. The power densities that can be achieved with the MSOFC in this application are shown in figure 4. The fuel cell power density is shown on the left y-axis, while the system power density is shown on the right y-axis. The fuel cell power density is very high because the fuel utilization is very low. Essentially pure hydrogen exists through the whole length of the fuel channels, and the average Nernst potential is about 1 V. For these calculations, the area-specific resistance was assumed to be 0.05 ohm-cm^2, which is expected to be achieved with further development of the MSOFC. An important feature of the system is the relationship between the fuel cell power density and the system power density. As the fuel cell power density becomes larger, the contribution of the balance-of-system begins to dominate the system weight. The fuel cell weight becomes small relative to the balance-of-system when the fuel cell power density exceeds about 20 kW/kg. For this system design, the system power density approaches

~4.5 kW/kg as an upper limit, and this power density is determined by the sizes of the heat exchangers required to heat the incoming hydrogen and oxygen and the insulating box for the high-temperature components.

MSOFC FABRICATION

The principal challenge to fabrication of the MSOFC structure is to match the sintering shrinkages of the four MSOFC materials: (1) the electrolyte, yttria-stabilized zirconia, (2) the interconnect material, strontium-doped lanthanum chromite, (3) the anode material, nickel-zirconia cermet, and (4) the cathode material, strontium-doped lanthanum manganite. The MSOFC structure is assembled while the tape-cast components are in an unfired (green), flexible state. The polymer binder in the tapes bond the tapes together as they are placed in contact and heated above the "glass transition" temperature of the polymer. The assembled structure is then appropriately supported and heated slowly to burn out the polymer. The structure is further heated to temperatures of about 1300 to 1400°C to sinter the materials and create permanent bonds at the points of contact. It is important that the shrinkages that occur during binder burnout and during sintering be precisely matched among the four materials. This matching of shrinkages has been accomplished satisfactorily during development of the MSOFC, and the results of this shrinkage matching are reported elsewhere (ref. 5).

One of the important objectives in development of the MSOFC has been reduction of the number of defects in the ceramic structure. Defects such as cracks allow the fuel and oxidant gases to mix, thus reducing the efficiency and, if the cross-leakage is severe, reducing the open-circuit potential. Defects such as non-bonds between the layers increases the overall fuel cell resistance because of the reduced cross-section of the conduction path. As the sintering shrinkages and the coefficients of thermal expansion have become better matched, the performance of the fuel cells have improved. For example, the improvement in open-circuit voltage with reduced number of cracks in the fuel cell is shown in figure 5. The large number of cracks during the early development stages of the MSOFC caused sufficient cross-leakage of fuel and oxidant to reduce the difference in oxygen potential across the electrolyte. Since the Nernst potential is proportional to the log of the ratio of oxygen partial pressure in the oxidant to that in the fuel, the open-circuit voltage decreases with increased cross-leakage. The current status of MSOFC development is such that essentially crack-free structures can be built and tested.

MSOFC PERFORMANCE

The performance of the MSOFC has approached the theoretical limit as a result of recent development efforts. The first MSOFC single cells had an area-specific resistance (ASR) of about 8 ohm-cm^2, and since that time the performance has improved dramatically to the present state-of-the-art ASR of about 0.4 ohm-cm^2. The theoretical limit of performance, based on materials resistances and elimination of all electrode/electrolyte interfacial resistances, is about 0.093 ohm-cm^2 for an electrolyte thickness of 50 μm. This ASR can be reduced to 0.05 ohm-cm^2 by reducing the electrolyte thickness to 25 μm. The interfacial resistances can be reduced with further development (1) by decreasing the spacing between conductive particles in the electrodes, (2) by increasing the thickness of the electrodes, and (3) possibly by placing a mixed electronic/ionic conductor at the electrolyte/electrode interfaces. These developments are expected to reduce the ASR to closely approach the bulk resistance limit.

The performance of multi-cell MSOFC stacks is significantly less attractive than the performance of single cells. Figure 6 shows the improvement in the performance of multi-cell stacks since the operation of the first stack in January 1986. While the performance improvement has been dramatic, it must be improved further to equal that of the single cells. The improvement in open-circuit potential is a result of improvements in fabrication methods, particularly in matching the sintering shrinkages of the four different MSOFC materials.

The difference between single cell and multi-cell performance is primarily due to interactions among the materials during the sintering process. A liquid-phase sintering aid is used to assist densification of the interconnect material. This sintering aid migrates throughout the MSOFC structure and affects the other materials, particularly the cathode. The cathode becomes dense and tends to migrate away from the electrolyte/cathode interface leaving voids in that critical area. This effect on the cathode reduces the performance of the multi-cell stacks.

Future needs for development of the MSOFC include: (1) a more easily sinterable interconnect material, (2) cathode materials that are more stable at the sintering temperature, (3) development of ancillary materials such as insulation, manifolds, cements, and current collectors, (4) optimization of MSOFC designs for specific applications, (5) development of MSOFC systems, and (6) quality control development, including improved control of source materials and development of nondestructive analysis methods for the MSOFC structure.

CONCLUSIONS

The feasibility of the MSOFC concept has been proven, and the performance has been dramatically improved. The differences in thermal expansion coefficients and firing shrinkages among the fuel cell materials have been minimized, thus allowing successful fabrication of the MSOFC with few defects. The MSOFC shows excellent promise for development into a practical power source for many applications from stationary power, to automobile propulsion, to space pulsed power.

ACKNOWLEDGMENT

This work was sponsored by the Defense Advanced Research Projects Agency of the U.S. Department of Defense under ARPA Order No. 4850. Argonne National Laboratory is operated for the U.S. Department of Energy under contract No. W-31-109-ENG-38.

REFERENCES

1. Fee, D. C., Steunenberg, R. K., Claar, T. D., Poeppel, R. B., and Ackerman, J. P., "Monolithic Fuel Cells," 1983 Fuel Cell Seminar Abstracts, Courtesy Associates, Inc., Washington, DC, p. 74, November 1983.

2. McPheeters, C. C., Dees, D. W., Dorris, S. E., and Picciolo, J. J., "Argonne Monolithic Solid Oxide Fuel Cell Fabrication," 1988 Fuel Cell Seminar Abstracts, Courtesy Associates, Inc., Washington, DC, p. 29, October 1988.

3. Onoda, G. Y. Jr., and Hench, L. L., *Ceramic Processing Before Firing*, John Wiley & Sons, New York, p. 411, 1978.

4. Richerson, D. W., *Modern Ceramic Engineering*, Marcel Dekker, Inc., New York, p. 206, 1982.

5. McPheeters C. C. et al., "Recent Advances in Monolithic Solid Oxide Fuel Cell Development," 23rd Intersociety Energy Conversion Engineering Conference, Vol. 2, Book No. 10272B, August 1988.

The submitted manuscript has been authored by a contractor of the U. S. Government under contract No. W-31-109-ENG-38. Accordingly, the U. S. Government retains a nonexclusive, royalty-free license to publish or reproduce the published form of this contribution, or allow others to do so, for U. S. Government purposes.

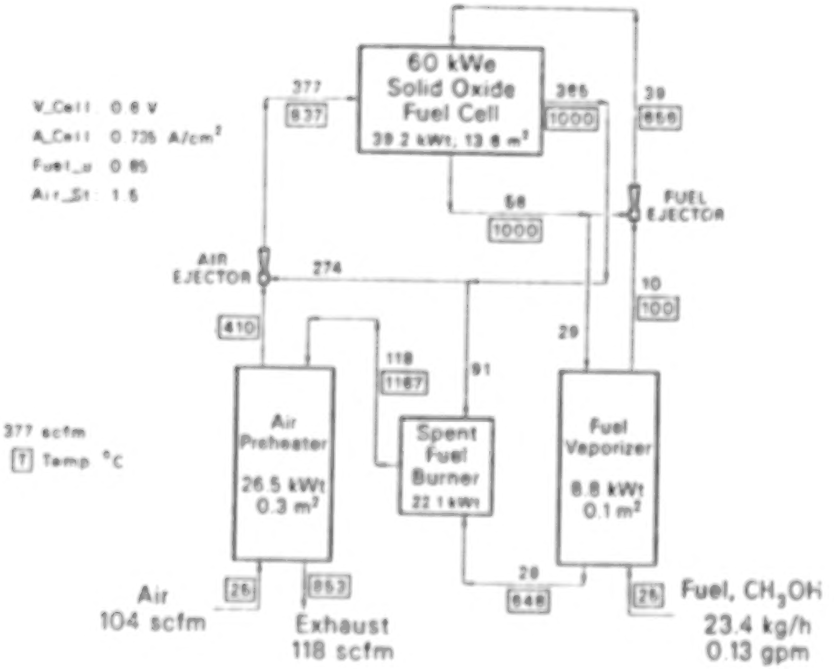
V_Cell: 0.6 V
A_Cell: 0.735 A/cm²
Fuel_u: 0.85
Air_St: 1.5
60 kWe
Solid Oxide
Fuel Cell
39.2 kWt, 13.6 m²
377
637
385
1000
39
656
58
1000
FUEL
EJECTOR
AIR
EJECTOR
274
10
100
410
118
1167
91
29
Air
Preheater
26.5 kWt
0.3 m²
Spent
Fuel
Burner
22.1 kWt
Fuel
Vaporizer
8.8 kWt
0.1 m²
377 scfm
? Temp °C
29
648
26
853
25
Air
104 scfm
Exhaust
118 scfm
Fuel, CH₃OH
23.4 kg/h
0.13 gpm

Figure 1. Methanol fueled MSOFC for vehicle propulsion.

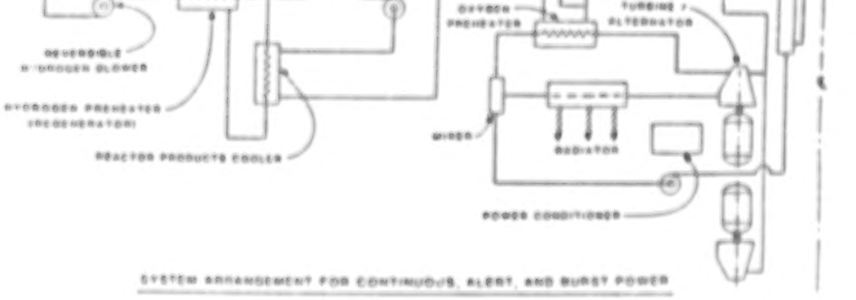
FUEL CELL SYSTEM
RANKINE SYSTEM
HYDROGEN / WATER STORAGE
OXYGEN / WATER STORAGE
RADIATOR
FUEL CELL STACK
REACTOR
SHIELD
H₂O
H₂
O₂
REVERSIBLE OXYGEN BLOWER
LPVG
OXYGEN PREHEATER
TURBINE / ALTERNATOR
REVERSIBLE HYDROGEN BLOWER
HYDROGEN PREHEATER (REGENERATOR)
REACTOR PRODUCTS COOLER
MIXER
RADIATOR
POWER CONDITIONER
SYSTEM ARRANGEMENT FOR CONTINUOUS, ALERT, AND BURST POWER

Figure 2. Space-based regenerative MSOFC system coupled with a nuclear reactor for pulse power.

The MSOFC Power System Is:

1) Simple in Design
2) All Solid State

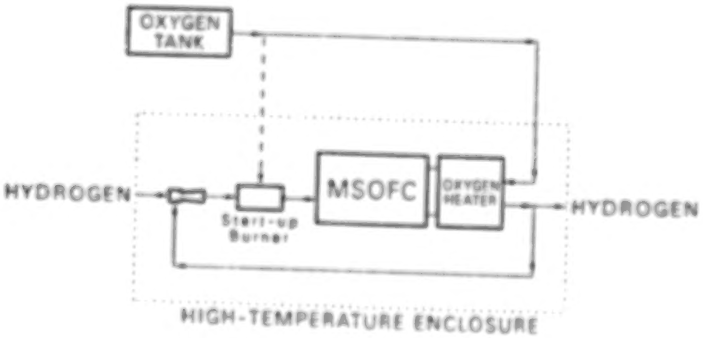
OXYGEN TANK
HYDROGEN
Start-up Burner
MSOFC
OXYGEN HEATER
HYDROGEN
HIGH-TEMPERATURE ENCLOSURE

Open-Cycle System Schematic

Figure 3. Simple open-cycle MSOFC system with no hydrogen regeneration and low fuel efficiency.

Monolithic Solid Oxide Fuel Cell
Open-Cycle System Power Densities
Can Exceed 4 kW/kg

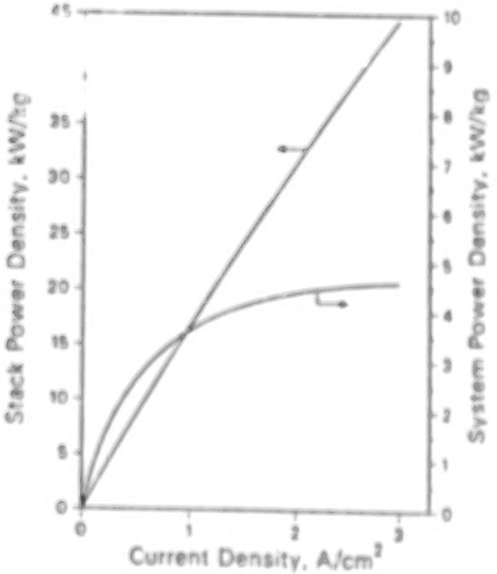

Figure 4. Stack and system power densities for a simple open-cycle space-based system.

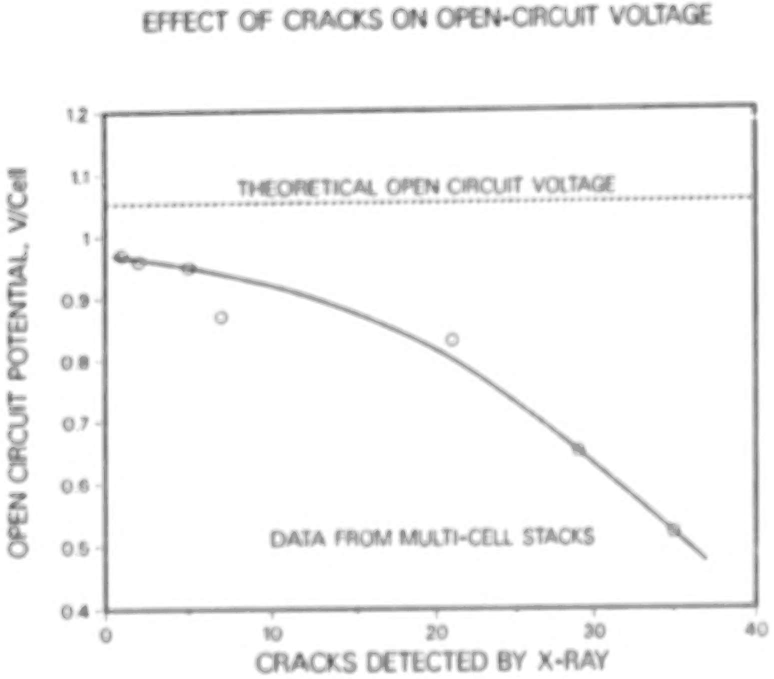

Figure 5. Improved MSOFC open-circuit voltage with reduction in ceramic defects.

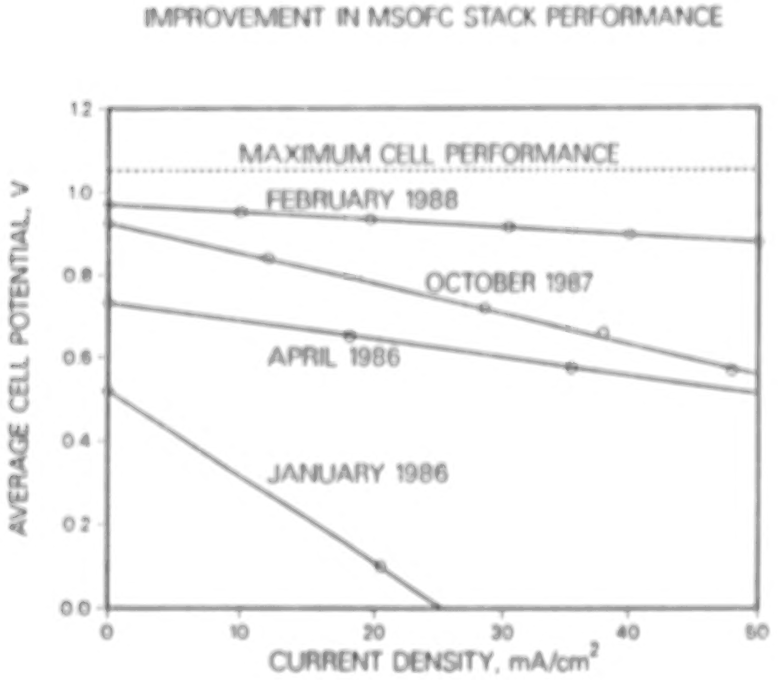

Figure 6. Improvement in multi-cell MSOFC stacks during development at Argonne.

THE ELECTROCHEMICAL GENERATION OF USEFUL CHEMICAL SPECIES FROM LUNAR MATERIALS*

Kan J. Tsai, Daniel J. Kuchynka and Anthony F. Sammells
Eltron Research, Inc.
Aurora, Illinois 60504

Electrochemical cells have been fabricated for the simultaneous generation of oxygen and lithium from a Li_2O containing molten salt (Li_2O-LiCl-LiF). The cell utilizes an oxygen vacancy conducting solid electrolyte, yttria-stabilized zirconia (YSZ), to effect separation between oxygen evolving and lithium reduction half-cell reactions. The cell, which operates at 700-850°C, possesses rapid electrode kinetics at the lithium-alloy electrode with exchange current density (i_o) values being $>60 mA/cm^2$. When used in the electrolytic mode, lithium produced at the negative electrode would be continuously removed from the cell for later use (under lunar conditions) as an easily storable reducing agent (compared to H_2) for the chemical refining of lunar ores. Because of the high reversibility of this electrochemical system, it has also formed the basis for the lithium oxygen secondary battery system which possesses the highest theoretical energy density yet investigated.

INTRODUCTION

The strategy being pursued for lunar ore refining is based upon electrochemical cells possessing the general configuration:

$$\text{Li alloy}/Li_2O\text{-LiCl-LiF molten salt}/\text{YSZ}/La_{0.89}Sr_{0.11}MnO_3$$

In practical electrolytic cells, lithium produced at the negative electrode would, after removal from the cell, be available for lunar ore refining via the general chemical reaction:

$$2Li + MO \longrightarrow Li_2O + M$$

where MO represents a lunar ore. Emphasis to this time has been on Fe_2O_3, TiO_2 and the lunar ore ilmenite ($FeTiO_3$), all of which have been shown chemically reducible by Li to give metals. The resulting Li_2O reaction product could then be removed from the solid-state reaction mixture by sublimation and reintroduced into the negative electrode compartment of the electrolytic cell to be electrolyzed again. Hence, this electrochemical approach provides a convenient route for the simultaneous generation of both metals and oxygen from lunar materials on the Moon's surface. It has previously been suggested that oxygen might be extracted from ilmenite by its initial chemical reduction by hydrogen, initially transported from Earth (ref. 1-3), and presumably requiring cryogenic storage on the Moon's surface. Other approaches discussed for the chemical reduction of lunar ores have included carbothermic reduction to give the desired metal (ref. 4,5). Previous work by others has also investigated the direct high temperature electrochemistry of simulated lunar materials (molten silicates), using platinum electrodes. Electrolysis of these melts demonstrated simultaneous oxygen evolution at the anode (ref. 6-10) and deposition of an impure metal-silicon alloy slag at the cathode (ref. 11-14). Nevertheless, this preliminary work showed feasibility for high temperature molten salt electrochemistry as an attractive approach for oxygen evolution and metal reduction from lunar type ores. In the approach being discussed here, oxygen evolution and lunar ore reduction are separated into distinct electrochemical and chemical steps. This strategy minimizes the opportunity for lunar ore originating impurities from entering the electrochemical cell and degrading performance.

---

*This work was supported by NASA Johnson Space Center under Contract No. NAS9-17991.

The reducing power of lithium is significantly greater than that of hydrogen. This fact can be summarized by the two general reactions:

$$H_2 + \tfrac{1}{2}O_2 \longrightarrow H_2O \qquad \Delta G = -68\text{kcal/mole} \ (25^\circ C) \qquad (1)$$

and

$$2Li + \tfrac{1}{2}O_2 \longrightarrow Li_2O \qquad \Delta G = -142\text{kcal/mole} \ (25^\circ C) \qquad (2)$$

The corresponding free energy of reaction between lithium and candidate metal oxides of interest at 1000°K are summarized in Table 1.

TABLE 1

	ΔG(kcal/mole)
$4Li + SiO_2 \rightarrow 2Li_2O + Si$	-28.0
$2Li + FeO \rightarrow Li_2O + Fe$	-53.9
$4Li + TiO_2 \rightarrow 2Li_2O + Ti$	-15.6
$6Li + Cr_2O_3 \rightarrow 3Li_2O + 2Cr$	-87.9

We estimate the free energy change associated with ilmenite reduction by lithium at 1000°K, corresponding to the overall reaction:

$$FeTiO_3 + 6Li \longrightarrow Fe + Ti + 3Li_2O \qquad (3)$$

to be $\Delta G = -62.2$kcal/mole. Hence, lithium would appear to be a sufficiently strong reducing agent for many of the transition metal oxides anticipated to be present on the Moon's surface.

The electrochemistry occurring in these cells possesses high reversibility and consequently has given us the opportunity to study the lithium/oxygen secondary battery. The overall electrochemistry occurring in this cell upon discharge/charge cycling can be represented by:

$$FeSi_2Li_x + \tfrac{1}{2}O_2(\text{air}) \underset{\text{charge}}{\overset{\text{discharge}}{\rightleftharpoons}} Li_2O(\text{in molten salt}) + FeSi_2 \qquad (4)$$

with overall capacity being dictated by the concentration of Li_2O that may be incorporated within the negative electrode compartment of this electrochemical cell. Although theoretical energy densities for a given battery system are often a poor indicator of the final practical energy density that might be achieved, it is of interest to note that the energy density for electroactive materials in the lithium-oxygen system calculates to 4082Wh/kg compared to 2211Wh/kg for the lithium-chlorine cell; the highest energy density secondary system investigated to this time. The significant technical observations to be discussed which make this an attractive secondary battery system are i) both electrodes possess high electrochemical reversibility,

ii) the anodic reaction upon cell charge involves the exclusive evolution of oxygen, and iii) a significant concentration of Li_2O can be incorporated into the Li_2O-LiCl-LiF ternary melt. A comparison of the lithium-oxygen secondary cell with other major conventions and advanced systems is shown in Table 2.

TABLE 2

Major secondary batteries for electrical energy storage in comparison to the lithium oxygen system

Battery System	Negative	Positive	OCP(V)	Theoretical Energy Density for Electroactive Matls. (Wh/kg)
Lead-Acid	Pb	PbO_2	2.0	238
Nickel-Cadmium	Cd	NiOOH	1.2	148
Nickel-Zinc	Zn	NiOOH	1.7	448
Zinc-Chlorine	Zn	Cl_2	2.12	829
Lithium-Iron Sulfide	Li(Al)	FeS	1.2	626
Sodium-Sulfur	Na	S	2.1	760
Lithium-Chlorine	Li	Cl_2	3.53	2211
Lithium-Oxygen	Li	O_2	2.3	4082

RESULTS AND DISCUSSION

Previous work performed in our laboratory (ref. 15) showed that the ternary molten salt system Li_2O-LiF-LiCl is an attractive candidate electrolyte for this electrochemical cell. The utility of this molten salt electrolyte was dependent, however, upon gaining some insight into the amount of Li_2O that could be accommodated in the LiF-LiCl ($70^m/o$) molten salt and its impact upon the resulting solid-liquidus curve. This was performed by progressively introducing Li_2O in 2-$5^m/o$ increments into a LiF-LiCl ($70^m/o$) binary mixture in a conventional conductivity type cell. After each Li_2O addition, the ternary molten salt mixture was initially heated to 550°C, at which temperature it became molten. The resulting molten salt ionic conductivity values were measured between stainless steel electrodes ($1cm^2$) placed 1.5cm apart during slow cell cooling so as to minimize interelectrode thermal gradients. The molten salt freezing point was detected by a dramatic decrease in measured ionic conductivity. The resulting solid-liquidus curve obtained for this ternary system is shown in Figure 1, which indicates that for Li_2O contents above $\simeq 18^m/o$ the molten salt goes into a two-phase region consisting of Li_2O ($18^m/o$),LiF ($24.6^m/o$),LiCl ($57.4\ ^m/o$) in direct contact with solid Li_2O. The important point here is that excess Li_2O could be introduced into the electrolyte cell and would not promote melt freezing.

Both half and full cell electrochemical measurements have been performed on this cell. Coulometric lithium deposition has been performed on both iron and iron silicide ($FeSi_2$) negative electrode substrates. Iron silicide was of interest since lithium deposition results in formation of a series of distinct electrochemically reversible lithium compounds up to the composition $FeSi_2Li_{10}$. This has not only permitted us to conveniently store lithium in the negative electrode compartment for the reversible lithium oxygen storage battery, but also acts as a substrate for wetting lithium, facilitating its later removal from the negative electrode compartment of the electrolytic cell. Preliminary current-potential characteristics of this electrode were performed in electrolytic cells possessing the general configuration shown in Figure 2. The charging current-potential curves for this cell (Figure 3) clearly show voltage plateaus associated with each ternary lithium compound. Electrode ki-

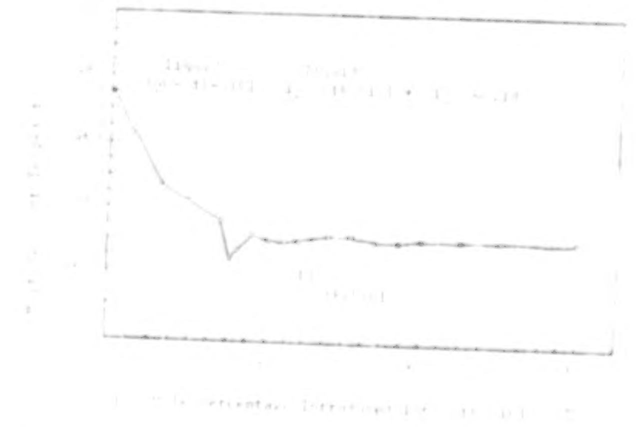

Figure 1. Solid-liquidus curve for Li_2O-LiF-LiCl molten salt as a function of Li_2O.

Figure 2. Schematic drawing of cell configuration used for the simultaneous electrolytic generation of lithium and oxygen. A) anode current collector; B) calcia or yttria stabilized zirconia; C) molten salt; D) $La_{0.89}Sr_{0.11}MnO_3$ anode; E) stainless steel or $FeSi_2$ cathode; F) furnace.

netics for this electrode were performed using a molten salt of composition Li_2O ($6.4^m/o$),LiF($28.1^m/o$),LiCl($65.5^m/o$) using $FeSi_2Li_x$ for the working and $SiLi_4$ for counter and reference electrodes. For voltage plateaus corresponding to the respective ternary alloys $FeSi_2Li_6$, $FeSi_2Li_8$ and $FeSi_2Li_{10}$ cyclic voltammetry scans (50mV/s) were performed ±200mV from its initial open circuit potential (OCP) with respect to the $SiLi_4$ reference. A representative current-overpotential curve is shown in Figure 4, which was analyzed by use of the Allen-Hickling relationship:

$$\log \frac{i}{e^{\alpha\eta F/RT} - 1} = \log i_o - \frac{\alpha\eta F}{2.303RT} \qquad (5)$$

where i_o was the exchange current density from which a direct estimation of relative electrode kinetics were determined, η was the electrode overpotential, α the transfer coefficient and the other symbols had their usual significance (ref. 16). Exchange current densities (i_o) were obtained from the intercept by plotting η versus $\log \frac{i}{e^{\alpha\eta F/RT} - 1}$. The dependency of i_o upon both cell temperature and lithium alloy composition is summarized in Table 3. These current-voltage measurements clearly showed the presence of rapid electrode kinetics at the negative electrode suggesting that this Faradaic process will not be the rate limiting process in the finally developed electrochemical cell.

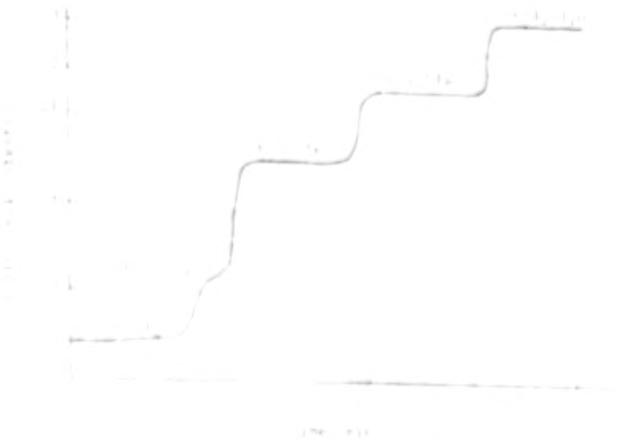

Figure 3. IR free charge curve for $FeSi_2$ in $28.5^m/o$ LiF, $66.5^m/o$ LiCl and $5^m/o$ Li_2O at 650°C vs $La_{0.89}Sr_{0.11}MnO_3/Pt$ (air). Current density $10mA/cm^2$.

Figure 4. Current-overpotential curve for the cell

$FeSi_2Li_{10}/Li_2O\text{-}LiF\text{-}LiCl/SiLi_4$

at 800°C. Initial open circuit potential -71mV with respect to $SiLi_4$ reference. Scan rate 50mV/sec.

TABLE 3

Cell Temperature °C	Measured Exchange Current Density i_o (mA/cm^2)		
	$FeSi_2Li_{10}$	$FeSi_2Li_8$	$FeSi_2Li_6$
650	49.7	50.6	43.7
700	54.5	54.7	50.9
750	56.0	57.2	55.6
800	64.5	65.7	58.2

In fully developed electrolytic cells we must facilitate the convenient removal of faradaically deposited lithium at the negative electrode. One of the major obstacles to achieve this is related to the high surface tension of Li at 700°C (320 dynes/cm) which compares to Hg (400 dynes/cm) at room temperature. Deposited lithium resident in a porous electrode structure, in the absence of wetting, can as a consequence prove difficult to physically remove via a proximate orifice. We have found, however, that both $SiLi_x$ and $FeSi_2Li_x$ can act as effective substrate sites for wetting faradaically deposited lithium, thereby providing a strategy for the subsequent continuous removal of lithium from the electrolytic cell. A schematic of the experimental arrangement used for comparing approaches for lithium removal is shown in Figure 5. Lithium could be conveniently removed from the cell by application of ≈5psi into the lithium chamber C, thereby enabling its transfer into glass trap D. In the event of lithium/molten salt mixtures being formed in the electrochemical cell, we have found that effective segregation into two distinct phases can be achieved if the stainless steel transfer tube between the electrolytic cell and lithium storage compartment is initially silicided to form a thin coating of $FeSi_2$. Subsequent reaction of this thin coating with lithium to give $FeSi_2Li_x$ will provide the necessary wetting characteristic necessary for promoting preferential lithium migration from the electrolytic cell.

Figure 5. Schematic diagram for simulated lithium removal process.
C) lithium containing chamber; D) lithium collecting chamber;
F) furnace; L) lithium; P) pressure gauge

As we have previously discussed, lithium is a strong reducing agent which should in principle, be able to reduce simulated lunar ores to the corresponding metal. This has been examined by investigating direct reaction between lithium and the respective metal oxides TiO_2, Fe_2O_3 and $FeTiO_3$. Here, thermal analyses were performed under both argon and vacuum (~100μ). Lithium and the metal oxide of interest were initially placed into a small boron nitride crucible located inside a 3/4" Swagelock union used as the reaction chamber. A chromel alumel thermocouple was placed in direct contact with the reaction mixture. Because of the anticipated high reducing ability of lithium, only 0.02g was used for each reaction with an excess of metal oxide being present. The reaction chamber was heated at 5°C/min. The inception of solid-state reaction was manifested by a rapid temperature increase in all cases investigated, indicating the reaction to be highly exothermic and irreversible. Thermal analyses for respectively Fe_2O_3 and TiO_2 are shown in Figure 6 A and B. The reaction product between Li and Fe_2O_3 was clearly shown to be elemental iron and could be conveniently removed with a magnet. Analysis of the reaction mixture between Li and TiO_2 was determined by initially dissolving with 37^w/o HCl. Here, unreacted TiO_2 was insoluble, where Ti became dissolved as $TiCl_3$ to give a dark blue solution. Quantitative determination of elemental Ti was then performed spectrophotometrically. Based upon the initial Li present in the reaction mixture, approximately 80% participated in promoting TiO_2 reduction to Ti. Temperatures experimentally observed for the inception of these reactions are summarized in Table 4 together with the corresponding calculated heat of reaction at each respective temperature.

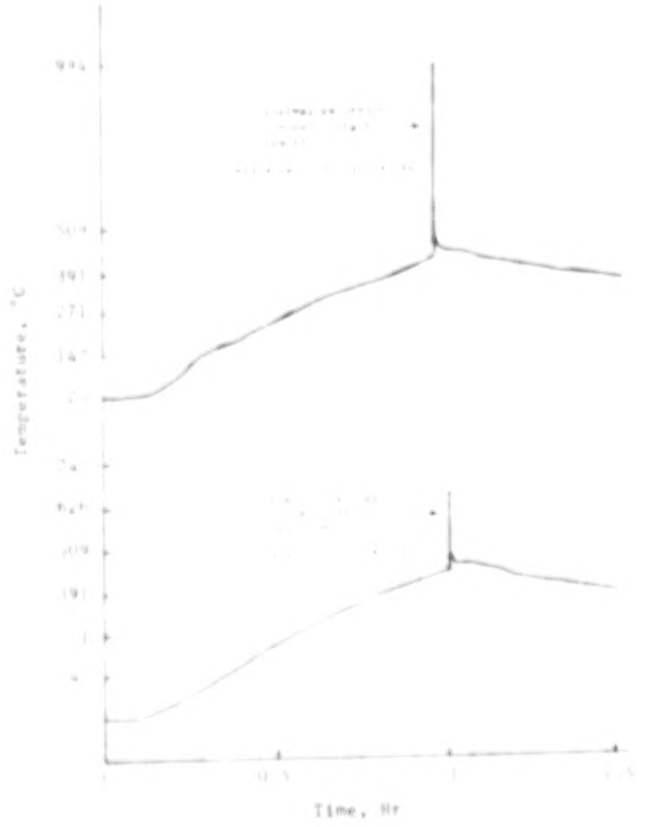

Figure 6. Thermal analysis for detection of solid-state reaction temperature between Li and Fe_2O_3 (excess) A, and TiO_2 (excess) B, under argon.

This electrochemical technology, as we have already discussed, is also compatible for a high energy secondary battery. Initial work (ref. 17) towards this goal focused upon electrochemical cell configurations analogous to that shown in Figure 2

TABLE 4

Experimentally observed temperatures and heat of reaction for the inception of reaction between lithium and the metal oxide of interest.

Metal Oxide	Temperature for Inception of Solid-State Reaction, °C	Heat of Reaction kcal/mole, Calc'd at Temperature
TiO_2	457	-71.6
Fe_2O_3	440	-244.8
$FeTiO_3$ (ilmenite)	432	--
Fe_2O_3+TiO_2 (1:1)	428	-157.2

where maintenance of an inert (Ar) atmosphere in the negative electrode component could be conveniently achieved (ref. 18). A preliminary charge-discharge curve for this type cell using a $FeSi_2Li_x$ negative electrode is shown in Figure 7. Again, the voltage plateaus observed correspond to the reversible formation of ferro silicon lithium alloys. Furthermore, it was found during cell charge that the volume of oxygen generated was in fact Faradaic, demonstrating that even in direct contact with halide containing molten salt, the solid electrolyte remains an exclusive oxygen anion conductor.

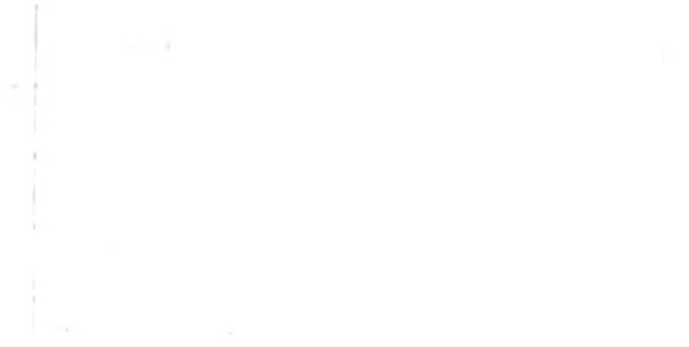

Figure 7. IR-free charge-discharge curve for the cell Li_xFeSi_2/(52.5-23.6-23.9)^m/o LiCl-LiF-Li_2O/ZrO_2(5^w/o CaO)/$La_{0.89}Sr_{0.11}MnO_3$/Pt at 20mA/cm^2 (at negative electrode). Total cell resistance 24Ω. Temperature 650°C.

For practical reversible lithium/oxygen batteries for terrestrial applications, however, we must identify a design which will enable us to operate in the atmosphere. This has been addressed by fabrication of small prototype cells possessing the general design shown in Figure 8. The design is based upon a 5cm high YSZ crucible possessing respective inside and outside diameters of 2.1 and 2.35cm (total volume 19ml). Cells were fabricated in the partially charged state using $FeSi_2Li_8$ as the negative electroactive material. Current collection from this electrode was via an aluminized nickel chromium alloy (Ni (76%), Cr (16%), Al (4.5%), Fe (3%), Y (trace), Haynes Alloy 214). The $La_{0.89}Sr_{0.11}MnO_3$ oxygen electrode was initially prepared (ref. 19) from a 15^w/o suspension in polyvinyl alcohol-ethylene glycol of the appropriate stoichiometric metal nitrates. Current collection from this region was via a Pt wire initially tightly coiled in this area. Synthesis of the perovskite electrocatalyst was achieved by heating in the atmosphere to ≈1000°C for 1h. Protection of the negative electrode compartment from direct contact to the atmosphere was achieved using a machined alumina cover (Cotronics, Inc.) whose residual porosity was removed by use of a coating of high density ceramic cement (Sauereisen #8), followed by curing at

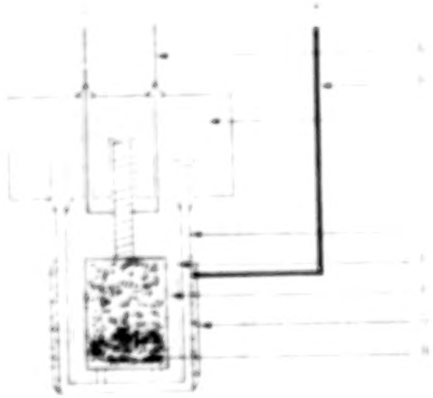

Figure 8. Schematic design of the lithium/oxygen secondary storage cell discussed in the text. A) current collector nickel-chromium (80:20) (-); B) platinum current collector (+) tightly wound around YSZ crucible; C) machined alumina cap; D) YSZ O^{2-} conducting solid electrolyte; E) zirconia felt separator; F) molten salt containing 66.5^m/o LiCl, 28.5^m/o LiF and 5^m/o Li_2O; G) $La_{0.89}Sr_{0.11}MnO_3$ electrocatalyst; H) $FeSi_2Li_8$ negative electrode

90°C for one day.

In partially charged cells fabricated here, the negative electrode compartment initially contained a molten salt of composition LiCl (66.5^m/o),LiF (28.5^m/o),Li_2O 5^m/o). This cell was operated in the atmosphere by initially heating to 600°C, at which temperature the open-circuit potential became 2.2V. Between 650° and 800°C the overall cell resistance decreased from 47Ω to 3.9Ω. This reflected the improved O^{2-} conductivity for the solid electrolyte at higher temperatures. E_a was found to be 16kcal/mole, similar to literature values (ref. 20). Current-potential and discharge curves for this cell are shown in Figure 9 (A and B).

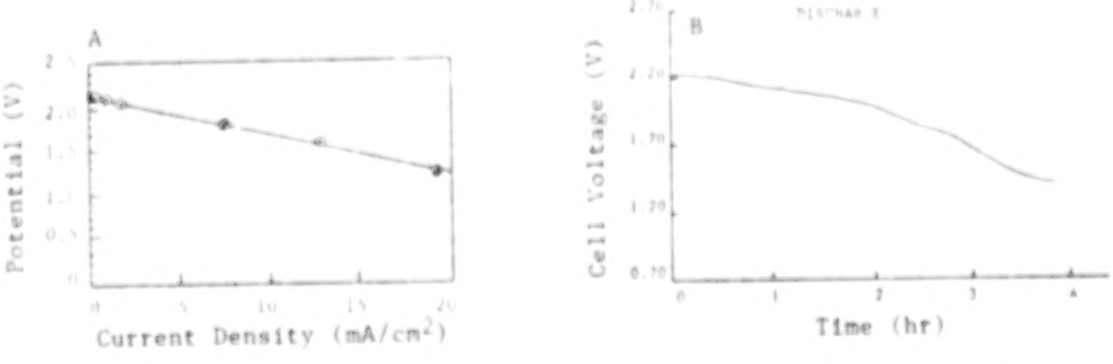

Figure 9. Current-potential and discharge curve for the lithium/oxygen cell at A) 800°C (R_{cell} = 3.9Ω) and B) 850°C at a C/50 rate (5.3mA/cm^2).

The above discussed results demonstrate that this electrochemical technology is evolving into a practical option for both the generation of chemical species on the

Moon's surface and as a high energy secondary battery for either terrestrial or lunar applications.

REFERENCES

1. H. P. Davis, Eagle Engin. Report #EE1 83-63, Houston (1983).
2. M. A. Gibson and C. W. Knudsen in "Lunar Bases and Space Activities of the 21st Century," NASA, 1984, p. 26.
3. E. Kibler, L. W. Taylor and R. J. Williams in "Lunar Bases and Space Activities of the 21st Century," NASA, 1984, p. 25.
4. W. C. Phinney, et. al., in "Space Based Manufacturing from Nonterrestrial Materials, Amer. Inst. of Aeronautics and Astronautics," New York (1977).
5. A. H. Cutler in "Lunar Bases and Space Activities of the 21st Century," NASA, 1984, p. 22.
6. K. W. Semkow and L. A. Haskin, Geochim. Cosmochim. Acta, 49, 1897 (1985).
7. K. W. Semkow and L. A. Haskin, Abstracts to Lunar Planet Sci., XVI, (1985) p. 761.
8. A. Ghosh and T. B. King, Trans. Metall. Soc., AIME, 245, 145 (1969).
9. J. K. Higgins, Glass Technol., 23, 90 (1982).
10. J. K. Higgins, Glass Technol., 23, 180 (1982).
11. D. S. Kesterke, U.S. Dept. of Interior Bureau of Mines Report of Invest. RI-7587, 1971.
12. D. J. Lindstrom and L. A. Haskin in "Space Manufacturing Facilities 3," T. Grey and C. Krop, Eds., Amer. Inst. Aeronautics and Astronautics, New York, 1979.
13. W. F. Carroll, Jet Propulsion Laboratory Report 83-36, 1983.
14. R. H. Lewis, D. J. Lindstrom and L. A. Haskin, Abstracts to Lunar Planet Sci., XVI, 1985, p. 489.
15. A. F. Sammells and K. W. Semkow, J. Power Sources, 22, 285 (1988).
16. P. A. Allen and A. Hickling, Trans. Faraday Soc., 53, 1626 (1957).
17. K. W. Semkow and A. F. Sammells, J. Electrochem. Soc., 134, 2084 (1987).
18. K. W. Semkow and A. F. Sammells, J. Electrochem. Soc., 134, 2088 (1987).
19. H.-M. Zhang, Y. Teraoka and N. Yamazoe, N. Chem. Lett., 665 (1987).
20. T. H. Etsell and S. N. Flengas, Chem. Rev., 70, 339 (1970).

A NEW CONCEPT FOR HIGH-CYCLE-LIFE LEO: RECHARGEABLE MnO_2-HYDROGEN

A.J. Appleby, H.P. Dhar, Y.J. Kim and O.J. Murphy
Center for Electrochemical Systems and Hydrogen Research
TEES-Texas A&M University
College Station, Texas 77843

The nickel-hydrogen secondary battery system, developed in the early 1970s, has become the system of choice for geostationary earth orbit (GEO) application. However, for low earth orbit (LEO) satellites with long expected lifetimes the nickel positive limits performance. This requires derating of the cell to achieve very long cycle life. A new system, rechargeable MnO_2-Hydrogen, which does not require derating, is described here. For LEO applications, it promises to have longer cycle life, higher rate capability, a higher effective energy density, and much lower self-discharge behavior than those of the nickel-hydrogen system.

INTRODUCTION

Space power systems designed for continuous high-power-output applications have most commonly been based on the use of photovoltaic panels. Since in all orbits satellites are subjected to a greater or lesser number of eclipses, a reliable means of energy storage and power load-leveling is required using reliable, maintenance-free secondary batteries. In the early 1970s, nickel-cadmium was the only proven long-lived secondary battery for use in space. Most of its long-term applications were in GEO communications satellites, for which there are two 45-day eclipse periods per year and one eclipse per eclipse-day in typical orbits. The eclipses are of variable duration, and reach a maximum of 1.2 h at the middle of the eclipse period. Over a ten-year satellite lifetime, a total of about 900 cycles are therefore required, varying from a maximum of medium discharge (60% depth of discharge, DOD) at the C/2 rate for 1.2 h, to shallow discharge, 60% DOD being a precautionary choice for long lifetime and reliable operation. Typical aerospace Ni-Cd cells can easily exceed 2000 cycles under these cycling conditions, but in a battery their energy density is little better than 20 $Wh\text{-}kg^{-1}$. In view of the importance of battery weight in determining overall power system weight, hence incremental satellite structural weight , new battery concepts offering higher specific energy were explored. As an illustration of the battery contribution to power system weight, state-of-the-art deployable photovoltaic (PV) panels have a specific power of 55 $W\text{-}kg^{-1}$, whereas the Ni-Cd battery under the above discharge conditions has a specific power of 16.7 $W\text{-}kg^{-1}$. Thus, 18.2 kg of PV array is required to produce a continuous 1 kW output, with an additional 1.2 kg (three-axis stabilization) to charge an 80% efficient battery over 22.8 h per eclipse-day, discharging in 1.2 h with a power output of 1 kW. Based on 16.7 $W\text{-}kg^{-1}$, such a battery would weigh 60 kg, thus demonstrating the driving force for reducing battery weight.

HIGH-ENERGY-DENSITY SATELLITE BATTERIES

The first attempt to reduce battery weight was the development of a regenerative fuel cell/electrolyzer (RFC) in the 1960s [1]. This consisted of a thin, lightweight pressure vessel containing pure noble metal negative and positive electrodes of fuel cell type, with a separator containing KOH electrolyte. A flexible sealed divider cut the pressure vessel into two volumes in the ratio 2 : 1 to store hydrogen produced at the negative and oxygen at the positive. The gases were recombined at the same electrodes. The system should be capable of many deep-discharge cycles, with indefinite cycle-life at the hydrogen electrode, and long life at the oxygen electrode provided that suitable electrocatalysts (e.g., gold-iridium) are used. A calculation shows that 54 Wh/kg is obtainable [2], assuming an Inconel 718 pressure vessel with a safety factor of 4. This is over twice the value for Ni-Cd. However, the state-of-the-art electrocatalyst technology could not offer a round-trip efficiency greater than about 50% due to oxygen electrode polarization. More importantly, the storage system was subject to cross-leaks, which limited reliability, lifetime, management of the excess water produced on discharge and consumed on charge, and proved to be a problem. In spite of these drawbacks, an updated version of this system using more recent technology may still have advantages for certain applications [2].

To avoid cross-leaks and electrolyte management problems, attention was transferred to metal-oxygen battery concepts. These can in principle show high energy density (for example, the zinc-oxygen couple has a practical energy density of 600 Wh-kg^{-1}), and the open volume of the pressure vessel (about 60% of the weight of the RFC) is small, since only oxygen storage is required. In consequence, zinc-oxygen systems (which do not have a water-mangement problem since the dicharge product is simply zinc oxide) were estimated to have practical energy densities on the order of 90 Wh-kg^{-1} [3]. However, like all alkaline zinc systems in stationary electrolyte, the negative showed dendrite formation and shape-change, resulting in limited cycle-life. The zinc electrode can also react explosively with excess oxygen on overcharge, which is accompanied by drying out. Finally, while the coulombic efficiency of the zinc-oxygen system is good, the oxygen electrode charge-discharge characteristics limit voltage efficiency to 60%. Since the corresponding cadmium system [3] has only the advantage of cycle life over zinc-oxygen, with a considerably poorer energy density, attention focused on metal-oxide/hydrogen systems, specifically nickel-hydrogen, which combined the best electrodes of the Ni-Cd and RFC.

THE NICKEL-HYDROGEN SYSTEM

The Ni-H_2 battery combined the two electrodes from the Ni-Cd battery and the RFC with the best electrochemical characteristics. Both operate close to reversibility, and give high coulombic efficiency. The battery was first described in the patent literature [4], and was developed from 1970 onwards, primarily at Comsat Laboratories [5]. No attempt was made to use specially-developed components for the battery. Compared with zinc-oxygen, it was immediately obvious that the nickel-hydrogen system would be conservative from the viewpoint of energy density. Aerospace Ni-H_2 positives of conventional construction have a typical capacity of 0.11 Ah/g, which is perhaps only 20% of that of a zinc negative, and hydrogen negative systems require twice the container volume and weight than those using oxygen positives. While a lightweight design, with a minimum container safety factor, might achieve 55 Wh-kg^{-1}, a more practical figure is 45 Wh-kg^{-1} on the single-cell level [5].

The Ni-H_2 system has no problems of electrolyte management, since the overall cell reaction [$NiOOH + 1/2H_2 \Rightarrow Ni(OH)_2$] does not involve formation or consumption of free water. This represents an advantage over both the RFC and the Ni-Cd system. The hydrogen electrode operates under benign conditions, at high hydrogen pressures (up to several hundred psi) and with maximum current densities of about 40 mA/cm^2 at the C rate. There is no evidence of change of hydrogen electrode performance with time under normal operating conditions. While the nickel electrode has an enviable record of longevity, it is still the life-limiting element in the battery. Since the nickel electrode operates in a starved electrolyte environment, any electrolyte loss from the separator can cause cell failure. With chemically-impregnated aerospace electrodes, failure occurred at about 2500 cycles under GEO cycling conditions with 50% overcharge per cycle. Corrosion of the nickel sinter, with consequent consumption of water, was identified as the cause of failure [6]. Improved lifetimes (to about 5000 cycles) were observed with under-impregnated electrodes, and with electrochemically impregnated electrodes [7], which have a more uniform distribution of active nickel hydroxide in the sinter structure [6].

On cycling, swelling of the nickel electrodes occurs, resulting from volume changes in the active material. Corrosion of the sinter in effect produces more active material, but the internal stresses created cause progressive breakdown of the sinter by the rupture of the "necks" between individual nickel particles. Since the electronic pathways through the sinter are thereby compromised, capacity slowly falls after going through a maximum early in life. Eventually, breakdown is total, and the cell ceases to function, even if electrolyte losses are made up. The situation is improved by using lower active material loadings, and by operating the electrodes at lower depths of discharge, keeping overcharge to a minimum. This demonstrates the effect of rate on cycle life.

For LEO applications, charge/discharge rates are not only much higher than those for GEO, but a far larger number of cycles is required. In an equatorial orbit, sunlight is 0.9 h, and the eclipse period is 0.6 h, with one charge-discharge cycle per orbit, or 5840 cycles per year. Consequently, for a guarantee of a ten-year lifetime, over 100,000 cycles would have to be reliably demonstated in laboratory testing. Thus far, 8000-12,000 cycles can be routinely demonstrated with low-loading, electrochemically impregnated electrodes. One aspect of recent work has been the effect of initial electrolyte concentration on cycle-life. It has been shown that life is at a maximum at a starting concentration of 26% KOH, when about 30,000 LEO cycles can be achieved with derated electrodes [8]. This seems to suggest that two different processes control electrode lifetime, one perhaps being charge acceptance of the nickel positive, which is favored at higher electrolyte concentrations, and the limiting effects of sinter corrosion, which also become more marked at high concentrations. However, in spite of this work, it would appear that the nickel electrode, at least in its present form, is marginal for long-term LEO use.

THE RECHARGEABLE MnO_2 POSITIVE

Electrolytic manganese dioxide has only a limited charging ability (about 50% of the first electron) [9]. However, in recent years a highly rechargeable form of MnO_2 has been demonstrated, in which both electrons can be reversibly charged and discharged. This consists of a material doped with bismuth (1-5 atom %), with birnessite structure [10-12]. It can be subjected to many thousands of rapid cycles (at the 12C rate in thin electrodes) and still shows no noticeable degradation in perfomance (Figure 1). It is quite indifferent to overcharge (no formation of soluble species) and to overdischarge. Unlike electrolytic MnO_2, both electrons discharge in the same potential range, giving a very flat discharge plateau and a more useful capacity to the voltage cut-off point, as Figure 2 shows for a cell with a zinc negative. In a benign environment (i.e., in the absence of certain impurities in the electrolyte) 85% of the two-electron capacity can be recovered over an indefinite number of cycles. Like Ni-H_2, MnO_2-H_2 has no water mangement problems, since the overall cell reaction is $MnO_2 + H_2 \Rightarrow Mn(OH_2)$. Finally, overall efficiency is estimated to be 78% (similar to Ni-H_2), and heat dissipation has similar characteristics to those of Ni-H_2.

At first sight, the proposal of using the modified MnO_2 positive combined with a hydrogen electrode does not make much sense, since the couple has a comparatively low voltage compared with that of nickel hydrogen (average plateau potential at LEO rates is approximately 0.7 V versus hydrogen at an average pressure of 24 atm). However, the low potential has certain operational advantages that are conducive to long life and low corrosion rates. In addition, since the modified MnO_2 positives can be operated at a nominal 85% of their two-electron capacity in long-term cycling, even at high rates, the positives are much lighter and have smaller volumes than nickel electrodes. Finally, microcalorimeter measurements (Figure 3) have established that the rate of the self-discharge reaction between MnO_2 and compressed hydrogen is much less than that for NiOOH. The mild corrosion environment allows the use of graphite powder additive as an electronic conductor in Teflon-bonded electrodes. With a material doped with 2 atom % bismuth, containing 15 wt % graphite and 7 wt % Teflon binder, the specific coulombic yield of the positive mix is 0.43 Ah/g to 85% DOD. Applied to a screen similar to those used for hydrogen electrodes, this value is reduced to 0.249 Ah/g.

COMPARISON BETWEEN MODIFIED MnO_2-H_2 AND Ni-H_2 FOR LEO USE

Table 1 shows a breakdown of component weights in a Ni-H_2 cell with a nominal capacity of 38.5 Ah (to 1.0 V at 23°C). The volume of the Inconel 718 container (with safety factor of 4) has been arranged to contain 38.5 Ah of hydrogen between 41 and 7 atm. To ensure very long cycle life under LEO conditions, the positive electrodes in such a system must be derated, typically to 40% of capacity. This requires a larger stack weight and volume, since the number of positives, negatives, separators, and gas streams, together with the total electrolyte volume, must be increased by 2.5. In consequence, the container weight and volume must be corresopondingly increased. Overall, the LEO Ni-H_2 cell has an effective specific energy of 22.2 Wh/kg (33.1 Wh/l), whereas the baseline Ni-H_2 has values of 44.9 Wh/kg and 51 Wh/l.

The final column contains the corresponding breakdown for LEO MnO_2-H_2. It can be seen that the smaller weight and volume of the positives results in a lighter and more compact cell than baseline Ni-H_2, although its specific energy is degraded by its lower operating voltage. However, in the LEO application it offers a specific energy of 32.6 Wh/kg, almost 50% higher than the purpose-designed Ni-H_2 cell with derated electrodes, intended for the same application. On a Wh/l basis, both systems have the same practical energy density.

CONCLUSIONS

The proposed modified MnO_2-H_2 cell operating at 0.7 V (nominal), with electrodes operating at 85% of two-electron capacity has the same volume energy density as Ni-H_2 operating with positives derated to 40% of capacity to achieve 25,000 or more LEO cycles. Its energy density on a weight basis is 50% greater (32.6 Wh/kg). The relatively low operating potential of the MnO_2 positive means that it operates in a mild environemt from the viewpoint of corrosion, ensuring long life with graphite as an electronically conducting element in the structure. Microcalorimeter studies have demonstrated a low self-discharge rate for the positive. In view of the above, and taking into account the difficulty of making nickel positives that can reliably offer 50,000 or more cycles, the secondary MnO_2-H_2 system deserves serious consideration for LEO use.

REFERENCES

1. Klein, M.; Costa, R.L.: "Electrolytic Regenerative H_2-O_2 Secondary Fuel Cells,", Proc. Space Technology and Heat Transfer Conf., Los Angeles, CA, 1970, American Society of Mechanical Engineers, New York, 1970, 70-Av/SpT-39.

2. Appleby, A.J.: *J. Power Sources* **22**, 377 (1988).

3. Klein, M.: Proc. 7th IECEC, Nat. Inst. Chem. Eng., Washington, D.C. 1972, p.729017.

4. Tsenter, B.I.; Sergeev, V.M.; Kloss, A.I.: U.S. Patent 3,669,744 (1972).

5. Dunlop, J.D.; Van Ommering, G.; Earl, M.W.: in D. H. Collins, ed., "Power Sources 6," Academic Press, London, 1977, p. 231.

6. Appleby, A.J.; Crepy, G; Feuillade, G.: Final Report, INTELSAT Contract No. IS-611, Comsat Laboratories, Clarksburg, MD, 1975.

7. Beauchamp, R.: U.S. Patent 3,653,067 (1972).

8. Lim, H.S.; Verzwyvelt, S.A.: *J.Power Sources* **22**, 213 (1988).

9. Kordesch, K.; Gsellman, J.; Peri, M.; Tomantschger, K; Chemelli, R.: *Electrochim. Acta* **26**, 1495 (1981).

10. Yao, Y.J.; Gupta, N; Wroblowa, H.S.: *J. Electroanal. Chem.* **223**, 107 (1987).

11. Wroblowa, H.S.; Gupta, N.: *J. Electroanal. Chem.* **238**, 93 (1987).

12. Dziecinch, M.A.; Gupta, N.; Wroblowa, H.S.: *J. Electrochem. Soc.* **135**, 2416 (1988).

TABLE I: CELL WEIGHT BREAKDOWN IN GRAMS

Component	Nominal Ni-H_2	LEO Ni-H_2	LEO MnO_2-H_2
Positives	348.6	870.5	154.4
Hydrogen Electrodes	72.0	180.0	72.0
Separators	35.1	87.8	35.1
Gas Screens	8.0	20.0	8.0
Electrolyte	159.0	397.5	159.0
Stack Total	622.7	1555.8	428.5
Center Rod and Insulator	14.3	35.8	14.3
Busbars and Tabs	41.4	41.4	41.4
Endplates	34.0	34.0	34.0
Nuts, Washers	4.6	4.6	4.6
Terminal Conductors	79.0	79.0	79.0
Internal Hardware	173.3	194.8	173.3
Pressure Shell	179.0	275.4	170.5
Weld Ring	35.0	35.0	35.0
Compression Seals	18.4	18.4	18.4
Container	232.4	328.8	223.9
Total Cell Weight	1028.4	2079.4	825.7
Total Cell Volume (ml)	836.0	1286.0	805.0
Specific Energy (Wh/kg)	44.9	22.2	32.6
Specific Energy (Wh/l)	51.0	33.1	33.5

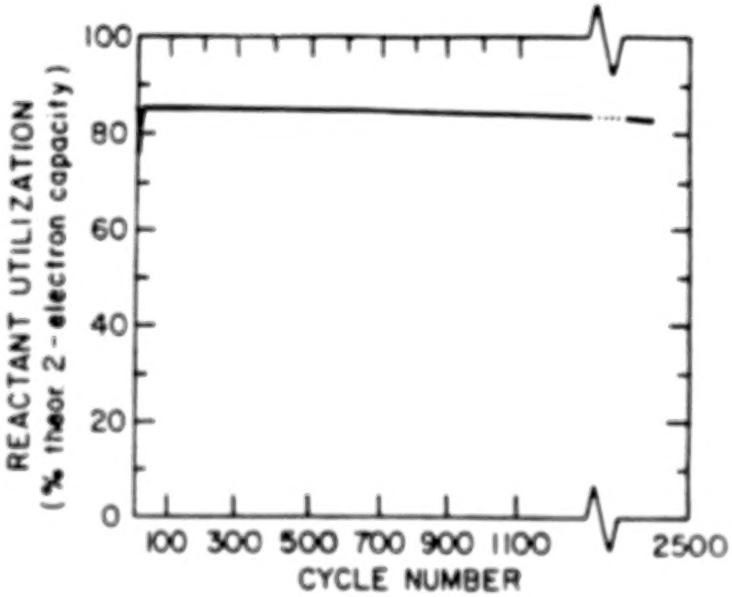

Figure 1: Reactant utilization versus cycle number for a modified MnO_2 electrode cycled at 6C in 9M KOH at room temperature

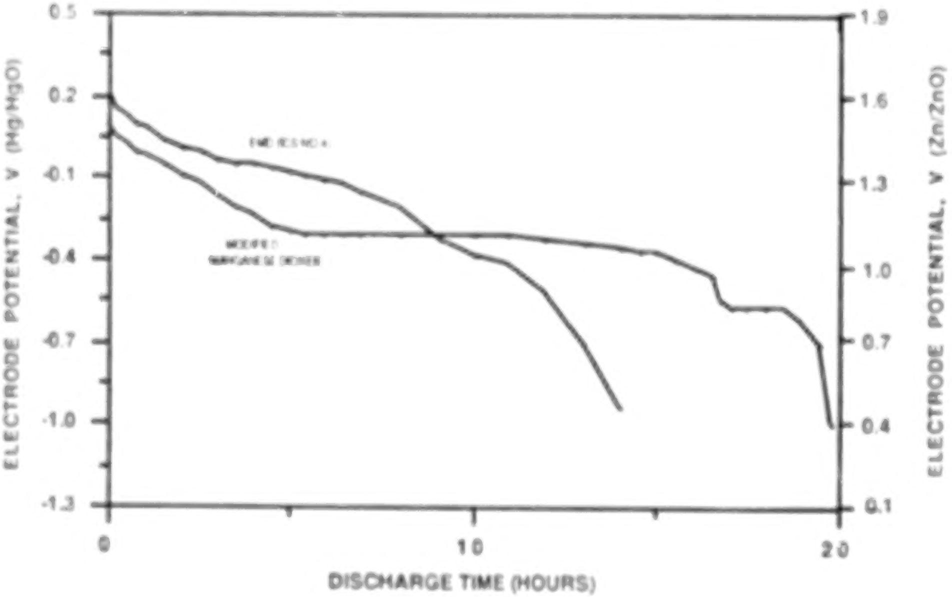

Figure 2: First discharge curve for electrolytic MnO_2 and modified MnO_2 obtained in 9M KOH at room temperature with a discharge current of 44 mA/gMn. Cathode mix: 85 wt% manganese dioxide, 10 wt% acetylene black and 5 wt% binder.

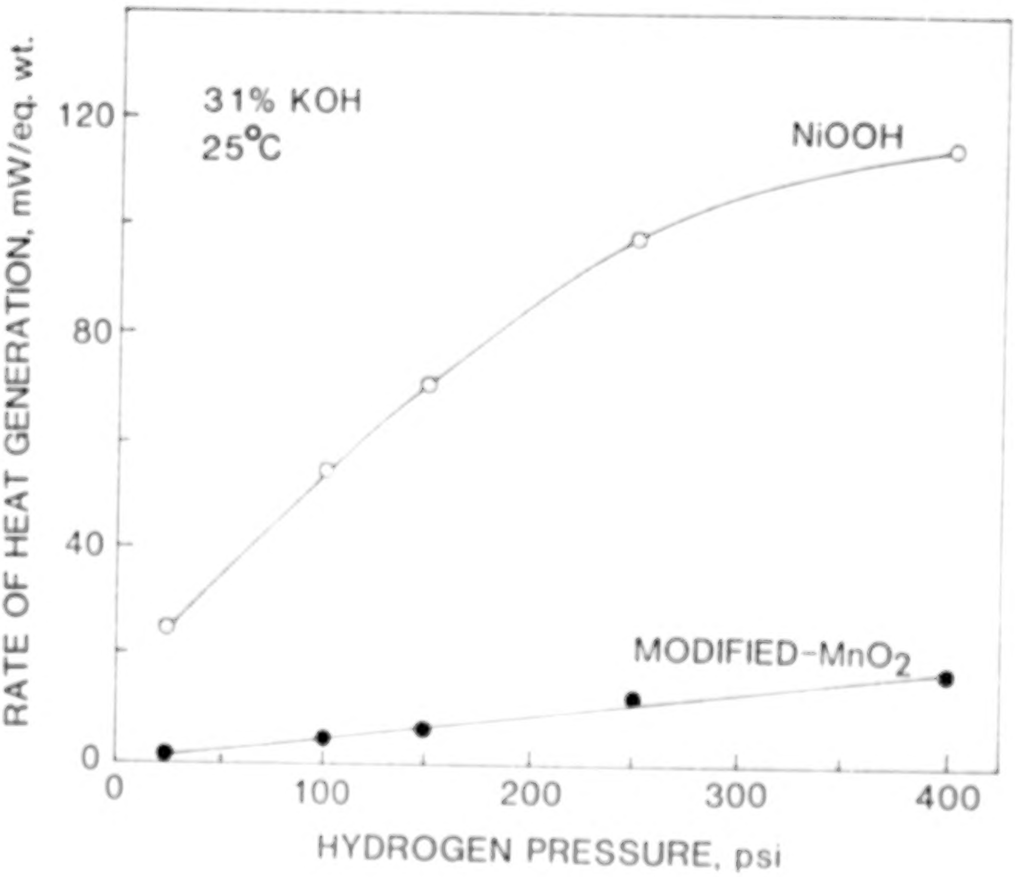

Figure 3: Heat generation rates as a function of hydrogen pressure from the reactions between hydrogen and NiOOH and bismuth-modified MnO_2. 0.1g oxide samples in 1.0 ml of 31 wt% KOH were used.

CHARACTERIZATION TESTING OF A 40 AHR BIPOLAR NICKEL-HYDROGEN BATTERY

Jeffrey C. Brewer
NASA Marshall Space Flight Center
Huntsville, Alabama 35812

Michelle A. Manzo
NASA Lewis Research Center
Cleveland, Ohio 44135

Russel P. Gemeiner
NASA Lewis Research Center
Cleveland, Ohio 44135

Extensive characterization testing has been done on a second 40 amp-hour (Ahr), 10-cell bipolar nickel-hydrogen (Ni-H_2) battery to study the effects of such operating parameters as charge and discharge rates, temperature, and pressure, on capacity, Ahr and watt-hour (Whr) efficiencies, end-of-charge (EOC) and mid-point discharge voltages. Testing to date has produced many interesting results, with the battery performing well throughout all of the test matrix except during the high-rate (5C & 10C) discharges, where poorer than expected results were observed. The exact cause of this poor performance is, as yet, unknown. Small scale 2" x 2" battery tests are to be used in studying this problem.

Low earth orbit (LEO) cycle life testing at a 40% depth of discharge (DOD) and 10°C is scheduled to follow the characterization testing.

INTRODUCTION

Space power systems of the future are projected to require power levels that extend far beyond the current levels of demand. In order to meet these increasing needs, improvements must be made to current energy-producing systems or new technologies must be developed. Over the past several years, LeRC has been actively engaged in the development of a bipolar configured Ni-H_2 battery. This battery system has the potential to meet some of these high-power needs of the future. In a continuing effort to develop this technology to a point where it can be used efficiently in space flight, LeRC has begun testing a second 40 Ahr, 10-cell bipolar Ni-H_2 battery.

Results from the tests on the first battery tested here at LeRC were very encouraging. The battery operated for some 10,000 LEO cycles at 40% DOD and produced promising results in most of a variety of characterization tests, as well (ref. 1). Following the completion of this test, work began on the design of the second bipolar battery in hopes of developing an improved battery.

BATTERY DESIGN

The basic design of this battery differs from that of the first battery only through slight modifications in the cell frames. Poor high-rate discharge performance and electrolyte leakage paths in the first battery led to these changes. It was thought, at the time, that a possible cause of the poor high-rate performance in the first battery was limited gas access to the reaction sites on the negative electrode. Gas-access area was thus increased by modifying the cell frame in an attempt to alleviate this problem. The gaskets were also changed in the cell frame design in an effort to improve the seals and thus better contain the electrolyte within the cells. In addition to these minor design changes, most of the individual components of the second battery came from different manufacturers (table I). The reasons vary as to why these component changes were made. The frame material, for instance, was changed from polysulfone to ABS (resins which are terpolymers of acrylonitrile, butadiene, and styrene) because of superior machining capabilities and mechanical stability of the material. The nickel electrode was changed simply because of availability. The other changes were based, at least in part, on more technical reasoning and on the desire to reduce the number of parts. Because of inconsistencies found in the previous H_2 electrode, Giner, Inc. was engaged in a development program to manufacture a suitable large area, single unit electrode for this application. In doing so, the previous three-piece electrode would be eliminated. A program was also undertaken with National Standard to develop a fibrex electrolyte reservoir plate (ERP) which would contain pores in the desired range and could be manufactured in one piece. The previous ERP was constructed from nickel foam from Brunswick which, due to the large area required and manufacturing limitations, resulted in a six-piece ERP. In an attempt to increase the effective current carrying area between the gas screen and the bipolar plate and to improve high rate performance, the gas screen was changed to a heavier, woven screen, as opposed to an expanded metal (Exmet) screen in the first battery. This change also created a large weight increase which makes it difficult to justify its use without major performance improvements. Finally, the electrolyte concentration was changed from 31% to 26% potassium hydroxide. This was done because of superior life seen in IPV Ni-H_2 testing (ref. 2). These multiple component changes, as well as different testing procedures and unique cell characteristics make it difficult to directly compare results from the two batteries. Some comparisons, however, are valid and will be made.

One feature consistent with the first battery is that both utilized an active cooling process. This is accomplished by pumping a coolant through alternate bipolar plates (cooling plates) in the battery stack. This enables temperature readings to be controlled very consistently and accurately throughout the entire cell. This is one advantage over IPV technology. In an IPV cell, temperatures in the stack can run 7°C hotter than the measured temperatures outside the cell (ref. 3).

PROCEDURES

After construction was complete, the battery was placed in a boiler plate pressure vessel, which was designed to meet safety requirements. Each cell was instrumented with voltage leads to measure individual cell voltages as well as a thermocouple attached to the bipolar plate in the hydrogen cavity to measure internal cell temperature. Additional thermocouples were placed on the exterior of the stack to get additional temperature measurements. The pressure vessel was equipped with a pressure transducer for measuring the hydrogen pressure, an oxygen sensor, and a relative humidity indicator. A Modicon programmable controller was used to run the test. All instrumented points were scanned and digitized every 18 seconds by a Neff multiplexer and stored by a central computer system for subsequent processing. The data could then be processed and received in both tabular and graphical form for each cycle.

Following the setup and checkout of the test hardware and data collection system, initial cycles were run to determine battery capacity. An initial capacity of 40 Ahrs was assumed. The capacity determination cycles basically consisted of a C/2 rate charge with a 5% overcharge followed by a C rate discharge to a battery voltage of 7.0 V or a low cell voltage of 0.5 V. "C" is defined as the rate at which the battery's capacity will be depleted in one hour. The low cell voltage cut-off of 0.5 V was used in order to prevent any cell from going negative and thus generating hydrogen. A C/4 drain to these same cut-off points followed this to complete the total cycle. As the cycles continued, the "C" value was adjusted several times until a consistent capacity was recorded, which was 40 Ahrs. While some of the formation cycles were run at 20°C and 200 psi, the baseline capacity determination cycles were run at 10°C and 200 psi.

Characterization tests were then run at a variety of charge and discharge rates, temperatures, and pressures. A full set of tests was run at 10°C and 200 psi at charge rates of C/4, C/2, and C, and discharge rates of C/4, C/2, C, 2C, 5C, 10C, and 5C pulse for each charge rate. Following this set of tests, subsets of this base characterization test were run at other temperatures and pressures. A C/2 rate charge was chosen as the charge rate to be used in these subsets. This selection was based not only on performance in the base characterization test, but also on performance in prior tests (ref. 4). A C/2 rate charge also allowed the cycles to fit better into an eight-hour day than if run at a lower rate. A subset of tests run at 20°C and 200 psi consisted of the identical discharge rates used in the base set paired with the C/2 charge rate. The remaining subsets (0°C at 200 psi, 30°C at 200 psi, and 20°C at 400 psi) consisted only of the C/4, C/2, C, and 2C rate discharges. Again, all were paired with the C/2 charge rate. Each individual test was run until three consistent cycles were recorded. Consistency was based on Ahr and Whr efficiencies. Each cycle consisted of a full charge (the amount of which was equal to the capacity out in the preceding discharge plus a set percentage of overcharge) followed by a full discharge to a battery voltage of 7.0 V or a low cell voltage of 0.5 V (hereafter known as the normal cut-off points). A C/4 drain followed all discharges run at a C/2 rate or higher.

A set percentage of overcharge was used in this test in order to ensure adequate charging as well as protect from unnecessary overcharging. This is compared to the first battery test where a set charge input was used for each cycle regardless of the capacity delivered in the previous discharge (ref. 1). A 5% overcharge was used initially; however, this proved to be insufficient to adequately recharge the battery so the overcharge was increased to 10%. This percentage maintained a stable capacity from cycle to cycle; however, to reduce any unnecessary overcharging, the percentage was dropped to 7% where stable capacities were once again realized. The overcharge amount thus stayed at 7% throughout the remainder of the characterization testing.

Due to a lack of adequate manpower, cycles were not run over the weekends or holidays. This extended wet-stand period allowed time for a weak, high-resistance cell to self-discharge considerably more than the other cells. This delayed the resuming of the characterization testing until after that cell could be brought back up to a state of charge similar to that of the other cells. It was found through trial and error that the weak cell could be maintained by trickle charging the fully charged battery at a C/150 to C/100 rate. This method produced much more consistent results than other methods that were tried and allowed characterization cycles to resume much more quickly.

RESULTS AND DISCUSSION

Due to the wide range of variables in this test, all of the relevant numerical data will not be enumerated here, but is summarized in tables II - VIII. Figures 1 - 4 contain pertinent voltage profiles from throughout the test.

Before discussion can begin on the specific results in the test, a general point needs to be made concerning the data to be discussed hereafter. It was mentioned earlier about the problems caused by a weak cell during extended wet-stand periods. This same weak cell created problems during the characterization cycles, as well. The discharges on most, if not all, of the early characterization cycles were terminated by a battery voltage of 7.0 V. This allowed good, accurate comparisons of data from cycle to cycle. The discharges, however, on the vast majority of characterization cycles were terminated by a low cell voltage of 0.5 V, while the overall battery voltage ranged from 7.1 to 10.4 V. Because most of the cycles thus had no common end-of-discharge (EOD) point, it was difficult to compare the basic, overall data between cycles. So, where it was helpful, capacity delivered to the 10.0 V point in the discharges was used to compare cycles in hopes of negating some of the distorting effects of the weak cell on the normal cut-off point data. Just what caused this cell to perform this way is unknown at this time; however, it is thought that shunt currents could be present which allowed an additional discharge path through which the cell self-discharged over night between cycles. This would explain the erratic behavior seen throughout the characterization cycles.

One additional comment about the data -- each data point represents the average value of the three most consistent cycles run at that particular set of test conditions.

Increasing the charge rate had little consistent effect on the capacity delivered to the normal cut-off points, although at lower charge rates the battery seemed to perform slightly better. Even the capacity delivered to 10.0 V showed no consistent trends (table II). Increasing the charge rate also had little consistent effect on the Ahr efficiency, but, due to the accompanying increase in battery charge voltage from an average of 15.52 V at the C/4 rate to 16.65 V at the C rate, caused an average decrease of 7.3% in the Whr efficiency, except at the 2C rate discharge where no significant changes were seen (table III). Thus, because of its desirable effect on Whr efficiency and lack of effect on other variables, a low charge rate would seem to be best; however, previous testing has suggested that a C/2 to C charge rate range should produce the optimum results (ref. 4). It is difficult, however, to directly compare results from this characterization test with the referenced test due to the fact that the nickel electrodes used in both tests came from different manufacturers. Electrolyte concentration was also different. These differences alone could account for the discrepancies seen between the two tests. In either case, though, results failed to show strong proof that there is clearly an optimum charge rate.

Increasing the discharge rate caused a consistent decrease in the capacity delivered over all temperatures and pressures except at 20°C and 400 psi where the capacity increased slightly from 46.03 Ahr to 47.46 Ahr at discharge rates of C/4 and C/2, respectively (table IV). The probable cause of this apparent increase in capacity delivered at the higher rate can be traced to the weak cell causing an early termination of the discharges run at the lower rate. Comparing the capacities at the 10.0 V point in the discharge supports this theory. At 10.0 V, an average capacity of 43.99 Ahr was delivered at the C/4 rate and 42.59 Ahr was delivered at the C/2 rate.

Because of the lower capacities delivered at the higher discharge rates, the resulting Ahr efficiencies also decreased across the board (table V). Also, as discharge rates increased, Whr efficiencies decreased over all temperatures and pressures due to the decrease in operating voltages that always accompany increasing discharge rates (tables VI & VII). In this report, operating voltages are reported as mid-point discharge voltages, which were calculated by averaging the following two data points: the voltage reading at 1/2 of the total discharge time and the voltage reading at the 20 Ahr out point. Discharge voltage profiles vs. capacity at all discharge rates can be seen in figure 1.

The discharge rate effects were all as anticipated; however, at high discharge rates of 5C and 10C, performance was very poor. Poor performance was also seen at these rates in the first battery (ref. 1); but, despite attempts to alleviate this problem through design and individual component changes, even poorer performance was seen in the second battery (figure 2). In the attempts to run a 10C discharge, the battery voltage dropped below 7.0 V within 30 seconds. Another 10C discharge was run and was allowed to continue past the normal cut-off points down to a low cell voltage of 0.1 V. This discharge lasted 3 minutes but the voltage did not begin to level off until around 4.5 V (figure 1). The 5C discharges lasted longer but, again, failed to level off above a battery voltage of 7.0 V. (tables IV - VI and figure 1). Only a 5C pulse (1 second on / 4 seconds off) discharge was able to produce meaningful results (tables IV & V and figures 1 & 3).

Several ideas have been discussed as to what could be causing this high-rate discharge problem. Limited gas access to the negative electrode was previously mentioned as a possible cause. The design changes mentioned earlier that were made in an attempt to alleviate this problem instead could have elevated the problem even more. This is based on the possibility that the holes drilled in the battery frame to allow gas access into the interior of the battery became filled with electrolyte and blocked free gas flow. One argument against this scenario is that the pressure of the gas flowing to and from the electrodes would keep the holes clear. Also, if gas access is the problem, then, based on the amount of H_2 located in the cavity adjacent to the negative electrode, initial voltage performance might be expected to be good but would fall off as the H_2 gas located in the cavity was used up. Data from the high-rate discharges showed no signs of good initial voltage performance and even showed signs of leveling off at a low voltage. A second possible cause is poor contact between the gas screen and the two surrounding components -- the negative electrode and the bipolar plate. Due to the large surface area of the bipolar stack components, uniform stack compression and the resulting surface contact between individual components is difficult to consistently maintain. A lack of adequate contact area would limit the current carrying capability and produce poor results especially at high current levels. Another possible cause is the Goretex backing placed on the H_2 electrode during the standard production process at Giner, Inc. Its presence could possibly be limiting the effective contact area between the H_2 electrode and the gas screen, thus hindering current flow. There was some initial concern about the possibility that this backing could cause current flow problems in a bipolar configuration; however, polarizations of up to 500 mA/cm^2 were operated successfully on a small scale prior to construction of the full size electrode. Perhaps the key point, once again, is the possible lack of uniform stack compression in a full scale battery configuration. One possible solution that has been discussed that could, at least, partially improve the contact between components is to weld the gas screen to the bipolar plate. This would assure adequate contact area between these two components, but would not improve the contact area between the H_2 electrode and the gas screen. The effects on performance that the Goretex backing has in a full scale battery as well as other possible problem areas are to be addressed in further testing. Small scale 2" x 2" battery tests will begin soon and will be used to evaluate some of these areas. Flooded capacity tests have already been done to evaluate the performance effects caused by varying the nickel electrode manufacturer and the electrolyte concentration. Electrodes from both manufacturers (Eagle Picher and Whittaker-Yardney) were tested at 10C, 5C, 2C, C, C/2, and C/4 discharge rates using 26, 31, and 40% KOH as electrolyte. Nickel was used as the counter electrode and amalgamated zinc was used as the reference electrode. Results from this test showed no signs of inferior high-rate performance by the Whittaker-Yardney nickel electrode used in the second battery (figure 4). On the contrary, these electrodes produced much more stable efficiencies and capacities at all discharge rates tested (table VIII). The Whittaker-Yardney electrodes shown in table VIII produced 76% of their low-rate (C/4) capacity at the high (10C) rate, while the Eagle Picher electrodes delivered only 39% of their low-rate capacity at the high rate. It is not possible, however, to completely rule out the nickel electrode as being responsible for the poor high-rate discharge performance. Because of the flooded conditions under which these capacity measurements were made, the ability of the different electrodes to perform under actual battery conditions was not addressed. Thus, it is entirely possible that under actual battery conditions the Whittaker-Yardney electrodes would not perform optimally and that the "starved" condition could lead to the type of poor performance that was seen at the high rates. Finally, it was not intended through these tests to directly compare the two manufacturers' electrodes. Neither manufacturer optimized the electrodes that were used; they simply supplied standard electrodes of the size requested.

Temperature variations between 0°C and 30°C produced some interesting results. As expected, an increase in temperature produced significant drops in EOC voltage due to the decrease in internal resistance that accompanies rising temperatures. Readings averaged 16.40 V at 0°C and 15.12 V at 30°C. As temperatures increased, the mid-point discharge voltages, however, showed a steady increase at all discharge rates except at C/4 where a 50 mV drop was seen between the temperatures of 0°C and 10°C. (table VII). The improved voltage performance seen at higher temperatures, however, did not directly translate into an increase in Whr efficiencies at all conditions (table VI). At the 2C rate discharge the Whr efficiency was the lowest (41.26%) at 30°C and the highest (53.43%) at 20°C. At the other three discharge rates, though, 30°C produced the highest efficiencies. The discrepancy at the 2C rate discharge can be, at least partially, attributed to a high EOD voltage of 10.3 V at 30°C compared to 7.2 V at 20°C. Whether or not the large percentage difference could have been completely overcome had the 30°C discharge run down to around 7.0 V is difficult to determine; but, certainly a large portion of it would have been. The effect that temperature had on total capacity out was equally interesting. For instance, as temperatures increased from 0°C to 20°C, capacity delivered to the normal cut-off points increased at the C/2 rate discharge from 41.19 Ahr to 47.68 Ahr, respectively, but fell off drastically at 30°C to 37.50 Ahr (table IV). This trend was consistent at all discharge rates and was also seen in the capacity data to the 10.0 V point in the discharge. Ahr efficiencies, however, seemed to be less consistently affected by temperature variations (table V). All of this data seems to support the use of temperatures as high as 20°C or even 30°C to produce optimum results. This agrees rather well with the data produced during the first battery test (ref. 1).

Increasing the H_2 pressure inside the vessel also produced some interesting results. Negligible change was seen in the EOC voltage between 200 and 400 psi as the voltage dropped from 15.62 V to 15.59 V, respectively; however, at 400 psi, an improvement was seen in the mid-point discharge voltage at all discharge rates (table VII). This was expected behavior because the increased pressure would increase the activity coefficient of the gas and thus improve its efficiency and voltage performance. When looking at the data measured to the normal cut-off points in the discharge, the capacity, and Ahr and Whr efficiencies all were less at the higher pressure, except at the C/4 rate discharge, where a slight increase in both Ahr and Whr efficiencies was seen (tables IV - VI). These were not expected results but, once again, the weak cell seems to be distorting the data by prematurely terminating the discharges during the 400 psi cycles. Although the capacity delivered to 10.0 V is still greater at 200 psi, the differences are not as great. Also, the Ahr and Whr efficiency differences can be reasonably eliminated by considering the high EOD voltages on the 400 psi cycles. Actually, the Whr efficiencies would have probably been greater at 400 psi had all discharges terminated at similar voltages. It certainly should illustrate that increasing or decreasing the pressure will have minimal effects on overall battery performance.

After completion of the characterization cycles, the battery was placed on LEO cycle life testing at 40% DOD and at 10°C.

CONCLUSIONS AND RECOMMENDATIONS

Despite the fact that a weak cell made it difficult to directly compare some of the data from cycle to cycle, there was enough evidence to see that the battery produced generally expected results and performed very well throughout the majority of the characterization test matrix. It is hoped and expected that the LEO cycle life test that has just begun will produce similarly encouraging results. One area that continues to be a problem, however, is the high-rate discharge performance of the battery. Even though improvements were not made in this area with this battery, several encouraging ideas have been mentioned as possible solutions to the poor high-rate performance problem. As mentioned earlier, several studies, including small scale 2" x 2" battery tests, will be done in hopes of pinpointing the area or areas responsible for the poor high-rate performance.

REFERENCES

1. Cataldo, R.L.: Parametric and Cycle Tests of a 40-A-hr Bipolar Nickel-Hydrogen Battery. 21st Intersociety Energy Conversion Engineering Conference, Vol. 3, pp. 1547-1553.

2. Lim, H.S.; and Verzwyvelt, S.A.: KOH Concentration Effect on the Cycle Life of Nickel-Hydrogen Cells. II. Accelerated Cycle Life Test. 21st Intersociety Energy Conversion Engineering Conference, Vol. 3, pp. 1601-1606.

3. Rogers, H.; Levy, Jr., E.; Stadnick, S.J.; and et al: Failure Mechanisms in Nickel-Hydrogen Cells, Final Report. December 1977, pg. 2-36.

4. Cataldo, R.L.: Test Results of a Ten Cell Bipolar Nickel-Hydrogen Battery. 18th Intersociety Energy Conversion Engineering Conference, Vol. 4, pp. 1561-1567.

Table I. - COMPONENT DIFFERENCES BETWEEN BATTERY 1 AND BATTERY 2

Component	Battery 1	Battery 2
Frame	Polysulfone - Old	ABS - New
Nickel electrode	Eagle Picher	Whittaker - Yardney
Hydrogen electrode	LSI	Giner
ERP	Ni foam - Brunswick	Ni felt - Nat'l Std
Gas screen	Exmet	Woven (Nat'l Std)
Separator	Asbestos	Asbestos
Electrolyte	31% KOH	26% KOH

Table II. - CHARGE RATE EFFECTS ON CAPACITIES DELIVERED TO NORMAL CUT-OFF VOLTAGES & TO 10.0 VOLTS AT 10°C AND 200 PSI; BATTERY EOD VOLTAGES SHOWN UNDER NORMAL CUT-OFF CAPACITY VALUES

Discharge Rate	Capacity to Normal Cut-offs			Capacity to 10.0 V		
	Charge rate			Charge rate		
	C/4	C/2	C	C/4	C/2	C
C/4	47.45 7.0	46.90 6.9	46.87 7.0	43.15	42.85	43.06
C/2	46.80 7.0	46.12 6.8	43.72 7.1	42.60	42.02	40.34
C	41.73 7.1	42.38 7.3	40.84 8.0	37.75	39.08	38.97
2C	35.92 7.1	37.93 7.1	37.17 7.4	20.88	21.52	24.27

Table III. - CHARGE RATE EFFECTS ON AHR & WHR EFFICIENCIES AT 10°C AND 200 PSI

Discharge Rate	Ahr Efficiency, %			Whr Efficiency, %		
	Charge rate			Charge rate		
	C/4	C/2	C	C/4	C/2	C
C/4	94.16	93.60	93.77	80.16	78.17	74.45
C/2	87.76	86.30	85.95	72.43	69.21	66.20
C	76.99	77.04	75.76	60.43	58.93	55.83
2C	67.09	67.72	70.39	46.62	45.65	46.32

Table IV. - CAPACITY DELIVERED TO NORMAL CUT-OFF VOLTAGES AT ALL TESTED CONDITIONS WITH A C/2 RATE CHARGE; BATTERY EOD VOLTAGES SHOWN UNDER CAPACITY VALUES

Discharge Rate	Capacity, Ahr					
	200 psi				20°C	
	0°C	10°C	20°C	30°C	200 psi	400 psi
C/4	42.15 9.7	46.90 6.9	50.49 7.4	40.71 7.9	50.49 7.4	46.03 8.9
C/2	41.19 10.4	46.12 6.8	47.68 ***	37.50 7.3	47.68 ***	47.46 7.5
C	38.32 9.3	42.38 7.3	44.20 7.3	35.48 9.2	44.20 7.3	38.82 8.7
2C	33.17 7.6	37.93 7.1	39.45 7.2	32.60 10.3	39.45 7.2	33.66 9.0
5C	###	15.43 7.0	22.24 6.9	###	22.24 6.9	###
5C Pulse	###	30.60 7.0	33.97 8.1	###	33.97 8.1	###

*** - No readings available due to data collection system errors

- 5C and 5C Pulse run only at 10°C and 20°C at 200 psi

Table V. - AHR EFFICIENCIES AT ALL TESTED CONDITIONS WITH A C/2 RATE CHARGE

Discharge Rate	Ahr Efficiency, %					
	200 psi				20°C	
	0°C	10°C	20°C	30°C	200 psi	400 psi
C/4	90.80	93.60	92.04	90.96	92.04	92.55
C/2	85.79	86.30	86.76	86.68	86.76	86.20
C	82.80	77.04	78.86	79.62	78.86	76.85
2C	72.67	67.72	72.39	72.23	72.39	68.38
5C	###	28.18	41.52	###	41.52	###
5C Pulse	###	52.08	65.18	###	65.18	###

- 5C and 5C Pulse run only at 10°C and 20°C at 200 psi

Table VI. - WHR EFFICIENCIES AT ALL TESTED CONDITIONS WITH A C/2 RATE CHARGE

Discharge Rate	Whr Efficiency, %					
	200 psi				20°C	
	0°C	10°C	20°C	30°C	200 psi	400 psi
C/4	75.90	78.17	77.92	79.99	77.92	80.09
C/2	69.28	69.21	***	75.29	***	71.52
C	61.67	58.93	63.69	68.32	63.69	63.64
2C	46.51	45.85	53.43	41.26	53.43	52.91
5C	###	15.35	24.82	###	24.82	###

*** - No readings available due to data collection system errors

- 5C and 5C Pulse run only at 10°C and 20°C at 200 psi

Table VII. - MID-PT. DISCHARGE VOLTAGES AT ALL TESTED CONDITIONS WITH A C/2 RATE CHARGE

Discharge Rate	Mid-Pt. Discharge Voltage, V					
	200 psi				20°C	
	0°C	10°C	20°C	30°C	200 psi	400 psi
C/4	12.90	12.85	12.95	13.20	12.95	13.10
C/2	12.40	12.45	12.65	13.00	12.65	12.80
C	11.45	11.72	12.15	12.60	12.15	12.45
2C	9.70	10.15	11.10	11.83	11.10	11.55

Table VIII. - CAPACITIES & AHR EFFICIENCIES FOR FLOODED ELECTRODE TESTS

Discharge Rate	Capacity, Ahr		Ahr Efficiency, %	
	EP31	WY26	EP31	WY26
C/4	0.64	0.43	71.95	73.07
C/2	0.63	0.41	71.19	70.48
C	0.59	0.40	66.54	68.00
2C	0.55	0.39	61.92	67.43
5C	0.47	0.37	52.63	62.86
10C	0.25	0.33	28.20	56.90

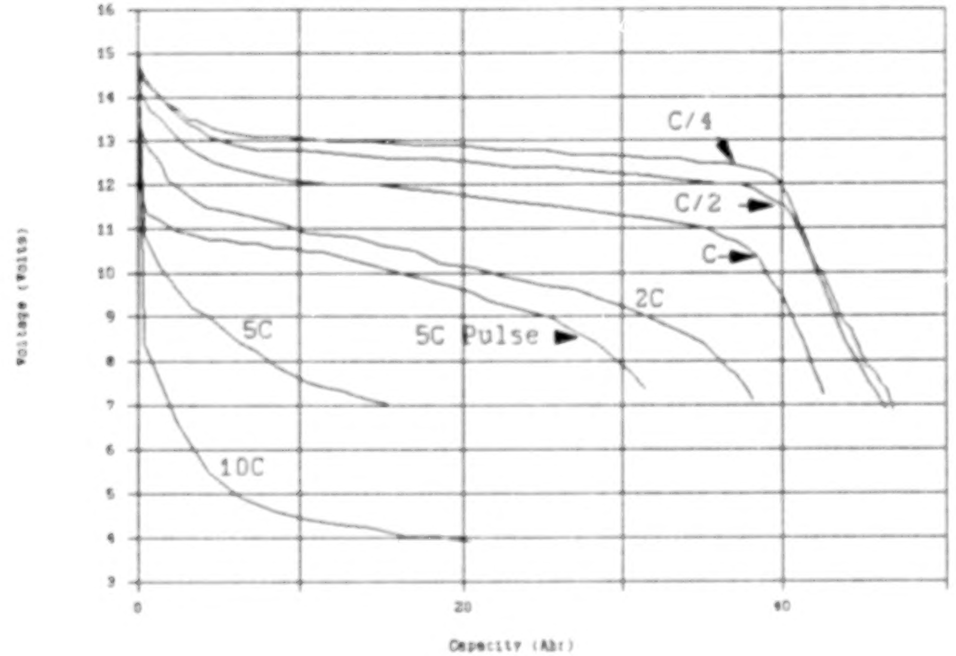

Figure 1. - Discharge voltage profiles vs. capacity for all discharge rates @ 10°C & 200 psi

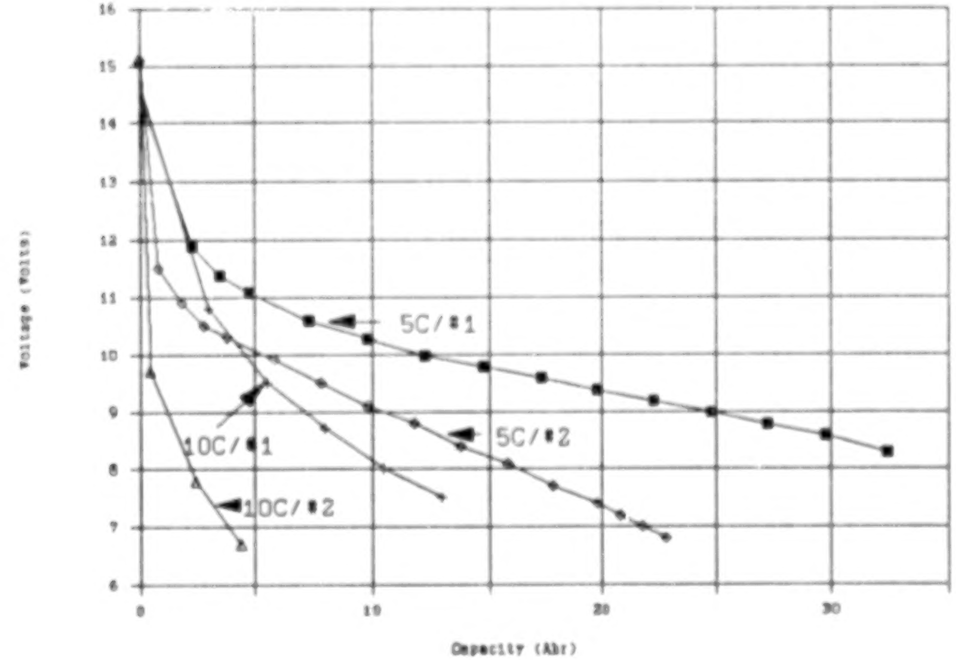

Figure 2. - 5C & 10C rate discharge voltage profile vs. capacity @ 20°C & 200 psi for battery 1 & battery 2

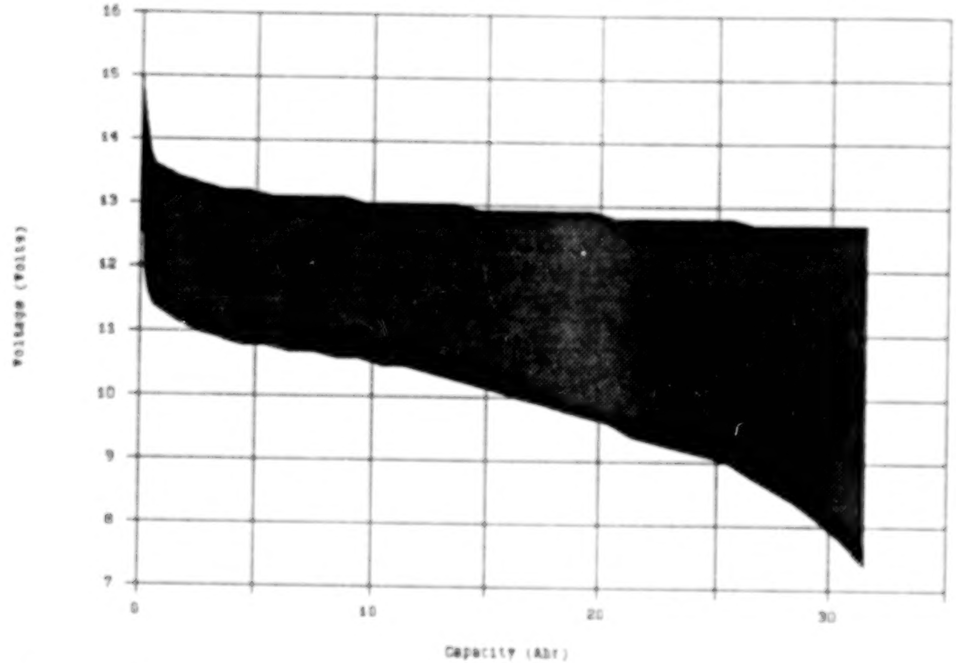

Figure 3. - 5C pulse (1 sec on / 4 sec off) discharge voltage profile vs. capacity @ 10°C & 200 psi

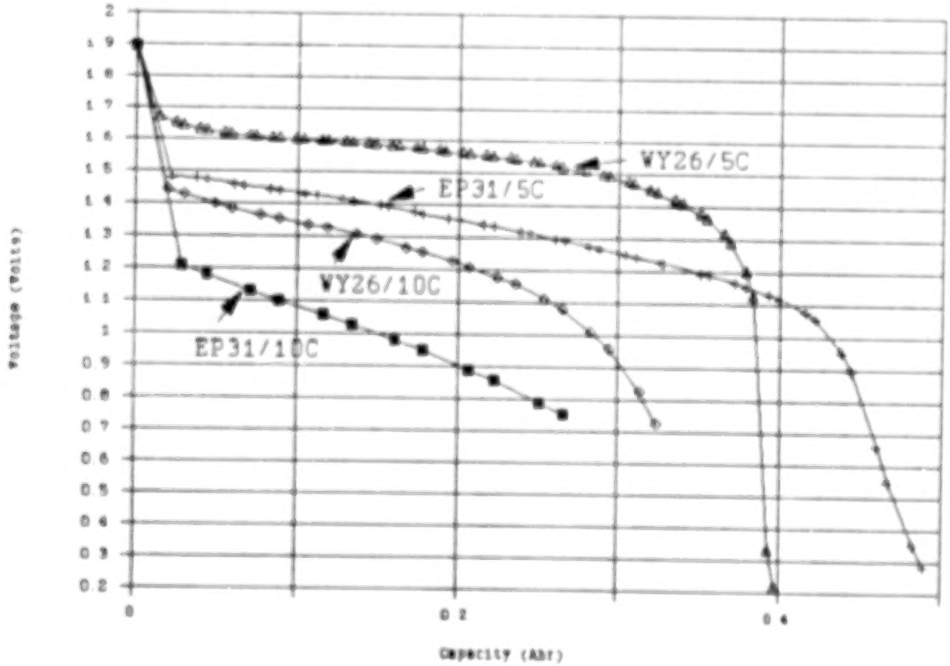

Figure 4. - 10C & 5C discharge voltage profiles vs. capacity during flooded electrode tests for Eagle Picher electrode in 31% KOH and Whittaker/Yardney electrode in 26% KOH

ADVANCED DOUBLE LAYER CAPACITORS

S. Sarangapani, P. Lessner, J. Forchione,
A. Griffith and A.B. LaConti
Giner, Inc.
Waltham, Massachusetts 02254

Work has been conducted that could lead to a high energy density electrochemical capacitor, completely free of liquid electrolyte. A three-dimensional RuO_x-ionomer composite structure has been successfully formed and appears to provide an ionomer ionic linkage throughout the composite structure. Capacitance values of approximately 0.6 F/cm^2 have been obtained compared 1 F/cm^2 when a liquid electrolyte is used with the same configuration.

INTRODUCTION

Electrochemical capacitors store energy by utilizing double layer and surface redox type processes. **Table I** compares energy density, power density, and cycle life figures for batteries, electrochemical capacitors, and conventional capacitors. The projected energy density for electrochemical capacitors are two orders of magnitude lower than that of batteries, but power densities (on the millisecond to second) time scale are three orders of magnitude higher. Energy density is much better than for conventional capacitors, but the nature of the electrochemical processes make the electrochemical capacitors suitable for relatively long pulses (milliseconds) and low to intermediate power applications.

Table I

Device	Wh/L	W/L	Cycle LIfe
Batteries	50-250	150	$<10^4$
Electrochemical Capacitors	5	$>10^5$	$>10^5$
Conventional Capacitors	0.05	$>10^8$	$>10^6$

Several applications of devices with the characteristics of electrochemical capacitors can be envisioned: lightweight electronic fuses, burst power for battery-powered vehicles and backup power for computer memory. The last application takes advantage of the high cycle life of electrochemical capacitors, instead of the high power density. Commercial devices, based on high surface area carbons and sulfuric acid and marketed by NEC under the SUPERCAP brand label, are already being sold for this application. Preliminary projections indicate that the advanced electrochemical capacitors that are being developed will have an order of magnitude higher specific energy and energy density than these carbon-based capacitors.

A simplified equivalent circuit of a single electrochemical capacitor cell is shown in **Figure 1**. A device consists of two electrodes separated by an electrolyte. Capacitances for metals and carbons in contact with aqueous solutions are 10-40 microfarads/real cm^2. Certain noble metal oxides in contact with aqueous solutions have capacitances in the range of approximately 150 microfarads/cm^2 (Kleijn and Lyklema, 1987). Materials in contact with organic solvent-electrolytes may also have high capacities. In addition, pseudocapacity due to fast surface redox reactions can contribute to energy storage which is accessible on a similar time scale as double layer energy storage. High surface area porous electrodes can be used to give capacitances up to several farads per geometric cm^2.

The equivalent circuit also illustrates several resistances present in the system. The resistance in parallel with the capacitance represents a leakage path. It should be as high as possible. The series resistance between the electrodes ultimately limits the power that can be delivered by the system. The major contributor to this is the resistance of the electrolyte between the electrodes. In addition, for practical systems using porous electrodes, the distributed electrolyte resistance in the electrode contributes to the series resistance.

Because of the decomposition of water, aqueous-based devices are limited to about 1 V per cell; organic-based devices may have higher cell voltages because organic solvents have higher decomposition voltages. To build up the voltage, several cells need to be stacked in series.

These physical principles provide an explanation for some of the figures of merit listed in Table 1. Energy density of electrochemical capacitors is lower than that of batteries because the capacitors use surface processes to store energy instead of bulk processes. However, these surface processes are accessible on a much shorter time scale than bulk processes giving the electrochemical capacitor a higher power density. Cycle life is greater than that of batteries because the surface processes result in no or small morphological changes in the material. In a sense, the electrochemical capacitor can be thought of as a specialized type of battery.

Some work has been conducted in the development of solvent-electrolyte-based electrochemical capacitors (Holleck,et al., 1988; Lee, et al., 1988). A problem with these systems is the possibility of electrolyte leakage. This can occur because of external pressure changes or gas evolution due to cell overcharge. The typical sulfuric acid electrolyte (3 to 4M H_2SO_4) is very corrosive and leakage could cause the module and ancillary equipment to be damaged or destroyed. This has led us to investigate devices where the liquid electrolyte is replaced by a solid ionomer electrolyte. Perfluorosulfonated ionomer electrolytes, such as Nafion(R), consist of a perfluoro polymer backbone to which sulfonic acid sites are permanently anchored. The only liquid or vapor present in these devices would be pure water.

(R) E.I. DuPont Trademark

The device concept is shown in Figure 2. The capacitor electrodes (high surface area metal oxides) are separated by thin sheets of ionomer membrane. Current collection is accomplished via lightweight foils or screens. The configuration allows the individual cells to be stacked into a module. The repeating element consists of the thin bipolar metal collector in intimate contact with a unitized particulate-solid ionomer composite structure.

The major challenge to be met when replacing the liquid electrolyte with the solid ionomer electrolyte is maintaining a high surface area electrode-electrolyte contact. A liquid electrolyte is sorbed into the macropores of the electrode and micropores down to about 100 Å by capillary action. An illustration of the type of composite that needs to be formed with the solid electrode-solid ionomer electrolyte structure is shown in Figure 3. A film of ionomer is needed from the face of the electrode in contact with the ionomer membrane separator extending back into the electrode toward the current collector. The electrode particulates must make intimate electronic contact with each other and with the current collector. Ideally, there is ionomer ionic linkage throughout the thin particulate-solid ionomer composite structure and extends from metal collector to metal collector.

There are several requirements for the electrode material to be used in the electrochemical capacitor. Most importantly, it should have a high double layer capacity and pseudocapacity on a real area basis. In order to have a high capacitance on a geometric area basis, the material should have a high surface area. The material should be able to be fabricated into a porous electrode forming a high surface area interface with the solid ionomer electrolyte and bonded to the ionomer membrane separator.

RuO_2 was selected as the electrode material to be studied initially because it meets all of these requirements. The oxide has a high double layer capacity of about 150 microfarads/real cm^2 (Kleijn and Lyklema, 1987). There is also a substantial pseudocapacity due to the surface reaction which can be written approximately as:

$$2RuO_2 + 2H^+ + 2e^- \longrightarrow Ru_2O_3 + H_2O \qquad [1]$$

This type of surface reaction in combination with double layer processes has been shown to be capable of sustaining high current densities on the millisecond scale (Holleck, et al., 1988; Lee, et al., 1988). RuO_2 can be made into a high surface area coating (Trasatti and Lodi, 1980) or as high surface area particulates (Balko, et al., 1980). Bonding of particulates to an ionomer membrane has been demonstrated for RuO_2 anodes for use in chlor-alkali cells (Coker, et al., 1980) where membrane and electrode assemblies with active areas of up to 35 ft^2 have been prepared.

EXPERIMENTAL METHODS

RuO_2 was prepared by thermal decomposition of $RuCl_3$ in a $NaNO_3$ flux (Balko, et al., 1980). The resulting powder was characterized by scanning electron microscopy (SEM), transmission electron microscopy (TEM), X-ray diffraction (XRD) and nitrogen surface area (BET method).

Two approaches were used to form the RuO_2-ionomer composite electrodes: 1) impregnation of a PTFE-bonded RuO_2 electrode with ionomer solution, and 2) mixing of ionomer solution with RuO_2 powder, followed by formation into an electrode. In all cases, the ionomer solution was 5% Nafion 117 in an alcohol-water mixture (Aldrich Chemicals).

The RuO_2-Nafion composite electrodes were hot-pressed to a Nafion 117 membrane. A diagram of the test cell is shown in **Figure 4**. The electrode arrangement for testing consisted of two electrodes pressed on opposite sides of the membrane. The membrane and electrode (M and E) assembly was held between two acrylic plates which contained a water reservoir to keep the M and E wet. A tail of the Nafion 117 membrane dips into a beaker of H_2SO_4 which contains a Hg/Hg_2SO_4 reference electrode. Some of the M and E assemblies had an integrally bonded Pt/air reference electrode.

The effectiveness of forming the extended RuO_2-ionomer interface and the maximum electrochemical limits of operation were assessed by using cyclic voltammetry. The electrode was cycled between voltage limits where only double layer and reversible surface redox processes occur. For double layer or surface processes, the current is related to sweep rate by:

$$i = C \frac{dV}{dt} \qquad [2]$$

where C is the capacitance of the electrode.

RESULTS AND DISCUSSION

Powder X-ray diffraction showed the material to be substantially RuO_2. There was some undecomposed $RuCl_3$ present. Nitrogen adsorption measurements gave surface areas near 50 m^2/g. The SEM photograph in **Figure 5** shows the particles to be pyramid-shaped and on the order of 0.1 to 5 microns in size. Clearly these surface areas cannot be explained on the basis of impermeable particles of this size. TEM examination of a 50 m^2/g powder (**Figure 6**) shows that the particles have considerable internal porosity with crystallites on the order of 200 Å. Assuming spherical particles of this diameter, the calculated specific surface area is about 40 m^2/g, which is in good agreement with the measured BET surface area. This powder was heat treated which reduced its surface area to 3 m^2/g. **Figure 7** shows that this surface area loss was due to the loss of the small size particles by sintering. This type of morphology in the oxide is not unexpected. The density of $RuCl_3$ is 3.1 g/cm^3, while RuO_2 has a density of 7 g/cm^3. When the decomposition reaction is accompanied by a large decrease in specific volume (as is the case here) the final products tend to have the external shape and dimensions of the precursor, but with many small voids (Volpe and Boudart, 1985). This appears to be the case here.

Voltammograms of a RuO_2 electrode bonded to a Nafion 117 membrane are shown in **Figure 8**. At potentials more negative than -0.4 V vs. $Hg/HgSO_4$, RuO_2 is irreversibly reduced to lower oxides (shown as the beginning of a reduction wave in Figure 8). Above about 0.5 V, oxygen evolution is possible. This gives a single cell a usable voltage of 0.9 V. In the intermediate region, the voltammogram is fairly flat with peaks due to reversible surface conversion of oxides as in Reaction 1. Trassati and Lodi (1980) have stated that the oxide cycles between the +3 and +4 states in the region of -0.3 to 0.3 V. The current in the potential region near 0.15 V was plotted against sweep rate to obtain capacitance.

The capacitances of 50 m^2/g powder bonded to the Nafion 117 membrane with no ionomer impregnation are about 0.15 F/cm^2. This capacitance is independent of RuO_2 loading. This is approximately one order of magnitude lower than the capacitance if the electrode was completely flooded with sulfuric acid.

Our most successful attempts to extend the area of electrode-electrolyte contact has been via the technique of suspending RuO_2 in a Nafion solution and spreading it onto the Nafion 117 membrane, followed by evaporation of the solvent. **Figure 9** shows the results obtained by using this technique with a low surface area powder and 5 wt% Nafion in the final electrode. Although the absolute values of capacitances are low, a clear correlation is seen between RuO_2 loading and capacitance. **Figure 10** shows that with a higher surface area powder, similar results can be achieved. Another technique is to form the electrode on a separate thin sheet, followed by transfer to the membrane. Figure 10 shows that this method gives similar results; it is also more amenable for making larger electrodes. Electrodes up to 25 cm^2 have been made with this technique.

SUMMARY

The all-solid electrochemical capacitor concept offers the advantage of greater reliability and safety. If the electrode-ionomer structure can be optimized further and sufficiently thin ionomer membrane separators can be developed, then the energy and power density for the all-solid capacitor should be comparable to other advanced electrochemical capacitors being developed (Lee, et al., 1988 and Table I). The techniques of sealing/water management, thermal management and power transfer/control are expected to be similar to scaled-up all-solid-state proton exchange membrane bipolar electrolysis devices (Coker, et al., 1982). These devices containing up to 100 bipolar elements (0.3 ft^2) have been marketed as reliable devices for over 5 years.

ACKNOWLEDGEMENT

This work is being supported by the Office of Naval Research under Contract No. N00014-88-C-0391.

REFERENCES

Balko, E.N., C.R. Davidson and A.B. LaConti. 1980. Solid Solutions of RuO_2 and IrO_2. J. Inorg. Nucl. Chem. 42:1778.

Coker, T.G., R.M. Dempsey and A.B. LaConti. 1980. Production of Halogens in an Electrolysis Cell with Catalytic Electrodes Binded to an Ion Transporting Membrane and an Oxygen Depolarized Cathode. U.S. Patent No. 4,191,618.

Coker, T.G., A.B. LaConti and L.J. Nuttall. 1982. Industrial and Government Applications of SPE$^{(R)}$ Fuel Cell and Electrolyzers. Paper published in *Proceedings of the Electrochemical Society Symposium on Membranes and Ionic and Electronic Conducting Polymers*. Case Western Reserve, Cleveland Ohio.

Holleck, G.L., B.H. Jackman and R.D. Rauh. May 1988. High Rate Electrodes for Pulse Power, Iridium Oxide and Ruthenium Oxide. Abstract No. 18, The 173rd Electrochemical Society Meeting, Atlanta, Georgia.

Kleijn, J.M. and J. Lyklema. 1987. The Electrical Double Layer on Oxides: Specific Adsorption of Chloride and Methylviologen on Ruthenium Dioxide. Journal of Colloid and Interface Science. 120:511.

Lee, Ho-Lun, G. Mason and K. Kern. 1988. Hign Power Pulse Energy System Concept. Final Report for ONR Contract No. N00014-87-C-0705.

Trasatti, S. and G. Lodi. 1980. Properties of Conductive Transition Metal Oxides with Rutile-Type Structure. In *Electrodes of Conductive Metallic Oxides Part A*. Chapter 7, S. Trasatti (Ed.), Elsevier, Amsterdam.

Volpe, L. and M. Boudart. 1985. Topotactic Preparation of Powders with High Specific Surface area. Catal. Rev. Sci. Eng. 27:515.

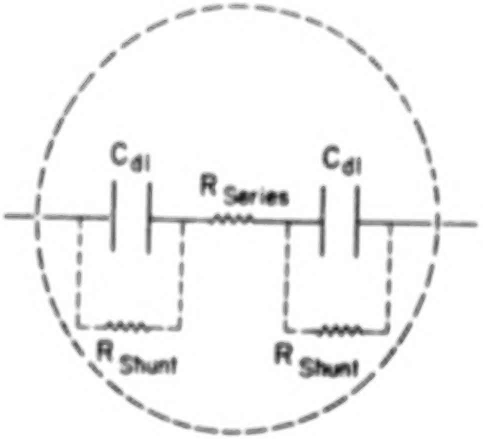

Figure 1. Simplified Equivalent Circuit of Electrochemical Capacitor Single Cell.

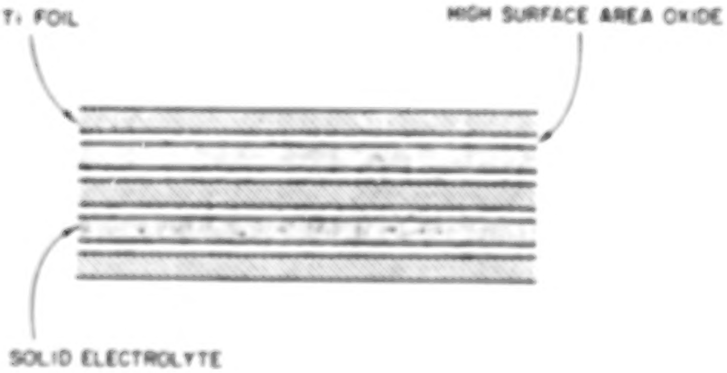
Ti FOIL
HIGH SURFACE AREA OXIDE
SOLID ELECTROLYTE

Figure 2. Unitized Electrochemical Capacitor Module.

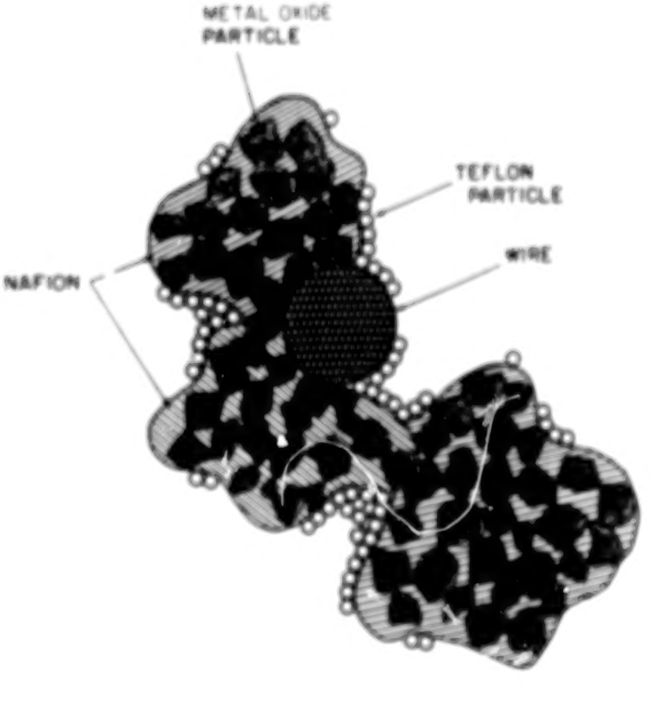
METAL OXIDE PARTICLE
TEFLON PARTICLE
WIRE
NAFION

Figure 3. Structure of Ionomer-Metal Oxide Composite Electrode.

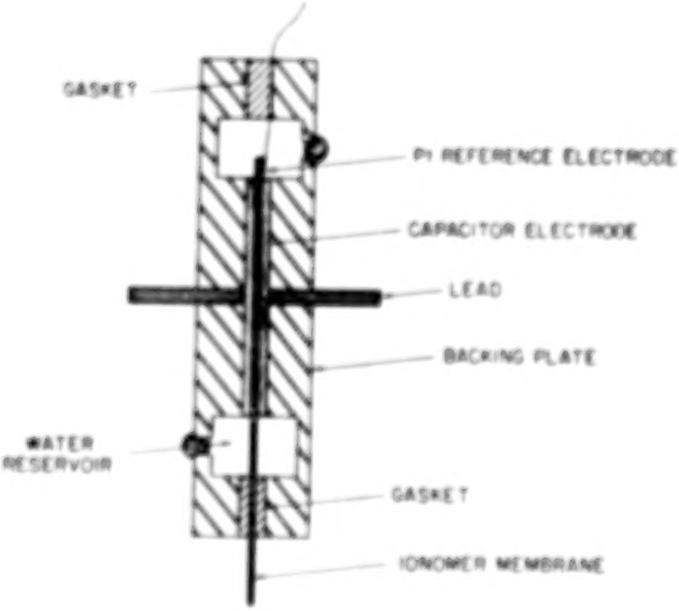
GASKET
Pt REFERENCE ELECTRODE
CAPACITOR ELECTRODE
LEAD
BACKING PLATE
WATER RESERVOIR
GASKET
IONOMER MEMBRANE

Figure 4. Test Fixture for All-Solid Capacitor Cell.

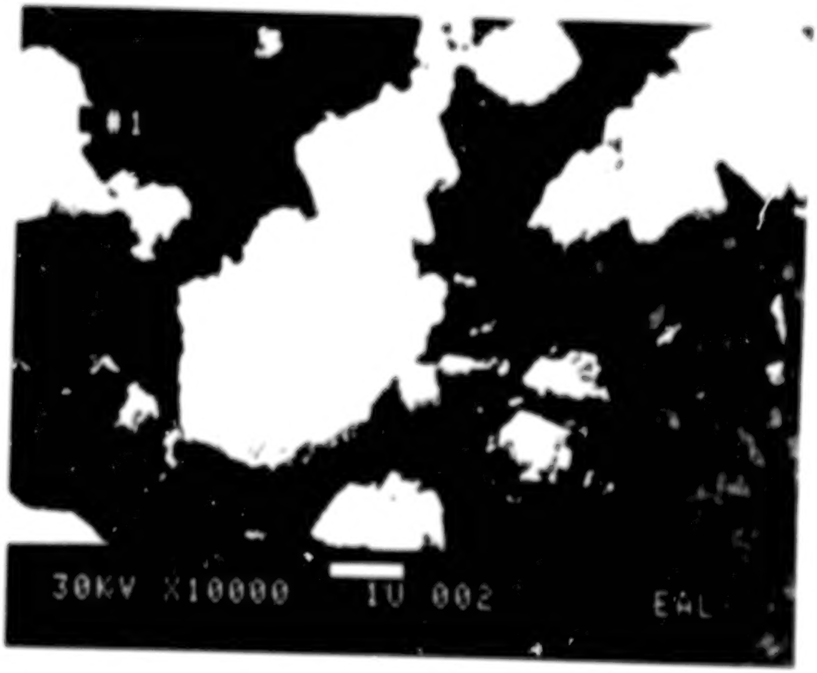
#1
30KV X10000 1U 002 EAL

Figure 5. SEM Photograph of RuO_2 Particulates.

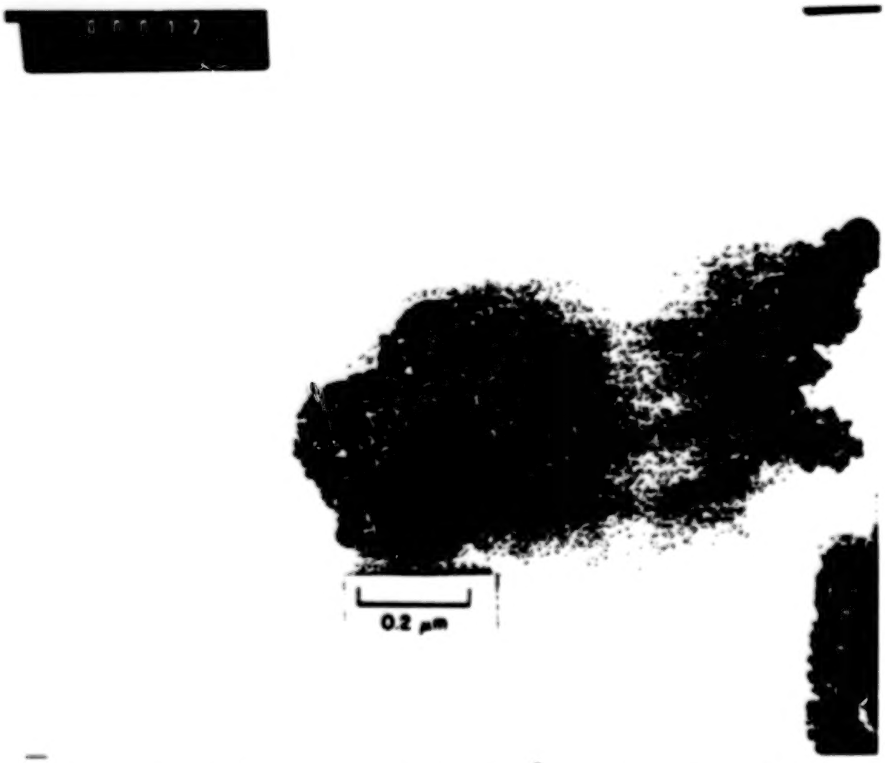

Figure 6. TEM Photograph of 50 m^2/g RuO_2 Particulates.

Figure 7. TEM Photograph of 3 m^2/g RuO_2 Particulates.

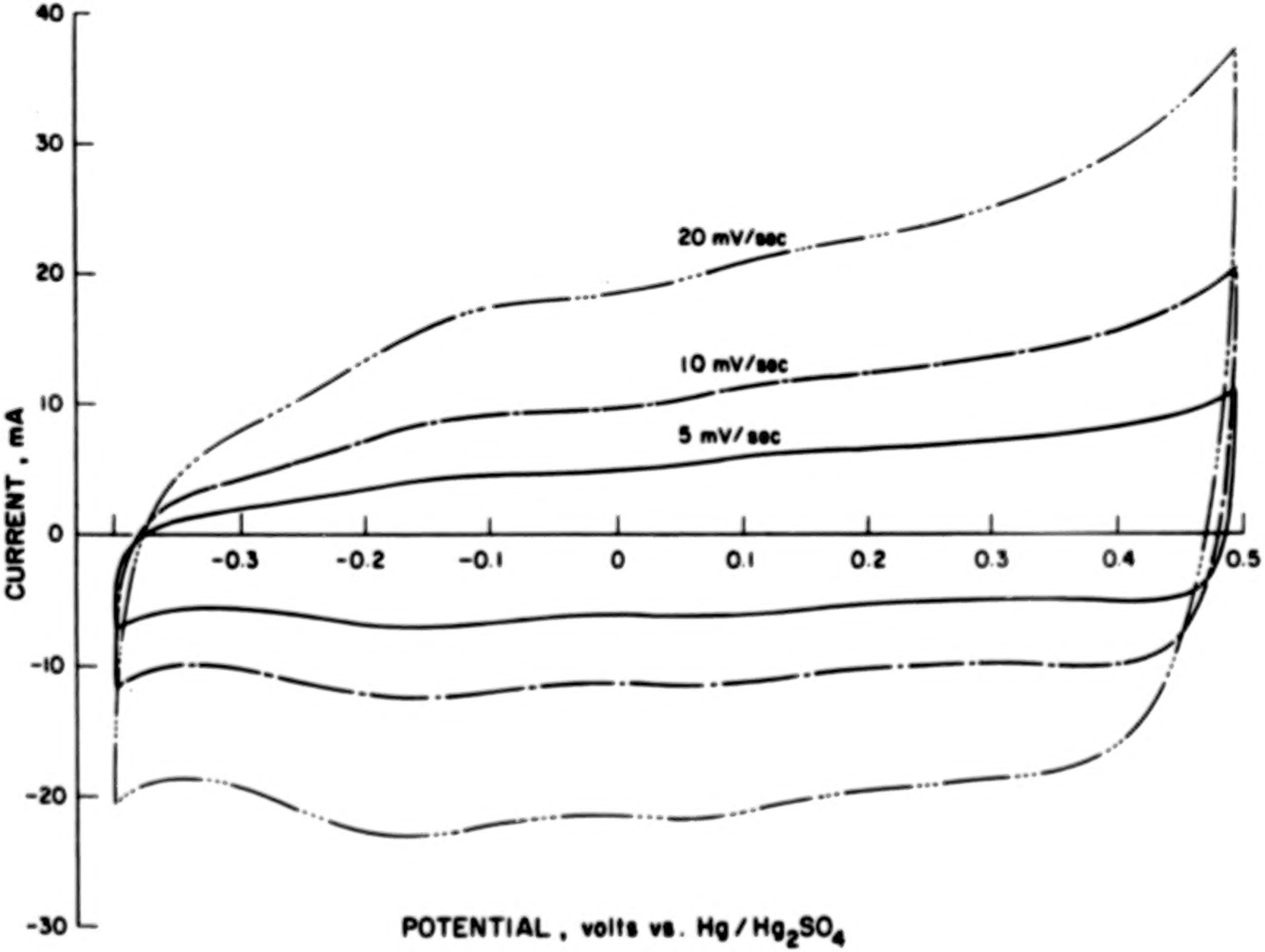

Figure 8. Voltammogram of RuO$_2$ Bonded to Nafion 117 membrane; 6.45 cm^2 Electrode.

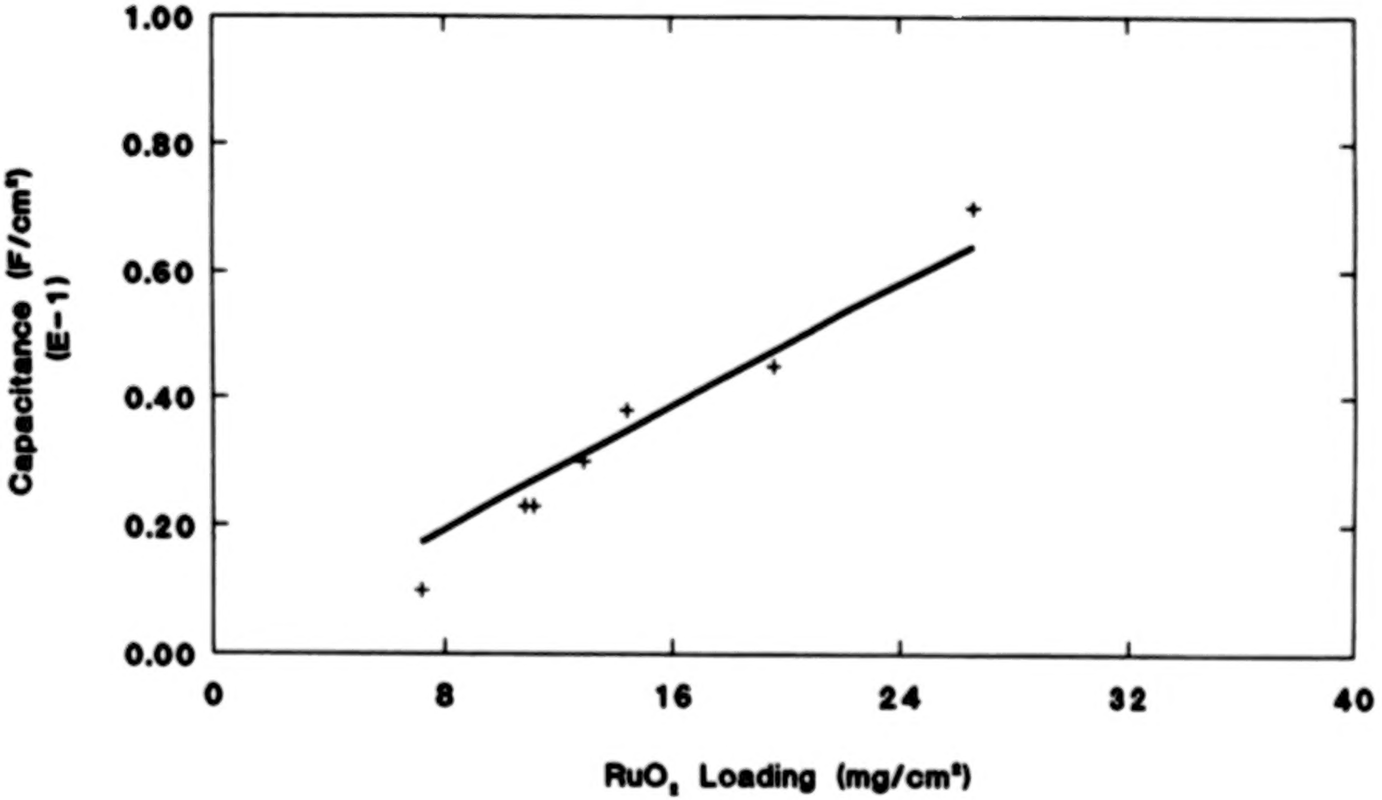

Figure 9. Capacitance Versus Loading for RuO_2 (Low Surface Area)-Nafion Electrodes Bonded to a Nafion 117 Membrane.

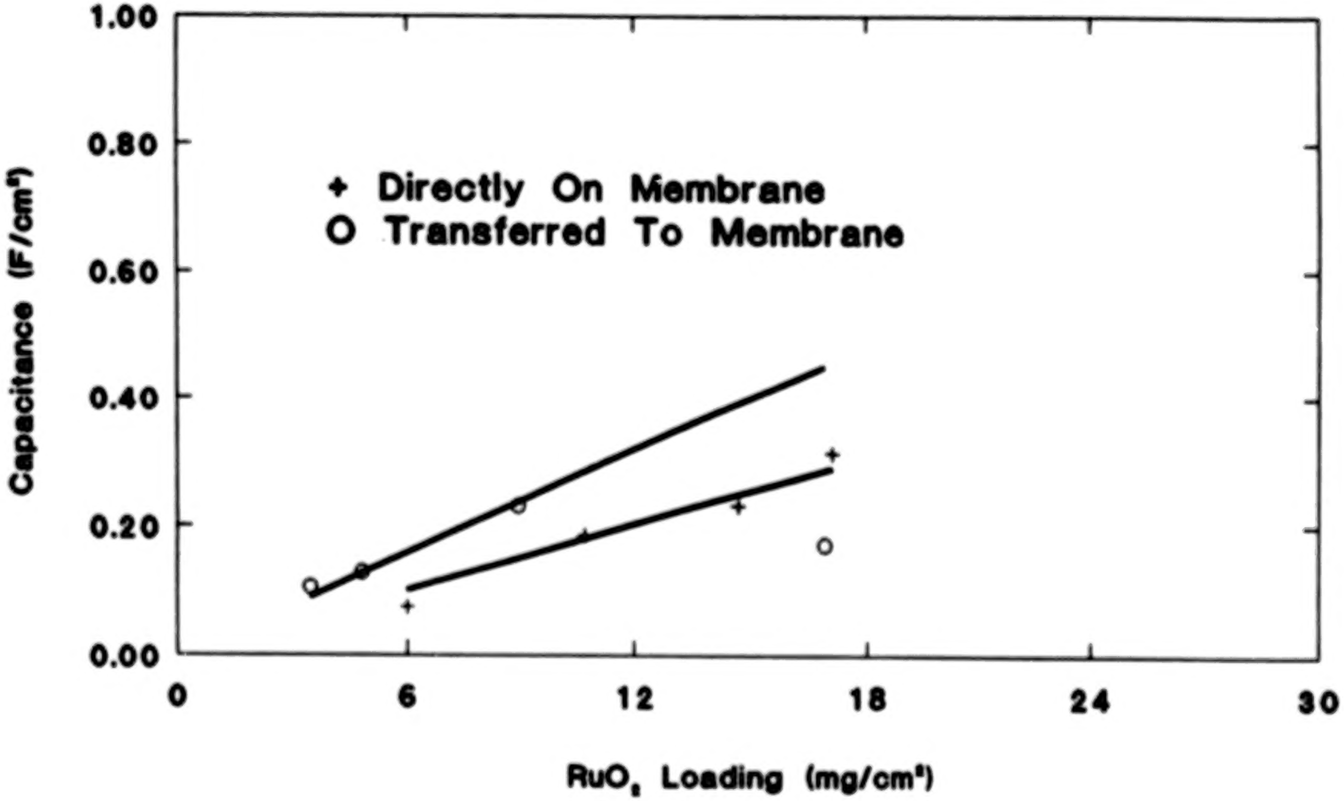

Figure 10. Capacitance Versus Loading for RuO_2 (High Surface Area)-Nafion Electrodes Bonded to a Nafion 117 Membrane.

RECENT ADVANCES IN SOLID POLYMER ELECTROLYTE FUEL CELL TECHNOLOGY WITH LOW PLATINUM LOADING ELECTRODES

Supramaniam Srinivasan, David J. Manko, Hermann Koch[1],
Mohammad A. Enayetullah and A. John Appleby
Center for Electrochemical Systems and Hydrogen Research
Texas Engineering Experiment Station
Texas A&M University System
College Station, Texas 77843

Of all the fuel cell systems only alkaline and solid polymer electrotyte fuel cells are capable of achieving high power densities (>1W/cm^2) required for terrestrial and extraterrestrial applications. Electrode kinetic criteria for attaining such high power densities are discussed. Attainment of high power densities in solid polymer electrolyte fuel cells has been demonstrated earlier by different groups using high platinum loading electrodes (4 mg/cm^2) . Recent works at Los Alamos National Laboratory and at Texas A&M University (TAMU) demonstrated similar performance for solid polymer electrolyte fuel cells with ten times lower platinum loading (0.45 mg/cm^2) in the electrodes. Some of the results obtained at TAMU are discussed in terms of the effects of type and thickness of membrane and of the methods of platinum localization in the electrodes on the performance of a single cell.

1 INTRODUCTION

1.1 Rationale for Selection of Solid Polymer Electrolyte Instead of Alkaline Electrolyte Fuel Cell System for Attainment of High Power Densities

Only the alkaline and solid polymer electrolyte fuel cell systems are capable of attaining high power densities (>1 W/cm^2). The pros and cons of the two fuel cell systems are best expressed as in Table 1. Even though the alkaline fuel cell systems developed by International Fuel Cells/United Technologies Corporation(1), for the Apollo and Space Shuttle Program, are in a highly advanced state and have functioned extremely well for the required missions, the solid polymer electrolyte fuel cell system is a stiff competitor for the alkaline fuel cell system, as is clearly evident in Table 1. There is already a sufficient Technology Base Development for the alkaline system at International Fuel Cells/United Technologies Corporation and several $100 M have been invested in this system. Even though a considerably lesser financial support has been provided for the solid polymer electrolyte system, it is in an advanced state of development, as evidenced by the progress made in the development of 1.5 kW systems by Ballard Technologies, Inc. in Vancouver, Canada (2) and by Ergenics Power Systems, Inc., in Wyckoff, New Jersey(3). Siemens(4) in Erlangen, Germany is also engaged in research, development and demonstration of high power density solid polymer electrolyte fuel cell systems for submarine applications. The work on solid polymer electrolyte fuel cell systems by these organizations has been with high platinum loading (4 mg/cm^2) electrodes. In the most recent work at Ballard, it has been reported that a current density (i) of 6 A/cm^2 has been attained at cell potential (E) of 0.5 V. The slope of the linear region in Ballard's E - i plot is 0.08 ohm cm^2. The performance of relatively high power densities (1A/cm^2 at 0.7V) in solid polymer electrolyte fuel cells with low platinum loading

---

[1] Exchange Graduate Student from Ruhr University, Bochum, Germany, FR.

TABLE 1

PROS AND CONS OF SOLID POLYMER ELECTROLYTE FUEL CELL SYSTEM OVERALKALINE ELECTROLYTE FUEL CELL SYSTEMS FOR (WPAFB'S) PROPOSEDAPPLICATION OF HIGH POWER DENSITY ELECTRIC GENERATION SYSTEMS

SOLID POLYMER ELECTROLYTE FUEL CELL SYSTEM	ALKALINE FUEL CELL SYSTEM
PROS	PROS
1. Electrolyte is a perfluorinated sulfonic acid membrane - only water need be added to it to make it conducting. 2. Excellent electrode kinetics of hydrogen oxidation in this electrolyte-overpotential at 2 A/cm^2 is only 20 mV. 3. Electrode kinetics of oxygen reduction faster in this electrolyte than in any other acid electrolytes. 4. Membrane has a high bubble pressure (even at thickness of order of 50µm) and is hence a good gas separator. 5. High power density attained approaching same level as in alkaline electrolyte, fuel cell.	1. The only well developed fuel cell system (kW level) for space application. 2. Best electrode kinetics of oxygen reduction at temperatures less than 200°C - low Tafel slope. 3. High conductivity of the electrolyte. 4. By operation at over 100 °C, water removal is simplified.
CONS	CONS
1. High cost of membrane 2. A more complex but manageable water management problem. 3. Insufficient data on stability of materials in SPE membranes, particularly at elevated temperatures.	1. Highly corrosive environment 2. Electrolyte has to be held in matrix to reduce ohmic drops. 3. Difficult to find matrix with required bubble pressure. 4. Electrolyte has to be replenished in matrix via electrolyte reservoir plate behind electrode. 5. Leak-proof seals in cells difficult. 6. Electrolyte degrades electrode structure. 7. Electrode kinetics of hydrogen oxidation considerably slower in alkaline than in solid polymer electrolyte.

electrodes was first demonstrated at Los Alamos National Laboratory by Srinivasan, Ticianelli, Derouin and Redondo (5-7).

The solid polymer electrolyte fuel cell system has major advantages over the alkaline fuel cell one in terms of lower operating temperature, ability to start from cold, and total lack of electrolyte management problems. From a cold (10°C) start-up, this system can be designed to give full power in under 30 seconds. The fuel cell system can easily be programmed for instant start-up by arranging a stack hydrogen dead-volume after the cut-off valve equal to twice the corresponding oxygen cut-off-dead-volume. Short-circuiting will rapidly reduce hydrogen and oxygen partial pressures to close to zero, with production of water that is sealed into the stack, and so will maintain the membrane in peak condition. Thus, a cold solid polymer electrolyte fuel cell stack can be safely and indefinitely left on open circuit, if prevented from freezing, and it can still be ready for rapid start-up. This is a great advantage compared with the high-performance alkaline fuel cell system, which must be maintained at the required minimum temperature to prevent electrolyte solidification, and whose open-circuit storage under these conditions is doubtful.

1.2 Necessary Electrode Kinetic Criteria for Attainment of High Power Densities

The heart of the fuel cell system is the electrochemical cell. Even though the electrode kinetics of the electrochemical cell have been adequately dealt with in books (8,9) and review articles in journals (10), it is worth recapitulating the electrode kinetic criteria for attainment of high power densities. As will be seen from the brief analysis presented below, the electrode kinetics of fuel cell reactions pose the critical issues and problems.

Firstly, there is no doubt that the only fuel cells which are capable of attaining high power densities are the ones using hydrogen and oxygen as reactants. Secondly, it has been clearly demonstrated that only the fuel cells with alkaline and perfluorinated sulfonic acid polymer electrolytes are capable of attaining high power densities. The main reason for this is that there is hardly any anion adsorption on electrocatalysts from these electrolytes and thus the poisoning of the oxygen reduction reaction is minimal. Thirdly, in fuel cells with both these electrolytes, mass transport limitations are not visible at current densities up to several A/cm^2. Under these conditions, the cell potential (E) - current (i) relations may be expressed by the equation:

$$E = E_o - b \log i - R\, i \qquad (1)$$

In perfluorinated sulfonic acids and their polymeric acids (for e.g., Nafion), the kinetics of hydrogen oxidation is extremely fast and the potential of the hydrogen electrode varies linearly with current density up to high current densities (a few A/cm^2) (7). In alkaline electrolytes, this is not the case because the exchange current density for this reaction is considerably less than in the perfluorinated sulfonic acids(11). However, the oxygen reduction reaction is faster in alkaline medium than in perfluorinated sulfonic acids. In both media, the relation between the oxygen electrode potential and current density is semi-logarithmic, and this accounts for the second term in the right hand side of Eq. 1. In this equation, b represents the Tafel slope for the oxygen reduction reaction. The first term on the right hand side, may be further expressed by:

$$E_o = E_r - b \log i_o \qquad (2)$$

where E_r is the reversible potential for the cell and i_o is the exchange current density for the oxygen reduction reaction. Differentiating equation (1), one obtains:

$$\frac{dE}{di} = -\frac{b}{i} - R \qquad (3)$$

At low current densities, the first term on the right hand side of Eq. 3 is predominant and is reflected in the high slope (which gradually decreases) of the cell potential - current density plot (see Fig. 1). At higher current densities, the second term becomes important and is responsible for the linear region in this plot. Contributions to R are from (i) the ionic resistance of the electrolyte; (ii) electronic resistance of the electrodes; (iii) charge transfer resistance of the hydrogen electrode; (iv) charge transfer resistance of the oxygen electrode which is due to the difference in the activation overpotential between the two current densities over which the slope was measured; and (v) any small contributions to mass transport resistances. As seen from figure 1, if mass transport becomes important there will be a rapid fall-off of cell potential with current density and thus only close to the limiting current density does mass transport control exert its influence. This apparently simplified equation applies over 3 decades of current density (1m A/cm^2 to 2 A/cm^2) for high power density solid polymer electrolyte fuel cells (see Section 3).

It is worthwhile at this stage to focus on the electrode kinetic requirements to attain high power densities by an examination of Equations (1 to 3) and Figure 1. Two factors clearly dominate the shape of the cell potential - current density relation: these are the Tafel parameters for the oxygen reduction reaction and the ohmic overpotential in the cell. The highest values of the exchange current density for oxygen reduction in porous gas diffusion electrodes is approximately 10^{-6} A/cm^2. The minimum value of R in Eq. 1 which has been reported is 0.05 ohm cm^2 for the alkaline fuel cell system (operating at 150°C and 8 atm) and 0.08 ohm cm^2 for the solid polymer electrolyte fuel cell system (operating at 95°C and 5 atm). In alkaline electrolytes, the Tafel slope for oxygen reduction on the best electrocatalyst (90% Au 10% Pt) is 0.04 V/decade, whereas in solid polymer electolytes it is 0.06 V/decade. The best reported cell performance in the alkaline fuel cell system is at a temperature of 150°C and 8-10 atm pressure. In the solid polymer electrolyte fuel cell system, most of the work has been carried out at close to 100°C, whereas the best, reported, performance by Ballard Technologies, Inc. is at 120°C. Use of a value of $E_r = 1.20$ V is a close approximation for the reversible potential of the fuel cell in both these environments. Thus at a current density of 3 A/cm^2, and a cell potential of 0.8 V(an expected performance of fuel cells for defense applications), one may write the following expressions for the exchange current densities of the oxygen reduction reaction:

Alkaline fuel cell:

$$0.8 = 1.20 + 0.04 \log i_o - 0.04 \log 3 - 0.05 \times 3 \qquad (4)$$

$$\therefore\ i_o = 1.7 \times 10^{-6}\ \text{A/cm}^2$$

SPE® fuel cell:

$$0.8 = 1.20 + 0.06 \log io - 0.06 \log 3 - 0.10 \times 3 \qquad (5)$$

$$\therefore\ i_o = 6.5 \times 10^{-2}\ \text{A/cm}^2$$

This simplified analysis signifies that the exchange current density for oxygen reduction in alkaline electrolyte must be equal to or greater than about 2×10^{-6} A/cm^2 (based on the geometric area of the electrode) to reach the specified goals. On the other hand, with the value of R (0.1 ohm cm^2) assumed for the solid polymer electrolyte, the exchange current density for the oxygen reduction reaction will have to be greater than 7×10^{-2} A/cm^2 (again based on the geometric area of the electrode). If, however, we were to assume the same value of R for the solid polymer electrolyte fuel cell as that for the alkaline fuel cell, the exchange current density for the oxygen reduction will have to be 2×10^{-4} A/cm^2. Considering the exchange current densities, which have been reported for oxygen reduction on smooth surfaces in alkaline ($i_o = 10^{-8}$ A/cm^2) and fluorinated sulfonic acid ($i_o = 10^{-7}$ A/cm^2) electrolytes at room temperature and assuming (i) an increase of these values by a factor of 10 for operation at elevated temperatures (150°C for the alkaline fuel cell system and

120°C for the SPE® fuel cell system); and (ii) a conservative value of 100 for the roughness factor of the porous electrodes, it should be possible to reach the desired goal of operation at 3 A/cm^2 and 0.8 V/cell, only if the slope of the linear region of the cell potential - current density is 0.05 ohm cm^2 or less.

1.3 A Snap-Shot Version of the Status of Solid Polymer Electrolyte Fuel Cell Technology

In three recent articles (5-7) the present status of the solid polymer electrolyte fuel cell technology is summarized. For detailed information, the reader is referred to these publications. In this paper a "snap-shot" version (Table 2) of the progress made in this field is presented. Table 2 demonstrates that significant progress has been made during the 1980's in solid polymer electrolyte fuel cell technology in spite of the fact that the funding for this program is miniscule compared to the investments made for the development of alkaline, phosphoric, molten carbonate and solid oxide fuel cells. In hardware production of solid polymer electrolyte fuel cells, Ballard Technologies Corporation and Ergenics Power Systems, Inc. have done extremely well. Both are at a stage where they can custom-make 1 1/2 kW power plants. However, these systems, as well as the previously developed ones by General Electric Company, contain electrodes with high platinum loadings (4 mg/cm^2). The first demonstration of high power density solid polymer electrolyte fuel cells with low platinum loading electrodes was by one of the authors in this paper (SS) and his coworkers at Los Alamos National Laboratory (LANL); a brief description of this work is presented in the next sub section.

1.4 A Synopsis of Advances in the Attainment of High Power Densities in Solid Polymer Electrolyte Fuel Cells with Low Platinum Loading Electrodes

Since the first Space Electrochemical Research and Technology (SERT) Conference, in which the results of the first set of investigations on solid polymer electrolyte fuel cells with low platinum loading electrodes were presented(5), there has been considerable progress in developing methods for the attainment of high power densities (about 0.7 W/cm^2) in such types of fuel cells. It must be noted that the Nafion (registered trademark of Dupont) membrane was used as the proton-conducting membrane in all these investigations. The methods used to attain the high power densities may be summarized as follows:

(i) optimization of the amount of Nafion impregnated into the electrode structure;
(ii) hot-pressing of the Nafion-impregnated electrodes to prepurified Nafion membranes at 120°C (close to glass transition temperature) and 50 atm pressure;
(iii) optimization of the humidification of the reactant gases at a temperature of 5°C for oxygen or air and 10-15°C for hydrogen above the cell temperature;
(iv) operation of the cell at elevated temperatures and pressures (say, 80° C and 5 atm); and
(v) localization of platinum by fabrication of electrodes with a higher percentage of platinum crystallites on high surface area carbon (i.e., supported electrocatalysts with 20 wt% Pt/C rather than 10%) while still maintaining the amount of Pt in the electrode (0.4 mg/cm^2) and by sputter-deposition of a thin film of platinum on the front surface (0.05 mg/cm^2), corresponding to 500 Å film a smooth surface).

By use of all these methods, it was possible to attain a current density of 1 A/cm^2 at a cell potential of 0.64 V with H_2/O_2 as reactants and 0.580 V with H_2/air reactants at 80°C and 3/5 atm pressure (3 on hydrogen and 5 on oxygen side).

The cell potential (E) - current density (i) plot fitted the equation (1). The electrode kinetic parameters for the cell E_0, b and R were calculated using a non-linear least squares fit of this equation to the experimental points. The slope of the Tafel line for oxygen reduction was found to be 0.050 to 0.060 V/decade and was independent of temperature.

TABLE 2

A SNAP-SHOT VERSION OF THE PROGRESS MADE IN SOLID POLYMER ELECTROLYTE FUEL CELL TECHNOLOGY

ORGANIZATION/ (PERIOD OF ACTIVITY)	PERFORMANCE	MAJOR ACCOMPLISHMENTS	MAJOR PROBLEMS
1. General Electric/Hamilton Standards-UTC (1958-present)	Gemini Fuel Cells - 1kW, 30kg 100 mA/cm^2 at 0.5 V; Significant improvement in performance whenNafion instead of polystyrene sulfonate used as electrolyte.	First major application of fuel cells; Breakthrough by utilizing perfluorinated sulfonic acid electrolyte membrane.	Pt-loading (4 mg/cm^2); Difficult water management; Mass transport limitations at lower current densities than expected with H_2/Air
2. Ballard Technologies Corporation Vancouver, Canada (1980 -)	Best performance 6A/cm^2 at 0.5 V with H_2O_2 ; Slope of E-i plot region 0.08 ohm cm^2 ; With H_2 /air 2A/cm^2 at 0.55 V	1.5 kW units built and tested; Use of Dow Membranes instead of Nafion significantly improves performance	Pt loading high (4 mg/cm^2); Lifetime not known.
3. Siemens, Erlangen Germany (1986 -)	Technology similar to General Electric/ Hamilton Standards -UTC; High power densities, same as Ballard, reported	Demonstration of high power densities	
4. Ergenics PowerSystems, Inc. (1984 -)	200 W units with hydride storage, built and tested - for power required by astronauts in spacewalks; Best performance reported 400 mA/cm^2 at 0.7 V	Novel approach for water management -internal transport of water from porous carbon behind electrode for humidification of gases and membrane; 1.5kw units custom-made.	High Pt loading (4 mg/cm^2); Performance on H_2 /O_2 is good; with H_2 /Air, mass transport limitations at current densities less than expected.
5. Los Alamos National Laboratory (1981 -)	2 A/cm^2 at 0.5 V attained in 5 cm^2 cells with H_2 /O_2 as reactants; 50 cm^2 cells designed and tested; Dow membrane gives best performance.	Low Pt loading electrodes (0.4 mg/cm^2); Localization of Pt near front surface of electrode to attain high power density; Optimization of humidification conditions of cell; Theoretically expected performance with air at current densities up to 1 A/cm^2 .	Program too electrochemical research oriented; Needs emphasis on engineering aspects - thermal and water management.
6. Texas A&M University (1987 -)	2 A/cm^2 at 0.6 V attained with H_2/O_2 as reactants in 5 cm^2 same current density; Cell potential 0.38 V 50 cm^2 cell design improved; Dow membrane gives best performance.	Alternate and more economical methods for Pt localization being developed; Initiated thermal and water management investigations.	Performance improvement necessary in low current density region to reach WPAFB's goals of 3 A/cm^2 at 0.8 V.

Since small variations in the parameter b give rise to misleading values of i_o, it was decided to use the current density at a cell potential of 0.900 mV (at this potential mass transport and ohmic effects are negligible and so also is the overpotential at the hydrogen electrode) as a measure of the electrocatalytic activity of the electrode for the oxygen reduction reaction. It is extremely important to have this value as high as possible to minimize the steep decrease of slope of the cell potential - current density region at very low values of curent densities. In the best case, i.e., with H_2/O_2 as reactants at 3/5 atm and 80°C in cells with electrodes composed of 20% Pt/C supported electrocatalysts and 0.4 mg Pt/cm^2 on to which a thin film of Pt was sputtered, the current density at 0.900 V was 160 mA/cm^2. Further, the calculated value of R (0.24 ohm cm^2) was quite close to the high frequency resistance (0.21 ohm cm^2), indicating the absence of mass transport overpotential over the measured current density range. The increase of cell potential with pressure, at constant current density, showed the expected semi-logarithimic dependence. The cyclic voltammetric technique was used to determine the electrochemically active surface area of the electrode. By use of this method, the platinum utilization of the electrode with the best configuration of electrodes (20% Pt/C 0.40 mg Pt/cm2 plus sputtered film (0.05 mg Pt/cm^2) was found to be about 15-20%. It was concluded in the second publication (7) since the SERT conference that to increase the power densities further, it is necessary to use membranes with higher specific conductivities and better water retention characteristics.

1.5 Scope of Present Work

The work described in the preceding sub-section was carred out by one of the authors (SS) of this paper and his former colleagues at LANL. This work has since then been continued in our laboratories with the objectives of increasing the power densities still further, as required for some applications (for example, silent mobile power source for transportation). While the work at LANL was focussed on developing on solid polymer electrolyte fuel cells using reformed hydrogen (steam-reforming of methanol), the work at our Center (CESHR) is concentrating on developing fuel cells using pure H_2 and O_2. As seen from the results in the preceding section, the "high priority" tasks which are envisioned to be important are (i) to develop methods, alternative to sputter-deposition to localize platinum near the front surface of the electrode and (ii) to reduce the ohmic overpotential in the cell. The reason for importance of the former is that sputter-deposition is not economically feasible compared to wet-chemical methods, which can be automated, for the large-scale modification of surfaces of electrodes for fuel cell systems with a reasonable power output (20 kw and higher). The methods, which are examined in this work for the deposition of a thin layer of Pt on the front surface of the electrodes are: (i) brushing the surface with a chloroplatinic acid solution (desired quantity and drying); (ii) brushing surface with platinum black particles suspended in Nafion solution; and (iii) electrodeposition of Pt. Two approaches were taken to reduce the ohmic overpotential in the cell: use of (i) thinner membranes and (ii) Dow membranes with better conductivity and water retention characteristics.

2 EXPERIMENTAL

2.1 Wet Chemical/Electrochemical Methods to Localize Platinum near Front Surfaces

The membrane and electrode (M&E) assemblies were fabricated using Protech porous gas diffusion electrodes (20% Pt/C, 0.4 mg/cm^2) and proton conducting polymer membranes (Dupont and Dow Chemical). Localization of an extra layer of platinum on the active surface of these electrodes was achieved by wet chemical methods: (i) brushing with Nafion solution containing unsupported Pt catalyst; (ii) chemical deposition of Pt from H_2PtCl_6 and (iii) electrochemical deposition of Pt also from H_2PtCl_6.

In the first method, 0.5 mg of fuel cell grade unsupported Pt catalyst (Prototech) was sonicated in 5% Nafion solution (0.6 ml) and two electrodes (each of 5 cm^2 area) were brushed with the mixture, using a soft printing brush, as uniformly as possible. The brushed electrodes were next dried in a vacuum oven at 70°C and then impregnated with Nafion in the manner described in previous publications (5-7), prior to fabrication of the M&E assembly. Chemical deposition of Pt (0.5 mg/cm2) was carried out by brushing the active surface of the electrodes with an appropriate amount of 1% H_2PtCl_6 solution in 0.05 M H_2SO_4, diluted with an equal volume of methanol; this was then followed by heat treatment of the electrodes for three hours at 200 °C in air. Electrodeposition of Pt, on the active side of Protech electrodes using the same H_2PtCl_6 (1%) - methanol (1:1 vol.), was carried out at a constant current density of 2 mA/cm^2 to deposit ~0.05 mg/cm^2 of Pt; a gold foil was used as anode during electrolysis.

2.2 Assembly of Single Cells and Performance Evaluation

The main components of a single cell assembly are as described in previous papers(5-7). The essential components are two graphite plates, the M&E assembly and gaskets containing the gas inlet and outlet and ribbed channels for the distribution of reactant gases behind the porous gas diffusion electrodes. The M&E assembly is positioned between two such graphite plates. The reference electrode (a small piece of fuel cell electrode) is embeded in the graphite plate on the anode side. Teflon coated fiberglass cloth gaskets are placed between the membrane and each of the graphite current collectors to prevent gas leakage and to avoid excessive compression of the electrodes. The current collection from the fuel cell uses a copper plate positioned behind each of the graphite plates. Compression of the overall assembly is made by means of two 1/4 inch thick stainless steel end plates and four bolts. Teflon sheets are used for electric insualtion of the single cell and the end plates. Though incorporation of a single cell in the test station with all its peripheral components (e.g., temperature controller, humidification chamber, flow meters, back pressure regulator) have also been described in the referenced publications, the components of the single cell and the test station are illustrated in Figs. 2&3 respectively. The performance evaluation was carried out using a microcomputer (IBM - XT) a power supply (HP 6033A) and a data acquisition unit (HP-3421A) interconnected through a GPIB bus. During performance evaluation, the fuel cell is connected in series with the power supply for its operation under galvanostatic load and cell potentials as well as half cell potentials versus current density data were recorded periodically. Measurements were made at different temperatures and pressures of reactant gases (H_2 at the anode and air/O_2 at the cathode).

3 RESULTS AND DISCUSSION

3.1 A Comparison of the Effects of the Suputter-Depostion and the Wet Chemical/ Electrochemical Methods on the Performance of Single Cells

As stated in Section 1, one of the main objectives of this work was to find alternatives to sputter-deposition to localize the platinum near the front surface of porous gas diffusion electrodes with low platinum loading electrodes. The cell potential current density plots (Fig. 4) show that fuel cells with the sputter-deposited and chloroplatinic acid treated electrodes exhibit similar performances throughout the entire current density range (1 to 2000 mA/cm^2). This is not so in the case of the of the fuel cell with electrodes on to which a thin layer of Pt black was deposited. A close examination of the linear E vs i (Fig. 4), as well as of the semi-logarithmic (E+ i R) vs log i (Fig. 5) plots shows that the oxygen electrode is only activation-controlled up to a current density or 1 A/cm^2. Fig. 5 and Table 3 illustrate that the fuel cell with H_2PtCl_6 treated electrodes shows a higher oxygen electrode performance than the electrodes with the Pt sputter-deposited and Pt/Nafion thin layers. This reflects a higher surface area of the H_2PtCl_6 treated electrode. The fuel cell with the Pt black treated electrodes have an unusually high slope in the linear region of the E-i

TABLE 3

Effect of Method of Deposition of Thin Layer of Platinum (0.05 mg/cm ^{2}) on Front Surface of Prototech Electrodes (20% Pt/C, 0.04 mg Pt/cm ^{2}) on Electrode Kinetic Parameters (see Eq. 1) for H_2/O_2 Solid Polymer Electrolyte Fuel Cell with 100 μm thick Nafion Membrane.

Membrane Type and Thickness	Cell Temperature	Pressure H_2/O_2	Electrode Kinetic Parameters for Cell Eo V	b V	R Ω/cm^2	Current Density at 0.9V mA/cm^2
Sputtered Pt	50	1/1	0.930	0.044	0.339	7
•	50	4/5	0.993	0.047	0.301	35
•	70	4/5	0.983	0.040	0.252	46
•	85	4/5	0.999	0.450	0.201	52
•	95	4/5	0.997	0.500	0.189	61
Unsupported Pt/Nafion, Brushed	50	1/1	0.964	0.052	0.501	12
•	50	4/5	0.956	0.048	0.452	48
•	70	1/1	1.024	0.059	0.505	10
•	70	4/5	1.014	0.052	0.462	51
•	85	4/5	1.008	0.045	0.414	61
•	95	4/5	1.005	0.044	0.368	35
H_2PtCl_6 in H_2O-CH_3OH-brushed	50	1/1	0.978	0.056	0.338	19
•	50	4/5	1.024	0.053	0.341	72
•	85	4/5	1.019	0.044	0.253	80
•	95	4/5	1.020	0.056	0.189	83

plot and the departure from linearity occures at a relatively low current-density. The slopes of the linear regions of the E-i plots in the other two cases are similar for identical operating conditions but not low enough to reach the desired goals of power density (See Section 1.2). However, it is encouraging to note that the wet chemical method of application of chloroplatinic acid followed by the heat-treatment provides electrodes which exhibit similar performances to the sputter-deposited ones.

3.2 Effects of Thickness of Membrane on Performances of Fuel Cells

Most of the LANL studies reported in references 5 to 7 used Nafion 117 membranes. Fuel cells with these membranes yield a slope of approximately 0.25 ohm cm^2 in the linear region of the E-i plot. If the resistance of the test cell fixtures (0.05 ohm cm^2) is subtracted from this value, the slope of the E-i (Table 3) plot (linear region) will be reduced to 0.20 ohm cm^2. This value is still too high to reach current density of 2 to 5 A/cm^2 at reasonable cell potentials (> 0.5V). Thus, in this work experiments were carried out with Nafion membranes having a thickness of 50 and100 µm and the results of fuel cell performance compared with those in fuel cells with the Nafion 117 membrane (thickness: 175 µm). The 100 µm membranes were of the "sweded type" (sweding was carried out to roughen the surfaces of the membrane and make it of uniform thickness). The performances of the fuel cells with the 50, 100 and 175 µm membranes are shown in Fig. 6. While the fuel cell with the Nafion 117 membrane begins to show mass transport limitations at a current density of 1 A/cm^2, this is not the case for the single cells with thinner Nafion membranes. The single cell with 100 µm membrane shows mass transport limitation at 1.8 A/cm^2 while the cell with 50 µm membrane shows no mass transport limitation up to the highest current density (2 A/cm2) of measurements.The electrode kinetic parameters extracted from these experimental results and using equation (1), are shown in Table 4. The agreement in the "pseudo i R" (all forms of overpotential which show a linear variation of potential with current density - mostly ohmic) corrected Tafel plots Fig. 7 for oxygen reduction in the cells with the 100 and 175 µm thick membranes are as expected. The sweded membrane (100 µm thick) shows a slightly higher resistance than expected on the basis of its thickness as compared to the thicker (175 µm) membrane (Table 4).

3.3 Dow Membranes: The Solution to Attainment of Super High Power Densities

In the work to date the highest power densities were attained by using Dow membranes as the electrolyte layer. A comparison of the performances of single cells using the Nafion and Dow membranes is illustrated in Fig. 8. The Nafion Membranes had thicknesses of 175 and 100 µm while the Dow membranes were 125 µm thick. It is natural to expect a thinner membrane to have a lower resistance but even if we take this into consideration the Dow membrane has a lower specific resistivity (i.e., higher specific conductivity) than Nafion. The reason for the higher specific conductivity of the Dow membrane than that of Nafion is that the monomer of the former may be represented by:

$$CF_2{=}\ CF\ O\ CF_2\ CF_2\ SO_3\ H \qquad (6)$$

while that of the later is:

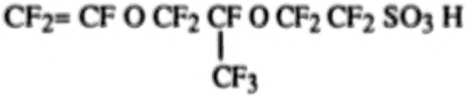

$$CF_2{=}\ CF\ O\ CF_2\ \underset{\underset{\displaystyle CF_3}{|}}{CF}\ O\ CF_2\ CF_2\ SO_3\ H$$

(7)

Hence, there are a greater number of sufonic acid groups in Dow polymer membrane than in the Nafion polymer membrane. Expressed in another manner, the Dow proton conducting polymer has a lower equivalent weight than Nafion.

TABLE 4

Effect of Thickness of Nafion Membrane and of Type of Membrane on Electrode Kinetic Parameters of H_2/O_2 Solid Polymer Electrolyte Fuel Cell with Prototech Electrodes (20% Pt/C, 0.40 mg Pt/cm^2) on to which a Thin Layer of Pt (0.05 mg/cm^2) was sputtered.

Membrane Type and Thickness	Cell Temperature	Pressure H_2/O_2	Electrode Kinetic Parameters for Cell			Current Density at 0.9V mA/cm^2
			Eo V	b V	R Ω/cm^2	
Nafion 117, 175µm	50	1/1	.946	.049	.475	7
•	50	3/4	1.003	0.048	.428	50
•	80	3/4	.951	0.037	.437	61
•	85	3/4	1.007	0.046	.298	70
Sweded Nafion 117, 100µm	50	1/1	0.964	0.052	0.339	12
•	50	4/5	0.956	0.048	0.301	48
•	70	4/5	1.024	0.059	0.252	10
•	85	4/5	1.008	0.045	0.201	61
•	95	4/5	1.005	0.044	0.189	35
•						
	50	1/1	.833	.061	.188	<1
Nafion 117, 50µm	50	1/1	.955	.061	.195	7
Dow Membranes	50	4/5	.995	.053	.157	42
•	70	1/1	.912	.062	.153	1.6
•						
	70	4/5	.994	.053	.116	43
•	85	4/5	1.002	.053	.111	62
•	95	4/5	1.000	.549	.110	54
•						

Figure 8 shows that the cell-potential current density plots overlap in the low current density region (say up to 50 mV). This means that the activation-controlled behavior is unaffected by the characteristics of the membrane (Dow vs Nafion, Nafion thick vs thin). One can easily interpret this result on the basis that the electrochemical reaction occurs to a large extent within the pores and the surface of the electrodes which are coated with the proton-conducting membranes. With increasing current density, the role of the membrane (type, thickness) is dominant and consequently the slopes of the linear region are different. One significant result is that the slope of the linear region in the cell with the Dow membrane (thickness 175 µm) is less than that in the cell with the Nafion membrane (thickness 100 µm) even thaough the thickness of the Dow membrane is greater than that of the Nafion membrane. This result can be explained by the fact that the Dow membrane has a higher specific conductivity than that of the Nafion membrane.

There is a second interesting observation in the E-i plots. The departure of the E-i plot from linearity at the higher current density appears to depend on the thickness of the membrane (cf the results with Nafion membrane 175 and 100 µm thick membrane) and the type (cf Dow membrane 125 µm vs Nafion 100 µm). Departure from linearity at the high current densities are associated with mass transport controlled processes. Generally, these are due to mass transport limitations of reactants reaching the active sites in the electrode or of products (or inert gases like N_2 when air instead of oxygen is used) away from the electrocatalytic sites. However, the electrode structures and conditions of humidification of reactant gases were identical in the three cases. It is very likely that transport processes within the membrane can be rate-limiting. The transporting species are protons, which migrate from the anode to the cathode under the influence of the electric field, and water molecules which are carried with the protons. It is estimated that 3-6 water molecules are transported with the protons. Due to the resulting concentration gradient of water molecules in the cell during operation one can expect water molecules to diffuse from the cathode to the anode. Mass transport limitations could occur due to any one or more of these processes. The Dow membrane shows a linear behavior up to a current density of 2 A/cm^2. This is not the case in the cell with the Nafion membrane which is slightly thicker than the Dow membrane. This result lends insight on different types of proton conduction (say Grotthus type in a Dow membrane vs classical proton transport through the electrolyte in Nafion). It is interesting to point out that in previous studies it was noted that when mass transport limitation begins on one electrode, it also sets in on the other at the same current density. A detailed modeling analysis of the mass transport processes is necessary to interpret the result in the higher current density range.

The electrode kinetic parameters for the cells were calculated as described briefly in section 1.2. The parameters E_0 and b are unaffected by the membrane. However, R, which represents the rate of increase of cell potential in a linear manner with the current density, depends on the membrane type and its thickness. The most significant contribution to R is the ionic resistance of the membrane, as has been shown previously using high frequency measurements (7). The striking result is that R is a factor of two less for the cell with the Dow membrane (thickness 125 µm) than for the one with the Nafion membrane. This result follows from the fact that the Dow membrane has a lower specific resistance. The calculated value of R is always slightly less than the slope of the linear region in the E vs i plot. For example for the cell with the Dow membrane operating at 95°C, the R is 0.110 while the slope of the linear region is 0.113. The reason for this is that the apparently linear slope of the E-i plot includes a small contribution of the charge transfer resistance of the oxygen reduction reaction. In the cells used in this work the test cell fixtures have a resistance of 0.05 ohm cm^2. If this is excluded from the values of R and of the slope of the E-i, line the resulting values are only 0.06 and 0.08 ohm cm^2 respectively. The latter value is the same as that of the slope of the E-i plot in the best Ballard Cells. Using the calculated values of R, the (E + Ri) vs log i plots (Fig.9) were made for the cells with the Dow (125 µm) and Nafion (100 µm) membranes operating at 95°C and 4/5 atm. The Tafel behavior is observed for the former cell over the entire current density range, whereas for the latter, there is departure from the Tafel line at the same current density as the one in the E-i plot where it departs from linearity.

Another resutl is worth mentioning. The half and single cell potentials are plotted as a function of current density (Fig. 10) for the cell with the Dow membrane. The hydrogen electrode exhibits a linear behavior throughout the entire current density range. The hydrogen overpotential at 2A/cm^2 is only 20 mV. Thus the charge transfer resistance due to the hydrogen electrode is only 0.01 ohm cm^2 which is a contribution of this electrode to the calculated R value or the measured slope of the cell potential vs current density plot.

4 CONCLUSIONS

The conclusions which may be drawn from these studies are:

(i) The chloroplatinic acid method of treatment of the electrodes provides a satisfactory alternative and considerably more economic method than sputtering for the deposition of a thin layer of Pt on the front surface of the electrodes, which is essential for the attainment of high power densities.

(ii) Use of thinner membranes is advantageous from the points of view of lowering the ionic resistance and lowering mass transport limitations at higher current densities.

(iii) Striking results have been obtained in cells with the Dow membrane which has a higher ionic conductivity , lesser mass transport limitations (H^+ and H_2O) and better water management characteristics than Nafion.

(iv) The performances of a solid polymer electrolyte fuel cells with low platinum loading electrodes are approaching those of the ones with ten times the platinum loading in respect to attainment of high power densities.

ACKNOWLEDGEMENTS

This work was supported by a contract from DARPA/ONR, Code 1113 ES. The authors are grateful to Dow Chemical (via Drs. Glenn Eisman and Jeffrey Gunshor), Freeport, Texas, for providing Dow polymer membranes used in this work.

REFERENCES

1. (a) J. K. Stedman, 1985 Fuel Cell Seminar Abstracts, P. 138. Courtesy Associates, Washington D. C. (1985).
   (b) R. Warnock, Wright-Patterson Air Force Base, Personal communication.

2. (a) D. Watkins, D. Kircks, D. Epp and A. Harkness, Proceedings of the 32nd Annual Power Sources Conferences, Cherry Hill, N.J., June 9-12, 1986. The Electrochemical Society, Inc. 590, (1986).
   (b) D. Watkins, Ballard Technologies Inc., personal communication, (1987).

3. O.J. Adlhart and M.J. Rosso, Ergenic Power Systems, Inc.,Wyckoff, NJ, Personal communication.

4. K. Strasser, Siemens, Erlangen, Germany FR, Personal communication.

5. S. Srinivasan, E.A. Ticianelli, C.R. Derouin and A. Redondo, J. Power sources, 22, 359 (1988).

6. E. Ticianelli, C.R. Derouin, A. Redondo and S. Srinivasan, J. Electrochem. Soc., 135, 2209 (1988).

7. Edson, A. Ticianelli, Charles R. Derouin and Supramaniam Srinivasan, J. Electroanal Chem., 251, 275-295 (1988).

8. J. O'M Bockris and S. Srinivasan, Fuel Cells: Their Electrochemistry, McGraw Hill Publishing Company, New York (1969).

9. A. J. Appleby and F. R. Fowkes, Fuel Cell Handbook, Van Nostrand Reinhold, New York (1988).

10. S. Srinivasan, J. Electrochem. Soc., 136, 41C (1989).

11. M. A. Enayatullah and J. O'M. Bockris, Proceedings of the Symposium on Electrode Materials and Processes for Energy Conversion and Storage, S. Srinivasan, S. Wagner and H. Wroblowa (eds.), Proceedings Volume 87-12, 256, The Electrochemical Society, Pennington, NJ (1987).

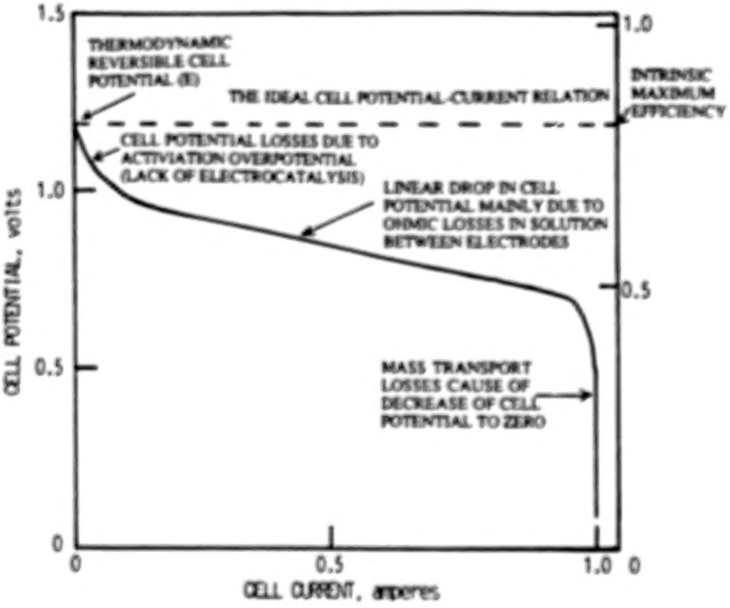

Figure 1. Typical plot of cell potential versus current for fuel cells illustrating regions of control by various types of overpotentials.

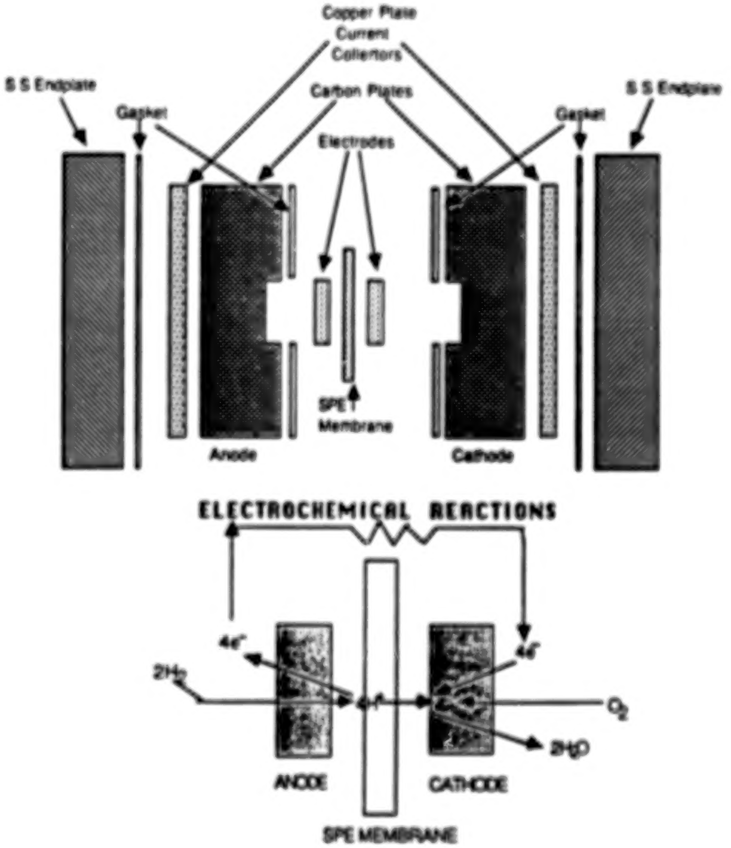
Copper Plate Current Collertors
S S Endplate
S S Endplate
Gasket
Gasket
Carbon Plates
Electrodes
SPE Membrane
Anode
Cathode
ELECTROCHEMICAL REACTIONS
4e⁻
4e⁻
2H₂
4H⁺
O₂
2H₂O
ANODE
CATHODE
SPE MEMBRANE

Figure 2. Schematic of solid polymer electrolyte fuel cell assembly.

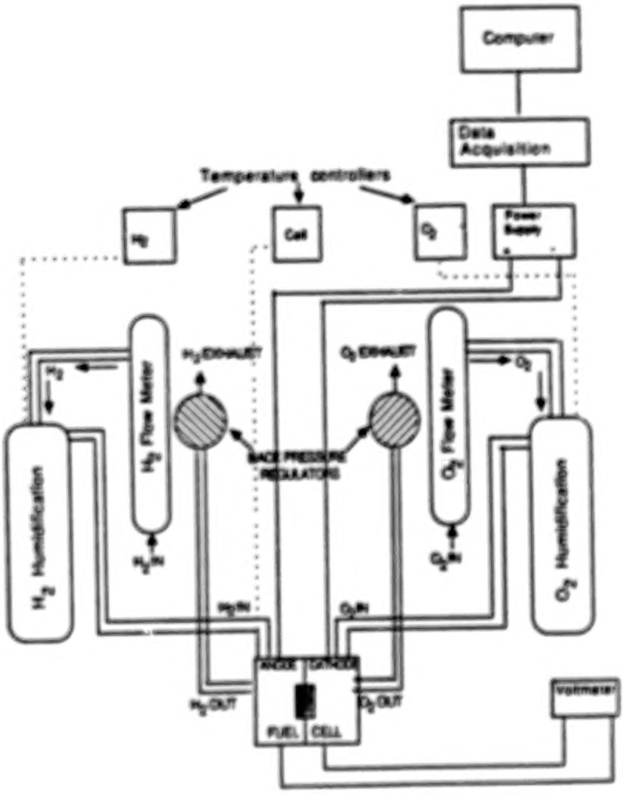
Computer
Data Acquisition
Temperature controllers
H2
Cell
O2
Power Supply
H2 EXHAUST
O2 EXHAUST
H2
O2
H2 Flow Meter
O2 Flow Meter
BACK PRESSURE REGULATORS
H2 Humidification
O2 Humidification
H2 IN
O2 IN
H2 IN
O2 IN
ANODE
CATHODE
H2 OUT
O2 OUT
FUEL
CELL
Voltmeter

Figure 3. Schematic of solid polymer electrolyte single cell test station.

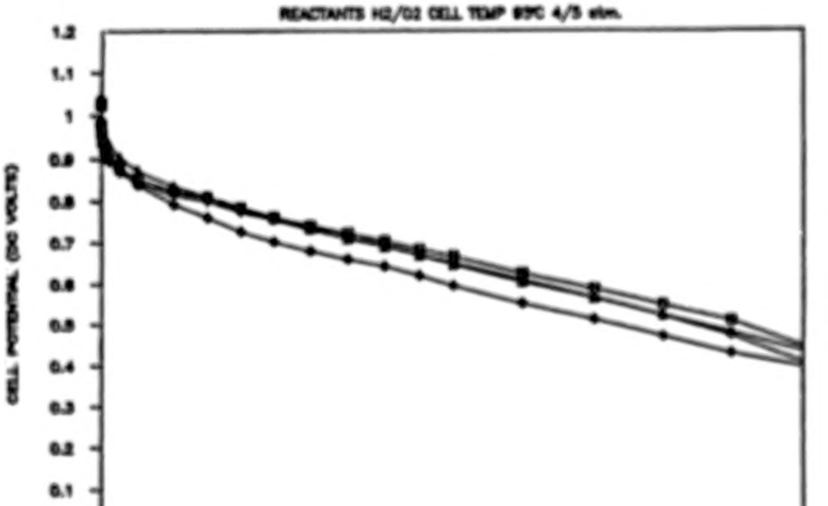

Figure 4. Cell potential vs. current density plots for single cells with electrodes having localized Pt layer deposited by different methods, all operating at 95°C and with H_2/O_2 at 4/5 atm. Sputter deposited (■), electrochemically deposited (+), chemically deposited from H_2PtCl_6 (Δ) and brushed with Nafion solution containing unsupported Pt (◇). Pt loading on each electrode: 0.45 mg/cm^2.

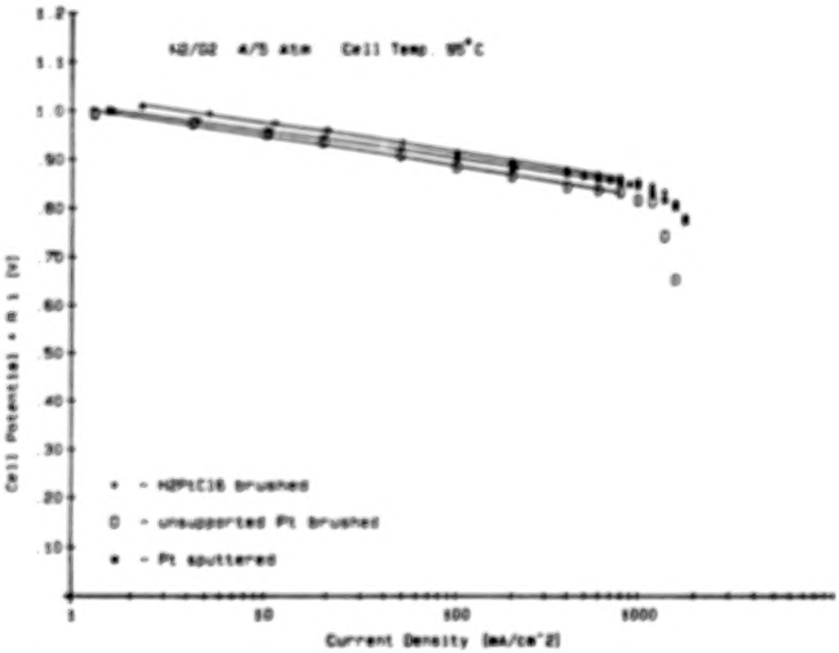

Figure 5. Plots of (E + iR) vs log I for single cells with electrodes having localized Pt layer deposited by different methods, all operating at 95°C with H_2/O_2 at 4/5 atm. sputter-deposited (●), chemically deposited from H_2PtCl_6 (+), and brushed with Nafion solution containing unsupported Pt (o). Pt loading on each electrode: 0.45 mg/cm^2.

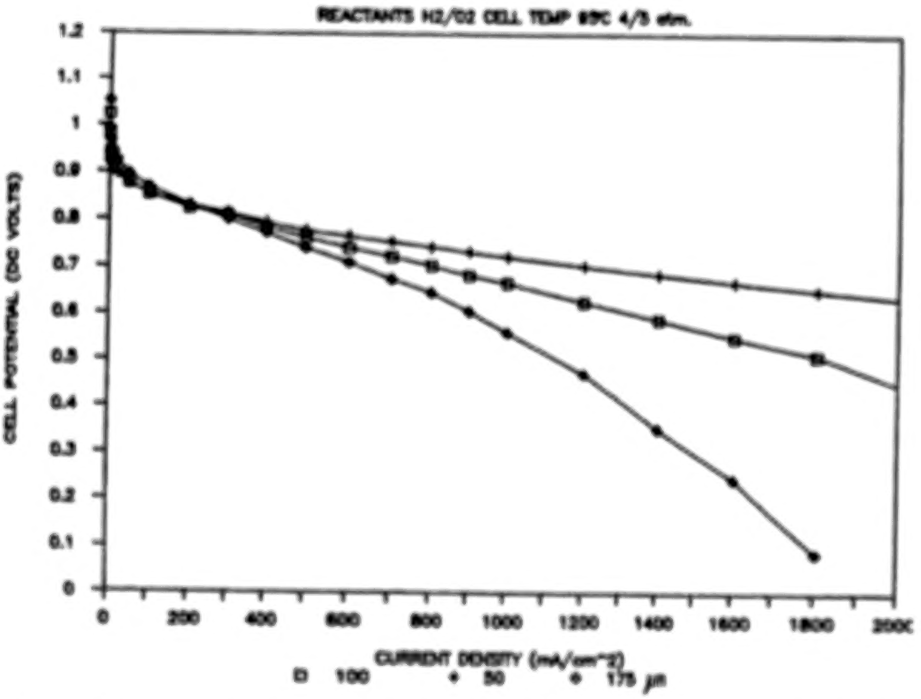

Figure 6. Cell potential vs current density plots for single cells with Nafion 117 membranes of two different thicknesses, operating at 95°C with H_2/O_2 at 4/5 atm. Nafion, thickness:175 μm (◆),100 μm (▫) and 50 μm (+) Pt loading on each electrode: 0.45 mg/cm^2.

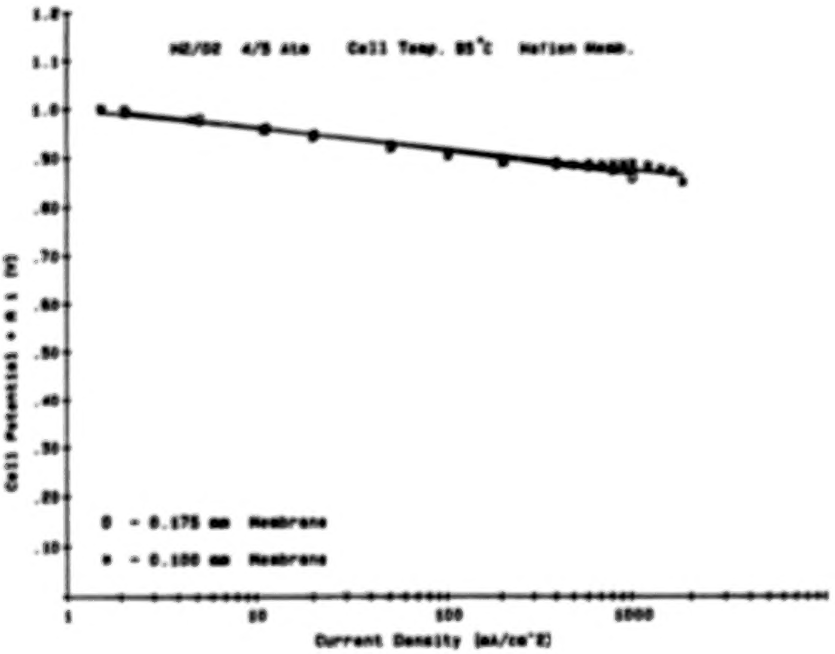

Figure 7. Plots of (E + iR) vs log i for single cells with Nafion membranes of two different thicknesses, operating at 95°C with H_2/O_2 at 4/5 atm. Nafion117, thickness: 175 µm (o) and 100 µm (•). Pt loading on each electrode: 0.45 mg/cm^2.

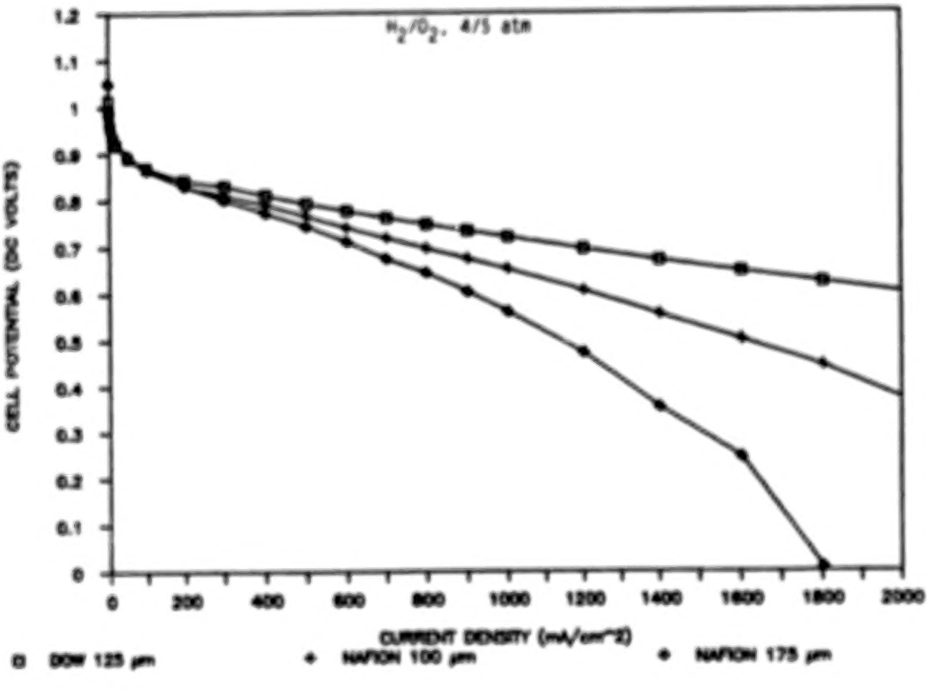

Figure 8. Cell potential vs current density plots for single cells with different membrane materials, operating at 95°C with H_2/O_2 at 4/5 atm. Dow membrane, 125 µm (▪), Nafion 117, 175 µm (◊), and Nafion 117 (sweded), 100 µm (+). Pt loding on each electrode: o. 45 mg/cm^2.

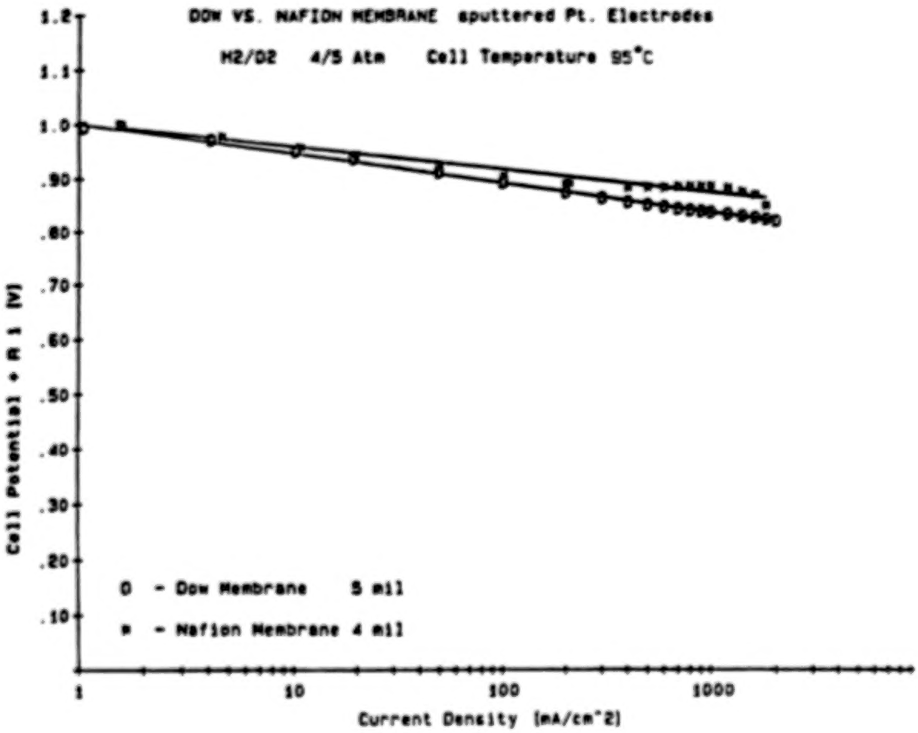

Figure 9. Plots of (E + iR) vs log i for single cells with different membrane materials, operating at 95°C with H_2/O_2 at 4/5 atm. Dow membrane, 125 µm (o), Nafion 117, 175 µm (*). Pt loading on each electrode: 0.45 mg/cm^2.

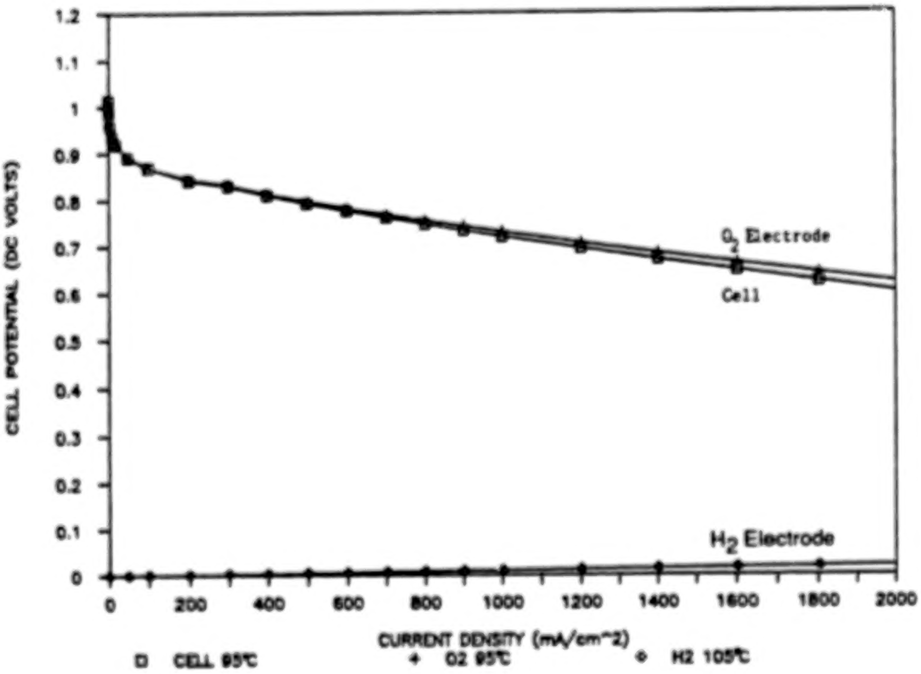

Figure 10. Cell and half cell potentials vs current density plots for a single cell with Dow membrane (thickness: 125 µm) and Pt-sputtered Prototech electrodes (Pt loading: 0.45 mg/cm^2) operating at 95 °C with H_2/O_2 at 4/5 atm.

THE APPLICATION OF DOW CHEMICAL'S PERFLUORINATED MEMBRANES IN PROTON-EXCHANGE MEMBRANE FUEL CELLS

G.A. Eisman
The Dow Chemical Company
Freeport, Texas 77541

Dow Chemical's research activities in fuel cells revolve around the development of perfluorosulfonic acid membranes useful as the proton transport medium and separator. The following work will outline some of the performance characteristics which are typical for such membranes.

INTRODUCTION

The use of fuel cells as a power source has been successful for manned space applications on short-lived missions as is evident from the Gemini, Apollo and Orbiter missions. In the latter two programs, the alkaline technology has been the system of choice; whereas the Gemini program experimented with the proton-exchange membrane technology (PEM). Although the alkaline technology has enjoyed a certain degree of popularity among the various fuel cell concepts for space applications, there are no clear-cut favorites for one fuel cell technology over others when the duty cycle becomes long as it would in extensive long-lived missions.

Until recently, the PEM fuel cell technology has been a laboratory curiosity except for a few brief missions during the Gemini program. Although attractive for many reasons, including long life (Ref. 1) and reduced failure rates as a result of pressure upsets (when compared to free electrolyte systems), the lower power and efficiency characteristics have kept the technology shelved. Recently, Dow Chemical developed a new perfluorosulfonic acid proton transporting ionomer which can be applied in fuel cells (Ref. 2-3). The results of tests with the Dow membrane as reported in the literature (Ref. 4-7), have demonstrated that the materials have a significantly reduced internal resistance. For fuel cells, this reduced resistance translates directly to performance and efficiency since a membrane with this characteristic results in significantly enhanced proton transport rates with a lower emf driving force.

The performance of a proton-exchange ionomer in a fuel cell is related to many factors, some of which include membrane ionic activity, hydration level, visco-elastic properties, as well as electrode characteristics, cell design, and mode of operation. This paper will be concerned with the properties of the Dow materials which are related to performance characteristics of a PEM fuel cell system.

EXPERIMENTAL

The Dow experimental membrane utilized in this study is characterized by having an ion-exchange capacity of 1.13 and being .013 cm in thickness. All cell tests were carried out in a single cell 50 cm^2 active area PEM fuel cell designed and built by the Hamilton-Standard Corp. for Dow Chemical. The cell is a modified version of the hardware delivered to Los Alamos National Laboratory under a transportation contract with Hamilton-Standard (NASA Contract #P.O. No.9-X53-D6272-1).

The current interrupt experiments were carried out using a home-made fast response switching device coupled to a Nicolet storage oscilloscope.

The membrane and electrode assemblies were fabricated using proprietary techniques. The electrode loadings were 2 mg/cm^2/side.

RESULTS AND DISCUSSION

Membrane Properties

The new perfluorosulfonic acid membranes recently introduced by Dow Chemical, as referenced above, exhibit significantly lower IR losses resulting in membranes which can be operated at ultra-high current (power) levels. This behavior is presented in Figure 1 along with the state-of-the-art performance characteristics for a commercially available fuel cell membrane manufactured by DuPont under the tradename Nafion ®. As can be seen from the data, the Dow materials can generate substantially higher current densities than systems utilizing the DuPont material. The voltage losses which appear to be great at 3500 amps/ft^2 (3771 amps/cm^2) are actually a result of using high resistant cell plates and hardware. It is approximated that the loss due to the cell hardware is close to 200 mv.

Although the membrane is capable of higher current levels, the attractive characteristic and one which will be critical for long space flights is the higher voltage at the lower current densities, i.e., 100 - 500 amp/ft^2. This enhanced voltage is a direct result of the reduced internal resistance of the membrane which is attributed mainly to the high sulfonic acid ionic content responsible for proton transport. The advantages of such a higher voltage are many, but the most important is an increase in the total electrochemical efficiency.

The Dow membrane is based on chemistry which leads to a reduced mass in the sidechain which is bonded to the long CF_2 backbone. Presented in Figure 2 is the chemistry for the synthesis of the monomer and the copolymerization step with the tetrafluoroethylene; while in Figure 3, the resultant structure is depicted. Also presented in Figure 3 for comparative purposes is the structure of DuPont's Nafion.

The membrane properties pertinent for fuel cell operation are tabulated in Table 1 for the Dow fuel cell membranes. Such characteristics as ionic conductivity, water permeability, gas permeation, and properties related to mechanical strength are listed. The data presented in the table covers a range rather than single data points because, at this time, Dow has prepared numerous membranes of different ion exchange capacity which all have been successfully tested in fuel cell operation.

Fuel Cell Test Results

The hardware used during the membrane performance tests is a modified version of the cell presented in Figure 4. The hardware utilizes carbon/Kynar plates with a 50 cm^2 active area. There is a heat exchanger on each side of the reactor compartment and an internal humidification compartment.

Presented in Figure 5 is a polarization curve of the membrane previously described. As can be seen from the figure, the membrane is capable of operating at high efficiencies at low current densities or lower efficiencies at high current densities. The resistance in the ohmic region is .220 ohm-cm^2 ($2.37 X 10^{-4}$ ohm-ft^2). This data contains the resistance of the package and therefore is not an IR free number. It should also be pointed out that the polarization data at each point was recorded only after the system appeared to reach equilibrium at the given current density. Figure 6 is a plot of the same data as Figure 5 but expanded in the region of 0 to 500 amps/ft^2.

Although steady-state performance can be achieved at any current density demonstrated in the polarization data of Figure 5, the voltage of the cell vs. time at a single current density (200 amps/ft^2) for a relatively short period of operation is presented in Figure 7. These data include predetermined shut-down periods on a daily basis. As can be seen from the plot, the voltage over the time element investigated was invariant.

Current interrupting was carried out in order to determine the electronic resistance effects of the hardware and remaining ionic resistance and over-voltage of the membrane and electrode package. The tests were carried out at 100 amps/ft^2 (and less) due to a limitation in the interrupting switching device. A typical result of the tests is depicted in Figure 8 for the current membrane under study. As can be seen from the data presented in the figure, the IR free component is approximately 15 mv at this current density and was measured at approximately 50 microseconds after the current break. This translates to an internal resistance of 3 milliohms at 100 amps/ft^2 (5 total amps) or .15 ohms-cm^2. When the IR free voltage (.933) at 100 amps/ft^2 is subtracted from the open circuit potential (1.05 V) the resulting voltage due to the membrane, membrane/electrode, and electrode overvoltages, amounts to approximately 117 millivolts. In order to determine the package ohmic contribution, the cell resistance is subtracted from the slope data. Such a calculation yields .07 ohm-cm^2 (.222 - .15 ohm-cm^2). A list of IR free values vs. at current densities between 25 and 100 amps/ft^2 are presented in Table 2.

In order to determine the response times for the membrane and electrode assembly in the Dow hardware utilizing a Dow perfluorosulfonic membrane, a series of tests was carried out not unlike the above whereby the current was "interrupted" numerous times. In these tests, the cell was allowed to reach equilibrium at the desired current density prior to the interruption. The cell voltage was monitored as a function of time and recorded (Figure 9) during each interruption. As can be seen from the data, the time required to shut the electronic component of the cell off was on the order of 50 microseconds. Such a rapid shut-down rate should be construed to be an advantage from an operating (safety) point of view.

In addition to proceeding from a power producing mode to open circuit, the response times were also monitored for when the system is at open circuit and then dropped across a resistance to generate the 100 amps/ft^2. The results of these tests are essentially identical to those when the current path was opened, both in behavior as well as response time.

For a power device to be practical the cell response time must be fast and efficient and without the generation of transients. In both of the above response time tests, the time required to reach various percentages of full power are presented in Table 3. In all cases, it is seen that the time to reach full "on" power was short, but in all cases 90% of full power was achieved within 80 milliseconds.

Finally, since the fuel cell was turned off and on several times throughout the test, it is important to demonstrate the reliability and resiliency of the PEM system by presenting polarization data after such system upsets. The series of polarization curves generated throughout the week-long run was carried out in order to determine if changes were occurring to the membrane/electrode assembly. Presented in Figure 10 is a series of current-voltage sweeps (IR included) taken at the times labeled on each curve. After the numerous on-off cycles, as determined from the polarization behavior, no apparent degradation was taking place.

CONCLUSIONS

The results of tests utilizing a new experimental membrane useful in proton-exchange membrane fuel cells were presented. The high voltage at low current densities can lead to higher systems efficiencies while, at the same time, not sacrificing other critical properties pertinent to membrane fuel cell operation. A series of tests to determine response times indicated that "on-off" cycles are on the order of 80 milliseconds to reach 90% of full power. The IR free voltage at 100 amps/ft^2 was determined and the results indicating a membrane/electrode package resistance to be .15 ohm-cm^2 at 100 amps/ft^2.

REFERENCES

1. McElroy, J., General Electric Co., Solid Polymer Electrolyte Fuel Cell Technology Program, Final Report. NASA Contract # Nas 9-15286, May, 1980, p 5.

2. Ezzell, B. R.; Carl, B.; Mod, W. A.; "Ion Exchange Membranes for the Chlor-Alkali Industry," AIChE Symposium Series, Houston, Texas, March, 1985, pp 49-51.

3. Eisman, G. A., "The Physical and Mechanical Properties of a New Perfluorosulfonic Acid Ionomer for use as a Separator/Membrane in Proton Exchange Processes," Proceedings of the 136Th Electrochemical Society Meeting, Boston, May, 1986.

4. Eisman, G. A., " The Application of a New Perfluorosulfonic Acid Ionomer in Proton-Exchange Membrane Fuel Cells: New Ultra-High Current Density Capabilities," Proceedings of the International Seminar on Fuel Cell Technology and Applications, The Netherlands, 26 October, 1987, pp 287-294.

5. Watkins, D., Canadian Fuel Cell Program. International Seminar on Fuel Cell Technology and Applications, The Netherlands, 26 October, 1987.

6. Vanderborgh, N. E.; Spirio, C. A.; Huff, J. R.; "Advanced Fuel Cell Systems for Transportation Applications," Proceedings of the International Seminar on Fuel Cell Technology and Applications, The Netherlands, 26 October, 1987, pp 253-262.

7. Hoadley, J., Lawrence, R., "Scale-up of a Proton-Exchange Membrane Fuel Cell," Proceedings of the Fuel Cell Seminar, Long Beach, CA, October, 1988, pp 263-266.

FIGURE 1
VOLTAGE–CURRENT POLARIZATION DATA

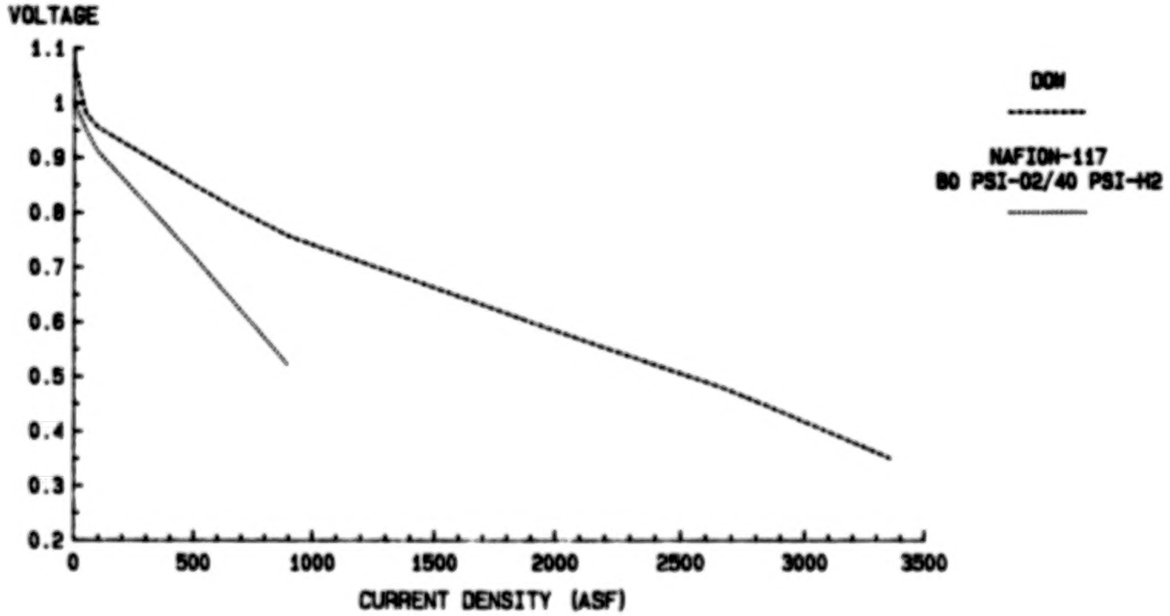

H2/O2 40/60 PSIG 80 C
2 MG/CM2/SIDE Pt

FIGURE 2

CHEMISTRY OF THE DOW CHEMICAL COMPANY

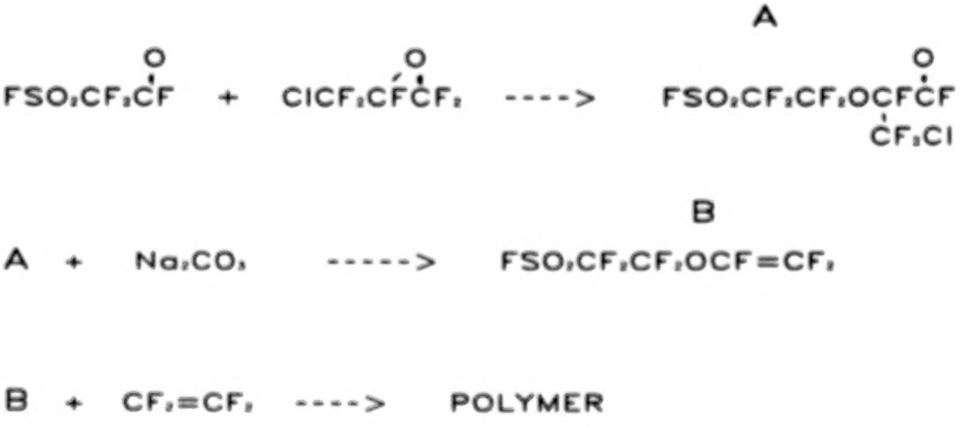

$$FSO_2CF_2\overset{O}{C}F + ClCF_2\overset{O}{CFCF_2} \text{ ----> } \overset{A}{FSO_2CF_2CF_2O\underset{CF_2Cl}{C}F\overset{O}{C}F}$$

$$A + Na_2CO_3 \text{ -----> } \overset{B}{FSO_2CF_2CF_2OCF{=}CF_2}$$

$$B + CF_2{=}CF_2 \text{ ----> } \text{POLYMER}$$

FIGURE 3
POLYMER STRUCTURES

DOW

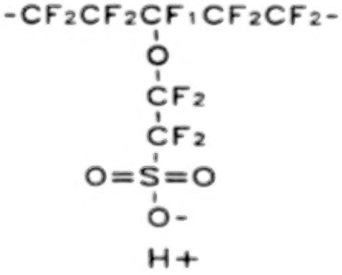

$$\begin{array}{c} -CF_2CF_2CF_1CF_2CF_2- \\ | \\ O \\ | \\ CF_2 \\ | \\ CF_2 \\ | \\ O=S=O \\ | \\ O^- \\ H^+ \end{array}$$

DUPONT NAFION

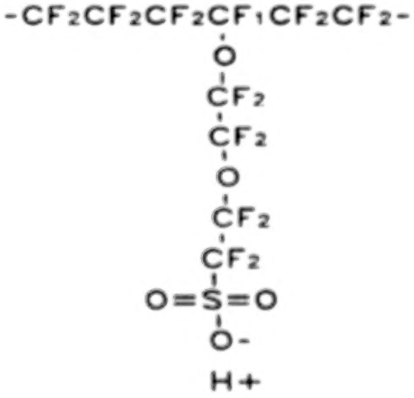

$$\begin{array}{c} -CF_2CF_2CF_2CF_1CF_2CF_2- \\ | \\ O \\ | \\ CF_2 \\ | \\ CF_2 \\ | \\ O \\ | \\ CF_2 \\ | \\ CF_2 \\ | \\ O=S=O \\ | \\ O^- \\ H^+ \end{array}$$

FIGURE 4
CELL HARDWARE

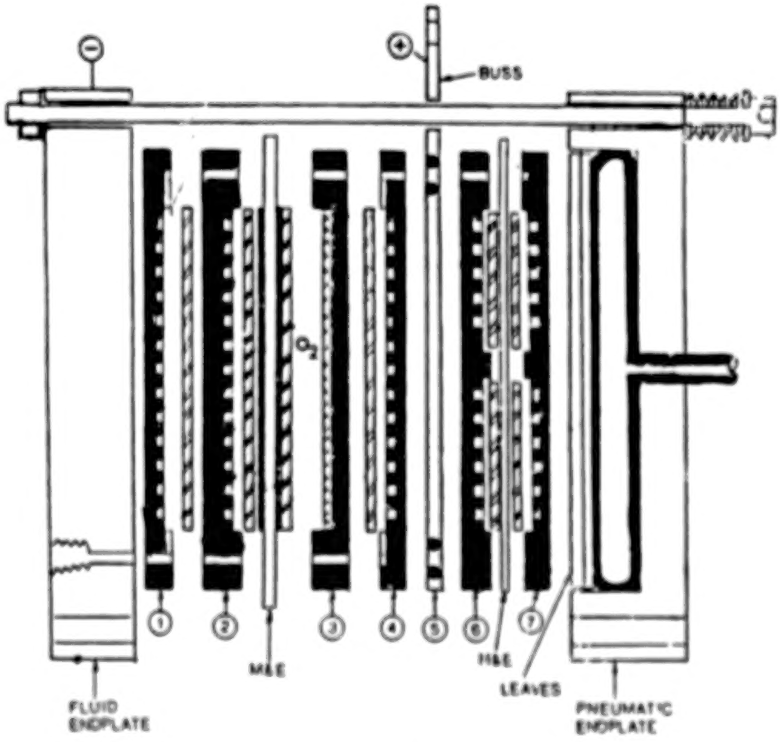
⊖
⊕
BUSS
O_2
①
②
M&E
③
④
⑤
⑥
⑦
M&E
LEAVES
FLUID ENDPLATE
PNEUMATIC ENDPLATE

FIGURE 5
VOLTAGE - CURRENT POLARIZATION DATA
HYDROGEN OXYGEN 80 C

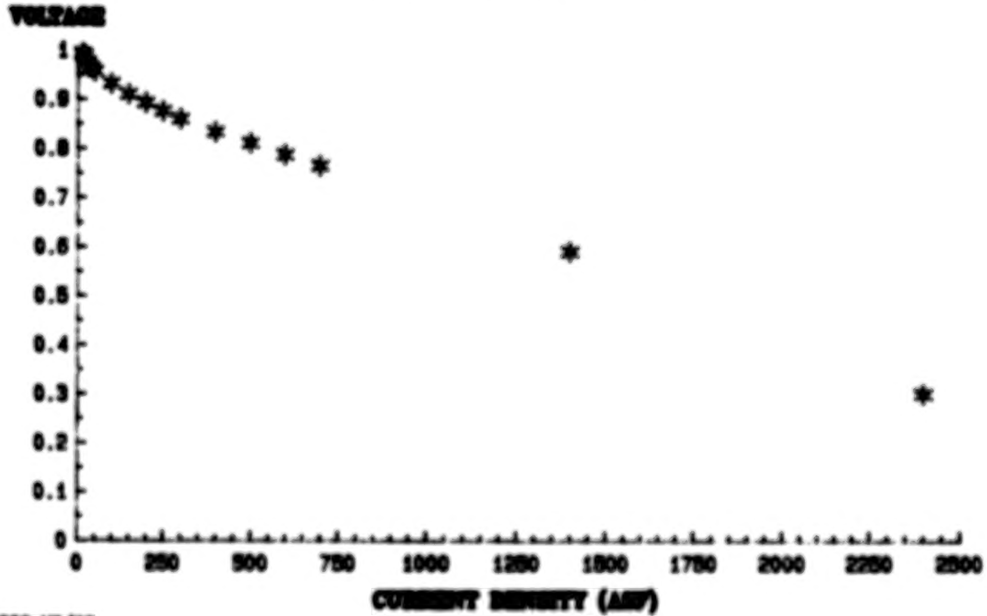

40/60 PSIG H2/O2
1.1 STOICH H2: 2 STOICH O2
2mg Pt/CM^2/SIDE

FIGURE 6
VOLTAGE-CURRENT POLARIZATION DATA
0 --> 500 ASF

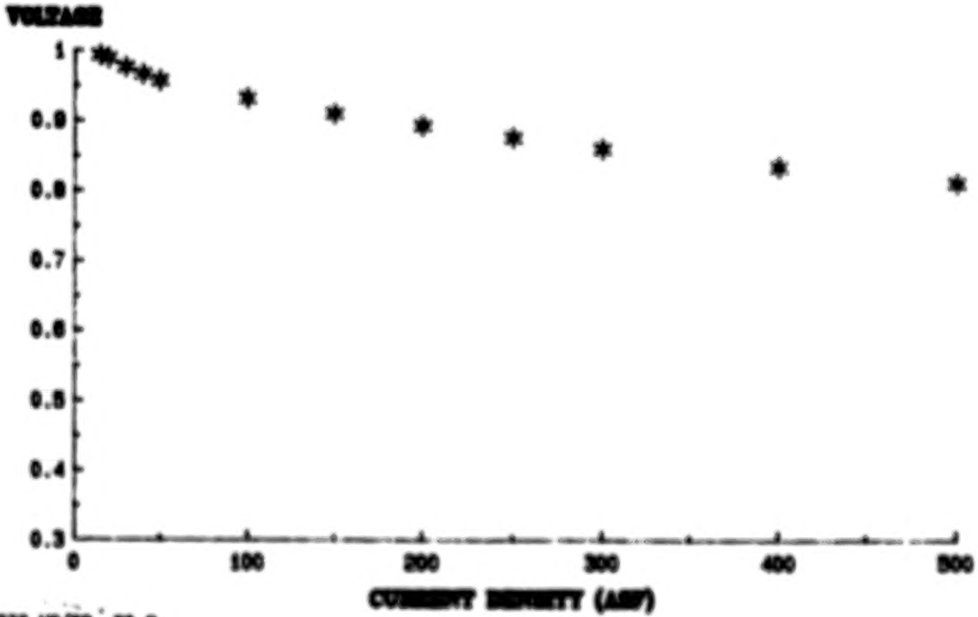

40/60 PSIG H2/O2 80 C
1.1 STOICH H2: 2 STOICH O2
2mg Pt/CM^2/SIDE

FIGURE 7
VOLTAGE VS. TIME (HRS)
200 ASF

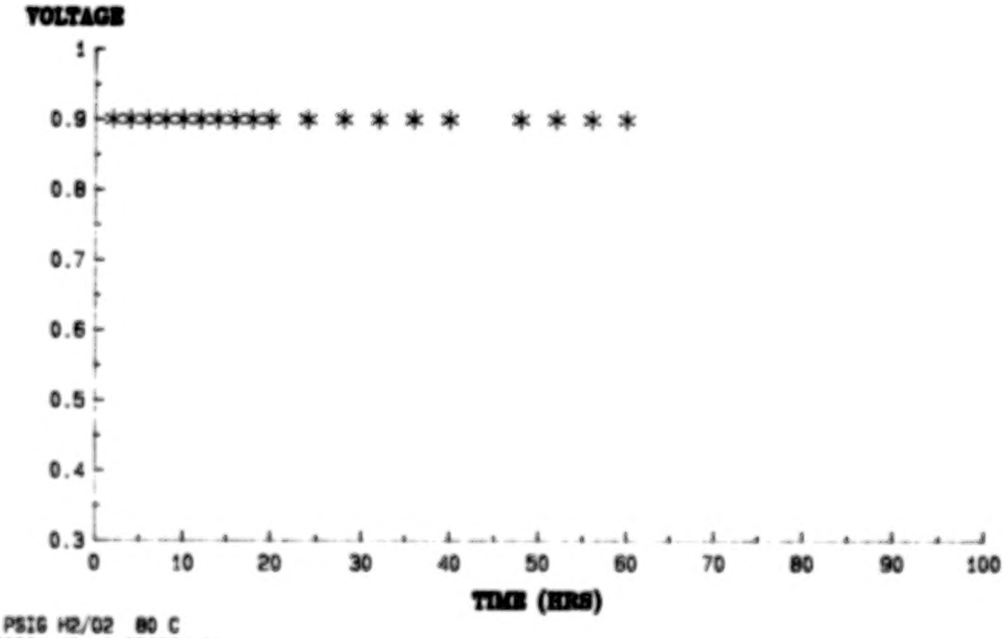

40/60 PSIG H2/O2 80 C
1.1 STOICH H2: 2 STOICH O2
2mg Pt/CM^2/SIDE

FIGURE 8

RESPONSE TIME 100 ASF ---> OCV

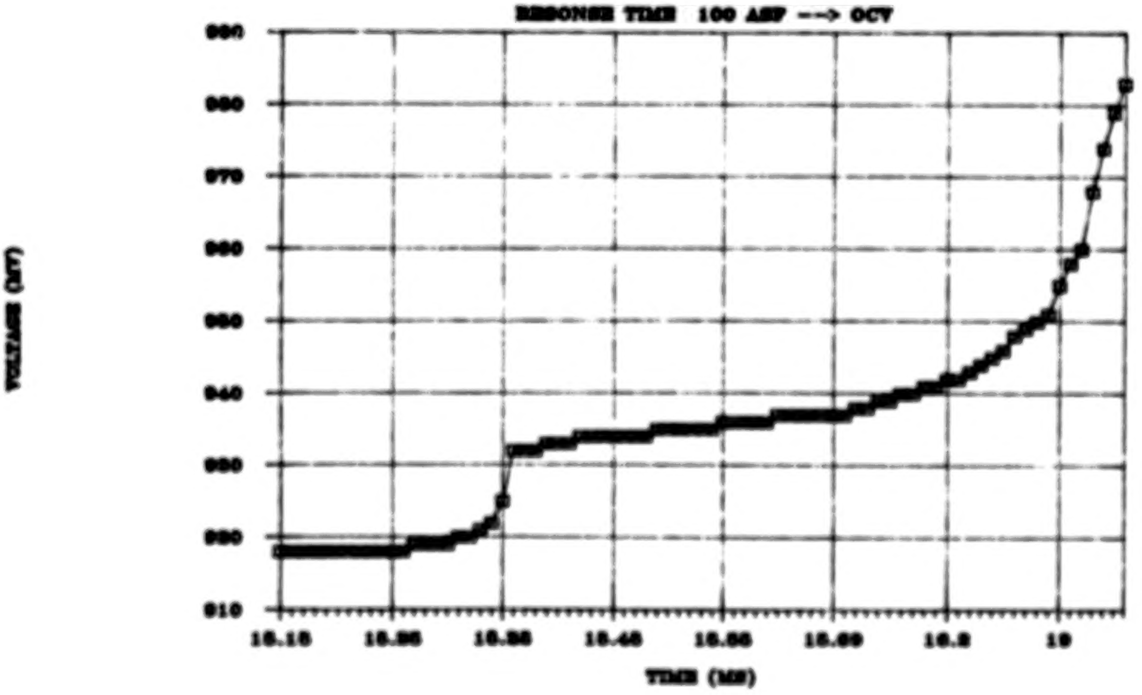

FIGURE 9
CURRENT INTERRUPTION
100 ASF --> OCV

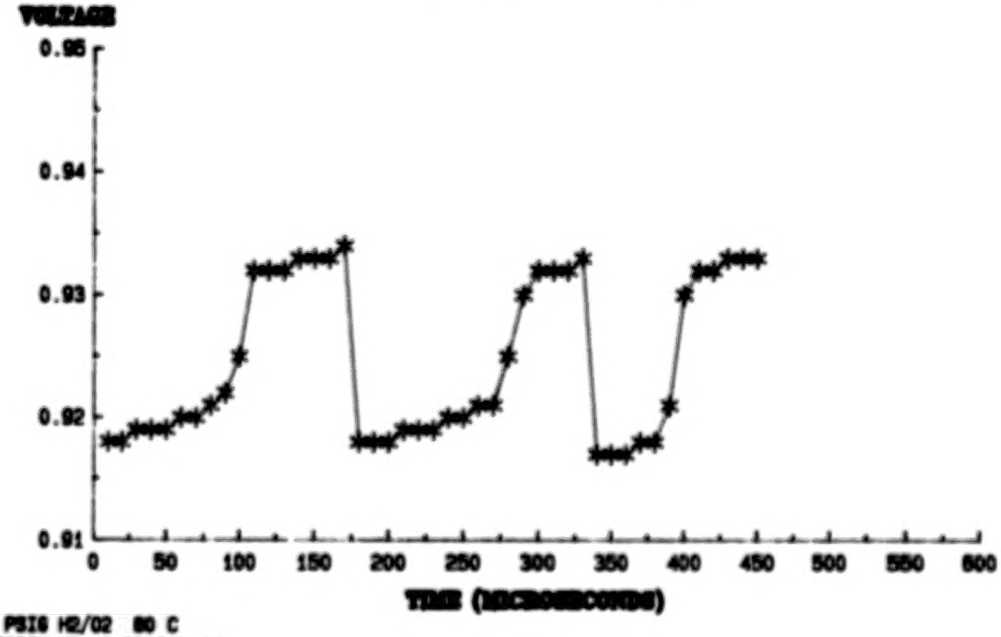

40/80 PSIG H2/O2 80 C
1.1 STOICH H2: 2 STOICH O2
2mg Pt/CM^2/SIDE

FIGURE 10
VOLTAGE VS. CURRENT DENSITY
POLARIZATION DATA VS. RUN TIME

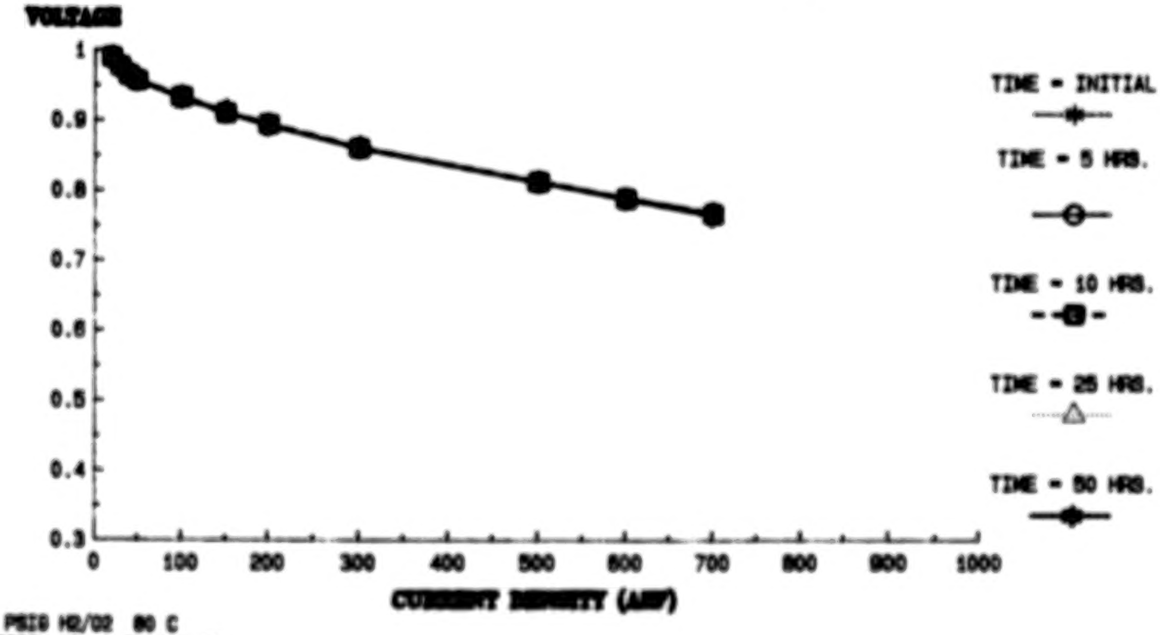

40/80 PSIG H2/O2 80 C
1.1 STOICH H2: 2 STOICH O2
2mg Pt/CM^2/SIDE

TABLE 1
MEMBRANE PROPERTIES

IONIC CONDUCTIVITY	.1 - .2 (OHM-CM)^-1
TENSILE STRENGTH	2500 - 4000 PSI
WATER UPTAKE	36 - 60%
WATER PERMEABILITY	4.5 x E-2 CC/(CM2*SEC)
GAS PERMEATION	
HYDROGEN	5 X E-9 CC-CM/(CM^2*CM Hg*SEC)
OXYGEN	2.5 X E-9

TABLE 2
IR FREE VOLTAGE VS. CURRENT DENSITY

CURRENT DENSITY (ASF)	IR FREE - CELL VOLTAGE(MV)
25	3
50	6
75	11
100	15

TABLE 3

RESPONSE TIME VS. PERCENT FULL POWER
OPEN CIRCUIT --> 100 ASF

% FULL POWER	TIME (MS)
10	2
20	5
30	8
40	12
50	16
60	21
70	28
80	41
90	51
97	81

OPEN CIRCUIT VOLTAGE	1.023 V
VOLTAGE AT 100 ASF	.915 V

HYDROGEN-OXYGEN PROTON-EXCHANGE MEMBRANE FUEL CELLS AND ELECTROLYZERS

R. Baldwin
NASA Lewis Research Center
Cleveland, Ohio 44135

M. Pham
NASA Lyndon B. Johnson Space Center
Houston, Texas 77058

A. Leonida, J. McElroy and T. Nalette
Hamilton Standard
Windsor Locks, Connecticut 06096

INTRODUCTION

Hydrogen-oxygen SPE fuel cells and SPE electrolyzers (products of Hamilton Standard) both use a Proton-Exchange Membrane (PEM) as the sole electrolyte. These solid electrolyte devices have been under continuous development for over 30 years. This experience has resulted in a demonstrated ten-year SPE cell life capability under load conditions.

Ultimate life of PEM fuel cells and electrolyzers is primarily related to the chemical stability of the membrane. For perfluorocarbon proton exchange membranes an accurate measure of the membrane stability is the fluoride loss rate. Millions of cell hours have contributed to establishing a relationship between fluoride loss rates and average expected ultimate cell life. Figure 1 shows this relationship. Several features have been introduced into SPE fuel cells and SPE electrolyzers such that applications requiring ≥ 100,000 hours of life can be considered.

Equally important as the ultimate life is the voltage stability of hydrogen-oxygen fuel cells and electrolyzers. Here again the features of SPE fuel cells and SPE electrolyzers have shown a cell voltage stability in the order of 1 microvolt per hour. That level of stability has been demonstrated for tens of thousands of hours in SPE fuel cells at up to 500 amps per square foot (ASF) current density. SPE electrolyzers have demonstrated the same stability at 1000 ASF.

Many future extraterrestrial applications for fuel cells require that they be self recharged (i.e., regenerative fuel cells). This requirement means that a dedicated fuel cell and a dedicated electrolyzer work in tandem as an electrical energy storage system. Some applications may find advantages with a unitized regenerative fuel cell (i.e., one cell that operates alternately as a fuel cell and as an electrolyzer). Electrical energy storage for earth orbits via hydrogen-oxygen regenerative fuel cell systems can have specific energies in excess of 50 watt-hours/kg (Ref. 1). For extraterrestrial surface electrical energy storage the hydrogen-oxygen regenerative fuel cell can have significantly increased specific energies:

- Mars Base - 500 Watt-hours/kg
- Lunar Base - 1000 Watt-hours/kg (Ref. 2)

To translate the proven SPE cell life and stability into a highly reliable extraterrestrial electrical energy storage system, a simplification of supporting equipment is required. Static phase separation, static fluid transport and static thermal control will be most useful in producing required system reliability. Although some 200,000 SPE fuel cell hours have been recorded in earth orbit with static fluid phase separation, no SPE electrolyzer has, as yet, operated in space.

Under NASA sponsorship a flight experiment of a unitized regenerative fuel cell is being studied. If selected for actual flight under the NASA OAST Outreach Project, several advanced features will be tested in space.

The objective of the flight experiment is to test the space viability of the incorporated features, and not to imply that the specific configuration of the flight experiment is optimum for any given extraterrestrial application. With a successful flight experiment, supported by terrestrial experiments, the system designer can select the proven advanced system features that are appropriate for any particular extraterrestrial application.

ULTIMATE CELL LIFE

The ultimate life of PEM fuel cells and electrolyzers, based on fluoride loss rate, assumes that the cell, stack and system designs are configured to prevent premature mechanical failures. With the elimination of mechanically induced failure, the fluoride loss rate has been found to be an excellent measure of the health and life expectancy of PEM cells.

The fluoride lost from the PEM cell is actually a degradation product of the perfluorocarbon membrane. It should, therefore, not be surprising to find the fluoride loss/ultimate life relationship. The Figure 1 relationship was primarily based on PEM cells using perfluorocarbon membranes in the 8 to 12 mils thickness range. The Figure suggests that perfluorocarbon membranes of less than 8 mils will have a similar ultimate life with a proportional loss of fluoride. This, of course, will only be verified when a large number of cells containing advanced thin perfluorocarbon membranes have accumulated substantial lifetimes.

The fluoride loss rate determination for non-evaporatively cooled PEM fuel cells can be directly measured in the liquid product water. Fluoride detection at the low ppb range can be made directly, while detection at the ppt range is accomplished by concentration techniques. To put the Figure 1 curve into everyday calibration, the following PEM fuel cell example is offered:

Cell Characteristics

Membrane Thickness - 10 mils
Current Density - 500 Amps per Square Foot (ASF)

Life Prediction Vs. Fluoride in Product H_2O

1,000 hours - 2 ppm
10,000 hours - 200 ppb
100,000 hours - 20 ppb

The fluoride loss rate determination for liquid anode feed PEM electrolyzers can be directly measured in the open loop "proton" water. The following PEM electrolyzer example is offered:

Cell Characteristics

Membrane Thickness - 10 mils
Current Density - 1000 ASF

Life Prediction Vs. Fluoride in Proton H_2O

1,000 hours - 140 ppb
10,000 hours - 14 ppb
100,000 hours - 1.4 ppb

Since long life of PEM cells has been inversely equated with fluoride loss rate, the designer can quickly determine the suitability of a given configuration for a particular application. Each manufacturer of PEM cells undoubtedly has his own proprietary techniques for the control of fluoride release rate.

SPE fuel cell and electrolyzer designers incorporate proprietary features into system configurations for extended life. One such demonstration SPE cell is within seven months of reaching 100,000 hours of high current density operation. Figure 2 displays this cell as it passed the ten year mark in May 1988. Two additional SPE test cells have accumulated over ten years of "uninterrupted" operation since the May 1988 milestone.

CELL VOLTAGE STABILITY

The voltage stability of PEM fuel cells and electrolyzers is a second very important feature for many applications. Experience has shown that features that provide a long cell life, as indicated by low fluoride release rates, do not necessarily equate long cell life with stable voltage. This is indeed unfortunate, as it makes it next to impossible to predict the long term voltage stability of a cell design from short-term tests.

In earlier SPE cell designs a reasonable voltage-change rate would unexpectedly turn to a high voltage-change rate. When unpredicted mechanisms were identified and corrective measures taken, the level and longevity of voltage stability improved. As one might imagine, the test, analysis, corrective action and retest cycles have taken many years to obtain the current level of voltage stability.

Figure 3 shows the voltage stability, as measured by voltage-change with time, of six SPE test units. The baseline configuration for SPE electrolyzers and SPE fuel cells is represented by SPE electrolyzer C and SPE fuel cell E. Both of these units have a voltage-change rate of 1 microvolt/cell hour at 1000 ASF and 500 ASF, respectively.

SPE electrolyzers A and B purposely deviate from the baseline configuration for application specific reasons. Both of these units represent a voltage-change rate of 7 microvolts/cell hour. This voltage-change rate is perfectly acceptable for the intended applications (i.e., electric utility hydrogen generation and nuclear submarine oxygen generation).

Like the SPE fuel cell baseline E, SPE fuel cell D displayed a voltage-change rate of 1 microvolt/cell hour. The unit D configuration, formally considered the SPE fuel cell baseline, is limited in current density. SPE fuel cell F had a voltage-change rate of 6 microvolts/cell hour and represents an earlier configuration which was part of the development data base leading to the present SPE fuel cell baseline.

The configurations of the baseline SPE electrolyzer and SPE fuel cell consist of a combination of patented and proprietary features. Each PEM electrolyzer and PEM fuel cell manufacturer will have their own features which, like the SPE devices, will have to be verified by the life test process.

EXTRATERRESTRIAL APPLICATIONS

Many of the future extraterrestrial applications for hydrogen-oxygen fuel cells and electrolyzers involve combining the two devices to produce the equivalent of a battery for electrical energy storage (see Figure 4). The so called regenerative fuel cell has the distinct advantage over traditional batteries in that power and energy are separated. One needs only to increase reactant storage, without increasing the reactor stack(s), to increase the stored energy. The results of this distinction is that the mass advantage of typical advanced batteries lose out to regenerative fuel cells when the discharge time is increased beyond a few tens-of-minutes.

Energy storage system sizing has been examined for a variety of extraterrestrial applications. The most favorable application of the hydrogen-oxygen regenerative fuel cell is the lunar base application because of the long charge/discharge time span. The studies have indicated the next best available energy storage technology (NaS battery) is more than ten times as massive as the hydrogen-oxygen regenerative fuel cell system.

The state-of-the-art of the hydrogen-oxygen regenerative fuel cell is not without disadvantages. Even considering the demonstrated lifetime and voltage stability of the SPE devices, the questions of efficiency and complexity must be considered.

The energy-out-to-energy-in ratio range generally accepted for state-of-the-art hydrogen-oxygen regenerative fuel cells is 55% to 65%. Advanced batteries operating at 75% energy storage efficiency or greater have the clear advantage in this characteristic. The primary reason for the lower hydrogen-oxygen regenerative fuel cell energy storage efficiency is related to electrode performance. Years of research have been invested to improve low-temperature electrode performance with only minor increases observed. Without a breakthrough in low-temperature electrode performance,the lower efficiency of the state-of-the-art low-temperature hydrogen-oxygen regenerative fuel cell is fundamental.

The efficiency of the hydrogen-oxygen regenerative fuel cell results in a greater energy input requirement for a fixed output when compared to advanced batteries. In the case of a photovoltaic power source, this means an increase in the size of the solar array. However, as charge times increase this differential mass becomes insignificant. An order-of-magnitude lower mass for the overall lunar base power system based on the hydrogen-oxygen regenerative fuel cell, as compared to advanced batteries, is still projected even when including the state-of-the-art photovoltaics.

Although the efficiency disadvantage of the hydrogen-oxygen regenerative fuel cell turns out to be insignificant in most extraterrestrial applications, the complexity of state-of-the-art regenerative fuel cells is much greater than most advanced batteries. The very feature that gives the hydrogen-oxygen regenerative fuel cell its significant mass advantage is responsible for its complexity. The complexity arises primarily due to the storage of reactants and products external to the reactors. These state-of-the-art complexities in hydrogen-oxygen regenerative fuel cells include:

- Fuel cell product water removal from the reactant chamber by dynamic reactant recirculation.
- Dynamic separation of the fuel cell product water from the reactant.
- Pumping electrolysis process water up to gas generation pressure.
- Temperature-controlled fluid recirculation in both fuel cells and electrolyzers.
- Separate dedicated fuel cells and electrolyzers.

In total, the state-of-the-art hydrogen-oxygen regenerative fuel cell system would use in the range of 4 to 6 rotating devices, not including redundancy, to provide fluid transport and/or phase separation. Additionally, on the order of twice as many individual cells would be required as would be needed for advanced batteries, simply because the batteries operate both in charge and discharge modes. The complexity, in terms of dynamic components and the large piece-part count, with double the number of cells, relegates the state-of-the-art hydrogen-oxygen regenerative fuel cell to a lower reliability than the more massive batteries.

The reliability of the hydrogen-oxygen regenerative fuel cell can be increased by component redundancies. This approach diminishes the mass advantage and adds to the system complexity. Our approach, of a unitized (reversible) hydrogen-oxygen regenerative fuel cell with static fluid and thermal control features, can improve reliability and reduce complexity, which further improves the mass advantage over advanced batteries.

SYSTEM SIMPLIFICATIONS

With complexity and lower reliability identified as the major concerns in hydrogen-oxygen regenerative fuel cells, manufacturers have begun to respond with a variety of approaches. In particular, SPE fuel cell and SPE electrolyzer designs are being directed toward reduced complexity. Specific developments include:

- Reversible SPE cell
- Passive fuel cell product water separation and removal
- Passive electrolyzer process water introduction
- Passive electrochemical gas pumping
- Passive heat management

Separate dedicated SPE fuel cells and SPE electrolyzers came into favor several years ago due to higher overall energy storage efficiency. It is true that in reversible SPE cells, the preferred SPE fuel cell catalyst results in poor electrolyzer performance and the preferred SPE electrolyzer catalyst results in poor SPE fuel cell performance. Compromise catalyst systems have been developed which bring the overall energy storage efficiency within 5% of the dedicated configuration. Figure 5 shows performance curves for these various configurations.

A specific application may find the 5% efficiency reduction as an acceptable trade for simplicity and mass reduction. Alternately, if the application dictates, by trade study, that discharge efficiency is of prime importance, a 10% energy storage efficiency reduction may be preferred while using optimized fuel cell catalyst.

Passive fuel cell product water separation and removal from the reactor stack in microgravity is certainly not a new idea. Both the Gemini and Biosatellite SPE fuel cells operated with passive wicking product water systems. These systems, however, operated only at low current densities with higher mass and volume structures.

Recent developments in passive water separation and removal from SPE fuel cells have involved separation of the liquid product water from the gaseous oxygen within the cell structure (Ref. 3). This approach, shown in Figure 6, eliminates the need for wicking and uses a hydrophilic separator plate in the oxygen cavity. Testing of this configuration has been very successful to date with operation demonstrated against gravity (i.e., product water separated upward from the cathode electrode). Figure 7 displays the performance of an SPE fuel cell with the passive product water removal feature operating against gravity.

The passive water vapor feed SPE electrolyzer developed during the seventies used a hydrated ion-exchange membrane to feed water vapor to the operating cell. This cell structure (shown in Figure 8) eliminated the need for separating liquid water from the products. However, close control of the water pressure was required. If the water pressure was significantly higher than hydrogen pressure, water hydraulically passed through the water feed barrier and exceeded the electrolysis rate. Conversly, if the water pressure was below the hydrogen pressure, an accumulation of hydrogen in the water feed chamber by normal diffusion resulted in water starvation.

Recently, an inovative feature has been incorporated into the passive water vapor feed SPE electrolyzer. This feature allows the water pressure to be well below hydrogen pressure without the concern of hydrogen buildup in the water feed chamber. The feature consists of electrifying the water feed membrane in order for it to function as an electrochemical hydrogen pump (Ref. 4). Figure 9 shows the electrification of the water feed membrane. The fraction of a watt required for each cell is considered a small penalty to pay for the elimination of the requirements for pumping water up to pressure and maintaining close pressure control.

The electrochemical hydrogen pump allows the water to be fed to the cell at any source pressure down to the cell water vapor pressure without any mechanical pumping. Figure 10 shows the water vapor feed SPE electrolyzer performance with water pressure 160 psi below hydrogen generation pressure.

Several thousand cell hours have now been accumulated on electrolyzer cells supported by the use of electrochemical hydrogen pumps.

The simplifying features described herein have all demonstrated successful operation in ground testing. Although passive fluid phase separation was successfully used in the Gemini and Biosatellite SPE fuel cell systems, none of the described simplifying features have actually flown in space.

THE FLIGHT EXPERIMENT

The planned unitized regenerative SPE fuel cell experiment makes use of the proven life and voltage stability features as well as the simplifying aspects. A basic fluid schematic of the flight experiment is shown in Figure 11. This figure shows one of several experiment options studied. If selected, the experiment will fly on a future Shuttle mission in a simulated low earth orbit energy storage configuration. The potential one week experiment should be of ample length to assess the performance of the various system simplification aspects.

During the experiment discharge cycle, hydrogen gas and oxygen gas are delivered to the reversible cell on a purely demand basis. The reversible cell converts these reactants into dc power with a current output of approximately 100 ASF. The product water, formed within the oxygen chamber as a liquid, contacts the porous plate. The spring bellows in the oxygen/water storage tank creates a pressure differential across the porous plate (O_2 > H_2O) of about 1 psi. The 1 psi is more than sufficient to force the product water through the hydrophilic porous plate at the generation rate, but, not nearly high enough to allow passage of oxygen gas.

The product water will be saturated with oxygen, and some small bubbles of oxygen gas will appear as the water pressure decreases by 1 psi as it passes through the porous plate; some oxygen will come out of solution. As this water passes through the water chamber of the water vapor feed barrier membrane, the oxygen gas and dissolved oxygen are converted to water at the positive electrode of the hydrogen pump. This oxygen is chemically consumed by combining with the diffusing hydrogen that otherwise is electrochemically pumped back to the hydrogen chamber. The water eventually delivered to storage is essentially free of dissolved gases. This is an important feature as the system pressures alternate up and down through the charge/discharge cycles.

At the end of the discharge period the pressures in the reactant storage tanks are at the reduced level and a load contactor is opened. This is followed by closing a power contactor to supply charge power to the reversible cell.

In the electrolysis charge mode, water vapor is fed to the operating electrolysis cell across the hydrogen compartment gap. Hydrogen and oxygen gases are delivered to their respective tankage and the system pressures rise. An accumulation of water in the reactant storage tankage is prevented by thermally matching the tankage with the operating cell and the fact that the produced gases are in fact subsaturated.

The electrochemical hydrogen pump milliwatt power draw continues through both the charge and discharge modes. This assures that hydrogen gas does not block the flow of water, and it also provides an actual measure of the amount of oxygen consumed during the discharge water desaturation step.

The entire experiment will be cold-plate mounted. Heat generated within the cell hardware is conducted to the base plate. Figure 12 is a photograph of the experimental hardware mock-up.

SUMMARY

In summary, a flight experiment is planned for the validation in a microgravity environment of several ground proven simplification features relating to SPE fuel cells and SPE electrolyzers. With a successful experiment these features can be incorporated into the designs of equipment for specific extraterrestrial energy storage applications.

REFERENCES

1. Appleby, J.: Regenerative Fuel Cells for Space Applications. Journal of Power Sources, 22 (1988) p.p. 337-385.

2. NASA Conference Publication 3016: September 12-13, 1988 p.p. 206

3. Leonida, A: Hydrogen/Oxygen Fuel Cells with In-Situ Product Water Removal. 33rd International Power Sources Symposium, June 13-16, 1988

4. Sedlak, J; Austin, F.; and LaConti, A: Hydrogen Recovery and Purification Using the Solid Polymer Electrolyte Electrolysis Cell. International Journal of Hydrogen Energy, (1981) Volume 6, p.p. 45-51

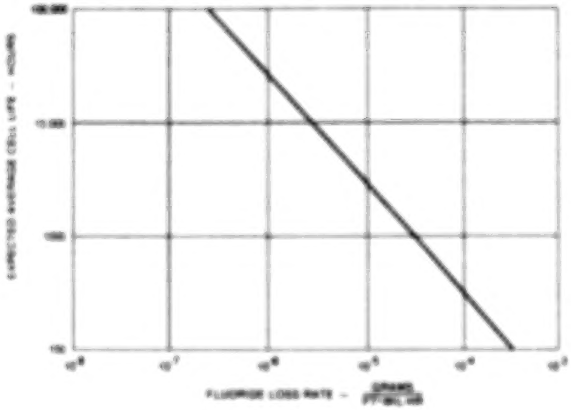

FIGURE 1. EXPECTED LIFETIMES OF SPE CELLS WITH PERFLUOROCARBON PROTON EXCHANGE MEMBRANES

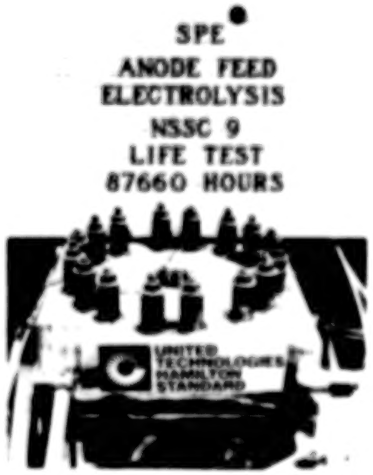
SPE
ANODE FEED
ELECTROLYSIS
NSSC 9
LIFE TEST
87660 HOURS
UNITED TECHNOLOGIES
HAMILTON
STANDARD

FIGURE 2. "UNINTERRUPTED" SPE ELECTROLYZER LIFE TEST

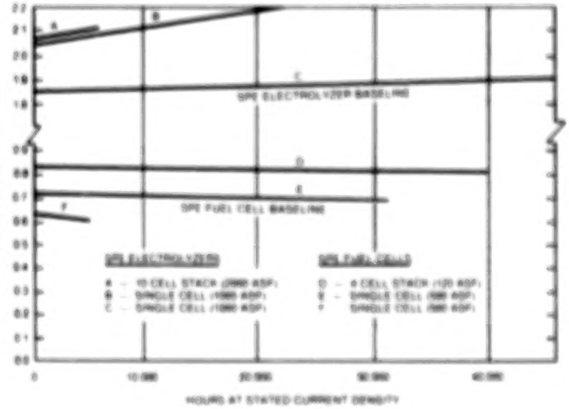

FIGURE 3. SPE CELL VOLTAGE STABILITY

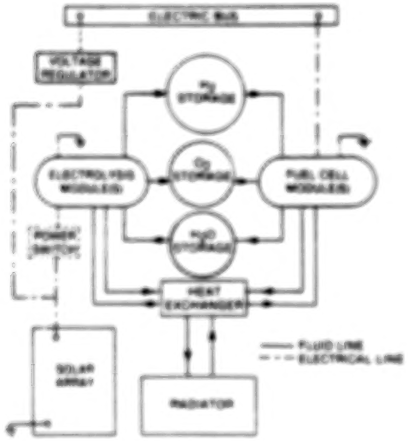
ELECTRIC BUS
VOLTAGE REGULATOR
H_2 STORAGE
ELECTROLYSIS MODULE(S)
O_2 STORAGE
FUEL CELL MODULE(S)
POWER SWITCH
H_2O STORAGE
HEAT EXCHANGER
SOLAR ARRAY
RADIATOR
FLUID LINE
ELECTRICAL LINE

FIGURE 4. HYDROGEN-OXYGEN REGENERATIVE FUEL CELL ENERGY STORAGE SYSTEM

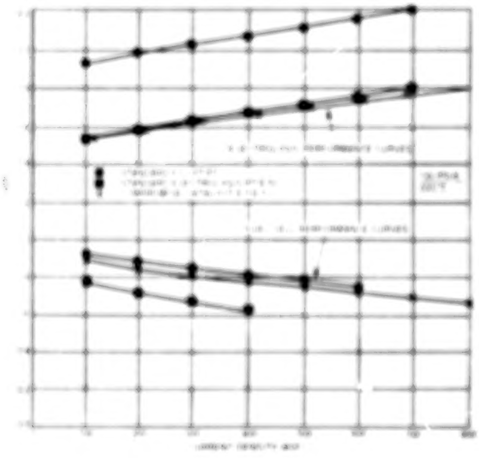

FIGURE 5. COMPARISON OF PERFORMANCE DURING FUEL CELL AND ELECTROLYSIS MODES

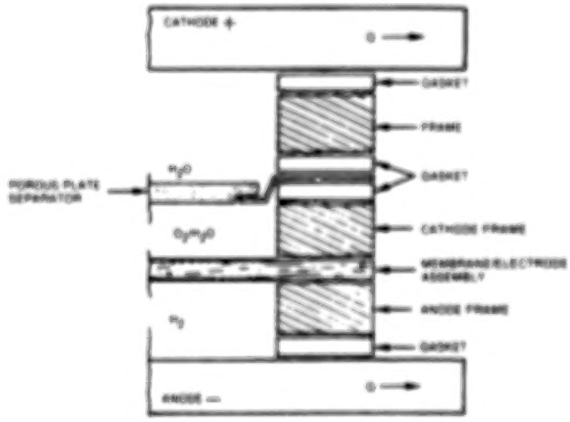
CATHODE +
O →
GASKET
FRAME
H_2O
POROUS PLATE SEPARATOR
GASKET
O_2/H_2O
CATHODE FRAME
MEMBRANE/ELECTRODE ASSEMBLY
H_2
ANODE FRAME
GASKET
ANODE –
O →

FIGURE 6. PASSIVE STATIC WATER REMOVAL SPE FUEL CELL — CROSS SECTION

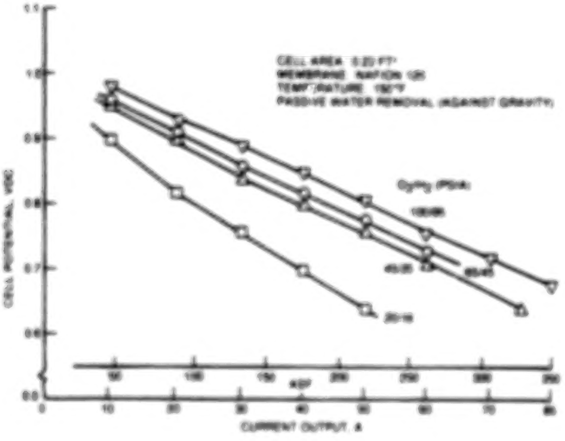

FIGURE 7. PASSIVE WATER REMOVAL SPE FUEL CELL PERFORMANCE AT 150°F

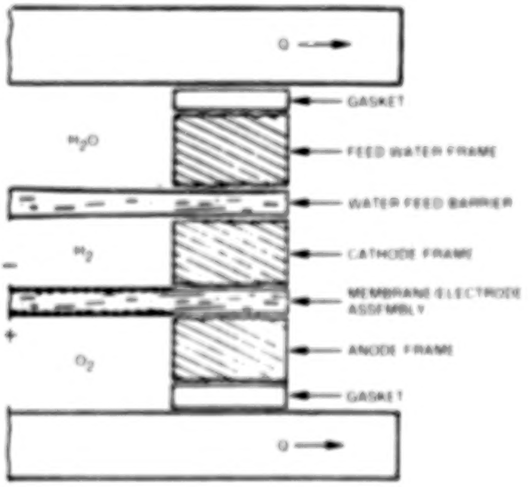
Q
GASKET
H₂O
FEED WATER FRAME
WATER FEED BARRIER
H₂
−
CATHODE FRAME
MEMBRANE ELECTRODE ASSEMBLY
+
O₂
ANODE FRAME
GASKET
Q

FIGURE 8. WATER VAPOR FEED SPE ELECTROLYZER

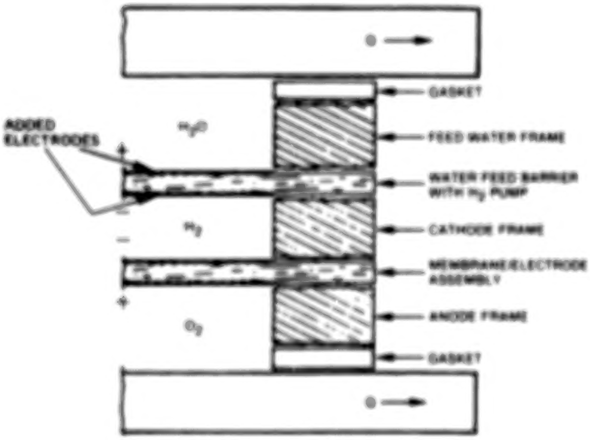
Q
GASKET
ADDED ELECTRODES
H₂O
+
FEED WATER FRAME
WATER FEED BARRIER WITH H₂ PUMP
−
H₂
−
CATHODE FRAME
MEMBRANE/ELECTRODE ASSEMBLY
+
O₂
ANODE FRAME
GASKET
Q

FIGURE 9. WATER VAPOR FEED SPE ELECTROLYZER WITH ELECTROCHEMICAL HYDROGEN PUMP

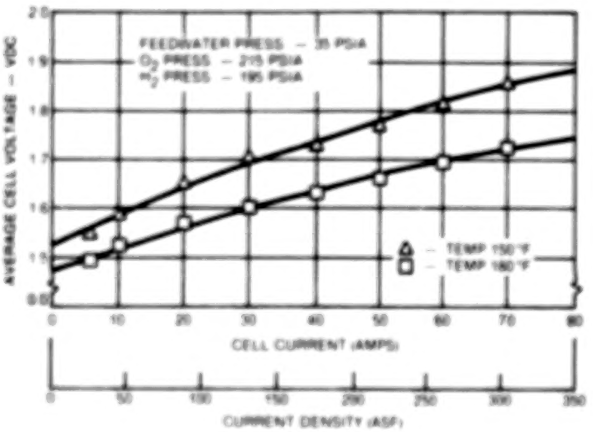

FIGURE 10. WATER VAPOR FEED SPE ELECTROLYZER PERFORMANCE

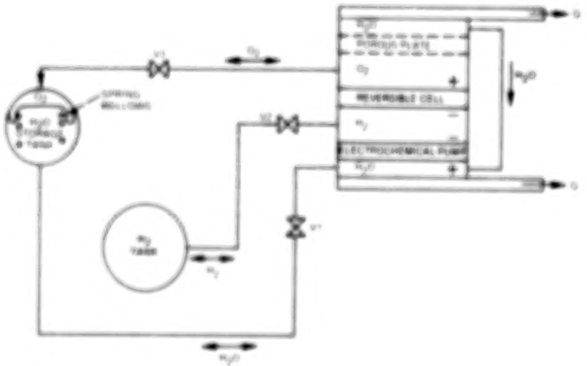
V1
O₂
O₂
SPRING BELLOWS
H₂O
STORAGE TANK
H₂O
POROUS PLATE
O₂
+
REVERSIBLE CELL
V2
H₂
−
−
ELECTROCHEMICAL PUMP
H₂O
+
H₂O
Q
Q
H₂ TANK
H₂
V1
H₂O

FIGURE 11. UNITIZED REGENERATIVE SPE FUEL CELL

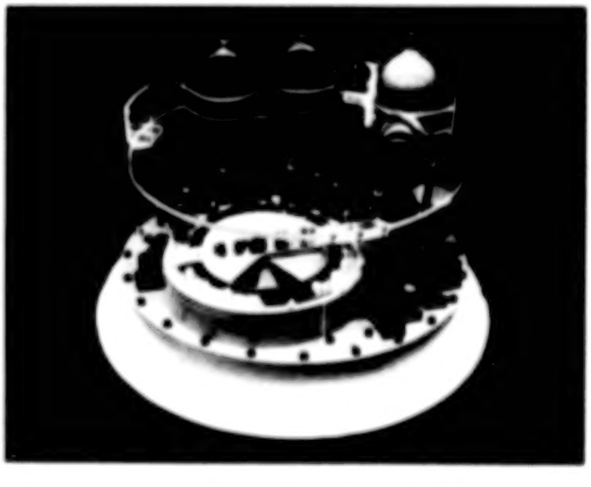

FIGURE 12. UNITIZED REGENERATIVE SPE FUEL CELL MOCK-UP

ELECTROCATALYSIS FOR OXYGEN ELECTRODES IN FUEL CELLS AND WATER ELECTROLYZERS FOR SPACE APPLICATIONS

Jai Prakash, Donald Tryk and Ernest Yeager
Case Center for Electrochemical Sciences
and the Chemistry Department
Case Western Reserve University
Cleveland, Ohio 44106

The lead ruthenate pyrochlore $Pb_2Ru_2O_{6.5}$ in both high and low area forms has been characterized using thermogravimetric analysis, X-ray photoelectron spectroscopy, X-ray diffraction, cyclic voltammetry and O_2 reduction and generation kinetic-mechanistic studies. Mechanisms are proposed. Compounds in which part of the Ru is substituted with Ir have also been prepared. They exhibit somewhat better performance for O_2 reduction in porous gas-fed electrodes than the unsubstituted compound. The anodic corrosion resistance of pyrochlore-based porous electrodes was improved by using two different anionically conducting polymer overlayers, which slow down the diffusion of ruthenate and plumbate out of the electrode. The O_2 generation performance was improved with both types of electrodes. With a hydrogel overlayer, the O_2 reduction performance was also improved.

INTRODUCTION

In most instances separate electrocatalysts are needed to promote the reduction of O_2 in the fuel cell mode and to generate O_2 in the energy storage- water electrolysis mode in aqueous electrochemical systems operating at low and moderate temperatures ($T \leq 200$ °C). This situation arises because, even with relatively high performance catalysts, the O_2 reduction and generation reactions are still quite irreversible with much overpotential. The potentials of the O_2 electrode in the cathodic and anodic modes are separated by typically 0.6 V and the states of the catalyst surface are very different. Interesting exceptions are the lead and bismuth ruthenate pyrochlores in alkaline electrolytes. These catalysts have high catalytic activity for both O_2 reduction and generation (1-6). Furthermore, rotating ring-disk electrode measurements provide evidence that the O_2 reduction proceeds by a parallel four-electron pathway (6). The ruthenates can also be used as self-supported catalysts to avoid the problems associated with carbon oxidation, but the electrode performance so far achieved in our laboratory is considerably less.

At the potential involved in the anodic mode the ruthenate pyrochlores have substantial equilibrium solubility in concentrated alkaline electrolyte. This results in the loss of catalyst into the bulk solution and a decline in catalytic

---

*This work was supported by the NASA-Lewis Research Center under Contract No. NAG3-964.

activity. Furthermore, the hydrogen generation counter electrode may become contaminated with reduction products from the pyrochlores (lead, ruthenium).

A possible approach to this problem is to immobilize the pyrochlore catalyst within an ionically conductive solid polymer, which would replace the fluid electrolyte within the porous gas diffusion O_2 electrode. For bulk alkaline electrolytes, an anion exchange polymer is needed with a transference number close to unity for the OH^- ion. Such a membrane may not block completely the transport of the lead and ruthenium, which are expected to be in complex anionic forms. Preliminary short term measurements with lead ruthenates using either 1) a partially fluorinated anion exchange membrane as an overlayer on the porous gas-fed electrode or 2) a hydrogel coating on the porous electrode indicate lower anodic polarization and similar cathodic polarization. With the hydrogel coating, there is also some enhancement of the performance at higher current densities.

EXPERIMENTAL

The pyrochlores were synthesized at CWRU using the alkaline solution technique of Horowitz et al (3). Samples of $Pb_2Ru_2O_{6.5}$ and $Pb_2[Ru_{1.67}Pb_{0.33}]O_{6.5}$ were also provided by Exxon. This method involves the reaction of the appropriate metal cations by precipitation and subsequent crystallization of the precipitate in a liquid alkaline medium (4 M KOH) in the presence of O_2 at ~75-90°C. The salts used were $Ru(NO)(NO_3)_3$, in aqueous solution, 1.5 % (w/v) from Strem, $IrCl_3 \cdot 3H_2O$ (Aldrich, Gold label) and $Pb(CH_3COO)_2 \cdot 3H_2O$ (MCB, reagent grade). The salts were added in the appropriate amounts to achieve the desired stoichiometries. The reactions were carried out for 24-72 h, until the supernatant solution was free of detectable amounts of the reactant metal ions. The suspension was filtered and washed with water and glacial acetic acid. The X-ray diffraction (XRD) was measured after a heat treatment (HT) in air at 300-350°C for 12 h. In some cases XRD was also run prior to the HT.

Thermogravimetric analysis was performed on a Perkin-Elmer 7 Series Thermal Analysis System with O_2 and N_2 purges at a temperature ramp rate of 15°C min^{-1}. X-ray photoelectron spectroscopy was obtained using a Varian IEE- 15 instrument.

A modification of the ring-disk electrode (RRDE) technique was used in which a thin PTFE-bonded porous coating of the pyrochlore was applied to a basal plane pyrolytic graphite disk, which was slightly recessed. PTFE suspension (Teflon T30B, Du Pont) was diluted with water and ultrasonically agitated with the pyrochlore and filtered with a 1 μm pore size polycarbonate filter membrane (Nucleopore). The resulting mixture was 5 wt % in PTFE solids. The semi-moist paste was kneaded with a spatula and then applied to the disk (either 0.196 or 0.45 cm^2) and spread evenly. Excess material was carefully removed from the edge of the disk. The layer was not allowed to dry in order to avoid cracking of the layer and was placed in the electrolyte solution. The amount of pyrochlore in the layer was determined after the experiment by first washing it in water, removing it, drying and weighing. The typical loading was 4-6 mg cm^2. The Au ring had a collection efficiency N of 0.177. The Teflon electrochemical cell had separate compartments for the working RDE or RRDE electrode, counter electrode (Au) and reference electrode (Hg/HgO, 1 M OH^-). The KOH solution was prepared from the solid (Fluka, puriss., p.a.) by dilution with triply distilled reverse osmosis water.

Porous gas-fed electrodes were fabricated as follows. Teflon T30B suspension was diluted approximately to 2 mg cm^{-3} in water and slowly added to an aqueous suspension of 38 mg of pyrochlore and 35 mg of air-oxidized (~1 h at 600°C) Shawinigan black (Chevron Chemical Co., Olefins and Derivatives Div., Houston, Texas). The suspension was filtered using a 1μm pore size filter membrane. The resulting paste was kneaded with a spatula until slightly rubbery, shaped into a 1.75 cm diameter disk in a stainless steel die using hand pressure and then pressed at a pressure of ~100 kg cm^{-2}. The disk was applied to a 0.5 mm thick disk of Teflon-carbon black hydrophobic backing material containing silver-plated nickel mesh (Electromedia Corp., Englewood, NJ). A final pressing was done at ~300 kg cm^{-2} at room temperature and then the disk was heat-treated at ~280°C for 2 h in flowing helium.

In some cases a 1.75-cm diameter disk of a partially fluorinated anion exchange membrane material (Type 4035, RAI, Hauppage, NY) was pressed onto the electrolyte side of the electrode at 200 kg cm^{-2}. In other experiments a mixture of poly(dimethyldiallylammonium)chloride (DMDAAC, 15 wt % in aqueous solution, Polysciences) and Nafion 117 (5 wt% in alcohol solution, Aldrich) was diluted by a factor of 6 by volume and painted onto the electrolyte side of the porous electrode and allowed to air-dry. The resulting hydrogel film was ~1.5 mg cm^{-2}.

The porous gas-fed electrode was placed in a special screw-cap-type Kel-F holder which holds the electrode vertically between a Pt foil current collector on the gas-side and a polyethylene-polypropylene rubber gasket on the electrolyte side. A stream of either air or O_2 was directed at the back of the electrode. The area exposed to the electrolyte was 0.97 cm^2. The O_2 reduction measurements were performed galvanostatically in 5.5 $\underline{M}$ KOH at 25°C with a fast-action potentiostat (BC-1200, Stonehart Associates) using the current interruption method to correct for solution-phase IR drop external to the gas-fed electrode.

RESULTS

Using the alkaline solution technique, a sample of $Pb_2Ru_2O_{6.5}$ was prepared with a reasonably high area (~35 m^2 g^{-1}) and some evidence of crystallinity (X-ray diffraction) even without further heat treatment. After heat treatment at ~350°C, the X-ray diffraction became very well resolved. This result is important because heretofore it has been assumed that in order to achieve high surface areas, it is necessary to prepare the lead ruthenate with some substitution of the Ru with Pb (7-8). Such "lead-rich" compounds are known to exhibit decreasing stability as the amount of substitution increases (1). The O_2 generation behavior of this $Pb_2Ru_2O_{6.5}$ sample was significantly better than for other lower area samples of the same stoichiometry that were examined with gas-fed electrodes.

Further characterization studies for $Pb_2Ru_2O_{6.5}$ are in progress in which the effect of the heat treatment is being examined. The thermogravimetric analysis (TGA), for example, indicates that ~0.8 moles of water are present before any heat treatment and are mostly removed at 800°C. The X-ray photoelectron spectra (XPS), however, did not show discernable changes in peak shapes or binding energies for Ru, Pb and O over the temperature range 100°C to 500°C, in which most of the water is lost.

Cyclic Voltammetry

The cyclic voltammetry (CV) for the $Pb_2Ru_2O_{6.5}$ thin porous coating is very complex. There is a large, gradually increasing anodic current on which are superimposed several small peaks (Fig. 1, a-e). On the back sweep there is a large cathodic peak. The charge under this peak (2.7×10^{-2} C) corresponds to ~12 % of the total possible charge expected for a single electron transfer to each Ru atom in the coating (~0.8 mg or 1.1×10^{-6} mol, yielding 0.214 C). From the crystal structure (9), there are 4 Ru atoms exposed on the face of each unit cell, whose edge is 10.253 A. This corresponds to ~6.3×10^{-10} mol cm^{-2}. The BET area of the $Pb_2Ru_2O_{6.5}$ sample used for the CV experiment was 6.0 $m^2\ g^{-1}$. Therefore, for a 0.8 mg sample, the surface area was ~ 48 cm^2, corresponding to 3.02×10^{-8} mol or 2.9×10^{-3} C for a 1-electron process for surface Ru atoms only. This value is one order of magnitude less than the observed charge of 2.7×10^{-2} C. One possible explanation is that ~10 monolayers are involved in a 1-electron process. On the other hand, for the valence states $(Pb^{2+})_2(Ru^{4.5+})_2(O^{2-})_{6.5}$, the following oxidation processes are possible over the potential range:

$$2\ Pb^{2+} \xrightarrow{-\ 4\ e^-} 2\ Pb^{4+}$$

$$2\ Ru^{4.5+} \xrightarrow{-\ 3\ e^-} 2\ Ru^{6+}$$

for a total of 7 electron transferred. This would still account for ~1.5 monolayer, if all 7 electrons are involved. Therefore, it appears that the overall process involves not only the surface but also the bulk ($1.5 < x < 10$ monolayers) of the material. If the process is indeed a 1-electron process, it may be assigned to the Ru(IV)/Ru(V) transition proposed by Edgell et al (2). The existence of the smaller peaks has not been explained thus far but may involve Ru atoms on the surface of the oxide undergoing successive electron transfers with both Pb and Ru going to higher valence states.

Oxygen reduction

The polarization curves for O_2 reduction on a thin porous coating of $Pb_2Ru_2O_{6.5}$ at a series of rotation rates are shown in Fig. 2. The corresponding ring currents for peroxide oxidation are very small, reaching a maximum of only ~5 % of the disk current (corrected for N) at the most negative potentials.

Kinetic analysis of the ring-disk results using the method of Wroblowa et al. (10) would lead to the conclusion that the O_2 reduction is proceeding via the direct 4-electron pathway to OH^-. In addition, the slopes of the i^{-1} vs. $f^{-1/2}$ plots (where f = rotation rate) correspond to an overall number of electrons being transferred of ~3.8. The porosity of the electrode causes complications in the interpretation of the data however. For example, if a catalyst is a good peroxide decomposer, it can appear that the O_2 reduction is proceeding by a direct 4-electron pathway even though the reaction is proceeding by a series pathway, with O_2 reduction to peroxide as the first step, followed by peroxide decomposition. Overall this would yield 4 electrons. The reason for the possible confusion is that the peroxide requires a relatively long time to diffuse out of the porous layer and during this time has a good opportunity to decompose. Even so, the significant potential range over which there is negligible peroxide picked up at the ring rather strongly indicates a 4-electron process.

Tafel plot of the mass-transport corrected currents for f = 2500 rpm in the potential range of +0.06 to -0.08 V is shown in Fig. 3. A linear relationship is obtained with a Tafel slope of -0.063 V (decade)$^{-1}$. This suggests a non-charge transfer step as rate determining following a fast outer-sphere electron transfer.

Oxygen reduction studies were also carried out over the pH range 11.9 to 13.9 keeping the ionic strength constant. The currents for O_2 reduction increased with decreasing concentration of OH^-. The half wave potential also became increasingly positive. The slopes of the mass transport-corrected Tafel plots were also almost identical over the above pH range. A reaction order of -0.5 with respect to OH^- concentration over this pH range was observed. This result together with the Tafel slope of -0.06 V (decade)$^{-1}$ is consistent with the following mechanism for O_2 reduction on the $Pb_2Ru_2O_{6.5}$ pyrochlore.

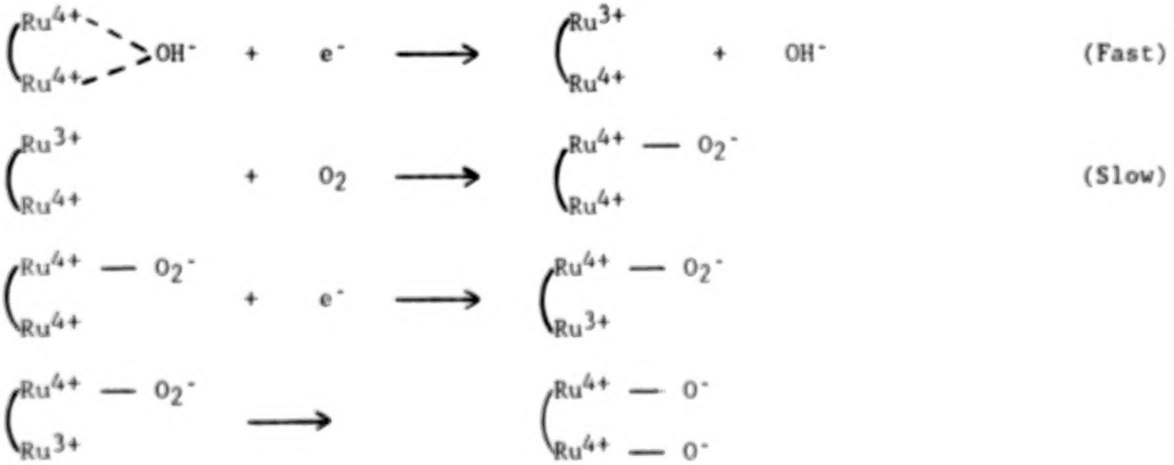
Ru4+ OH- + e- → Ru3+ Ru4+ + OH- (Fast)
Ru3+ Ru4+ + O2 → Ru4+ — O2- Ru4+ (Slow)
Ru4+ — O2- Ru4+ + e- → Ru4+ — O2- Ru3+
Ru4+ — O2- Ru3+ → Ru4+ — O- Ru4+ — O-

followed by a series of further steps resulting in the overall process

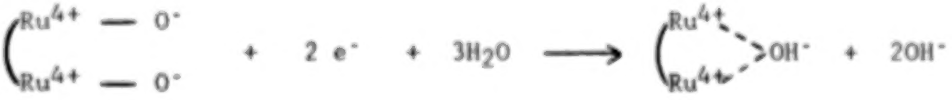

which would not generate solution-phase peroxide.

Oxygen generation

O_2 generation studies were carried out over a range of pH (11 to 14) at a constant ionic strength. The catalyst was incorporated in a porous electrode (geometric area = 4.8 cm^2) using Teflon T30B as the binder with a Ni screen current collector and heat treated at 280°C for 2 h in an inert atmosphere. The Tafel slope at room temperature varied from 0.032 to 0.038 V (decade)$^{-1}$. A reaction order of 1.0 was found with respect to OH^- concentration over this pH range. A reaction mechanism consistent with the reaction order is proposed as follows.

$$S^{z} + OH^{-} \underset{k_{-a}}{\overset{k_a}{\rightleftharpoons}} (SOH)^{z+} + e^{-} \qquad \text{(Fast)}$$

$$(SOH)^{z+} \xrightarrow{k_b} (SOH)^{z+1} + e^{-} \qquad \text{(Slow)}$$

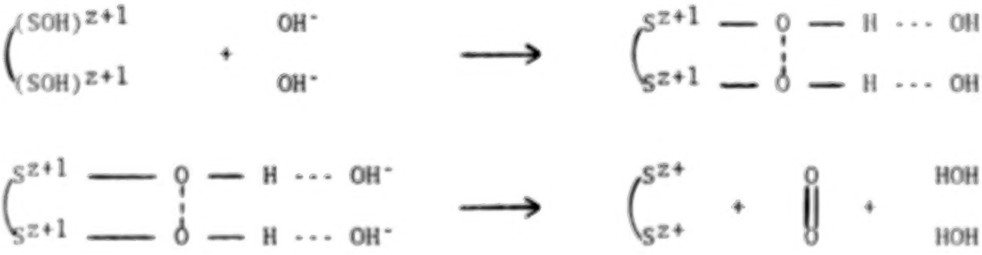

This mechanism is similar to the one proposed for O_2 generation on RuO_2 electrodes (11).

Gas-fed electrode measurements

The electrochemical behavior, including the O_2 reduction and generation activity as well as the stability in the anodic mode can be modified by substituting a part of either the Pb or Ru with other metals. One such type of substitution which was examined is that of Ir for Ru in the B site. Ir is expected to be more resistent to anodic dissolution than Ru (13). The ionic radii are very similar (11) and the lattice parameters for $Pb_2Ru_2O_{6.5}$ and $Pb_2Ir_2O_{6.5}$ are very similar (9). Thus there is probably a continuous range of solid solutions possible. Horowitz et al. mentioned that such compounds are possible to prepare using the alkaline solution technique (7) but have not presented electrochemical results for compounds of this type. Two compounds were prepared in our laboratory and the X-ray diffraction indicates a single pyrochlore phase.

Although the effects on the O_2 reduction are slight, they are encouraging (Fig. 4). The effects on the O_2 generation were also slight (Fig. 5). It is not clear at present to what extent these effects might be due to changes in the wetted catalyst surface area.

Another approach to inhibiting the anodic dissolution of Ru is to use a conductive solid ionomer either as replacement for the liquid electrolyte within the porous O_2 cathode or as an overlayer on the solution side of the electrode. Even though the dissolved species are anionic, (RuO_4^{2-}, $HPbO_2^{-}$, PbO_3^{2-}) they should diffuse relatively slowly in such ionomers due to size effects. Two types of ionomers were used in this preliminary work. The first was a partially fluorinated anion exchange membrane (RAI 4035) as an overlayer. The second was a hydrogel coating which consisted of a mixture of poly(dimethyldiallylammonium)chloride (DMDAAC) and Nafion (14). The RAI membrane exhibited a definite effect in slowing down the release of ruthenate into the solution when an electrode made from $Pb_2[Ru_{1.67}Pb_{0.33}]O_{6.5}$ was in the O_2 generation mode.

The pre-cast ionomer layer was not expected to have a significant effect on the O_2 reduction and this turned out to be the case (Fig. 6). With the hydrogel coating, however, the ionomers can come into more intimate contact with the catalyst in the porous layer and possibly improve the performance through an increase in the O_2 concentration associated with the polymer fluorocarbon backbone. A small improvement in the performance for O_2 reduction at high current densities was observed for the hydrogel-coated electrode and this is quite encouraging (Fig. 6). With both ionomers there was an improvement in the O_2 generation performance (Fig. 7). This was not expected but can be explained by pointing out that the inhibition of the anodic dissolution would slow down the progressive changes in the surface composition of the material that would occur during the dissolution.

ACKNOWLEDGEMENT

This research has been supported by NASA through the Lewis Laboratory and the Department of Energy through a subcontract with Lawrence Berkeley Laboratory. Samples of two pyrochlores were kindly supplied by Dr. H. S. Horowitz of Exxon. The assistance of Mr. Wesley Aldred is acknowledged in carrying out the gas-fed electrode measurements. Helpful discussions are also acknowledged with Dr. Martin Shingler concerning the pyrochlore crystal structure.

REFERENCES

1. H. S. Horowitz, J. M. Longo and H. H. Horowitz, J. Electrochem. Soc., 130, 1851 (1983).
2. R. G. Edgell, J. B. Goodenough, A. Hammett and C. C. Naish, J. Chem. Soc., Faraday Trans. I, 79, 893 (1983).
3. H. S. Horowitz, J. M. Longo, H. H. Horowitz and J. T. Lewandowski, in "Solid State Chemistry in Catalysis", ACS symposium Series No. 279, R. K. Grasselli and J. F. Brazdil, Editors, pp. 143-163, American Chemical Society, Washington, D.C. (1985).
4. C. Iwakura, T. Edamoto and H. Tamura, Bull. Chem. Soc. Jpn., 59, 145 (1986).
5. J. A. R. Van Veen, J. M. Van Der Eijk, R. De Ruiter and S. Huizinga, Electrochim. Acta, 33, 51 (1988).
6. J. Prakash, R.E. Carbonio, M. Razaq, D. Tryk and E. Yeager, 173rd Meeting of the Electrochemical Society, Atlanta, GA, May, 1988, Ext. Abst., 88-1, 503 (1988).
7. H. S. Horowitz, J. M. Longo and J. T. Lewandowski, U. S. Patent 4,225,469, September 30, 1980.
8. H. S. Horowitz, J. M. Longo and J. T. Lewandowski, Mat. Res. Bull., 16, 489 (1981).
9. J. M. Longo, P. M. Raccah and J. B. Goodenough, Mat. Res. Bull., 4, 191 (1969).
10. H. S. Wroblowa, Y. C. Pan and G. Razumney, J. Electroanal. Chem., 69, 195 (1976).
11. W. O'Grady, C. Iwakura, J. Huang and E. Yeager, in "Proceedings of the Symposium on Electrocatalysis", M. Breiter, Editor, pp. 286-302, The Electrochemical Society, Pennington, NJ (1974).
12. R. D. Shannon and C. T. Prewitt, Acta Cryst., B25, 925 (1969).
13. M. Pourbaix, " Atlas of Electrochemical Equilibria in Aqueous Solutions," pp. 343-349, 373-377, Pergamon, Oxford (1966).
14. M. S. Hossain, D. Tryk, E. Yeager and A. Gordon, 171st Meeting of the Electrochemical Society, Philadelphia, PA, May 1987, Ext. Abst., 87-1, pp. 466.

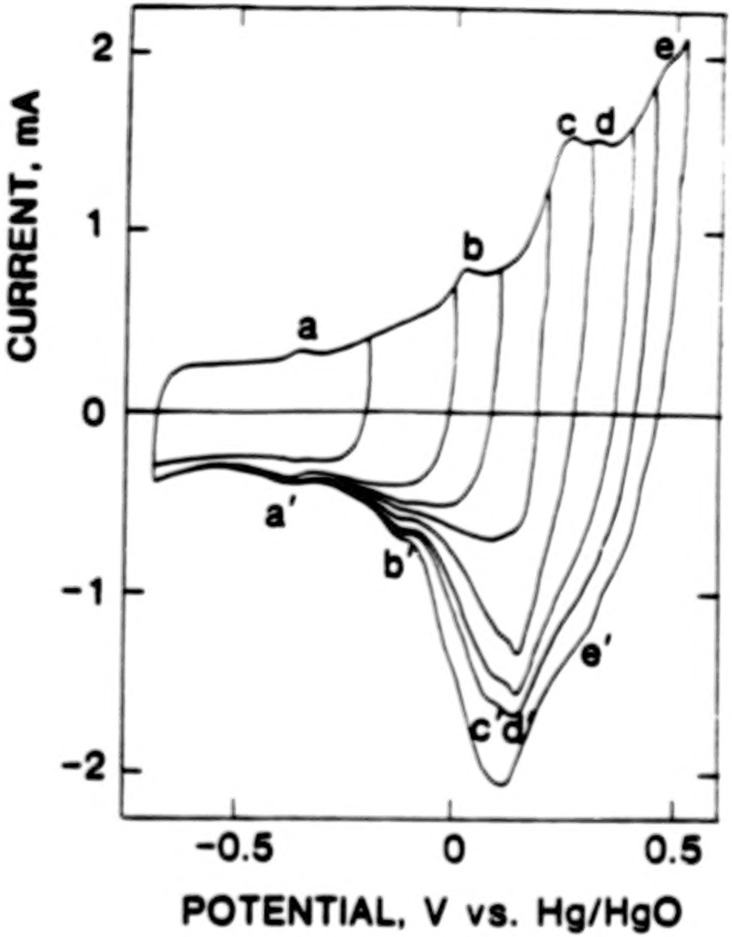

Fig. 1. Cyclic voltammetry for $Pb_2Ru_2O_{6.5}$ in the form of a thin porous coating on an ordinary pyrolytic graphite disk in N_2-saturated 1 M KOH at 22°C. The coating contained 4.0 mg cm^{-2} pyrochlore and 0.21 mg cm^{-2} Teflon T30B. Electrode area was 0.196 cm^2. The sweep rate was 20 mV s^{-1}.

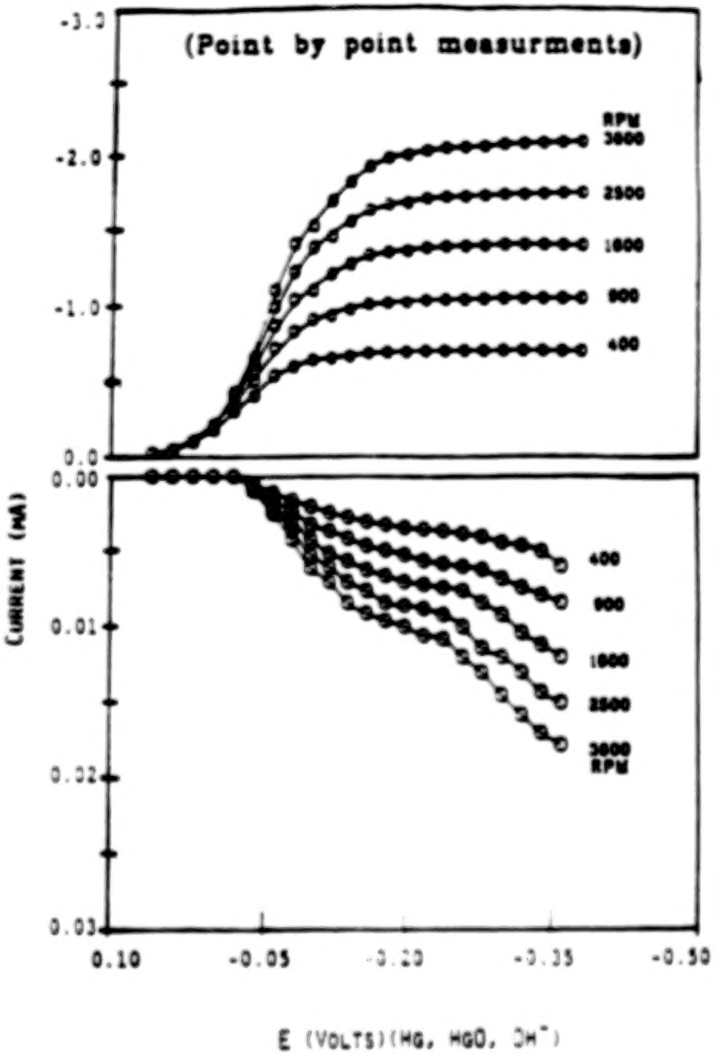

Fig. 2. Rotating ring- disk polarization curves for O_2 reduction on a thin porous coating of $Pb_2Ru_2O_{6.5}$ in O_2-saturated 1 M KOH. Electrode area was 0.45 cm^2. Collection efficiency was 0.177. Rotation rates were as shown. The composition of the coating was as shown in Fig. 1.

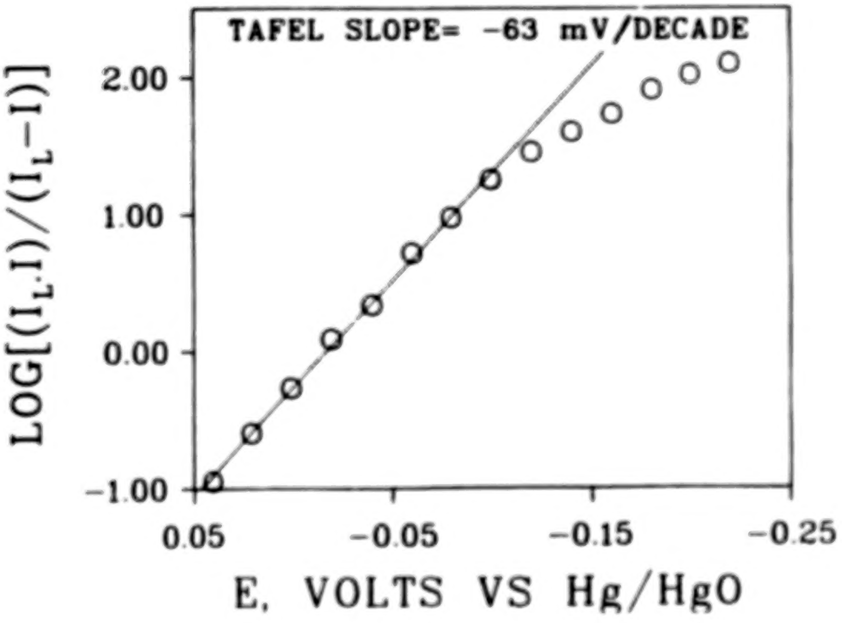

Fig. 3. Tafel plot for O_2 reduction on $Pb_2Ru_2O_{6.5}$ (thin porous coating) in O_2-saturated 1 M KOH. The current values (in mA) for 2500 rpm from Fig. 2 were corrected for mass transport using I_L = 1.75 mA.

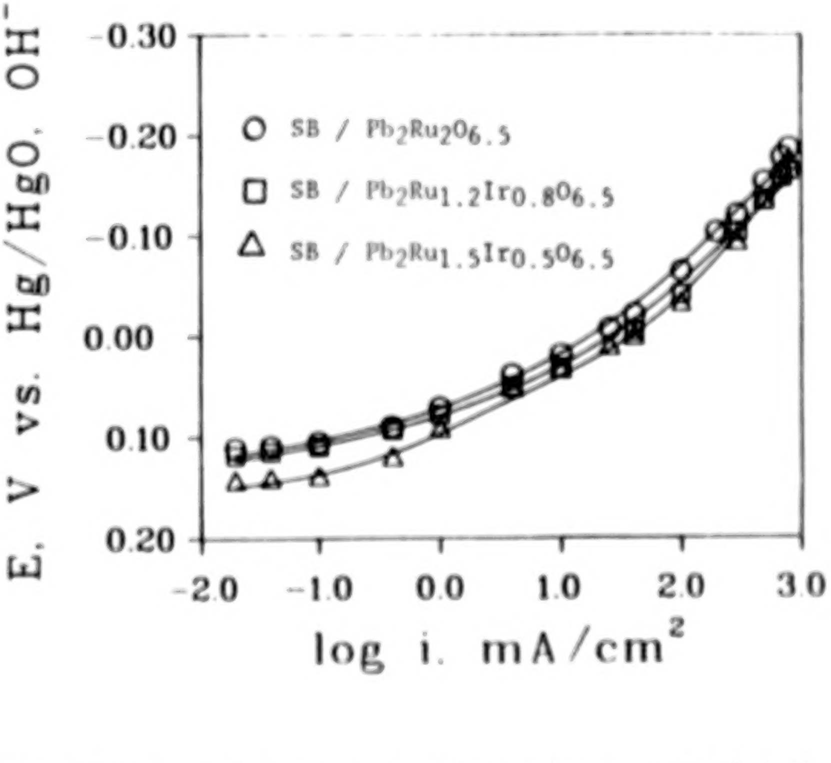

Fig. 4. Polarization curves for O_2 reduction with porous O_2-fed (1 atm) electrodes in 5.5 M KOH at 25°C. The electrode contained 15.8 mg cm^{-2} pyrochlore, 14.6 mg cm^{-2} air-oxidized Shawinigan black and 12.2 mg cm^{-2} Teflon T30-B and was heat-treated at 280°C for 2 h in flowing helium.

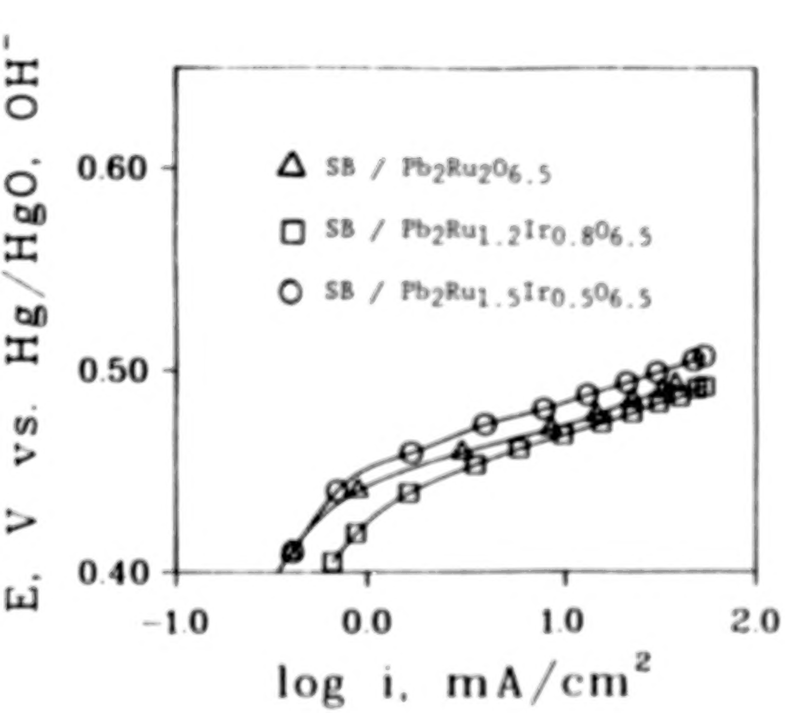

Fig. 5. Polarization curves for O_2 generation with the porous electrodes of Fig. 4.

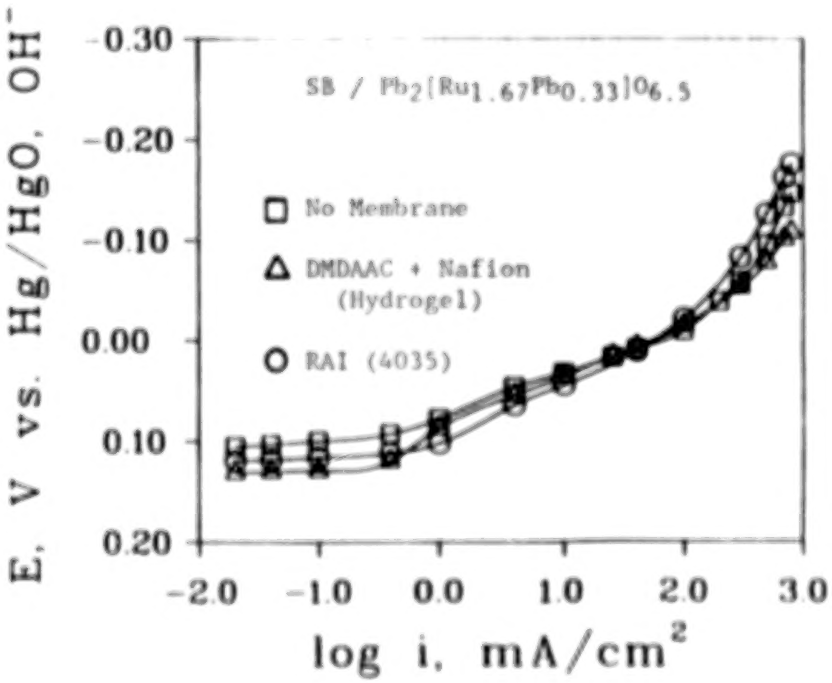

Fig. 6. Polarization curves for O_2 reduction with porous O_2-fed (1 atm) electrodes in 5.5 M KOH at 25°C. The preparation of the hydrogel coating for curve 2 is described in the text. The RAI membrane was pressed onto the solution side of the electrode.

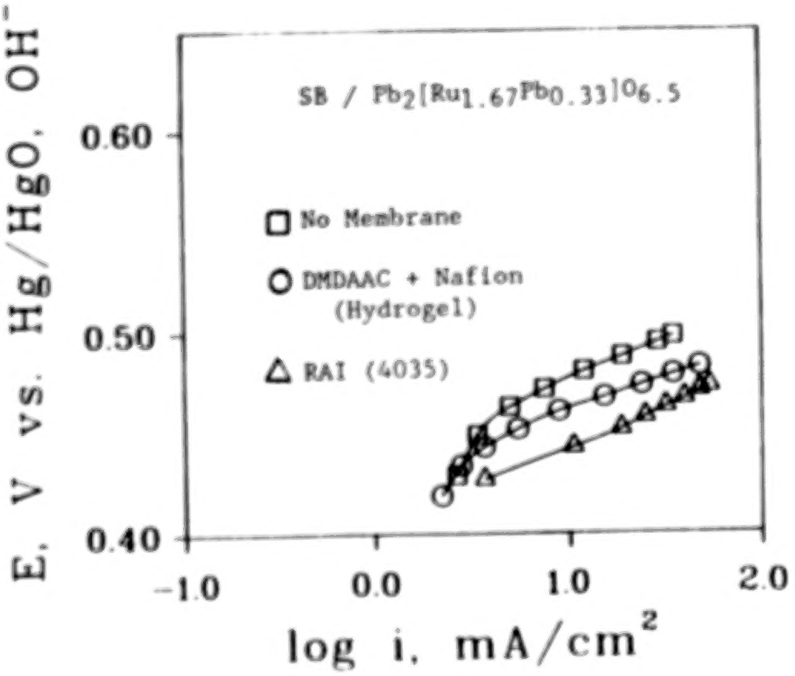

Fig. 7. Polarization curves for O_2 generation with the porous electrodes of Fig. 6.

OXYGEN ELECTRODES FOR RECHARGEABLE ALKALINE FUEL CELLS - II*

L. Swette and N. Kackley
Giner, Inc.
Waltham, Massachusetts 02254

The primary objective of this program is the investigation and development of electrocatalysts and supports for the positive electrode of moderate temperature single-unit rechargeable alkaline fuel cells. Approximately six support materials and five catalyst materials have been identified to date for further development.

INTRODUCTION

Viable candidate materials for moderate temperature single-unit rechargeable alkaline fuel cells must meet the following requirements: 1] good electrical conductivity (a more demanding requirement for supports than electrocatalysts); 2] high resistance to chemical corrosion and electrochemical oxidation and/or reduction; 3] electrocatalysts, in addition, must exhibit high bifunctional electrocatalytic activity (O_2 evolution and reduction). Advanced development requires that the materials be prepared in high surface area forms, and may also entail integration of various candidate materials, e.g., one or two electrocatalysts distributed on a less active support material.

Candidate support materials have been drawn from transition metal carbides, borides, nitrides (Ti, Zr, Hf, Nb) and oxides (La, Sr, Cr, Mo, W, Mn, Ni) which have high conductivity (>1 ohm-cm^{-1}). Candidate catalyst materials have been selected largely from metal oxides of the form ABO_x (where A = Pb, Cd, Mn, Ti, Zr, La, Sr, Na, and B = Pt, Pd, Ir, Ru, Ni, Co) which typically have been investigated and/or developed for one function only, either O_2 reduction or O_2 evolution. The electrical conductivity requirement for catalysts may be lower, especially if integrated with a higher conductivity support. For initial evaluation, materials have been purchased when available; subsequently, in-house preparations have been attempted, to affect surface area and composition, if necessary.

Candidate materials of acceptable conductivity are typically subjected to corrosion testing in three steps. Preliminary corrosion testing consists of exposure to 30% KOH at 80°C under oxygen for about 5 days. Materials that survive chemical testing are examined for electrochemical corrosion activity; the material is held at 1.4 V versus RHE in 30% KOH at 80°C for 15 to 20 hours.

---

*This work is being supported by Nasa Lewis Research Center under the direction of Dr. William Fielder, Contract No. NAS3-24635.

An acceptable anodic current is on the order of a few microamps/mg of material. For more stringent corrosion testing, and for further evaluation of electrocatalysts (which generally show significant O_2 evolution at 1.4 V), samples are held at 1.6 V or 0.6 V for about 100 hours. The surviving materials are then physically and chemically analyzed for signs of degradation (visual examination, electron microscopy, X-ray diffraction).

To evaluate the bifunctional oxygen activity of candidate catalysts, Teflon-bonded electrodes are fabricated and tested in a floating electrode configuration (Ref. 1). Many of the experimental materials being studied have required development of a customized electrode fabrication procedure. For preliminary testing, catalysts of interest should show <500 mV polarization (from 1.2 V) in either mode at 200 mA/cm^2. In advanced development, the goal is to reduce the polarization to about 300-350 mV.

MATERIALS INVESTIGATED

Candidate Supports:
$LaNiO_3$ $LiNiO_x$ NbO_2 MoO_2 WO_2 HfB HfN TiN ZrN ZrC

Candidate Electrocatalysts:
$PbPdO_2$ $Pb_2(Ir_{2-x}Pb_x)O_{7-y}$ $Pb_2(Ru_{2-x}Pb_x)O_{7-y}$ $Na_xPt_3O_4$ $La_{.5}Sr_{.5}CoO_3$
$La_{.5}Sr_{.5}MnO_3$ $YBa_2Cu_3O_x$ $PtTi_{23}O_x$ $RuTi_{12}O_x$ $RuMn_{10}O_x$ $RuMn_2O_x$

Reference materials:
O_2 reduction
10% Pt/Au (Johnson-Matthey, 11 m^2/g)
10% Pt/Vulcan XC-72 Carbon (Johnson-Matthey, Pt: 130 m^2/g)

O_2 evolution
Pt black (Englehard, 25 m^2/g)

SOURCES OF CANDIDATE MATERIALS

Candidate materials for both catalysts and supports were purchased, if commercially available in powder form, as the most efficient approach for preliminary evaluation (electrical conductivity, chemical and electrochemical stability). Such materials offer the advantage of an economical purchase of a material of known purity in a quantity (5-25 g) sufficient for preliminary qualification, and particularly for disqualification. The disadvantage is that most of the commercially available materials have surface areas in the range from low (<10 m^2/g) to very low (<1 m^2/g). Consequently, most commercial materials that survive preliminary screening must be prepared in a higher surface area form, in-house or by a custom fabricator, for effective evaluation as potential catalysts and/or supports.

In many cases, especially for candidate catalysts, commercial materials were not available. Preparation methods described in the literature, either specific for the material or as a general model, were used when deemed appropriate to the material requirements in terms of electrical conductivity, surface area, etc.

CHARACTERIZATION OF CANDIDATE SUPPORT MATERIALS

Candidate material preparations are typically analyzed by X-ray diffraction (XRD) for chemical characterization. The objective of preparing fine powder materials, however, is generally in conflict with obtaining sharp XRD patterns (because of the line-broadening characteristic of high surface area powders); thus the quality of these results is sometimes compromised. Firing materials for a longer time or at a higher temperature usually increases the crystallinity and improves XRD results, but at the expense of decreased surface area and some uncertainty about the composition of the higher surface area material. In some instances, materials of interest have been re-analyzed after extended corrosion testing by XRD and/or scanning electron microscopy (SEM), to check for changes in composition, reaction products and changes in morphology. SEM has also been used occasionally to observe the particle size range of powders.

The electrical conductivity of candidate materials is estimated by compressing a small volume (e.g., 0.5-1 cc) of the powder at about 12,000 psi between metal pistons within an insulating cylinder; the resistance of the powder is measured directly, across the metal pistons, with an ohmmeter. If the resistivity thus measured is low (<5 ohm-cm), the resistance is redetermined by measuring the voltage drop across the powder under the flow of sufficient current to generate easily measured current and voltage signals. The more accurate 4-point method of measuring resistance has not been used because of the larger sample volume requirement.

Surface areas of candidate materials are determined by the BET nitrogen adsorption method using a Micromeritics Flowsorb II 2300 instrument. The samples are typically outgassed at 150°C in the vent stream of the instrument, or at ~100°C in vacuum. All measurements reported have been made with 30% N_2 in He.

A summary of the measured physical characteristics of candidate materials is presented in Table I. As a result of these measurements, the following materials were eliminated from further consideration due to inadequate electrical conductivity: NbO_2, $PtTi_{23}O_x$, $RuTi_{12}O_x$, $RuMn_{10}O_x$, and possibly $La_{.5}Sr_{.5}MnO_3$. The $La_{.5}Sr_{.5}CoO_3$ sample had a very low surface area but good electrical conductivity and thus remained a candidate for further testing. The $LiNiO_x$ sample had both low surface area and marginal conductivity; XRD analysis, however, indicated a second phase of lithium carbonate (which might be leached out), consequently, this material was also retained for further testing.

STABILITY TESTING

A preliminary assessment of the chemical stability of the candidate support materials is made by exposing the as-prepared powder to 30% KOH at 80°C under an oxygen atmosphere. Indications of chemical reaction between the support material and the KOH are color change of the solution or powder, evolution of gas, dissolution of the powder, weight change, and combinations of these phenomena. After exposure for up to 5 days, the remaining powder is filtered out and weighed to determine weight change, if any; small weight changes (e.g., <5%) have an equal probability of being within experimental error for the measurement (weighing, filtering, washing, drying, weighing), and need to be evaluated in conjunction with other observations.

For an initial assessment of the electrochemical stability of candidate support materials and catalysts, the steady-state anodic current is measured in the range of 1.0 to 1.4 V versus RHE in 30% KOH at 80°C. The powder to be tested is blended with polytetrafluoroethylene (PTFE, DuPont type 30 Teflon™ suspension) at about 10-20% by weight and heated to 275-325°C, to try to achieve a suitable compromise between physical integrity and good electrolyte penetration. A pure gold mesh is used as the current collector and the electrode is suspended vertically in solution to prevent gas bubble occlusion of the surface. If the anodic current observed, after initiation of potentiostatic control, drops to the microamp range, the system is allowed to equilibrate overnight; the steady-state anodic current is then recorded. In a second stage of testing (~100 hours), candidate materials are subjected to higher potentials (1.6 V) representative of oxygen evolution conditions, and lower potentials (0.6 V) representative of oxygen reduction conditions. The latter is intended to place electrochemical stress on the materials used in the oxide form.

The value of residual anodic current measured by these methods is not an unequivocal indicator of electrochemical stability. A low value of anodic current (e.g., a few microamps/mg) is necessary but not sufficient to demonstrate corrosion resistance since the powder may passivate or delaminate from the current collector and exhibit a deceptive value. At the other extreme, a high current may represent the onset of oxygen evolution rather than corrosion, especially in the case of catalytic materials. Finally, the gold current collector always exhibits a base level of anodic current (5-10 microamps/cm^2). Consequently, the anodic current values measured must be combined with other observations such as weight loss or gain, color changes, microscopic examination (SEM, TEM) and analysis (EDAX, XRD, etc.).

Observations on chemical stability are summarized in **Table II**. Electrochemical stability measurements are recorded in **Tables III** and **IV**.

Three candidate materials were eliminated from consideration due to evidence of chemical instability when the sample powders were exposed to KOH at 80°C under O_2: **HfB**, **HfN**, and **$YBa_2Cu_3O_x$**. Two additional materials were eliminated due to dissolution during electrochemical stress testing at 1.6 V: **MoO_2** and **WO_2**. As a result of these screening tests, the following materials remain as potential candidates for further investigation, and may be classified as follows:

Supports:
TiN, ZrC, ZrN

Catalytic Supports:
$LaNiO_3$, $LiNiO_x$, $La_{.5}Sr_{.5}CoO_3$

Electrocatalysts:
$PbPdO_2$, $Na_{.8}Pt_3O_4$, $Pb_2(Ir_{1.33}Pb_{.67})O_{7-y}$,
$Pb_2(Ru_{1.35}Pb_{.65})O_{7-y}$, $RuMn_2O_x$

TM - Teflon is a trademark of E.I. DuPont Corp.

The following observations were made on these materials:

TiN: The coarse commercial powder (40 microns) and the low surface area Giner, Inc. preparation (1 micron, 2.3 m^2/g) appeared to be quite stable up to 1.4 V vs. RHE. The latter material, held at 1.6 V for more than 100 hours, had a slight surface discoloration, but otherwise, showed no evidence of reaction (e.g., no weight change). Post-test XRD analysis indicated a strong TiN pattern (a = 4.240 angstroms), no TiO_2, and a few lines possibly due to a silicate, phosphate or carbonate.

The higher surface area material (TiN_x, Univ. of Calif.) similarly appeared relatively stable in the chemical test (very small amount of white floc visible, quantitative weight change measurement not successful) and anodically up to 1.4 V. Post-test XRD analysis showed a strong TiN pattern and three additional lines that might be attributed to a phase such as potassium titanate. When the electrode was held at 1.6 V, however, the material was largely lost, apparently by dissolution. A gold-catalyzed TiN electrode was also found to be very reactive. After electrochemical testing, the surface of the electrode had degraded to a refractory non-conductive material. Post-test XRD analysis again showed a second phase (much stronger) consistent with the first analysis (potassium titanate?). Based on these results, it appears that the non-stoichiometric TiN_x ($x = 0.72$-0.86), although promising in terms of the high surface area achieved, is unstable at anodic potentials. Based on other results, TiN remains a candidate support material under investigation.

ZrC: The commercially available material was a coarse (40 microns), low surface area powder with about 2% Hf impurity. During the initial period of the chemical stability test, gassing was observed; this was attributed to dissolution of the Hf impurity (weight change measurements were not successful). In three repetitions of electrochemical testing, the anodic currents measured at 1.4 V were very low, 0.2 to 0.7 microamps/mg, equivalent to the background current measured on the gold current collector. In testing at 1.6 V vs. RHE from 50 to 100 hours, there was a visible loss of material, as well as a measurable weight loss (e.g., ~40%), but this could not be distinguished from physical shedding during oxygen evolution, and there was no other evidence of reaction. This material remains a potential candidate support under development with emphasis on higher surface area preparations.

ZrN: The commercially available material, a coarse, low surface area powder, also appeared to be fairly inert in all stability tests. A weight loss of about 9% was recorded for a 14-day chemical exposure test. The anodic current at 1.4 V was at a background level (0.2 microamps/mg) and there were no signs of degradation after a week of oxygen evolution (1.6 V in 30% KOH at 80°C). This material also remains under development primarily to produce high surface area powder.

$LaNiO_3$: The commercial material has proven to be quite stable in all corrosion testing. Since $LaNiO_3$ is also catalytic (Ref. 2) oxygen evolution currents were measured at 1.4 V vs. RHE. After extended testing at 1.6 V and 0.6 V, XRD analysis still indicated a strong, unchanged pattern for $LaNiO_3$. Attempts to prepare materials with surface areas greater than ~5 m^2/g have been unsuccessful to date.

$LiNiO_x$: XRD analysis of the commercial sample (labeled "$LiNiO_2$") indicates a strong second phase of lithium carbonate. This may account for the weight loss recorded in chemical testing. It is anticipated that a more well-defined material will be stable, somewhat catalytic, and a potential support material. Higher surface area in-house preparations will be investigated.

$La_{.5}Sr_{.5}CoO_3$: This commercial compound was quite conductive, but very low in surface area. It showed a 28% weight loss in the chemical test but did not appear to be reactive (or very catalytic) at anodic potentials. Higher surface area preparations will be attempted for further investigation as a support.

$PbPdO_2$: The classical preparations of this material, by high temperature firing of the mixed oxides (Ref. 10) or hydroxide co-precipitates, have generally resulted in fairly non-conductive powders (Ref. 11), limiting our ability to evaluate the material. It remains of interest because it has shown catalytic activity on a carbon support (Ref. 11). A recent preparation by a novel method has yielded a quite conductive material with the correct XRD pattern for $PbPdO_2$. In the limited chemical test performed to date, the material showed no weight change or other signs of reaction, and will be investigated further.

$Na_{.8}Pt_3O_4$, prepared at Giner, Inc. (Batch #1), had moderately high surface area and good conductivity. After 17 days of corrosion testing, primarily at 1.6 V vs. RHE, there were no signs of degradation or changes in appearance (no XRD data), and the electrode showed a similar level of anodic polarization at 200 mA/cm^2 (~400 mV) as a freshly-prepared electrode (~385 mV). This material continues to show promise as a bifunctional oxygen electrode catalyst, as discussed in the next section.

$Pb_2(Ir_{1.33}Pb_{.67})O_{7-y}$: In our initial investigation of this material (Ref. 11) it was found to be unstable in 30% KOH at 80°C (e.g., 23 microamps/mg at 1.0 V vs. RHE); at 1.6 V, the material showed substantial physical changes. More recently, this same material was refired at 500°C. This had the effects of improving its crystallinity and decreasing its reactivity below 1.4 V. The test electrode survived 24 hours at 1.6 V, but delaminated from the current collector at 0.6 V. It is anticipated that this material will be prepared in different compositions and by alternative methods for further investigation.

$Pb_2(Ru_{1.35}Pb_{.65})O_{7-y}$, prepared in several batches by a different method (Ref. 8) than the Pb-Ir pyrochlore above, was obtained in a crystalline form at low temperature. The resulting materials, however, were unstable under most test conditions, as evidenced by yellow coloration of all test solutions. Heat treating the 3rd batch of this compound at 400°C resulted in a substantial reduction in surface area (73 --> 30 m^2/g) and stabilized the compound in the chemical test (no coloration of the solution). This material is under active investigation.

$RuMn_2O_x$: This material has been subjected to very limited investigation to date; it shows evidence of instability similar to that observed for the Ru pyrochlore discussed above. Efforts are now concentrated on stabilizing this catalyst by thermal treatments and alternative preparations.

OXYGEN ELECTRODE PERFORMANCE TESTING

Oxygen electrode performance testing is implemented in a floating electrode cell (Ref. 1) in 30% KOH at 80°C using a 1 cm x 1 cm electrode sample. Pure oxygen is fed to the cell through a water presaturator. To fabricate a test electrode, a powder sample is blended with PTFE (DuPont type 30 Teflon suspension) in the range of 15-40% by weight, as an approximate function of surface area. The Teflon catalyst blend is then applied to a gold-plated Ni mesh with a porous Teflon backing (1-micron pores), dried and thermally processed at 330-360°C. It is frequently necessary to try other Teflon-catalyst compositions and fabrication procedures to achieve an adequate balance in the hydrophobic/hydrophilic properties of the electrode.

The testing sequence is usually an oxygen reduction polarization test followed by an oxygen evolution polarization test, applying small potential steps sufficient to yield a few data points in each log-decade of current density from 1 to 1000 mA/cm^2. The potentials are controlled, and compensated for iR loss, with a Princeton Applied Research model 173 potentiostat. Collecting oxygen evolution data entails frequent interruptions to remove trapped gas bubbles. After an oxygen evolution test, electrodes are sometimes too flooded to rerun an oxygen reduction test. Development of an electrode structure adequate for bifunctional operation with these candidate electrocatalysts is an independent research task; some experience, gained in the development of Pt black bifunctional hydrogen electrodes, will be beneficial to this effort.

The best performance data for each of the catalysts, as well as data for the reference materials (10% Pt/Au, 10% Pt/C and Pt black), are shown in **Figure 1**. The following observations were recorded:

$\underline{\mathbf{RuMn_2O_x}}$ exhibited exceptional oxygen evolution performance, and moderate oxygen reduction performance, in the limited testing performed to date. Unfortunately, this batch of material was not stable, as evidenced by the reddish coloration of the test solutions in this test and in the earlier corrosion tests. We are currently investigating methods of stabilizing this catalyst by thermal treatment and/or doping.

$\underline{\mathbf{Pb_2(Ir_{1.33}Pb_{.67})O_{7-y}}}$ (fired at 400°C) gave good performance at lower current densities for both oxygen reduction and evolution, but polarized rapidly above 100 mA/cm^2, suggesting a poor electrode structure. This preparation was also unstable as discussed under stability testing. The sample refired at 500°C was corrosion tested but not performance tested. Further preparation and testing of this catalyst is planned.

$\underline{\mathbf{Pb_2(Ru_{1.35}Pb_{.65})O_{7-y}}}$, prepared by the low temperature process described (Ref. 8), showed from good (Batch #1) to exceptional (Batch #3) activity for oxygen reduction, as presented in **Figure 2**. All of these preparations were unstable in KOH, however. Post-thermal treatment at 400°C (Batch #3) stabilized the material but resulted in a loss in performance, coincident with the loss in surface area. Oxygen evolution performance was generally very poor with the exception of Batch #1, as shown in Figure 1. Performance of all materials was typically transient and non-reproducible. This catalyst is still under investigation with emphasis on stability and oxygen evolution performance.

$Na_{.8}Pt_3O_4$ - Performance data for two separate preparations of this catalyst are shown in Figure 1. The data for Batch #2 is the more recent and represents improvements in electrode structure as well. This material is the best candidate bifunctional oxygen electrode catalyst developed to date in terms of both stability and oxygen reduction/evolution performance. The emphasis in further development is on increasing the surface area and preparing larger quantities of material. Deposition on a support will be attempted also, when a suitable, stable, high surface area support material has been developed.

Au/TiN_x: Gold was deposited on the high surface area TiN_x, by a Giner, Inc. proprietary process, to investigate the feasibility of catalyzing this support. The surface area was increased from about 38 m^2/g to 51 m^2/g, indicating an average particle size of about 25 nm. Electron microscopic examination of this material at NASA, by Dr. William Fielder, indicated the presence of particles in this range as well as larger agglomerates of particles. The material could not be tested electrochemically because of the instability of the TiN_x, as discussed above, but indicates the potential feasibility of catalyst deposition on this novel support.

ACKNOWLEDGEMENTS

We would like to acknowledge the assistance of Prof. B.L. Chamberland of the University of Connecticut in the selection and identification of numerous materials tested in this program.

REFERENCES

1. Giner, J.; and Smith, S.: A Simple Method for Measuring the Polarization of Hydrophobic Gas Diffusion Electrodes. Electrochem. Technol., vol. 5, 1967, p. 59.

2. Otagawa, T.; and Bockris, J.O'M.: Lanthanum Nickelate as Electrocatalyst: Oxygen Evolution. J. Electrochem. Soc., vol. 129, 1982, p. 2391.

3. Zhang, H-M.; Teraoka, Y.; and Yamazoe, N.: Preparation of Perovskite-type Oxides with Large Surface areas by Citrate Process. Chemistry Letters, 1987, p. 665.

4. Baythoun, M.S.G.; and Sale, F.R.: J. Mater. Sci., vol. 12, 1982, p. 2757.

5. Schwartz, K.B.; Prewitt, C.T.; Shannon, R.D.; Corliss, L.M.; Hastings, J.M.; and Chamberland, B.L.: Neutron Powder Diffraction Study of Two Sodium Oxides: $Na_{1.0}Pt_3O_4$ and $Na_{0.73}Pt_3O_4$. Acta Cryst., vol. 38, 1982, pp. 363-368.

6. Shannon, R.D.; Gier, T.E.; Carcia, P.F.; Bierstedt, P.E.; Flippen, R.B.; and Vega, A.J.: Synthesis and Properties of Platinum Metal Oxides of the Type $M_xPt_3O_4$. Inorg. Chem., vol. 21, no. 9, 1982, pp. 3372-3381.

7. Horowitz, H.S.; Longo, J.M.; and Lewandowski, J.T.: Lead Ruthenium Oxide, $Pb_2[Ru_{2-x}Pb_x^{4+}]O_{6.5}$. Inorganic Synthesis, vol. 22, John-Wiley & Sons, New York, 1983, pp. 69-72.

8. Horowitz, H.S.; Longo, J.M.; and Lewandowski, J.T.: Method of Making Lead and Bismuth Pyrochlore Compounds Using an Alkaline Medium and at Least One Solid Reactant Source. U.S. Patent No. 4,225,269, Sept. 30, 1980.

9. Adams, R.; and Shriner, R.L.: Platinum Oxide as a Catalyst in the Reduction of Organic Compounds. III. Preparation and Properties of the Oxide of Platinum Obtained by the Fusion of Chloroplatinic Acid with Sodium Nitrate. J. Am. Chem. Soc., vol. 45, 1923, p. 2171.

10. Lazarev, V.B.; and Shaplygin, I.S.: Properties and Structure of $PbPdO_2$. Zh. Neorg. Khim., vol. 24, 1979, pp. 885-889.

11. Swette, L.; and Giner, J.: Oxygen Electrodes for Rechargeable Alkaline Fuel Cells. J. of Power Sources, vol. 22, 1988, pp. 399-408.

TABLE I - PHYSICAL CHARACTERIZATION OF CANDIDATE MATERIALS

Material	Source [Reference]	Surface Area (m^2/g)	Elect. Conduct. $(ohm\text{-}cm^{-1})$
$PbPdO_2$	Giner, Inc. #4	4	0.74
$Na_{.8}Pt_3O_4$	Giner, Inc. #1 [5,6]	21	50
	Giner, Inc. #2 [5,6]	17	56
$Pb_2(Ir_{1.33}Pb_{.67})O_{7-y}$	Giner, Inc. #1 (400°C) [7]	24	40
$Pb_2(Ru_{1.35}Pb_{.65})O_{7-y}$	Giner, Inc. #1 [8]	55	41
	Giner, Inc. #2 [8]	35	30
	Giner, Inc. #3 [8]	73	33
	Giner, Inc. #3 (400°C) [8]	30	26
$PtTi_{23}O_x$	Giner, Inc. #1 [9]	79	(poor)
$RuTi_{12}O_x$	Giner, Inc. #1 [9]	73	(poor)
$RuMn_{10}O_x$	Giner, Inc. #1 [9]	38	(poor)
$RuMn_2O_x$	Giner, Inc. #1 [9]	62	2.9
$La_{.5}Sr_{.5}CoO_3$	CheMaterials (Basic Vol.)	0.1	105
$La_{.5}Sr_{.5}MnO_3$	CheMaterials	9	0.14
$YBa_2Cu_3O_x$	Duke University	0.04	1.3
$LaNiO_3$	CheMaterials	5	5-10
	Giner, Inc. #1 [2]	4	46-109
	Giner, Inc. #2 [3]	6	(poor)
$LiNiO_x$	CheMaterials	0.8	0.4
NbO_2	Alfa Prod. (Morton-Thiokol)	N/M	(poor)
MoO_2	Alfa Prod.	N/M	3.4
WO_2	Alfa Prod.	N/M	3.5
HfB	Aesar (Johnson-Matthey)	N/M	2.1
HfN	Aesar	N/M	1.7
ZrN	Alfa Prod.	0.3	91
ZrC (2% Hf)	Aesar	1	125
TiN	Alfa Prod.	N/M	390
	Giner, Inc.	2.3	440
	Univ. of California #2	56	0.34
	Univ. of California #3	38	N/M
	Univ. of California #5	21	14
Au/TiN	Giner, Inc./U. Calif. #3	51	0.37

TABLE II - RESULTS OF STABILITY TESTS OF SELECTED CANDIDATE MATERIALS.

Codes: **NVR - No Visible Reaction**
SR - Slight Reaction (C = Color, G = Gas)
D - Dissolved
N/M - Not Measured

Material	**Source [Reference]**	**Weight Change (%)**	**Observations**
$PbPdO_2$	Giner, Inc. #4	+0.7	NVR
$Na_{.8}Pt_3O_4$	Giner, Inc. #1 [5,6] Giner, Inc. #2 [5,6]	N/M N/M	NVR NVR
$Pb_2(Ir_{1.33}Pb_{.67})O_{7-y}$	Giner, Inc. #1 (400°C) [7]	N/M	NVR
$Pb_2(Ru_{1.35}Pb_{.65})O_{7-y}$	Giner, Inc. #1 [8] Giner, Inc. #2 [8] Giner, Inc. #3 [8] Giner, Inc. #3 (400°C) [8]	N/M N/M -20 N/M	SR-C SR-C SR-C NVR
$RuMn_2O_x$	Giner, Inc. #1 [9]	-14	SR-C
$La_{.5}Sr_{.5}CoO_3$	CheMaterials	-28	NVR
$La_{.5}Sr_{.5}MnO_3$	CheMaterials	-15	NVR
$YBa_2Cu_3O_x$	Duke University	N/M	SR-C
$LaNiO_3$	CheMaterials Giner, Inc. #1 [2]	N/M -25	NVR NVR
$LiNiO_x$	CheMaterials	-29	NVR
MoO_2	Alfa	N/M	NVR
WO_2	Alfa	N/M	NVR
HfB	Aesar	-100	D-C/G
HfN	Aesar	-100	D-C/G
ZrN	Alfa	-9	NVR
ZrC (2% Hf)	Aesar	N/M	SR-G
TiN	Alfa Giner, Inc. Univ. of California #2	N/M N/M N/M	NVR NVR SR-C

TABLE III - ELECTROCHEMICAL STABILITY MEASUREMENTS ON SELECTED CANDIDATE MATERIALS

Material	Source [Reference]	Anodic Current (µA/mg) at 1.0-1.4 V (vs. RHE)				
		1.0	1.1	1.2	1.3	1.4
$Na_{.8}Pt_3O_4$	Giner, Inc. #1 [5,6]	1.5	1.0	1.3	2.3	800
$Pb_2(Ir_{1.33}Pb_{.67})O_{7-y}$	Giner, Inc. #1 (400°C) [7]	23	---	32	50	---
	Giner, Inc. #2 (500°C) [7]	---	---	0.4	2.0	6.0
$Pb_2(Ru_{1.35}Pb_{.65})O_{7-y}$	Giner, Inc. #1 [8]	---	1.1	4.9	530	2400
$RuMn_2O_x$	Giner, Inc. #1 [9]	---	---	4.0	---	600
$La_{.5}Sr_{.5}CoO_3$	CheMaterials	0.8	---	---	---	3.5
$LaNiO_3$	CheMaterials	---	---	---	0.1	18
	Giner, Inc. #1 [2]	---	---	---	---	0.9
$LiNiO_x$	CheMaterials	0.1	0.1	0.1	0.2	4.0
MoO_2	Alfa	16	---	---	---	0.7
		0.2	1.5	2.0	1.5	2.0
WO_2	Alfa	2.5	---	---	---	0.3
		---	---	---	---	0.4
		20	---	---	---	---
ZrN	Alfa	0.4	0.4	0.4	0.4	0.2
ZrC (2% Hf)	Aesar	0.5	1.1	1.2	0.7	0.7
TiN	Alfa	0.2	0.2	0.2	0.2	0.2
	Giner, Inc.	0.4	0.4	0.6	0.5	0.6
	Univ. of California #2	1.0	2.0	2.0	1.0	3.5
	Univ. of California #3	0.4	0.9	1.3	0.5	1.5
	Univ. of California #5	1.3	1.3	1.2	0.5	0.2

TABLE IV - ELECTROCHEMICAL STRESS TESTS ON SELECTED CANDIDATE MATERIALS

Material	Source [Reference]	Stress Test Hours at 1.6, 0.6 V		Observations (Wt. Change)
		1.6 V	0.6 V	
$Na_{.8}Pt_3O_4$	Giner, Inc. #1 [5,6]	120	70	No signif. deterior.
$Pb_2(Ir_{1.33}Pb_{.67})O_{7-y}$	Giner, Inc. #1 (400°C) [7]		112	Cracking, shrinkage
	Giner, Inc. #2 (500°C) [7]	24	72	Delamin. at 0.6 V
$Pb_2(Ru_{1.35}Pb_{.65})O_{7-y}$	Giner, Inc. #1 [8]	50	2.5	Color in soln. (-40%)
$RuMn_2O_x$	Giner, Inc. #1 [9]	70		Color in soln. (-17%)
$La_{.5}Sr_{.5}CoO_3$	CheMaterials	64		NVR (-7%)
$LaNiO_3$	CheMaterials	75	46	XRD-No evidence of react
$LiNiO_x$	CheMaterials	114	3.5	Mat. loss (-72%)
MoO_2	Alfa	20		Delamin. at 1.6 V
		1		Dissolved at 1.6 V
WO_2	Alfa	48		Delamin. at 1.6 V
		37	6	Dissolved at 1.6 V
		(16 hrs @ 1 V)		Dissolved at 1.0 V
ZrN	Alfa	169	17	No signif. deterior.
ZrC (2% Hf)	Aesar	48	17	Mat. loss (-38%)
TiN	Giner, Inc.	105		Surf. color change (0%)
	Univ. of California #3	46		Part. dissolved
	Univ. of California #5	3		XRD anal.-Ktit.? (+5%)

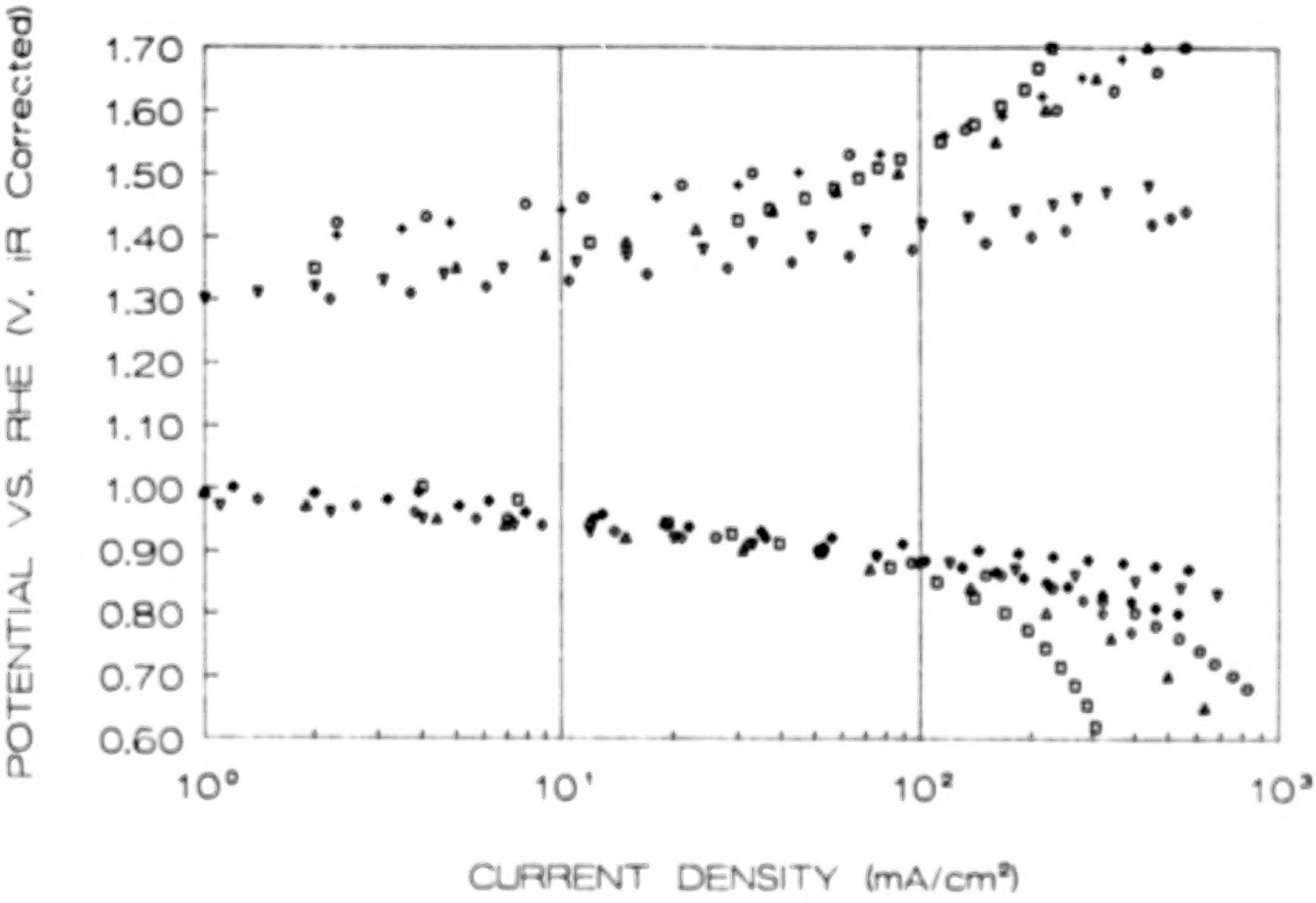

Figure 1. **Bifunctional Oxygen Catalyst Performance in 30% KOH at 80°C.**

◆ 10% Pt/Au (15 mg/cm^2); + Pt black (10 mg/cm^2);
◆ 10% Pt/C (1 mg Pt/cm^2); ◇ RuMnO$_x$, #1 (26 mg/cm^2);
□ PbIrO$_x$ (19 mg/cm^2); ○ PbRuO$_x$ (20 mg/cm^2);
△ Na$_{.8}$Pt$_3$O$_4$, #1 (20 mg/cm^2); ▽ Na$_{.8}$Pt$_3$O$_4$, #2 (20 mg/cm^2);

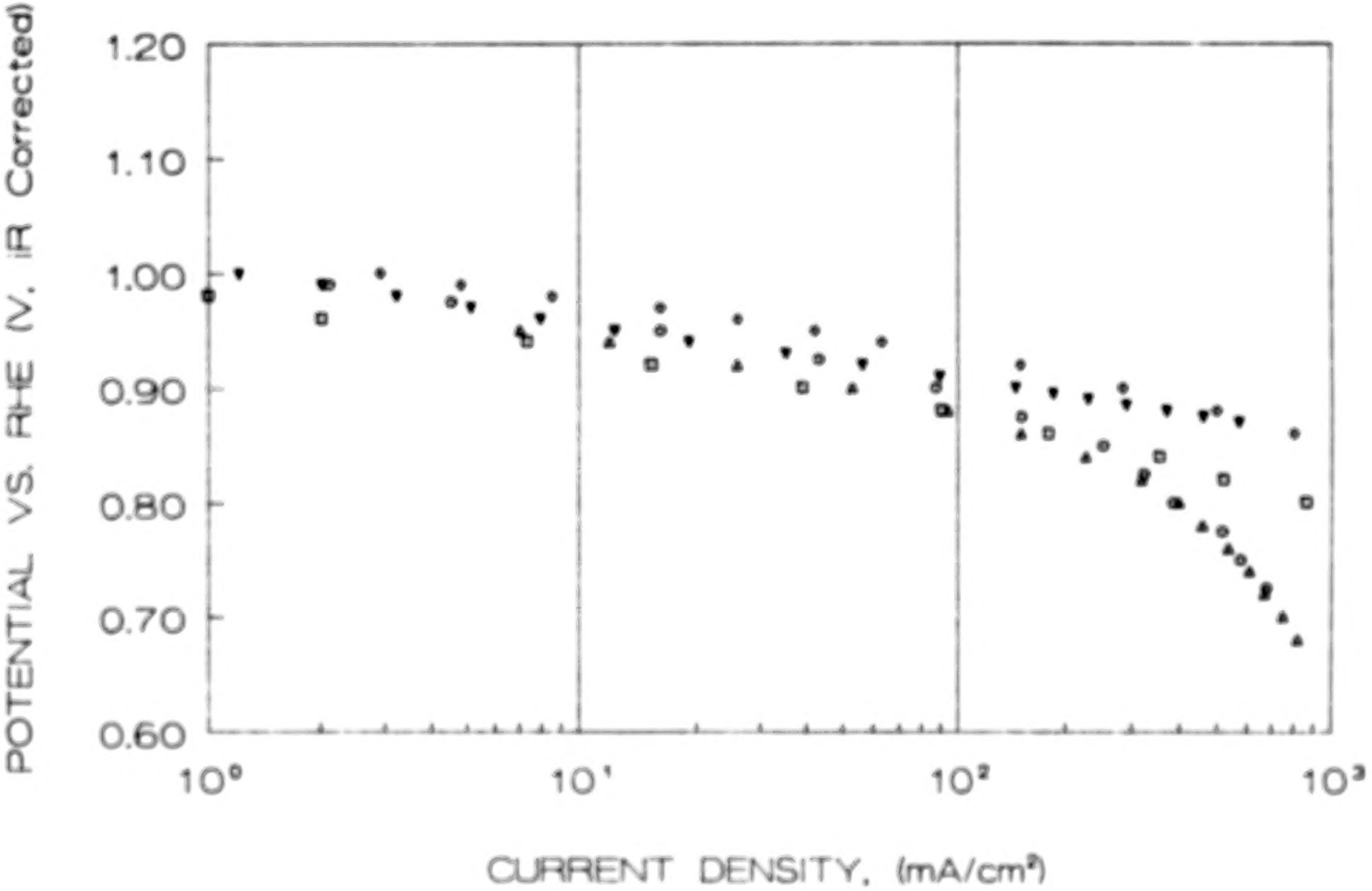

Figure 2. O_2 Reduction Performance of Lead Ruthenate Preparations in 30% KOH at 80°C.
▼ 10% Pt/Au; △ PbRuO$_x$ #1; ○ PbRuO$_x$ #2; ◇ PbRuO$_x$ #3; □ PbRuOx #3, 400°C

NON-NOBLE ELECTROCATALYSTS FOR ALKALINE FUEL CELLS

S. Sarangapani, P. Lessner, M. Manoukian and J. Giner
Giner, Inc.
Waltham, Massachusetts 02254

INTRODUCTION

Noble metals, when used as electrocatalysts for oxygen reduction in metal-air batteries and fuel cells, suffer from the disadvantages of high cost, susceptibility to poisoning and sintering. Carbons activated with macrocyclics have attracted increasing attention as alternative electrocatalysts for oxygen reduction (Yeager, 1984). Initial activity of these catalysts is good, but performance declines rapidly. Pyrolyzing the macrocyclic on the carbon support leads to enhanced stability and the catalyst retains good activity (Wiesener, 1986). The exact nature of the catalytic sites after pyrolysis is still under investigation (Scherson, et al., 1983; McBreen, et al., 1987).

Despite this promising method of treating macrocyclic activated carbon catalysts, the performance decay is still too large to be acceptable. Part of the stability problem occurs because the catalytic layer on the carbon surface is, at most, a few monolayers thick. The approach described here is designed to develop bulk doped catalysts with similar structures to pyrolyzed macrocyclic catalysts. The transition metal and coordinated ligands are dispersed throughout the bulk of the conductive carbon skeleton.

Two approaches to realizing this concept are being pursued, both involving the doping of a carbon precursor followed by high temperature pyrolysis to form a M-N-C catalyst. In one approach, the precursor is a solid phase ion exchange resin. Two resins have been selected for doping. One is IRC-50 (**Figure 1a**) which is a weak cation exchange resin that contains no nitrogen in its backbone or exchange groups. The transition metal and nitrogen are introduced by either exchanging a transition-metal (such as Fe^{+3} from $FeCl_3$) and nitrogen (from NH_4OH) sequentially or exchanging a chelation compound (such as $Fe(bipy)_3^{2+}$). The other ion exchange resin chosen was Chelite-C (**Figure 1b**) which contains a nitrogen-containing iminodiacetic acid exchange group. Exchange of a simple transition metal salt results in metal-nitrogen coordination before pyrolysis.

In the second approach, gas phase precursors are mixed in a reactor and pyrolyzed to form the catalyst. Acetylene (C_2H_2) is used as the carbon source, ammonia (NH_3) as the nitrogen source, and an iron-containing organometallic as the transition metal source.

EXPERIMENTAL METHODS

Chelation compounds for doping the IRC-50 resin have included Fe(bipy)$_3$SO$_4$, Co(bipy$_3$)Cl$_2$, Fe(phen)$_3$SO$_4$, Co(NH$_3$)$_6$Cl$_2$, and Co(en)$_3$Cl$_3$. Doping is carried out by mixing the resin with a solution of the dopant and agitating the mixture at 80°C for 3 hours. The doped resin is dried and then placed in a tube furnace. The resin is pyrolyzed under an NH$_3$ atmosphere at temperatures near 900°C.

The gas phase precursors are pyrolyzed in a vertical tube furnace at temperatures near 1100°C. The C$_2$H$_2$, NH$_3$, and iron-containing organometallic are introduced at the top of the furnace. Product is collected in a water trap at the bottom of the furnace or inside the tube.

Electrodes are prepared from the bulk doped carbons by mixing the catalyst with PTFE and spreading onto a Ag-plated Ni screen.

Electrochemical tests are performed using the floating electrode technique (Giner and Smith, 1967). The electrolyte is 30% KOH and the temperature is held at 80°C. The electrodes are tested galvanostatically and the measurements are corrected for external ohmic losses. Potentials are reported versus a dynamic hydrogen electrode (DHE).

The catalysts are analyzed for their carbon, hydrogen, nitrogen, and metal content. Some catalysts have also had BET surface areas determined using a Micromeritics Flowsorb II surface area analyzer.

Mossbauer spectroscopy has been used in an attempt to identify the species present in the iron-containing catalysts. This work is being done in conjunction with Professor Daniel Scherson at Case Western Reserve University.

RESULTS AND DISCUSSION

A. Electrochemical Tests

Figure 2 compares the electrochemical performance of catalysts prepared from IRC-50 doped from solutions of Fe(bipy)$_3$SO$_4$, Co(en)$_3$Cl$_3$, Co(bipy)$_3$SO$_4$, Co(NH$_3$)$_6$Cl, and FeCl$_3$-NH$_4$OH with CoTMPP adsorbed and pyrolyzed on Vulcan XC-72. There is a large improvement in performance on changing the dopant solution from FeCl$_3$-NH$_4$OH to Fe(bipy)$_3$SO$_4$ with the same resin and pyrolysis conditions. The Fe(bipy), Co(en), and Co(hex) systems show a performance that is 50-80 mV less at 100 mA/cm^2 than the CoTMPP on Vulcan XC-72. The surface areas of Co(en), Co(hex) and Fe(bipy), doped carbons are in the same range as CoTMPP doped Vulcan XC-72. The differences in the kinetic region may be attributed to the differences in the surface concentrations of the catalyst. The earlier dropoff of performance may be due to either ohmic losses in the structure or hindrance to oxygen transport. The Co(bipy) system shows somewhat poorer performance; stoichiometric analysis of the Co(bipy) system showed that only 1% Co was incorporated in the final catalyst (compared to 10% for iron) and, therefore, doping conditions need to be adjusted.

The next set of experiments examines two different approaches for the synthesis of "Fe-N" complexes. **Figure 3** compares the performance of the IRC-50 Fe(bipy) system with Chelite-C doped with FeCl$_3$. In the first system, the Fe is already coordinated with nitrogen in the bypyridine complex. Introducing this complex into the ion exchange resin, allows bulk-doping and ensures molecular level interaction between the carbon and the "Fe-N" complex. In the second system, the resin has a backbone that contains nitrogen and coordinates with the iron. In addition to differences in the density of the exchange sites (which determines the metal/nitrogen ratio) in these two systems, the molecular interactions are bound to be different which may result in differences in oxygen reduction performance. The carbon prepared from the chelating resin shows essentially the same performance in the kinetic region, indicating that the nature of the Fe-N complexes may be similar regardless of their method of preparation, as long as covalent type interactions are ensured as opposed to purely ionic type interactions. At higher current densities, there are some differences in the performance of these systems, which may be attributed to the non-optimized electrode preparation. It is also quite possible that the stabilities of these complexes may vary widely. Preliminary examination of the catalysts using Mossbauer spectroscopy indicates that the IRC-50 and Chelite-C systems contain one species in common and one species each that is unique to that catalyst.

Figure 4 shows the results of performance measurements on catalysts from gas phase precursors. The undoped carbon prepared from gas pyrolysis shows very poor performance. Addition of the Fe and N has a dramatic effect on performance. The surface area of the Fe/N doped carbon in this figure, is only 19 m^2/g and the nitrogen/metal mole ratio is 0.46. Studies are in progress to improve both these factors.

B. Characterization of Catalysts

The catalysts are routinely analyzed for carbon, hydrogen, nitrogen, and metal content. **Table I** shows the stoichiometry calculated for some typical catalysts. There is still some unknown that is not accounted for in the C, H, N, M. Some of this unknown is oxygen which comes from the COO^- groups in the resin and exposure of catalyst to the atmosphere. The oxygen is present in the form of metal oxides. However, a calculation of the maximum weight percentage of oxygen present in this form shows that it is not enough to account for all of the unknown. The sample of IRC/Fe(bipy) was also sent for Si analysis. Some Si is present, but Si or SiO_2 does not account for all of the unknown. Emission spectroscopy was conducted to determine if any other heavy metals are present. Only minor amounts were present. The sample was sent for sulfur analysis which showed that some sulfur was present. This sulfur is probably from the sulfate group in the $Fe(bipy)_3SO_4$. This is because some of the dopant is imbibed in the pores of the IRC-50 instead of being ionically bound to the COO^- groups.

BET surface areas of catalysts prepared from the doped ion-exchange resin precursors are in the range of 100-300 m^2/g. When the IRC-50 resin with no dopant was pyrolyzed, the surface area was less than 5 m^2/g. This is consistent with work in progress which indicates that the presence of the metal dopant has a large effect on the nature of the pyrolysis process.

CONCLUSIONS

The doping of solid phase precursors followed by pyrolysis or the co-pyrolysis of gas phase precursors has allowed us to produce catalysts with good activity toward oxygen reduction. Efforts are currently underway to better understand the reasons for the catalytic activity of the bulk doped catalysts with a view toward further improving their activity.

ACKNOWLEDGEMENT

This work is supported by the United States Department of Energy under Contract No. DE-AC02-87ER80500.M001. We would like to thank Professor Daniel Scherson for providing the sample of CoTMPP adsorbed on Vulcan XC-72 and performing the Mossbauer spectroscopy on the catalyst samples.

REFERENCES

Giner, J. and S. Smith. 1967. A Simple Method for Measuring the Polarization of Hydrophobic Gas Diffusion Electrodes. Electrochem. Technol. 5:59.

McBreen, J., W.E. O'Grady, D.E. Sayers, C.Y. Yang, and K.I. Pandya. 1987. An EXAFS Study of Pyrolyzed Metal Macrocyclic Electrocatalysts. In Electrodes, Materials and Processes for Energy Conversion and Storage, S. Srinivasan, S. Wagner, H. Wroblowa (Eds.). Electrochemical Society Proceedings. 87-12.

Scherson, D.A., S.L. Gupta, C. Fierro, E.B. Yeager, M.E. Kordesch, J. Eldridge, R.W. Hoffman, and J. Blue. 1983. Cobalt Tetramethoxyphenyl Porphyrin - Emission Mossbauer Spectroscopy and O_2 Reduction Electrochemical Studies. Electrochim. Acta. 28:1205.

Wiesener, K. 1986. N_4-Chelates as Electrocatalyst for Cathodic Oxygen Reduction. Electrochim. Acta. 31:1073.

Yeager, E. 1984. Electrocatalysts for O_2 Reduction. Electrochim. Acta. 29:1527.

TABLE I

Catalyst	Wt%					Surface Area (m^2/g)
	C	H	N	M	Unk	
IRC 50/Fe(bipy)	70.70	0.75	2.36	9.60	16.59	310.5
IRC 50/Co(bipy)	85.86	0.19	0.210	1.18	12.56	87.3
IRC 50/Co(en)	88.42	0.31	0.620	10.8	0	150.4
IRC 50/Co(hex)	96.28	0.29	0.10	2.63	0.7	205.3
Chelite-C/Fe	79.6	0.22	0.190	13.5	6.4	191.1
Gas Phase Carbon	99.00	0.5	---	---	0.5	
Gas Phase/Ferrocene Derivative	78.34	0.34	1.38	12.00	7.90	19

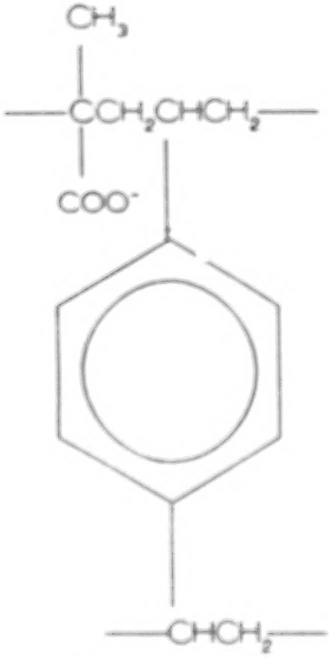
CH3
CCH2CHCH2
COO-
CHCH2

Figure 1a: Structure of IRC-50 Weak Acid Ion Exchange Resin.

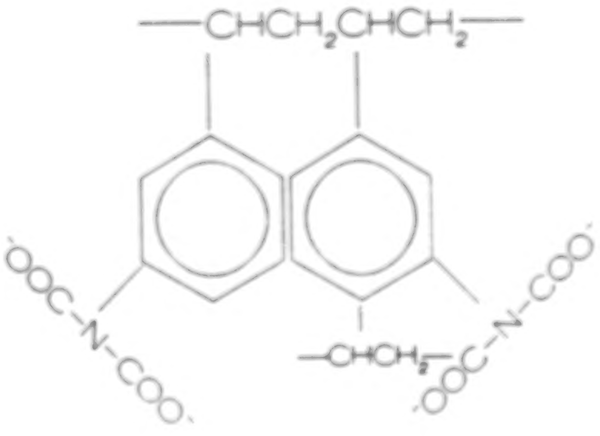
CHCH2CHCH2
-OOC-N-COO-
CHCH2
C-N-COO-
-OOC

Figure 1b: Structure of Chelite-C.

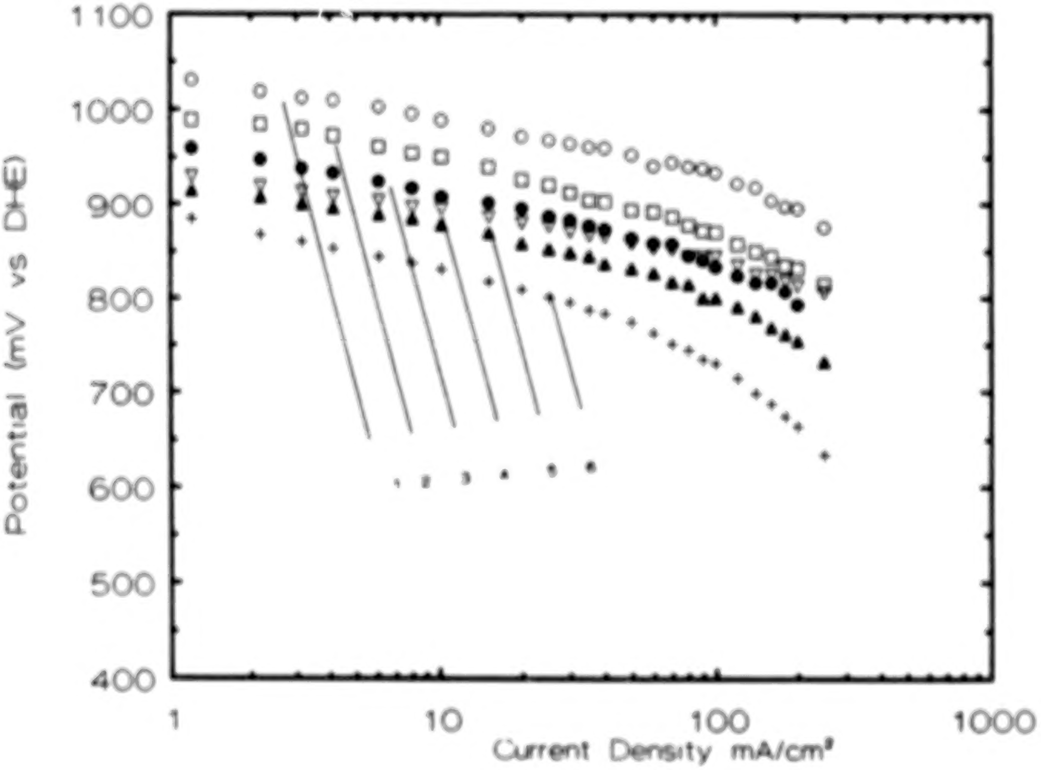

Figure 2: Polarization curves for O_2 reduction with porous electrodes in 7M KOH at 80°C.
Curve 1: 4.8% w/w Co-TMPP on XC-72 carbon.
Curve 2: IRC-50 + Fe (added as bipyridyl complex).
Curve 3: IRC-50 + Co (added as the hexamine chloride).
Curve 4: IRC-50 + Co (added as tris ethylenediamine cobalt(III) chloride).
Curve 5: IRC-50 + Co (added as bipyridyl complex).
Curve 6: IRC-50 + Fe (added as the chloride) + N (added as NH_4OH).

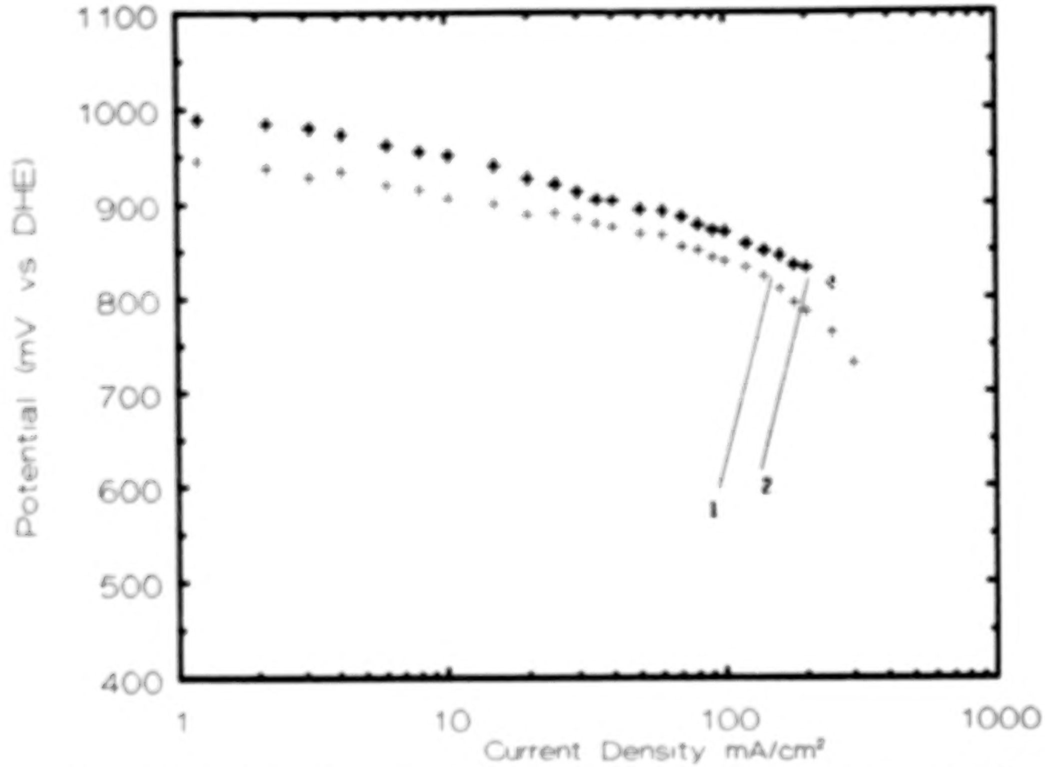

Figure 3: Polarization Curves for O_2 Reduction With Porous Electrodes in 7M KOH at 80°C.
Curve 1: Chelite-C + Fe (added as the chloride) Pyrolyzed at 900°C.
Curve 2: IRC-50 +Fe (added as the bipyridyl complex), Pyrolyzed at 900°C.

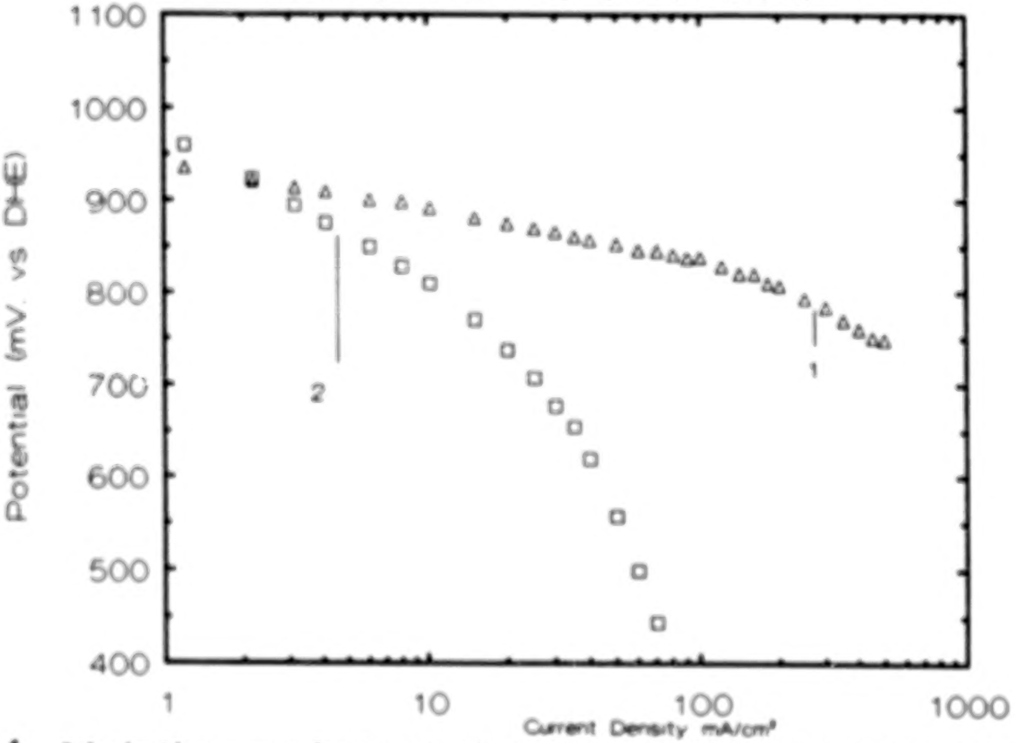

Figure 4: Polarisation curves for O_2 reduction with porous electrodes in 7M KOH at 80°C.

Curve 1: Electrode was made with pyrolysed
C_2H_2 + Fe (added as dimethylaminoethylferrocene).
Curve 2: pyrolysed C_2H_2 (1000°C).

CORROSION TESTING OF CANDIDATES FOR THE ALKALINE FUEL CELL CATHODE

Joseph Singer and William L. Fielder
NASA Lewis Research Center
Cleveland, Ohio 44135

Current/voltage data have been obtained for specially made corrosion electrodes of some oxides and of gold materials for the purpose of developing a screening test of catalysts and supports for use at the cathode of the alkaline fuel cell. The data consist of measurements of current at fixed potentials and cyclic voltammograms. These data will have to be correlated with longtime performance data in order to fully evaluate this approach to corrosion screening.

INTRODUCTION

Preliminary screening of materials intended for oxygen reduction performance electrodes for the alkaline fuel cell is desirable in order to minimize the number of long term test electrodes that might otherwise be required. Moreover, a section from a performance electrode would not be as satisfactory as a specially made corrosion electrode for this purpose because the latter should be made much more wettable and intended for submersion in the electrolyte.

EXPERIMENTAL

1. Materials

$NiCo_2O_4$ spinel was synthesized by co-precipitation, in the manner of Tseung and Botejue (1985). This material was characterized in Singer et al (1987); its surface area is 70 m^2/g. The pyrochlore $Pb_2Ru_2O_{6.5}$ was synthesized after the method of Horowitz (1978, 1983); its surface area is 101 m^2/g. Two gold standards, or blanks, were employed. One was the gold wire screen used as the substrate for the oxides; the other was a piece from an actual working electrode as used in Orbiter fuel cells, comprising 20 mg/cm^2 of Au-10% Pt of surface area 12 m^2/g and about 30 wt % PTFE (Teflon).

2. Electrode Fabrication

Pure Au wire screen was the substrate in the oxide electrodes. The screen was 50 mesh, of 0.25 in. wire; approximately 0.5 cm^2 surface area of wire was included in the submerged part of the oxide electrodes whose loadings were about 25 mg/cm^2. The IFC Orbiter electrode yielded a BET surface area of 2000 cm^2 in the electrode.

3. Measurements

4 mm x 10 mm rectangular cuts of the fabricated electrodes were microtorch spot welded to the 0.020 inch gold wire lead with a 4 mm x 2 mm piece of Au foil enfolding the clear area of the electrode and the wire. The contacted electrode was immersed in the floating half-cell of Giner (1967) within the cylindrical cage into which the reference electrode faces (Fig. 1). The immersion included all the active material and a minimum of the clean gold above it. The Teflon bracket of the half-cell shown in Figure 1 which is used to contact the dry side of working electrodes, was completely removed. The electrolyte was 30% KOH, the counter electrode was Pt or Au foil, and N_2 with about 1 ppm O_2 was passed through a 30% KOH bubbler before the cell. Most measurements were made at 24° C. Stirring was found to be detrimental.

Currents at fixed voltages were measured with a PAR 173 potentiostat with a 376 attachment leading into a recorder or a voltammeter. The O_2 reduction range between 1.0 and 0.6v (RHE) was of most interest for observing corrodibility, although some data were taken beyond these limits.

RESULTS

The current obtained from the gold wire screen, which was used as the collector-substrate for all the materials except the IFC electrode, is shown in Figure 2. The rapid drop to a steady current of a few microamps is noted. The log-log plot was found generally useful for extrapolation to long times.

The IFC Au-Pt electrode, based on a pure gold wire screen of denser mesh than used in the other electrodes, required a longer time to fall to the same microamperage than required by the bare gold wire (Figure 3). Figure 4 shows the more rapid fall to a lower current for the same electrode at 0.6v than at 0.3v.

The cyclic voltammograms of Figures 5 and 6 show appreciable differences between the bare gold wire and the Orbiter teflonated gold electrode.

Corrosion currents obtained with the Pb-Ru pyrochlore and the Ni-Co spinel electrodes are shown, respectively, in Figures 7 and 8. Cyclic voltammograms for these two specimens are given in Figures 9, 10, and 11.

DISCUSSION

The final currents obtained with the two gold standards are of the order of microamps. It may be assumed that most of this is due to trace O_2 in the environment. The IFC electrode may be expected to be most efficient at reacting with trace O_2, having been optimized as a porous hydrophobic-backed reduction electrode. Perhaps another type of gold electrode standard could be envisaged, namely a corrosion type designed for maximum wetting, using pure Au colloid and minimum Teflon.

The cyclic voltammograms of the gold specimens show sensitivity to absorption of trace oxygen species at 0.925v (RHE) = 0 volts (Hg/HgO); the IFC electrode plainly shows, in addition, its Pt content, in its resemblance to Pt cyclic voltammograms throughout the literature (Will, 1966). The sharp rise in current above 500v (Hg/HgO) is due to O_2 evolution, which itself would supply O_2 to both gold electrodes in addition to the ca. 1 ppm in the N_2 gas supply, and to back diffusion and leakage of air. In summary, the very low currents rapidly obtained in Figures 2, 3, and 4 indicate a satisfactory standard for relative non-corrodibility.

The pyrochlore used in this work is part of a study to make an improved material with the expectation of improving its stability reproducibly. Whether the present data indicate progress in this direction cannot yet be stated; however, Figures 7, 9, and 10 obtained with this pyrochlore synthesis show no drastic corrosion, in agreement with Horowitz (1983). This surmise is fortified by comparison with the spinel data of Figures 8 and 11. $NiCo_2O_4$ has been reported to be unstable to reduction potentials (King and Tseung (1974) which is one reason it was used in this study. During the performance represented by Fig. 8 a black coating developed on the counter electrode. This was dissolved in HCl. Ni and Co were found, with about 6 times as much Co as Ni; however, no attempt was made to relate this finding quantitatively to the corrosion data.

Comparisons of corrosion tests, like these reported, with longtime performance electrode tests, will have to be made to evaluate this type of screening. The present preliminary work suggests that this approach is worth pursuing.

CONCLUSIONS

Corrosion test screening of candidates for the oxygen reduction electrode of the alkaline fuel cell has been applied to two substances, the pyrochlore $Pb_2Ru_2O_{6.5}$ and the spinel $NiCo_2O_4$. The substrate gold screen and a sample of the IFC Orbiter Pt-Au performance electrode were included as blanks. The pyrochlore data indicate relative stability, although nothing yet can be said about long term stability. The spinel was plainly unstable. For this type of testing to be validated, comparisons will have to be made with long term performance tests.

Acknowledgement

The collaboration of PSI Technology Company of Andover, MA, under Contract NAS3-25199, in the preparation of the oxides and their electrodes used in this study is herewith acknowledged. The provision of a sample of Orbiter electrode by Dr. Ron Martin of IFC is gratefully acknowledged.

REFERENCES

Giner, J. and Smith, S. (1967): Electrochem. Tech. 5, 59.

Horowitz, H. S., Longo, J. M., and Lewandowski, J. T. (1978): U. S. Patent 4, 129, 525.

Horowitz, H. S., Longo, J. M., and Horowitz, H. H. (1983): J. Electrochem. Soc. 130, 1851.

King, W. J. and Tseung, A. C. C. (1974): Electrochem. Acta, 493.

Singer, J. and Fielder, W. L. (1987): NASA TM 100239.

Tseung, A. C. C. and Botejue, J. (1986): Int. J. Hydrogen Energy 11, 125.

Will, F. (1966): J. Electrochem. Soc. 112, 481.

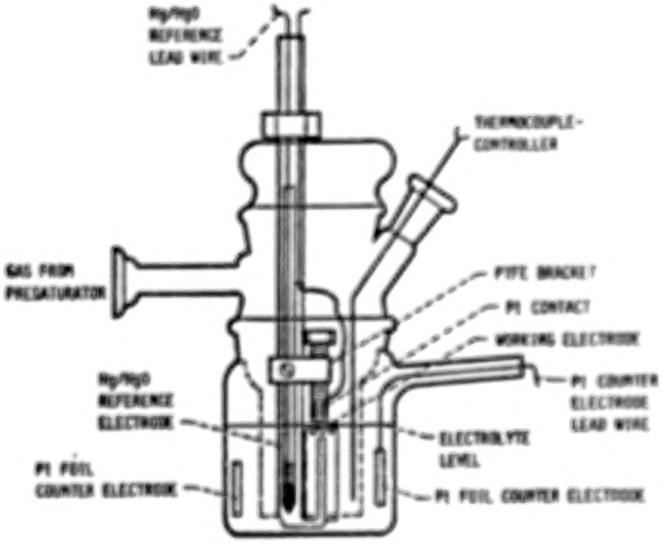
Hg/HgO
REFERENCE
LEAD WIRE
THERMOCOUPLE-
CONTROLLER
GAS FROM
PRESATURATOR
PTFE BRACKET
PT CONTACT
WORKING ELECTRODE
PT COUNTER
ELECTRODE
LEAD WIRE
Hg/HgO
REFERENCE
ELECTRODE
ELECTROLYTE
LEVEL
PT FOIL
COUNTER ELECTRODE
PT FOIL COUNTER ELECTRODE

FIG. 1. FLOATING HALF-CELL

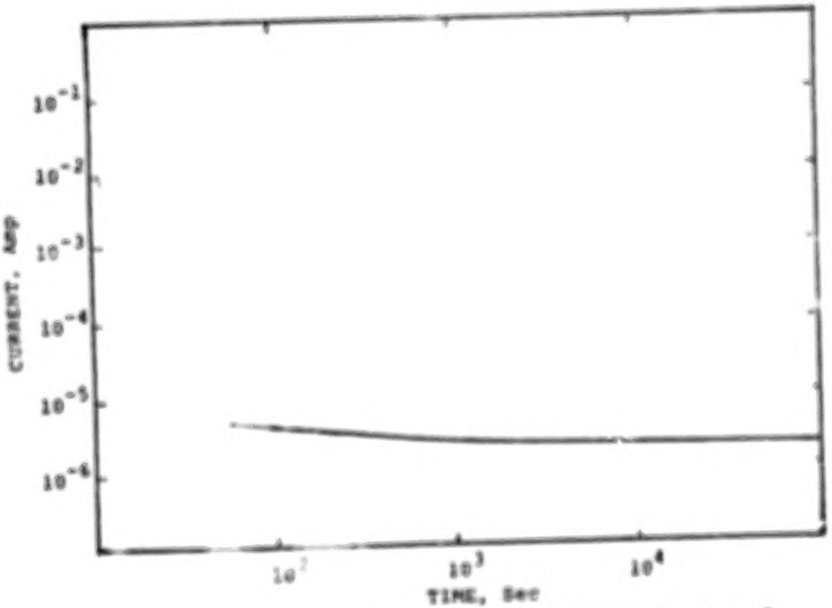

Gold Wire Screen 0.300 V(RHE); 24 deg C

FIG. 2. CORROSION CURRENT

IFC Au-Pt ORBITER ELECTRODE

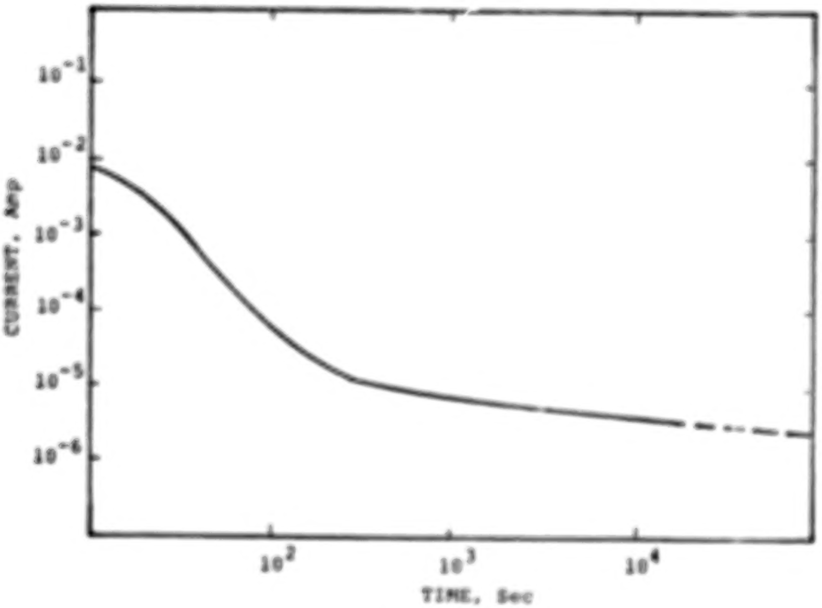

0.300 V(RHE); 24 deg. C

FIG. 3. CORROSION CURRENT

IFC Au-Pt ORBITER ELECTRODE

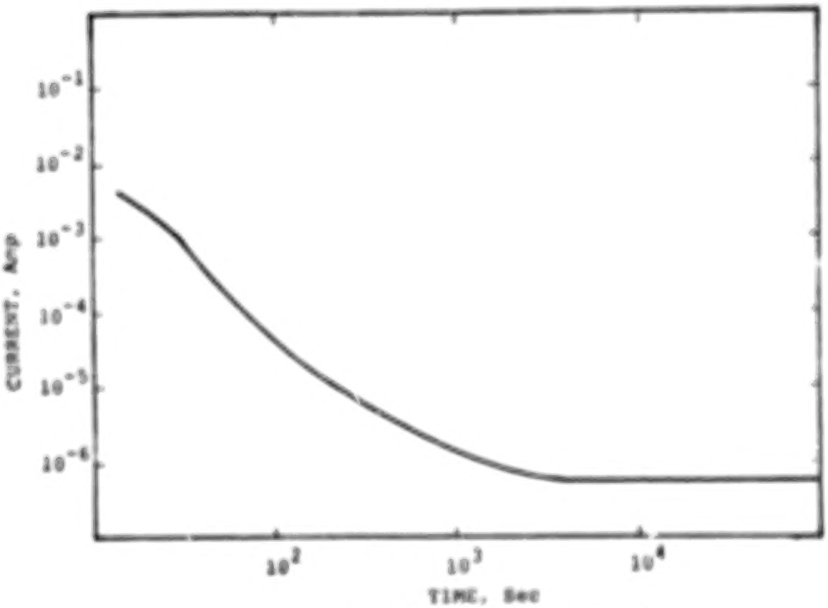

0.600 V(RHE); 24 deg. C

FIG. 4. CORROSION CURRENT

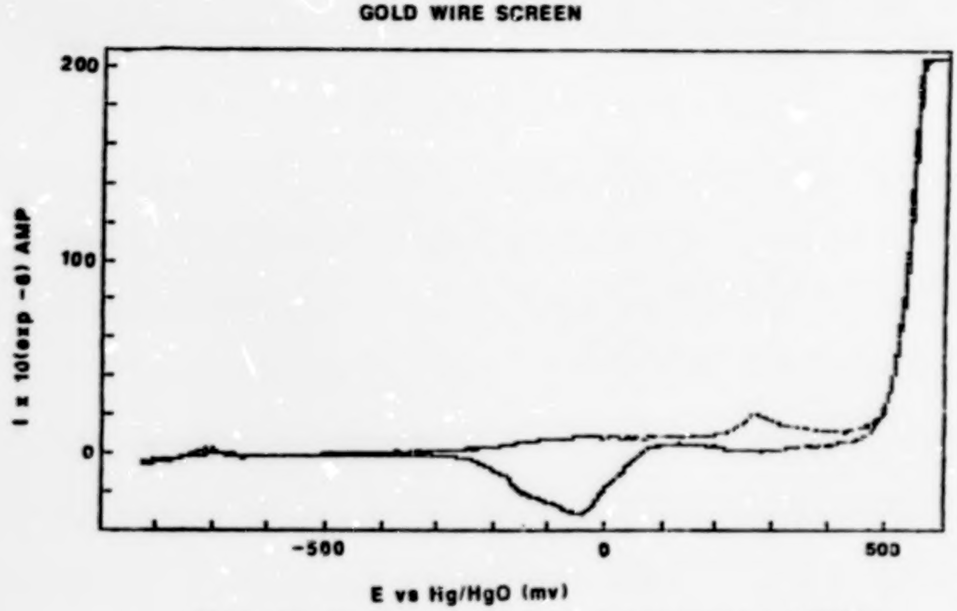

GOLD WIRE SCREEN

Sweep: 600 to -826 mv, 1 mv/s, 80 deg. C, Nitrogen, 30%KOH

FIG. 5 CYCLIC VOLTAMMOGRAM; GOLD WIRE SCREEN

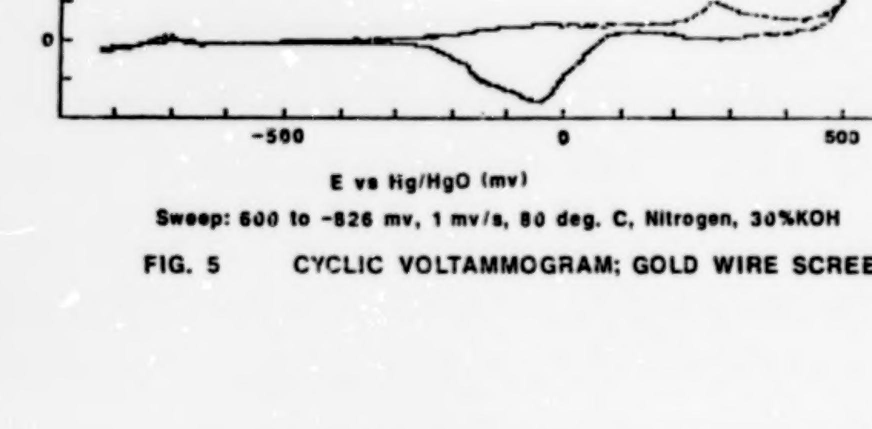

IFC Au-Pt ORBITER ELECTRODE

Sweep: 564 to -706 mv, 1 mv/s, 24 deg.C, Nitrogen, 30%KOH

FIG. 6 CYCLIC VOLTAMMOGRAM

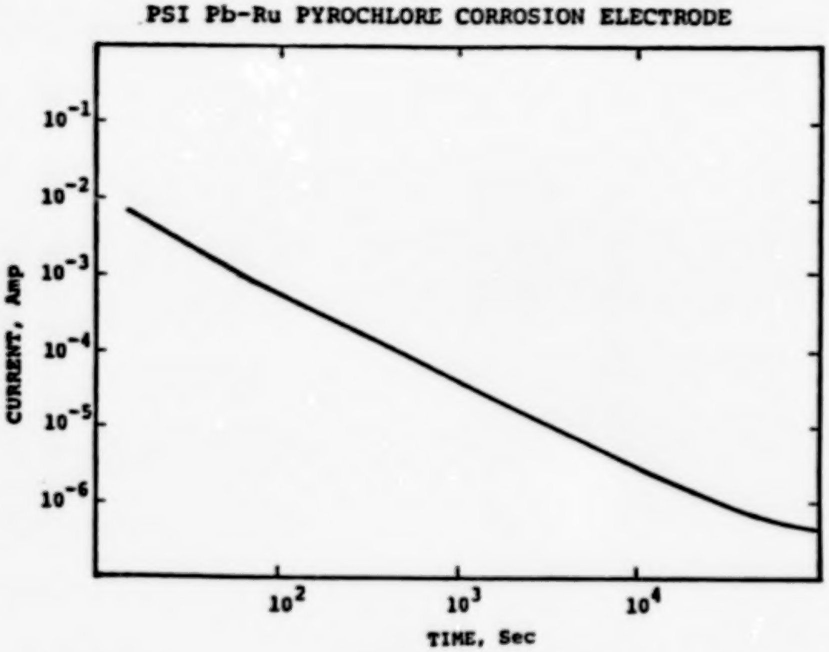
PSI Pb-Ru PYROCHLORE CORROSION ELECTRODE

0.700 V(RHE); 24 deg. C
FIG. 7 CORROSION CURRENT

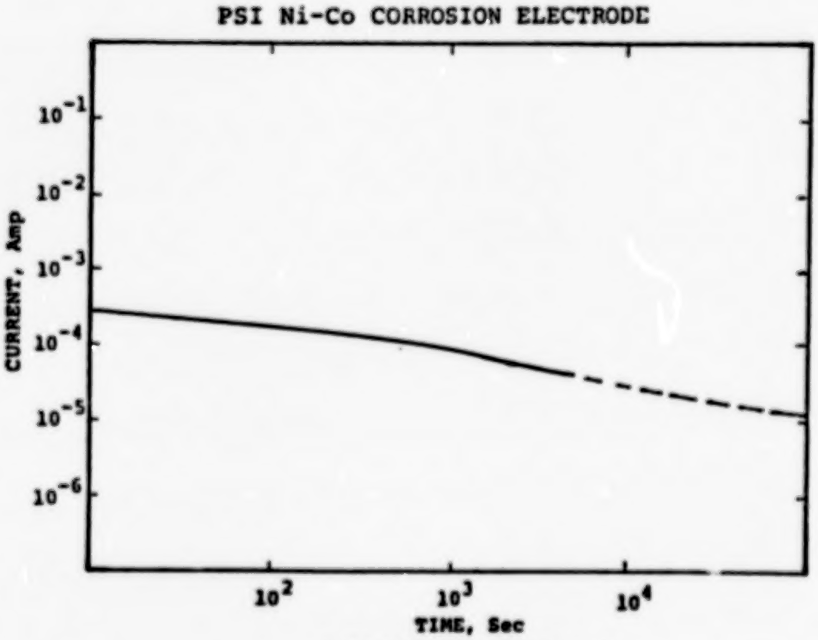
PSI Ni-Co CORROSION ELECTRODE

0.600 V(RHE); 24 deg. C.
FIG. 8 CORROSION CURRENT

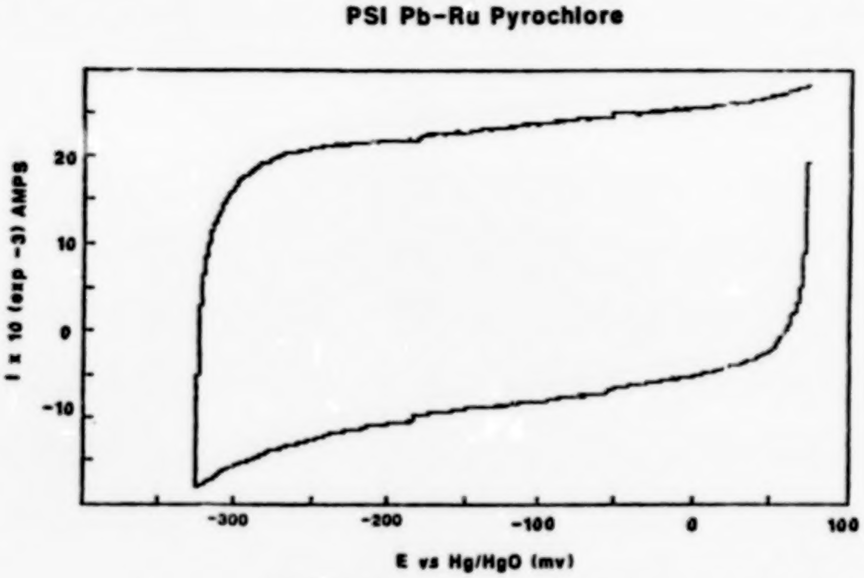

Sweep: 74 to -326 mv, 1 mv/s, Nitrogen, 30% KOH

FIG. 9 CYCLIC VOLTAMMOGRAM

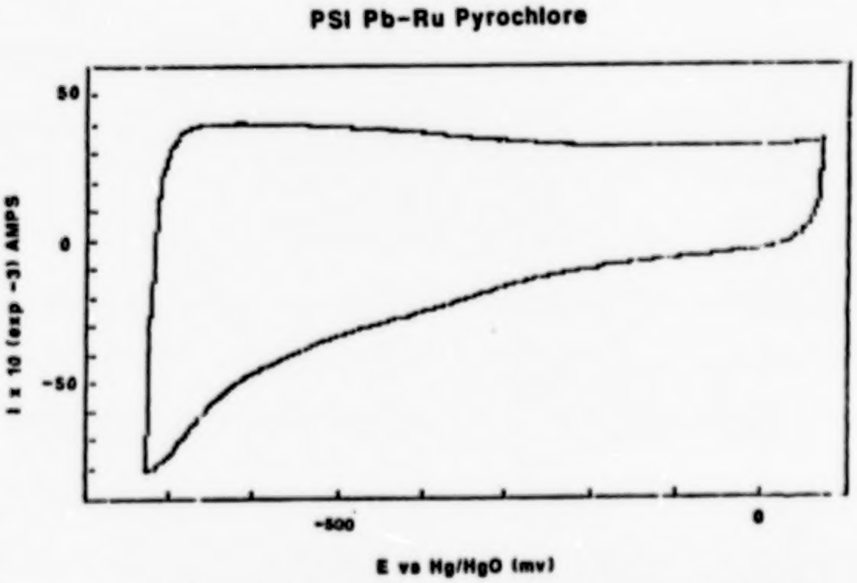

Sweep: 74 to -726 mv, 1 mv/s, 24 deg. C, Nitrogen, 30% KOH

FIG. 10 CYCLIC VOLTAMMOGRAM

NI-Co SPINEL CORROSION ELECTRODE

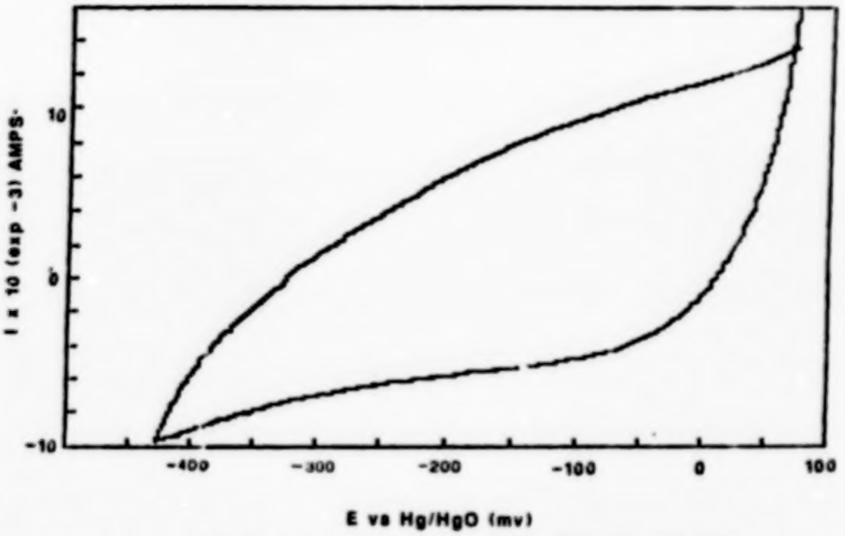

Sweep: 74 to -326 mv,80 deg. C, Nitrogen, 30% KOH

FIG. 11 CYCLIC VOLTAMMOGRAM

STRUCTURAL COMPARISON OF NICKEL ELECTRODES AND PRECURSOR PHASES*

Bahne C. Cornilsen, Xiaoyin Shan and Patricia Loyselle
Michigan Technological University
Houghton, Michigan 49931

In this paper we summarize our previous Raman spectroscopic results and discuss important structural differences in the various phases of active mass and active mass precursors. Raman spectra provide unique signatures for these phases, and allow one to distinguish each phase, even when the compound is amorphous to x-rays (*i.e.* does not scatter x-rays because of a lack of order and/or small particle size). The structural changes incurred during formation, charge and discharge, cobalt addition, and aging will be discussed. The oxidation states and dopant contents are explained in terms of the nonstoichiometric structures.

INTRODUCTION

Nickel electrode active mass has traditionally been classified in terms of two distinct cycles, defined in equations 1 and 2 (ref. 1).

$$\begin{tikzcd}
\alpha\text{-Ni(OH)}_2 \arrow[r, dashed] \arrow[d, "\text{aging}"] & \gamma\text{-NiOOH} & (1) \\
\beta\text{-Ni(OH)}_2 \arrow[r, dashed] & \beta\text{-NiOOH} \arrow[u, "\text{overcharging}"'] & (2)
\end{tikzcd}$$

The four end-member phases have been named on the basis of x-ray diffraction pattern similarities between electrochemical materials and chemically prepared materials, α-Ni(OH)$_2$, β-Ni(OH)$_2$, and γ-NiOOH (ref. 2).

Our research has shown that these materials can be distinguished using Raman spectroscopic analysis (ref. 3,4). The unique spectral signatures found for the various phases allow definition of these structures and reflect significant variations. The two cycles in equations 1 and 2 differ in degree of nickel deficit nonstoichiometry. The nonstoichiometric structural model proposed in reference 3 provides a framework in which the electrochemical properties can be understood. The lattice structures of active mass are non-close

---

[*] This work was supported by NASA Lewis Research Center Grant No. NAG 3-519

packed. The structural difference between the α/γ and the β/β cycles as not previously understood (ref. 5). β-$Ni(OH)_2$, the traditional close packed model of discharged active mass, is not present in active mass. Reanalysis of the x-ray diffraction patterns for charged active mass and γ-NiOOH has supported a non-close packed structure, nickel oxyhydroxide type structure, in agreement with vibrational spectra (ref. 4). We define structural details and inter-relations between these materials, including the structures of the cobalt containing cathodic-α and active mass (ref. 3,6).

To distinguish the active mass structural phases from the other structures, we shall use prefixes, 2α, 3γ, 2β, and 3β (ref. 3). This allows retention of the historical name indicative of intra-layer structure measured by the x-ray patterns, but also allows delineation of important structural differences. The structures of non-close packed active mass are defined in terms of NiO_2 layers which exhibit a nickel deficit, and therefore can contain foreign cations, and interlamellar cation sites. These are defined in terms of atom sites present in the $R\bar{3}m$, NiOOH type lattice (ref. 4). The nonstoichiometric formulae written in this paper express these two types of sites, nickel or proton sites, and the dopants on them, by writing the former ahead of the oxygen pair and the latter after the oxygen pair.

EXPERIMENTAL

Preparations of the cathodic-α, ordered β-$Ni(OH)_2$, disordered β-$Ni(OH)_2$, and active mass phases (2α, 3γ, 2β, or 3β) have been described previously (ref. 3,4). Chemical analyses indicate that the disordered β-phases exhibit a nickel deficit ($x < 0.16$) with empirical formulae consistent with $Ni_{1-x}(2H)_x(OH)_2$. The empirical formula for cathodic-α was obtained in the same manner.

Cobalt (5%) containing cathodic-α phase was electrochemically deposited on nickel foil (10 min.), from aqueous nitrate solution (0.5 M), at a current density of 4.6 mA/cm^2. Cobalt containing active mass has been produced by charging these thin films in 0.5 M KOH. The low KOH concentration minimizes aging. Cyclic voltammetry was used to cycle the films between 0.25 and 0.55 V (with respect to a 0.5 M Hg/HgO reference electrode) at a 7.8 mV/min. scan rate.

The spectra and structures for the above active mass are comparable to those found in commercial electrodes cycled to 80% depth of discharge (DOD) and charged to 120% of full charge (20% excess accounts for oxygen evolution during charge). Active mass is defined as the material or materials found in a "formed" electrode which are reproducibly observed during charge and discharge cycling.

Raman spectra were collected with a Ramanor HG.2S Spectrophotometer with photon counting electronics. Multi-scan spectra were required to provide adequate signal-to-noise ratio. The excitation was the 514.5 nm line from an argon ion laser (10-20 mW on the sample).

RESULTS AND DISCUSSION

The band positions in the Raman spectra of active mass precursors, in active mass itself, or other related phases are summarized in Table I (ref. 3,4). These spectra provide unique signatures allowing distinction of each phase. The basic structural unit in each of these materials is the NiO_2 layer, which contains interstitial, octahedral nickel atoms within a pair of close packed oxygen planes. For the ideal crystal lattice the proton sites are interlamellar (between NiO_2 layers); however, for a defective crystal, protons may occur within an NiO_2 layer (possibly on or near empty nickel atom sites). The structural relationship between two NiO_2 layers (layer stacking), the proton positions, and the internal structure for each NiO_2 layer influence the space group symmetry and therefore the spectral selection rules. The spectral selection rules control the number and relative intensities of the Raman and infrared vibrational bands. The 4000 to 2000 cm^{-1} region of the spectrum contains vibrational modes which reflect the symmetry and bonding of protons to oxygen atoms. The 600 to 200 cm^{-1} region of the spectrum contains Ni-O lattice modes, involving motion within the two-dimensional layers. The number of lattice modes can be influenced by layer stacking interactions. The wavenumber positions of vibrational modes depend on the chemical structure and bond strengths, and therefore vary with oxidation state and/or nonstoichiometry.

Ordered and Disordered β-$Ni(OH)_2$

The β-$Ni(OH)_2$ structure is the best characterized, being the only compound in this series which has been studied in single crystal form (ref. 7,8). The Raman spectrum (Table I) of this highly ordered, crystalline phase contains only one O-H stretch and three lattice modes (one is very weak) (ref. 4). This spectrum agrees with theoretical selection rules predicted on the basis of the known crystal structure. The NiO_2 layer stacking is known to be close packed in this structure. The three lattice modes originate from the intra-layer Ni-O modes and from inter-layer interaction between the close packed layers present in this stacking sequence (ABAB).

A disordered form of β-$Ni(OH)_2$ exhibits a Raman spectrum which is quite distinct in comparison with the above ordered compound (ref. 4). It contains two additional O-H stretching modes and one additional lattice mode (see Table I), but is otherwise identical. This shows that the basic structure is that of β-$Ni(OH)_2$, but with additional features which relate to an empirical formula with $Ni/OH < 0.5$. A structural model of a hydrated β-phase with interlamellar water can be written as shown in equation 3.

$$Ni(OH)_2 \cdot yH_2O \qquad (3)$$

The lack of molecular water vibrations in both the IR and Raman spectra suggest this hydrated model is inadequate. The lattice parameters observed for these disordered-β materials are comparable to those of ordered β-$Ni(OH)_2$, and do not provide room for interlamellar H_2O molecules. Therefore this model is inadequate.

An alternative formulation with an equivalent stoichiometry, where $x = y/(2 + y)$, can be written (equation 4).

$$Ni_{1-x}\,(2H)_x\,(OH)_2 \qquad (4)$$

Nickel vacancy disorder is proposed based on the empirical nickel deficit ($x < 0.16$) and the vibrational spectra. A second type of disorder is possible. Layer stacking disorder is likely, based upon x-ray line broadening (ref. 9). Recent EXAFS analyses support the nonstoichiometric model (ref. 10).

Charged Active Mass and Discharged Active Mass

The chemically oxidized γ-NiOOH structure is the prototype for charged active mass (ref. 4). This non-close packed NiOOH type structure contrasts sharply with the close packed β-$Ni(OH)_2$ structure. The two lattice modes (Table I) and the lack of an O-H stretching mode originate from the non-close packed layer stacking (ABBCCA) and interlamellar hydrogens on centric lattice sites. This structure has been supported by reinterpretation of the x-ray diffraction pattern (ref. 4).

Both forms of charged active mass (3β- and 3γ-NiOOH) exhibit the same selection rules which indicates that they have similar structures (ref. 3). This crystal structure together with the point defect structure allow one to understand the origin of the variable formulae and oxidation states. The key difference between the 3β- and 3γ-NiOOH phases is the magnitude of the nickel deficit and the resultant point defect structures (see Table II). The nickel deficit is constant within each cycle. The 3γ-phase generally contains potassium as well. The amount of potassium uptake is determined by the nickel deficit, *i.e.* the nickel vacancies are filled with potassium. The ramifications of this nonstoichiometric structure upon the electrochemical properties are significant (ref. 3). The differing oxidation states allow the α/γ cycle to have a greater capacity. The nonstoichiometry and point defects also control proton diffusion and electron conduction.

Discharged active mass (2α- and 2β-phases) displays spectra and selection rules similar to those for charged active mass (ref. 4). We propose a similar non-close packed layer structure. The nickel deficit in each is comparable to that in the respective charged phase (see Table II).

The wavenumber positions vary with charge state and defect content (see Table I) as the active mass is charged and discharged. The α/γ bands are higher in energy (wavenumber position) than the β/β bands. This shift parallels the increased nickel deficit observed for the α/γ phases. Therefore, the change in defect structure is also reflected in the band positions. The energy of a vibrational mode is proportional to the bond strength (i.e. force constant). An increase in oxidation state normally leads to an increase in wavenumber (ref. 11). The mechanism by which the nickel deficit influences wavenumber is the same, in that the change in nonstoichiometry induces an increase in average oxidation state and thereby, an increase in wavenumber.

The traditional structures proposed for discharged active mass (2α and 2β) are β-$Ni(OH)_2$ or the so-called α-phase structure (ref. 2). The Raman spectra of discharged active mass clearly demonstrate that formed and cycled materials are not isostructural with β-$Ni(OH)_2$ (compare spectra in Table I) (ref. 3). The Raman spectrum of a chemically precipitated α-phase also differs from that of discharged active mass (see Table I). Therefore, the structures of chemical-α and 2α or 2β differ as well. The structural difference between discharged active mass (2α) and a cathodic-α phase precursor is more subtle and will be discussed below.

Implications of the Nonstoichiometric Structure of Active Mass

The oxidation state maximum seen for 3γ is +3.67. This oxidation state is predicted for a defect structure which incorporates potassium on 0.25 vacant nickel sites. With a +1 dopant (K) on the nominal Ni(III) site, only 2 electron holes remain per site to ionize and to form two Ni(IV) species. Ionization provides 0.5 moles of Ni(IV), equation 5, giving an average oxidation state of 3.67 for the total 0.75 moles of nickel per mole of compound.

$$Ni^{+4}_{0.5}\ Ni^{+3}_{0.25}\ (K^{+})_{0.25}\ OOH \qquad (5)$$

Discharge of this material reduces the nickel, but the 0.25 protons on the nickel vacancies produce an average nickel oxidation state of 2.25 for the 2α-phase (see Table II). It is apparent that the nickel cannot be reduced completely to 2.00 because the lattice requires charge balance and the vacant nickel site (nominally 2+ on the discharged lattice) holds only one proton (based upon the empirical formula).

The 3γ point defect structural model explains how Ni(IV) ions can be introduced into the nominally Ni(III), NiOOH-type crystal lattice. In order for the average oxidation state of nickel to exceed 3+, a nickel deficit is required. The 3β structure (Table II) demonstrates that the nickel deficit is not the only prerequisite to an oxidation state above 3+. The dopant content, three protons on the nickel vacancy, reduces the average oxidation state to 2.9 in this case.

It has been observed that the nickel vacancies are invariably filled with protons or alkali metals, and that the excess monovalent cations fit exactly on the vacancies, within reasonable experimental error. When alkali metals are low, one to three protons can be found per vacancy. When sufficient alkali is present in the formula, it generally fills the vacancy. Therefore, when writing formulae, we have chosen to place potassium or sodium on the nickel vacancy sites in preference to interlamellar sites. We do this to demonstrate correlation of potassium content and vacancy content. This observation appears to suggest that the potassium on nickel site positioning is fact; however, it is important to realize that this may be coincidence. We have no positive, experimental evidence to prove this, nor to disprove it. It can be said that the potassium does stabilize the nickel deficit.

Thus the point defect structure (nickel deficit and dopant K or H contents) controls both the maximum oxidation state and the minimum oxidation state. Needless to say, the oxidation state change between the two extremes controls the electrode capacity. The same logic applies to the β/β cycle, with the result that the narrower oxidation state range leads to a lower capacity. Therefore, the nonstoichiometric model allows one to understand the variable oxidation states of nickel active mass as well as the variable capacities.

Cathodic-α Precursors of Active Mass

The two Raman lattice modes observed for cathodically deposited electrode-precursor materials are consistent with a non-close packed structure. Although the cathodically deposited α-phase materials exhibit a broad O-H stretching mode, the lattice mode region differs little from that of discharged active mass (Table I) (ref. 4). Therefore the two structures are related in terms of layer stacking. X-ray powder diffraction data also reflects this similarity (ref. 1,2). However, the O-H stretching mode indicates that there are differences in water content and/or proton bonding. This structural difference may be significant.

The lattice mode positions (see Table I) for the cathodic-α phase are lower than for the discharged active mass phases (2α and 2β). This shift is related to the difference in bond strengths associated with a small change in oxidation state. The cathodic-α material is green and is Ni(II). The oxidation states of the dark discharged active mass are greater than 2 (see Table III).

The empirical formula of a cathodic-α material is written in Table II. The nickel-oxygen ratio in these materials is generally lower than for discharged active mass. This can be caused by either additional molecular water (equation 6) or a more extensive nickel deficit (equation 7).

$$Ni_{0.75}(2H)_{0.25}(OH)_2 \cdot 0.33\,H_2O \qquad (6)$$

$$Ni_{0.65}(2H)_{0.35}(OH)_2 \qquad (7)$$

We favor the molecular water explanation because the Raman spectrum of cathodic-α displays O-H stretching modes which are typical of water. The hypothetical nickel deficit in equation 7 is also greater than 0.25; the 0.35 value is larger than seen in other materials to date.

The above results show that discharged active mass, charged active mass, and cathodic-α phases are non-close packed and related in structure. The proposal of this structure for the α-phases disagrees with literature which suggests close packed inter-layer stacking (ref. 1). The literature powder pattern has been assigned a low reliability in the JCPDS file (ref. 12) and has been questioned in the literature (ref. 13). Further research is needed to understand how the excess "water" is incorporated structurally.

Cobalt-Containing Nickel Electrodes: Precursors and Active Mass

Raman spectra of cobalt containing precursors, i.e. cathodically deposited materials, are distinct and differ from that of cobalt-free, cathodic-α phase (ref. 6). The Raman spectrum of a 5% cobalt, cathodic-α displays two Raman bands at 460 and 530 cm^{-1} (Figure 1). The wavenumber positions are identical to those observed with no cobalt, but the intensity ratio for the two bands is inverted. A very weak O-H stretching mode is observed at 3652 cm^{-1}. The weakness of this band and the intensity reversal distinguish the cobalt-free and cobalt containing spectra. These changes reflect the significant influence of cobalt addition. Changes in the electronic structure of the solid when the cobalt solid solution is formed apparently change the bonding enough to change the polarizability of these lattice modes. Raman intensities depend directly upon the polarizability tenser associated with each normal vibration.

However, the spectral selection rules do not change with cobalt addition for these cathodically deposited materials. The spectra are therefore consistent with a non-close packed structure, with the cobalt going into solid solution on the nickel sites. We propose the layer stacking is ABBCCA, similar to active mass.

Formation and cycling of the above materials produces an active mass material that displays Raman spectra similar to those of cobalt-free, nickel electrode active mass (ref. 3). The fact that the active mass spectral selection rules do not change upon cobalt addition indicates that the cobalt is incorporated in solid solution, and that a non-close packed structure is retained. The previous discussion of active mass structure applies to cobalt containing active mass as well.

Cobalt addition introduces a structure that is intermediate between the β/β and α/γ stoichiometries. Both the Raman spectral positions (550 and 474 cm^{-1}, charged) and empirical formulae suggest this (ref. 3). The recent cobalt-containing empirical formula reported by Braconnier *et al.* can be recast in nonstoichiometric form in equation 8 (ref. 14). The nickel deficit obtained is 0.19, falling between the cobalt-free β/β and α/γ values, as expected based upon Raman spectral positions. It is apparent that the cobalt stabilizes an increased cation deficit.

$$Ni_{0.57}\ Co_{0.24}\ K_{0.17}\ Na_{0.02}\ OO\ H_{0.92}\ Na_{0.08} \qquad (8)$$

STRUCTURAL AND CHEMICAL CHANGES

The Formation Process

Both cathodic-α and active mass are nonstoichiometric and non-close packed. Therefore no change in layer stacking is required during the formation process. If the cathodic-α precursor contains a significant nickel deficit, then the change in nickel nonstoichiometry during formation can be minimal. For example, a cathodic-α (equation 6) would form an active mass as defined in equation 9 if no change in nickel deficit occurred. A net loss in "water" is evident as well as a change in oxidation state.

$$Ni_{0.75}\ (2H)_{0.25}\ OOH_{2.0}\cdot 0.33\ H_2O + 0.25\ OH^- \text{ ------> } \qquad (9)$$
$$Ni_{0.75}\ (2H)_{0.25}\ OOH_{2.0} + 0.58H_2O + 0.25e^-$$

The formation of active mass from a more stoichiometric precursor would also involve creation of nickel vacancies. The final nickel deficit characterizing an active mass need not be equal to nor controlled by the deficit in the precursor-α. The formation process can increase the nickel deficit to form more optimal active mass.

Transformation of a cathodic-α to active mass involves a change in proton incorporation or bonding, as demonstrated by the loss of the O-H stretching mode upon formation. This change in the spectrum is consistent with our proposal that the cathodic-α contains molecular water which is removed or lost during formation.

A stoichiometric precursor with close packed stacking, such as β-$Ni(OH)_2$, must undergo major structural change upon formation into nonstoichiometric, non-close packed active mass. Both transformation from close packed to non-close packed layer stacking and vacancy creation are required. It is likely that layer shearing and defect formation processes would slow the formation process for such starting materials. Furthermore, shape and volume changes are expected to be much greater for such a precursor. It is likely that these would reduce the electrode mechanical integrity as well. We propose that the reason that cathodically deposited materials are successful precursors to active mass is intimately tied to the minimal structural change required during the formation process.

Charge and Discharge Cycling and Transformation from β/β to α/γ Cycles

Shifts in band position during charging and discharging of cobalt-free active mass directly reflect changes in the structure and bonding which occur as the nickel oxidation state varies (Table I). The wavenumbers increase during charging and drop on discharge as discussed earlier. The general charge-discharge reaction can be written as shown in equation 10. K^+ may replace x of the protons to give the α/γ cycle. If no overcharging occurs the structural changes are simply changes in proton content and oxidation state. No change in defect structure or layer stacking is required.

$$\mathrm{Ni}_{1-x}\,(nH)_x\,OOH_2 + [1+x(n-1)]\,OH^- \;\text{------>}\; \mathrm{Ni}_{1-x}\,H_x\,OOH_{1.0} + [1+x(n-1)]\,H_2O + [1+x(n-1)]\,e^- \qquad (10)$$

Overcharging a 3β-material induces the 3γ-phase (ref. 2). As seen in the nonstoichiometric formulae (Table II) the materials in the two cycles display different nickel deficits. We propose that overcharging induces the higher level of nonstoichiometry to accommodate the higher oxidation state formed during overcharge. The resultant point defect structure allows a greater change in oxidation state, which provides the higher capacity observed for the α/γ cycle. A significant amount of potassium is introduced when 3γ is produced. It is apparent that the potassium and the increased nickel deficit are important to the stability of this structure.

Once formed, retention of the α/γ cycle might be expected. However, further cycling will allow transformation back to the β/β cycle with a concomitant reduction in nickel deficit and potassium content. Furthermore, these are not the only structural changes expected with this model. One mechanism for return to the β/β cycle involves aging of discharged-α to disordered β-$Ni(OH)_2$ (as described below), with subsequent cycling and re-formation back into the β/β cycle. The intermediate structure is close packed (disordered β-$Ni(OH)_2$). Because this mechanism involves a change in layer-layer stacking, density and volume changes are expected. Therefore, both mechanical stability and capacity would be reduced. This is consistent with experimental observations.

Aging in KOH

The product of KOH aging of a cathodic-α was found to be "deactivated-α" by Barnard *et al.* (ref. 15). The Raman spectrum of such an aged material shows that it is a nonstoichiometric, disordered-β compound (ref. 4). Barnard *et al.* observed a β-like x-ray pattern as well, but did not differentiate it as a nonstoichiometric material (ref. 9).

The Role of Cobalt Addition

The mechanisms by which cobalt has a beneficial effect on electrode properties can now be discussed in terms of the structures and structural changes already defined. Cobalt is incorporated in solid solution with nickel in cathodic-α and active mass. All three materials are non-close packed. Cobalt stabilizes nickel deficit nonstoichiometry that is higher than for cobalt-free systems. This structure enhances electrochemical properties, including a higher nickel oxidation state.

Another role of the cobalt additive appears to be in stabilizing a cathodically deposited precursor structure with enhanced nonstoichiometry which is structurally similar to optimal active mass. The very weak O-H stretching mode observed with cobalt addition is a measure of a water, proton and defect content more like that of active mass. This will improve mechanical stability by minimizing the density and volume changes during formation. The optimal nonstoichiometry and point defect structure will also optimize the electronic and protonic diffusion processes.

CONCLUSIONS

Optimal nickel active mass is non-close packed and nonstoichiometric, as is cathodic-α. The formation process transforms precursor phases into this structure. Therefore, the precursor nonstoichiometry and disorder, or lack thereof, influences the final active mass structure and the rate of formation. Aging to less active material or incorporation of less than optimum nonstoichiometry reduces capacity. The role of cobalt addition can be appreciated in terms of structures favored or stabilized by the dopant.

The unique spectral signatures found for the various phases allow differentiation of these materials and reflect significant structural variations. Most importantly, the layer stacking is clearly indicated by Raman spectroscopic analysis. The nonstoichiometry allows one to understand the oxidation states and electrochemical properties. An optimum active mass will exhibit an enhanced nickel deficit, providing a maximum change in oxidation state, and will resist aging. How formation of such a material can increase mechanical stability is discussed in terms of a structurally similar precursor-α.

This new structural understanding provides a basis upon which one can study the subtle structural effects induced by empirical parameters such as cobalt concentration or electrolyte concentration. With such information the electrode structure can be tuned to provide optimal electrochemical properties. It should be possible to relate optimal structure of a precursor-α and of formed active mass to properties during cycling. Furthermore the potential of Raman spectroscopy for quality control purposes appears bright because the spectra vary qualitatively to mirror both major and subtle variations.

REFERENCES

1. Bode, H.; Dehmelt, K.; and Witte, J.: Zur Kenntnis der Nickelhydroxidelektrode--I. Uber Das Nickel (II)-Hydroxidhydrat, Electrochim. Acta, Vol. 11, 1966, pp. 1079-1087.

2. Bode, H.; Dehmelt, K.; and Witte, J.: Zur Kenntnis der Nickelhydroxidelektrode. II. Uber die Oxydationsprodukte von Nickel(II)-hydroxiden, Z. Anorg. Allg. Chem., Vol. 366, 1969, pp. 1-21.

3. Loyselle, P. L.; Karjala, P. J.; and Cornilsen, B. C.: A Point Defect Model For Nickel Electrode Structures, Proc. Symp. on Electrochemical and Thermal Modeling of Battery, Fuel Cell, and Photoenergy Conversion Systems, J. R. Selman and H. C. Maru eds., Electrochemical Society, Pennington, NJ, 1986, pp. 114-121.

4. Cornilsen, B. C.; Karjala, P. J.; and Loyselle, P. L.: Structural Models for Nickel Electrode Active Mass. J. Power Sources, Vol. 22, 1988, pp. 351-357.

5. Oliva, P.; Leonardi, J.; Laurent, J. F.; Delmas, C.; Braconnier, J.; Figlarz, M.; Fievet, F.; and deGuibert: Review of the Structure and the Electrochemistry of Nickel Hydroxides and Oxyhydroxides., J. Power Sources, Vol. 8, 1982, pp. 229-255.

6. Shan, X.; Loyselle, P. L.; and Cornilsen, B. C.: Structural Influence of Cobalt Addition to the Nickel Electrode, Abstract 79, 174th Electrochemical Society Meeting, Chicago, IL, October 14, 1988.

7. De Wolff, P. M.: Joint Committee on Powder Diffraction Standards Card No. 14-117.

8. Szytula, A.; Murasik, A.; and Balanda, M.: Neutron Diffraction Study of $Ni(OH)_2$. Phys. Stat. Sol. B., Vol. 43, 1971, pp. 125-128.

9. Barnard, R.; Randell, C. F.; and Tye, F. L.: Studies Concerning the Ageing of Alpha and Beta $Ni(OH)_2$ in Relation to Nickel-Cadmium Cells. Power Sources 8, J. Thompson, ed., Academic Press, London, 1981, pp.401-423.

10. Loyselle, P. L.; Cornilsen, B. C.; Condrate, R. A.; and Phillips, J. C.: X-ray Absorption Study of Beta Nickel Hydroxides, Abstract 77, 174th Electrochemical Society Meeting, Chicago, IL, October 14, 1988.

11. Nakamoto, K.: Infrared and Raman Spectra of Inorganic and Coordination Compounds, John Wiley & Sons, New York, 1978.

12. Bode, H.: Joint Committee on Powder Diffraction Standards Card No. 22-444.

13. McEwen, R. S.: Crystallographic Studies on Nickel Hydroxide and the Higher Nickel Oxides. J. Phys. Chem., Vol. 75, 1971, pp. 1782-1789.

14. Delmas, C.; Braconnier, J. J.; Borthomieu, Y.; and Hagenmuller, P.: New Families of Cobalt Substituted Nickel Oxyhydroxides and Hydroxides Obtained by Soft Chemistry, Mat. Res. Bull., Vol. 22, 1987, pp. 741-751.

15. Barnard, R.; Randell, C. F.; and Tye, F. L.: Studies concerning charged nickel hydroxide electrodes. I. Measurement of reversible potentials, J. Appl. Electrochem., Vol. 10, 1980, pp. 109-125.

Table I. - Raman Band Positions (cm^{-1}) Characterizing Solid Phases Present in Active Mass, or Related to Active Mass (ref. 3,4)

Spectrum Type:	I	II	III	IV	V				
Structural Designation:	Ordered β-$Ni(OH)_2$	Disordered β-$Ni(OH)_2$	Cathodic α-$Ni(OH)_2$	Chemical α-$Ni(OH)_2$	Active Mass 2α	3γ	2β	3β	Assignment
		3687							
		3600							νH_2O
			3650	3650					--------
	3583	3580							
					536	559	532	550	
			530						Ni-O Lattice Mode
					470	476	468	468	
		519							
			462	464					
	453	448							
	378								
	313	312							

Table II. - Comparison of Empirical and Nonstoichiometric Formulae.

Structural Designation	Typical Empirical Formula Ni	O	H	K	(Ref.)	Nonstoichiometric Structural Formula
Ordered β-Ni(OH)$_2$	1.00	2.00	2.00		*	β-Ni(OH)$_2$
Disordered β-Ni(OH)$_2$	1.00	2.35	2.70		*	$Ni_{0.85}(2H)_{0.15}(OH)_{2.0}$
Cathodic α-Ni(OH)$_2$	1.00	3.10	4.20		*	$Ni_{0.75}(2H)_{0.25}OOH_{2.0}\cdot 0.33H_2O$
2α	1.00	2.67	3.09		15	$Ni_{0.75}(H)_{0.25}OOH_{2.1}$
3γ	1.00	2.68	1.36	0.33	15	$Ni_{0.75}(K)_{0.25}OOH_{1.0}$
2β	1.00	2.25	2.25		15	$Ni_{0.89}V_{0.11}OOH_{2.0}$
3β	1.00	2.25	1.72	0.03	15	$Ni_{0.89}(3H)_{0.08}(K)_{0.03}OOH_{1.2}$

* This work

Table III. - Solid State Structural Characteristics of Active Mass or Active Mass Precursors Based on Spectral Analysis.

Structural Designation:	Ordered β-Ni(OH)$_2$	Disordered β-Ni(OH)$_2$	Cathodic α-Ni(OH)$_2$	Chemical α-Ni(OH)$_2$	Active Mass			
					2α	3γ	2β	3β
(Preparation Method:)	(recrystallized)	(rapid ppt., aged alpha)	(electrochemical)	(rapid ppt.)	(Electrochemical)			
Layer-Layer Stacking	hcp	hcp	ncp	ncp	ncp	ncp	ncp	ncp
Ni Average Oxid. State*	2	2	2	2	2.25	3.67	2.25	2.75
Stoichiometry	stoi.	non.	non.	non.	non.	non.	non.	non.
Crystalline Order	ord.	dis.	dis.	dis.	dis.	dis.	dis.	dis.
Molecular Water Content	no	slight	possible	possible	no	no	no	no

hcp = hexagonal close packed, ncp = non-close packed
stoi. = stoichiometric, non. = nonstoichiometric
ord. = ordered, dis. = disordered

* Active mass oxidation states from ref. 15.

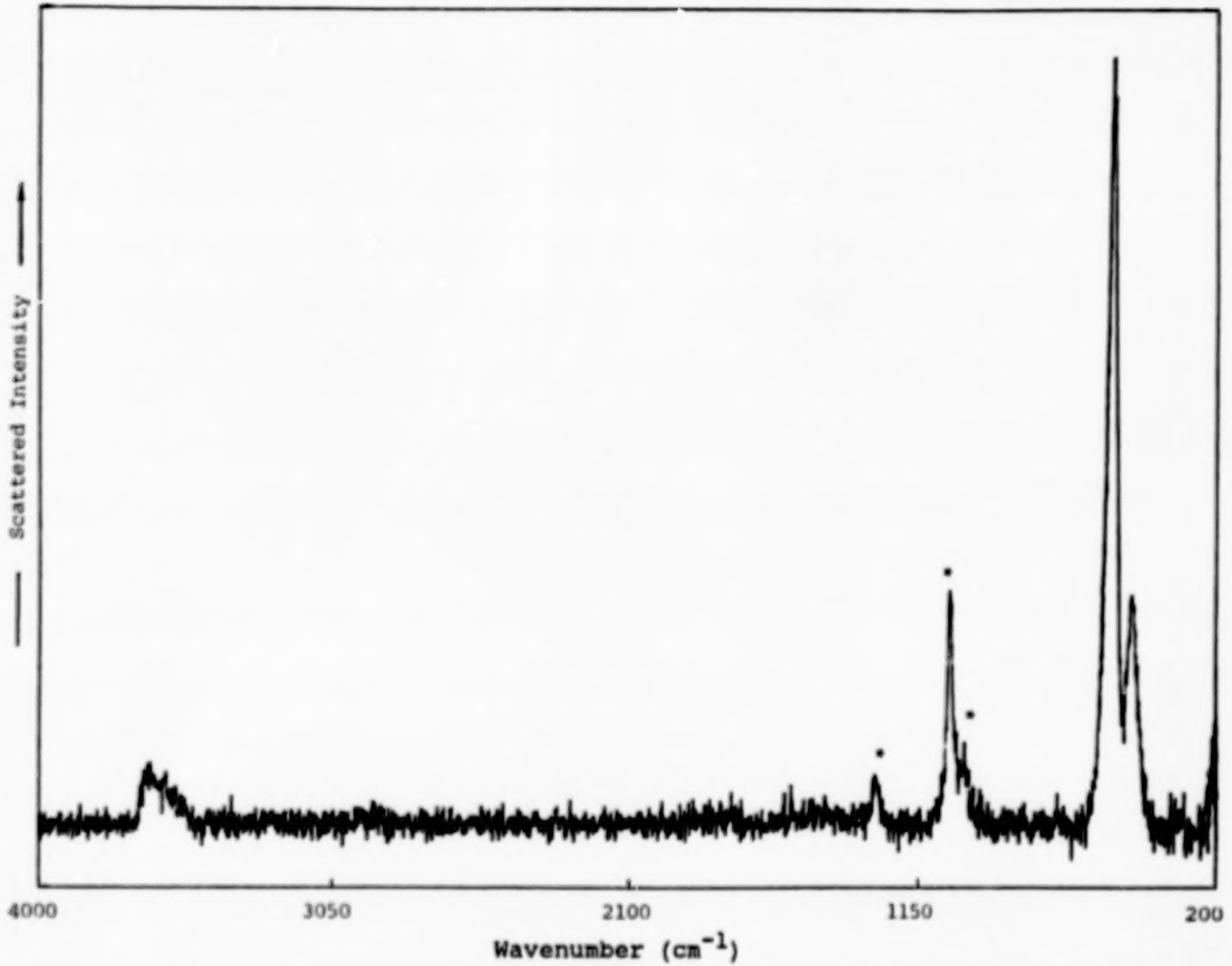

Figure 1. - Raman spectrum of cathodic-α nickel electrode with 5% cobalt additive. Bands marked with an asterisk are nitrate vibrational modes.

IMPEDANCE STUDIES OF Ni/Cd AND Ni/H_2 CELLS USING THE CELL CASE AS A REFERENCE ELECTRODE

Margaret A. Reid
NASA Lewis Research Center
Cleveland, Ohio 44135

Impedance measurements have been made on several Ni/Cd and Ni/H_2 flightweight cells using the case as a reference electrode. For these measurements the voltage of the case with respect to the anode or cathode is unimportant provided that it remains stable during the measurement of the impedance. In the cells measured so far, the voltages of the cell cases with respect to the individual electrodes differ from cell to cell even at the same overall cell voltage, but they remains stable with time. The measurements can thus be used to separate the cell impedance into the contributions of each electrode, allowing improved diagnosis of cell problems.

INTRODUCTION

Many impedance studies have been carried out on Ni electrodes and Ni/Cd and Ni/H_2 cells. Some studies have been made while the cells or electrodes were being discharged (refs. 1-2), others at various open circuit voltages (refs. 3-6). The impedances have been found to be strongly dependent on depths of discharge and/or voltage and on the procedure used to obtain the measurements. The studies have been similar qualitatively but not quantitatively.

In order for impedance to be used as a diagnostic tool for individual cells, more reproducible measurements must be obtained. It would also be desirable to be able to separate the contributions of the individual electrodes, especially for Ni/Cd cells. With Ni/H_2 cells one can almost always assume that any problems are due to the Ni electrode or separator and that the hydrogen electrode behaves reasonably reversibly. In this case the cell impedance is essentially that of the nickel electrode plus the ohmic contributions from the separator and electrolyte. However, with Ni/Cd cells, the Cd electrode can sometimes be the cause of poor cell performance although it usually causes fewer problems than the Ni electrode. For a sealed cell with no reference electrode, there is currently no satisfactory way of determining which electrode is behaving poorly without opening the cell and performing postmortem analyses.

This paper discusses preliminary measurements of impedance on flightweight Ni/Cd and Ni/H_2 cells using the case as a reference electrode in order to determine the impedance of each individual electrode. Although measurements so far have been limited, the method appears valid. We are reporting it at this time because of the urgent need for better diagnostic procedures for space-qualified Ni/Cd and Ni/H_2 cells.

EXPERIMENTAL PROCEDURE

Impedance measurements were made using the Solartron 1250 Frequency Response Analyzer coupled with a Solartron 1286 Electrochemical Interface. Measurements were made on two flightweight 50 AH Ni/Cd cells from General Electric Corporation (now Gates) which had undergone acceptance testing several years ago and which had subsequently been stored in the short-circuit condition. One was from a lot which had Cd electrodes which had been determined to be faulty from testing of other cells of the lot, the other was believed to have a good Cd electrode. At the time of testing, the cells had been stored for about six years. They were measured in the as-received condition, partially charged at 1 A for 5 hours, discharged at 1 A to 0.1 V, where they were measured again. They were then charged at 5 A (C/10) for 16 hours, discharged at 10 A (C/5) to 0.1 V and equilibrated at 1.275V. The impedances were then measured at room temperature from 100 Hz to 0.0025 Hz with a RMS signal of 1 mV (peak to peak signal of 2.828 mV).

The Ni/H_2 cell studied was a 50 AH flightweight cell from Hughes which had completed acceptance tests and been cycled 900 real-time LEO cycles, followed by three years on open-circuit. The cell was charged to 1.275 V and equilibrated overnight. Impedance measurements were then taken of the total cell and the individual electrodes. The cell was then charged several times at C/10 for 18 hours and discharged at C/2 to 1.00 V. Following this it was cycled at 60% DOD for three LEO cycles (55 minutes charge, 35 minutes discharge, 5% overcharge). Impedance measurements were taken again after equilibration of the cell at 1.275 V. The same parameters for the impedance measurements were used as with the Ni/Cd cells.

RESULTS AND DISCUSSION

A simplified circuit diagram for an electrochemical cell is shown in Figure 1. A real cell usually has additional circuit elements including inductance due to the physical arrangement of the plates, modifications due to the porous nature of the electrodes, and adsorption capacitances and resistances. However, this simplified circuit diagram serves as a good first approximation. If the impedance of one of the electrodes is several orders of magnitude less than that of the other as is usually the case with Ni/H_2 cells, one of the RC loops can be neglected, and the impedance of the cell can be treated as essentially that of the electrode with the higher impedance. The impedance data can be plotted in a number of different ways (ref.7). Bode plots (the log of the magnitude of the impedance vs the log of the frequency) are useful for comparing data that vary by orders of magnitude. Nyquist or complex plane plots (the real or in-phase component of the impedance vs the imaginary or out-of-phase component) are helpful in determining the ohmic and kinetic resistances and double-layer capacitances, and the slope of the Warburg plot (either the real or imaginary component vs the inverse square root of the angular frequency) gives information about the diffusion process (a large slope corresponds to slow diffusion). Figure 2 shows a typical Nyquist plot of a well-behaved Ni/H_2 cell at a voltage where the kinetic resistance is low. The impedance in this case is essentially that of the Ni electrode. The left intercept with the x-axis is the ohmic resistance, and the diameter of the semicircle gives the kinetic resistance. The right-hand portion of the curve is caused by slow diffusion processes. Similar plots are obtained with Ni/Cd cells (refs. 4-6), and the bulk of the impedance is also usually due to the Ni electrode. At low voltages, the diffusion portion of the curve may merge with the kinetic portion.

If the impedance of the cell varies from that of the typical cell, or if there is reason to suspect problems with the Cd or H_2 electrodes, it would be desirable to separate the impedance into the contributions from each individual electrode. This study was undertaken in order to see if the use of the cell case would enable such a separation.

In studying the impedances of cells containing Ni electrodes, the problem arises as to the best voltage or voltages for carrying out the measurements. It has been found that the impedances of Ni electrodes in the charged state (i.e., at higher voltages) are very low and do not vary much from one electrode to another or from one manufacturer to another. However, at low voltages corresponding to almost completely discharged electrodes, impedances rise by several orders of magnitude. Figure 3 is the Bode diagram for the magnitude of the impedance vs frequency for a typical electrode showing the changes with voltage as well as with frequency. Figures 4 and 5 show how the kinetic resistance and the Warburg slope change abruptly by several orders of magnitude as the voltage is lowered. At very low voltages (cell voltages of less than 1.000 V or electrode voltages below about 0.050 V vs the Hg/HgO electrode) the impedances are very large, and there is a great deal of scatter. We have found that equilibrium cell voltages of 1.150 to 1.275 V (corresponding to voltages of the Ni electrode vs the Hg/HgO electrode of about 0.200 to 0.325 V) give sufficient differentiation of the impedances with less scatter than at lower voltages. The measurements reported below were taken at cell voltages of 1.275 V.

We have also found significant differences at low voltages between electrodes from different manufacturers in addition to small differences between individual electrodes from the same manufacturer. This is not important if one is comparing cells from a single manufacturer, but must be taken into account if comparisons are made between electrodes or cells from different sources.

Recent studies in our laboratories have also indicated that measurements of impedances of the Ni electrode are more reproducible if the cells or electrodes are equilibrated at the voltage of interest. Equilibration times required vary from a few minutes for highly charged electrodes to several hours or overnight or longer for electrodes at low voltages. The voltage range described above allows reasonable equilibration times of 15 min to several hours depending of the electrode and the magnitude of the change from the initial voltage to the equilibrium voltage desired.

The voltage of the Cd electrode is reasonably stable, and it can be used as a reference electrode although it is less satisfactory than the Hg/HgO electrode (ref. 8). If the electrode is partially charged so that there is a reasonable amount of both metallic Cd and $Cd(OH)_2$ present, the potential should be quite close to the theoretical value (E^0=0.809 V vs

SHE). Thus if the voltage of the cell case vs the Cd electrode is fairly constant, we can assume that the cell case voltage is not changing significantly.

The voltages of the cell cases with respect to the Cd and Ni electrodes at various times are given in Table I. We see that the voltages of the case vs the Cd electrodes are quite stable, especially over short periods of time, while the voltage of the Ni electrode vs the case varies gradually with time. Although it is only necessary that the case voltage remain constant during the impedance measurement, it is interesting to speculate as to what electrode reaction is determining the potential of the case. The standard voltages of several possible couples are presented in Figure 6 along with the couples for the Ni and Cd electrode reactions, the Hg/HgO reference electrode and the case voltages for the two Ni/Cd cells studied.

Flightweight Ni/Cd cells have stainless steel cases. If we compare the data in Table I with the values in Figure 6, we see that the potential of the case with respect to Cd for cell L13-012 is somewhat higher than that of the $Fe(OH)_3/Fe(OH)_2$ potential, that of the other cell is not close to that of any obvious couple. There are no other metal/metal oxide potentials in this voltage range that could reasonably be considered as the source of this potential. Thus the potential-determining reaction cannot be determined at this time, but since the potential is stable for a reasonable time period, determination of the impedance using the case as the reference is feasible. The potential may be a mixed potential or it may be affected by organic components from degradation of the separator.

Impedance measurements were made on the complete cell and on each of the electrodes individually using the case as a reference. Figure 7 shows the arrangement of the leads for each measurement. The voltage between the two reference electrodes was maintained constant during the measurement. The experiments were interrupted several times during the course of the measurements of the individual electrode impedances to see if the cell voltage and the voltage of the electrode which was not being measured had changed. If the cell voltage had fallen (in no case this was more than 3-4 mV), the cell was again brought to the initial voltage before the measurements were continued.

The results are plotted either as Bode plots or Nyquist plots. The Nyquist measurements were corrected for ohmic resistance since it was not known initially whether the sum of the ohmic resistances between the case and the individual electrodes would equal the ohmic resistance between the two electrodes. (The results of the measurements subsequently showed that this was unnecessary, that each of the resistances between the case and the individual electrodes was half that of the ohmic resistance of the complete cell). The corrected impedance for the two electrodes was added together at each frequency to give a calculated impedance for the complete cell. This calculated impedance was then compared to the experimental impedance for the cell (which had also been corrected for ohmic resistance). The values were essentially the same except at low frequencies where the impedances are higher and the scatter greater, indicating that the method is valid.

Figure 8a is the Nyquist plot for the impedances in cell L13-012, the cell which was presumed to have a poor Cd electrode. It can be seen that the sum of the impedances for the individual electrodes at each frequency is equal to the measured impedances for the total cell. The same behavior is shown in Figure 8b for cell L07-220, from a lot with "good" Cd electrodes.

Figure 9a compares the impedances of the "good" and "bad" Cd electrodes using the Bode representation. The impedance of the "bad" Cd electrode in cell L13-012 is higher at low frequencies (diffusion controlled region) by half an order of magnitude. Figure 9b is the comparable plot for the Ni electrodes. In this case the low frequency impedance of the Ni electrode in cell L13-012 is lower than that in cell L12-220. The Nyquist plots are shown in Figure 10.

The values of the kinetic resistances, Warburg slopes, and electrode capacitances that can be obtained by analysis of the data using the circuit diagram for an individual electrode are not reported, since we believe that the cells had not been cycled sufficiently after the open-circuit or short-circuited storage to obtain reproducible results. The data are presented primarily to describe the method and indicate its probable validity. However, we feel that the results are qualitatively correct.

The data for the Ni/H_2 cell after cycling are presented in Figure 11. The Bode representation is used since the nickel electrode impedance and the hydrogen electrode impedance differ by about two orders of magnitude. The impedance parameters are given in Table II.

In both sets of measurements of the Ni/H_2 cell the voltage of the cell case was not as stable as with the Ni/Cd cells. Sometimes the voltage was close to the Ni potential, at other times close to potential of the H_2 electrode. During the measurements of the impedance of the Ni electrode the case potential remained stable, i.e., the cell voltage after the measurement was essentially the same as before, and no appreciable DC current was noticed. However, during the measurement of the impedance of the hydrogen electrode the cell voltage changed by several hundred mV and a large DC current was noticed. We suspect that the instability of the case voltage may be due to the difference in the case material from that of the Ni/Cd cells. The case of the Ni/H_2 flightweight cell is made of Inconel, while that of the Ni/Cd cells is steel. The voltages of the case vs Ni in nine boilerplate Ni/H_2 cells housed in standard steel pressure vessels are in the same range as those of the two Ni/Cd cells described above and seem to be as stable as in the Ni/Cd cells. The difference is thus probably due to the case material rather than the difference in the negative electrode or separator. Despite the changes in voltage of the case in the Ni/H_2 cell, the results are believed to be qualitatively correct.

CONCLUSIONS

Preliminary experiments indicate that the cell case can be used as a reference for Ni/Cd cells. The case can also probably be used as a reference for Ni/H_2 cells, although the potential of the case does not appear to be as stable as with the Ni/Cd cells. These measurements can be used to help determine which electrode is responsible for loss of performance. We are now cycling these Ni/Cd cells to determine changes in impedances of the individual electrodes with cycle life. We hope to make more measurements on a variety of Ni/Cd and Ni/H_2 cells from different lots to see if the cell and electrode impedances can be correlated with cycle life.

REFERENCES

1. Zimmerman, A., Martinelli, M.R., Janecki, M.C., and Badcock, C.C., J. Electrochem. Soc., 129 (1982), 289.

2. Barton, R.T., Hughes, M., Karunathilaka, S.A.G.R., and Hampson, N.A., J. Appl. Electrochem., 15 (1985) 399.

3. Lenhart, S.J., Macdonald, D.D., and Pound, B.G., J. Electrochem. Soc., 135 (1988) 1063.

4. Haak, R., Ogden, C., and Tench, D., J. Power Sources, 12 (1984) 289.

5. Comtat, M., Delorme, P., Baron, F., and Capel, A., Proc. ESA Session at 16th Annual IEEE PESC (ESA SP-230, May 1985.)

6. Reid, M.A., Extended Abstracts of the 174th Electrochemical Society Meeting, Chicago, IL, Oct. 1988, 122.

7. Bard, A.J., and Faulkner, L.R., Electrochemical Methods. Wiley, (1980) 316.

8. Salkind, A.J., and Bruins, P.F., J. Electrochem. Soc., 109, (1962) 356.

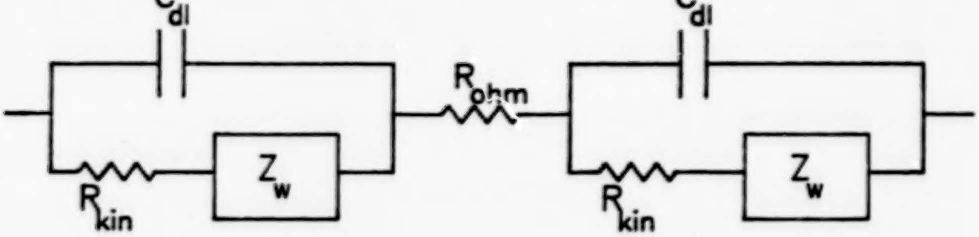
C_{dl}
R_{ohm}
C_{dl}
R_{kin}
Z_w
R_{kin}
Z_w

Fig. 1. Simplified circuit diagram for an electrochemical cell.

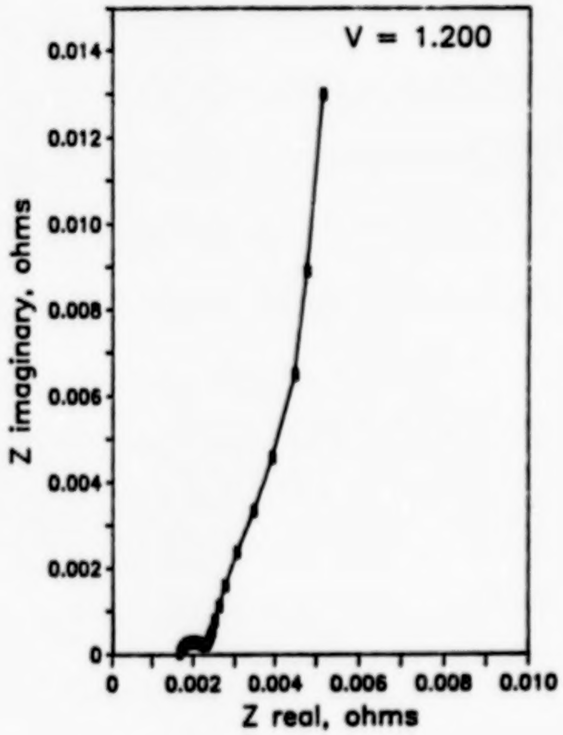

Fig. 2. Nyquist plot of impedance of typical 65 AH Ni/H_2 cell being tested for Space Station Freedom.

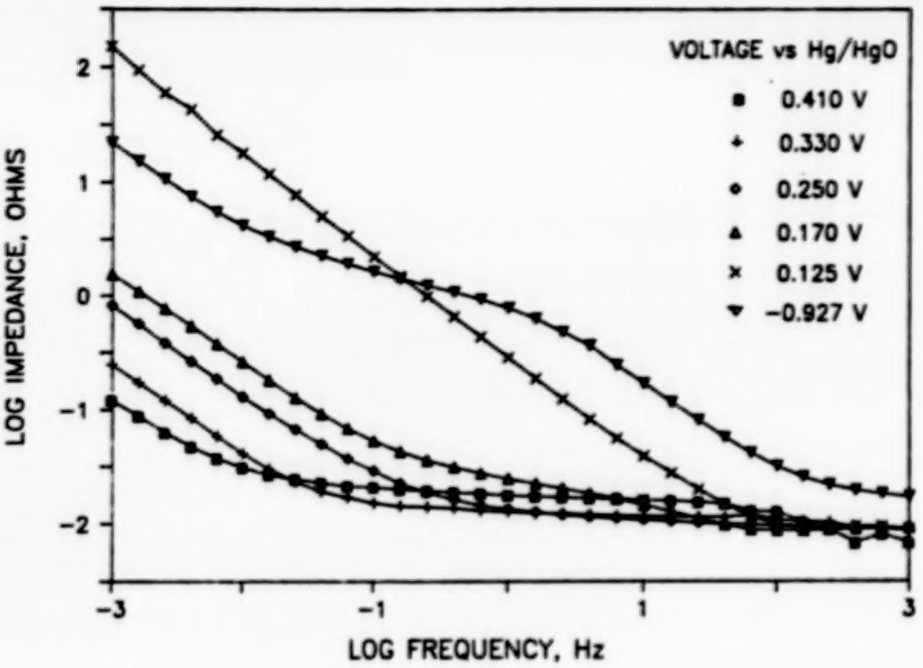

Fig. 3. Dependence of impedance on voltage for a Gates electrode, 42.9 cm^2, 31% KOH, after 12 cycles.

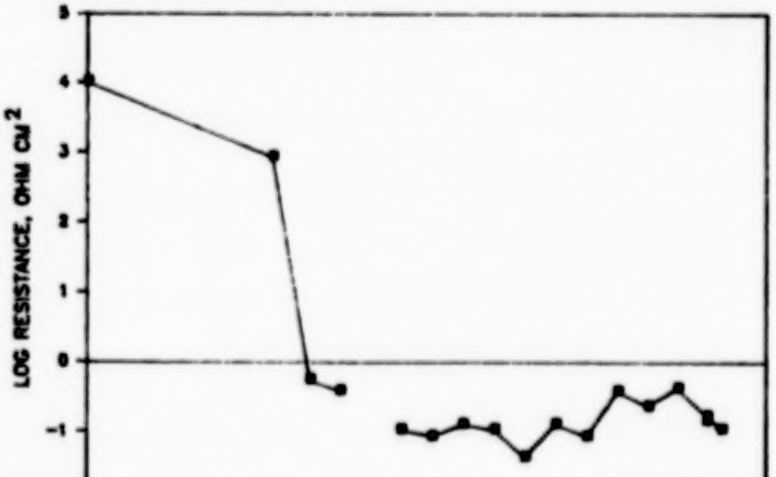

Fig. 4. Changes of kinetic resistance with voltage, Gates electrode, normalized.

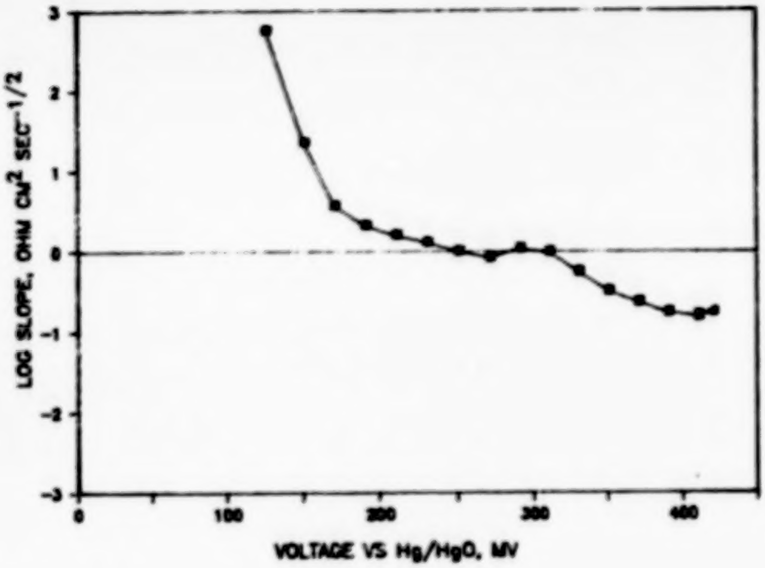

Fig. 5. Changes of Warburg slope with voltage, Gates electrode, normalized.

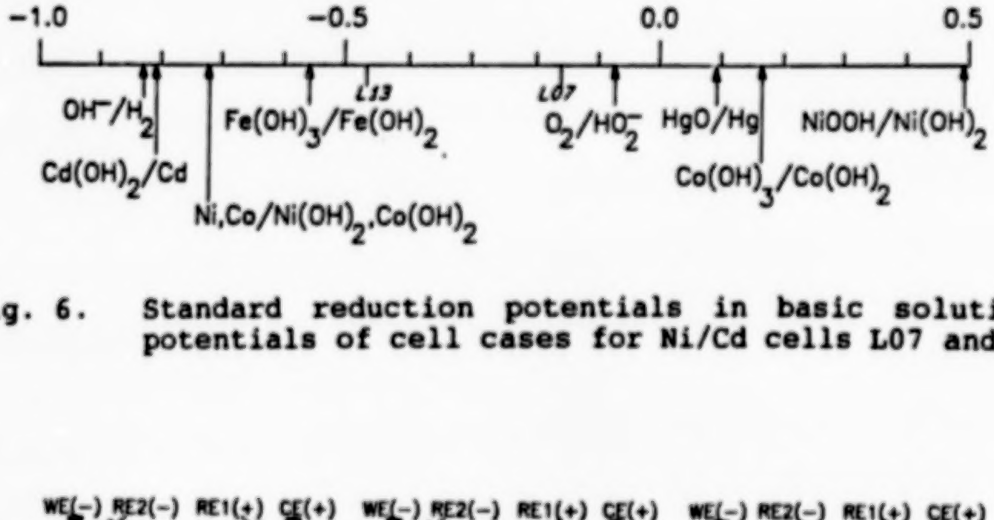
−1.0
−0.5
0.0
0.5
L13
L07
OH^-/H_2
$Cd(OH)_2/Cd$
$Ni,Co/Ni(OH)_2,Co(OH)_2$
$Fe(OH)_3/Fe(OH)_2$
O_2/HO_2^-
HgO/Hg
$NiOOH/Ni(OH)_2$
$Co(OH)_3/Co(OH)_2$

Fig. 6. Standard reduction potentials in basic solution and potentials of cell cases for Ni/Cd cells L07 and L13.

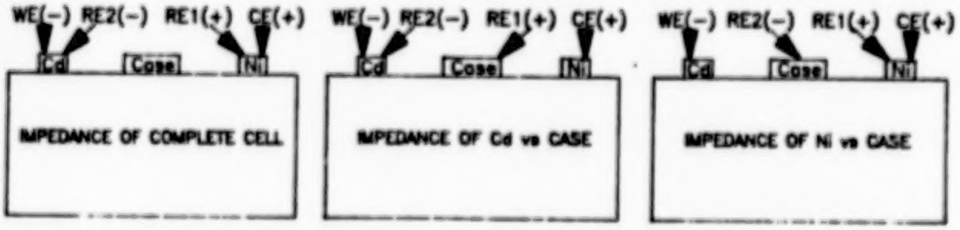
WE(−) RE2(−) RE1(+) CE(+)
Cd
Case
Ni
IMPEDANCE OF COMPLETE CELL
WE(−) RE2(−) RE1(+) CE(+)
Cd
Case
Ni
IMPEDANCE OF Cd vs CASE
WE(−) RE2(−) RE1(+) CE(+)
Cd
Case
Ni
IMPEDANCE OF Ni vs CASE

Fig. 7. Arrangement of leads for impedance measurements.

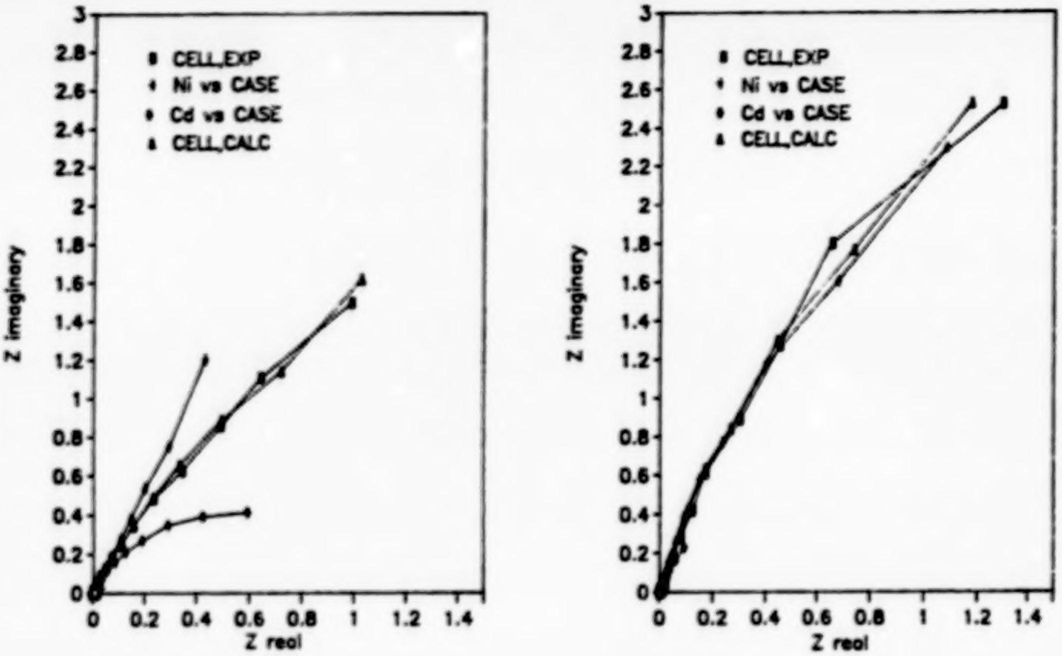

Fig. 8. Comparison of sums of individual electrode impedances of Ni/Cd cells with experimental cell impedances, Nyquist plot. Cell voltage = 1.275 V. a) Cell L13, b) Cell L07. (Scale of axes is unequal in order to show data more clearly.)

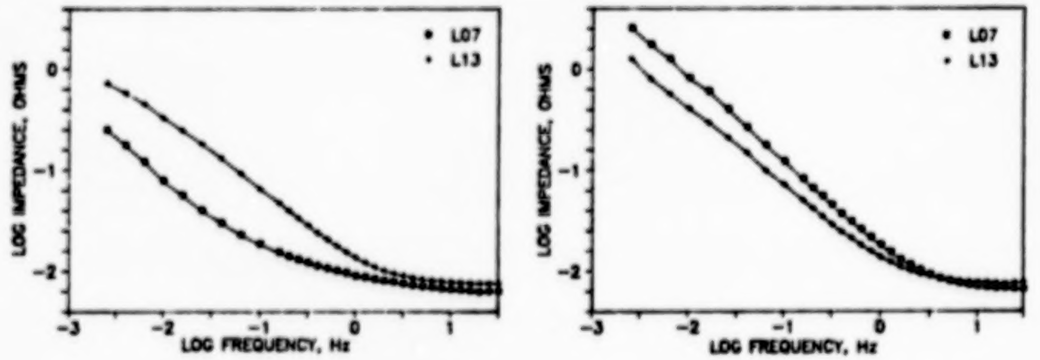

Fig. 9. Impedances of individual electrodes in cells L07 and L13, Bode plot. Cell voltage = 1.275 V. a) Cd electrodes, b) Ni electrodes.

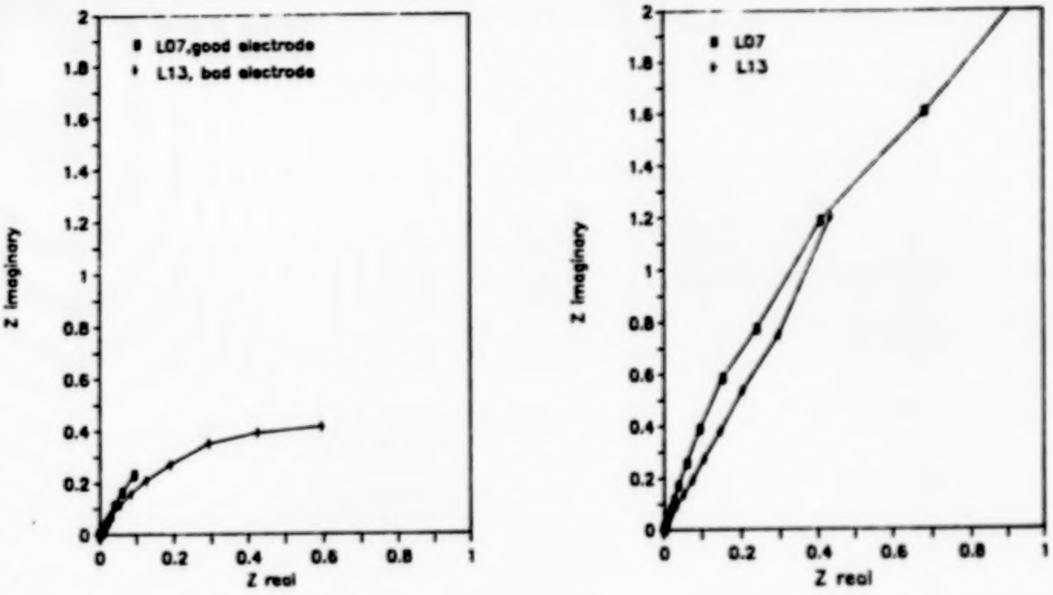

Fig. 10. Impedances of individual electrodes of cells L07 and L13, Nyquist plot. Cell voltage = 1.275 V. a) Cd electrodes, b) Ni electrodes. (Scale of axes is unequal in order to show data more clearly.)

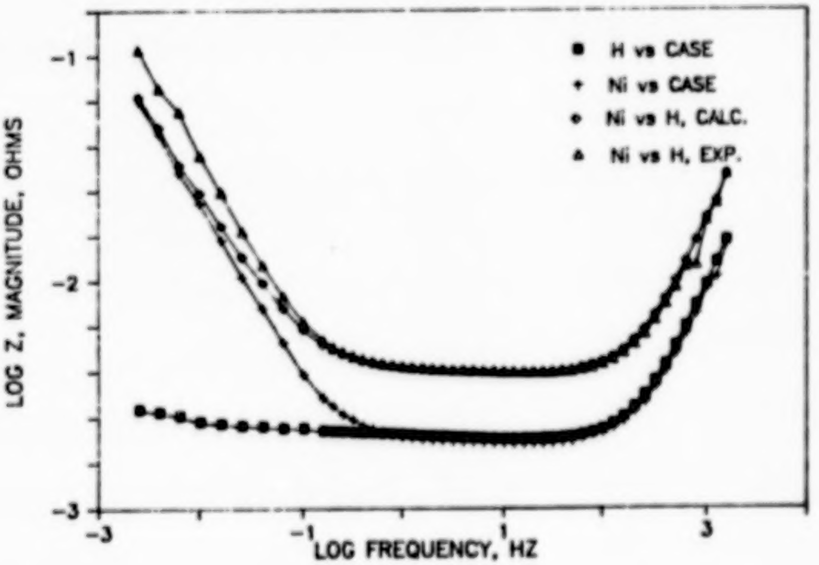

Fig. 11. Comparison of sums of individual electrode impedances in 50 AH Ni/H_2 cell with experimental cell impedance, Bode plot. Cell voltage = 1.275 V.

Table I. VOLTAGES OF CASES OF Ni/Cd CELLS VS INDIVIDUAL ELECTRODES.

Cell L13–012	At Time of Impedance	Overnight Stand	After Recharge	Two Months OCV
Cell Voltage	1.275	1.181	1.275	0.243
Case vs Cd	0.350	0.350	0.349	0.318
Ni vs Case	0.925	0.831	0.926	–0.076
Cell L07–275				
Cell Voltage	1.275			0.413
Case vs Cd	0.648			0.631
Ni vs Case	0.627			–0.218

Table II. IMPEDANCE PARAMETERS FOR Ni/H_2 50 AH CELL.

	R_{ohm} (mOhm)	R_{kin} (mOhm)	SLOPE	CAPACITANCE (Farads)
COMPLETE CELL	4.00	–	.0063	–
NI vs CASE	1.96	–	.0041	–
H vs CASE	2.05	–	.000056	–

THE APPLICATION OF ELECTROCHEMICAL IMPEDANCE SPECTROSCOPY FOR CHARACTERIZING THE DEGRADATION OF $Ni(OH)_2$/NiOOH ELECTRODES

D.D. Macdonald and B.G. Pound
SRI International
Menlo Park, California 94025

and

S.J. Lenhart
Ford Aerospace
Palo Alto, California 94303

Electrochemical impedance spectra of rolled and bonded and sintered porous nickel battery electrodes were recorded periodically during charge/discharge cycling in concentrated KOH solution at various temperatures. A transmission line model (TLM) was adopted to represent the impedance of the porous electrodes, and various model parameters were adjusted in a curve fitting routine to reproduce the experimental impedances. Degradation processes for rolled and bonded electrodes were deduced from changes in model parameters with electrode cycling time. In developing the TLM, impedance spectra of planar (non-porous) electrodes were used to represent the pore wall and backing plate interfacial impedances. These data were measured over a range of potentials and temperatures, and an equivalent circuit model was adopted to represent the planar electrode data. Cyclic voltammetry was used to study the characteristics of the oxygen evolution reaction on planar nickel electrodes during charging, since oxygen evolution can affect battery electrode charging efficiency and ultimately electrode cycle life if the overpotential for oxygen evolution is sufficiently low.

Transmission line modeling results suggest that porous rolled and bonded nickel electrodes undergo restructuring during charge/discharge cycling prior to failure. The average pore length and the number of active pores decreases during cycling, while the average solid phase resistivity increases. The average solution phase resistivity remains relatively constant during cycling, and the total porous electrode impedance is relatively insensitive to the solution/backing plate interfacial impedance.

INTRODUCTION

Porous nickel electrodes are used in a number of secondary alkaline battery systems, including nickel-iron, nickel-zinc, nickel-hydrogen and nickel-cadmium cells. Each of these batteries must ultimately meet several performance criteria: high specific power, high specific energy, low cost, and long cycle life. At present, the viability of these batteries is often limited by the degradation of the electrode materials. In some cases, the nickel plate is life-limiting (Ref. 1).

A number of irreversible degradation processes affect the performance of porous nickel battery electrodes. Like all porous electrodes, nickel plates can exhibit electrolyte exhaustion within the pores leading to mass transport and ohmic overpotential losses that reduce cell power. Faradaic efficiency losses from cycle-and temperature-dependent parasitic processes, such as oxygen evolution, can reduce charging efficiency. Also, the structural integrity of porous nickel electrodes frequently is inadequate to endure the mechanical stresses that arise during charge/discharge cycling. Resistive degradation of substrate particle-particle bonds can result from these stresses, and/or the active material may progressively separate from the current collector further reducing the performance of the electrode on cyclic charging and discharging.

In this paper, we report a study of the degradation of porous nickel battery electrodes in alkaline media upon cyclic charging/discharging. Electrochemical impedance spectroscopy is used as the principal experimental tool. Impedance studies of both planar and porous nickel battery electrodes in alkaline solutions have been published previously, but much of this work was restricted to relatively narrow frequency ranges because of limitations with experimental instrumentation (Ref. 2-5). Also, some investigators report impedance data for the total cell rather than the individual electrodes (Ref. 6,7), while other studies have dealt with electrodeposited (thick) oxide films (Ref. 8).

TRANSMISSION LINE MODEL

An understanding of how the properties of porous nickel electrodes are altered during cycling is developed in this study by adopting a transmission line model (Ref. 9,10) for the impedance of the porous mass. The model is adopted from Lenhart, Chao, and Macdonald (Ref. 11) and Park and Macdonald (Ref. 12), and differs from classical TLMs in two ways. First, the model used here recognizes the finite thickness of a practical battery electrode. Accordingly, the electrochemical behavior of the porous mass will be partly determined by processes that occur at the base of the pore between the current collector (backing plate) and the solution (impedance Z', Figure 1), provided that the frequency is sufficiently low that the penetration depth of the AC wave is of the same order as the thickness of the porous mass. Secondly, the model assumes a finite resistance for the active solid phase in order to account for the resistive degradation of particle-particle contacts caused by internal stresses.

As with most porous electrode models developed to date, several simplifying assumptions are made in order to render the mathematics tractable. Thus, the pores are assumed to be parallel right cylinders, and any radial and axial electrolyte concentration gradients within the pores are neglected. Furthermore, average pore electrolyte and solid phase resistances are used. A uniform layer of active material is assumed to line the walls of the pores, and charge storage processes along the walls are represented by a position-independent interfacial impedance Z. In this work, an equivalent circuit representing the interfacial impedance, Z, and the backing plate impedance, Z', are deduced from planar nickel electrode impedances.

The mathematical details of the modified transmission line model have been described in previous publications (Ref. 11,12) and are discussed only briefly here. The equivalent electrical circuit for a single pore in discretized form is shown in Figure 2, in which R_m and R_s represent the resistance of the solid current-carrying phase per unit pore length (ohm/cm), and the resistance of the solution phase per unit pore length (ohm/cm), respectively. The interfacial impedance, Z, is a specific impedance per unit pore length, (ohm cm^2/cm), so Z/dx has units of ohms. The current collector or backing plate impedance Z' has units of ohms, and is assumed to be independent of pore length.

Current and potential distributions within the porous system, and the total impedance, were derived (Ref. 11,12) by application of circuit analysis equations to a typical discrete unit. The total impedance of n one-dimensional parallel pores was found to be:

$$Z_T = \frac{1}{n}\left\{\frac{R_m R_s \ell}{R_m + R_s} + \frac{2\gamma^{1/2} R_m R_s + \gamma^{1/2}(R_m^2 + R_s^2)\, C + \delta\, R_s^2 S}{\gamma^{1/2}(R_m + R_s)\,(\gamma^{1/2} S + \delta\, C)}\right\} \qquad (1)$$

where

$\gamma = \frac{R_m + R_s}{Z}$, $\delta = \frac{R_m + R_s}{Z'}$, $C = \cosh(\gamma^{1/2}\ell)$, and $S = \sinh(\gamma^{1/2}\ell)$.
If A is the total projected area of the porous electrode, and $(1-\theta)$ is the fraction of that area occupied by pores, then $\theta A/n$ is the film area per pore, and $(1-\theta)A/n$ is the average pore area per pore. The solution phase resistance per pore becomes $\rho_s n\ell/(1-\theta)A$, and the resistance of the current-carrying solid phase is $\rho_m n\ell/\theta A$, where ρ_s and ρ_m are the resistivities (ohm cm) of the solution and solid phases, respectively, and ℓ is the pore length. The resistances R_s and R_m in Figure 2 are therefore

$$R_s = \rho_s\, n/(1-\theta)A \qquad \text{(ohm/cm)} \qquad (2)$$

$$R_m = \rho_m\, n/\theta A \qquad \text{(ohm/cm)} \qquad (3)$$

If the specific impedances (ohm cm^2) of the pore wall and pore base are Z and Z', respectively, then the impedance of the pore wall and pore base per pore are $Z_w/2\pi r l$ and $Z_b/\pi r^2$, where r is the average pore radius. Since the average pore area is $(1-\theta)A/n = \pi r^2$, the average pore radius is given as

$$r = \left(\frac{(1-\theta)\,A}{\pi n}\right)^{1/2} \qquad (4)$$

and the impedance per unit pore length as:

$$Z = \frac{Z_w \ell}{2\pi r \ell} = \frac{Z_w}{2} \left(\frac{n}{\pi A (1-\theta)}\right)^{1/2} \qquad (5)$$

Similarly, the backing plate or current collector impedance Z' per pore is found to be

$$Z' = \frac{Z_b}{\pi r^2} = \frac{Z_b n}{(1-\theta)A} \qquad (6)$$

The above expressions for R_m, R_g, Z and Z' are used in Equation 1, which now describes the impedance of a three dimensional porous electrode. The expressions for Z and Z' are determined from planar electrode impedances, as discussed in the Results Section.

EXPERIMENTAL

Test Cell

A three electrode cylindrical PTFE cell was used for all experiments with the working electrode positioned horizontally near the bottom of the cell. A platinum counter electrode and a Hg/HgO reference electrode were positioned over the working electrodes. The cell provided input ports for the electrolyte solution, for high purity argon gas purging, and for a PTFE coated copper/constantan thermocouple. High purity argon purging gas was deoxygenated in two zinc/vanadyl sulfate gas washing bottles. An 8 molal KOH electrolyte solution with 1% LiOH was used for all experiments and was prepared from reagent grade KOH and LiOH in double distilled, deionized water. The small LiOH addition was made to conform with other previously reported battery cycling experiments. Lithium additions are usually regarded as beneficial to porous electrode performance (Ref. 13,14,15,) although recent experiments (Ref. 16) showed little effect on capacity during cycling.

All potentials reported here are relative to the Hg/HgO reference electrode. A paste of Hg/HgO was inserted in a PTFE container above the solution, and contact with the electrolyte was provided by cotton fibers in a PTFE capillary. No liquid junction correction was required with this arrangement, since the reference and working electrodes were in contact with the same electrolyte. From the reaction

$$HgO + H_2O + 2e^- \rightleftharpoons Hg + 2OH^- \qquad (7)$$

the potential of the Hg/HgO reference in 8 molal KOH was calculated to be

-0.008V (SHE) using the following values for the activity of water and OH^-: a_{H_2O}(298°K, 8m KOH) = 0.5545, E° = 0.0984 V and $a_{OH^-} = (m_{OH^-})\gamma_\pm = m_{KOH}\gamma_\pm$ = (8molal)(5.902) from Pound et al. (Ref. 17).

Three kinds of nickel working electrodes were used: a planar nickel electrode, rolled and bonded porous electrodes, and sintered porous electrodes. The planar nickel specimen was cut from a rod of 99.5% nickel. It was polished to a 0.05 micron alumina powder finish and was rinsed with distilled water. Typically less than 10 minutes elapsed between polishing and polarizing the sample, and only a few seconds elapsed between solution contact and polarization.

The porous electrodes used in this study were prepared by commercial electrode fabricators. The active material in the rolled and bonded electrodes was supported by a PTFE "web" making up 1 w/o of the total electrode material; the remainder being 30% graphite, 1% cobalt hydroxide, and hydrated nickel hydroxide. The graphite served as the current carrier to the backing plate, and the cobalt was added to increase capacity during cycling (Ref. 18). A capacity of 0.29 A hr/gm was reported based on a one electron transfer from nickel hydroxide to nickel oxyhydroxide. The structural features of the sintered electrodes were very different from the rolled and bonded electrodes. For the former, nickel powder was sintered to a nickel wire mesh, and NiOOH was chemically deposited in the pores. The sintered nickel metal (and not graphite) carried the current to/from the wire mesh, which served as a backing plate. The capacity was 0.015 A hr/cm^2 projected (flat) area.

Experiments were performed at temperatures ranging from 0 to 100°C. The temperature was controlled to within ± 2°C as indicated by a thermocouple inside the test cell.

Cyclic Voltammetry

Only planar nickel electrodes were studied by cyclic voltammetry. Freshly polished nickel electrodes were inserted into the cell and, on contact with the electrolyte, were polarized to -850 mV. The solution and cell were then heated or cooled to the desired temperature. After temperature stabilization, a triangular potential/time perturbation was applied to the cell via a coupled function generator and potentiostat.

Various sweep rates from 1 to 100 mV/s were employed, and the potential was swept from below the hydrogen evolution potential to well above the oxygen evolution potential before reversing the sweep direction. At a given temperature, E/I traces were first recorded at 100 mV/s, then at progressively lower sweep rates. After the lowest sweep rate voltammogram was recorded, E/I traces were recorded at consecutively higher sweep rates up to 100 mV/s. The voltammograms reported here were reproducible to within ± 3 mV and ± 0.5 mA/cm^2 on the potential and current scales, respectively.

Electrochemical Impedance Spectroscopy

Impedance data were recorded with either a Solartron 1172 or 1250 Frequency Response Analyzer. For all impedance measurements, the Solartron sine wave output was superimposed on an applied DC bias from a Princeton Applied Research Model 173 potentiostat. Solartron potential and current input leads were taken directly from the cell and not from the potentiostat electrometer and current output jacks. A unity gain voltage follower based on an AD 521J operational amplifier was placed between the cell and the potential input of the Solartron to avoid polarizing the reference electrode. The amplifier had a differential input impedance of 3 X 10^8 ohms, and a flat frequency response (± 1%) at unity gain to 75 kHz. The voltage follower was accurate to 0.1 mV DC relative to a digital voltmeter.

Planar electrode impedance spectra were recorded over a range of DC potentials. Impedances were usually measured sequentially without repolishing the electrode between measurements. Electrodes were first polarized for two hours at the lowest potential of a given measurement sequence (typically -150 mV). The impedance spectrum was recorded, followed by a potential step (usually 100 mV) to the next highest potential. After one hour at the higher potential, another impedance spectrum was recorded. This procedure was normally repeated up to about 500 or 600 mV.

Porous electrode impedances were recorded in the fully discharged condition (0 mV). They were recorded periodically after selected numbers of charge/discharge cycles. The cycling process is described below, and one hour elapsed at constant potential (0 mV) before impedance spectra were recorded.

Charge/Discharge Cycling

Porous electrodes were cycled at constant current using an ECO Model 545 Galvanostat/Electrometer. Various charging currents were used, but the electrodes were always discharged at twice the charge rate. They were usually charged to 100% of rated capacity, and were fully discharged (100% DOD) on each cycle. Four or five "conditioning" cycles were completed before impedance data were recorded.

The galvanostat provided for automatic current reversal at selected potentials by presetting front panel potentiometers. However, in most cases, it was necessary to use constant charging and discharging times. Two timers were used to control switches connected to charge and discharge trigger inputs on the galvanostat. When charging efficiency was less than 100%, it was necessary to stop the discharging current before the end of the set discharge time. A voltage comparator based on an LM 311 amplifier was constructed and included in the timer circuitry to stop the discharging current prematurely at any selected potential until the next charging cycle started.

RESULTS AND DISCUSSION

Planar Electrodes - Cyclic Voltammetry

Cyclic voltammetry was used to determine the extent of oxygen evolution during nickel hydroxide oxidation. Oxygen evolution is a parasitic reaction during charging of nickel battery electrodes, and oxygen gas bubble formation may contribute to electrode degradation by generating internal stresses within the electrode pores. The large KOH concentration and elevated temperatures used in this study serve to enhance oxygen evolution by decreasing the overpotential.

For most cycling experiments, only one anodic oxidation peak, appearing at about 500mV, was recorded prior to oxygen evolution. Similarly, only one oxyhydroxide reduction peak at about 300mV was observed on the reverse sweep. Similar voltammograms have been reported for nickel in various alkaline solutions (Ref. 14,19).

At the highest sweep rate of 100mV/s, no steady state voltammogram was observed even after cycling continuously for over 19 hours (Figure 3). Both the anodic peak currents and anodic charge were found to increase steadily with time, but at a decreasing rate. Cathodic peak currents and the associated cathodic charge were difficult to determine since the cathodic current base line was obscured by the oxygen evolution current. However, minimum and maximum values for the cathodic parameters were estimated. For the first few tens of cycles, results indicate that more charge is consumed during hydroxide formation on the cathodic sweep than is liberated during oxyhydroxide formation on the preceding anodic sweep ($q_c > q_a$). This is possible if oxygen becomes trapped within the film or does not desorb from the film/electrolyte surface rapidly, and is reduced during the subsequent cathodic sweep (Ref. 20). After several additional cycles, the anodic charge becomes larger than the cathodic charge ($q_a > q_c$). This suggests that athe nickel substrate oxidizes during cycling and possibly that some film dissolution occurs.

Cycling time at 100 mV/s had only a minor effect on the proximity of the hydroxide oxidation peak to the oxygen evolution line at ambient temperature. The anodic peak potentials initially decreased and then increased with cycling time, but overall the changes were small, as indicated in Figure 3.

Anodic peak potentials were closer to oxygen evolution curves at higher temperatures. Figure 4 shows voltammograms at 0, 45, and 100°C after 10 cycles at 100 mV/s. Nickel hydroxide oxidation and oxygen evolution are within about 100 mV at 100°C compared with more than 200 mV at 0°C. The separation decreases primarily because of the shift in the equilibrium potential for oxygen evolution to more negative values and a decrease in the overpotential for this reaction. Furthermore, at higher temperatures, the anodic peak shifts closer to the oxygen evolution line with increasing cycle time (Figure 5). In a relatively short time, the anodic peak disappears completely from the voltammogram trace (Figure 6), although the presence of the cathodic peak indicates that nickel hydroxide oxidation occurs simultaneously with oxygen evolution. At 100°C, anodic peak shifting is even more rapid, while at 0°C virtually no peak shifting with cycle time is observed.

As noted by Macdonald and Owen (Ref. 21) and by McKubre and Macdonald (Ref. 19), the reversible potential for oxygen evolution is more negative than that for $Ni(OH)_2/NiOOH$ at all temperatures of interest. The appearance of the nickel hydroxide oxidation peak on the voltammograms is due to a high overpotential for oxygen evolution. However, as the temperature is increased, the overpotential is reduced, such that at 80°C and after extensive cycling a distinct oxidation peak is no longer observed. This phenomenon may have serious consequences for porous nickel electrode performance in concentrated alkali solutions at elevated temperatures, because oxygen evolution in the pores will occur simultaneously with charging. As noted previously, gas formation within the pores may contribute significantly to internal tensile stresses that can rupture particle-particle ohmic contacts within the active mass. Also, oxygen evolution represents a significant parasitic process that will lower the coulombic efficiency of the porous electrode over a charge/discharge cycle.

The anodic charge and peak current associated with nickel hydroxide oxidation increase considerably at higher temperatures, suggesting that more active material is present on the electrode surface. If film thickness is assumed to be proportional to anodic charge, then thicker films are formed at higher temperatures in a given number of cycles. A proportionality between charge and film thickness is supported by the work of McKubre and Macdonald (Ref. 19) where no evidence of film dissolution in rotating ring disc experiments is reported. This indicates that an increased battery electrode capacity might be anticipated if battery electrodes are operated at higher temperatures, but of course any advantage may be offset by the decrease in the oxygen evolution overpotential noted above.

Planar Nickel Electrodes - Electrochemical Impedance Spectroscopy

The transmission line model requires a knowledge of the interfacial electrolye/pore wall and electrolyte/backing plate impedances. It is assumed in this work that these impedances can be described by the impedance of a planar electrode in the same electrolyte. This assumption can be supported by several arguments. First, neglecting pore wall curvature, the basic structure of the sintered battery electrode at the electrolyte/pore wall interface, consisting of the metal, film, and electrolyte, should be similar to that for a planar electrode. The structure of the rolled and bonded porous electrodes deviates somewhat from this geometry but it is similar if the graphite is regarded as a substitute for the metal phase. Second, a concentrated electrolyte was selected for this study, so electrolyte depletion within the pores of the porous electrode should be minimal, particularly after one hour at constant DC bias prior to the measurement of the AC impedance spectra. The electrolyte concentration at the pore wall should be approximately the same as that at the film/electrolyte interface for a planar electrode.

In this study, an equivalent circuit for planar electro-oxidized (thin) film electrode impedances is used as the interfacial impedance input to the transmission line model. It can be argued that planar thick film electrode impedances should be used, since the active material in nickel battery electrodes is typically chemically or electrochemically deposited to a relatively large thickness within the pores. However, thick films themselves can be porous. Electro-oxidized thin films have comparatively smooth surfaces and are more suitable for use as interfacial impedances in the transmission line model.

Impedance spectra were recorded in sequences of increasing applied DC bias. Figures 7 and 8 show a typical sequence of ambient temperature Bode plots of log $|Z|$ vs. log ω, and phase angle vs. log ω, respectively, where $|Z|$ is the impedance magnitude, ω is the angular frequency ($2\pi f$), and the phase angle is the arc tangent of the ratio of the imaginary and real parts of the measured impedance. Impedance magnitudes are found to decrease with increasing potential, and a large decrease is observed when the nickel oxyhydroxide phase is formed at 500 mV. Phase angles generally show two maxima within the frequency range studied. The high frequency maximum shifts sharply to lower frequencies at 500 mV corresponding to the film transformation from nickel hydroxide to oxyhydroxide. However, both the magnitudes and the phase angles exhibit similar features above and below the nickel hydroxide/oxyhydroxide transition.

Impedance data were relatively unaffected by the potential step increments used in the DC bias sequences. In one test sequence, an electrode was polarized at 0 mV for one hour prior to an impedance spectrum measurement, then was cycled potentiodynamically between -800 mV and 600 mV at 100 mV/sec for 90 minutes. Following this, the impedance spectrum was again recorded at 0 mV after a one hour polarization at this potential. Both impedance spectra were virtually identical indicating that prior polarization to higher potentials does not significantly affect the planar electrode impedance spectra. It also suggests that charge/discharge cycling in of itself will not significantly affect the solution/pore wall impedance in the transmission line model.

Planar electrode impedance spectra were also recorded at other temperatures (Figures 9 and 10). Spectra were similar at all temperatures from 23°C to 100°C. However, at 0°C the high frequency relaxation shifted markedly to lower frequencies, and only the beginning of the low frequency relaxation is observable at the minimum frequency employed (6 mHz). At higher temperatures, higher minimum frequencies were used to avoid data scattering from noise, and again only the beginning of the lower frequency relaxation is observable. Despite the restricted view of the low frequency relaxation, the features of the elevated temperature data appear very similar to the ambient temperature spectra discussed above.

The planar electrode impedance spectra described above were modeled with the equivalent circuit shown in Figure 11. Mathematical impedance expressions derived from this circuit were used in the transmission line model, together with best fit component values (ie. capacitances, resistances and Warburg coefficients) obtained from a curve fitting technique.

An (infinite thickness) Warburg diffusion impedance was used in the equivalent circuit because previous results by Chao, Lin, and Macdonald (Ref. 22), Liang et al (Ref. 23), Madou and McKubre (Ref. 8), and Zimmerman et al. (Ref. 7) indicated that a diffusion impedance dominated the low frequency spectra over a wide potential range. Best fit component impedance values in each of the equivalent circuits were determined by minimizing the weighted sum of squares differences between the experimental and calculated impedance data. An example of fitted data using the circuit shown in Figure 11 and a spectrum recorded at 0 mV DC bias is shown in Figure 12. Clearly the essential features of the experimental data are reproduced by the model. Table 1 lists the best fit equivalent circuit parameter values at several potentials.

Porous Rolled and Bonded Electrodes

The transmission line model (TLM) contains eight independent variables. Two of these variables are the pore wall and backing plate interfacial impedances that are taken as planar nickel electrode impedances in this study. Planar electrode impedances are each described by four component impedance elements that may be frequency and DC bias dependent, as described in the previous section. A total of 16 independent variables are used to describe the impedance of porous nickel battery electrodes.

The TLM is used in this section to model porous electrode degradation processes. Each of the 16 variables in the model were first determined as accurately as possible in separate experiments. Impedance spectra were then calculated from the model and were compared to porous nickel electrode impedance spectra. Adjustments to key parameters allow the calculated spectra to progressively follow experimental impedances during degradation induced by galvanostatic cycling at various temperatures. The TLM clearly showed cycle dependent trends in several variables, and these trends are consistent with experimental observations, as described below.

Initial estimates of transmission line model parameters for rolled and bonded electrodes were selected as follows:

1. Pore wall and backing plate impedances, Z and Z', can be represented by planar electrode frequency dispersions from either experimental data or best fit calculated data derived from the equivalent circuits shown in Figure 11. The circuit shown in Figure 11 and its best fit component values (Table 1) at 0 mV DC bias were selected for this work.

2. Scanning electron microscope examination of rolled and bonded electrodes indicated that about 15000 pores were visible (at 100X) on electrodes of area 1.27 cm^2 given two "conditioning" charge/discharge cycles to their rated capacity. The smallest pores on the electrode surface could not readily be resolved at 100X and were not counted.

3. The initial average pore length, l, was approximated as the thickness of the electrodes (0.11 cm).

4. The projected electrode area was 1.27 cm^2 for rolled and bonded electrodes.

5. The total surface area of a rolled and bonded electrode after two conditioning cycles was found to comprise approximately 33% pores.

6. The KOH concentration in the pores was assumed to be constant along the length and radius of the pores since a high KOH concentration was used. While this assumption may not be strictly obeyed, the KOH/H_2O conductivity data of Lown and Thirsk (Ref. 22) shows that a 60% increase in conductivity is realized by halving the KOH concentration from 8 molar to 4 molar. This is within a factor of two. Therefore, the solution resistivity was approximated as a constant of 3.1 ohm cm for an 8 molar solution from the Lown and Thirsk data.

7. The solid phase resistivity, ρ_m, was difficult to estimate. The rolled and bonded electrodes contain principally graphite and nickel hydroxide. Graphite has a resistivity of about 0.0014 ohm cm (Ref. 25) while the resistivity of nickel hydroxide can be as much as ten or twelve orders of magnitude larger at 0 mV as indicated by planar electrode impedances. In this work, the graphite was assumed to determine the solid phase resistivity, so an initial estimate of ρ_m was taken as 10 ohm cm.

Bode plots calculated by direct substitution of the above parameters in the TLM were compared with impedances for a rolled and bonded electrode cycled twice at 23°C, with 40 minutes charging to rated capacity, and 20 minutes for 100% depth of discharge (DOD). The experimental impedance spectrum was measured after the electrode was held in the fully discharged condition at 0 mV for one hour. The features of the experimental impedance spectrum were present in the calculated spectrum. However, the fit of the calculated curve was relatively poor. Parameter value assignments were adjusted with a design optimization software package (OPTDES) written at Brigham Young University. OPTDES uses a set of design variables to minimize or maximize one or more objective functions defined by the user in a user-supplied Fortran subroutine. Four optimization algorithms were used in succession for each curve fitting.

OPTDES was used to minimize the sum of squares residuals (in the Nyquist plane) defined as the objective function in the Fortran subroutine. In a typical optimization sequence, interfacial and backing plate impedances for 0 mV applied DC bias plus the electrode area were first held constant, while the remaining variables were optimized. Then some or all of the component impedances in the interfacial and backing plate impedance expressions were allowed to vary along with the other design variables.

Curve fitting procedures indicated that small adjustments to several parameters significantly reduced the sum of squares error between the experimental and calculated impedance spectra (Figures 13 and 14). These parameter adjustments from the initial value assignments are discussed below.

1. The pore length, ℓ, required for the "best" fit of the experimental data is about three times the electrode thickness (0.35 cm compared with 0.11 cm thickness). This suggests that tortuosity along the pores increases the active pore length by this amount.

2. The best fit number of pores is about 23000, whereas about 15000 pores could be resolved in a 100X SEM photomicrograph. This may indicate that smaller pores (not counted in the photomicrograph) are not inactivated by their relatively larger solution resistance, $\rho_s l/a$, where a represents the cross sectional area of a pore.

3. The optimized surface coverage of pores $(1-\theta)$ was 0.33. This is in good agreement with the initial estimate of 0.3.

4. From Equation 4, the average pore radius can be calculated from the optimized number of pores and the surface coverage fraction of pores given above. The calculated average radius is 24 μm, which agrees well with the pore sizes observed in the SEM photomicrographs.

5. The optimized resistivities of the solid and solution phases were 9.3 and 4.5 ohm cm, respectively. Predicted values were 10 and 3.1 ohm cm, again in reasonable agreement.

6. The pore wall impedance, Z, required a small change to improve the fit with experimental data. Specifically, the smaller (high frequency) capacitance was decreased to about 7 μF from 43 μF at 0 mV DC bias. The latter number was obtained from the 0 mV, 23°C planar electrode impedance spectra as described in the previous section. Smaller capacitances (around 29 μF) were obtained in a similar manner for planar electrode impedances at lower potentials (-150 mV). Therefore, the smaller capacitnce required to fit the porous electrode data at 0 mV may be due to the potential drop across the porous electrode. The pore wall impedance input to the TLM represents an interfacial impedance averaged along the pore wall. If a potential drop occurs along the pore, then the pore wall impedance expression is selected at the average potential. The decreased (optimized) capacitance suggests that the average potential is lower than 0 mV, and therefore, that a potential drop exists across the electrode.

Experimentally, the porous electrode is polarized anodically at 0 mV, so the sign of the potential drop predicted by the TLM is in agreement with that imposed on the electrode in the cell.

7. The backing plate impedance, Z', had little effect on the shape of the calculated impedance spectra. This result supports the previous findings of a large pore length, and a large number of pores. Both of these parameters are proportional to the average solution resistance per pore $(\rho_s n\ell/(1-\Theta)A)$ and when large cause a redirection of current to the solid phase (away from the solution/backing plate interface.)

8. The remaining variables in the pore wall interfacial impedance (specifically the resistance, R, capacitance, C_1, and Warburg coefficient in Figure 12 were not optimized. Attempts to optimize these variables always resulted in slightly smaller sum of squares error, but with simultaneous distortions of the calculated spectrum. The optimization software found pathways to reduce the sum of squares error by skewing the features of the calculated spectrum. This may indicate that the best fit curves shown in Figures 13 and 14 represent only localized sum of squares minima and that a better fit might be found. More likely, it shows only that the optimization software can, in some cases, reduce sum of squares residuals on curves with complex shapes by unrealistic (albeit creative) manipulation of a large number of variables. In this study, the reproduction of the essential features of the experimental impedance spectrum is considered more important than a smaller sum of squares error.

Cycle Dependence

Impedance spectra for rolled and bonded electrodes at ambient temperature are shown in Figures 15 and 16 after 2, 12, and 27 galvanostatic charge/discharge cycles. Impedance magnitudes increase with cycle number at intermediate frequencies, while phase angle maxima decrease at low frequencies and increase at high frequencies. This behavior can be modeled by optimizing TLM parameters to minimize the sum of squares error between experimental and calculated impedance data. Parameter adjustments are discussed below:

1. The optimized active pore length decreased from 0.35 to 0.28 to 0.20 cm after cycles 2, 12, and 27, respectively. A considerable amount of the active material had spalled from the electrode by the end of 27 cycles, and was found scattered throughout the test cell. This could account for the decreased pore length. However, the electrode also swelled during the test, and after 27 cycles, the net thickness at the center of the electrode was actually larger than the original

thickness. The active material remaining on the surface of the electrode was easily flaked off, suggesting that the solid phase particles farthest from the backing plate were not active. The solid phase resistivity between these outer particles may have been so large that they did not participate in the electrochemical processes, and the pore length effectively decreased.

2. Cycle dependent adjustments to the solid phase resistivity, ρ_m, supports the above assertion that the outer particles were not active. The average solid phase resistivity changed from 8.9 to 13.2 to 12.4 ohm cm after 2, 12, and 27 cycles. The increase from the initial value is readily explained by particle-particle bond damage or breakage during the swelling process. Sloughing of the outer particles suggests that a resistivity gradient developed across the electrode, with the highest resistivity at the outer particles.

3. Optimized solution resistivities, ρ_s, remained virtually constant throughout the cycling process. Resistivities after 2, 12, and 27 cycles were 4.5, 4.9, and 4.0 ohm cm, respectively. Cycle independence was predicted since the KOH concentration was large making electrolyte depletion or exhaustion within the pores unlikely.

4. TLM modeling showed that the number of active pores, n, decreased from 23000 to 8500 to 3300 during this cycling sequence. A reduced number of active pores with cycling might be explained by "restructuring" and solid phase particle-particle bond breakage which inactivates many of the pores.

5. The optimized pore coverage fraction, $(1-\theta)$, decreased slightly during cycling, from 0.33 to 0.27, and 0.25 after 2, 12, and 27 cycles. This is also consistent with the gradual inactivation of pores during cycling.

6. According to the TLM, the potential drop across the porous electrode diminished somewhat with increasing cycle number. The optimized smaller capacitance in the pore wall interfacial impedance increased from 7 uF after cycle 2, to 34 uF after cycle 27. This indication of a cycle dependent decreasing potential drop is also readily explained. The resistance of the solid and solution phases per pore ($\rho_m nl/\theta A$ and $\rho_s\ n\ell/(1-\theta)A$, respectively) can be regarded as indicators of the potential drop across the porous electrode at a given DC bias. Both resistances decrease with increasing cycle number principally because of the decreasing pore length and number of pores, and the potential drop decreases accordingly.

Temperature Dependence

AC impedance spectra for rolled and bonded electrodes at 0 mV were measured at 0 and 40°C during their cycle life. The data had the same features as those at ambient temperature, suggesting that electrode degradation processes are similar at these temperatures.

No rolled and bonded impedance spectra were successfully recorded at 60°C or at 100°C. Electrodes failed in less than one or two cycles, and each test was terminated before impedance spectra were recorded. Failure was associated with severe spalling of the active material and the inability of the electrode to carry the imposed galvanostatic current within the output voltage range provided by the galvanostat.

The cyclic voltammetric results presented earlier show that oxygen evolution occurs rapidly during nickel hydroxide oxidation at 60°C and higher temperatures. Oxygen evolution and the associated bubble pressures within the pores are apparently major contributors to the rapid electrode degradation at higher temperatures. Slow swelling and sloughing at lower temperatures may also be related to the relatively slower oxygen evolution reaction rate.

Porous Sintered Electrodes

The effect of cycling current, cycle number, and temperature on the impedance data for a sintered electrode are shown in Figures 17-20. In all cases, the impedance components vary in a relatively simple manner with log ω. Log $|Z|$ typically decreases approximately linearly and then becomes constant with increasing frequency, while ϕ exhibits just one maximum over the frequency range studied. The decrease in ϕ to approximately 0° and the corresponding independence of $|Z|$ with frequency indicates that the impedance of the electrode is largely resistive for a large part of the frequency range.

Effect of Cycle Number

The impedance spectra were essentially independent of cycle number over the temperature range from 0° to 60°C, as shown in Figures 17-19. (The small shift in the impedance at 0°C is believed to be due to oxygen contamination late in the electrode cycle life.) Even up to failure, the spectra over this temperature range showed only small changes with cycling. The only indication of an impending failure was a slight fluctuation in the electrode potential just preceding failure. Moreover, the sintered electrodes did not exhibit any sloughing or swelling after failure as did the rolled and bonded electrodes.

Effect of Charge/Discharge Current

Impedance spectra obtained after cycling at high currents (26-min charge to capacity and 14-min for 100% DOD) and low currents (80-min charge to capacity and 40-min for 100% DOD) are shown in Figure 20. The frequency response of |Z| and ϕ were virtually identical for the two sets of cycling currents, indicating that there was no discernible degradation of the electrode structure within the range of currents used.

Effect of Temperature

The shapes of the Bode plots were independent of temperature, but the values of the impedance components did show some variation. The principal changes were (1) a decrease in the value of log |Z| at low frequencies, (2) an increase in the frequency of the phase angle maximum, and (3) a shift in the inflection of the log |Z| curve to higher frequencies.

At 100°C, failures occurred in the first few cycles even at low cycling currents based on an 80-min charging time. The impedance data at this temperature exhibited scatter due to noise, and measurements of the second harmonic indicated that the electrode response to a 10 mV rms AC perturbation was not linear. The AC perturbation signal was reduced to 3 mV, but the second harmonic was still too large.

The impedance spectra for the sintered electrodes differed from those for the rolled and bonded electrodes in several respects. Galvanostatic cycling of a rolled and bonded electrode, unlike a sintered electrode, has a marked effect on the impedance components, as shown in Figures 15 and 16. In addition, the curve for log |Z| shows more than one inflection, and ϕ exhibits two maxima over the frequency range studied. The first maximum in ϕ occurs in a similar frequency range to that for the sintered electrode, implying that it is associated with the active material whereas the second maximum is evidently related to the electrode structure.

The data for the rolled and bonded electrode, as discussed above, can be represented by a transmission line model, and parameters such as pore length and solid phase resistivity obtained from the model changed with cycle number. However, the impedance data for the sintered electrodes were not analyzed using the TLM because the changes in the impedance spectra were not sufficiently clear to render useful information on the degradation mechanism. The sintered electrodes are clearly more robust than are the rolled and bonded electrodes and hence are much more resistant to restructuring and rupture of the ohmic contacts in the active mass. Accordingly, we do not believe that our failure to detect changes in the impedance spectra represents a shortcoming of electrochemical impedance spectroscopy for studying electrode degradation phenomena but simply that the sintered electrodes are resistant to restructuring under the cycling regime employed in this work.

SUMMARY AND CONCLUSIONS

Transmission line modeling results indicate a set of parameter changes with cycle number that are consistent with experimental observations. Initial estimates and measurements of individual parameter values compare favorably with parameter values determined by curve fitting to real rolled and bonded electrode impedances at 0 mV and at 23°C. Rolled and bonded electrode impedances measured at 0 and 40°C behave similarly to those at ambient temperature, and similar parameter changes with cycle number are indicated.

Specific changes with cycle number at 23C are:

1. The average pore length decreases with cycle number, but always remains larger than the thickness of the electrode.

2. The average solid phase resistivity increases with cycle number.

3. The solution resistivity within the pores remains virtually unchanged during the cycle life of the electrodes.

4. The number of active pores decreases during cycling.

5. The average resistance per pore of the solution and solid phases decreases during cycling, and the potential drop across the electrode decreases accordingly.

6. The total porous electrode impedance is relativley insensitive to the solution/backing plate interfacial impedance. This indicates that little current flows along the entire pore length in the solution.

Rolled and bonded electrodes break down rapidly when cycled at 60 and 100°C. Cyclic voltammetric results at elevated temperatures show that the oxygen evolution reaction proceeds at a significant rate concurrent with the electrode charging reaction after the first few voltammetric cycles. Rapid rolled and bonded electrode breakdown during galvanostatic cycling at elevated temperatures is probably due to parasitic oxygen evolution processes.

Conversely, sintered electrode impedances do not change during galvanostatic cycling, and failures occur abruptly after a relatively large number of cycles. However, breakdown also occurred rapidly at 100°C, indicating that oxygen evolution processes may also affect sintered electrode cycle life.

ACKNOWLEDGMENTS

The authors gratefully acknowledge the financial support of this work by The U.S. Dept. of Energy through LBL under Contract No. 712955.

REFERENCES

1. Katz, M. H., McLarnon, F. R., Cairns, E. J., in Battery Division Extended Abstracts, The Electrochem. Soc., Fall Meeting, Oct. 17-21, 1982, p. 24.

2. Silverman, D. C., Corrosion , Vol. 37, No. 9, Sept. 1981, pp. 546-548.

3. Glarum, S. H., Marshall, J. H., J. Electrochem. Soc., Vol. 129. No. 3, March 1982, pp. 535-541.

4. Weininger, J. L., Breiter, M. W., J. Electrochem. Soc., Vol. 111, No. 6,June 1964, pp. 707-712.

5. Sathyanarayana, S., Venugopalan, S., Gopikanth, M. L., J. Applied Electrochemistry, Vol. 9, 1979, pp. 125-139.

6. Zimmerman, A. H., Janecki, M. G., in "Proceedings of the Symposium on The Nickel Electrode," Gunther, R. G., and Gross, S. eds., JES, Vol. 82-4, 1982, pp. 199-215.

7. Zimmerman, A. H., et al., J. Electrochem. Soc., Vol. 129, No. 2, Feb. 1982, pp. 289-293.

8. Madou, M. J., McKubre, M.C.H., J. Electrochem. Soc., Vol. 130, No. 5, May 1983, pp. 1056-1061.

9. De Levie, R., Electrochimica Acta, Vol. 8, 1963, pp. 751-780.

10. De Levie, R., in "Advances in Electrochem. and Electrochem. Eng.," P. Delahy, ed., Vol. 6, Interscience, New York, 1969, pp. 329-398.

11. Lenhart, S. J., Chao, C. Y., Macdonald, D. D., in "Proceedings 16th Intersociety Energy Conversion Engineering Conference, ASME, New York, Aug. 9-14, 1981, pp. 663-666.

12. Park, J. R., Macdonald, D. D., Corrosion Science, Vol. 12, No. 4, 1983, pp. 295-315.

13. Tuomi, D., J. Electrochem. Soc., Vol. 112, No. 1, Jan. 1965, pp. 1-12.

14. Weininger, J. L., in "Proceedings of the Symposium on the Nickel Electrode," Gunther, R. G. and Gross, S. eds., J. Electrochem. Soc., Vol. 82-4, 1982, pp. 1-18.

15. Takehara, Z., Kato, M., Yoshizawa, S., Electrochimica Acta, Vol. 16, 1971, pp. 833-843.

16. Maskalick, N. J., Buzzelli, E. S., in Battery Division Abstracts, The Electrochem. Soc., Fall Meeting, Oct. 17-21, 1982, p. 24.

17. Pound B. G., Singh, R. P., Macdonald, D. D., J. Power Sources, Vol. 18, p. 1 1986.

18. Pickett, D. F., U.S. Air Force Technical Report AFAPL-TR-75-34, Part I, Oct. 1975.

19. McKubre, M.C.H., Macdonald, D. D., J. Energy, Vol. 5, 1981, p. 368.

20. Sattar, M. A., Conway, B. E., Electrochemical Acta, vol. 14, 1969, pp. 695-710.

21. Macdonald D. D., Owen D., "The Electrochemistry of Nickel Metal in Lithium Hydroxide Solutions at 22, 170, and 250°C." High Temperature High Pressure Electrocemistry in Aqueous Solutions, Eds. R. W. Staehle, D. deG. Jones, and J. E. Slater, National Association of Corrosion Engineers, Houston, 1976.

22. Chao, C-Y, Lin, L.F., Macdonald, D. D., J. Electrochem. Soc., Vol. 129, 1982, 1874.

23. Liang, R., Pound, B., Macdonald, D. D., Electrochem. Soc., Ext. Abstr., 84-2, 1984, 356

24. Lown O. A., Thirsk H. R., Trans. Farad. Soc., Vol. 67. No. 1, 1971, p. 132.

25. Handbook of Chemistry and Physics, Weast R. C. ed., CRC Press Inc., 1974, p. F 159.

Table 1

EQUIVALENT CIRCUIT PARAMETERS
($1.27\ cm^2$ Electrode Area)

E (mV vs Hg/HgO/8m KOH)	C_2 (μF) DC Bias Sequence #1	C_2 (μF) DC Bias Sequence #2	C_1 (μF) DC Bias Sequence #1	C_1 (μF) DC Bias Sequence #2	R(Ω) DC Bias Sequence #1	R(Ω) DC Bias Sequence #2	$\sigma(\Omega/sec^{1/2})$ DC Bias Sequence #1	$\sigma(\Omega/sec^{1/2})$ DC Bias Sequence #2
-150	180		25.1		595		5900	
0	343	296	35.0	43.4	560	875	10400	8250
100		501		52.5		780		8850
200	541	671	55.0	70.6	530	736	5050	6880
300		756		86.4		770		4075
400		839		126.0		700		2500
500	1320	1130	950	891	430	415	870	485

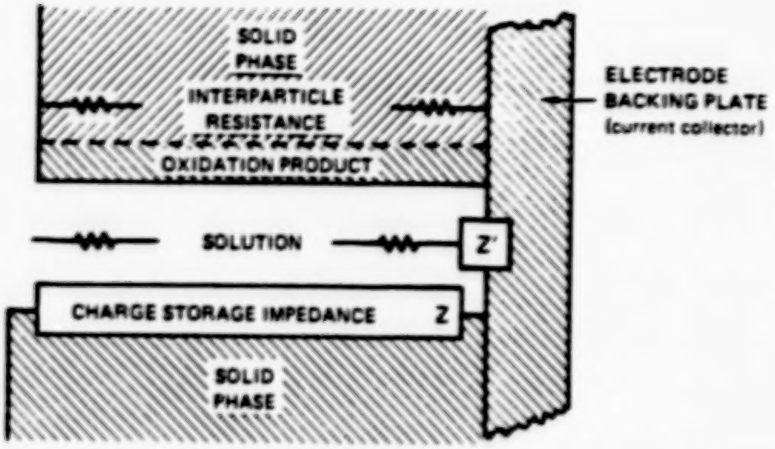
SOLID PHASE
INTERPARTICLE RESISTANCE
OXIDATION PRODUCT
ELECTRODE BACKING PLATE (current collector)
SOLUTION
Z'
CHARGE STORAGE IMPEDANCE
Z
SOLID PHASE

FIGURE 1 RIGHT CYLINDRICAL MODEL OF IDEAL SINGLE PORE

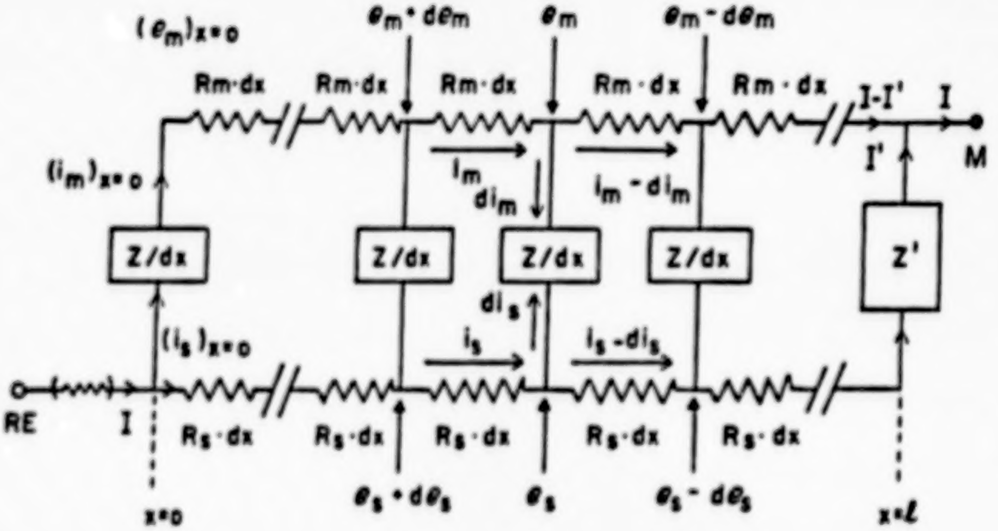
$(e_m)_{x=0}$
$e_m + de_m$
e_m
$e_m - de_m$
$R_m \cdot dx$
$I - I'$
I
I'
M
$(i_m)_{x=0}$
i_m
di_m
$i_m - di_m$
Z/dx
Z'
$(i_s)_{x=0}$
di_s
i_s
$i_s - di_s$
RE
$R_s \cdot dx$
$e_s + de_s$
e_s
$e_s - de_s$
x=0
$x = \ell$

FIGURE 2 DISCRETIZED FORM OF TRANSMISSION LINE MODEL FOR A POROUS BATTERY ELECTRODE OF FINITE THICKNESS

e_m and e_s are potentials in the metal and solution phases respectively.

i_m and i_s are currents in the metal and solution phases, respectively.

I and I' are the total current and the current flowing across the electrode backing plate/solution interface at the base of the pore, respectively.

RE and M designate the reference electrode and current collector locations respectively.

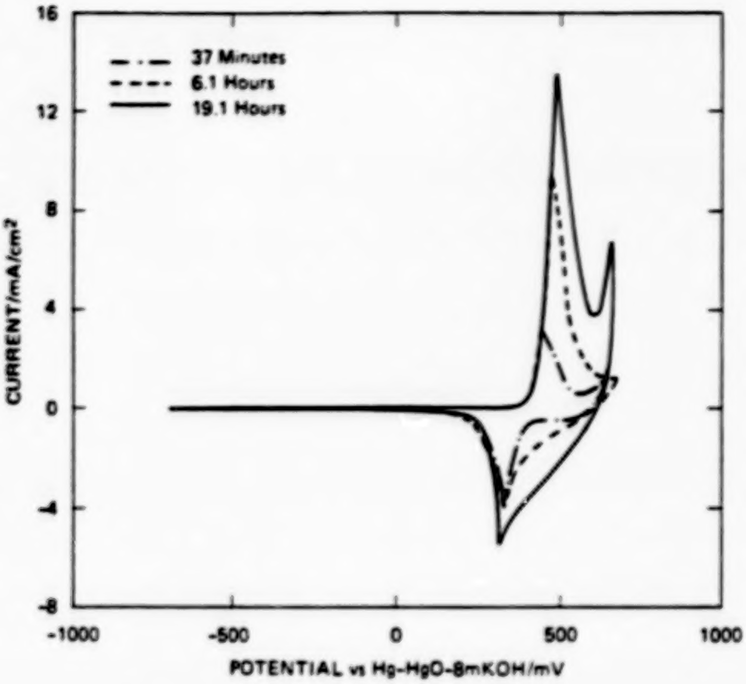

FIGURE 3 VOLTAMMOGRAMS FOR PLANAR Ni ELECTRODE IN 8 m KOH + 1% LiOH AT 23°C AS A FUNCTION OF CYCLING TIME. VOLTAGE SWEEP RATE = 100 mV/s

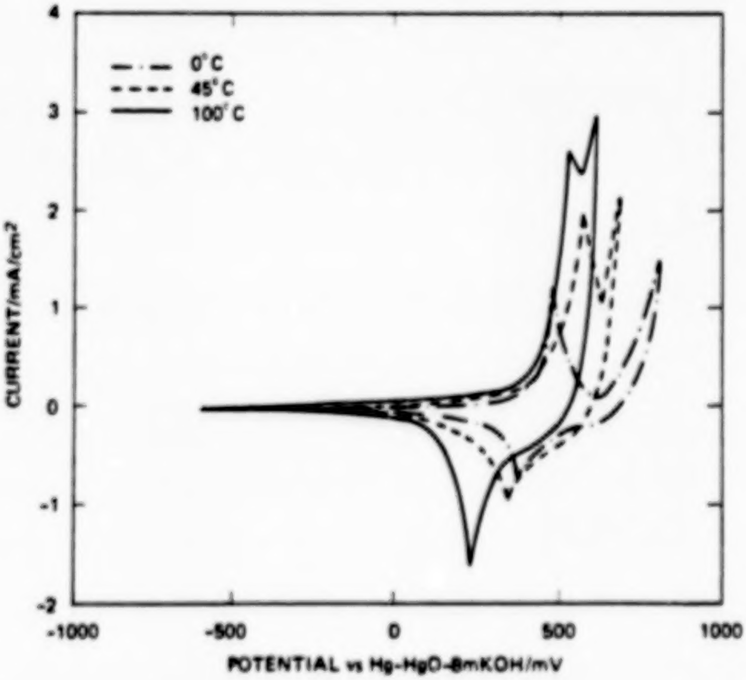

FIGURE 4 VOLTAMMOGRAMS FOR PLANAR Ni IN 8 m KOH + 1% LiOH AT VARIOUS TEMPERATURES AFTER 10 CYCLES AT 100 mV/s

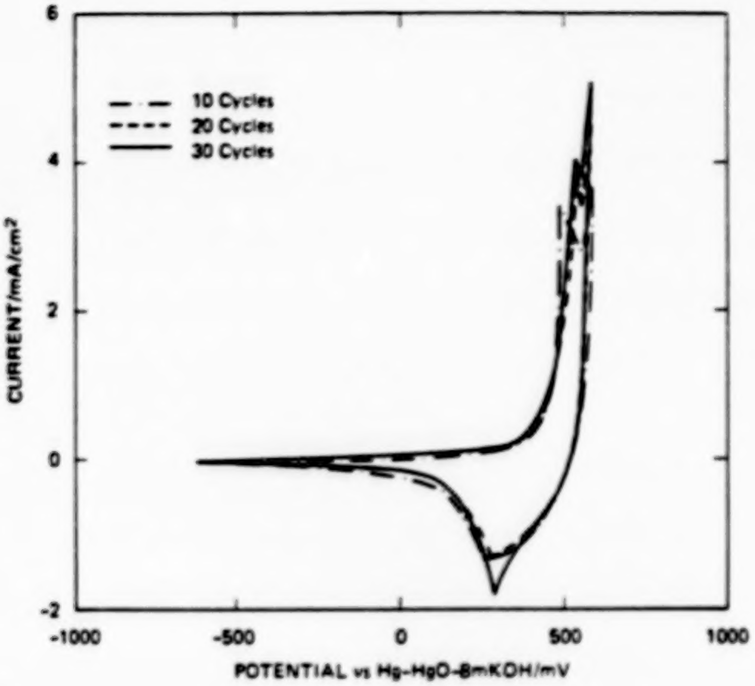

FIGURE 5 VOLTAMMOGRAMS FOR PLANAR Ni IN 8 m KOH + 1% LiOH AT 80°C, 100 mV/s AND 10, 20 AND 30 CYCLES

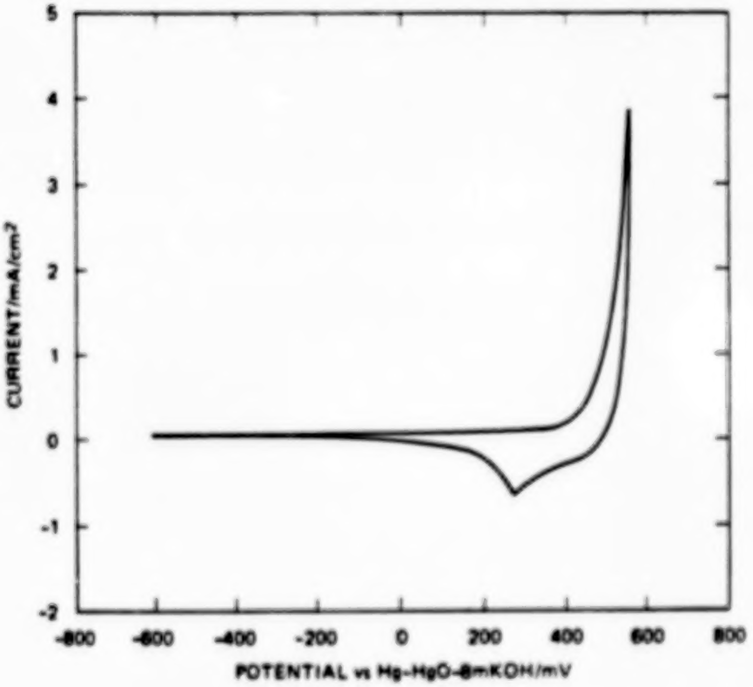

FIGURE 6 VOLTAMMOGRAM FOR PLANAR Ni in 8 m KOH + 1% LiOH AT 80°C, 20 mV/s, CYCLE 81

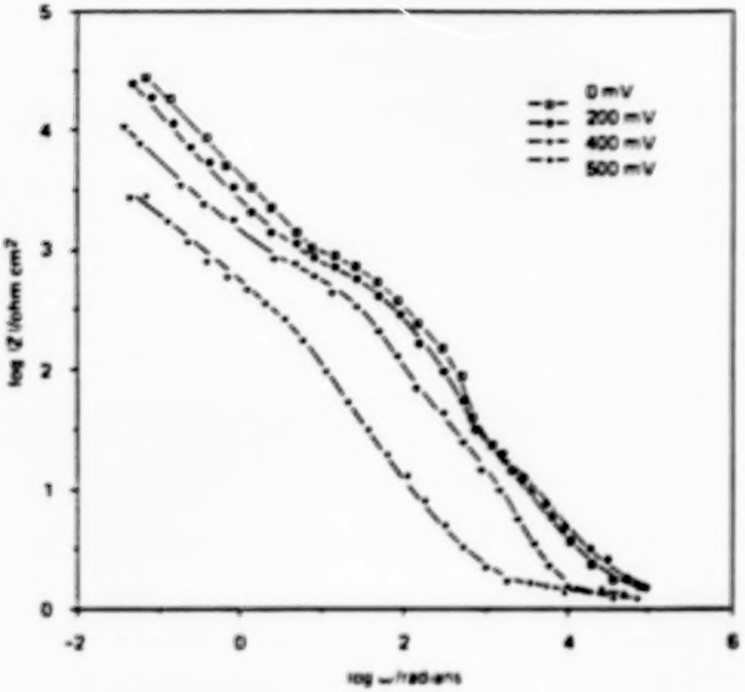

FIGURE 7 AMBIENT TEMPERATURE log |Z| vs log ω DATA FOR PLANAR Ni ELECTRODES IN 8 m KOH + 1% LiOH OVER A RANGE OF APPLIED DC BIAS

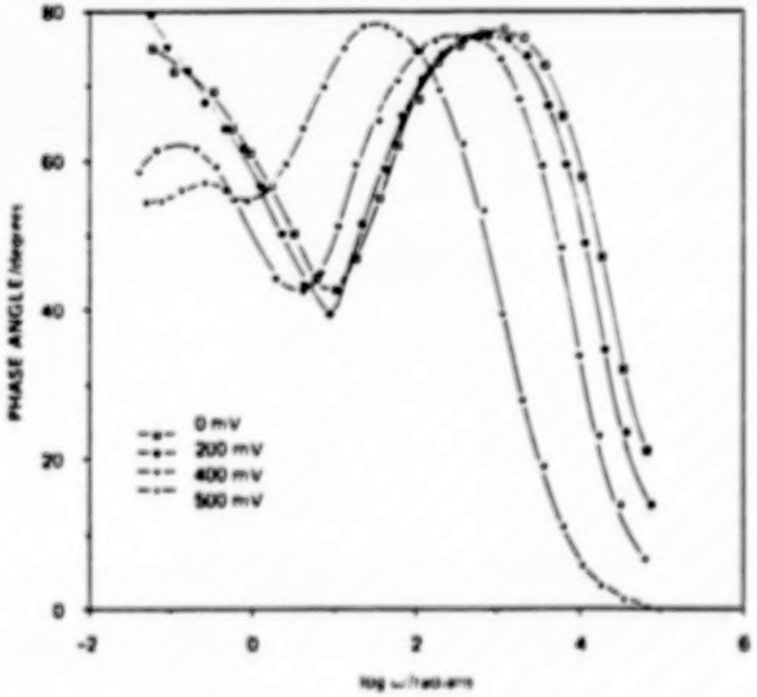

FIGURE 8 PHASE ANGLES CORRESPONDING TO DATA IN FIGURE 7

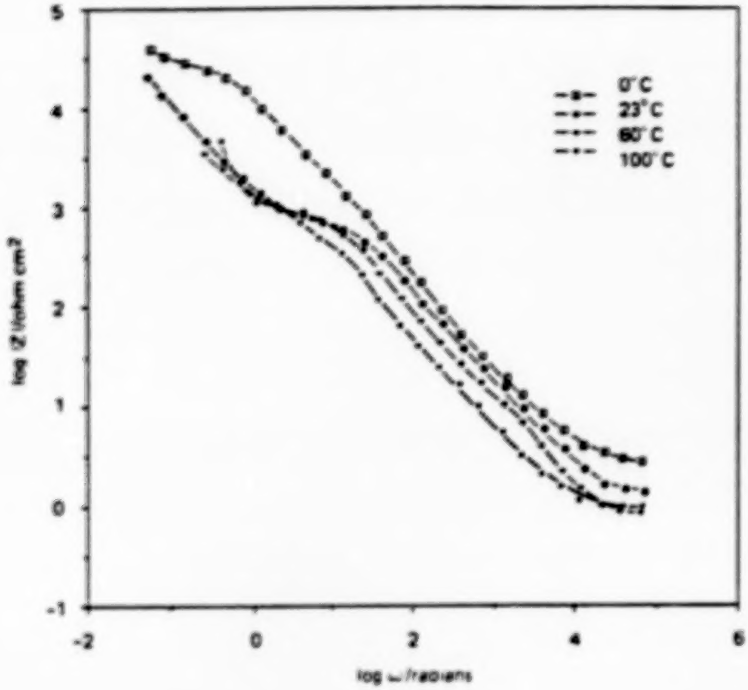

FIGURE 9 IMPEDANCE SPECTRA AT VARIOUS TEMPERATURES FOR A PLANAR N
ELECTRODE IN 8 m KOH + 1% LiOH AT 200 mV

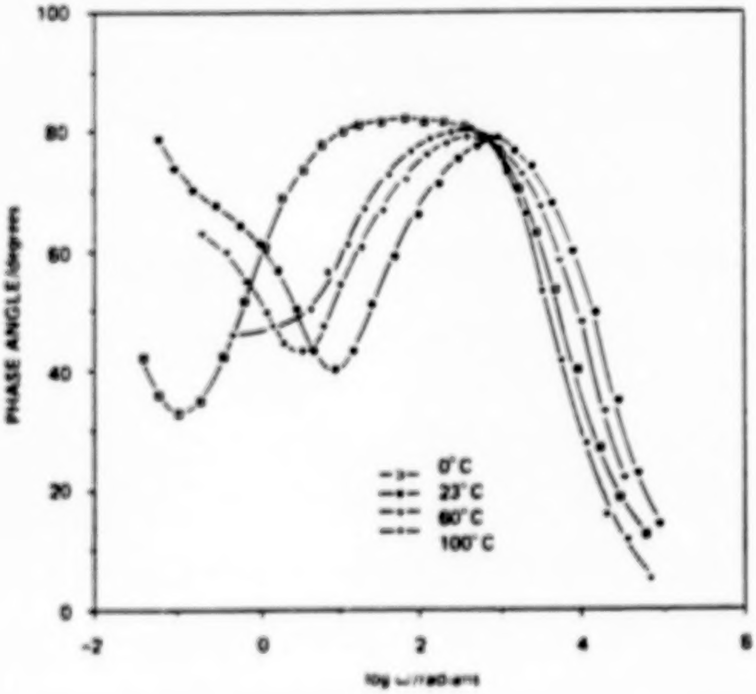

FIGURE 10 PHASE ANGLES CORRESPONDING TO DATA IN FIGURE 9

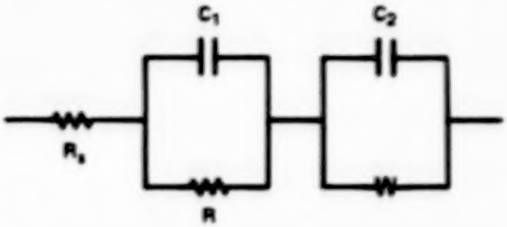

FIGURE 11 AN EQUIVALENT CIRCUIT FOR PLANAR NICKEL ELECTRODE IMPEDANCES IN 8 m KOH + 1% LiOH

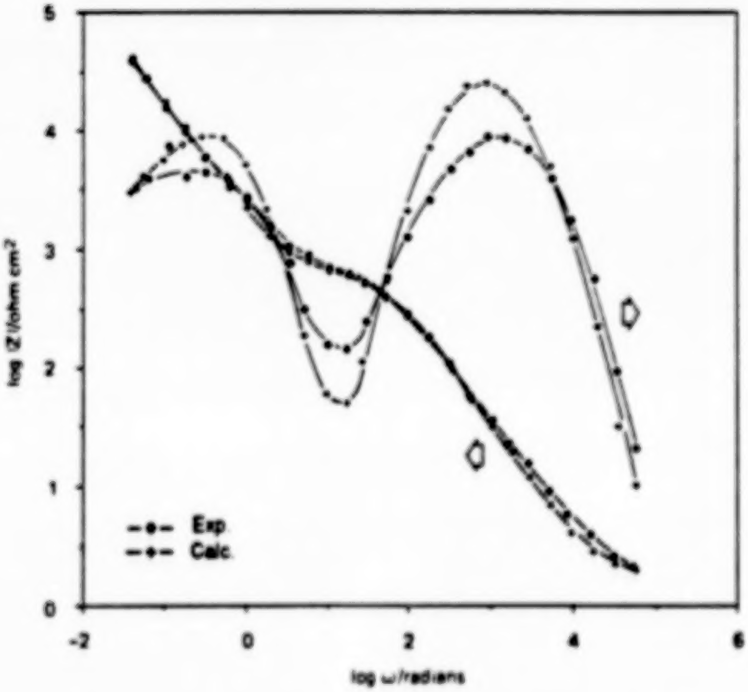

FIGURE 12 EXPERIMENTAL AND CALCULATED IMPEDANCE SPECTRA AT 0 mV APPLIED DC BIAS USING THE EQUIVALENT CIRCUIT IN FIGURE 11 FOR IMPEDANCE CALCULATIONS. (23°C)

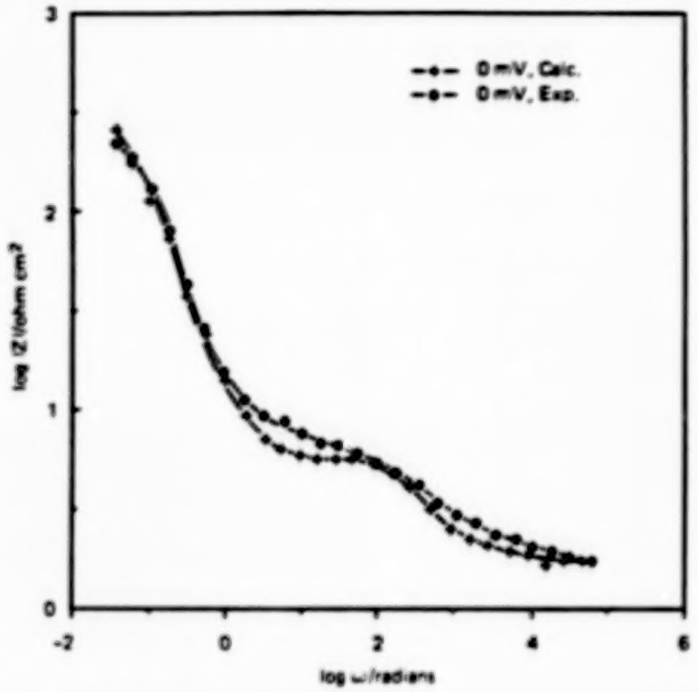

FIGURE 13 EXPERIMENTAL AND CALCULATED log |Z| vs log ω DATA AT 0 mV AND 23°C FOR A ROLLED AND BONDED POROUS ELECTRODE CYCLED TWICE. (40 min CHG TO CAPACITY AND 20 min TO 100% DOD.) CALCULATED SPECTRUM DETERMINED FROM OPTIMIZED TLM PARAMETERS DESCRIBED IN TEXT.

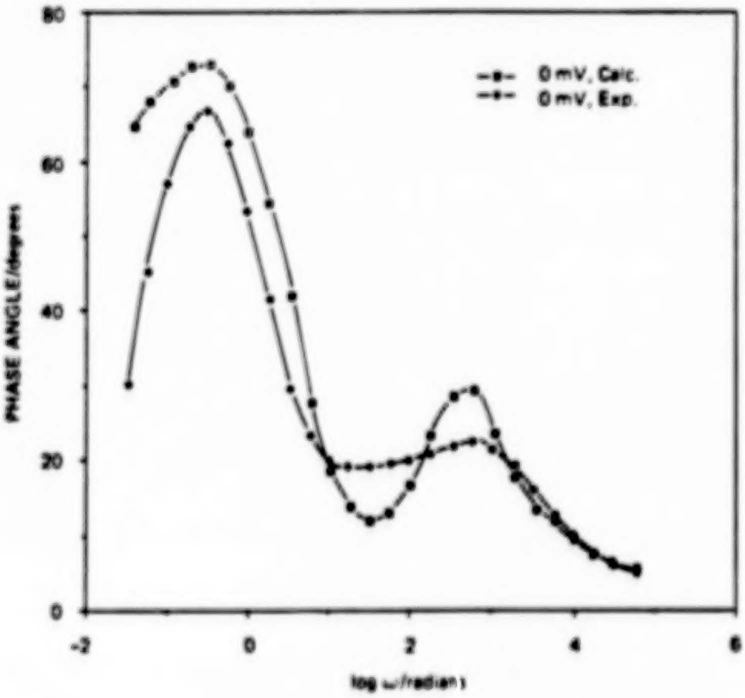

FIGURE 14 PHASE ANGLES CORRESPONDING TO DATA SHOWN IN FIGURE 13

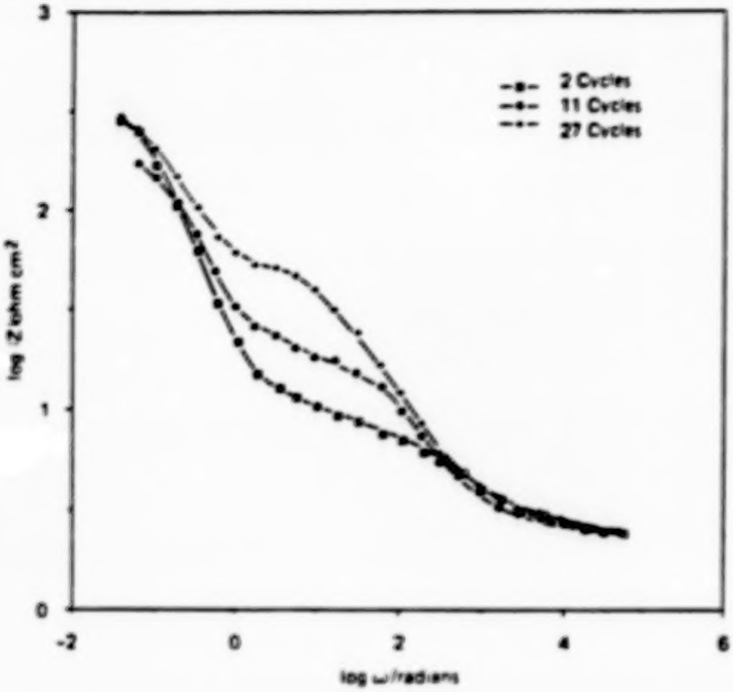

FIGURE 15 EXPERIMENTAL log |Z| vs log ω DATA FOR A ROLLED AND BONDED POROUS ELECTRODE AT 0 mV AND 23°C AFTER VARIOUS CYCLES. (40 min CHG TO CAPACITY AND 20 min TO 100% DOD.)

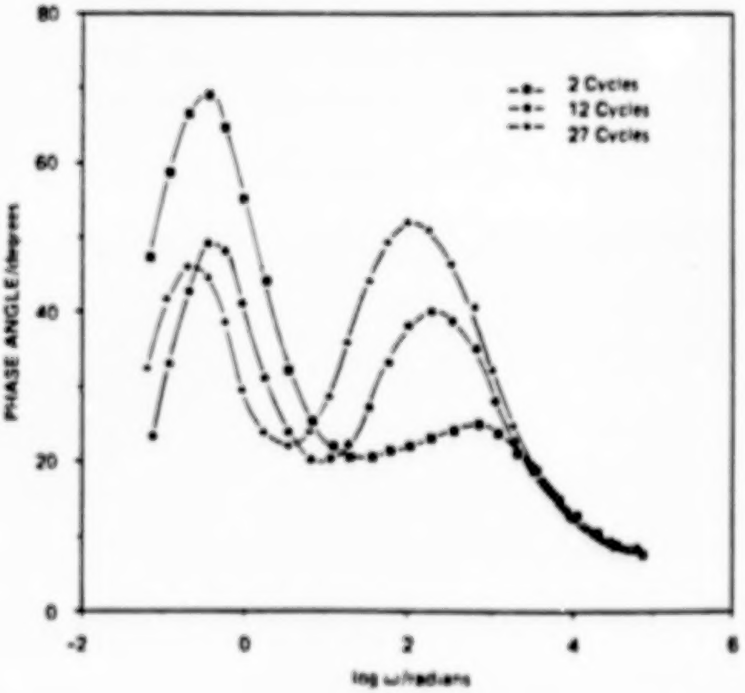

FIGURE 16 PHASE ANGLES CORRESPONDING TO DATA SHOWN IN FIGURE 17

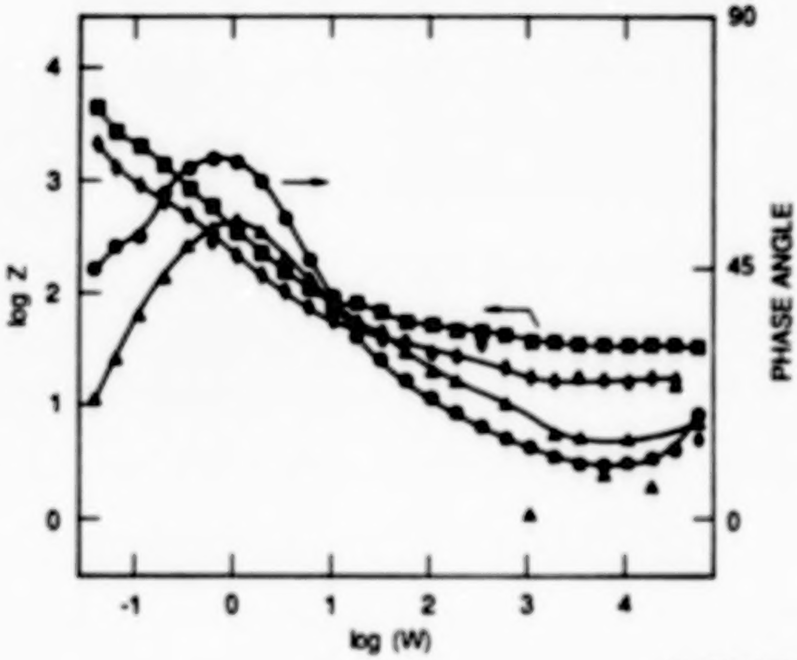

RA-350543-29

FIGURE 17 BODE PLOTS OF IMPEDANCE DATA FOR A SINTERED ELECTRODE AT 0°C AND 0 V AFTER 5(■, ●) AND 186 (⧫, ▲) GALVANOSTATIC CYCLES

(26-min. charge to capacity with 14-min discharge to 100% DOD).

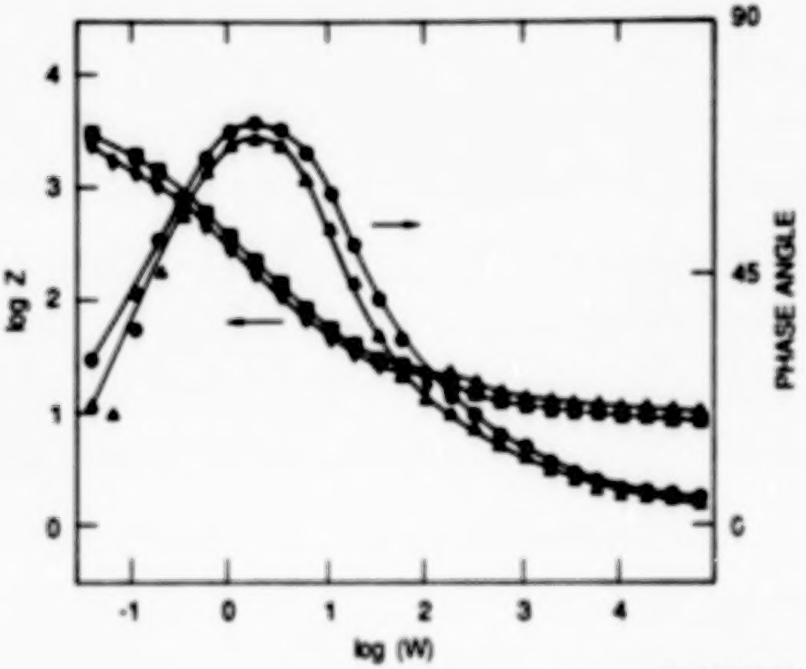

RA-350543-30

FIGURE 18 BODE PLOTS OF IMPEDANCE DATA FOR A SINTERED ELECTRODE AT 23°C AND 0 V AFTER 5(■, ●) AND 275 (◆, ▲) GALVANOSTATIC CYCLES

(26-min. charge to capacity with 14-min discharge to 100% DOD).

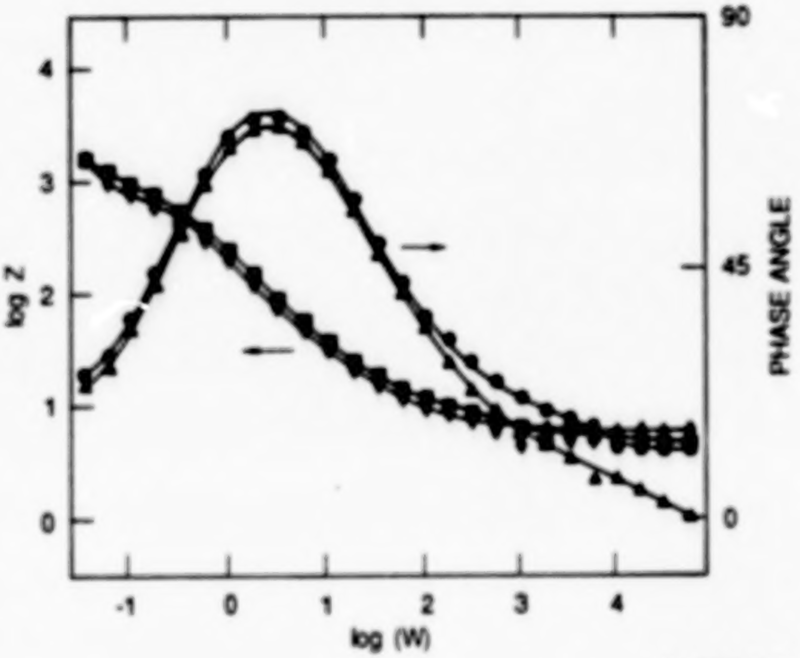

RA-350543-31

FIGURE 19 BODE PLOTS OF IMPEDANCE DATA FOR A SINTERED ELECTRODE AT 60°C AND 0 V AFTER 6(■, ●) AND 172 (♦, ▲) GALVANOSTATIC CYCLES

(26-min. charge to capacity with 14-min discharge to 100% DOD).

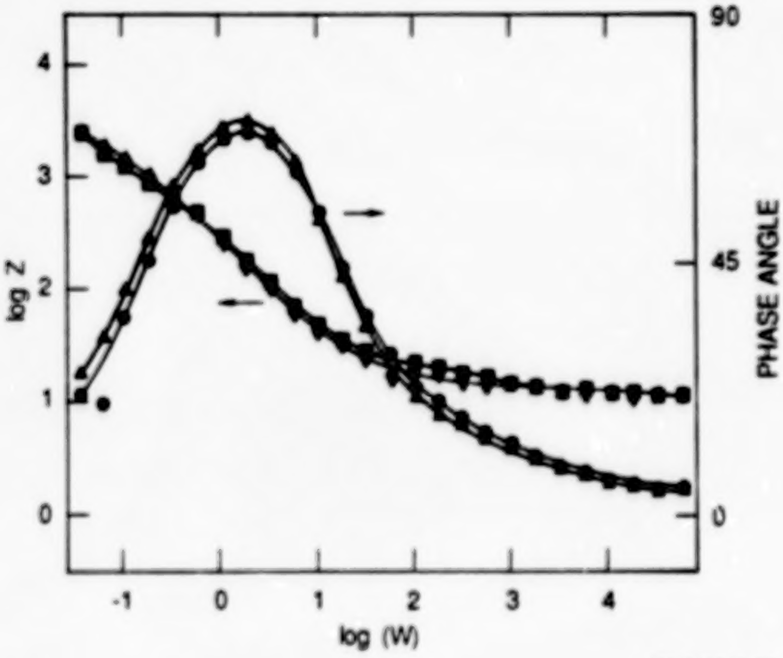

RA-350543-32

FIGURE 20 BODE PLOTS OF IMPEDANCE DATA FOR A SINTERED ELECTRODE AT 23°C AND 0 V AFTER CYCLING AT HIGH CURRENTS(■, ●) AND LOW CURRENTS(♦, ▲)

(High currents = 26-min. charge to capacity with 14-min discharge to 100% DOD; low currents = 80-min charge to capacity and 40-min discharge to 100% DOD).

KOH CONCENTRATION EFFECT ON THE CYCLE LIFE OF NICKEL-HYDROGEN CELLS. IV. RESULTS OF FAILURE ANALYSES

H.S. Lim and S.A. Verzwyvelt
Hughes Aircraft Company
Los Angeles, California 90009

KOH concentration effects on cycle life of a Ni/H_2 cell have been studied by carrying out a cycle life test of ten Ni/H_2 boiler plate cells which contain electrolytes of various KOH concentrations. Failure analyses of these cells were carried out after completion of the life test which accumulated up to 40,000 cycles at an 80% depth of discharge over a period of 3.7 years. These failure analyses included studies on changes of electrical characteristics of test cells and component analyses after disassembly of the cell. The component analyses included visual inspections, dimensional changes, capacity measurements of nickel electrodes, scanning electron microscopy, BET surface area measurements, and chemical analyses. Results have indicated that failure mode and change in the nickel electrode varied as the concentration was varied, especially, when the concentration was changed from 31% or higher to 26% or lower.

INTRODUCTION

Long cycle life has been demanded for a Ni/H_2 cell at deep depth of discharge cycles used in spacecraft applications, especially for a low earth orbit (LEO). We have reported earlier that cycle life of Ni/H_2 cells was improved tremendously by using lower KOH concentrations in electrolyte than conventional 31% KOH[1]. The cycle life has been improved as much as nine times by simply changing the concentration to 26% (by weight) from a conventional value of 31%. A cycle life test has been completed for ten Ni/H_2 cells containing electrolytes of various KOH concentrations ranging from 21 to 36%. In the present paper, we report failure analysis results of these cells which include studies on changes of cell performance and cell components after cell disassembly. We have also studied electrochemical behavior of the cycled nickel electrodes. This result will be reported later.

EFFECTS OF KOH CONCENTRATION ON CYCLE LIFE

A cycle life test was carried out in a 45-min LEO regime at 80% depth of discharge on ten Ni/H_2 boiler plate cells containing electrolytes of 21 to 36% KOH. Test period covered 3 years and 8 months and accumulated up to 39,573 life cycles. Details of the cycle regime have been reported earlier.[1] Life test results are summarized in Table 1. All cells of relatively short cycle life (BP3 to 6) failed by low end-of-discharge voltage (EODV), while all cells of long cycle life (BP1, 2, 9, and 10) failed the cycling test due to a "soft" short formation which was indicated by rapid self-discharge. Fully charged cells discharged completely in 30 to 35 h. The effect of the concentration on cycle life is shown in Figure 1 and 2. The cycle life to 0.9 V of EODV peaked at 26% KOH showing tremendous improvement (about nine times) over the conventional electrolyte of 31% KOH, but the life decreased sharply when the concentration was lowered further below 26%. If the voltage criteria for failure was lowered to 0.5 V, however, KOH concentrations as low as 21% also gave the extreme long life (Fig. 2). This rather drastic change in cycle life by a small change in the voltage criteria was due to development of a large capacity having a low discharge voltage (about 0.8 V) plateau which is often refered as "the second plateau."[illegible]

TABLE 1. LIFE TEST RESULTS OF Ni/H$_2$ CELLS AT 80% DEPTH-OF-DISCHARGE

CELL NO.	[KOH] %	NO.CYCLE TO 0.9 V	NO.CYCLE TO 0.5 V	TOTAL NO.CYCLES	FAILURE MODE
BP1	21	5,047	>38,191	38,191	SOFT SHORT
BP2	26	39,230	>39,573	39,573	SOFT SHORT
BP3	26	4,329	9,241	9,241	LOW EODV
BP4	31	2,979	3,275	3,286	LOW EODV
BP5	31	3,620	4,230	4,230	LOW EODV
BP6	36	1,268	1,845	1,845	LOW EODV
BP7*	21	1,037	6,508	9,402	LOW EODV
BP8	26	>30,549	>30,549	30,549	REMOVED
BP9	26	23,598	>24,594	24,594	SOFT SHORT
BP10	23.5	4,803	28,495	28,495	SOFT SHORT

* CYCLED AT 70% DEPTH-OF-DISCHARGE (DOD) FROM 1644 TO 4644 CYCLES AND AFTER 6508 CYCLES.

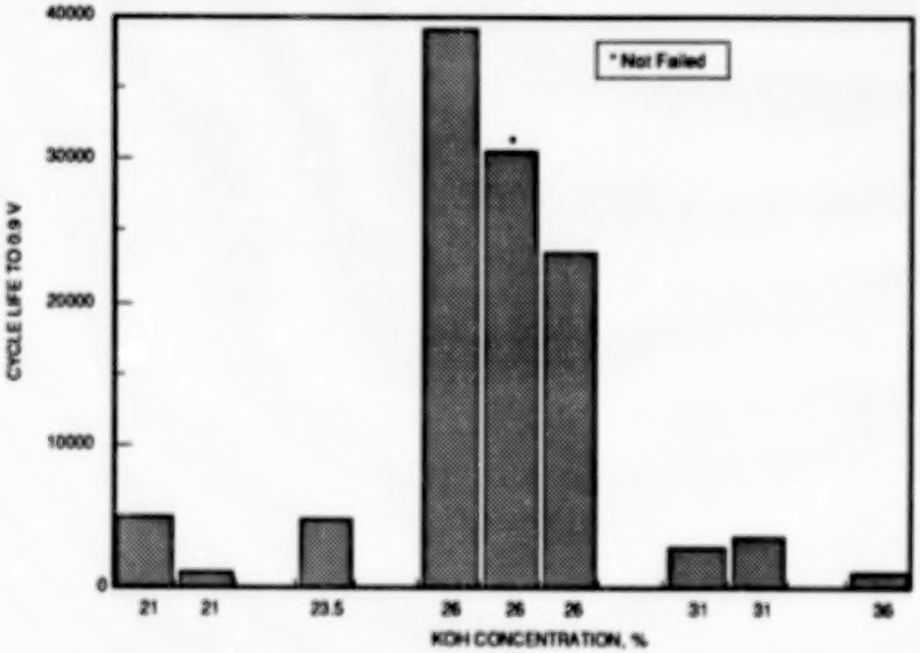

FIGURE 1. COMPARISON OF CYCLE LIFE TO 0.9 V OF Ni/H$_2$ CELLS WITH VARIOUS KOH CONCENTRATIONS IN THE ELECTROLYTE.

CHANGE OF CELL CHARACTERISTICS AFTER LIFE TEST

A series of duplicate to triplicate capacity measurements were carried out before and after the cycle life test using various charge and discharge rates in order to evaluate the rate effects on cell capacity. The charge rate effect was studied by measuring cell capacity at C/2 discharge rate to 1.0 V after charging them at C/10 rate for 16 h, C/2 rate for 160 min, C rate for 80 min, and 2C rate for 40 min, respectively. The discharge rate effect was studied by measuring cell capacity at various discharge rates (C/10, C/2, 1.0C, 1.37C, 2.0C, 2.74C, and 4.0C) to 1.0 V after charging them at C rate for 80 min. Internal resistance of cells was evaluated from mid-discharge voltages at various discharge rates.

Charge Rate Effects on Cell Capacity - Initial and end-of-life (EOL) capacity values are plotted against charge rates in Figure 3 and 4. The capacities of all cells improved as the charge rate increased from 0.1 to 0.5 C rate. This trend was more pronounced after the cycle test. Further increase in charge

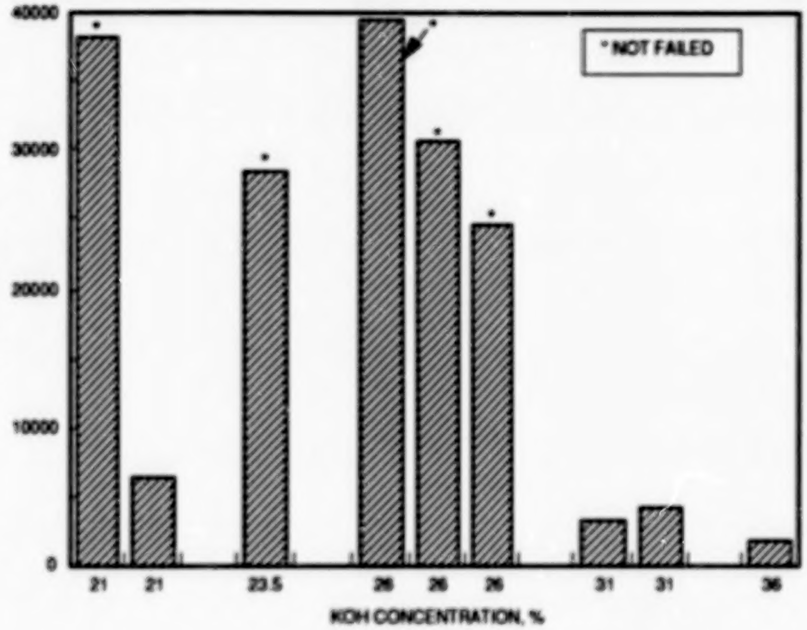

FIG. 2. COMPARISON OF CYCLE LIFE TO 0.5 V OF Ni/H_2 CELLS WITH VARIOUS KOH CONCENTRATIONS IN THE ELECTROLYTE.

rate over 0.5 C did not affect capacity of cells with high KOH concentrations (31 and 36%) while capacity of cells with low KOH concentrations improved slightly at 1 C rate. Capacities of all cells leveled off for the charge rates between 1 and 2 C. Although absolute values of the capacity decreased after life test with exception of BP8 and 10, general pattern of the charge rate dependence did not change with the cycle test.

Effects Of Discharge Rates On Capacity - Initial and EOL capacity values are plotted against discharge rates in Figure 5 and 6. Capacity of cells in general decreased slightly as discharge rate increased. This dependence of the capacity on discharge rate became more pronounced after the life test. We had also observed such dependence earlier with another group of 31% KOH cells.[2]

Cell Resistance - Plots of mid-discharge voltages (measured during the initial and EOL capacity tests) against the discharge current gave good straight lines as shown in Figure 7 for an illustration. The slopes of these lines represent the values of cell resistance. The cell resistances before and after the cycle life test are summarized in Table 2. Cell resistance did not appear to have changed significantly after the cycle life test except for BP1, BP3, and BP10. BP1 showed a significant reduction of the resistance. BP3 which had a defective current collector tab on one of the H_2 electrodes showed a significant increase. Overall, the change in the cell resistance with cycling appear to be too small to account either for the change of capacity dependence on discharge rate or to be the cause of cell failure.

COMPONENT ANALYSES AFTER CELL TEARDOWN

After the post-life-test capacity measurements, test cells were charged for 80 min at C rate and then discharged at C/2 rate to 0.5 V followed by shorting them with a 1.0-Ω resistance for a minimum of 24 h before disassembly of the cells for component study. This study included visual inspections during the

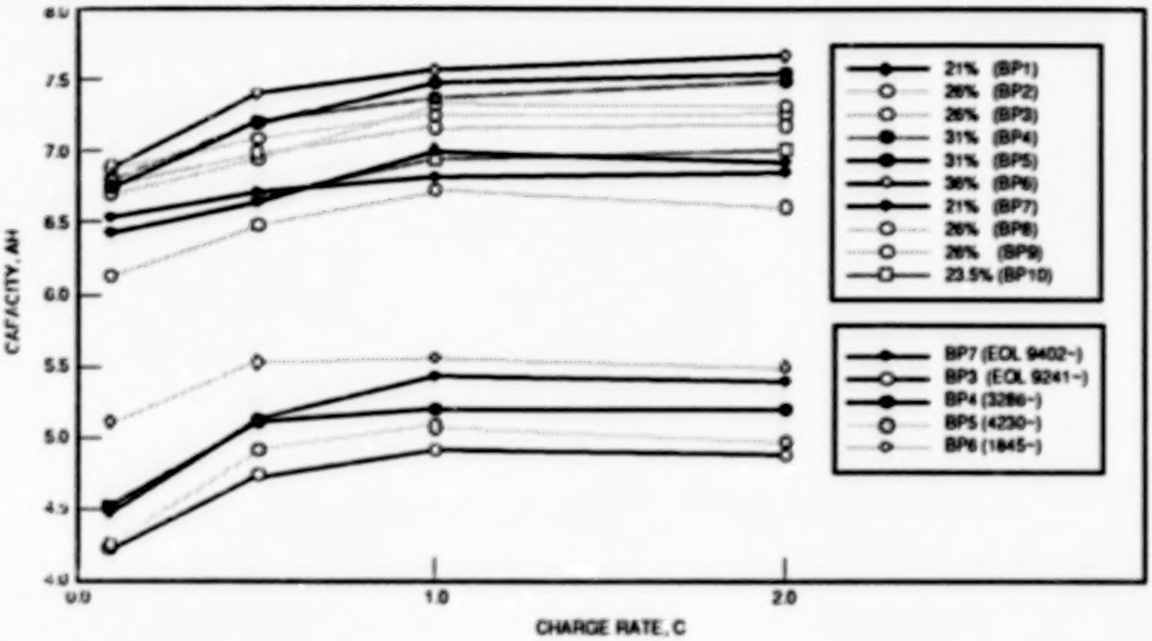

FIGURE 3. PLOTS OF INITIAL AND EOL CAPACITIES VS. CHARGE RATES. CAPACITY WAS MEASURED BY 0.5 C RATE DISCHARGE TO 1.0 V AFTER CHARGING AT VARIOUS RATES: 0.1 C RATE FOR 16 H, 0.5 C FOR 160 MIN., 1.0 C FOR 80 MIN., OR 2.0 C FOR 40 MIN.

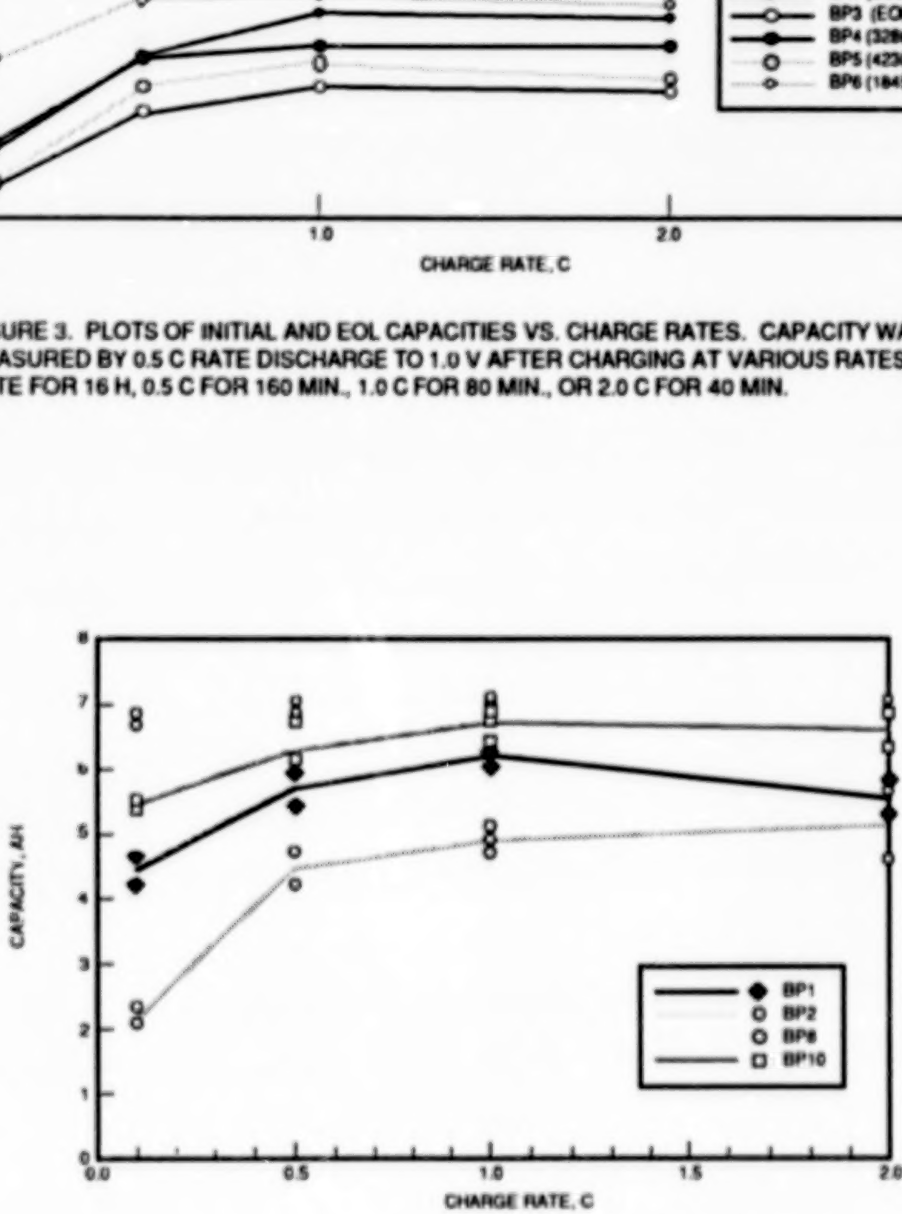

FIGURE 4. PLOTS OF EOL CAPACITIES VS CHARGE RATES. CAPACITY WAS MEASURED BY 0.5 C RATE DISCHARGE TO 1.0 V AFTER CHARGING AT VARIOUS RATES: 0.1 C RATE FOR 16 H, 0.5 C FOR 160 MIN., 1.0 C FOR 80 MIN., OR 2.0 C FOR 40 MIN.

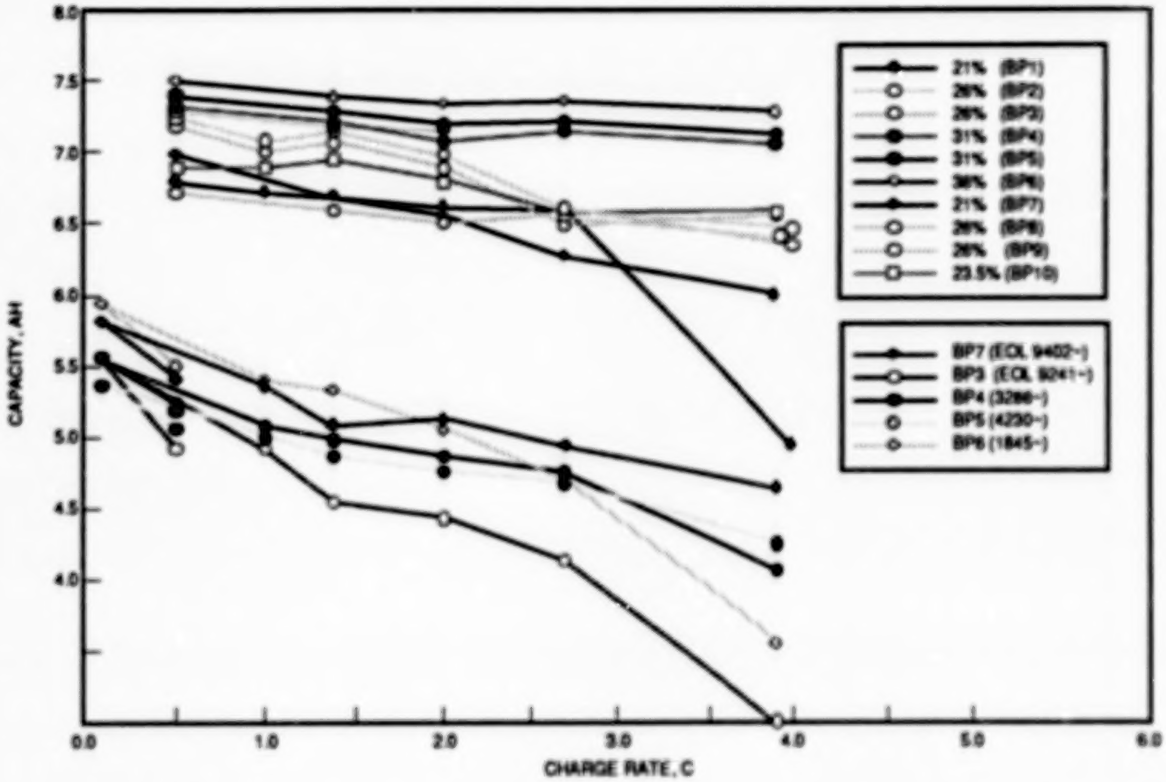

FIGURE 5. PLOTS OF INITIAL AND EOL CAPACITIES VS. CHARGE RATES. CAPACITY WAS MEASURED BY DISCHARGING CELLS AT VARIOUS RATES TO 1.0 V AFTER 1.0 C RATE CHARGE FOR 80 MIN.

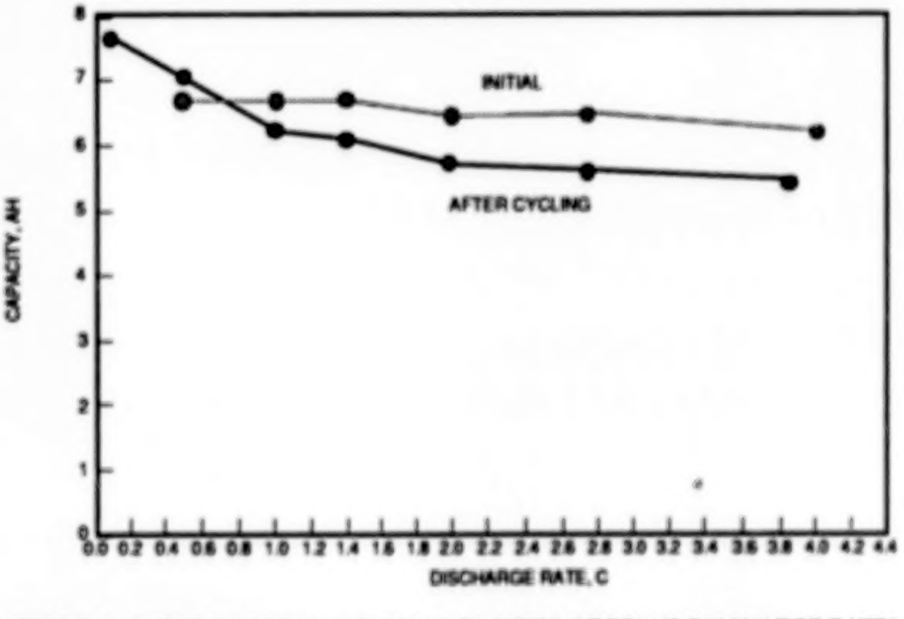

FIGURE 6. PLOTS OF INITIAL AND EOL CAPACITIES OF BP8 VS DISCHARGE RATES. CAPACITY WAS MEASURED BY DISCHARGING THE CELL AT VARIOUS RATES TO 1.0 V AFTER 1.0 C RATE CHARGE FOR 80 MIN.

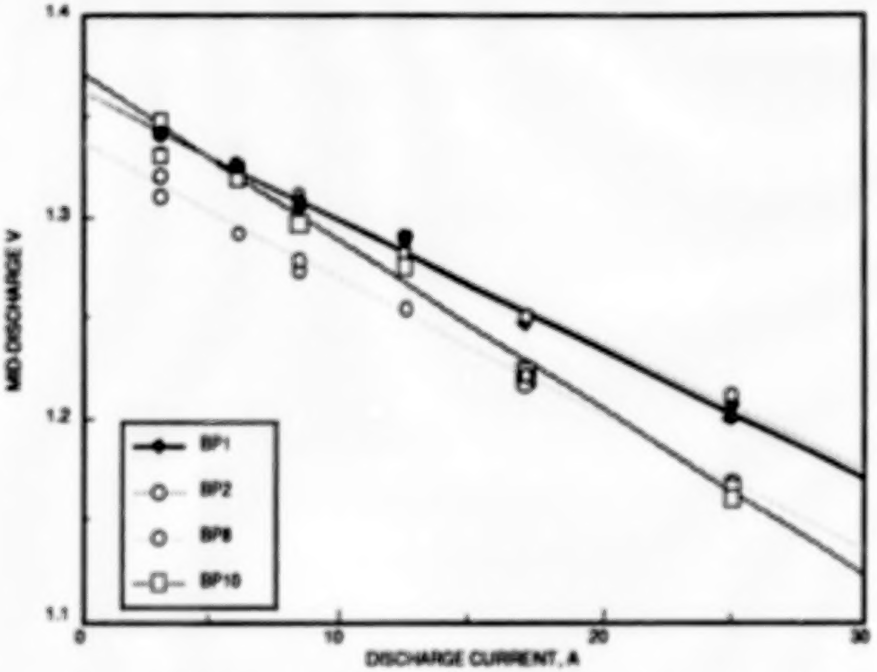

FIGURE 7. PLOTS OF MID-DISCHARGE VOLTAGES OF TEST CELLS VS DISCHARGE RATES FOR END-OF-LIFE PERFORMANCE TEST.

TABLE 2. CELL RESISTANCE (R) MEASURED FROM MID-DISCHARGE VOLTAGES.

CELL NO.	KOH %	NUMBER OF CYCLES	INITIAL R mΩ	EOL R mΩ	CHANGE mΩ	CELL P* PSIG
BP1	21.0	38,191	10.83	6.36	- 4.47	615
BP2	26.0	39,573	(5.89)	6.26	+ 0.37	705
BP3	26.0	9,241	7.53	9.69	+ 2.16	130
BP4	31.0	3,286	7.15	8.26	+ 1.11	150
BP5	31.0	4,230	7.09	6.96	- 0.13	225
BP6	36.0	1,845	7.61	8.49	+ 0.88	160
BP7	21.0	9,402	7.30	7.14	- 0.16	130
BP8	26.0	30,549	6.59	6.71	+ 0.12	0
BP10	23.5	28,495	6.57	8.24	+ 1.67	635

* PRESSURE PRIOR TO DISASSEMBLY.

disassembly, electrode thickness measurements (without washing and drying), scanning electron microscopy (SEM) of the cross-section of cell stacks, surface area measurements using BET technique, measurements of nickel electrode capacity and discharge voltages in flooded electrolyte cells, and chemical analyses of the nickel electrodes.

Visual Inspections - Conditions of cell stack and its components have been inspected carefully during disassembly of cycled cells. These inspections included wetness of components, degree of loose black nickel active material ("black powder") on cell components, penetration of the active material through the separator, adhesion of hydrogen electrode to gas screen, and integrity of nickel and hydrogen electrodes. Observations which appear to be important are summarized as follows:

- Wetness of the electrode and the degree of "black powder" formation increased noticeably as one approached the bottom of the stack (no.6 unit cell) from the top (no.1 unit cell). The observation on wetness change indicated that gravitational effect on the electrolyte distribution is substantial even in this relatively short stack. The observation on "black powder" formation appears to indicate that a wetter unit cell might have been used more heavily than a drier unit cell.

- Electrodes from BP7 (21% KOH; 9402 cycles) showed noticeably less "black powder" on the adjacent separator and in gas screen than those from high KOH concentration cells which had lower number of cycles. The black powder in the gas screen was found only in the peripheral area of the stack with BP7 while it was found all over the screen with the other cells which were cycled less than BP7. However, the 21% KOH cell (BP1; 38,191 cycles) which were cycled much longer showed heavy black powdering. It appears that rate of black powder formation is reduced as KOH concentration decreased.

- Electrical lead (tab) of #5 H_2 electrode of BP3 was not firmly attached (defective weld) to the electrode while its paired nickel electrode and separator appeared new (almost without the black powder). This observation strongly indicates that the cause of the poor performance of this cell from the beginning was due to this poor electrical contact. The BP3 should be considered as an anomalous cell.

- All nickel electrodes from cells which had extremely long cycle life ($\geq$24,594 cycles) showed "mushy" appearance indicating that some active material has loosened and squeezed out of the sinter structure. This indication was confirmed by scanning electron microscopic (SEM) pictures as will be discussed later in this report.

- All cells which had extremely long cycle life ($\geq$24,594 cycles) showed the following: Outer edges of gas screen were welded to Teflon layer of the H_2 electrodes. Damage with partially lost electrode material were apparent on parts of peripheral area of electrode stacks. The outer coined nickel electrodes was badly eroded. These observations indicated that violent recombinations of O_2 with H_2 had occurred around peripheral area of electrode stacks during the cycling test period.

Pressure Changes - Gas pressure of test cells in the fully discharged state were measured just before their disassembly using a mechanical pressure gauge. This was done in order to determine the net pressure change during the cycle life test. Gas composition was analyzed using a gas chromatograph. Gases in all cells were pure hydrogen within experimental error. Results on pressure readings are shown in Table 2. Long cycled cells (BP1, 2, and 10) showed roughly 470 psi higher pressure than those of relatively short cycle life (BP4, 5, and 6). (BP8 might have leaked slowly.) Although the long term sealing reliability of presently used boiler plate cell cases was questionable as discussed earlier,[16] the pressure increase in long cycled cells has be real. This pressure increase appears to be due to nickel corrosion from the sintered plaques probably according to equation (1):

$$Ni + 2H_2O \longrightarrow Ni(OH)_2 + H_2 \qquad (1)$$

Dimensional Changes of Stack Components - Thickness of nickel electrodes was measured by a micrometer at three different locations on each electrode before and after cycling. The thickness after cycling was measured both before and after rinsing out the electrolyte and drying. These two values agreed with each other within experimental error. The average values of these measurements for each electrode are tabulated in Table 3. Long cycled electrodes (BP2 and BP8) showed expansion values up to 80% of the original thickness. These long cycled electrodes showed heavy extrusion of active material out of the electrode into voids of the gas screen. Typically imprints of gas screen are clearly visible when gas screen is separated from the electrode. The high value of expansion (up to 80%) was due to contribution of this extruded material.

Average expansion values of electrodes from individual cells are plotted against number of cycles in Figure 8. The expansion values appear to fall on a straight line eventhough the individual cells have different KOH concentrations. This observation appears to indicate that the expansion rate on long term cycling is rather insensitive to KOH concentration which is contrary to our earlier understanding.[3,4,5] The expansion itself does not appear to be the main cause of electrode or cell failure.

TABLE 3. NICKEL ELECTRODE EXPANSION AFTER CYCLE TEST IN NI/H_2 CELLS WITH VARIOUS KOH CONCENTRATIONS.

CELL (%KOH) (CYCLE NO)	ELECTRODE I.D.	THICKNESS AFTER CYCLING,* MM	THICKNESS BEFORE CYCLING, MM	EXPANSION* %
BP1 (21%) (31,191)	28-05(#1, TOP)	1.166	0.761	53.4
	28-04(#2)	1.141	0.758	50.5
	24-03(#5)	1.268	0.737	71.8
	24-01(#6, BOTTOM)	1.225	0.751	63.2
BP2 (26%) (39, 573)	20-01(#1)	1.310	0.732	79.0
	20-02(#2)	1.274	0.739	72.5
	19-05(#5)	1.341	0.737	81.8
	19-06(#6)	1.327	0.735	76.1
BP3 (26%) (9641)	25-01(#1)	0.930	0.768	21.1
	26-02	0.933	0.744	25.3
	35-03(AN)	0.762	0.750	1.6
	35-04(#6)	0.947	0.753	25.7
BP4 (31%) (3275)	25-09(#1)	0.837	0.727	15.1
	26-03	0.814	0.732	11.2
	26-09	0.819	0.755	8.5
	27-07 (#6)	0.778	0.744	4.6
BP5 (31%) (4230)	22-02 (#1)	0.809	0.738	9.6
	22-03	0.814	0.732	13.6
	22-09	0.785	0.721	8.9
	20-03 (#6)	0.758	0.755	0.4
BP6 (36%) (1845)	27-03(#1)	0.816	0.744	9.6
	27-05	0.777	0.720	7.8
	35-08	0.785	0.724	8.4
	35-09(#6)	0.771	0.723	6.7
BP7 (21%) (9402)	05-05(#1)	0.876	0.748	17.2
	05-06(#2)	0.916	0.746	22.7
	21-07(#3)	0.929	0.755	23.1
	21-08(#4)	0.949	0.755	25.6
BP8 (26%) (30,549)	21-05(#1)	1.225	0.728	68.2
	21-01(#2)	1.286	0.762	68.7
	03-06(#5)	1.297	0.727	78.4
	03-02(#6)	1.304	0.719	81.3
BP9(26%) (24,594)	03-03(#1)	1.217	0.736	65.4
	04-07(#2)	1.229	0.735	63.2
	04-07(#5)	1.233	0.741	66.4
	06-07(#6)	1.208	0.752	60.6
BP10 (23.5%) (28,495)	04-03(#1)	1.330	0.751	77.2
	16-05(#2)	1.281	0.736	74.1
	16-02(#5)	1.353	0.760	78.0
	16-09(#6)	1.285	0.746	72.1

* MEASURED VALUES INCLUDE EXTRUDED ACTIVE MATERIAL INTO VOIDS OF GAS SCREEN.

Thickness of stack components including separator and gas screen was also measured from SEM picture of cross-section of cell stack. The results are shown in Figure 9 as a function of the number of cycles. Dimension of unit cell was generally unchanged with cycling. Nickel electrode expansion was again roughly linear with the number of cycles. Separator and gas screen were compressed as the nickel electrode expanded.

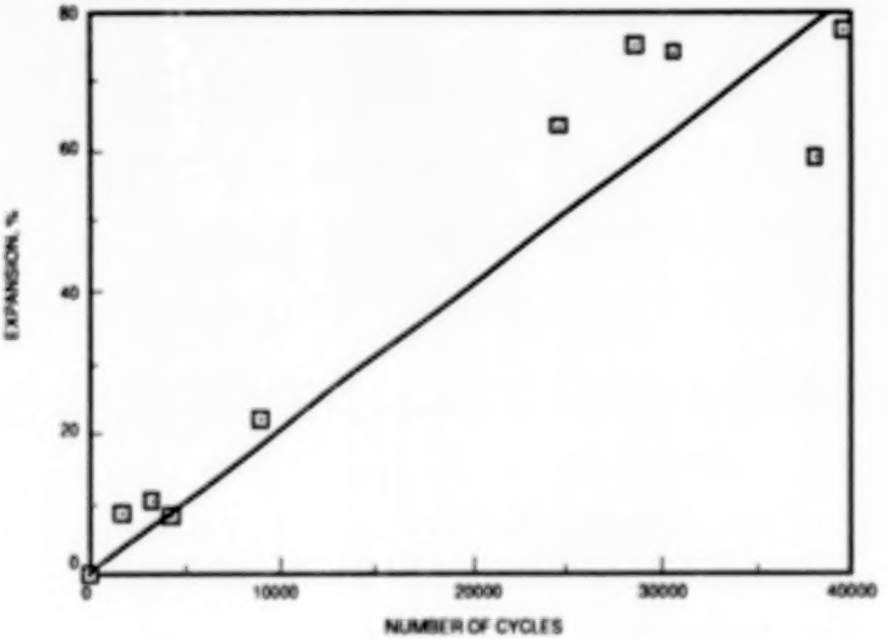

FIGURE 8. A PLOT OF NICKEL ELECTRODE EXPANSION VS. NUMBER OF CYCLES.

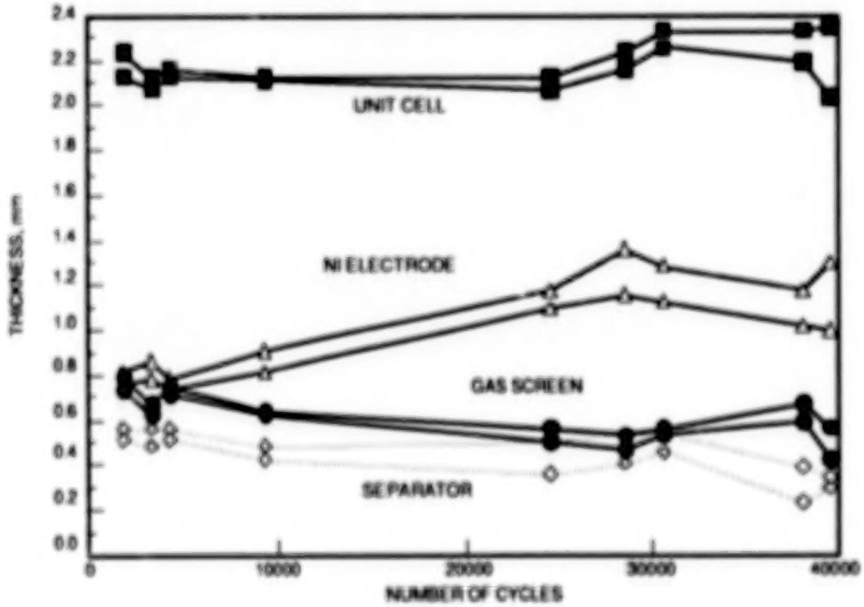

FIGURE 9. PLOTS OF CELL STACK COMPONENTS
THICKNESS AS A FUNCTION OF CYCLING.

TABLE 4. FLOODED CAPACITIES OF NICKEL ELECTRODES FROM CYCLED CELLS. #1: TOP ELECTRODE OF THE STACK. #6 BOTTOM ELECTRODE OF THE STACK. A NEW ELECTRODE HAD 1.24 AH FOR AN AVERAGE VALUE.

CELL NO. %	KOH CONC.	CAPACITY OF #1 ELECTRODE, AH				CAPACITY OF #6 ELECTRODE, AH				CAPACITY RATIO #6 / #1
		1ST	2ND	3RD	AV.	1ST	2ND	3RD	AV.	
BP1	21	1.17	1.18		1.18	1.24	1.24		1.24	1.05
BP2	26	1.18	1.17		1.17	1.25	1.24		1.25	1.07
BP3	26	0.99	1.00	1.00	1.00	0.70	0.69	0.70	0.70	0.70
BP4	31	1.16	1.11	1.12	1.13	0.73	0.77	0.79	0.76	0.67
BP5	31	0.98	0.96	0.98	0.97	0.69	0.70	0.71	0.70	0.72
BP6	36	0.98	1.08	1.17	1.08	0.69	0.81	0.81	0.77	0.72
BP7	21	0.95	0.93	0.93	0.94	1.01	1.02	1.01	1.01	1.08
BP8	26	1.21	1.15		1.18	1.13	1.11		1.12	0.95
BP10	23.5	1.26	1.26		1.26	1.24	1.24		1.24	0.98
(AFTER CHANGING ELECTROLYTE)										
BP1	31	1.11	1.10		1.11	1.16	1.15		1.16	1.04
BP2	31	1.13	1.23		1.18	1.16	1.15		1.16	0.98
BP3	31	1.02	1.04	1.03	1.03	0.75	0.77	0.77	0.76	0.74
BP4	31	1.14	1.14	1.14	1.14	0.79	0.80	0.80	0.80	0.70
BP5	31	1.01	1.03	1.03	1.02	0.72	0.72	0.72	0.72	0.72
BP6	31	1.04	1.04	1.03	1.04	0.69	0.70	0.70	0.70	0.68
BP7	31	1.02	1.06	1.05	1.04	1.03	1.09	1.08	1.07	1.03
BP8	31	1.21	1.20		1.21	1.06	1.05		1.06	0.88
BP10	31	1.21	1.20		1.21	1.21	1.20		1.21	1.00

Electrode Capacity in a Flooded Cell - Capacities of two nickel electrodes from each failed cell were measured in a flooded cell at C/2 discharge rate after charging C/10 for 18 to 19 hours. One electrode was from the top of the cell stack (#1) and the other was from the bottom of the stack (#6). Two to three capacities were measured in an electrolyte of the same KOH concentration as the original test cell and then all electrolytes were changed with 31% KOH for additional three capacities. The results are summarized in Table 4. With and exception of BP3 which was an anomalous cell, the capacity loss of nickel electrodes in low KOH concentration (21 to 26%) cells was relatively low and independent of the electrode position (#1 or #6) despite long cycling. With higher KOH concentrations (31 to 36%), however, the capacity of bottom (#6) nickel electrode was roughly 30% smaller than top (#1) electrode of the same cell. It appears that the cause of this faster degradation of the electrodes from the bottom (#6) than those from the top (#1) of the stack was originated from the variation of the electrolyte content from the top to the bottom. Cell teardown showed that the bottom part (#6) of the stack had much more electrolyte than the top part (#1) due to gravitational segregation. The wetter electrode pair (#6) is expected to pass higher current throughout the cycle test than the drier pair (#1) which was in parallel electrical connection. This uneven current distribution would have caused heavier usage of the #6 electrode than the #1. This heavy usage appears to cause a severe capacity decrease in higher KOH concentrations while the decrease is relatively minor in low KOH concentrations. No apparent relationship was found between the capacity decrease and the electrode expansion.

Chemical Analyses - Chemical Analyses results of electrolyte composition of cycled cells are shown in Table 5. The overall electrolyte concentrations in long cycled cells (BP2, BP8, and BP10) was increased by 3 to 4% from the initial value, indicating possible nickel plaque corrosion. Carbonate concentration which was negligible initially increased slightly in all cycled cells. The amount of carbonate build-up was roughly proportional to logarithmic number of cycles as shown in Figure 10. A possible source of carbonate might be corrosion of plaque which may contain about 0.1 % (by wt.) of carbon because it is made of carbonyl nickel powder (INCO Type 287).[6]

TABLE 5. COMPOSITION OF ELECTROLYTE FROM CYCLED CELLS.

CELL NO.	INITIAL CONC. OF KOH, %	KOH, % AS KOH	K_2CO_3, % AS KOH	TOTAL K^+ ION, % AS KOH	SAMPLING TECHNIQUE
BP2	26	25.5	5.27	30.77	SOXHLET*
BP3	26	23.6	2.7	26.3	BOTTOM OF CELL
BP4	31	28.0	3.3	31.3	BOTTOM OF CELL
BP6	36	33.2	2.5	35.7	BOTTOM OF CELL
BP7	21	17.3	4.0	21.3	BOTTOM OF CELL
BP8	26	24.03	5.07	29.1	SOXHLET*
BP10	23.5	21.6	5.1	26.7	SOXHLET*

* SOXHLET EXTRACTION OF #3 & 4 UNIT CELLS.

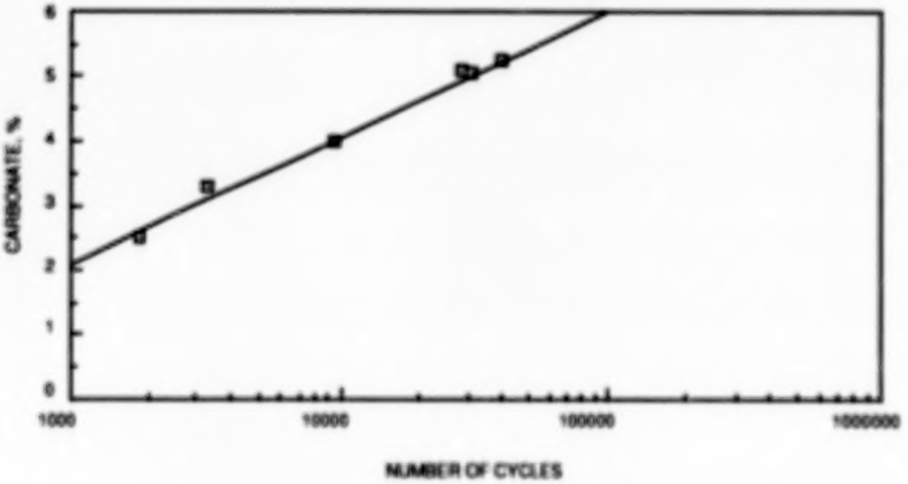

FIGURE 10. A PLOT OF CARBONATE BUILD-UP VS. NUMBER OF CYCLES.

TABLE 6. RESULTS OF CHEMICAL ANALYSES OF NEW AND CYCLED NICKEL ELECTRODES FROM BP CELLS. NUMERICAL VALUES IN THIS TABLE INDICATE AMOUNTS IN MMOLES/G OF ACTIVE MASS

	NEW 27-08	BP1	BP2	BP4	BP6	BP8	BP10
NI° (SINTER)							
TITRATION (A)	8.29	4.92	3.70	7.79	8.41	4.99	4.59
AA	8.20	4.59	3.27	6.49	7.47	4.59	4.20
NI (II&III); TITRATION (B)	4.90	7.24	8.10	5.14	4.77	7.32	7.19
CO (II&III); AA	0.67	0.55	0.57	0.61	0.57	0.57	0.59
NI (III)	1.50	0.90	1.78	0.58	0.80	2.60	1.40
TOTAL NI & CO TITRATION	13.40	12.06	11.94	12.20	12.56	12.23	11.87
(A) + (B)	13.19	12.16	11.80	12.93	13.18	12.31	11.78
(A) / [(A)+(B)], %	62.85	40.46	31.36	60.25	63.81	40.54	38.96

Chemical Analyses results of new and cycled nickel electrodes from test cells are shown in Table 6. Active material content (amount of total ionic Ni and Co in nickel electrode) is plotted against number of cycles in Figure 11. This content increased with cycling indicating that nickel plaque may be corroded gradually with cycling. Experimental data fit roughly to a linear corrosion rate of 0.1 Å/cycle (Curve A of Fig. 11).

In order to see if Pt was carried over the nickel electrode from adjacent H_2 electrode in BP cells in which soft shorts were developed. Elemental analyses (spectrographic) was carried out on outer edge of nickel electrodes from a few cycled cells. Analysis results of a nickel electrode from BP9 showed a considerable amount of Pt (0.25%) while Pt was not detected from a new electrode and detected only in trace level (less than 0.01%) in electrodes from BP2 and BP5. Considering both BP2 and BP9 had soft shorts, this non-uniform distribution of Pt might be due to a violent O_2 recombination ("popping") at peripheral edge as a probable mechanism of Pt migration.

Scanning Electron Microscope (SEM) - SEM pictures of a cross-sectional view of cell stack components were taken as a part of the failure analyses. Sample pictures of the components from cycled cells are shown in Figures 12, 13, and 14. BP6 (36%), which failed after relatively short cycling (1845 cycles), showed no apparent sign of expansion or deformation of stack components. However, long cycled cells, BP9 and BP2 (24,594 and 39,573 cycles, respectively) showed signs of heavy nickel electrode expansion, nickel active material migration, rupture of nickel sinter substrate, and deformation of other components such as separator, H_2 electrode, and gas screen material. It is interesting to note that despite the heavy expansion and sinter rupture in the long cycled electrodes, they suffered relatively small capacity decrease indicating that these changes are not direct causes of the electrode failure.

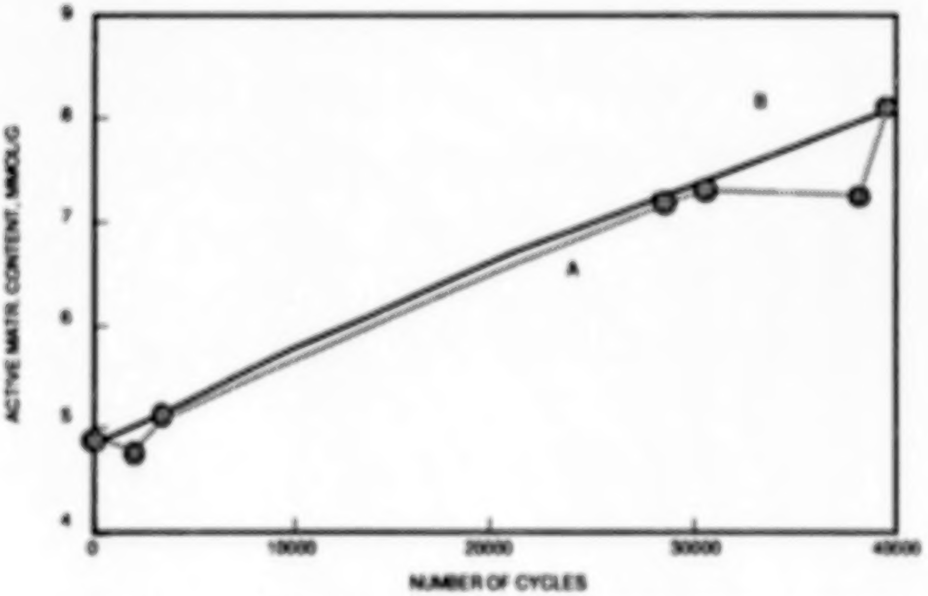

FIGURE 11. A PLOT OF ACTIVE MATERIAL CONTENT (TOTAL IONIC NICKEL AND COBALT) OF NICKEL ELECTRODE VS NUMBER OF CYCLES.

DISCUSSIONS

Cycle life of a nickel electrode increased greatly as the KOH concentration decreased in the electrolyte, although initial capacity of a nickel electrode decreases slightly as the concentration decreases reported earlier[16]. The cycle life increased more than twice when the concentration was decreased from 36 to 31%. Although results with very low KOH concentration (21 to 23.5%) was complicated due to unusable low voltage secondary plateau formation[15], the cycle life improved roughly nine times when the concentration was reduced to 26% from conventional value of 31%.

The failure mechanisms of a Ni/H_2 cell with a low KOH concentration (26% or lower) and one with a high KOH concentration (31% or higher) appears to be different from each other. High concentration cells failed on cycling by a gradual fading of nickel electrode capacity after relatively small number of cycles (1845 to 4230), while low concentration cells failed on cycling after a large number of cycles (mostly 25,000 to 40,000) by a "soft" short formation without an excessive capacity decrease of nickel electrodes. As a result of the tremendous difference in the number of cycles, heavy electrode expansion and active material migration and extrusion were observed in the long life low KOH concentration cells, but relatively small physical changes are present in the failed nickel electrodes in the high KOH concentration cells. However, we have observed much less "black powder" formation in BP7 (21% KOH) after 9402 cycles than in BP4 (31% KOH), BP5 (31% KOH), and BP6 (36% KOH) which were tested for less than half as many cycles as BP7, indicating that some physical changes occur at much reduced rate in low KOH concentrations.

The observation that no significant internal resistance change of cells despite heavy electrode expansion causing sinter rupture and active material migration and extrusion appears to indicate that the conductivity of nickel sinter may not be the controlling factor in electrode failure. We speculate that the capacity fading mechanism might involve crystallographic and micro morphological changes of active material. All long life cells failed eventually on cycling due to a "soft" short formation without an excessive capacity decrease of nickel electrodes as shown in Table 4. The positive identification of Pt on a nickel electrode (spectrographic analysis result) appear to indicate that the short might be due to the Pt on nickel electrode. This Pt might act as an hydrogen electrode while it is electrically shorted to the nickel electrode through a layer of high resistance nickel oxide/hydroxide material. An alternate mechanism might involve a short between nickel and hydrogen electrodes via extruded nickel active material in the gas screen area.

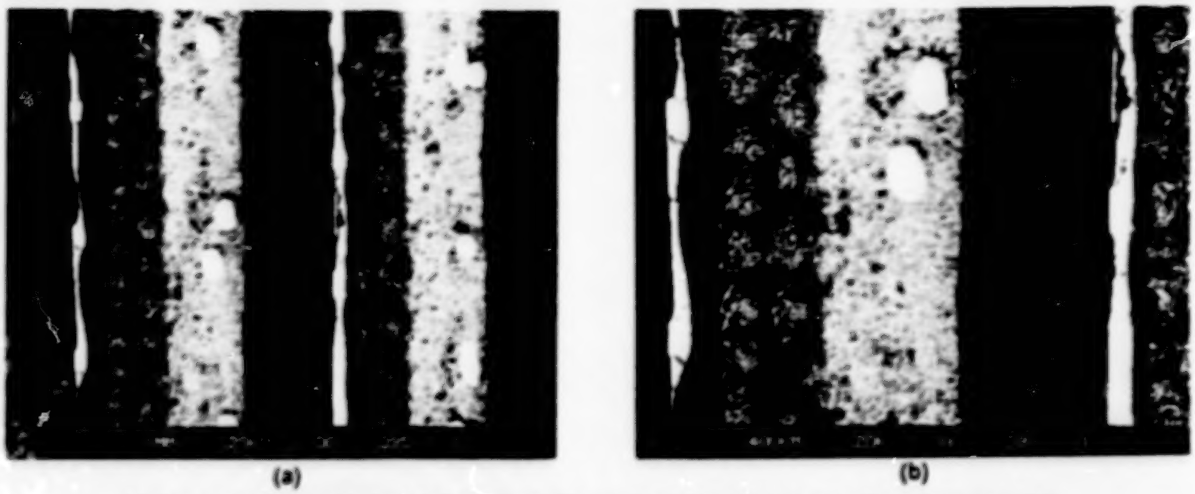

(a) (b)

FIGURE 12. SEM CROSS-SECTIONAL VIEW OF (A) #3 AND #4 CELLS AND (B) EXPANDED VIEW OF LOCAL AREA OF BP6.

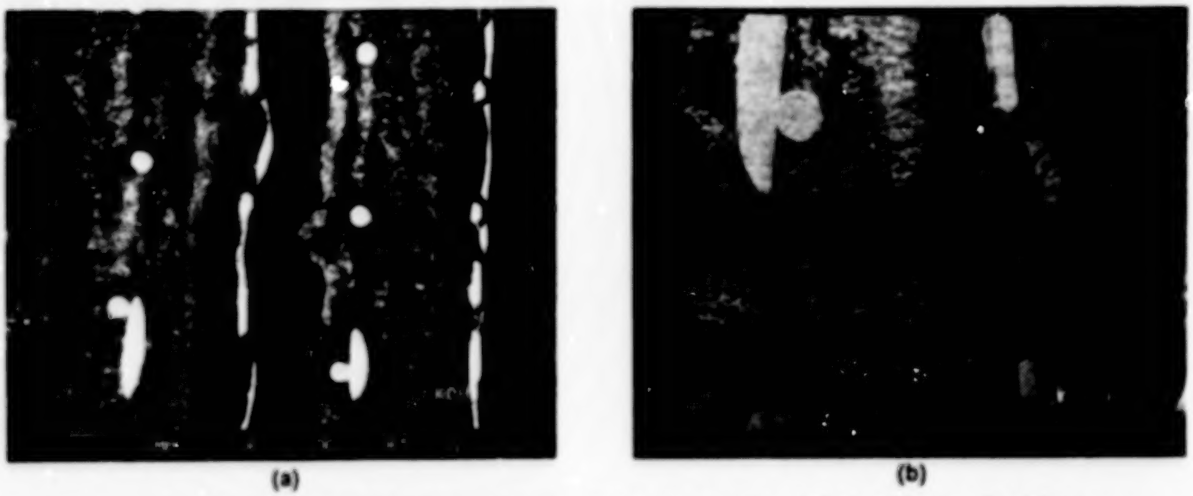

(a) (b)

FIGURE 13. SEM CROSS-SECTIONAL VIEW OF (A) #3 AND #4 CELLS AND (B) EXPANDED VIEW OF LOCAL AREA OF BP9.

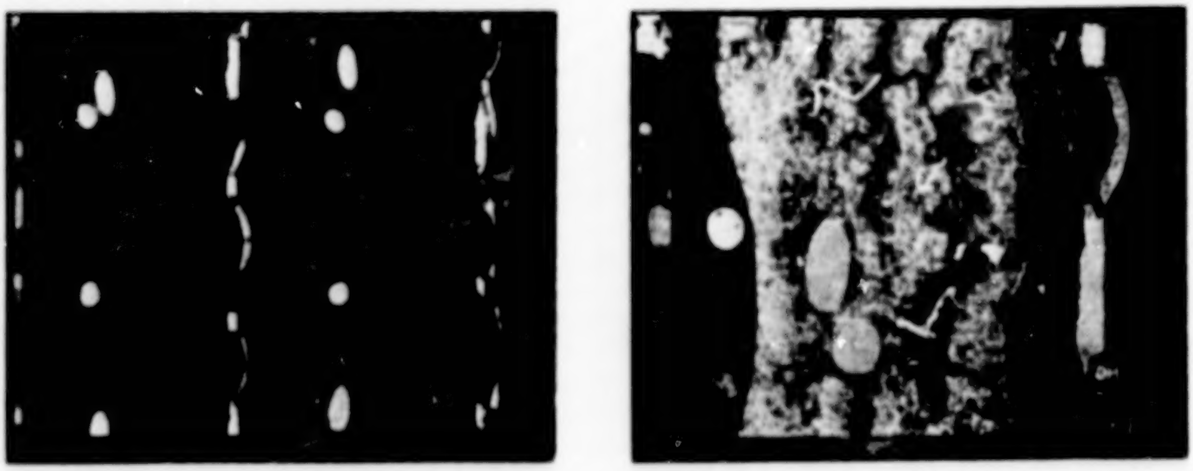

(a) (b)

FIGURE 14. SEM CROSS-SECTIONAL VIEW OF (A) #3 AND #4 CELLS AND (B) EXPANDED VIEW OF LOCAL AREA OF BP2.

ACKNOWLEDGMENT

We would like to acknowledge NASA-Lewis Research Center for its support for this study (Contract NAS 3-22238; Project Manager: John Smithrick).

REFERENCES

1. (a) H. S. Lim and S. A. Verzwyvelt, "KOH Concentration effect on the cycle life of nickel-hydrogen cells." Proc. 20th IECEC, August 1985, p. 1.165. (b) H. S. Lim and S. A. Verzwyvelt, "Cycle life of nickel-hydrogen cells. II. Accelerated cycle life test," Proc. 21st IECEC, August 1986, p. 1601. (c) H. S. Lim and S. A. Verzwyvelt, "KOH concentration effect on the cycle life of nickel-hydrogen cells. III. Cycle life test," J. Power Sources, 22, 213 (1988).

2. (a) H.S. Lim, "Long life nickel electrodes for nickel-hydrogen cells", Final Report of Phase I, NAS 3-22238, NASA Cr-174815. December, 1984; (b) H.S. Lim and S. A Verzwyvelt, "Long life nickel electrodes for a nickel-hydrogen cell: I. Initial Performance," Proc. 18th IECEC, August 1983, p. 1543; (c) H.S. Lim and S. A Verzwyvelt, "Long life nickel electrodes for a nickel-hydrogen cell: Cycle life test," Proc. 31st Power Sources symposium, June 1984, Cherry Hill, NJ. p. 157; (d) H.S. Lim and S. A Verzwyvelt "Long life nickel electrodes for a nickel-hydrogen cell: Results of an accelerated test and failure analyses." Proc. 19th IECEC, August 1984, p. 312

3. H. S. Lim and S. A. Verzwyvelt, 'Nickel electrode expansion and the effect of LiOH additive." Proc. 20th IECEC, August 1985, p. 1.104.

4. M. P. Bernhardt and D. W. Mauer, Proc. 29th Power Sources Conf. 1980, Electrochemical Society, p. 219.

5. P.P. McDermott, "Analysis of Nickel Electrode Behavior in an Accelerated Test." Proceedings of Symposium on the Nickel Electrode, Proc. Vol. 82-4, R. G. Gunther and S. Gross Eds. (The Electrochemical Society, Pennington, NJ, 1982), p. 224.

6 V. A. Tracy, "The properties and some applictions of carbonyl-nickel powdwers," Powder Metallurgy, 9, 54 (1966).

ADVANCES IN LIGHTWEIGHT NICKEL ELECTRODE TECHNOLOGY

Dwaine Coates, Gary Paul and Paul Daugherty
Eagle-Picher Industries, Inc.
Electronics Division
Joplin, Missouri 64802

Studies are currently underway to further the development of lightweight nickel electrode technology. Work is focused primarily on the space nickel-hydrogen system and nickel-iron system but is also applicable to the nickel-cadmium and nickel-zinc systems. The goal is to reduce electrode weight while maintaining or improving performance thereby increasing electrode energy density. Two basic electrode structures are being investigated. The first is the traditional nickel sponge produced from sintered nickel-carbonyl powder. The second is a new material for this application which consists of a non-woven mat of nickel fiber. Electrodes are being manufactured, tested, and evaluated at the electrode and cell level.

INTRODUCTION

Eagle-Picher has been involved in nickel electrode development for a number of years in association with many different battery systems. Our current work with the nickel-hydrogen system dates back to 1969 and has evolved from previous work with aerospace nickel-cadmium and zinc-air battery cells. The goal throughout has been to increase the energy density of the nickel positive electrode (and hence the battery) while maintaining a satisfactory level of performance. For space applications, performance includes sufficient useful life as well as cell electrical characteristics.

The goal of increasing cell energy density provided the original impetus for the development of the nickel-hydrogen system. Replacing the heavy cadmium negative electrode of the nickel-cadmium cell with a lightweight catalytic gas electrode provided a substantial savings in weight. Nickel-hydrogen cell designs have been continuously refined over the years to remove even more system weight. However, cell pressure vessels and structural components can be reduced in weight only to a finite degree due to safety considerations and launch dynamics requirements. Common pressure vessel battery designs hold some promise for further weight reductions but are not currently being used in production programs.

The best opportunity for further weight savings without serious deviation from existing flight cell designs would appear to lie in the electrochemically active cell components. The nickel electrodes account for about forty percent of the total finished weight of a current design flight production nickel-hydrogen cell. Therefore even a small increase in the energy density of the electrode would amount to a substantial benefit at the cell and battery level.

The nickel electrode consists of two basic components. These are the active material and the support matrix. Active material utilization has been optimized in past efforts and probably can't be increased much past current levels. The most likely opportunity for weight reduction is in the structural matrix of the electrode which houses the active material. For conventional sintered nickel-carbonyl powder electrodes this would require producing a higher porosity matrix, a lighter weight current collector/substrate, or a thicker electrode. Use of a nonwoven mat of nickel fibers as an alternative lightweight, high porosity matrix is also being explored.

SINTERED NICKEL CARBONYL POWDER ELECTRODES

The production of battery electrodes from sintered nickel carbonyl powder is a well established technology and has been extensively investigated and reviewed. However, work is still being done to further refine the process for high reliability, long life, and weight-critical applications. Two basic processes are currently in use to produce electrodes for the nickel-hydrogen system. One is a dry powder method in which each individual plaque is hand-laid in a mold one at a time. The second is a wet slurry process in which the plaque is produced in a continuous roll. Both methods use a similar nickel wire mesh substrate and sintering process and yield a similar product.

Once the porous nickel matrix is obtained it must be loaded with active material to produce a working electrode. The chemical impregnation method used for many years to produce nickel-cadmium electrodes has been entirely replaced by an electrochemical process in the nickel-hydrogen system. Electrodes are produced in either an aqueous solution or an aqueous/alcohol solvent system. Both processes have the advantage of loading the active material in one impregnation step rather than many repeated cycles as in the chemical process. Other advantages of electrochemical impregnation include improved cycle life, utilization, and dimensional stability.

Electrodes produced by the wet slurry method and the dry powder method exhibit relative advantages to each other. Both processes are characterized by extensive quality control provisions (e.g. strict, tight tolerance requirements from raw materials, operational process steps and finished component testing) in recognition of their criticality to the finished product. The slurry process is a continuous-feed, more efficient, and less operator-dependent process. The current-collector substrate is automatically centered in the electrode structure by the nature of the process. This provides electrical and structural benefits. The material has high mechanical strength in terms of both tensile and bend properties. Slurry type plaque hold up to the rigors of electrode processing and handling resulting in a low attrition rate during the multi-step production process. The slurry type material better accepts attachment of electrical conductors by resistance welding without forming cracks in the heat affected zone and surrounding sinter. Part of the slurry production process involves a wet oxidation step which covers the surface of the plaque with a thin passive oxide layer. This serves to provide a more durable product with low susceptibility to mechanical damage or chemical corrosion. Most importantly, slurry type electrodes exhibit good dimensional stability and should provide a longer cycle life at higher depths-of-discharge.

Electrodes produced by the dry powder method possess inherent battery weight and energy density advantages. Dry powder process electrodes have a higher porosity structural matrix. This results in a higher active material to inactive substrate weight ratio and greater energy density. Dry powder electrodes also are manufactured with a greater electrode thickness. Increasing the thickness of the electrode has a net effect of increasing cell energy density by requiring fewer electrodes and associated cell components to achieve the same ampere-hour capacity.

Historically, applications of the space nickel-hydrogen system have been with slurry type electrodes impregnated by the aqueous electrochemical method. This extensive data base has been previously reviewed (Reference 2) and includes five major satellite programs (18 launches total) which are currently operating in orbit with nickel hydrogen batteries on board. The ideal electrode, therefore would be one which combines the mechanical strength and dimensional stability of slurry process plates with the higher porosity and greater electrode thickness associated with dry powder process plates.

Accordingly, manufacturing parameters were adjusted to produce several lots of 35 mil thick slurry process plaque with porosities ranging up to 86%. These plaque retained 60 to 80 percent of the nominal mechanical strength of normal 80% porosity, 30 mil thickness slurry plaque. Each lot was impregnated and formed by normal manufacturing procedures, and two plates from each lot were subjected to a standard flooded capacity measurement and a 200 cycle stress test. All plates tested exhibited satisfactory utilization numbers in the 120 to 130% range. However, a growth versus porosity plot of the 200 cycle, 10C stress test data (Figure 1) shows that there is currently a breakover point at around 83% porosity beyond which the amount of electrode growth becomes excessive. Thickness growth is undesirable as it has been previously identified as a major contributor in long term cycle failure of nickel-hydrogen cells (Reference 1).

Two lots with porosities of 82.7% and 84% were selected for further cycling. These plates underwent a total of 1000 stress test cycles with a visual inspection for physical integrity and growth measurements conducted at the completion of 200, 600, and 1000 cycles. Flooded capacity tests were run at the conclusion of each 200 cycle increment. None of the plates blistered or suffered a loss of capacity during the 1000 cycles of testing. Thickness increase peaked at 600 cycles for both lots. The 82.7% porosity lot exhibited less than 6% thickness increase after the completion of 1000 cycles.

Figure 2 shows the relationship between electrode growth and active material loading on a grams per cubic centimeter of void volume basis. This 200 cycle 10C stress test data suggests that the loading of high porosity slurry plates can be increased beyond current flight acceptable levels and thereby increase the energy density.

The goal of future development work is to push the breakover point demonstrated in Figure 1 beyond 84% porosity through further refinement of slurry process manufacturing parameters. Impregnation and formation of these high porosity slurry plaque will take place in Eagle-Picher's new nickel-electrode production facility. This facility has been expressly designed and dedicated to the space nickel-hydrogen system. As noted above, in recognition of the criticality of the component, the facility was designed from the group up for full automated computer process control. The generated process data forms the basis for a quality control statistical analysis with "real-time" feed-back provisions offering continuous, detailed process control.

Improved tank flow characteristics, greater solution volume to plaque area ratios, automated cycling and pH control, an oil-cooled balancing resistor network for equal current distribution, and computerized monitoring and recording of production parameters will allow tighter control and reproducibility of the manufacturing process. Slurry process electrodes with nominal porosities of 82% have already been produced in Eagle-Picher's existing facility, evaluated at the electrode level, and are currently being assembled into cells. It is anticipated a nominal mass saving of approximately 10% will be achieved at the finished cell level.

NON-WOVEN NICKEL FIBER ELECTRODES

Work has been done over the last several years on a non-woven nickel fiber material as a possible replacement for conventional sintered nickel powder type plaque. The material is manufactured by the National Standard Company under the trade name Fibrex (TM) and has received renewed interest recently. It has the potential for substantial improvements in energy density and material cost reduction. Some of the previous work with fiber mat had been unsuccessful because of problems in loading the active material and the resulting dimensional instability of the finished nickel electrode. The major problems appeared to be due to the open structure and large pore size of the mat and its lack of mechanical strength.

More recent work has been conducted mostly in relation to the nickel-iron battery system under the Dual Shaft Electric Propulsion (DSEP) Program funded by the United States Department of Energy (DOE). This investigation has been undertaken due to the development of a nickel fiber mat which has been cross-linked with battery grade nickel powder. This material has the potential for providing the necessary mechanical strength and dimensional stability required for long cycle life battery electrodes. Current work is focused on adjusting the fiber to powder ratio and the sintering conditions to achieve an optimum electrode for a given cell design. Cross-sectional strengths have been increased by a factor of ten over the earlier materials. The fiber mat promises good performance and design versatility through close control of electrode parameters such as weight, strength, surface area, pore size, and thickness. A 12% savings in weight over the sintered powder electrode is realized solely due to the elimination of the grid wire support/current collector structure not required by the mat. Further weight savings may be achieved from the higher porosities and active material loading obtainable from the fiber mat.

The problems associated with loading the active material into the fiber mat have been overcome in part by applying a periodic reverse impregnation process. The method is essentially the same as the normal aqueous electrochemical process except that the polarity of the electrodes is periodically reversed during impregnation. Periodic current reversal is commonly used in the metal plating industry to promote a more uniform deposited film on the work piece. It appears to have a similar load leveling effect in impregnating nickel electrodes with active material. Work is underway to continue investigation of plating/deplating current densities and cycle times to achieve optimum results. This method has an additional benefit of yielding a 20% higher ampere-hour efficiency in loading the plate over the normal constant current process.

Nickel-iron cells have been constructed and tested using electrodes produced from a 50% fiber/50% powder nickel fiber mat. The porosity of the plates was 75%, the thickness 0.040 inches and the nickel fiber diameter 20 microns. The plates were impregnated through two cycles due to inadequate active material weight gain after the first cycle. After formation in aqueous potassium hydroxide the plates had an average active material loading of 1.54 grams per cubic centimeter of void volume (g/ccvv). A plate was assembled into a test cell and 50 cycles were performed at 100% DOD (Figure 3). On-going research is now exploring sinter porosities up to 85 to 90% which will offer specific energy advantages.

Additional testing was developed for use in the DSEP Program to determine the best electrode design for optimum power capabilities. The test is composed of a base discharge at a C/2 rate with 2.25C rate pulses at 95%, 75%, 50%, and 20% of the working capacity. Testing was performed on fiber electrodes (Figure 4) with normal sintered electrodes as a control. It was concluded that the sinter electrode gives greater instant power within the first three pulses. However, the sinter electrode appears to increase in impedance over the discharge cycle more than the fiber electrode. The fiber electrode also yields a greater utilization of active material per gram than the sinter electrode. The fiber electrode could be developed to supply more power over the discharge curve by improving its dimensional stability. This would increase the contact area of the fibers thus lowering the internal resistance of the plate.

Further investigation into the utilization and electrochemical efficiency of the fiber electrode was made by Dr. Alvin J. Salkind and Associates. This was accomplished by a subcontract from the base technology contract with DOE for the development of the nickel-iron battery.

Testing was performed comparing the rate capability of 0.063 in. thick sintered and fiber nickel plates at various states of charge (SOC) but the fiber-based plate supported higher current densities at the lower SOC of 25%. The impregnation loading level of the fiber nickel plate was much lower than the standard sintered plate, with a consequent reduction of capacity.

The marked differences in scope and ability to sustain heavy loads at a low state of charge may be only a consequence of the relatively low active material content of the fiber plate. However, it seems likely that the fiber material can be loaded higher and still perform as well as a sintered plate of comparable active material density.

CONCLUSION

Considerable progress has been made toward improving the nickel electrode for high reliability, long cycle life space applications. The goal has been to increase energy density while maintaining currently acceptable flight program active material loading levels. In addition, the goal has been to significantly advance the level of quality control provision implementation and the level of quality control process data utilization for enhanced, "real-time", total process control. Electrodes produced for early nickel-hydrogen flight cell programs had an average energy density of about 0.135 ampere-hours per gram. Current flight production programs have achieved energy densities at the electrode level more than 20% greater than that value at the same active material loading on a grams per cubic centimeter of void volume basis. This translates into a substantial weight savings at the finished flight level.

Further increases should be attainable in the near future within the scope of current production technology. The main thrust of Eagle-Picher's future research work will be to develop a mechanically strong, thick, high porosity nickel electrode. Current data suggests that this electrode will more likely be produced using the wet slurry manufacturing process; but, work will continue with both the slurry and dry powder processes.

Nickel fiber mat appears to be a promising replacement for the traditional nickel sinter substrate. Preliminary testing has shown it to be a viable battery electrode with distinct weight advantages. Work will be continued towards the further development of optimized fiber electrodes for nickel battery systems.

In addition to superior physical performance and enhanced component quality, it is anticipated both of the above electrode substrate materials will eventually result in overall system cost reductions.

ACKNOWLEDGEMENTS

The authors wish to acknowledge the Department of Energy Funding of the Dual Shaft Electric Propulsion Program and the National Standard Company for providing fiber mat material in support of the non-woven nickel fiber electrode work. Much of the early basic testing and evaluation work on nickel sinter was performed by the Communication Satellite Corporation Laboratories funded by the International Telecommunications Satellite Organization.

REFERENCES

1. Coates, D.K., Barnett, R.M.: Nickel-Hydrogen Cell Life Testing, 23rd Intersociety Energy Conversion Engineering Conference, Volume 2, 1988, pp. 483-488.

2. Miller, L.: The Ni-H_2 Battery System: A Space Flight Application Summary, 23rd Intersociety Energy Conversion Engineering Conference, Volume 2, 1988, pp. 489-492.

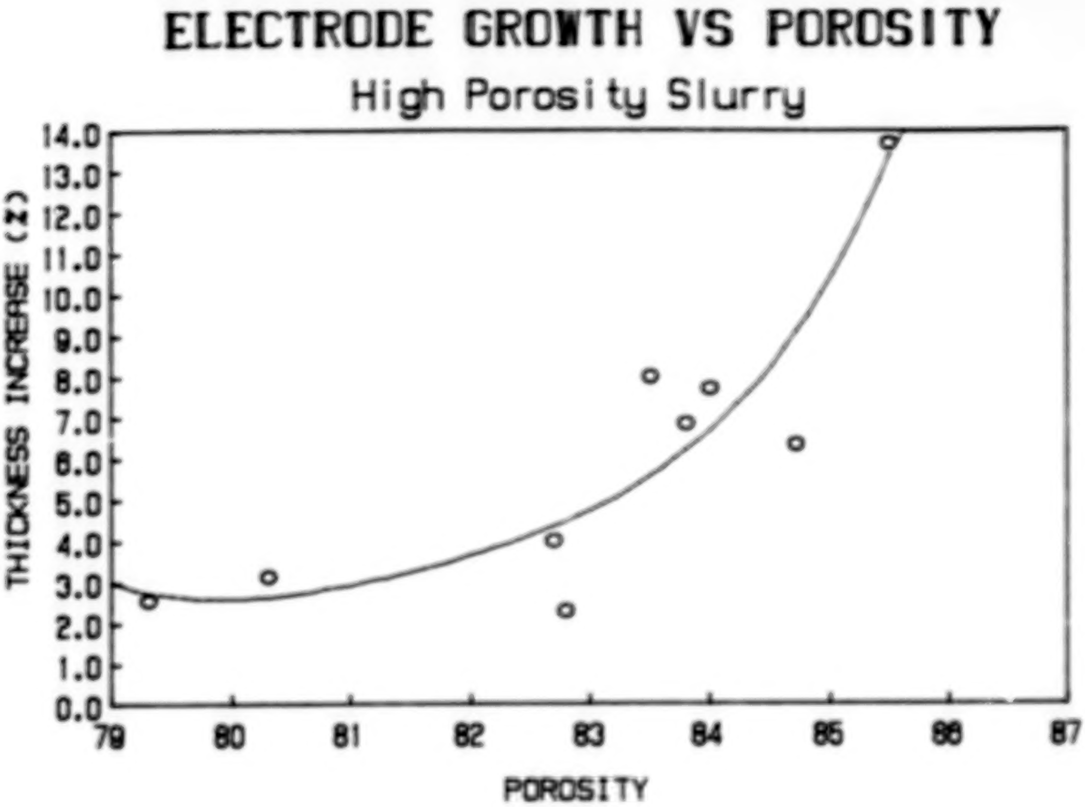

FIGURE 1

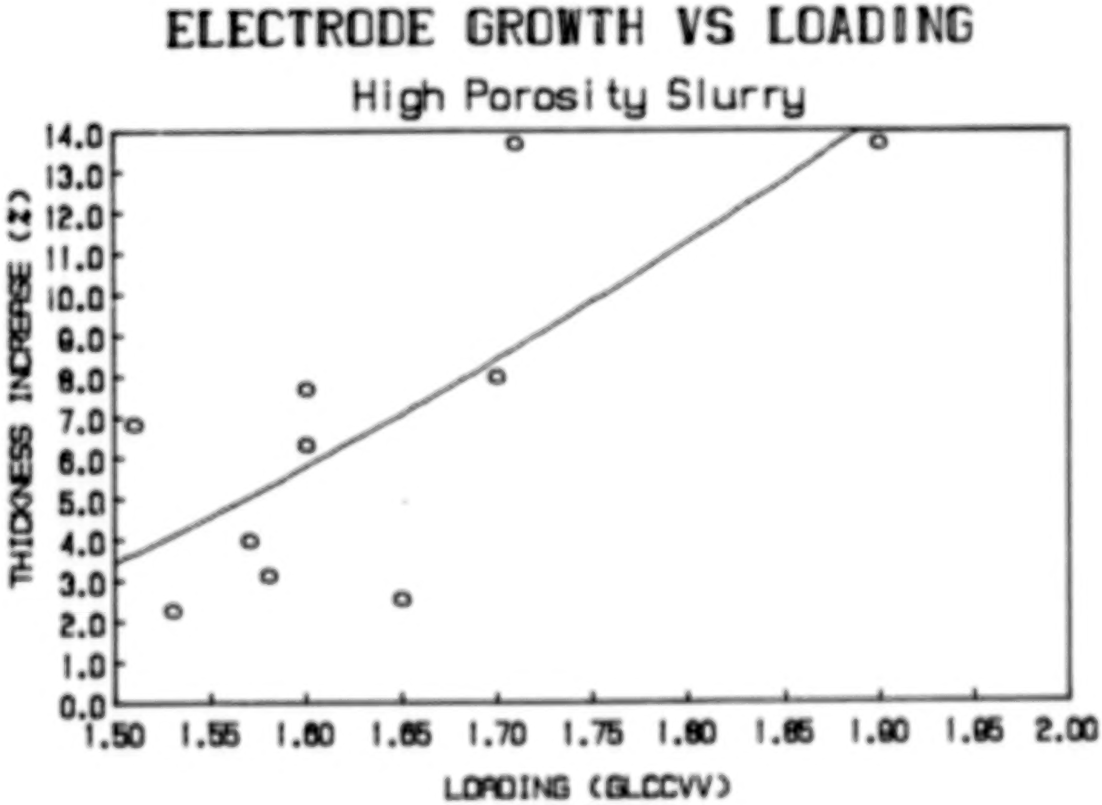

FIGURE 2

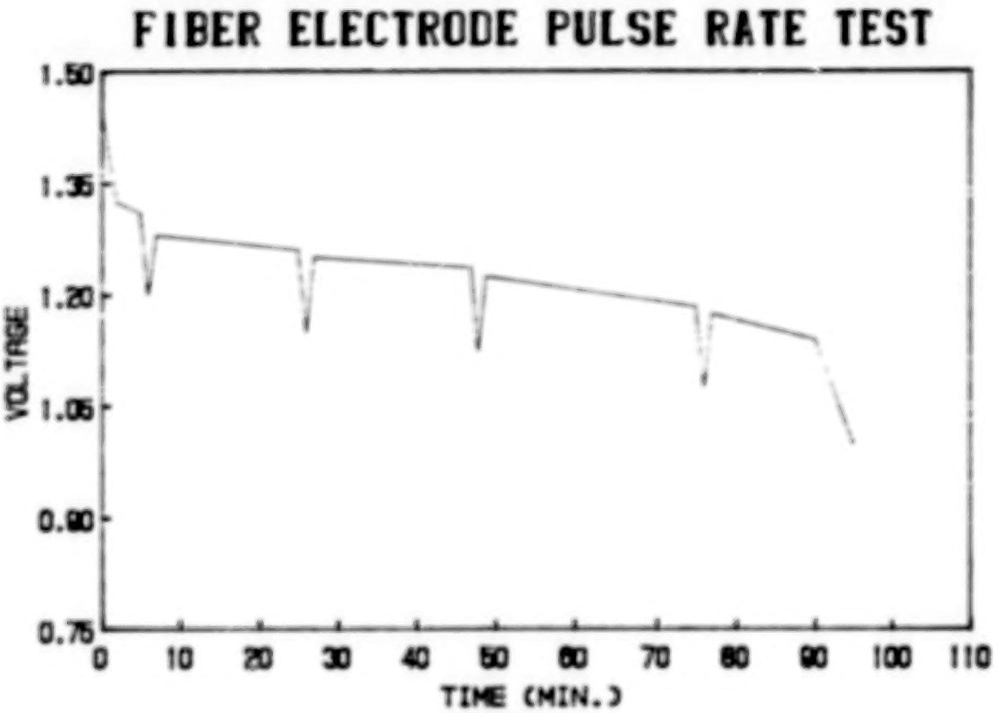

FIGURE 3

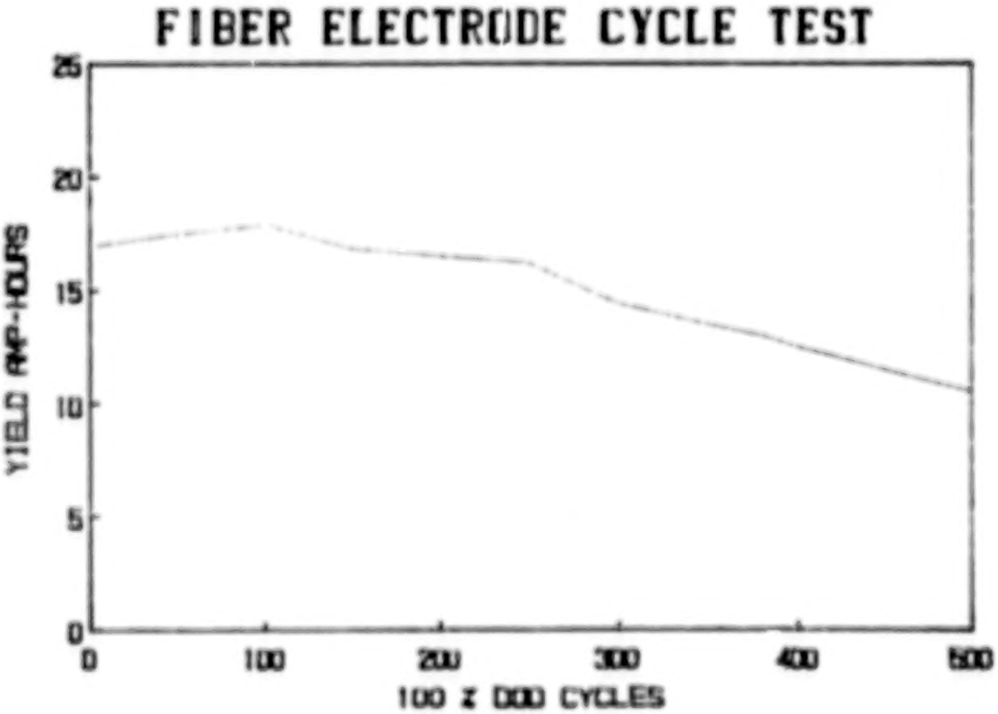

FIGURE 4

FIBER NICKEL ELECTRODE

VOLTAGE VS. DISCHARGE RATE & SOC

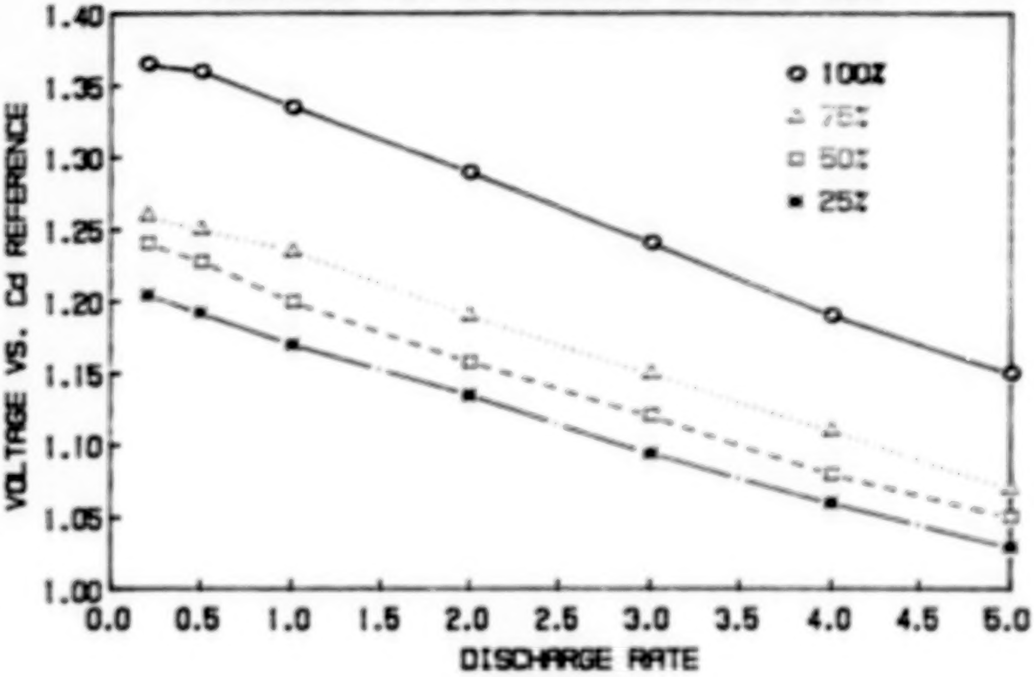

FIGURE 5

SINTERED NICKEL ELECTRODE

VOLTAGE VS. DISCHARGE RATE & SOC

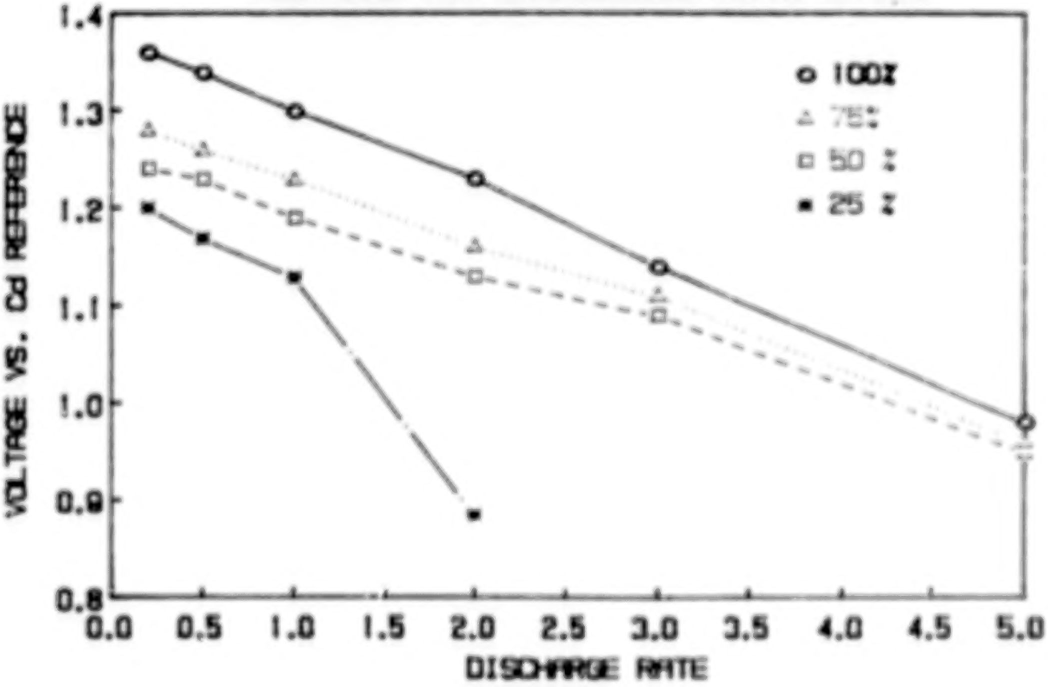

FIGURE 6

MULTI-MISSION Ni-H_2 BATTERY CELLS FOR THE 1990's

Lee Miller, Jack Brill and Gary Dodson
Eagle-Picher Industries, Inc.
Joplin, Missouri 64802

A sufficient production, test and operational database is now available to permit design technology optimization for the next decade. The evolved battery cell design features standardized technology intended to support multiple type missions (e.g. both GEO and LEO). Design analysis and validation test cells demonstrate that improved performance plus attractive specific-energy characteristics will be achieved.

INTRODUCTION

In the year 1988 Eagle-Picher Industries (EPI) surpassed the production point of 10,000 space type Ni-H_2 battery cells. Approximately 25,000,000 battery cell hours of space flight operation have now been accumulated. Multiple test cell groups continue to undergo real-time and accelerated life testing. Real-time GEO testing has now exceeded 13 years and LEO testing over six (6) years. Accelerated LEO testing has exceeded 40,000 cycles.

Several design technologies evolved in the accumulation of this extensive data-base. Performance comparisons and post-test destructive physical analysis (DPA) have proven useful in the evaluation of the advantages and disadvantages of the various design technologies. Sufficient data is therefore available to propose a more standard, optimized battery cell design capable of supporting multiple types of missions for the next decade.

BATTERY CELL DESIGN

The following design summary proposes a baseline cell design. If optional technology is available which has been tested and proven, then it is noted in parenthesis.

Pressure Vessel (PV)

A single girth weld design is proposed with opposing axial compression terminal seals as shown in Figure 1. (For volume critical or other special applications, the terminals may be located at 45° off-set positions on either the same PV end or at opposing ends.)

In accordance with MIL-STD-1522A, EPI has established and qualified an "in-house" fracture critical vessel inspection capability which permits customizing the cell design maximum-expected-operating-pressure (MEOP) and vessel wall thickness for the specific mission application.

Electron Beam Welding

All PV joining will be accomplished by the electron beam (EB) process. EPI has procurred a FERRANTI Sciaky 60 KV, 250 mA EB welder for "in-house" capability and control. A large vacuum chamber was selected to permit equipment modifications for high precision, multiple cell self-indexing, fully automated welding.

Electrode Stack

The electrode stack will feature "pineapple slice" geometry for optimum thermal, mechanical and electrical characteristics (refer to Figure 1). The positive electrodes will be configured in a "back-to-back" arrangement. Depending upon capacity the design will feature a single or dual stack arrangement. For capacities of 50 Ampere-Hours (A-H) or less, a single stack is generally used.

PV Wall Coating

The PV will feature a porous zirconium oxide wall coating to serve as an electrolyte return (wick) and reservoir. (A combination electrolyte transport and catalyzed wall coating design for enhanced gas management is also offered.)

Positive Electrode

A high mechanical strength (1500 psi minimum), slurry sinter positive electrode is utilized for long term dimensional stability. An electrode thickness of 0.03 inches (0.076 cm) is incorporated to maximize the quantity of electrodes and thus minimize operational current densities. A moderate active material loading level of 1.65 grams/cm^3 of void volume is specified.

Negative Electrode

A standard teflonated catalyzed electrode with a platinum loading of 8 milligrams/cm^2 is featured. (Platinum loading reductions of up to an order of magnitude are also available).

Separator

In consideration of long term availability, electrolyte reserve provisions and low impedance (particularly at lower temperatures), a two (2) layer zirconium oxide (Zircar) material design is featured. (A combination asbestos/Zircar design is also available. In addition, for mass critical missions a single layer asbestos or Zircar design is offered.)

Electrolyte

A 31% potassium hydroxide solution will be incorporated in the standard cell. (For missions with a large number of cycles or high depths of discharge, a 26% solution is offered for positive electrode stress reduction.)

Gas Management

The more open structural characteristics of the Zircar separator material poses additional problems with respect to oxygen gas management (reference Figure 2). The proposed cell design will incorporate provisions which are intended to redirect the oxygen gas flow away from the positive electrode-to-separator interface during overcharge.

Stack Growth Accommodations

To accommodate potential electrode stack dimensional growth and to maintain appropriate stack load under dynamic stress, a spring type device is employed. The device incorporated in the proposed cell design offers significant advantages over the Belleville washer design employed in several cell types. The spring constant for the proposed device can be reproducibly controlled and maintained in the manufacturing process. In addition, load uniformity is maintained over much greater length of travel at approximately one fourth the mass of equivalent Belleville washers.

80 A-H CELL DESIGNS

Battery cells rated at 80 A-H are being produced and validation cells have been placed on test. This program may serve as an example for projecting mass and volume characteristics for the proposed cell design. Figures 3 through 6 represent summaries of computer projections for the most influential technology option, separator type and design.

The design analysis of the proposed $Ni-H_2$ battery cell was performed on a TRS-80, Model 100 portable computer. The specific application software was coded in an extended version of BASIC. The program constructs a detailed model of the cell design via established electrochemical, physical and material performance formulas.

The 80 A-H cells for a program have now progressed sufficiently to permit model accuracy verification.

Attribute	Model Accuracy
Mass	0.2%
Capacity	0.2%
Length	0.1%

CELL TEST DATA

Typical battery cell conditioning and Acceptance Test data are presented in Tables 1 and 2, respectively. To permit a level of performance comparison, data was selected for a single layer asbestos and a single layer Zircar separator cell design.

These same two (2) test cell groups are part of a larger test cell group now undergoing real-time GEO life cycle testing in accordance with the test profile presented in Figure 7. Typical end-of-discharge voltage (EODV) performance is compared graphically in Figure 8.

CONCLUSION

A multi-mission $Ni-H_2$ battery cell has been produced and is successfully undergoing validation testing. The cell design has assimilated the optimal, space flight proven technology which has evolved from a 15 year, 10,000 production unit, 25,000,000 flight cell hour database. Its standardized features should now support missions through the 1990's with minimal need for design requalification and dedicated cycle life testing.

TABLE 1. Performance Comparison of 80 Ampere-Hour Cells During Sealed Conditioning Cycles*

	EOC V		1 Hr DV		Cap. (A-H)	
Cycle	#1	#2	#1	#2	#1	#2
1	1.535	1.534	1.220	1.233	88	86
2	1.527	1.525	1.218	1.233	85	85
3	1.537	1.533	1.215	1.234	84	85

Notes:
- * Charged C/10 for 16 hours, discharged C/2, 10°C.
1. Design #1 = Asbestos Separator, 8 cells on test.
2. Design #2 = Zircar (1) Separator, 3 cells on test.
3. All data values are group averages.

TABLE 2. Performance Comparison of 80 Ampere-Hour Cells During Acceptance Test Cycles*

	EOC V		1 Hr DV		Cap. (A-H)	
Test	#1	#2	#1	#2	#1	#2
25°C	1.491	1.486	1.204	1.211	73	71
-5°C	1.595	1.585	1.140	1.188	82	84
10°C	1.530	1.515	1.185	1.205	87 (77)**	86 (84)**

Notes:
- * Charged C/10 for 16 hours, discharged C/1.6.
- ** Discharge to 1.1 volts.
1. Design #1 = Asbestos Separator, 8 cells on test.
2. Design #2 = Zircar (1) Separator, 3 cells on test.
3. All data values are group averages.
4. Cells were subjected to 30 "burn-in" cycles between Conditioning and Acceptance Testing. Cycle = 12 hour; 75% DOD in 1.2 hours, 1.25 C/D return in 10.8 hours, 10°C.

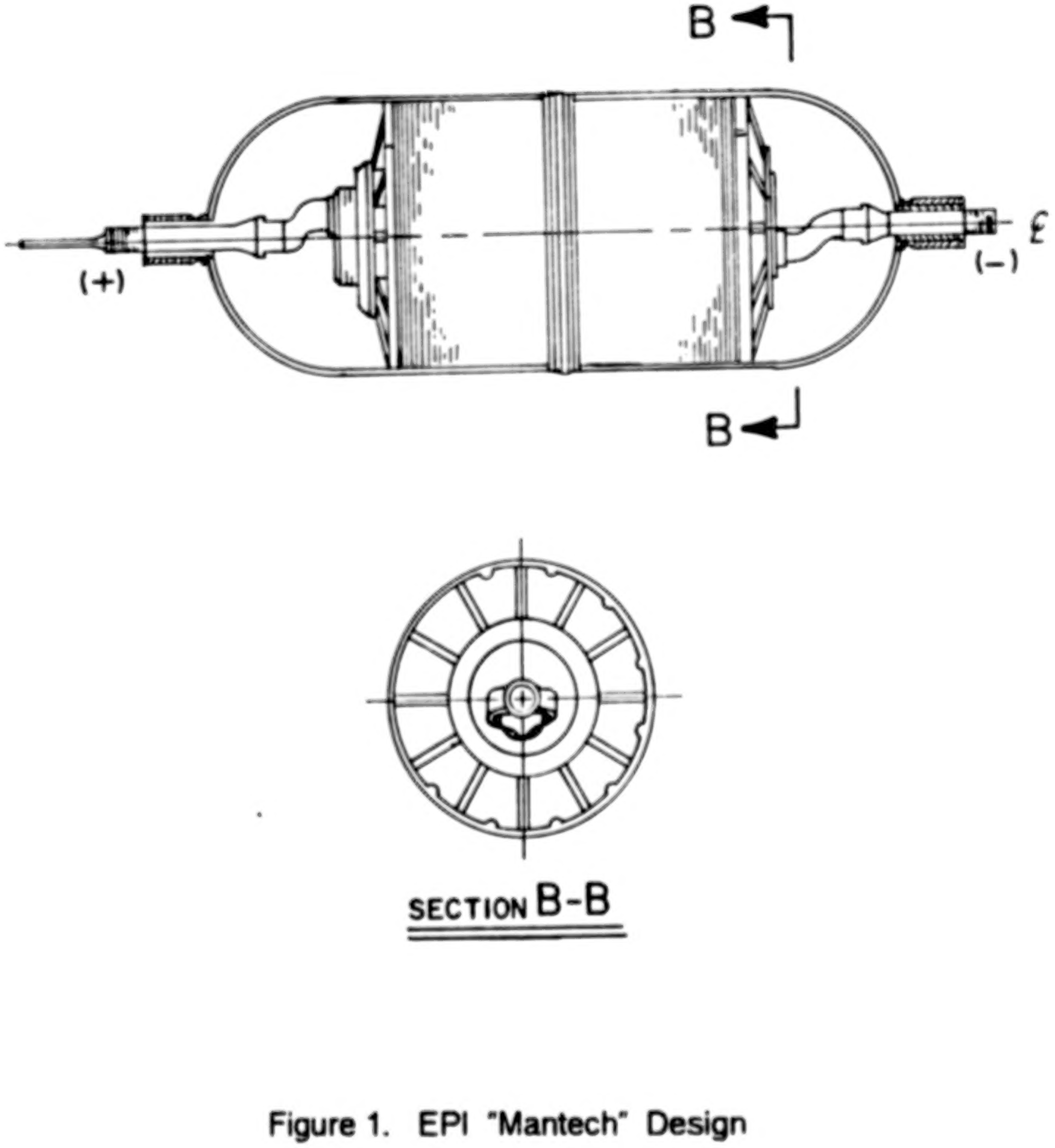

SECTION B-B

Figure 1. EPI "Mantech" Design

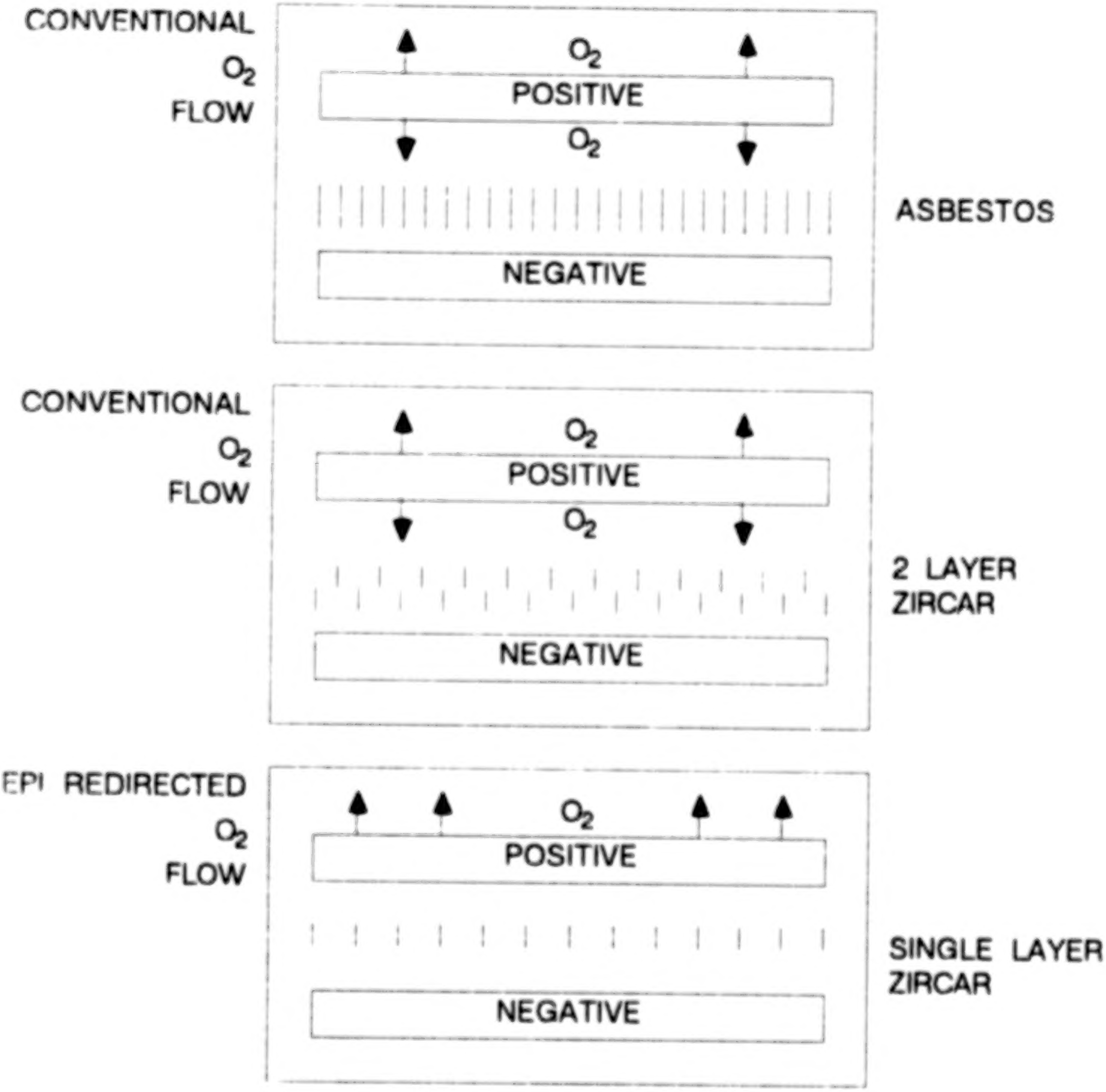
CONVENTIONAL
O_2
FLOW
O_2
POSITIVE
O_2
ASBESTOS
NEGATIVE
CONVENTIONAL
O_2
FLOW
O_2
POSITIVE
O_2
2 LAYER
ZIRCAR
NEGATIVE
EPI REDIRECTED
O_2
FLOW
O_2
POSITIVE
SINGLE LAYER
ZIRCAR
NEGATIVE

Figure 2. NiH_2 Separator Design Technology

Battery Cell Design Parameters (Input):	Value:
1. Rated Cell Capacity (A-Hr)	80.000
2. Cell Capacity Margin (%)	10.000
3. Cell Residual Capacity (%)	25.000
⋮	
Battery Cell Design Features (Output):	**Value:**
1. Nominal Cell Mass (Gms)	1991.280
2. Nominal Cell Capacity (A-Hr)	88.476
3. Cell Specific Energy (W-Hr/Kg)	54.207
4. Pressure Vessel Length (in)	10.123
5. Total Cell Length (in)	13.373
6. Total Cell Length (cm)	33.968
7. Cell Diameter (in)	3.506
8. Cell Diameter (cm)	8.905
⋮	

Figure 3. Baseline 80AH Rated (2 Layer Zircar Separator) Cell Design

Battery Cell Design Parameters (Input):	Value:
1. Rated Cell Capacity (A-Hr)	80.000
2. Cell Capacity Margin (%)	10.000
3. Cell Residual Capacity (%)	25.000
⋮	
Battery Cell Design Features (Output):	**Value;**
1. Nominal Cell Mass (Gms)	1947.790
2. Nominal Cell Capacity (A-Hr)	88.476
3. Cell Specific Energy (W-Hr/Kg)	55.417
4. Pressure Vessel Length (in)	10.021
5. Total Cell Length (in)	13.271
6. Total Cell Length (cm)	33.707
7. Cell Diameter (in)	3.506
8. Cell Diameter (cm)	8.905
⋮	

Figure 4. Option #1 80AH Rated (Asbestos / Zircar Separator) Cell Design

Battery Cell Design Parameters (Input):	Value:
1. Rated Cell Capacity (A-Hr)	80.000
2. Cell Capacity Margin (%)	10.000
3. Cell Residual Capacity (%)	25.000
⋮	
Battery Cell Design Features (Output):	**Value:**
1. Nominal Cell Mass (Gms)	1858.410
2. Nominal Cell Capacity (A-Hr)	89.271
3. Cell Specific Energy (W-Hr/Kg)	58.604
4. Pressure Vessel Length (in)	9.643
5. Total Cell Length (in)	12.893
6. Total Cell Length (cm)	32.749
7. Cell Diameter (in)	3.506
8. Cell Diameter (cm)	8.905
⋮	

Figure 5. Option #2 80AH Rated (1 Layer Asbestos Separator) Cell Design

Battery Cell Design Parameters (Input):	Value:
1. Rated Cell Capacity (A-Hr)	80.000
2. Cell Capacity Margin (%)	10.000
3. Cell Residual Capacity (%)	25.000
⋮	
Battery Cell Design Features (Output):	**Value:**
1. Nominal Cell Mass (Gms)	1803.090
2. Nominal Cell Capacity (A-Hr)	88.476
3. Cell Specific Energy (W-Hr/Kg)	59.865
4. Pressure Vessel Length (in)	9.505
5. Total Cell Length (in)	12.755
6. Total Cell Length (cm)	32.397
7. Cell Diameter (in)	3.506
8. Cell Diameter (cm)	8.905
⋮	

Figure 6. Option #3 80AH Rated (1 Layer Zircar Separator) Cell Design

FIGURE 7. Cycle Test, Cell Temperature Vesus Time

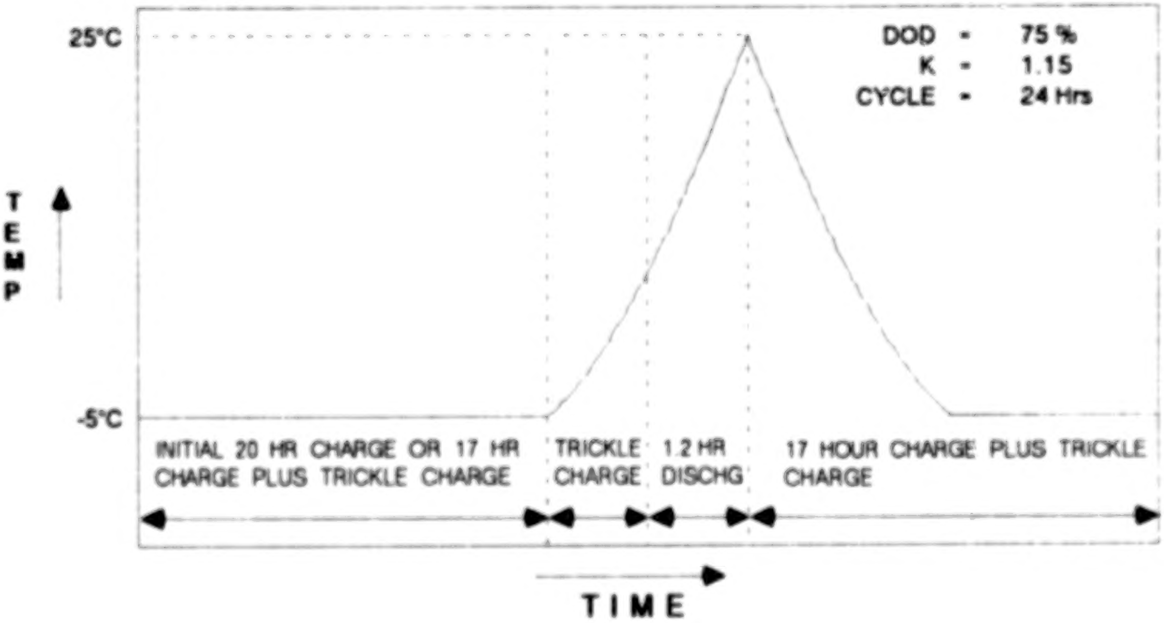

FIGURE 8. Real-time GEO Life Cycle Test End-of-Discharge Voltage

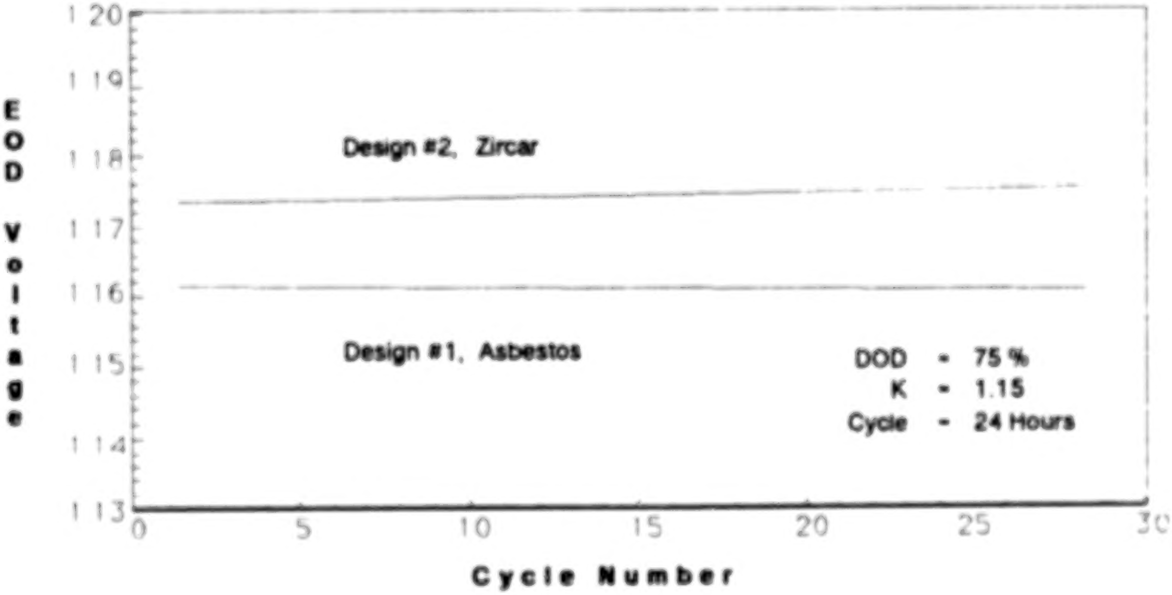

NICKEL-HYDROGEN CAPACITY LOSS ON STORAGE

Michelle A. Manzo
NASA Lewis Research Center
Cleveland, Ohio 44135

A controlled experiment evaluating the capacity loss experienced by nickel electrodes stored under various conditions of temperature, hydrogen pressure, and electrolyte concentration was conducted using nickel electrodes from four different manufacturers. It was found that capacity loss varied with respect to hydrogen pressure, and storage temperature as well as with respect to electrode manufacturing processes. Impedance characteristics were monitored and found to be indicative of electrode manufacturing processes and capacity loss. Cell testing to evaluate state-of-charge effects on capacity loss were inconclusive as no loss was sustained by the cells tested in this experiment.

INTRODUCTION

Nickel-hydrogen batteries are rapidly becoming accepted for use in low-earth-orbit and geosynchronous orbit applications. With their increased use, it has become evident that the storage procedures commonly used for nickel-cadmium cells are not adequate for the nickel-hydrogen system. Frequently cells that have been stored, under varied conditions, have exhibited a significant loss of capacity. However, much of the data available on capacity loss has been confusing and often conflicting. (ref. 1-6) As a result, members of the Electrochemical Technology Branch at the NASA Lewis Research Center conducted a controlled determination of the capacity loss exhibited by nickel electrodes when exposed to different storage conditions.

A comprehensive test matrix was developed to evaluate the capacity loss characteristics of nickel electrodes from four different manufacturers. Two types of tests were run; individual electrode tests, which involved flooded capacity and impedance measurements before and after storage under varied conditions of temperature, hydrogen pressure, and electrolyte concentration; and cell tests which primarily evaluated the effects of state of charge on storage. The electrode tests were run using electrodes from Gates Aerospace Batteries (GAB), Whittaker-Yardney (W/Y), Hughes (HAC), and Eagle Picher-Joplin (EP). The cell tests were run only with Hughes electrodes. The cell tests evaluated capacity loss on cells stored open circuit, shorted and trickle charged at C/200 following a full charge.

The results indicate that capacity loss varies with the specific electrode manufacturing process, storage temperature and storage pressure. In general, electrodes stored at low temperatures or low hydrogen pressures exhibited a smaller loss in capacity over the twenty-eight day storage period than those stored at high pressure or high temperature. The capacity loss appears to correlate with the level of cobalt in the nickel electrode, with a greater capacity loss observed in electrodes with higher cobalt levels. Impedance measurements appear to correlate well with capacity loss for a given type of electrode but do not correlate well with the capacity loss observed between electrodes fabricated by different manufacturers. There was a definite correlation between the electrode potential measured immediately following storage and the measured capacity loss. The cell storage tests indicated a temporary capacity loss in cells stored discharged in the open-circuit condition and shorted. The cell stored on trickle charge did not exhibit a loss of capacity.

EXPERIMENTAL

NICKEL ELECTRODE STORAGE TEST PROCEDURES

Before Storage Flooded Capacity Measurements

Fifteen electrodes were obtained from each of four nickel-hydrogen cell manufacturers for the capacity loss on storage test matrix. The following manufacturers supplied electrodes for this study: Eagle Picher-Joplin, Hughes, Gates Aerospace Batteries, and Whittaker/Yardney. The characteristics of the electrodes are summarized in Table 1. The electrodes were divided, by manufacturer, into two groups of thirty each for the flooded capacity measurements. Three electrodes from each manufacturer were subjected to the same set of test and storage conditions.

The initial capacity was estimated for electrodes from each manufacturer. Where capacity differences existed between electrodes in the groups tested together, test parameters (charge and/or discharge rates) were adjusted to accommodate the sub groups of electrodes. Since electrodes of varying capacity were tested in the same series string, relative "C" rates may have varied; however, in all cases the before storage and after storage measurements were made in the same way. (The C rate will discharge the nominal electrode capacity in one hour.) Since the variable of interest was percent change in capacity, it was felt that the results would be valid and comparable.

The flooded capacity measurements were made using a nickel counter electrode and an amalgamated zinc reference electrode. 31% KOH was used for the majority of measurements. One group from each manufacturer was tested in 26% KOH for a measure of capacity retention vs electrolyte concentration. The initial formation charges were run at C/7.5 or C/10 for 16 hours. The electrodes were discharged at the C/4 or C/5 rate. Formation cycles were run until a uniform capacity was obtained on consecutive cycles. This usually took six to seven cycles for each group of electrodes. An average formation capacity was obtained for each electrode.

Based on the formation capacity, C/2 charge and C/4 discharge cycles, with a C:D of 1.12 to 1.15, were planned for the electrode capacity measurements. However, as stated above, the grouping of electrodes of unequal capacities lead to relative "C" rates varying from C/4 to C/5.25 on discharge. A total of five to six capacity determination cycles were run. An average before storage capacity was determined for each electrode.

Before Storage Impedance Testing

Following the pre-storage capacity measurements the electrodes were left in KOH in the discharged state until impedance measurements could be made. A Princeton Applied Research 5208 Two-Phase Lock In Analyzer coupled with a Princeton Applied Research Potentiostat-Galvanostat Model 273 was used to make the impedance measurements. Impedance tests were run from .0007 Hz to 5.65 Hz. All electrodes were tested in the discharged state, following equilibration at 0.2 volts for 1 hour vs a Hg/HgO reference electrode.

One electrode from each group of three was also measured in the charged state. The electrode was charged at approximately the C/3 rate for 1/2 hour, then equilibrated at 0.4 volts vs Hg/HgO for 1 hour before measuring impedance. Following the impedance measurements, the electrodes were returned to 0.2 volts by discharging at rates similar to those used in the capacity measurement cycles and equilibrated there for 1 hour before storage.

Storage Procedures

As testing on groups of six electrodes that were to be subjected to the same storage conditions, (three from each manufacturer in the sub group) was completed, the electrodes were installed in a vessel and put on storage stand for twenty-eight days. Storage conditions and their identifying codes are described in Table 2. Storage temperature, hydrogen pressure, and electrolyte concentration were the parameters that were varied.

All electrodes were stored in the discharged state, open circuited; in boiler plate pressure vessels, stacked on cores that approximate flight hardware. They were separated by gas screens. No mechanical pressure was exerted on the stack.

The vessels were evacuated and backfilled with hydrogen to the desired pressure. The zero psig vessels were backfilled with hydrogen then the pressure was released until the gauge read zero. The vessels were then stored under the appropriate conditions and monitored to ensure that the desired storage conditions were maintained throughout the twenty-eight day storage period.

After Storage Procedures

The electrodes were removed from the vessels following twenty-eight days of storage at the specified conditions. The electrodes were placed in a solution of KOH at the proper concentration. Open circuit voltages were measured vs Hg/HgO as soon as possible following removal from storage. Impedance measurements were made in the discharged state at the electrode open circuit potential over the same frequency ranges as the before storage measurements.

The electrodes were then set aside, flooded with the proper concentration KOH, until the entire group of thirty electrodes had completed storage and initial impedance evaluation at the specified conditions. The after-storage capacity measurements were made in the flooded state following the same procedures used for the initial capacity measurements. Again five to six cycles were run and the results averaged. The average before and after capacities were compared in order to determine the percent change in capacity for each electrode. Data from the groups of three was also averaged for comparison purposes.

Following the after-storage capacity measurements, impedance was measured after equilibration at 0.2 volts for 1 hour as in the before capacity measurements. After storage measurements were not made at 0.4 volts.

NICKEL-HYDROGEN CELL STORAGE TEST PROCEDURES

Cell Construction Parameters

Representative cells were built to evaluate state of charge on storage in completed cells. Due to electrode availability and configuration, only nickel electrodes from Hughes were used for this portion of the study. Three stacks composed of three pairs of electrodes per stack were constructed. The standard Air Force recirculating design configuration was used. The hydrogen electrode used was of the standard Air Force design. The separator used for all three cells was a potassium titanate/polyethylene blend prepared under a grant with Miami University.

Before Storage Impedance Measurements

The cell impedances were measured following activation. Impedances were measured at the cell open circuit voltage over the range of 0.0007 Hz to 5.65 Hz.

Before Storage Capacity Determination Procedure

The formation procedure used on the cells was similar to that used on the nickel electrodes. The cells were charged at C/10 for 16 hours and discharged at the C/4 rate. Capacity to 1.0 volt was measured. The formation cycles were repeated until a stable capacity was achieved. Four cycles were run.

The pre-storage capacity was determined at the C/2 charge rate with a 10% overcharge and a C/4 discharge to 1.0 and 0.1 volts. Nine pre-storage capacity determination cycles were run.

The impedance measurements were repeated before storing the cells. The measurements were made at open circuit following the discharge to 0.1 volts at C/10. They were made over the same frequency range as the before formation measurements.

Storage Procedures

The storage procedures and conditions for the cells are summarized below. Cell 1 was discharged at the C/4 rate to 1.0 volts then discharged at C/10 to 0.1 volts. The cell was then stored at room temperature in the open circuit state for twenty-eight days. Cell 2 was discharged under conditions similar to those used for cell 1 then stored at room temperature, shorted through a 1 ohm resistor for twenty-eight days. Before storage, cell 3 was charged at the C/2 rate with a 10% overcharge. The cell was then trickle charged at C/200 for the twenty-eight day storage period. In order to emphasize any pressure effects, all cells were stored at room temperature and at 500 psi hydrogen.

After Storage Procedures

Following storage for twenty-eight days, the cells were charged and discharged as in the pre-storage capacity measurements. The cells were charged at C/2 with a 10% overcharge and discharged at C/4 to 1.0 and 0.1 volts. A number of cycles were run and capacity trends were monitored.

Impedance tests were repeated following the after-storage capacity measurements.

RESULTS AND DISCUSSION

Nickel Electrode Storage Tests

Capacity Loss Measurements

The capacity loss suffered as a result of storage at the various conditions is summarized in Figures 1 and 2. Figure 1 compares capacity loss as a function of storage conditions for each of the electrode manufacturers. In general, electrodes stored in 31% KOH, at 500 psi, and room temperature experienced the greatest loss in capacity. This was consistent for all four manufacturers. Storage at -20 deg C helped to minimize the capacity loss even at hydrogen pressures of 500 psi. The low temperature storage resulted in a .6 to 13% decrease in capacity loss with other storage parameters remaining constant. Similar reductions, 4 to 13%, were achieved by reducing the storage pressure from 500 psi to 50 psi. No additional reduction in capacity loss was achieved by reducing the storage pressure to ambient conditions. Electrolyte concentration appeared to have a minimal impact on capacity loss with storage in the presence of hydrogen.

Figure 2 compares the capacity loss as a function of electrode manufacturer for each of the storage conditions. Nickel electrodes from Hughes exhibited the greatest capacity loss for all storage conditions. This may be a result of the impregnation method or the concentration of cobalt in the electrodes. Hughes is the only one of the manufacturers whose electrodes were tested that uses an alcoholic impregnation process; all others use aqueous methods. The Hughes electrodes also have the highest cobalt level of those tested (Table 1). It has been postulated that cobalt segregation in reducing environments may be responsible for performance changes in nickel electrodes (ref. 7). Thus cobalt levels may effect the capacity loss characteristics as well. In order to evaluate the effects of cobalt concentration, electrodes impregnated by the same process have been prepared with 5% and 10% cobalt levels for impedance testing and capacity loss on storage evaluation.

In general, the capacity loss experienced by electrodes from the manufacturers other than Hughes was minimal; less than 5%. In fact the Eagle Picher electrodes experienced a slight increase in capacity measured after storage compared to that measured before storage.

Impedance Measurements

Electrodes from each manufacturer exhibited characteristic impedance behavior when measured in 31% KOH, at 0.2 volts vs Hg/HgO as shown in Figure 3. However, when measured at 0.4 volts vs Hg/HgO, the impedance spectra were similar for all four types of electrodes and could not be differentiated. It appears that the diffusion resistance increases abruptly as the electrode voltage decreases (ref. 8). This in turn effects the kinetic resistance term. The point at which, and the extent to which the diffusion resistance increases appears to vary with manufacturing process as well as previous cycle history.

The electrode model used for the impedance studies is shown in Figure 4. The impedance values that were compared for the various electrodes are for what is generally referred to as kinetic resistance, R_k. The kinetic resistance is a measure of the resistance to electron transfer. The ohmic resistance is not a valid parameter for the electrode tests as the measurements were made in the flooded state and as such the ohmic resistance becomes a measure of the resistance of the electrolyte to the reference electrode. Since impedance was measured before storing the electrodes, the 'pre-storage' measurements on all electrodes, with the exception of those tested in 26% KOH, were made at the same conditions for all electrodes, i.e. room temperature and 31% KOH. The initial, pre-storage kinetic resistance measurements generally ranged between 0.5 and 2 m-ohms. The post-storage impedance values are shown as a function of storage conditions and electrode manufacturer in Figures 5 and 6. There was no direct correlation in the changes in R_k as a function of storage conditions or electrode manufacturers. The impedance values seem to correlate with the capacity loss observed within a group but not between groups. Electrodes that experienced a capacity loss after storage also exhibited changes to the impedance spectra while those with no capacity loss did not (Figure 7).

The measurement of cell voltage upon removal from storage seemed to correlate very well with the capacity loss measured in the electrode tests. The Hughes electrodes stored at 500 psi and room temperature lost 15% to 18% of their initial capacity. They were also the only electrodes to have a negative voltage vs Hg/HgO immediately following storage. In general, the lower the electrode voltage upon removal from storage the greater the capacity loss. Table 3 shows the electrode voltage vs Hg/HgO upon removal from storage for each of the manufacturers at the various storage conditions. The voltage upon removal is an indicator of the amount of active material reduction that has taken place in the nickel electrode. The impedance then follows from the voltage change. In general, the lower the voltage, the higher the electrode impedance.

Cell Tests

The capacity to 1.0 and 0.1 volts vs cycles for the cell storage tests are shown in Figures 8-10. The results for the cell stored discharged/open circuit and the cell stored in the shorted condition are similar. In both cases the cells exhibited a capacity loss of 17-18% when comparing the cycles immediately prior to and after storage. This capacity loss was in the same range as that seen for Hughes electrodes stored under similar pressure and temperature conditions in the electrode portion of this study. The electrode stored at 500 psi and room temperature experienced an average 15% loss in capacity over the twenty-eight day storage period. However, the capacity loss experienced by the cells was recovered within eight cycles as shown in Figures 8 and 9. This does not agree with the electrode studies which showed essentially no increase in capacity during the after-storage cycling. The storage test was repeated on the same cells and similar results were obtained the second time around.

The cell stored charged then trickle charged at C/200 for twenty-eight days showed no degradation in capacity due to storage. A plot of the capacity obtained vs cycles for cell 3 is shown in Figure 10. It should be noted that the difference between the capacity to 1.0 volt and the capacity to 0.1 volt increased after the storage period. The capacity to 1.0 volt remained constant while the total cell capacity increased.

The cell tests showed no indication of irrecoverable capacity loss as a result of storage for any of the conditions tested. Capacity recovery which occurs within twenty cycles of storage is not considered a problem.

Comparison of impedance measurements made before and after storage were inconclusive. There was a great deal of scatter in the data and the absence of a reference electrode complicated the measurements.

CONCLUSIONS AND RECOMMENDATIONS

Capacity loss appears to be related to the hydrogen pressure in the vessel. Low temperatures, (-20 deg C) seem to negate the effects of the high pressure. KOH concentration has minimal effect on capacity loss. Nickel electrodes from Hughes showed the highest capacity loss. This may be related to impregnation process and/or cobalt levels in the electrodes. The storage tests run to evaluate the effect of state-of-charge on storage showed essentially no capacity loss for any of the conditions of storage evaluated.

The capacity loss on storage study provided much valuable information relating to the interactions of temperature, pressure and electrolyte concentration with nickel electrodes from various manufacturers. However, in some cases, conflicting results were produced, specifically in the correlation of the electrode data with the cell storage data. As mentioned above, areas requiring further study have been identified and are being pursued. Impedance work is continuing and as a greater understanding of the data is achieved further correlations may be made and a deeper understanding gained from the present study.

ACKNOWLEDGEMENTS

The work described in this paper represents a group effort. The following individuals were involved in completing the study: Olga Gonzalez-Sanabria and John Smithrick developed the test matrix used to evaluate electrodes from the various manufacturers. John Smithrick coordinated efforts with the manufacturers and obtained the electrodes necessary to perform the work. Michelle Manzo planned, scheduled and coordinated the overall test scheme, set up the flooded capacity measurement apparatus, and monitored the storage of the electrodes. Jeffrey Brewer, Doris Britton, and Olga Gonzalez-Sanabria were responsible for running the flooded capacity test measurements before and after electrode storage. Randall Gahn wired the data acquisition system for capacity loss measurements, prepared pressure vessels for both the cell tests and electrode storage tests, and built and tested the cells for the state-of-charge storage evaluation testing. Margaret Reid provided all of the impedance measurements on both the electrodes and cells. Jo Ann Charleston organized and plotted the results. Patricia O'Donnell and Lawrence Thaller served as advisors to the effort.

REFERENCES

1. McDermott, J.: Low-Earth-Orbit Testing of Nickel-Hydrogen Cells. 21st IECEC, Advancing Toward Technology Breakout in Energy Conversion, August 1986, pp. 1516-1520.

2. Vaidyanathan, H.; Dunlop, J.: Capacity Maintenance for Intelsat VI Nickel-Hydrogen Cells. 21st IECEC, Advancing Toward Technology Breakout in Energy Conversion, August 1986, pp. 1516-1520.

3. Vaidyanathan, H.: Long-Term Storage of Nickel-Hydrogen Cells. Space Electrochemical Research and Technology Conference, NASA Lewis Research Center, Cleveland, Ohio, April 1987, Proceedings, pp 41-48, NASA Conference Publication 2484, pp. 41-48.

4. Smithrick, J.: Effect of Storage and LEO Cycling on Manufacturing Technology IPV Nickel-Hydrogen Cells. Energy New Frontiers, 22 IECEC, August 1987, pp.878-881.

5. Vaidyanathan, H; Earl, M.: Capacity and Pressure Variation of Intelsat VI Nickel-Hydrogen Cells with Storage and Cycling, 1988 IECEC Proceedings, pp. 471-475.

6 Hartjen, G. L.; Applewhite, A. Z.; Hall, A. M.:Storage and Testing of 220 Ampere-Hour Nickel-Hydrogen Battery Cells in Low Earth Orbit, 1988 IECEC Proceedings, pp.363-366.

7. Zimmerman, A. H.: Nickel-Hydrogen Cell Positive Electrode Studies: Cobalt Segregation in Reducing Environments, Report

SD-TR-87-64, The Aerospace Corporation, El Segundo, CA, May 1987.

8. Reid, M. A.: Impedance Studies of Ni-Cd and Ni-H_2 Cells Using the Cell Case as a Reference Electrode, Space Electrochemical Research and Technology Conference, NASA Lewis Research Center, Cleveland, Ohio, April 1989.

Table 1
Nickel Electrode Characteristics

Characteristic	Hughes	Eagle-Picher	Whittaker Yardney	Gates
Plaque type	Dry Powder	Slurry	Slurry	Dry powder
Plaque porosity (%)	80	80	80	80
Impregnation process	Alcoholic	Aqueous	Aqueous	Aqueous
Loading level (g/cc void)	1.60	1.65	1.68	1.63
Cobalt level (mole %)	10	5	5	*
Thickness (mils)	30	30	35	31 or 37

* Proprietary information

Table 2
Nickel Electrode Storage Conditions

H2 Pressure (psig)	Temperature (deg C)	KOH Concentration (%)	Code
500	RT	31	HPRT31
50	RT	31	MPRT31
0	RT	31	APRT31
500	RT	26	HPRT26
500	-20	31	HPLT31

Table 3
Nickel Electrode Voltages After Storage
(Measured vs Hg/HgO)

Storage Condition	Electrode Manufacturer			
	Hughes	Eagle Picher	Whittaker Yardney	Gates
HPRT31	-0.765	0.173	0.032	0.170
MPRT31	0.186	0.198	0.191	0.200
APRT31	0.212	0.240	0.216	0.244
HPLT31	0.199	0.230	0.221	0.233
HPRT26	-0.365	0.216	0.073	0.216

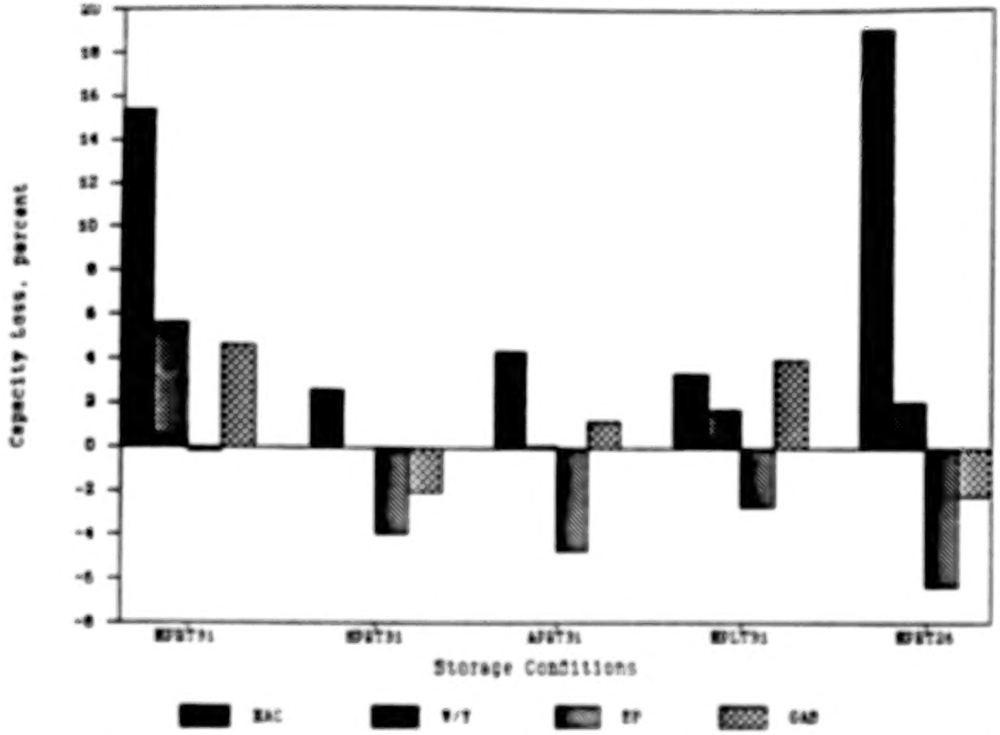

Figure 1 Capacity Loss vs Storage Conditions for Nickel Electrodes from Various Manufacturers

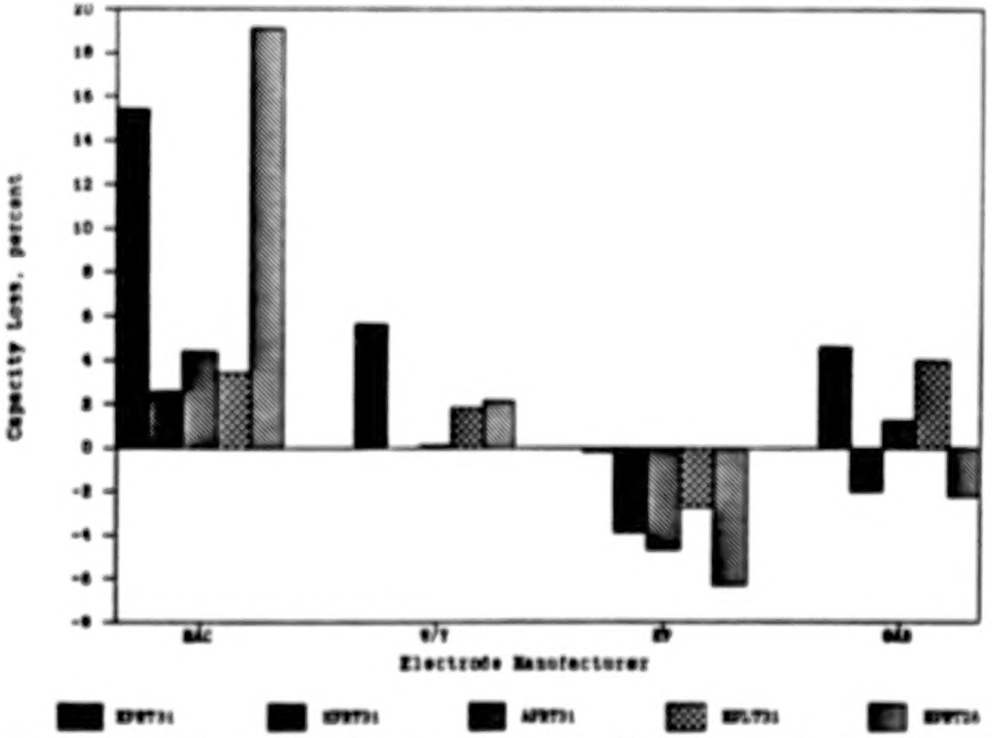

Figure 2 Capacity Loss vs Nickel Electrode Manufacturer for Various Storage Conditions

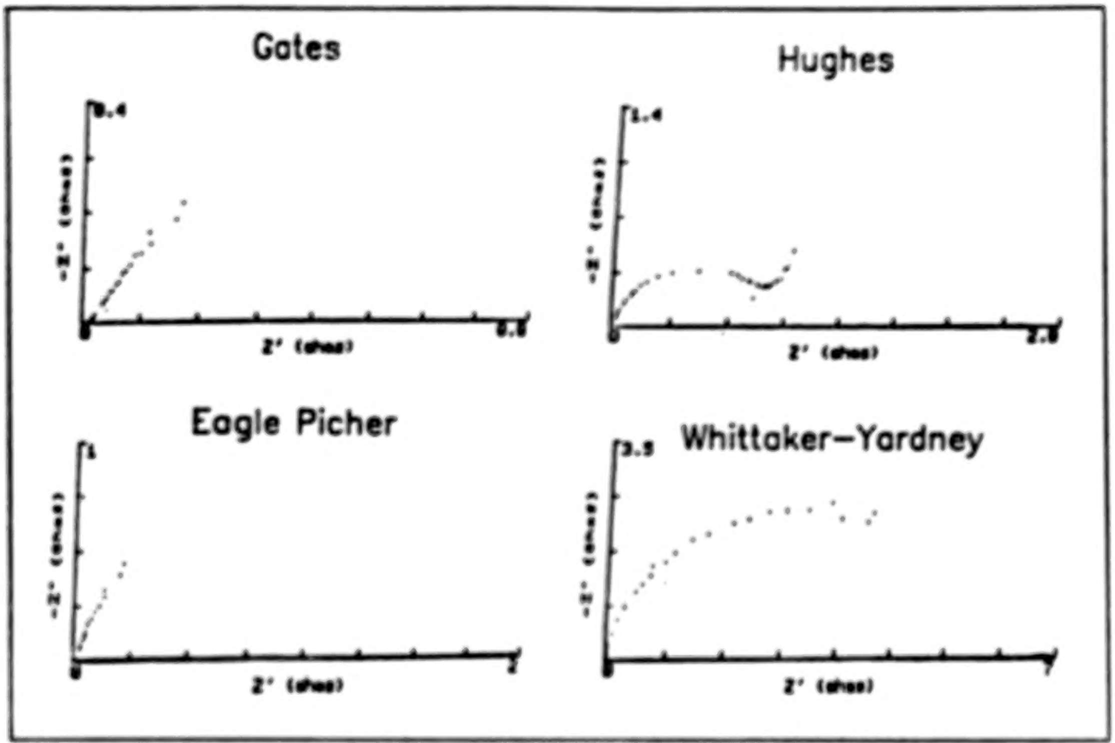

Figure 3 Representative Impedance Curves for Nickel Electrodes from the Various Manufacturers Impedance measured at 0.2 volts vs Hg/HgO

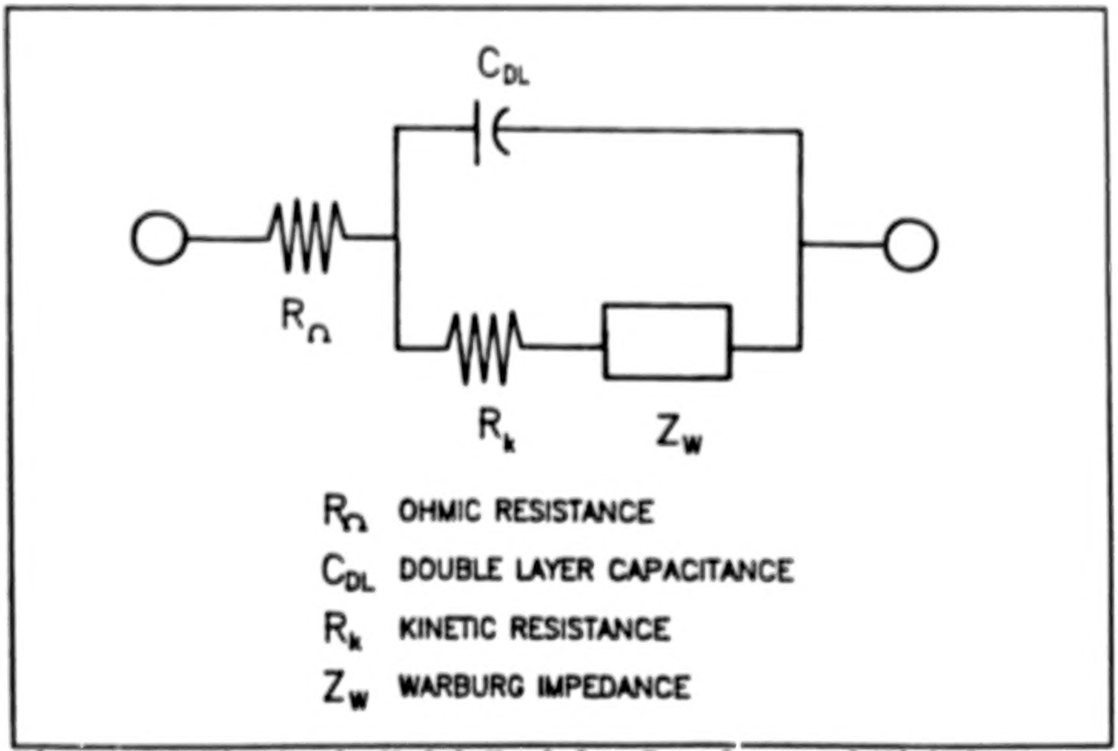
C_{DL}
R_{Ω}
R_k
Z_W
R_{Ω} OHMIC RESISTANCE
C_{DL} DOUBLE LAYER CAPACITANCE
R_k KINETIC RESISTANCE
Z_W WARBURG IMPEDANCE

Figure 4 Electrode Model Used for Impedance of Nickel Electrodes in Storage Studies

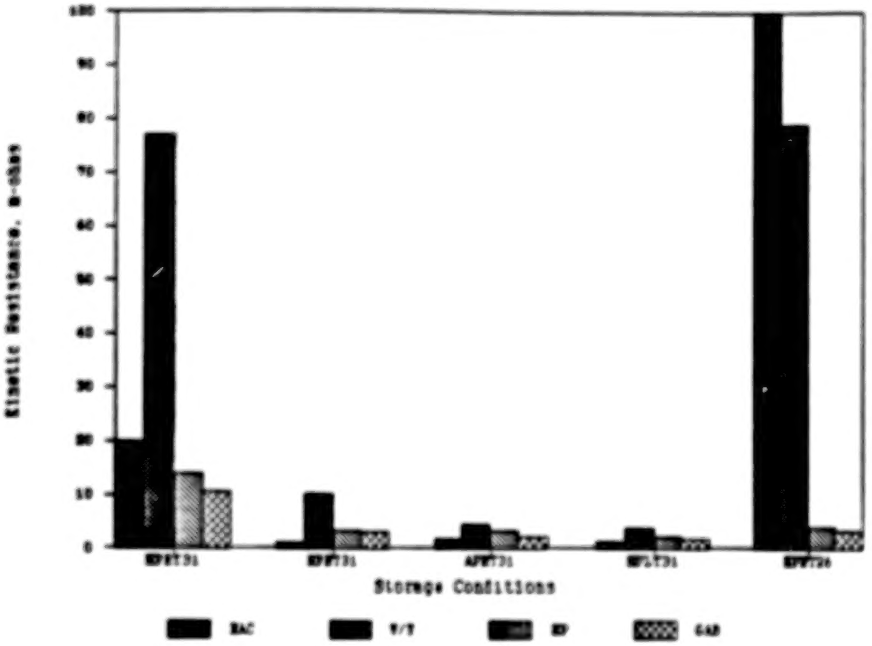

Figure 5 After Storage Impedance (Rk) vs Storage Conditions for Nickel Electrodes from Various Manufacturers

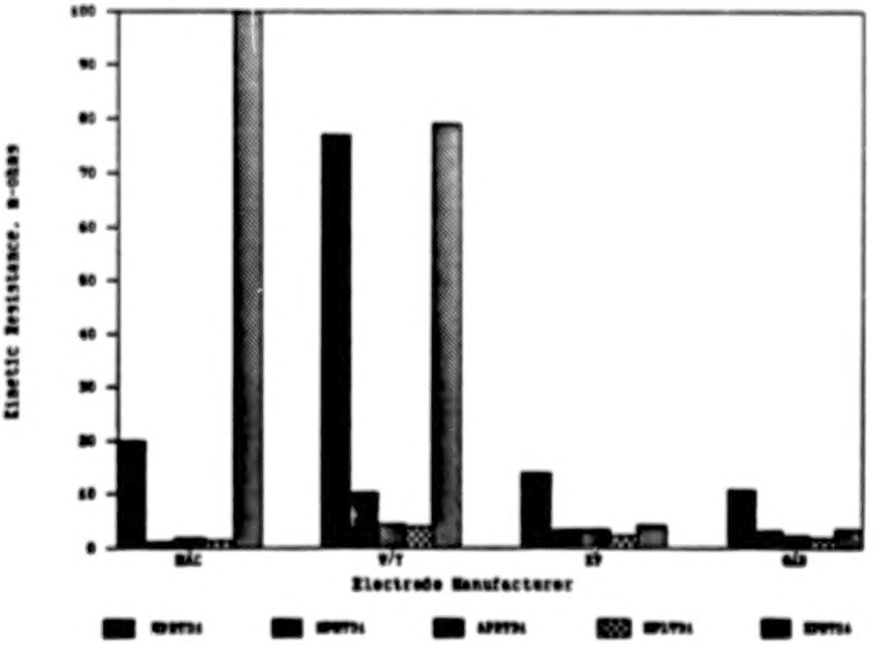

Figure 6 After Storage Impedance (Rk) vs Nickel Electrode Manufacturer for Various Storage Conditions

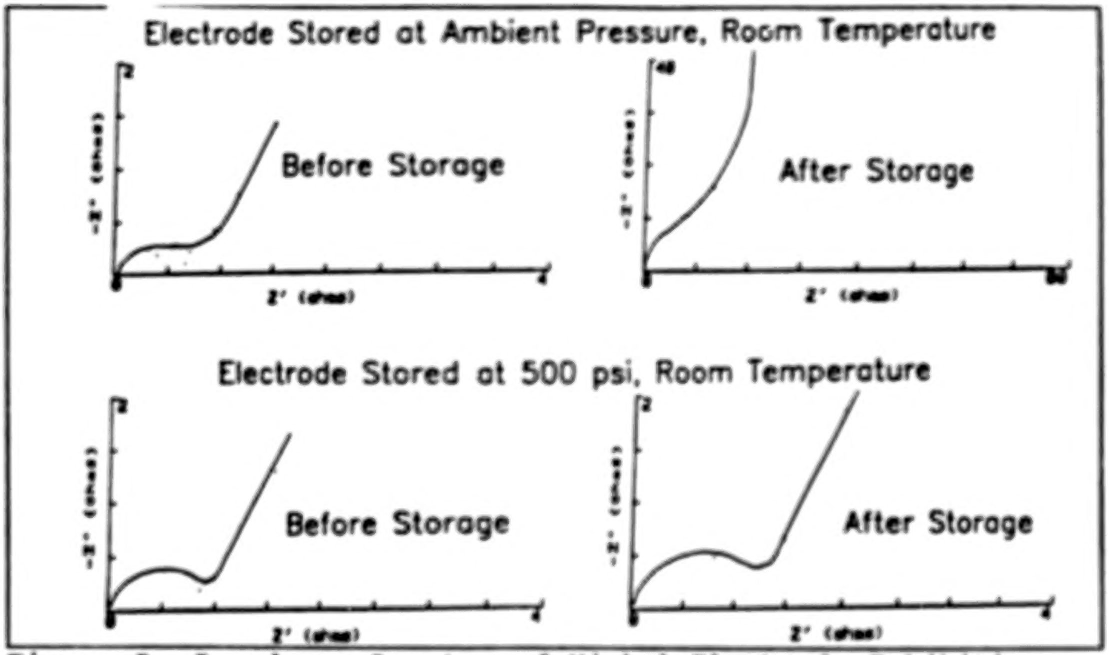

Figure 7 Impedance Spectra of Nickel Electrode Exhibiting Capacity Loss After Storage (shown at top) Compared to Impedance Spectra of Nickel Electrode That Did Not Exhibit Capacity Loss (shown at bottom)

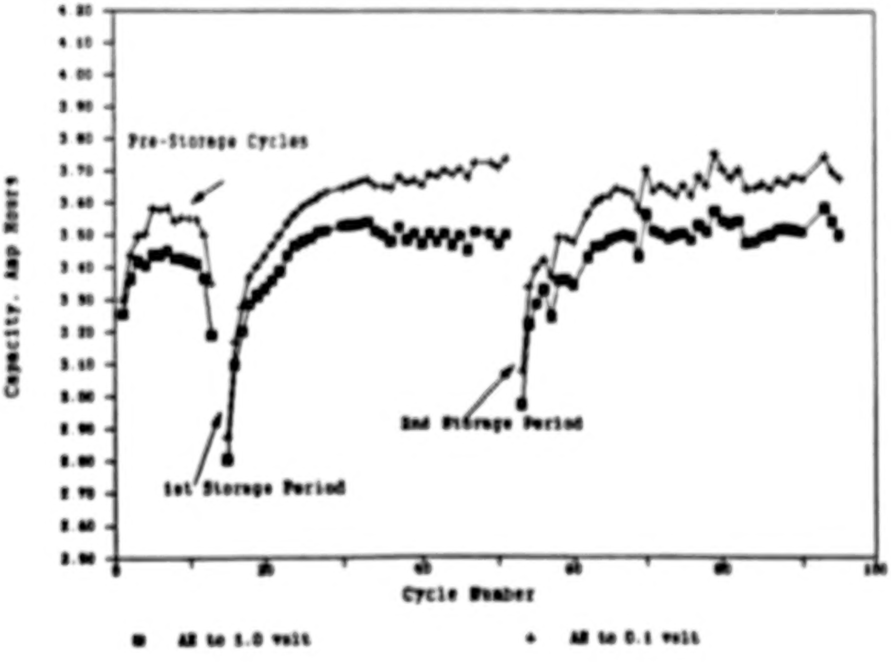

Figure 8 Capacity vs Cycles for Nickel-Hydrogen Cell Stored Discharged in the Open Circuit State

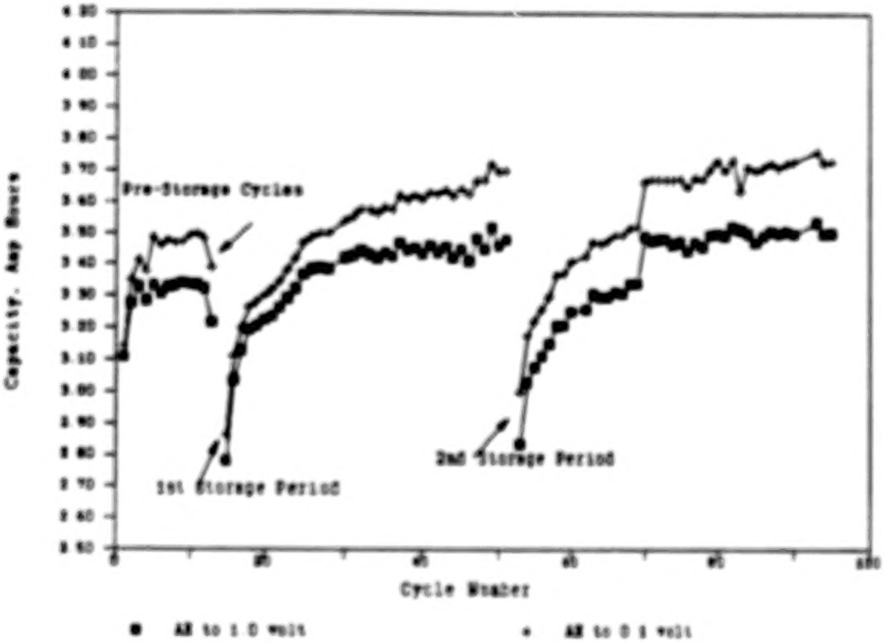

Figure 9 Capacity vs Cycles for Nickel-Hydrogen Cell Stored Discharged, Shorted

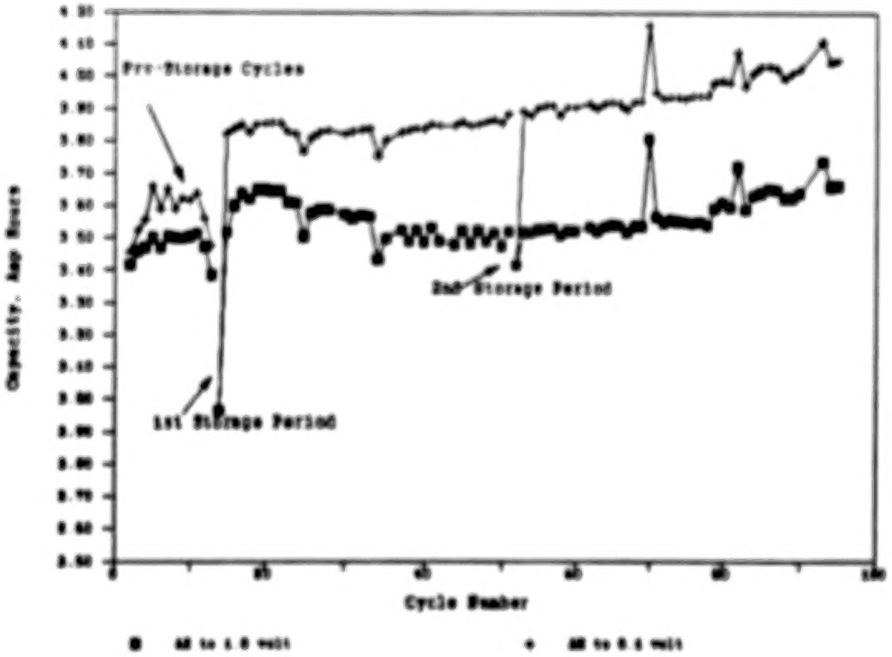

Figure 10 Capacity vs Cycles for Nickel-Hydrogen Cell Stored on Trickle Charge at C/200

SODIUM-SULFUR BATTERY FLIGHT EXPERIMENT DEFINITION STUDY*

Rebecca Chang
Ford Aerospace Corporation
Space Systems Division
Palo Alto, California 94303

and

Robert Minck
Ford Aerospace Corporation
Aeronutronic Division
Newport Beach, California 92663

The need for high power space systems is anticipated within the next 10 to 20 years. Examples are the Space Station, co-orbiting platforms, geostationary orbit (GEO) platforms, and space based radar satellites and some classified high power missions. Sodium sulfur (NaS) batteries have been identified as the most likely successor to nickel hydrogen ($Ni-H_2$) batteries for space applications. One advantage of the NaS battery system is that the useable specific energy is two to three times that of $Ni-H_2$ batteries. This represents a significant launch cost savings or increased payload mass capabilities. NaS batteries support NASA OAST's proposed Civil Space Technology Initiative goal of a factor of two improvement in spacecraft power system performance, as well as the proposed Spacecraft 2000 initiative.

The NaS battery operates at between 300 and 400°C, using liquid sodium and sulfur/polysulfide electrodes and solid ceramic electrolyte[1,2,3]. The transport of the electrode materials to the surface of the electrolyte is through wicking/capillary forces. These critical transport functions must be demonstrated under actual microgravity conditions before NaS batteries can be confidently utilized in space.

Ford Aerospace Corporation, under contract to NASA Lewis Research Center, is currently working on the NaS battery space flight experiment definition study. The objective is to design the experiment that will demonstrate operation of the NaS battery/cell in the space environment with particular emphasis on evaluation of microgravity effects. Experimental payload definitions have been completed and preliminary designs of the experiment have been defined.

* The work at Ford Aerospace Corporation is sponsored by NASA Lewis Research Center under contract NAS3-25355.

INTRODUCTION

The NaS battery cell, pioneered by Ford Motor Co., is seen as one of the most attractive battery systems for spacecraft power systems. The primary advantage of this system is its high energy density, which can reach 150 WH/kg at C-rate discharge at the cell level. The NaS battery offers a combination of system level advantages:

- Mass and volume effectiveness
- High round-trip efficiency
- Heat rejection at high temperature
- Simplicity of battery integration
- Competitive acquisition costs

Nominal NaS cell operating parameters are shown and compared with typical Ni-Cd and Ni-H_2 cell data in Table 1. Unusual performance features for the NaS cells are the high cell operating voltages, high roundtrip efficiency and high operating temperature which minimizes the radiator area and cost. Potential cost savings are illustrated in Table 2. It is obvious that the battery mass savings are translated into spacecraft launch cost savings or payload capability increase. Using Ni-H_2 systems as a reference, it can save in launch cost from 1.1 to 1.7M$/KW for the GEO missions and 0.2 to 0.4M$/KW for the LEO missions. For example, a 2.5 KW aerospace NaS battery concept design which weighs 31.8Kg while a 2.5 KW Ni-H_2 battery weighs 30.5 kg.

The NaS battery is a particularly good energy storage system for high power satellite missions. A parametric study comparing the operational storage candidates for a 75 KW satellite mission has been performed by Ford Aerospace and the results are shown in Table 3[1]. The NaS battery looks the most favorable with respect to the other storage systems.

The NaS battery cells operate at between 300 and 400° C. The liquid electrode materials rely on the wicking actions for transport to and from the electrolyte interface to support routine cyclic operation. Current developmental space cells have been designed to have adequate wicking, but this critical function must be demonstrated under actual orbital microgravity conditions before NaS batteries can be confidently applied in space. The primary objective of the Ford Aerospace study is to define the specific experimental design required for successful demonstration of NaS battery/cells under space environments.

CELL OPERATIONS AND SELECTIONS

NaS cells as shown in Figure 1 utilize a solid ceramic electrolyte known as β"-alumina to separate anode (sodium) and cathode (sulfur/sodium polysulfide) reactants and to provide a conductive path for sodium ions during operation. The transport of the electrode materials to the surface of the electrolyte is through wicking/capillary forces. A metal protection tube limits the flow of sodium into the reaction zone, thus providing for safe operation of the cell. Since only small amounts of the sodium are available for reaction, a quick, explosive reaction is not possible to occur even in the case of a broken electrolyte tube. The sulfur is contained in the outer part of the cell, imbedded in a carbon fiber mat. The carbon fiber mat improves the electrical conduction path for the sulfur electrode.

At the cell operating temperature, the reactants are at liquid state. During discharge of the cell, the sodium splits into positive ions, which are transported across the electrolyte, and negative electrons, which are carried up by the current collector to the external circuit. Once the sodium ions are transported across the ceramic electrolyte, they join with the sulfur to form a sodium-polysulfide (Na_2S_5). As the cell is further discharged, the Na_2S_5 reacts with sodium to form other sodium polysulfides such as Na_2S_4 and Na_2S_3. Charging the cell results in the opposite reactions taking place with the sodium-polysulfides being dismantled into sodium ions and sulfur. The sodium ions are then transported back across the electrolyte to the sodium electrode.

The proposed flight experiment cells which are rated 40AH are derived from the Ford Aerospace baseline SATBAT-2 cells. The physical characteristics of the cells are summarized as follows and typical 40AH cells are shown in Figure 2.

Cell Capacity (Ah): 40.0
Outer diameter (cm): 3.6
Cell length (cm): 23.0
Cell Mass (g): 519.0

FLIGHT EXPERIMENT JUSTIFICATIONS AND OBJECTIVES

NaS cells differ from most batteries in that they contain molten anodic and cathodic reactants. Ability of the NaS cells to efficiently charge and discharge is critically dependent upon the favorable spatial distribution of the fluid reactants with respect to their interface with the solid beta"-alumina ceramic electrolyte. Fluid motion and reactant morphology are particularly critical for NaS cell operation since the sulfur/sodium-polysulfide catholyte reactants form three immiscible phases during recharge, two of which are non-conductive: molten sulfur, void volume, and Na_2S_5. Should an unfavorable distribution occur, a blocking layer could develop and restrict cell operation.

Terrestrial cell designs incorporate preferential wetting, capillarity and/or graded resistance within the sulfur electrode to maintain efficient operation. Such cells have been developed to operate effectively at high rate and to yield high specific energy and specific power. However, the characteristics of NaS cells under microgravity conditions are unknown because of the uncertain role of gravity in controlling the distribution and consolidation of the separate reactant phases. These effects can only be determined by testing in orbit with 3-axis stabilized spacecraft because it is not possible to simulate low gravity conditions for sufficiently long times to represent cycling or the large equilibration time constraints associated with the sluggish fluids.

The main purpose of the NaS battery/cell flight experiment is to validate the application of NaS battery technology to space power applications. The principal objective of the flight experiment definition study is to design an experiment that will demonstrate operation of the battery/cells under space environments with particular emphasis on evaluation of microgravity effects which are specially critical for 3-axis stabilized spacecrafts. These can be categorized in the followings:

I. To evaluate cell charge and discharge characteristics as affected by the fluid reactant distributions.
II. To determine reactant distributions under microgravity conditions.
III. To understand current and thermal distributions within the cells.
IV. To evaluate freeze/thaw effects.
V. To evaluate multi-cell early LEO (Low Earth Orbit) cycle life.

The approach is to select only those tests that are critical and expected to differ under microgravity conditions. Spin stabilized satellite batteries can be tested on the ground, thus a test to simulate this application in space is not needed. Warm launch has an advantage that the cells in space will require less energy and time to heat up from the warm launch temperature to its final operating temperature. However, the demonstration of the cell survivability to the launch environments can be confirmed on the ground by test followed by electrical cyclic testings. Therefore, the warm launch test need not be included in the experiment.

DESCRIPTION OF PROPOSED EXPERIMENTS

Five tests have been identified in the NaS battery flight experiment definition study to meet the above objectives. Each of these tests will be summarized in the following sections.

I. CELL CHARACTERIZATION TEST
II. REACTANT DISTRIBUTION TEST
III. CURRENT/TEMPERATURE DISTRIBUTION TEST
IV. FREEZE/THAW TEST
V. MULTI-CELL LEO CYCLE TEST

The test cells will be Ford Aerospace baseline 40AH cells except Test III cells which will be specially instrumented with extra thermocouples and voltage probes.

Our general testing philosophy is to have most of the space cells evaluated under various conditions on the ground prior to launch, in the space, and after cells are brought back to earth to provide before-during-after data comparison. Additional control cells will be assigned to an identical ground test to provide additional comparative data base.

I. CELL CHARACTERIZATION TEST

NaS cells will be evaluated under various test conditions in space under two temperature ranges, 275°C and 350°C. Once orbit has been stabilized, the cells will be heated to operating temperatures and the test sequence performed. The charge/discharge cycle variables have been established to cover a sufficiently wide range of parameters to address a majority of anticipated space applications. Pulse loads will be imposed during the discharge. Each cell will be instrumented with power leads, voltage sense leads and a thermocouple pair, all which will penetrate the thermal insulation barrier for connection to ambient temperature connector panels. During the charge/discharge cycle, each cell voltage will be periodically measured.

II. REACTANT DISTRIBUTION TEST

After completion of Test I, the cells will be discharged into their 1-phase region and placed on open circuit to accurately determine their state-of-charge. Each state of charge of the cell will be adjusted to a composition ranging from Na_2S_3 to Na_2S_5.

III. CURRENT/TEMPERATURE DISTRIBUTION TEST

This test will determine the spatial variations of electrode reactions and current densities within the sulfur electrode continuously throughout the electrical cycles while being operated under microgravity conditions. This information will support analysis and assessment of test results of Test I and II, and will provide direction of possible modification of the sulfur electrode design should that prove necessary.

The distribution of internal current densities and electrode reactions will be measured continuously during the electrical cycles by measuring its small ohmic losses. Specially instrumented cells will be fabricated to incorporate a multitude of voltage probes on the positive current collector. In addition to the external thermocouples located at the top, middle, and bottom of the cell container, internal thermocouples on the inside electrolyte tube wall will also be installed at respective locations to measure the temperature gradients. Three sets of voltage probes shall be used to provide information about circumferential uniformity.

IV. FREEZE/THAW TEST

Cells will be evaluated for the freeze/thaw cycles. Cells will be initially heated up to operating temperature and evaluated electrically, followed by several freeze/thaw cycles. On the last day of the flight experiment, cells will be again evaluated electrically to determine the effects of the freeze/thaw under microgravity conditions. The cells will be cooled for reentry.

V. MULTI-CELL LEO CYCLE TEST

NaS cells will be series connected and evaluated in the 90 minute orbit regime. Cells will be cycled at a high rate discharge for 36 minutes and followed by a charge for 54 minutes. It is almost impossible to evaluate the life cycle of the NaS cells in such short experiment duration. However, the proposed LEO cycle will provide an early life real time LEO operational experience and demonstrate the multi-cell operation. Information obtained will be definitely valuable for full size battery scaling-up.

SYSTEM IMPLEMENTATION AND CARRIER OPTIONS

A variety of payload carriers, shown in Figure 3, including Middeck Modular Locker, Get Away Special, Hitchhiker G, and Hitchhiker M have been reviewed[5]. Concerns such as electrical power, mass load/structure, and mounting orientation have been considered as factors for carrier selections. From the preliminary design of the five tests, the total weight of the enclosures, batteries, and support equipments is estimated to be a total of less than 100 lbs. The experiment will occupy a space approximately 3.0'x3.0'x1.5'.

SUMMARY AND CONCLUSION

NaS batteries have been identified as the most likely successor to space Ni-H_2 or Ni-Cd batteries, primarily due to a mass reduction by a factor 2-3 over Ni-H_2 and by a factor of 4 over Ni-Cd. This yields major launch cost reductions or payload mass improvements. NaS batteries support NASA OAST's proposed Civil Space Technology Initiative goal of a factor of two improvement in spacecraft 2000 initiative. Since Ni-H_2 and Ni-Cd batteries have been space flight proven, it is essential to have the flight experiment to establish a national space technology base to demonstrate the operation of the NaS battery for space applications.

ACKNOWLEDGEMENT

The authors wish to thank our colleagues for technical assistance and the support of this work from NASA Lewis Research Center under contract No. NAS3-23355.

REFERENCES

1. R.W.Minck & C.R.Halbach, "Characteristics of Sodium-Sulfur Cells for Diverse Applications", Proceeding of the 17th IECEC, 1982, P.557
2. H.L.Haskins, M.L.McClanahan, and R.W.Minck, "Sodium-Sulfur Cells for High-Power Spacecraft Batteries", Proceeding of the 18th IECEC, 1983, P.1465
3. D.M. Allen, "sodium-Sulfur Satellite Batteries: Cell Test Results and Development Plans", Proceedings of the 19th IECEC, 1984, P.163
4. C.W.Koehler & A.Z.Applewhite, and A.M.Hall & P.G.Russell, "Bipolar Nickel-Hydrogen Battery Development", Proceeding of the 20th IECEC, 1985
5. NASA Marshall Space Flight Center, "STS Investigators Guide"

Table 1. SPACE BATTERY OPERATING PARAMETER COMPARISON

Battery System	Condition	Average Cell Voltage (V)		Roundtrip Efficiency (%)	Discharge Dissipation (kWt/kWe)	Operating Temperature (C)	Typical DOD (%)
		Charge	Discharge				
Ni/Cd	GEO	1.43	1.22	80	0.18	0-20	45-60
	LEO	1.45	1.23	80	0.17	0-20	15-22
Ni/H_2	GEO	1.45	1.25	80	0.20	0-20	68-80
(IPV)	LEO	1.47	1.27	80	0.18	0-20	28-40
Ni/H_2	GEO	1.45	1.26	82	0.19	0-20	68-80
(bipolar)	LEO	1.46	1.28	82	0.27	0-20	28-40
Na/S	GEO	2.10	1.83	87	0.18	300-400	50-80
	LEO	2.15	1.80	84	0.21	300-400	35-50

Table 2. Sodium/Sulfur Batteries Offer Spacecraft Mass Savings

Battery System	Condition	Mass Performance	Volume Performance	Cost vs Ni/H2		Life Years
				Prod	Launch	
Ni/Cd	GEO	55-90 kg/kW	30-55 l/kW	1.1	+ 1.0-1.5 M$/kW	5-7
	LEO	70-140 kg/kW	40-85 l/kW	1.6	+ 0.3-0.5 M$/kW	5-5
Ni/H_2	GEO	35-60 kg/kW	60-120 l/kW	1	0	10-15+
(IPV)	LEO	35-70 kg/kW	60-150 l/kW	1	0	5-8
Ni/H_2	GEO	35-60 kg/kW	25-45 l/kW	1.2	0	10-15+
(Bipolar)	LEO	35-70 kg/kW	25-55 l/kW	1.2	0	5-8
Na/S	GEO	13-25 kg/kW	40-120 l/kW	1.2	- 1.1-1.7 M$/kW	5-(a)
	LEO	11-20 kg/kW	30-85 l/kW	1.2	- 0.2-0.4 M$/kW	1-(a)

a) requires demonstration

TABLE 3. ENERGY STORAGE SYSTEM OPTIONS COMPARISON

	ENERGY STORAGE SUBSYSTEM OPTIONS						
PARAMETER	RFC H_2-O_2	RFC H_2-O_2	BIPOL Ni-H_2	IPV Ni-H_2	Ni-Cd	Na S	FLY WHEEL
ROUND TRIP EFFICIENCY (%)	55	60	77	75	75	82	82
DEPTH-OF-DISCHARGE (%)*	38	38	38	38	20	38	38
MASS (kg)	2100	2500	3300	4100	9500	1500	4200*
VOLUME (m^3)	9.3	9.9	2.5	6.6	5.2	1.9	4.0*
WASTE HEAT/CYCLE (kW h)	42	34	15	17	17	11	11
ECLIPSE HEAT REJECTION (kW)	57	55	17	18	17	17	9
TEMPERATURE (°C)	80	80	10	10	10	350	35
CHARGE POWER REQUIREMENT (kW)	98	90	74	76	76	66	66

*IN ALL CASES, EXCEPT Ni-Cd CONTROLLED BY ONE ORBIT HALF POWER REQUIREMENT FOLLOWING A FULL POWER ECLIPSE

*EXCLUSIVE OF CONTAINMENT

FIGURE 1. SCHEMATIC OF NaS CELL

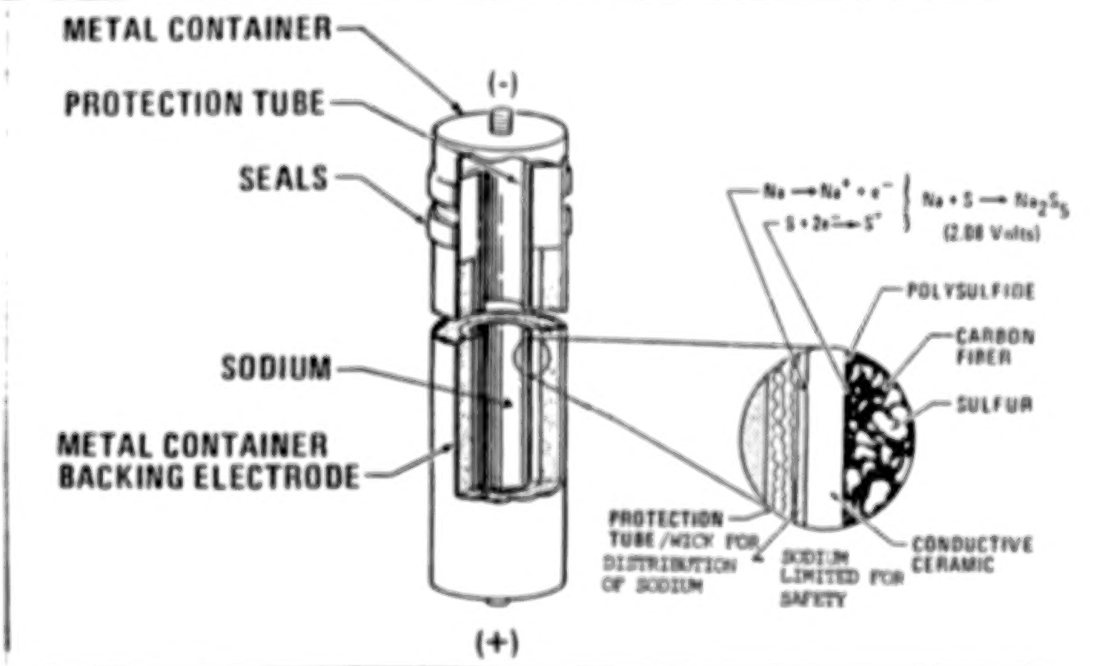
METAL CONTAINER
PROTECTION TUBE
SEALS
(-)
SODIUM
METAL CONTAINER
BACKING ELECTRODE
(+)
Na → Na⁺ + e⁻
S + 2e⁻ → S⁼
Na + S → Na₂S₅
(2.08 Volts)
POLYSULFIDE
CARBON FIBER
SULFUR
PROTECTION TUBE/WICK FOR DISTRIBUTION OF SODIUM
SODIUM LIMITED FOR SAFETY
CONDUCTIVE CERAMIC

FIGURE 2. FORD AEROSPACE NaS CELLS

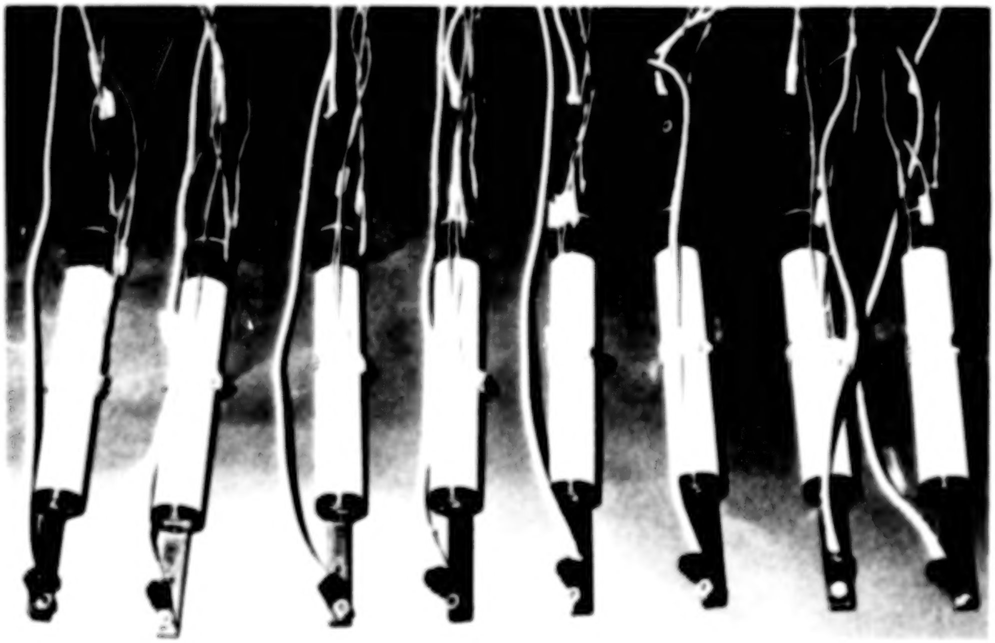

FIGURE 3. PAYLOAD CARRIER OPTIONS

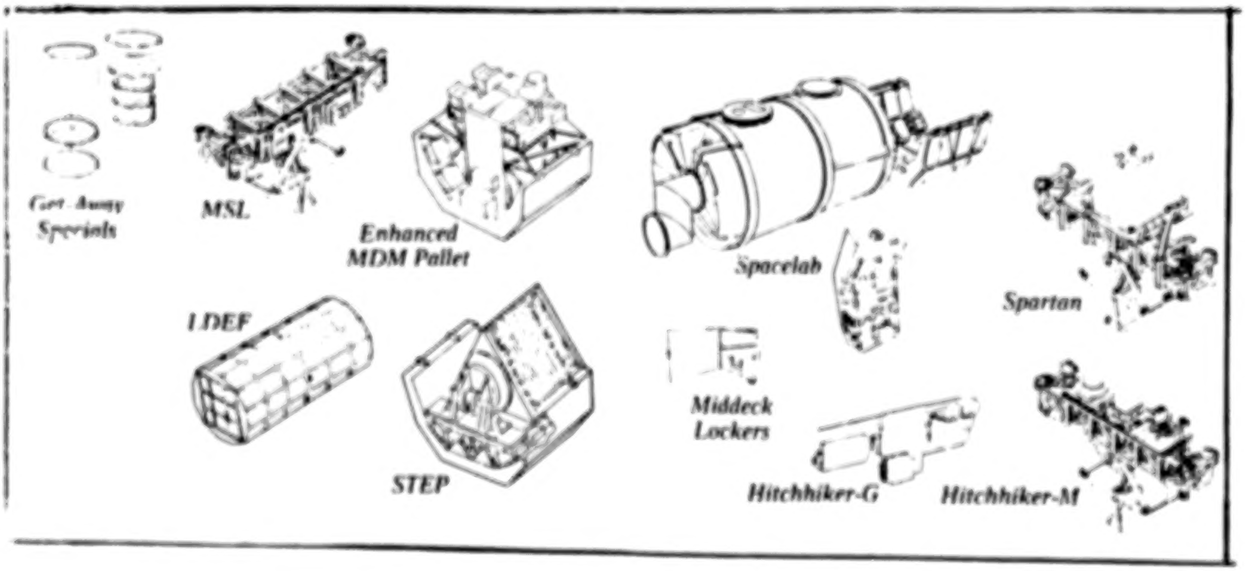
Get Away
Specials
MSL
Enhanced
MDM Pallet
Spacelab
Spartan
LDEF
STEP
Middeck
Lockers
Hitchhiker-G
Hitchhiker-M

ADVANCED HIGH-TEMPERATURE BATTERIES

P.A. Nelson
Argonne National Laboratory
Argonne, Illinois 60439

Recent results for Li-Al/FeS_2 cells and a bipolar battery design have shown the possibility of achieving high specific energy (210 Wh/kg) and high specific power (239 W/kg) at the cell level for an electric vehicle application. Outstanding performance is also projected for sodium/metal chloride cells having large electrolyte areas and thin positive electrodes.

INTRODUCTION

Work has been under way for about two decades on high-temperature batteries having lithium or sodium negative electrodes. These efforts have met with some success, but the original promise of very high specific energy and power has not been achieved for practical battery systems. This paper discusses some recent new approaches to achieving high performance for lithium/FeS_2 cells and sodium/metal chloride cells.

A comparison of the voltages and theoretical specific energies for several high-temperature cell couples is shown in Table I. The fraction of the theoretical specific energy that can be achieved for practical cells differs markedly among the couples shown in Table I. The important factors in determining that fraction are the voltages of the cells and the densities of the reactants and the discharge products. The densities of the materials have a surprisingly important effect on the achievable specific energy, as is discussed in more detail below.

LITHIUM/DISULFIDE BATTERIES

The main problems for the development of successful Li-Al/FeS_2 cells have been (1) instability of the FeS_2 electrode, which has resulted in rapidly declining capacity, (2) the lack of an internal mechanism for accommodating overcharge of a cell, thus requiring the use of external charge control on each individual cell, and (3) the lack of a suitable current collector for the positive electrode other than expensive molybdenum sheet material. Much progress has been made at ANL in solving the first two problems, and a new approach to cell design may result in a solution for the materials problem.

The disulfide electrode discharges along two major voltage plateaus, as shown in Fig. 1 (ref. 1). It has been found practical to limit the amount of lithium in the negative electrode to stop the discharge at the end of the first major plateau, with a final discharge product of Li_2FeS_2. Although, this limits the theoretical specific energy to about 475 Wh/kg (second row, Table I, based on Li-50 atom % Al), the positive electrode can be fabricated as a much denser electrode without provision for the large volume of Li_2S produced in operating on the lower voltage plateau.

The early problem on the stability of the FeS_2 electrode involved the disassociation of FeS_2 at high voltages on charge with the formation of polysulfide ions, which dissolve in the electrolyte and then result in deposition of lithium sulfide in the separator region.

Thomas D. Kaun at Argonne National Laboratory studied this stability problem and also sought to achieve higher energy and power by the incorporation of dense FeS_2 electrodes operated only on the upper voltage plateau (ref. 2,3). He found that the use of dense FeS_2 electrodes not only improves the specific energy but also improves the electrode conductivity and results in higher power. In most of the earlier work, the electrolyte was the LiCl-KCl eutectic (m.p., 352°C), which required operation of the cell at about 450°C because of polarization of the electrolyte with high composition gradients at high operating rates. Kaun introduced the use of an LiCl-LiBr-KBr electrolyte having a lower melting point and a broader liquidus range than those of the LiCl-KCl electrolyte, permitting operation at 400°C. The combination of these changes improved the electrode utilization by 50% and doubled the power capability of the electrode at 80% depth-of-discharge (Fig. 2). These changes also resulted in a dramatic improvement in cycle life capability, as shown in Fig. 3.

Another key improvement has been the development of a chemical overcharge protection mechanism (ref. 4). By providing an excess of lithium relative to the aluminum or other alloy elements, a high lithium activity at the negative electrode is reached at the end of charge. This results in an increase in the dissolved lithium concentration in the electrolyte as the cell approaches full charge and, thus, about a twentyfold increase in the rate of self-discharge for the cell. By maintaining a low trickle-charge rate for several hours at the end of the charge, cells that are only partially charged have an opportunity to come to full charge, while fully charged cells tolerate the overcharging by the increase in the self-discharge rate.

Recently work has begun on bipolar Li-Al/FeS_2 cells. The bipolar configuration reduces the amount of nonactive material required in the cell, and it provides a simpler design for the use of a coated material to reduce the cost of the disulfide electrode current collector. A schematic of the experimental cells now under development is shown in Fig. 4.

Researchers at ANL have used the results of cell tests to project the performance of Li-Al/FeS and Li-Al/FeS_2 cells in both the bicell and bipolar configuration. The results are summarized in Table II. The capacity and power at the end of discharge (EOD) of the four types of lithium/sulfide cells in Table II were selected to be appropriate for the Eaton DSEP van being developed by Chrysler and Eaton in a program for the Electric and Hybrid Propulsion Division of the Department of Energy. The specific energy of the multiplate monosulfide cell is essentially that which has been already achieved in the laboratory, but the specific power assumes about a 50% improvement, which is expected to be achieved with thinner electrodes. The bipolar monosulfide calculations are based on the electrode performances used for the multiplate cells, with the weight of the cell calculated by adding the weight of individual parts. The bipolar monosulfide cell would be approximately 7-1/2 in. in diameter and have electrodes 7-in. in diameter. The performance of the disulfide bicell is based on results achieved in the laboratory for smaller cells, with the weight calculated from the individual components. The calculations for the disulfide bipolar cell were based on the monosulfide bipolar calculations, with substitution of parts as necessary for the disulfide conditions.

Table III gives the projected performance for batteries constructed for the Eaton DSEP van. These results are based on the projected cell performances of Table II. The initial range of the vehicle with a new battery would be 125 miles. At the end of battery life it would be 100 miles. The energy storage required of the battery was adjusted for the total weight of the vehicle, including the battery, to achieve the desired vehicle range (Table III). It should be noted that the vehicle weight is a function of the battery weight, being 1649 kg plus the battery weight. The power at the end of discharge and at the end of battery life is sufficient for accelerating the vehicle to 50 mph in 20 s. With new batteries, for which the powers at the end of battery discharge are given in the table, the acceleration would be approximately 20% more rapid than at the end of life.

The number of parallel strings in the batteries varies from one for the monosulfide multiplate to three for the bipolar batteries. For the bipolar batteries, each string would be housed in a separate insulating container of approximately 10-in. O.D.

Tests of very thin Li-Al/FeS_2 cells are appropriate for pulsed power applications. Figure 5 shows the apparatus used by Laszlo Redey (ref. 5) for a pulsed discharge measurement, and Fig. 6 shows the results that were achieved in a discharge of approximately one millisecond. The calculated results show a specific power of 82.7 kW/kg and a power-to-energy ratio of 574 W/Wh (Table IV).

SODIUM/METAL CHLORIDE BATTERIES

Sodium/sulfur batteries and sodium/metal chloride batteries have demonstrated good reliability and long cycle life. For applications where very high power is desired, new electrolyte configurations would be required.

The sodium/metal chloride cells are related to sodium/sulfur cells in that they both use molten sodium negative electrodes and a β"-alumina solid electrolyte. The sodium/metal chloride system was invented in South Africa and is now being developed under the direction of Anglo America of South Africa. The principal organizations involved in this development effort include Harwell and Beta Research and Development Ltd. of England and Zebra Power Systems of South Africa.

The sodium/metal chloride cells, unlike the sodium/sulfur cells, utilize a secondary liquid NaCl-$AlCl_3$ electrolyte in the positive electrode in conjunction with an active material of metal chloride such as $FeCl_2$ or $NiCl_2$ (ref. 6-16). Because the NaCl and the metal chloride are insoluble in NaCl-$AlCl_4$ at the operating conditions, the NaCl-$AlCl_3$ electrolyte acts only to transfer sodium ions within the positive electrode. The cells can be operated at temperatures down to 160°C (the melting point of the liquid electrolyte), but are typically operated in present development work at 250°C to improve the kinetics of the positive electrodes.

The voltages and theoretical specific energies are given in Table I, and the overall reactions for the Na/$FeCl_2$ and Na/$NiCl_2$ cells are shown below:

$$2Na + FeCl_2 = 2NaCl + Fe$$

$$2Na + NiCl_2 = 2NaCl + Ni$$

An important feature of the metal chloride cells is that they are commonly fabricated in the uncharged state. For the Na/$FeCl_2$ cell, iron powder is mixed with NaCl powder and pressed into a positive electrode. The NaCl-$AlCl_3$ electrolyte is added to the top of the positive electrode material as a dry powder, and the cell is charged after heating to the operating temperature. An important feature of fabricating the Na/MCl_2 cells in the uncharged state is that the reactants are relatively inexpensive and easily purified. The iron powder required for the Na/$FeCl_2$ cell is considerably less expensive than the nickel powder required for the Na/$NiCl_2$ cell, an obvious cost advantage, but the Na/$NiCl_2$ cell has better potential performance.

Most of the work on Na/$FeCl_2$ and Na/$NiCl_2$ cells described in the published literature (ref. 6,7) is on cells of 100 Ah or even larger capacity. Batteries of such cells are already being tested in electric vehicles and appear to be rugged and reliable. This reliability results from connecting the cells into a single series-connected string. Unlike Na/S cells, Na/MCl_2 cells usually fail in the closed circuit condition. Large Na/MCl_2 cells can be connected in series, with the loss of a cell resulting only in the loss of voltage associated with that cell and essentially no loss of ampere-hour capacity for the entire battery.

The consequence of fabricating such large cells with a single beta-alumina electrolyte tube is that the cells have only moderate power and large voltage drops when discharged at the three-hour rate. Also, to achieve even moderate discharge rates for the thick positive electrodes requires a high volume fraction of molten salt electrolyte. This adds to the weight and, coupled with the large reduction in voltage from that of an open circuit, results in achieving a low fraction of the theoretical specific energy. As an example, Na/$NiCl_2$ battery cells of 100-Ah capacity were reported to achieve a specific energy of about 109 Wh/kg and have a cell resistance of 9 mΩ (ref. 8). When these cells were operated in a 60-cell battery, the energy was reduced to 88 Wh/kg and 95 Wh/L, which are less than the desired values for an advanced battery. However, the small reduction in specific energy of the battery compared to that of the cells is encouraging and results from the high density and high packing density of the cells. The life of both the cells and the batteries is reported to be excellent (1000 cycles).

An important feature of the Na/MCl_2 cell is that, in the positive electrode, the MCl_2 material is in thermodynamic equilibrium with the metallic constituent (iron or nickel) and does not appear to attack current collector materials made of the same metal. In contrast, polysulfides in the positive electrode of sodium/sulfur cells tend to attack most metals and alloys except, perhaps, chromium and molybdenum, which are quite useful as coatings.

We believe that much higher specific energies and powers than those achieved in the studies reported in the literature are possible with sodium/metal chloride cells. One indication of this is the high utilizations reported for Na/$FeCl_2$ cells at low current densities with relatively thick electrodes (ref. 7).

The sodium/metal chloride cell appears to have several unique characteristics. These include: (1) the cell failures are usually in the short-circuit mode, which provides very good battery reliability, (2) the reaction of sodium and either $FeCl_2$ or $NiCl_2$ following the fracture of an electrolyte is mild with only a slight temperature rise, a good safety feature, and (3) high active material densities and high packing density for the cells result in a high calculated volumetric energy density for the battery and a lightweight, compact battery insulating case.

To take advantage of these good features, the low power of the present cell design must be circumvented by increasing the greater electrolyte surface area, which could make possible the use of thinner positive electrodes.

One approach to designing high-performance sodium/metal chloride batteries is to design very small cells with small-diameter, thin-walled electrolyte tubes. Calculations at ANL indicate that for this approach the cells would have to be less than 5 Ah in capacity for the electric vehicle application and, thus, may result in high-cost cell fabrication and complex cell interconnection.

A more promising approach is to develop an electrolyte structure consisting of many long, small-diameter tubes connected to a single header. The sodium could be located either inside or outside the tubes. If the sodium is located inside the tubes, the segregation of the sodium into separate compartments is a good safety feature, and the heat which is developed in the positive electrode on discharge would be more easily transmitted to the wall of the cell from outside of the tubes. Whether the sodium is located inside or outside the tubes, each tube may be provided with an individual current collector wire, which can be sealed into the individual tubes. With this design approach, the header may be constructed of a metal that is compatible with the positive electrodes (nickel, for instance). Individual tubes could be sealed into the header with glass. It may be possible to retain some of the flexibility provided by the metal header and permit some movement between the individual electrolyte tubes, thus avoiding high stresses and cracking that might result for a rigid header structure.

Another approach is to develop a flat-plate electrolyte structure such as that shown in Fig. 7. Individual current collector wires could be sealed into the square pockets, which are probably most appropriate for containing the sodium electrode material.

A comparison of the characteristics of the three types of electrolyte configurations (single large tube, multiple tube, and flat-plate compartmented) is shown in Table V. A design cell capacity for each of these configurations is shown on the top row of the table. The 100 Ah capacity for the single large tube is typical of that now used in sodium/metal chloride cells. Cell capacities of 200 Ah are assumed for a multiple-tube cell and a flat-plate cell having compartmented electrolytes. To achieve the assumed capacities for the respective cells, 100 tubes are needed for a multiple tube cell, and 6 electrolyte structures are needed for the flat-plate compartmented cell.

These structures in the assumed sizes provide considerably more electrolyte area than that in the single large tube cell. The larger electrolyte areas coupled with the thinner wall thicknesses of the electrolytes result in much lower voltage losses through the electrolytes, as shown in the table. The electrolyte dimensions selected for Table V are only representative of high surface area designs and could be adjusted to achieve a wide range of power-to-energy ratio.

The voltage losses that develop in the positive electrode are also alleviated by the use of electrolytes having high surface areas. In presently operated sodium/metal chloride cells, the loading density of the positive electrode is frequently about 0.25 Ah/cm^3. This would result in a radial width for an annular positive electrode of 10.5 mm. At the high current densities required for the small electrolyte area, the voltage loss in this electrode would be very high. At the lower current densities for the high surface area designs, higher loading densities should be possible, and a value of 0.35 Ah/cm^3 was assumed in Table V. For cells with this higher loading density and higher electrolyte surface area, the thicknesses of the positive electrodes are much lower than that for the present single tube cell design. Thus, for these cells, the voltage loss in the positive electrode would also be low even though the fraction of liquid electrolyte in the electrode is lower that that for most of the cells reported to date.

Comparing the two types of high-surface-area electrolyte configurations considered in Table V, indicates that each has advantages. The multiple tube configuration probably requires less new development effort for electrolyte fabrication. Also, the tubular electrolytes would be more easily sealed into a header than the flat-plate electrolytes. The flat-plate compartmented design provides a more advantageous shape for the positive electrode than the multiple tube configuration. For the flat-plate cell, the positive electrodes would consist merely of flat plates pressed against a positive current collector sheet. Provision for the current collector and the loading of the positive electrode in the multiple tube cell would be complex, but clever designs may solve these problems.

CONCLUSION

Much improvement is possible in the performance of advanced batteries over that which has been achieved thus far. Future efforts in development of both lithium and sodium anode high-temperature batteries are expected to result in batteries that meet the goals that were originally set when development efforts were first initiated: specific energy of about 220 Wh/kg, specific power of 440 Wh/kg and a life of 1000 cycles.

ACKNOWLEDGMENT

The author thanks J. E. Harmon for editorial review of the manuscript. The work reported was funded by the U.S. Department of Energy, Conservation and Renewable Energy, under contract No. W-31-109-ENG-38.

REFERENCES

1. Tomczuk, Z., B. Tani, N. C. Otto, R. F. Roche, and D. R. Vissers. J. Electrochem. Soc., Vol. 129, p. 925 (1982).

2. Kaun, T. D. J. Electrochem. Soc., Vol. 132, p. 3063 (1985).

3. Kaun, T. D., T. F. Holifield, and W. H. DeLuca. Lithium Disulfide Cells Capable of Long Cycle Life. Ext. Abstracts, 174th ECS Mtg., p. 71, Chicago, IL (Oct. 1988).

4. Kaun, T. D., T. F. Holifield, M. N. Nigohosian, and P. A. Nelson. Development of Overcharge Tolerance in Li/FeS and LiFeS$_2$ Cells. Ext. Abstracts, 174th ECS Meeting, Vol. 88-21, p. 67, Chicago, IL (Oct. 1988).

5. Redey, L. Proc. 22nd IECEC Mtg., Philadelphia , PA, Vol. 2, p. 1091 (1987).

6. Molyneux, J., G. Sands, S. Jackson, and I. Witherspoon. IECEC Meeting, Philadelphia, PA, p. 975 (1987).

7. Bones, R. J., J. Coetzer, R. C. Galloway, and D. A. Teagle. J. Electrochem. Soc., Vol. 134, p. 2379 (1987).

8. Dell R. M., and R. J. Bones. Proc. 22nd IECEC Mtg., Philadelphia, PA, p. 1072 (1987).

9. Tilley, A. R., and R. M. Bull. Proc. 22nd IECEC Mtg., Philadelphia, PA, p. 1078 (1987).

10. Sudworth, J. L., R. C. Galloway, and D. S. Dermott. Electric Vehicles, Vol. 73, p. 14 (Autumn 1987).

11. Wright, M. L., and J. L. Sudworth. Ext. Abstr., Electrochem. Soc. Mtg., Honolulu, HI, p. 149 (October 1987).

12. Coetzer, J. J. of Power Sources, Vol. 18, p. 377 (1986).

13. Coetzer, J., and M. J. Nolte. U.S. Patent 4,592,969 (1986).

14. Bones, R. J., J. Coetzer, R. C. Galloway, and D. A. Teagle. Ext. Abstr., Electrochem. Soc. Mtg., San Diego, CA, p. 1122 (October 1986).

15. Coetzer, J., and M. M. Thackeroy. U.S. Patent 4,288,506 (1986).

16. Coetzer, J., R. C. Galloway, R. J. Bones, D. A. Teagle, and P. Mosely. U.S. Patent 4,546,005 (1985).

The submitted manuscript has been authored by a contractor of the U. S. Government under contract No. W-31-109-ENG-38. Accordingly, the U. S. Government retains a nonexclusive, royalty-free license to publish or reproduce the published form of this contribution, or allow others to do so, for U. S. Government purposes.

TABLE I. COMPARISON OF HIGH-TEMPERATURE CELL COUPLES

System	Positive Electrode Discharge Product	Average Open Circuit Voltage, V	Theoretical Specific Energy, Wh/kg
Li-Al/FeS	Li_2S,Fe	1.34	460
Li-Al/FeS_2	Li_2FeS_2	1.67	475
Li-Al/FeS_2	Li_2S, Fe	1.50	630
Na/$FeCl_2$	NaCl, Fe	2.35	728
Na/$NiCl_2$	NaCl, Ni	2.59	794
Na/S	Na-$S_{1.5}$	2.01	760

TABLE II. LITHIUM/SULFIDE CELLS--PROJECTED PERFORMANCE

Based on Eaton DSEP Van Requirements

Characteristic	Monosulfide Multiplate	Monosulfide Bipolar	Disulfide Bicell	Disulfide Bipolar
Capacity, Ah	313	92	137	87
Specific Energy, Wh/kg	112	160	175	210
Specific Power at EOD, W/kg	127	182	199	239
Weight, g	3410	686	1250	663
Volume, cm^3	1310	250	455	240

TABLE III. LITHIUM/SULFIDE VAN BATTERIES--PROJECTED PERFORMANCE

Basis: Eaton DSEP Van
Vehicle Weight: Base, 1376 kg; load, 273 kg; total, 1649 kg + battery weight
Range: 125 miles (range at end of battery life: 100 miles)
Energy Usage: 0.194 Wh/tonne-mile (FUDS cycle)
Power Requirement (end of discharge, end of battery life): 23 kW/tonne (0-50 mph/20 s)
Electronic Control: 400 A max, 200 V max open-circuit voltage

Characteristic	Monosulfide Multiplate	Monosulfide Bipolar	Disulfide Bicell	Disulfide Bipolar
Cells per Battery	150	450	224	336
Number of Parallel Strings	1	3	2	3
Capacity (FUDS Cycle), kWh	56.4	49.4	49.0	46.8
Power at EOD,[a] kW	64	56.3	55.7	53.3
Specific Energy, Wh/kg	83	127	132	167
Specific Power, W/kg	94	144	151	190
Weight, kg	680	390	370	280
Cell Fraction of Battery Wt	0.75	0.80	0.75	0.80
Volume, L	415	227	225	163
Dimensions, in.	59Lx43Wx10H	59Lx10D(3)[b]	42Lx33Wx10H	42Lx10D(3)[b]
Rate of Heat Loss, W	300	200	200	200

---

[a] 20% additional power over requirement is provided for new batteries to allow for battery degradation.

[b] Dimensions shown are for each of three modules.

TABLE IV. DESIGN AND PERFORMANCE DATA FOR Li-Al/FeS_2 CELL DISCHARGE FOR 1-ms AT 440°C

Components:	
Positive Electrode	FeS_2
Separator	BN + MgO
Electrolyte	LiF-LiCl-LiBr
Negative Electrode	Li-Al
Bipolar Plate	Mo
Design Parameters:	
Mass, g/cm^2	0.292
Thickness, cm	0.123
Area Loading, mAh/cm^2	42
Electrolyte Condition	flooded
Performance Parameters:	
Measured:	
Area Specific Impedance, $mohm\text{-}cm^2$	41
Area Specific Power, W/cm^2	24.1
Derived:	
Specific Energy, Wh/kg	144
Specific Power, kWh/kg	82.7
Power Density, kW/L	196
Power to Energy, W/Wh	574

TABLE V. ELECTROLYTE CONFIGURATION AND KEY CELL PARAMETERS

	Electrolyte Configuration		
	Single Large Tube	Multiple Tube	Flat-Plate Compartmented
Cell Capacity @ 3-h Rate, Ah	100	200	200
Electrolyte			
Number of Elements	1	100	6
Active Length, cm	30	18	18
Outside Dimensions	3.0-cm dia	0.5-cm dia	0.4 x 9.0 cm
Wall Thickness, mm	1.5	0.4	0.4
Electrolyte Outside Area, cm^2	283	2830	1950
Current Density, 3-h Rate, mA/cm^2	118	24	34
Voltage Loss @ 1.5 C Rate at the Following Resistivities			
6 ohm-cm,[a] V	0.50	0.03	0.04
50 ohm-cm, V	-	0.23	0.31
100 ohm-cm, V	-	0.46	0.62
Positive Electrode (central sodium)			
Loading Density,[b] Ah/cm^3	0.25	0.35	0.35
Thickness, mm	10.5[c]	1.5[d]	2.9[e]

---

[a] Resistivity of β''-alumina at 250°C is about 6 ohm-cm

[b] Based on rated capacity of cell

[c] Radial width of annulus

[d] Average radial width of annulus (irregular shape)

[e] Half-thickness of flat electrode reacted on both faces

Electrolyte: LiCl-KCl Eutectic
Temperature: 417°C
Current Density: 12 mA/cm^2

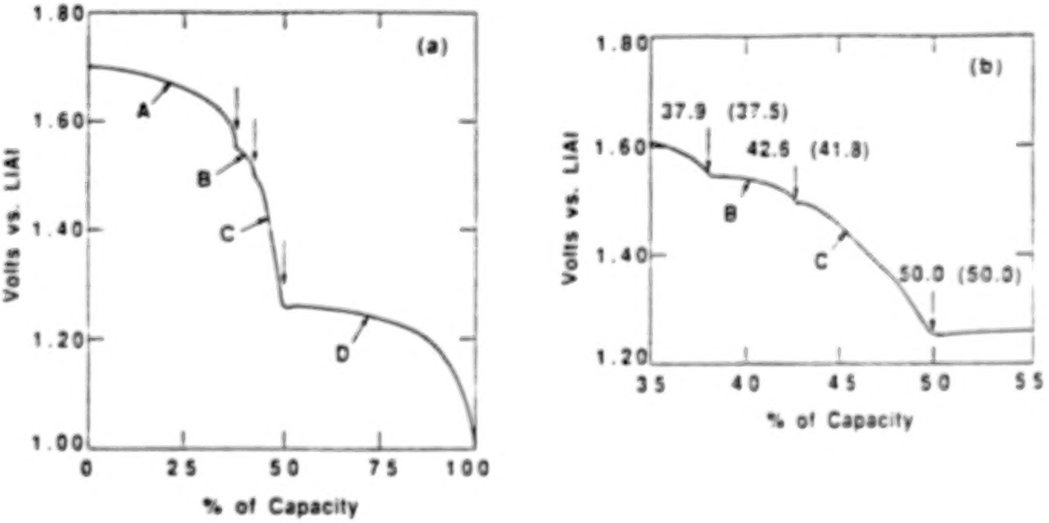

$$FeS_2 \xrightarrow{A} Li_3Fe_2S_4 \xrightarrow{B} Li_{2-x}Fe_{1-x}S_2 + Fe_{1-x}S \xrightarrow{C} Li_2FeS_2 \xrightarrow{D} Li_2S + Fe$$

FIGURE 1. DISCHARGE CURVE FOR LiAl/FeS$_2$ CELL.

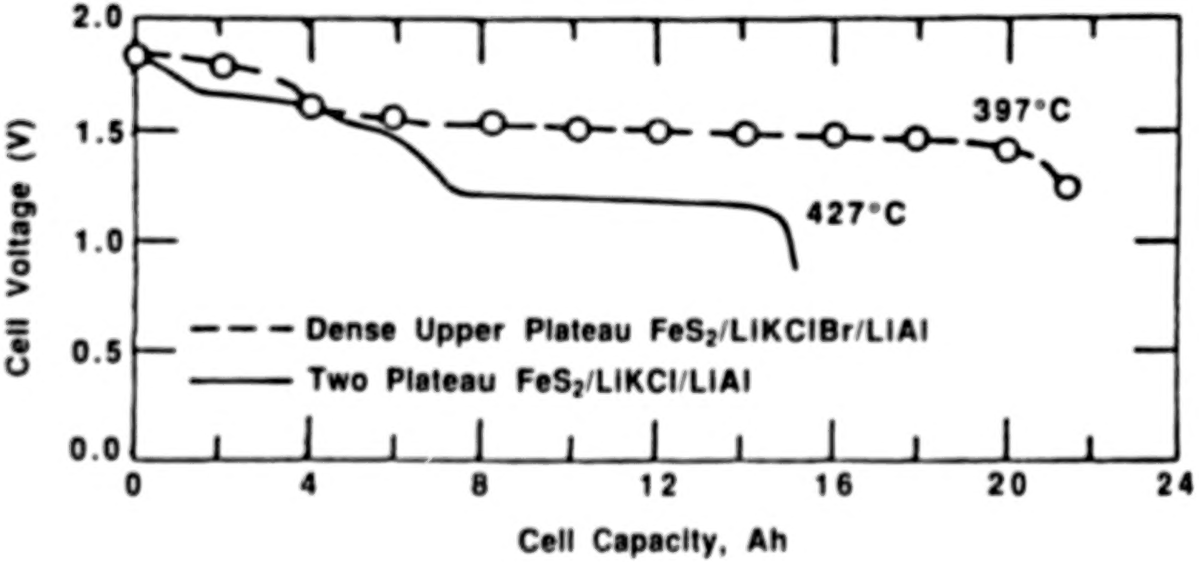

FIGURE 2. VOLTAGE VS. CAPACITY FOR TWO TYPES OF DISULFIDE ELECTRODES HAVING 24-Ah LOADINGS.

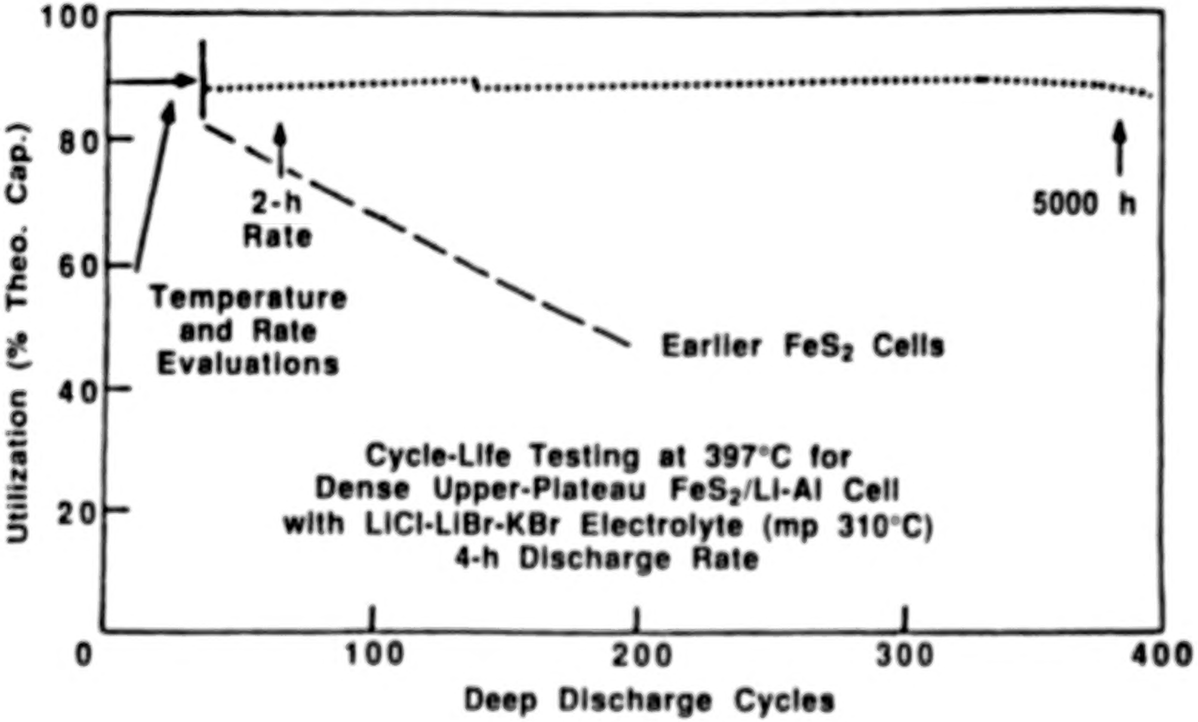

FIGURE 3. CYCLE LIFE TESTING OF DENSE UPPER-PLATEAU OF FeS_2 CELL.

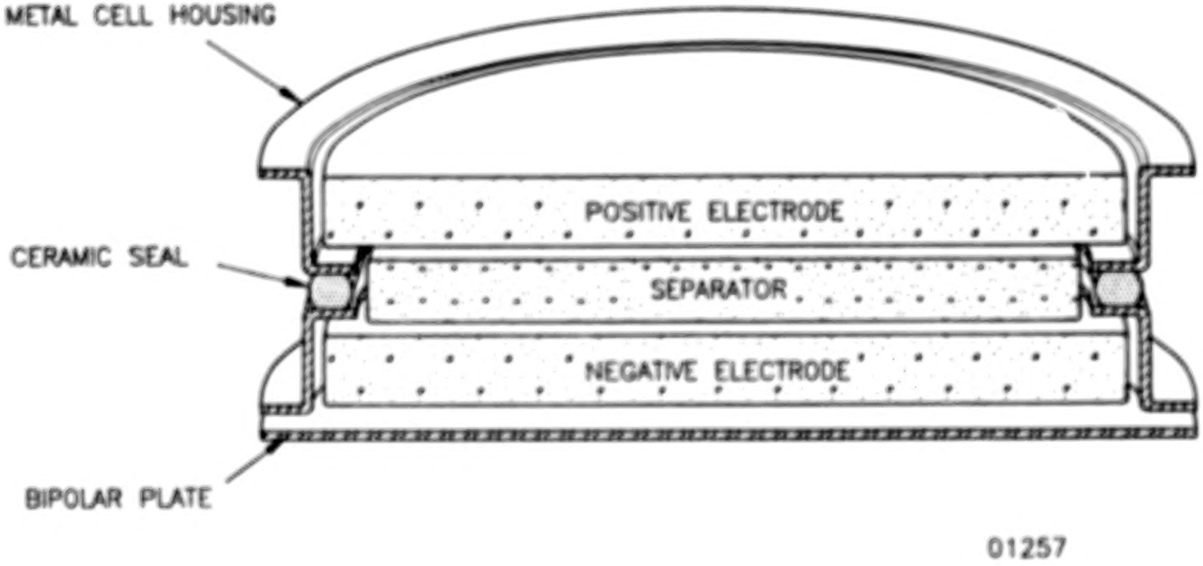
METAL CELL HOUSING
POSITIVE ELECTRODE
CERAMIC SEAL
SEPARATOR
NEGATIVE ELECTRODE
BIPOLAR PLATE
01257

FIGURE 4. BIPOLAR LITHIUM/IRON SULFIDE CELL CONCEPT.

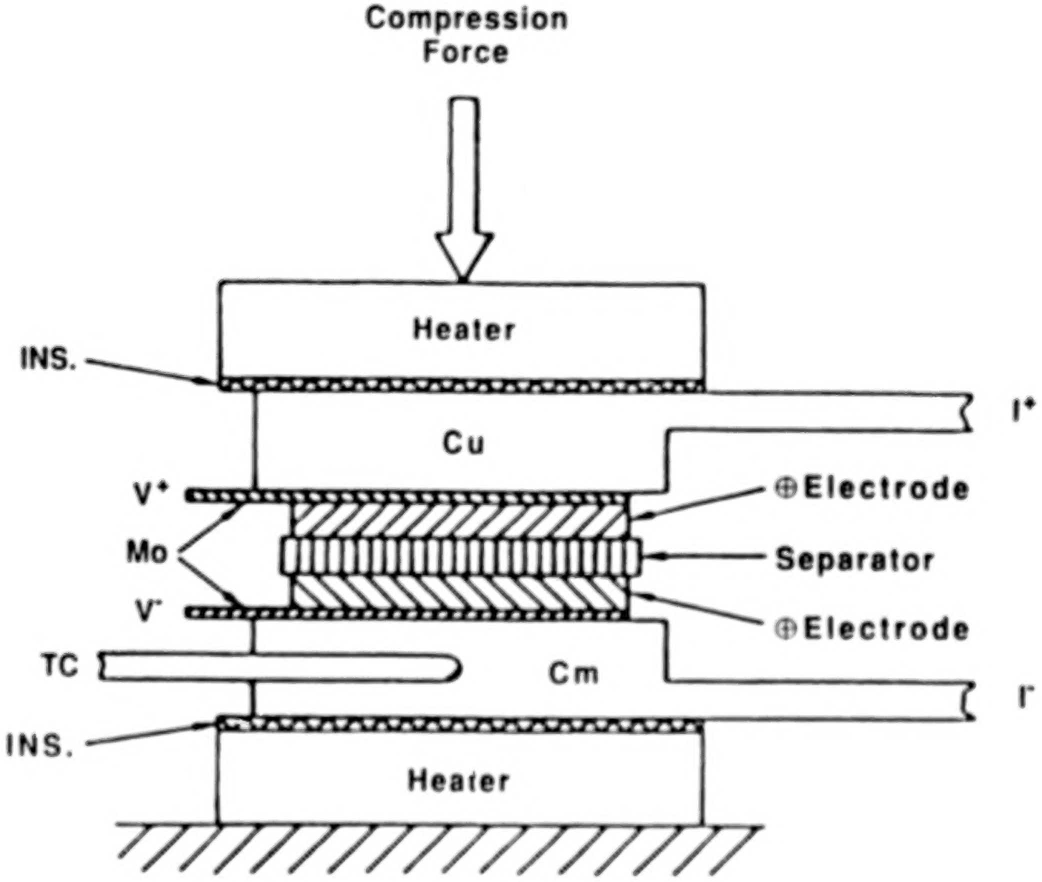
Compression Force
Heater
INS.
Cu
I+
V+
⊕Electrode
Mo
Separator
V-
⊕Electrode
TC
Cm
I-
INS.
Heater

FIGURE 5. APPARATUS FOR PULSED DISCHARGE MEASUREMENTS ON Li-ALLOY/FeS_2 CELLS.

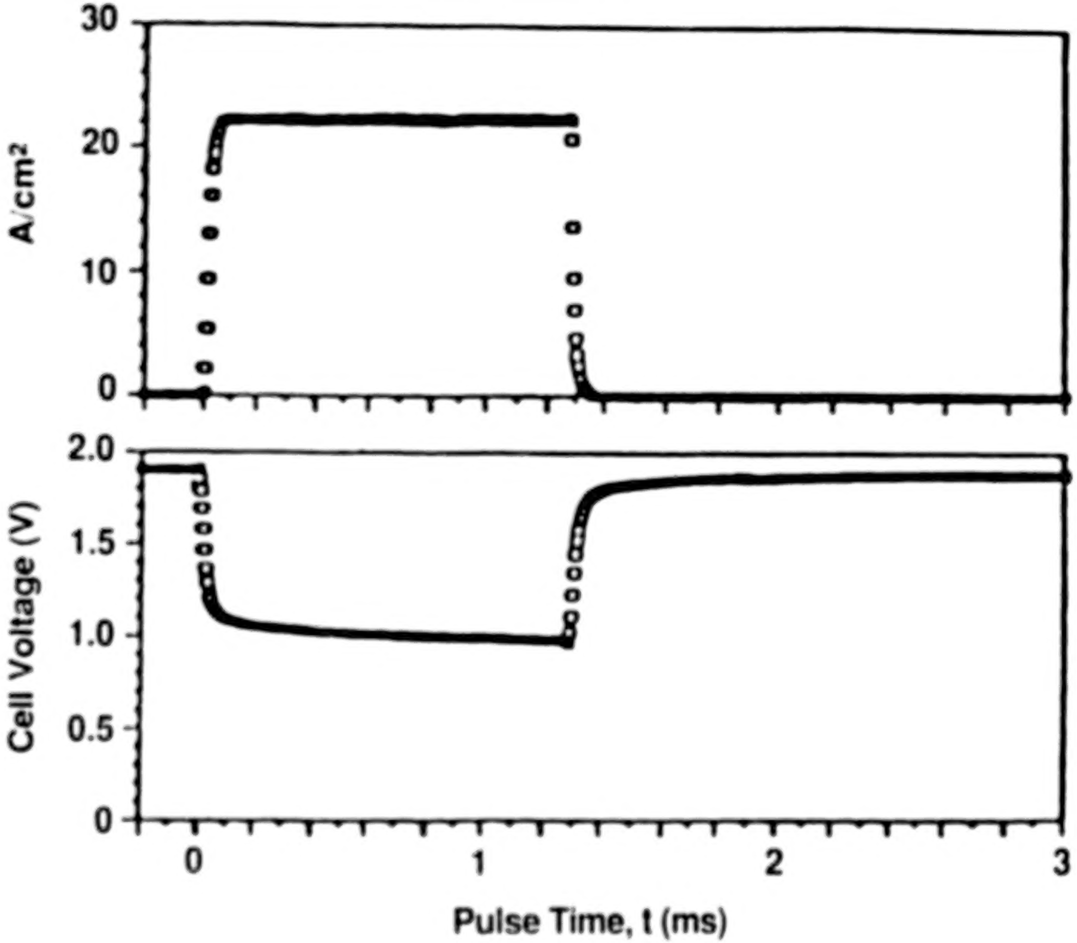

FIGURE 6. CURRENT DENSITY AND VOLTAGE FOR 1-mS POWER PULSE FOR Li-Al/FeS$_2$ CELL ACHIEVING 24.1 W/cm^2 AT 490°C, SAMPLING INTERVAL IS 5 μs.

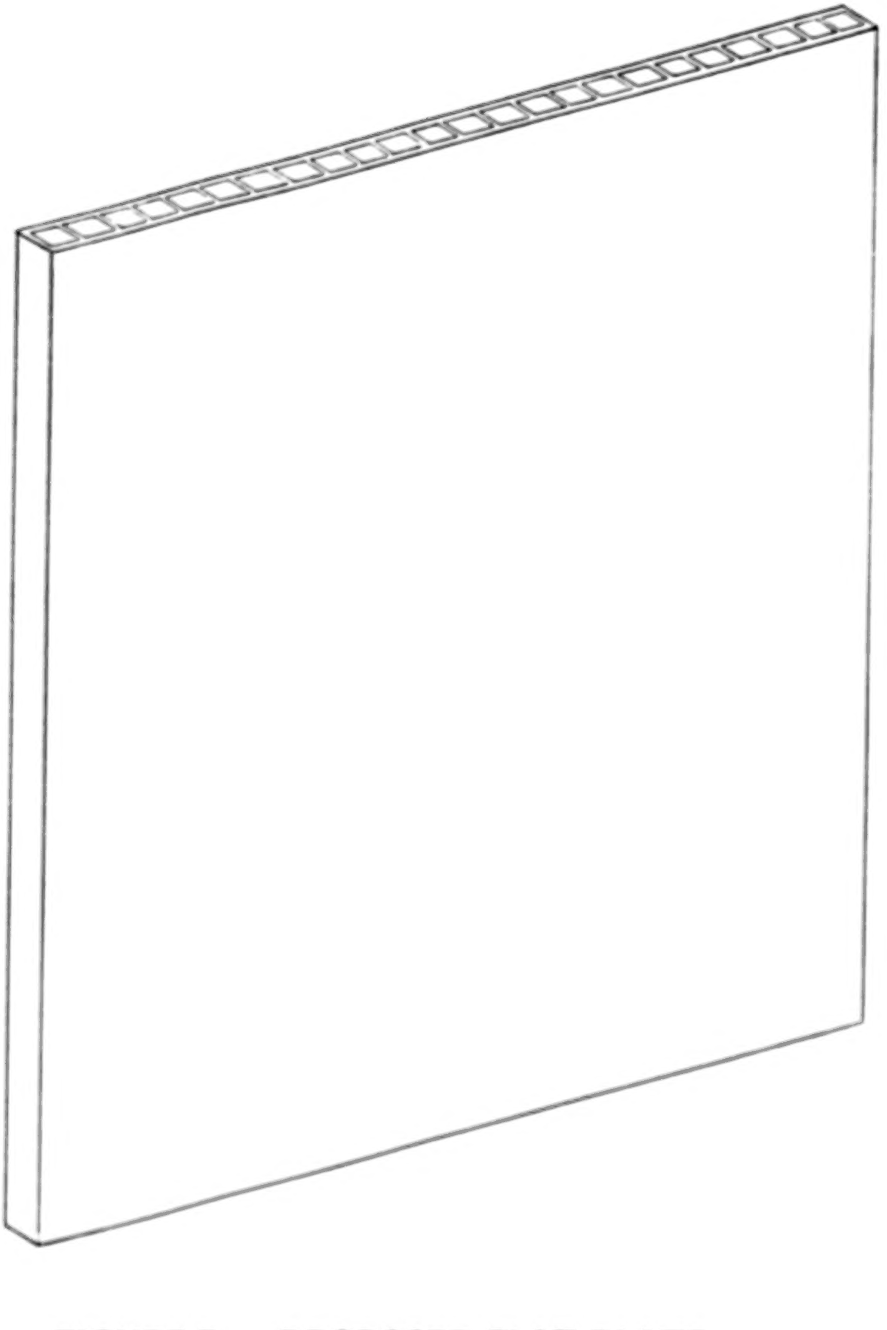

FIGURE 7. PROPOSED FLAT-PLATE β''-ALUMINA ELECTROLYTE FOR SODIUM METAL CHLORIDE CELL.

ADVANCES IN AMBIENT TEMPERATURE SECONDARY LITHIUM CELLS

S. Subbarao, D.H. Shen, F. Deligiannis,
C-K. Huang and G. Halpert
Jet Propulsion Laboratory
California Institute of Technology
Pasadena, California 91109

JPL is carrying out a NASA/OAST sponsored R & D program on the development of ambient temperature secondary lithium cells for future space applications. The goal of the program is to develop secondary lithium cells with a 100 Wh/kg specific energy and capable of 1000 cycles at 50% DOD. The approach towards meeting these goals initially focused on several basic issues related to the cell chemistry, selection of cathode materials and electrolytes and component development. We have examined the performance potential of Li-TiS_2, Li-MoS_3, Li-V_6O_{13} and Li-$NbSe_3$ electrochemical systems. Among these four, the Li-TiS_2 system was found to be the most promising system in terms of achievable specific energy and cycle life. Major advancements to date in the development of Li-TiS_2 cells are in the areas of cathode processing technology, mixed solvent electrolytes, and cell assembly. This paper summarizes these advances made at JPL on the development of secondary lithium cells.

INTRODUCTION

Ambient temperature secondary lithium batteries have several intrinsic and potential advantages including higher energy density, longer active shelf life, and lower self discharge over conventional Ni-Cd, Ni-H2, Pb-acid and Ag-Zn batteries. Successful development of these batteries will yield large pay-offs such as 2-3 fold increase in energy storage capability and a longer active shelf life of 2 to 4 years over these systems. A detailed analysis of the strengths and weakness of secondary lithium batteries has indicated that these batteries are suitable for applications requiring less than 1 kW power and limited cycle life. Some of the projected space applications of these batteries are for Mars Rover, planetary space craft/probes, astronaut equipment, and geosynchronous spacecraft.

Several ambient temperature secondary lithium systems such as: Li-TiS_2, Li-MoS_2, Li-$NbSe_3$, Li-MnO_2, Li-V_2O_5 etc. are currently under development for consumer and defense applications (1). Most of these systems are still in the research stage while a few of them are commercially available in small capacities (less than 1 Ah). Performance of the cells that are commercially available fall short of meeting the space application requirements (2).

Under a NASA OAST sponsored program, Jet Propulsion Laboratory is developing ambient temperature secondary lithium cells for future space applications. The primary objective of the program is to develop ambient temperature secondary lithium cells with 100 Wh/kg specific energy while delivering 1000 cycles at moderate depths of discharge (50%). The major thrusts of this program are to improve cycle life and safety of these cells. Approach has involved work in three areas: 1) chemistry and material research, 2) component development and interactions, and 3) performance and safety. This paper describes the advances made at JPL to date in these areas.

CHEMISTRY AND MATERIAL RESEARCH

Attempts to improve the performance capability of the state of art secondary lithium cells has been inhibited by the unavailability of materials with the desired properties and poor understanding of the cell chemistry(3). For these reasons the major emphasis of this effort has been directed towards identifying candidate electrode materials and a stable electrolyte and developing fundamental understanding of materials and cell chemistry. Some of the specific objectives in this area are : 1) Selection of a cathode material with a theoretical specific energy greater than 400 Wh/kg providing more than 1000 cycles, 2) Identification of an electrolyte that is stable towards lithium and has a conductivity greater than 10^{-3} ohm-^{1}-cm^{-1}, 3) Evaluation of the use of lithium alloys and other materials with low equivalent weight (40 gm/eq) to extend the cycle life performance and safety of the cells and 4) Development of concepts for overcharge/overdischarge protection of cells. Significant progress was made by JPL in the first three above topics as described below.

Cathode Materials

Cathode materials required for these cells must possess several desirable properties such as high specific energy, good electrochemical rechargeability, good electronic conductivity, high lithium diffusivity, and chemical compatibility towards electrolyte. Several materials have been reported in the literature for use in secondary lithium batteries (3). These materials can be classified into two categories: transition metal chalcogenides (TiS_2, MoS_3, MoS_2, $NbSe_3$, etc.) and transition metal oxides (V_2O_5, V_6O_{13}, MnO_2, CoO_2,etc.). Lithium is inserted into these host structures electrochemically during discharge (Figure 1). Ideally, the host lattice may undergo only a minor structural change during lithium intercalation/insertion process (discharge), and return to its original state after charging process (the deintercalation). Four of these materials (TiS_2, MoS_3, V_6O_{13}, and $NbSe_3$) were selected for detailed examination. These four materials were evaluated for their performance (specific energy, and cycle life) in experimental cells. In order to overcome poor cycle life performance of the lithium electrode, a high lithium to positive electrode ("cathode") ratio (6:1) was used in these experimental cells. Major emphasis of this study was focussed on determining the cycle life capabilities of these cathode materials. The results of these studies are summarized in Table I. The results clearly indicate that the most promising cathode material is TiS_2 in view of its long cycle life performance capability and realizable specific energy. The second material of choice is $NbSe_3$. Even though MoS_3 and V_6O_{13} have higher theoretical specific energy, the materials showed poor cycle life performance and low useful specific energy. These studies led to the selection of TiS_2 as the candidate cathode material for further studies with electrolytes and anode materials.

Electrolytes

The ideal electrolyte required for ambient temperature secondary lithium cells must exhibit high conductivity, wide electrochemical operating window, high stability towards lithium, and compatibility with cathode materials and separator, low density, and low viscosity. Some of the electrolytes that have been investigated for this application are THF, 2-MeTHF, Methyl Formate, and Propylene Carbonate (4). These single solvent electrolytes provide only limited cycle life capability because of their reactivity towards lithium. It has been suggested (5) that the use of mixed solvent electrolytes may alleviate this problem due to the formation of a beneficial passivating film on the lithium anode and the synergistic effects associated with the use of the selected mixed solvents. A number of mixed solvent electrolytes are currently being investigated in our laboratory for use in Li-TiS_2 cells. These electrolytes contain 2-MeTHF and THF as the base solvents and Ethylene Carbonate(EC), Propylene Carbonate (PC) and 3-Methylsulfolane(3-MeS) as the co-solvents. The important properties such as conductivity, stability towards lithium and lithium cycling efficiency of these mixed solvent electrolytes were evaluated . Conductivity of the electrolytes was determined by standard methods. Stability of the electrolytes towards lithium was investigated by microcalorimetry. The heat evolved from the uncycled experimental cells in open circuit condition was measured at 25°C with a heat conduction Hart Scientific microcalorimeter. The cycling efficiency of lithium in various electrolytes was determined by cycling experimental Li-TiS_2 cells. The lithium cycling efficiency/ figure of merit (FOM) was calculated using the relationship:

$$F.O.M._{Li} = \frac{\text{total accumulated discharge capacity}}{\text{theoretical Li capacity}}$$

Comparative performance of selected electrolytes is summarized in Table II. Among the co-solvents investigated, EC appears to be a promising co-solvent. The mixed solvent electrolytes containing EC (EC/THF, EC/2-MeTHF, EC/THF/2-MeTHF, EC/3-MeS/2-MeTHF) showed higher conductivity and improved stability towards lithium compared to the electrolytes containing no EC (based on open circuit stand tests and microcalorimetry). The AC impedance and FTIR studies (6) indicated that the improved performance of EC/2-MeTHF electrolyte may be due to the formation of a thin $LiCO_3$ film on the surface of the lithium electrode. From the results it can also be observed that EC containing electrolytes yielded higher FOM values than other electrolytes. A FOM of 38.5 was obtained with 10%EC+90%2-MeTHF electrolyte and this is 33% higher than the FOM of the bench mark 2-MeTHF electrolyte (29.5). Although the achievement of this FOM represents a significant advancement, the FOM value presently remains lower than the target objectives (FOM - 80) . Work is continuing to identify an electrolyte that can meet program targets.

Lithium Alloys

The limited cycle life performance of ambient temperature lithium cells is primarily attributed to the reactivity of the lithium anode with organic electrolytes. One method for reducing the reactivity of the lithium anode towards the electrolyte is by the use of lithium alloys as anode materials. Further, the use of lithium alloy anodes may also improve the safety of the cells. Six lithium alloys were selected for preliminary experimental evaluation after a detailed review of the literature. These alloys are Li-Al, Li-Si, Li-Sn, Li-Zn, Li-Pb, Li-Cd. All these materials are basically lithium rich alloys. These materials were selected based on their electrochemical potential, equivalent weight, lithium diffusivity, reversibility and thermodynamic stability towards organic electrolytes. Some of the important properties of these alloys are summarized in Table III. Experimental evaluation of these alloys was initiated on these anodes and is in progress.

COMPONENT DEVELOPMENT AND INTERACTIONS

Component characteristics and cell design also play a significant role on cell performance. For this reason, work is in progress on the fabrication of TiS_2 cathodes and design analyses. Details of the progress made in these two areas are described below.

TiS_2 Cathode Processing

The rate capability and faradaic utilization of TiS_2 cathode are dependent on the chemical composition of TiS_2, nature of the binder, additives/ conducting diluents, as well as thickness and porosity of the electrode. TiS_2 processed by the vapor transfer method was found to show higher faradaic utilization compared to the TiS_2 materials procured from commercial sources (Table IV). This improved performance was found to be associated with purity and stoichiometry of the material. Hence, it was decided to use TiS2 prepared in house by the improved vapor transport method in our future studies.

During cycling the cathode undergoes a volume change due to the intercalation/deintercalation of Li into/from TiS_2 crystal lattice. The electrode structure must be capable of accommodating these changes, otherwise it will disintegrate during cycling. Studies carried on various binder materials identified EPDM as the most suitable binder material for the construction of TiS_2 cathodes (7). Three methods : brushing, rolling, and pressing methods were examined for the fabrication of TiS_2 cathodes. The brushing method was found to be suitable for the fabrication of small electrodes in the glove box. The rolling and pressing methods offered several advantages including amenability to scale up, and uniform loading. Typical characteristics of the electrodes fabricated by various methods is given Table V. Work is in progress to understand the relationships between electrode properties and performance.

Design Trade off Studies

Some of the important parameters to be considered in the design of secondary lithium cell are ratio of electrode capacities, operating current density, electrolyte composition and quantity, case and grid materials and cell size. A computer program was developed (8) to understand the influence of these parameters on specific energy and to optimize the cell design. The results of these studies indicated that a specific energy of 80-100 Wh/kg is achievable for high capacity cells(>20 Ah). The negative to positive electrode capacity ratio has minimal effect on specific energy of the cells. A high anode to cathode capacity is required to account for the degradation of Li electrode and to achieve maximum cycle life. Cells cannot operate at current densities higher than 2 mA/cm^2 because of the poor conductivity of the electrolyte. The cell case is the major contributor to cell weight(Fig. 2). Among the active materials, Li contributes the least to the overall weight. The collector grids contribute more to the weight than does lithium alone. The use of titanium cases and aluminum grids will reduce cell weight considerably. Experimental work is in progress to determine the influence of some of the important parameters on the cycle life performance of the cells.

CELL PERFORMANCE AND SAFETY

An assessment was made of the status of secondary lithium cells by experimental evaluation of Li-MoS_2, Li-$NbSe_3$ and Li-TiS_2 cells. Li-MoS_2 and Li-$NbSe_3$ cells (AA) were procured from the industry. The Li-TiS_2 cells were fabricated in house with non-optimize and cell hardware. These cells were evaluated for their charge/discharge characteristics, rate capability and cycle life. Performance characteristics of these cells is summarized in Table VI. These cells have a cycle life of 100-250 cycles at moderate discharge rates (C/5). Li-$NbSe_3$ cells exhibited high specific energy and Li-MoS_2 cells showed long cycle life. The low specific energy and cycle life of 5 Ah cells may be due to the non-optimize cell design and cell hardware. Some of the important problems identified are formation of soft shorts during cycling at low discharge rates (C/10) and inferior performance at low depth of discharge in Li-MoS2 system. Evaluation of the safety of these cells is in progress.

CONCLUSIONS

Li-TiS_2 system appears to be the most promising system, among the ambient temperature secondary lithium systems examined, in view of its higher realizable specific energy and cycle life. Use of mixed solvent electrolytes was found to improve the cycle life of this system. Among the various electrolytes examined, 1.5 M $LiAsF_6$/ EC + 2-MeTHF mixed solvent electrolyte was found to be more stable towards lithium. Experimental cells activated with this electrolyte exhibited more than 300 cycles at 100% DOD. Design trade off studies of this system indicated that a practical specific energy of 80-100 Wh/kg is achievable in 20 Ah cells and higher. The technology of these cells is still far from meeting the requirements of planetary space missions. Significant progress is still needed, particularly with respect to cycle life, tolerance to over-charge and over-discharge, safety and cell size. Many of these key problems require significant scientific and technological innovations in the areas of electrolyte technology, alternative lithium based anode materials, new additives and cell design.

ACKNOWLEDGEMENTS

This work represents one phase of research performed by Jet Propulsion Laboratory, California Institute of Technology sponsored by the National Aeronautics and Space Administration under contract NAS-7-918.

REFERENCES

1) B. B. Owens, "Survey of Lithium Ambient Temperature Secondary Systems", Fifth International Seminar on Lithium Battery Technology and Applications, Deerfield Beach, Fla, March 1989.

2) S. Subbarao et al, "Ambient Temperature Secondary Lithium Batteries for Space Applications", Proceedings of the Fourth Annual Battery Conference on Applications and Advances, Long Beach, CA, January, 1989.

3) K. M. Abraham, "Status of Rechargeable Positive Electrodes for Ambient Temperature Rechargeable Batteries", J. Power Sources 7, 1(1981).

4) V. R. Koch " Advances in Organic Electrolytes for Rechargeable Lithium batteries", Fourth International Seminar on Lithium Battery Technology and Applications, Deerfield Beach, Fla, March 1988.

5) S. Tobishima, M. Arakawa, T. Hirai and J. Yamaki, Journal of Power Sources, 20, P. 293-297 (1987).

6) D. H. Shen, S. Subbarao, F. Deliagiannis, and G. Halpert, " Evaluation of Mixed Solvent Electrolytes for Ambient Temperature Secondary Lithium Cells", Proceedings of the 33rd International Power Sources Symposium, p.45, (1988).

7) S. P. S. Yen, D. H. Shen, and R. B. Somoano, Journal of Electrochemical Society, 130, P.5, May (1983).

8) D. H. Shen, S. Subbarao, S. P. S. Yen and R. B. Somoano, Journal of Power Sources, 18, P127-131 (1986).

TABLE I. PERFORMANCE COMPARISION OF SELECTED CATHODE MATERIALS

MATL	OP. VOLTAGE	SPECIFIC ENERGY THEO.	SPECIFIC ENERGY EXPTL.	CYCLE LIFE 100% DOD
TiS_2	2.1	473	401	>600
MoS_3	1.9	717	243	40-60
V_6O_{13} (NS)	2.15	622	323	30-50
$NbSe_3$	1.8	412	351	>100

TABLE II PROPERTIES OF SELECTED ELECTROLYTES

ELECTROLYTE	CONDUCTIVITY 10^{-3} (OHM^{-1}-CM^{-1})	STABILTY TO LITHIUM (microwatts)	LITHIUM CYCLING EFFICIANCY (FOM)
THF	13.7	90	3
2-MeTHF	3.4	25	28
10%EC+90%THF	14.6	84	4
10%EC+90%2-MeTHF	6.2	16	38
20%PC+90%2-METHF	6,1	24	-
25%3-MeS+75%2-MeTHF	3.6	-	10
50%THF+50%2-MeTHF	8.9	-	20

* HEATOUT PUT ON OCV (MICROCALORIMETRY STUDIES)

** DISCHARGE/CHARGE CURRENT DENSITY = 2/1 mA/cm2

TABLE III. PROPERTIES OF LITHIUM ALLOYS

ALLOY	EQ. WT (g/eq)	E vs Li (mV)	Ah/g	DIFFUSIVITY (cm^2/sec)	SP. ENERGY* (Wh/kg)
Li	6.9	0	3.86	—	473
$Li_{2.5}Al$	18.3	141	1.46	10^{-4} **	403
Li_2Si	21.0	332	1.28	10^{-5} **	356
$Li_{4.5}Pb$	68.1	400	0.39	10^{-8} ***	253
$Li_{5.6}Sn$	34.2	263	0.78	10^{-5} **	337
$Li_{1.5}Zn$	68.9	106	0.39	10^{-9} ***	295

* CALCULATED FOR LI-TIS$_2$ SYSTEM
** 400° C
*** 25° C

TABLE IV. PROPERTIES OF TiS_2 RAW MATERIAL

SOURCE	STIOCHIOMETRY (S : Ti)	IMPURITIES	AP. DENSITY (g/cc)	FARADAIC UTILIZATION (% THEO.)
JPL	1.99	O	0.80	95
DEGUSSA	1.97	Cl	o.48	75
CERAC	2.18	Cl,S	0.32	60

TABLE V. PROPERTIES OF TIS$_2$ CATHODES

PROPERTY	BRUSHING	ROLLING	PRESSING
THICKNESS (mil)	15+2	20+2	16+2
LOADING (mg/cm2)	48+5	66+5	54+5
POROSITY (%)	56+2	56+2	54+2
CAPACITY (mAh/cm2)	12+1	16+1	13+1

FIG. 1.STRUCTURE AND INTERCALATION OF Li IN TiS_2

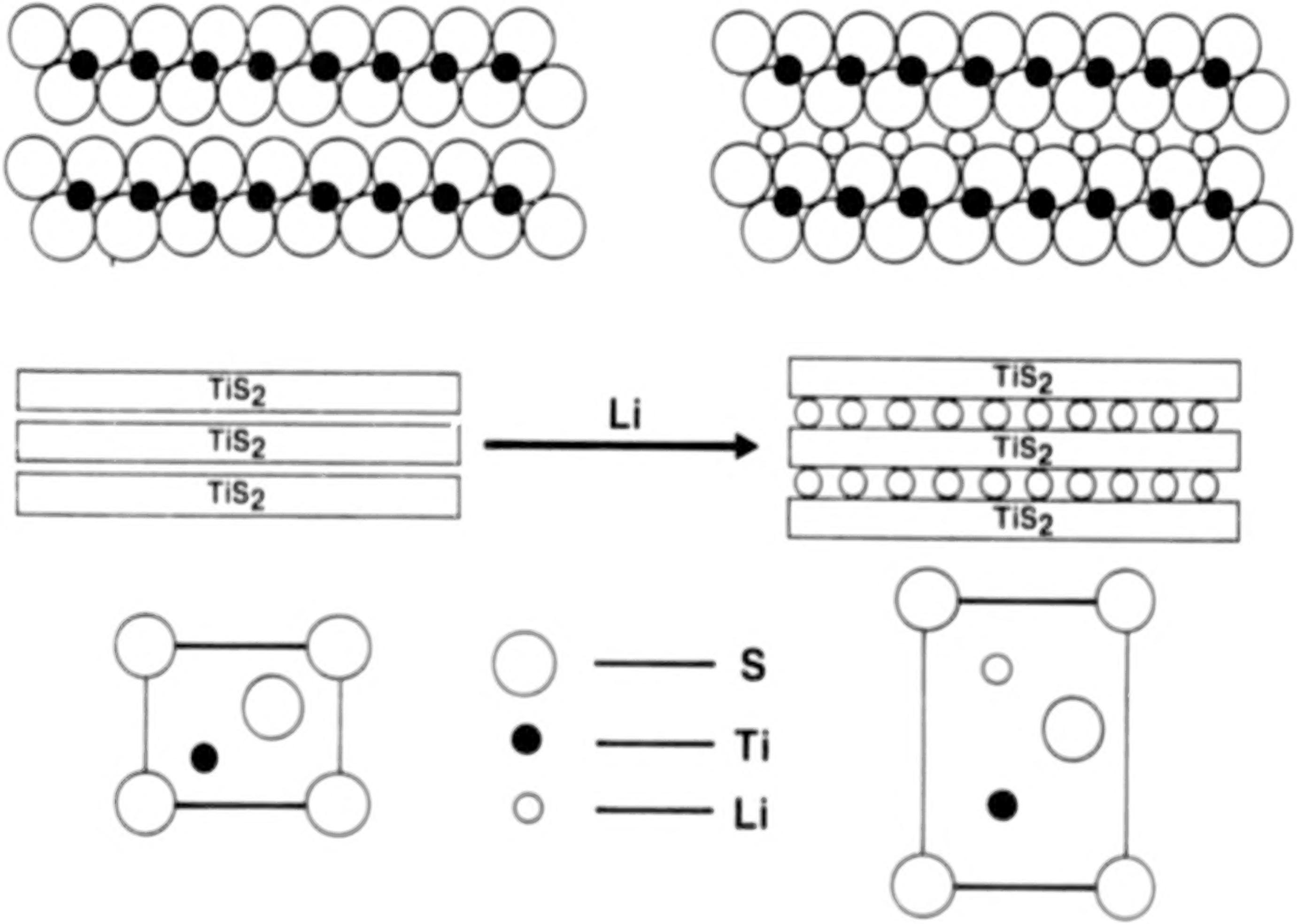
TiS_2
TiS_2
TiS_2
Li
TiS_2
TiS_2
TiS_2
S
Ti
Li

FIG.2. 5 Ah Li-TiS2 CELL WEIGHT BUDGET

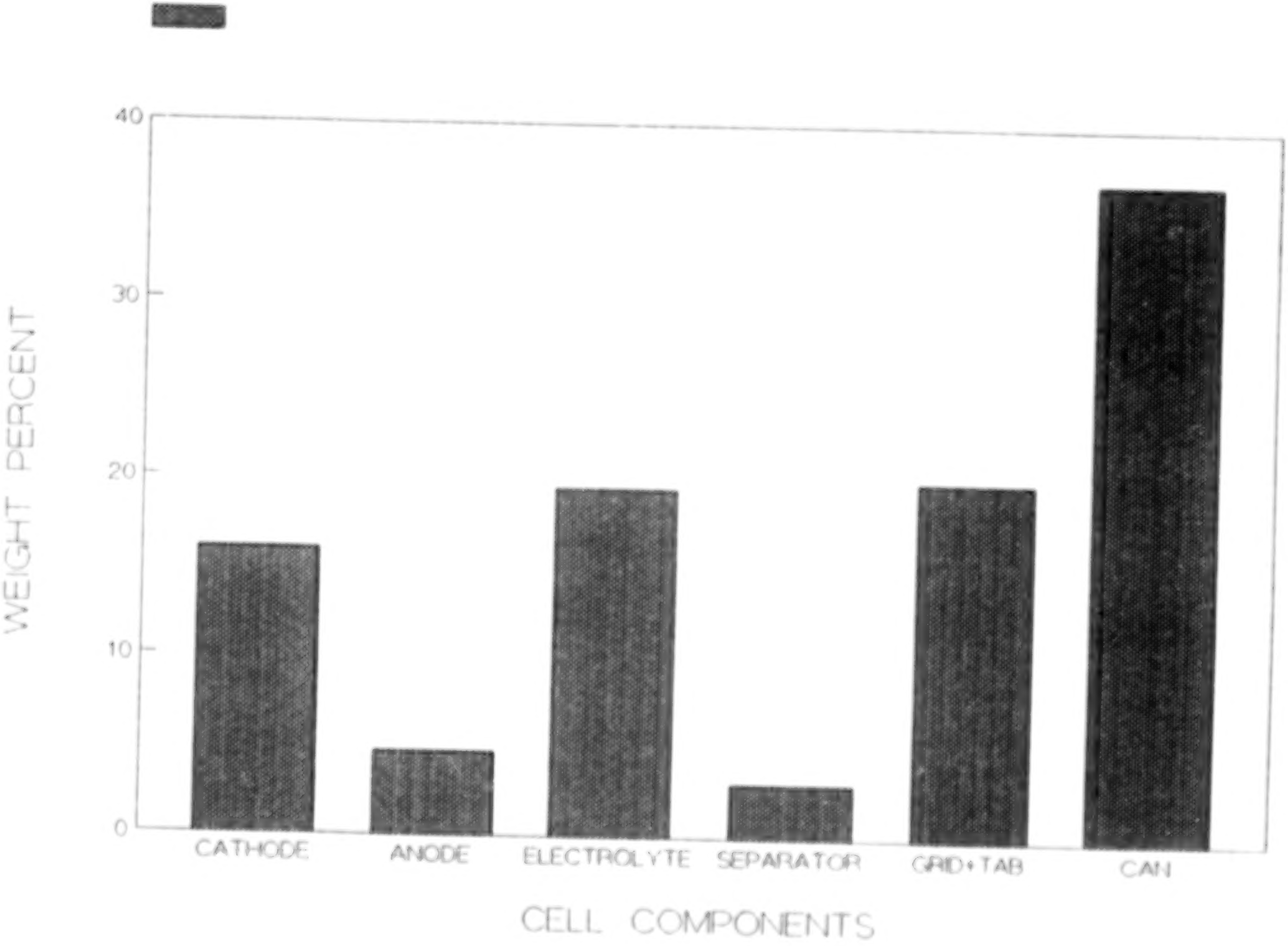

SPACE ELECTROCHEMICAL RESEARCH & TECHNOLOGY CONFERENCE

NASA LEWIS RESEARCH CENTER APRIL 11-13, 1989

ADVANCED CONCEPTS

CHAIRPERSON: A. J. APPLEBY

CO-CHAIRPERSON: MICHELLE MANZO

APRIL 12, 1989

SPACE ELECTROCHEMICAL RESEARCH & TECHNOLOGY CONFERENCE

NASA LEWIS RESEARCH CENTER APRIL 11-13, 1989

SUMMARY

ADVANCED CONCEPTS

- COLD FUSION

LAST YEAR'S ADVANCED CONCEPTS

- HIGH TEMPERATURE BATTERIES:
  - COMPOSITE SOLID ELECTROLYTES
  - BIPOLAR Li Al - Fe S_2, Li Al - S, (?) Li - O_2
  - NEW MATERIALS
- HIGH TEMPERATURE FUEL CELLS
  - MONOLITHIC AND PSEUDOMONOLITHIC
  - NEW ELECTROLYTES
- LOW TEMPERATURE SYSTEMS
  - ULTRACAPACITORS
  - NEW Li SYSTEMS
  - NEW COUPLES AND DESIGNS

SPACE ELECTROCHEMICAL RESEARCH & TECHNOLOGY CONFERENCE

NASA LEWIS RESEARCH CENTER APRIL 11-13, 1989

APPLICATIONS WILL DETERMINE WHICH ADVANCED SYSTEM IS BEST

- **FOR LEO, REQUIREMENTS ARE**
  - HIGH ENERGY DENSITY
  - HIGH CYCLE LIFE (>30,000 CYCLES)
  - HIGH POWER DENSITY

  POSSIBLE CANDIDATES: SOLID ELECTROLYTE SYSTEMS; RFC's
- **FOR PLANETARY ROVER, REQUIREMENTS ARE**
  - HIGH ENERGY DENSITY
  - VERY HIGH POWER DENSITY
  - 1000 CYCLES

  POSSIBLE CANDIDATES: LiAl-FeS$_2$, FUEL CELL, Na/BETA/METAL CHLORIDES
- **FOR SPACE PROBES, MANPACK, SMALL GEO SPACECRAFTS**
  - HIGH ENERGY DENSITY
  - SMALL SIZE
  - 1000 CYCLES
  - LOW TEMPERATURE OPERATION (5-20°C)

  POSSIBLE CANDIDATES: AMBIENT TEMP. LITHIUM, POLYMER ELECTROLYTE SYSTEMS
- **FOR MOON BASE OR MARS OUTPOST, REQUIREMENTS ARE**
  - EXTREMELY HIGH ENERGY DENSITY
  - EXTREMELY HIGH RELIABILITY

  POSSIBLE SYSTEMS: NUCLEAR, RFC

SPACE ELECTROCHEMICAL RESEARCH & TECHNOLOGY CONFERENCE

NASA LEWIS RESEARCH CENTER APRIL 11-13, 1989

COLD FUSION

- IF TRUE, WILL RADICALLY CHANGE THINKING
- BASELOAD FOR LUNAR BASE
- POSSIBLY PROPULSION: SPECIFIC POWER IS KEY, ESPECIALLY IF NO SHIELDING REQUIRED
- MUST GIVE HIGH-QUALITY HEAT (300° C FOR RANKINE, PREFERABLY 1000° C, BRAYTON, OTHERS)
- IMPLEMENTATION OF 1000 C, MOLTEN ^{6}LiD?
- SMALL SYSTEMS: STIRLING, Na HEAT ENGINE, POSSIBLY THERMIONICS, THERMOELECTRICS
- CLASSICAL CYCLES SINCE NO γ - OR n - TO ELECTRICITY DEVICES EXIST
- QUESTIONS: STANDBY POWER CAPABILITY?

  LOAD-LEVELING BATTERIES OR REGENERATIVE FUEL CELLS WILL BE NECESSARY, OR OFF-PEAK POWER CAN BE USED FOR PROPELLANT MANUFACTURE
- WHILE EXCITING, IF TRUE, WILL TAKE A LONG TIME TO IMPLEMENT. SO WE NEED TODAY'S SYSTEMS AND LAST YEAR'S NEW CONCEPTS. RISK LEVEL - VERY HIGH. REQUIRES & CONFIRMATION IF APPLICABLE, SYSTEMS & MATERIALS DEVELOPMENT

TIME FRAME: 2015+

EFFORT: AS FISSION

SPACE ELECTROCHEMICAL RESEARCH & TECHNOLOGY CONFERENCE

NASA LEWIS RESEARCH CENTER APRIL 11-13, 1989

HIGH TEMPERATURE BATTERIES

- COMPOSITE SOLID ELECTROLYTES
  - IMPROVEMENTS IN NaS AND OTHER SYSTEMS (Na/TRANSITION METAL CHLORIDES, Li SYSTEMS)
  - REQUIRE NEW GEOMETRIES, BETTER PACKAGING
  - LOWER TEMPERATURES OF CHLORIDE SYSTEMS MAY GIVE BETTER LIFE
  - SHOULD BE VERY SAFE (INSOLUBLE CHLORIDES IN $NaAlCl_4$; $NaFeCl_4$ UNSAFE)
- LiAl-FeS_2 BIPOLAR: 210 Wh/kg
  REQUIRE Mo-PLATED BIPOLAR COLLECTOR, SEALS
- Li/O_2 (?)
- LiAl-S, SOLID ELECTROLYTE: 300 Wh/kg
- NEW HIGH-TEMPERATURE MATERIALS, e.g., COATED CARBON-CARBON (INSULATING OR CONDUCTING, HIGHLY CORROSION RESISTANT)

SERT89 001 5

SPACE ELECTROCHEMICAL RESEARCH & TECHNOLOGY CONFERENCE

NASA LEWIS RESEARCH CENTER APRIL 11-13, 1989

HIGH TEMPERATURE FUEL CELLS

- MONOLITHIC AND PSEUDOMONOLITHIC STRUCTURES (EXTRUSION, ETC)
- MONOLITHIC ELECTROLYZERS (MAY USE WITH LOW-TEMPERATURE FUEL CELL)
- LOW-TEMPERATURE SOLID ELECTROLYTES FOR FUEL CELLS

SERT89 001 5

SPACE ELECTROCHEMICAL RESEARCH & TECHNOLOGY CONFERENCE

NASA LEWIS RESEARCH CENTER APRIL 11–13, 1989

LOW-TEMPERATURE SYSTEMS

- **20,000 J, 5 Wh/kg ULTRACAPACITORS**
  - HIGHER VOLTAGE REQUIRED (ORGANICS, LOW TEMPERATURE MOLTEN SALTS)
  - HIGHER FARADAIC PSEUDOCAPACITANCE (250 $\mu F/cm^2$)
  - HIGHER AREAS
- **LI POLYMER ELECTROLYTES**
  - NEW STRUCTURES (OTHER THAN PEO/$CF_3SO_3^-$)
  - AUTONOMOUS Li CONDUCTORS
- **Li - METAL OXIDE CATHODES (CoO_2, MnO_2)**
  - PROBLEM OF CHARGE POTENTIAL WINDOW
- **NEW AQUEOUS COUPLES (H_2-Bi/MnO_2, etc)**
- **NEW DESIGNS WITH OLD COUPLES (BIPOLAR, e.g., WITH Ni/H_2)**
- **RELIABLE, TRUE "SINGLE-CAN" REGENERATIVE FC/ELECTROLYZER**

[illegible]

SPACE ELECTROCHEMICAL RESEARCH & TECHNOLOGY CONFERENCE

NASA LEWIS RESEARCH CENTER APRIL 11–13, 1989

GENERAL COMMENTS

- **RELIABILITY vs WEIGHT & COST TRADE-OFF FOR SPACECRAFT**
  - HIGH CAPABILITY (LOW WEIGHT, VOLUME, ETC.) MUST BE CONSISTENT WITH RELIABILITY
- **MOST FUNDS ARE SPENT ON EXISITING SYSTEMS. NEW SYSTEMS NEED A RELIABILITY ANALYSIS BEFORE FUNDS ARE COMMITTED FOR PILOT PRODUCTION OF INAPPROPRIATE DESIGNS FOR MISSION**
- **ACCELERATED TESTING REQUIRED: WEIBULL AND OTHER ANALYSIS**
- **RISK LEVEL**
  - IS THERE A WAY OUT IF THE APPROACH DOES NOT WORK? ARE THERE ALTERNATIVE OPTIONS?
  - OPTIONS AVOID RISK
- **TIME FRAME, LEVEL OF EFFORT**
  - VARIABLE FROM TRANSFER TO PRIVATE SECTOR; SMALL EFFORT TO (FOR FUSION, IF TRUE) MASSIVE PROGRAM

[illegible]

SPACE ELECTROCHEMICAL RESEARCH & TECHNOLOGY CONFERENCE

NASA LEWIS RESEARCH CENTER APRIL 11-13, 1989

HYDROGEN-OXYGEN FUEL CELLS AND ELECTROLYZERS

CHAIRPERSON	JAMES HUFF
CO CHAIRPERSON	PAUL PROKOPIUS

APRIL 12, 1989

HYDROGEN-OXYGEN FUEL CELLS AND ELECTROLYZERS

FUTURE MISSIONS BENEFITED

- NEAR-EARTH
- PATHFINDER
- UNSPECIFIED - AS YET UNDEFINED

[illegible]

NEAR-EARTH MISSIONS

- INTEGRATED FUEL CELL - ELECTROLYZER

PATHFINDER

- LONG-LIFE, RELIABLE, EFFICIENT PEM AND ALKALINE FUEL CELLS AND ELECTROLYZERS

SPACE ELECTROCHEMICAL RESEARCH & TECHNOLOGY CONFERENCE

NASA LEWIS RESEARCH CENTER APRIL 11-13, 1989

UNDEFINED MISSIONS

- LONG-LIFE, RELIABLE, EFFICIENT, COMPACT PRIMARY OR REGENERATIVE FUEL CELL SYSTEMS

SPACE ELECTROCHEMICAL RESEARCH & TECHNOLOGY CONFERENCE

NASA LEWIS RESEARCH CENTER APRIL 11-13, 1989

THESE SYSTEMS ARE ENABLING FOR THE INDICATED MISSIONS

SPACE ELECTROCHEMICAL RESEARCH & TECHNOLOGY CONFERENCE

NASA LEWIS RESEARCH CENTER APRIL 11-13, 1989

TECHNOLOGY ISSUES

- COMPONENT LIFE TESTS IN FULL PLANAR AREA HARDWARE
  - FAILURE MECHANISMS
  - REACTANT CROSSOVER
  - CORROSION
  - DEVELOPMENT OF PREDICTIVE MODELS

SPACE ELECTROCHEMICAL RESEARCH & TECHNOLOGY CONFERENCE

NASA LEWIS RESEARCH CENTER APRIL 11-13, 1989

DEVELOPMENTAL NEED

- PASSIVE SYSTEM OPERATION FOR HIGH RELIABILITY

SPACE ELECTROCHEMICAL RESEARCH & TECHNOLOGY CONFERENCE

NASA LEWIS RESEARCH CENTER APRIL 11-13, 1989

RESEARCH ISSUES

NO PROVISION FOR LONG-TERM RESEARCH IN MISSION DRIVEN PROGRAMS

SPACE ELECTROCHEMICAL RESEARCH & TECHNOLOGY CONFERENCE

NASA LEWIS RESEARCH CENTER APRIL 11-13, 1989

NICKEL ELECTRODE WORKSHOP

CHAIRPERSON: ALBERT ZIMMERMAN

CO-CHAIRPERSON: MARGARET REID

APRIL 12, 1989

SPACE ELECTROCHEMICAL RESEARCH & TECHNOLOGY CONFERENCE

NASA LEWIS RESEARCH CENTER APRIL 11-13, 1989

ADVANCED NICKEL ELECTRODE TECHNOLOGY

- LIGHTWEIGHT NICKEL ELECTRODES (OPTIMIZED FOR HIGH ENERGY DENSITY)
  - SINTERED
  - FIBER
- NICKEL ELECTRODES OPTIMIZED FOR LONG CYCLE LIFE
  - OPTIMIZED SUPPORTING POROUS STRUCTURES
- TECHNOLOGY MAINTENANCE

SPACE ELECTROCHEMICAL RESEARCH & TECHNOLOGY CONFERENCE

NASA LEWIS RESEARCH CENTER APRIL 11-13, 1989

APPLICATIONS

- LIGHTWEIGHT Ni ELECTRODES
  - MODERATE CYCLE LIFE (~ 1000 CYCLES, > 50% DOD)
  - HIGH ENERGY DENSITY (~ 100 Wh/kg)
  - MARS ROVER
- LONG-LIFE Ni ELECTRODES
  - > 30,000 CYCLES (50% DOD)
  - SPACE STATION
  - 10-20 YR (GLOBAL CHANGE TECHNOLOGY MISSIONS)
- TECHNOLOGY MAINTENANCE
  - ASSURE HIGH RELIABILITY FOR EVOLVING TECHNOLOGY

SPACE ELECTROCHEMICAL RESEARCH & TECHNOLOGY CONFERENCE

NASA LEWIS RESEARCH CENTER APRIL 11-13, 1989

CRITICAL TECHNOLOGY NEEDS

- **STRUCTURAL INSTABILITY**
  - SWELLING
  - EXTRUSION
  - LOSS OF OHMIC CONTACT WITH CURRENT COLLECTOR
- **IMPROVED ACTIVE MATERIAL MECHANICAL PROPERTIES**
  - ADDITIVES
  - ELECTROLYTE
- **IMPROVED TEST PROCEDURES (TECHNOLOGY SUPPORT)**
  - ACCELERATED/REAL TIME
  - LOT CONFIRMATION TESTING
  - ROUTINE DPA OF CELL ON LOT BASIS
- **MODELING**
  - INPUTS - IMPEDANCE, PORE DISTRIBUTIONS, ETC.
  - ANALYTICAL METHODS
    - CORRELATION OF ELECTROCHEMICAL AND STRUCTURAL CHARACTERISTICS

SPACE ELECTROCHEMICAL RESEARCH & TECHNOLOGY CONFERENCE

NASA LEWIS RESEARCH CENTER APRIL 11-13, 1989

RESEARCH NEEDS

- **CAUSES FOR STRUCTURAL INSTABILITY**
  - ACTIVE MATERIAL MOVEMENT/SHEDDING
  - SINTER FRACTURING
  - SHORTING: DETECTION AND CAUSES
- **CORROSION RATES**
  - INHIBITION
  - ACCELERATING FACTORS
- **ADDITIVES**
  - IMPROVED CHARGE EFFICIENCY
  - IMPROVED CAPACITY (INCREASED UTILIZATION OF Ni)
- **ELECTROLYTE CONCENTRATION - EFFECTS ON PERFORMANCE**
- **INTERACTIONS WITH HYDROGEN GAS**
  - STORAGE
  - SELF-DISCHARGE
  - EFFECT ON CAPACITY, SECOND PLATEAU EFFECTS

RESEARCH NEEDS

- **TESTING**
  - CHARGE CONTROL METHODS
- **SCALE-UP**
  - EVALUATE PRESENT ASSUMPTIONS OF LINEAR SCALING
  - EXAMINE LIFE TEST DATA AND FAILURE MODES
- **FUNDAMENTAL ELECTROCHEMISTRY OF Ni ELECTRODE PROCESSES**
  - APPLICATION OF NOVEL ANALYTICAL TECHNIQUES (CALORIMETRY, NEUTRON SCATTERING, ACOUSTIC EMISSION, NOISE SPECTRUM ANALYSIS, EXAFS)

SUMMARY

- **CELLS CONTAINING Ni ELECTRODES ARE ONLY ESTABLISHED LONG CYCLE LIFE TECHNOLOGY**
  - RELIABLE
  - SAFE
- **IMPROVEMENTS SHOULD BE SUPPORTED AND ARE ACHIEVABLE**
  - OPTIMIZATION FOR HIGH ENERGY DENSITY
  - OPTIMIZATION FOR LONG CYCLE LIFE
- **TECHNOLOGY MAINTENANCE PROGRAM SHOULD BE INSTITUTED**
  - ASSURE CONTINUED RELIABILITY
  - SMOOTHLY TRANSITION ADVANCED TECHNOLOGY INTO PRACTICE

SPACE ELECTROCHEMICAL RESEARCH & TECHNOLOGY CONFERENCE

NASA LEWIS RESEARCH CENTER APRIL 11-13, 1989

WORKSHOP ON ADVANCED RECHARGEABLE BATTERIES

G. HALPERT AND J. SMITHRICK

SPACE ELECTROCHEMICAL R&T CONFERENCE

APRIL 12, 1989

SPACE ELECTROCHEMICAL RESEARCH & TECHNOLOGY CONFERENCE

NASA LEWIS RESEARCH CENTER APRIL 11-13, 1989

APPLICATIONS

	PRIORITY	CHARGE/ DISCHARGE DURATIONS	TYPICAL OPERATIONAL CYCLES REQUIRED			TYPICAL PEAK POWER AND ENERGY STORAGE REQUIRED (5 MINUTES)
			ACTUAL	QUAL*	DESIRED	
1	OUTER PLANETARY ORBIT	C - 2 hr D - 0.7 hr	500	1,000	2,000	0.5 C (1 kWh)
2	INNER PLANETARY ORBIT	C - 2 hr D - 0.7 hr	3,000	6,000	10,000	1.5 C (2 kWh)
3	GEO	C - 22.8 hr D - 1.2 hr	1,500	2,000	4,000	1.5 C (5 kWh)
4	PLANETARY ROVER	C - 12 hr D - 3 hr	300	600	800	1.3 C (3 kWh)
5	LUNAR BASE	C - 11 DAYS D - 17 DAYS	80	160	350	0.02 C (5 MWh)
6	LEO	C - 1 hr D - 0.6 hr	30,000	35,000	50,000	1.1 C (25 kWh)

GEO = GEOSYNCHRONOUS ORBIT
LEO = LOW EARTH ORBIT
*QUAL = MINIMUM NUMBER OF CYCLES NEEDED TO QUALIFY FOR APPLICATION

SPACE ELECTROCHEMICAL RESEARCH & TECHNOLOGY CONFERENCE

NASA LEWIS RESEARCH CENTER APRIL 11-13, 1989

OTHER NASA APPLICATIONS

- FREE FLYERS
- ROBOTICS
- OMV
- ASTRONAUT EQUIPMENT
- PENETRATORS/PROBES
- TETHERED S/C

SPACE ELECTROCHEMICAL RESEARCH & TECHNOLOGY CONFERENCE

NASA LEWIS RESEARCH CENTER APRIL 11-13, 1989

ASSUMPTIONS

- NO COST CONSTRAINTS
- TECHNOLOGY DEMONSTRATION - LEVEL 5 ASSUMES LIMITED TESTING TO VERIFY CAPABILITY
- BIPOLAR TECHNOLOGY - NOT A LIMITATION
- SPECIFIC ENERGIES BASED ON BATTERY CAPACITY

SPACE ELECTROCHEMICAL RESEARCH & TECHNOLOGY CONFERENCE

NASA LEWIS RESEARCH CENTER APRIL 11-13, 1989

CANDIDATES FOR LARGE POWER SYSTEMS (>2.5 kWh)

"BEST CASE ANALYSIS"

SYSTEM	PROJECTED SPECIFIC ENERGY (Wh/kg)	APPLICATIONS	YEAR FOR PROJECTED TECHNOLOGY DEMO (LEVEL 5)
Na - S	150	4,5	2000
Na - S	150	3,6	2010
Na - S	200	4,5	2010
Na - S	200	3,6	2015
Li (Al) - FeS_2	175	4,5	2000
Li (Al) - FeS_2	175	3	2010
Na - MCl_2	160	4,5	2000
Na - MCl_2	160	3,6	2010
Adv Ni-H_2	70	3,4,5	1995
Adv Ni-H_2	70	6	2000

SPACE ELECTROCHEMICAL RESEARCH & TECHNOLOGY CONFERENCE

NASA LEWIS RESEARCH CENTER APRIL 11-13, 1989

CANDIDATES FOR SMALL POWER SYSTEMS (<2.5 kWh)

"BEST CASE ANALYSIS"

SYSTEM	PROJECTED SPECIFIC ENERGY (Wh/kg)	APPLICATIONS	YEAR FOR PROJECTED TECHNOLOGY DEMO (LEVEL 5)
LI - SOLID CATHODE (TiS_2, $NbSe_3$, V_6O_{13})	100	1	1990
(SAME AS ABOVE)	100	3	1995
LI - SOLID CATHODE (CoO_2)	200	1,3	2005
LI - P.E. - SOLID CATHODE	200	1,3	2005
(SAME AS ABOVE)	200	2	2010

*P.E. = POLYMERIC ELECTROLYTE

SPACE ELECTROCHEMICAL RESEARCH & TECHNOLOGY CONFERENCE

NASA LEWIS RESEARCH CENTER APRIL 11-13, 1989

TECHNOLOGY ISSUES

Na-S (200 Wh/kg)

- REDESIGN CELL/BATTERY (200 Wh/kg)
- CORROSION FOR LONG-LIFE APPLICATIONS (>2 YRS)
- ELECTROLYTE SEALING
- CONTROL OF FAILURE MODE
- FREEZE/THAW
- LARGE SYSTEMS (2.5-100 kWh)
- STATE-OF-THE-ART - 140 Wh/kg
- PROBABILITY OF SUCCESS - 80%

CH-[illegible] SERT 10

SPACE ELECTROCHEMICAL RESEARCH & TECHNOLOGY CONFERENCE

NASA LEWIS RESEARCH CENTER APRIL 11-13, 1989

TECHNOLOGY ISSUES

U.P. Li-(Al)-FeS_2 (175 Wh/kg)

- CELL REDESIGN
- CORROSION FOR LONG-TERM APPLICATION
- HERMETIC SEAL FOR CELL
- ELECTROLYTE AND SEPARATOR MODIFICATION
- CELL EQUALIZATION
- STATE-OF-THE-ART - 140 Wh/kg
- PROBABILITY OF SUCCESS - 60%

CH-[illegible] SERT 11

SPACE ELECTROCHEMICAL RESEARCH & TECHNOLOGY CONFERENCE

NASA LEWIS RESEARCH CENTER APRIL 11-13, 1989

TECHNOLOGY ISSUES

Na - MCl_x (160 Wh/kg)

- CELL REDESIGN
- CHEMISTRY CLARIFICATION
- TECHNOLOGY RESIDES OUTSIDE U.S.
- SEAL DEVELOPMENT
- TIME-DEPENDENT FAILURE MECHANISMS IDENTIFIED
- FREEZE/THAW IS REPORTED AS A NON-ISSUE
- PROBABILITY OF SUCCESS - 50%

[illegible]

SPACE ELECTROCHEMICAL RESEARCH & TECHNOLOGY CONFERENCE

NASA LEWIS RESEARCH CENTER APRIL 11-13, 1989

TECHNOLOGY ISSUES

ADVANCED $Ni\text{-}H_2$ (70 Wh/kg)

- MODIFY SUPPORT STRUCTURES FOR COMPONENT, CELL AND BATTERY
- TECHNOLOGY FLIGHT DEMO/QUALIFIED
- PROBABILITY OF SUCCESS - 95%

[illegible]

SPACE ELECTROCHEMICAL RESEARCH & TECHNOLOGY CONFERENCE

NASA LEWIS RESEARCH CENTER APRIL 11-13, 1989

TECHNOLOGY ISSUES

Li - SOLID CATHODE (200 Wh/kg)

- Li RECHARGEABILITY
- ELECTROLYTE STABILITY AND CONDUCTIVITY
- HIGHER ENERGY LONG-LIFE CATHODES REQUIRED (CoO_2)
- SCALE-UP FROM CONSUMER SIZES
- SAFETY
- PROBABILITY OF SUCCESS - 60%

GHJ589 SERT 04

SPACE ELECTROCHEMICAL RESEARCH & TECHNOLOGY CONFERENCE

NASA LEWIS RESEARCH CENTER APRIL 11-13, 1989

TECHNOLOGY ISSUES

LI - POLYMER ELECTROLYTE - SOLID CATHODE (200 Wh/kg)

- MANUFACTURING PROCESSING OF P.E.
- P.E. COMPOSITION AND CONDUCTIVITY
- INTERFACIAL CONTACT
- PROBABILITY OF SUCCESS - 60%

GHJ589 SERT 05

NASA
National Aeronautics and
Space Administration

Report Documentation Page

1. Report No. NASA CP-3056	2. Government Accession No.	3. Recipient's Catalog No.
4. Title and Subtitle Space Electrochemical Research and Technology (SERT) 1989		5. Report Date December 1989
		6. Performing Organization Code
7. Author(s) Richard S. Baldwin, Editor		8. Performing Organization Report No. E-4708
		10. Work Unit No. 506-41-21
9. Performing Organization Name and Address National Aeronautics and Space Administration Lewis Research Center Cleveland, Ohio 44135-3191		11. Contract or Grant No.
		13. Type of Report and Period Covered Conference Publication
12. Sponsoring Agency Name and Address National Aeronautics and Space Administration Washington, D.C. 20546-0001		14. Sponsoring Agency Code

15. Supplementary Notes

16. Abstract

This document contains the proceedings of NASA's second Space Electrochemical Research and Technology Conference, held at the NASA Lewis Research Center April 11-13, 1989. The objectives of the conference were to examine current technologies, research efforts, and advanced ideas, and to identify technical barriers which affect the advancement of electrochemical energy storage systems for space applications. The conference provided a forum for the exchange of ideas and opinions of those actively involved in the field, with the intention of coalescing views and findings into conclusions on progress in the field, prospects for future advances, areas overlooked, and the directions of future efforts. Related overviews were presented in the areas of NASA advanced mission models. Papers were presented and workshops were conducted in four technical areas: advanced concepts, hydrogen-oxygen fuel cells and electrolyzers, the nickel electrode, and advanced rechargeable batteries. This document contains the overviews, the technical papers, and summaries of the technical workshops.

17. Key Words (Suggested by Author(s)) Electrochemistry; Fuel cells; Batteries; Electrocatalyst; Nickel electrode		18. Distribution Statement Unclassified – Unlimited Subject Category 44	
19. Security Classif. (of this report) Unclassified	20. Security Classif. (of this page) Unclassified	21. No of pages 364	22. Price* A16

NASA FORM 1626 OCT 86

*For sale by the National Technical Information Service, Springfield, Virginia 22161

NASA-Langley, 1989

National Aeronautics and
Space Administration
Code NTT-4

Washington, D.C.
20546-0001

Official Business
Penalty for Private Use, $300

SPECIAL FOURTH-CLASS RATE
POSTAGE & FEES PAID
NASA
Permit No. G-27

POSTMASTER: If Undeliverable (Section 158
Postal Manual) Do Not Return

358